Solid-State Emitting Organic Fluorogens with Diverse Associated Photophysical Properties: From Synthesis to Multifarious Optical and Bioimaging Applications

THESIS

Submitted in partial fulfilment
of the requirements for the degree of

DOCTOR OF PHILOSOPHY

by

SHOUVIK BHUIN

ID. No. 2018PHXF0409H

Under the Supervision of

Prof. **Manab Chakravarty**

BITS Pilani
Pilani | Dubai | Goa | Hyderabad

BIRLA INSTITUTE OF TECHNOLOGY AND SCIENCE, PILANI

2024

BIRLA INSTITUTE OF TECHNOLOGY AND SCIENCE, PILANI

CERTIFICATE

This is to certify that the thesis titled "***Solid-State Emitting Organic Fluorogens with Diverse Associated Photophysical Properties: From Synthesis to Multifarious Optical and Bioimaging Applications***" submitted by **Shouvik Bhuin** ID No **2018PHXF0409H** for award of Ph.D. of the Institute embodies original work done by him under my supervision.

Signature of the Supervisor: Manas Chakravarty

Name in capital letters: MANAS CHAKRAVARTY

Designation: Professor

Date: 29th April '2023

❖ Acknowledgements

I sincerely thank my supervisor, ***Prof. Manab Chakravarty,*** for selecting me as a CSIR SRF (Senior Research Fellow) in a CSIR-funded project in 2018 to provide a break-through in my career and allowing me to pursue a Ph.D. in his highly esteemed laboratory in the Department of Chemistry, BITS-Pilani Hyderabad Campus. I ever remember his continuous support, tireless guidance, and encouragement.

I remain with my heartiest thanks to my professor collaborators, ***Prof. & Administrative Dean, Perumal Yogeeswari***, ***Prof. Onkar Prakash Kulkarni***, ***Prof. Chanchal Chakraborty***, ***Dr. Pralok K. Samanta***, and ***Prof. Subit Kumar Saha*** from BITS-Pilani Hyderabad Campus. I also thank ***Prof. Apurba Lal Konar***, IISER Bhopal, and ***Prof. Moloy Sarkar*** from NIISER, Bhubaneswar. I thank my DAC members, ***Prof. Anupam Bhattacharya*** and ***Prof. Durba Roy,*** for their hearty help and suggestions. I would also like to thank the Vice-Chancellor of BITS-Pilani, ***Prof. V. Ramgopal Rao,*** and the Director of BITS-Pilani Hyderabad Campus, ***Prof. G. Sundar*** of BITS-Pilani, DRC Convener ***Prof. Tanmay Chatterjee***, and the HOD of the Chemistry Department, ***Prof. Sounak Roy***.

I take the opportunity to endlessly thank my research scholar collaborators and well-wishers ***Ms. Purbali Chakraborty***, ***Dr. Pravesh Kumar Sharma***, ***Dr. Sayantan Halder***, ***Dr. Susmita Roy***, ***Mr. P. Sivasakthi, Dr. Shweta Vinod Pawar, Mr. Pavar Sai Kumar, Dr. Dwaipayan Bhattacharya,*** *and* ***Mr. Debabrata Chakraborty***.

Especially without the help of ***Ms. Purbali Chakraborty***, the biological experimentations and bioimaging explorations were just impossible for me. I remain ever grateful to her for the same and appreciate it from my core entity. Again, a very special thanks to ***Prof. P. Yogeeswari*** for her memorable role as a scientific advisor in my bioimaging research.

I earnestly thank ***Mr. Adarash Kumar Shukla*** *(Kancha)* and ***Ms. Savita*** *(Kanchi)* for being my true friends and emotional support during both my sunny and rainy days.

I would like to thank ***Dr. Adinarayana Nandikolla***, ***Mr. Yogesh Mahadu Khetmalis, Ms. Reeshma Rameshan, Mr. Maddukuri Naveen Naidu,*** and ***Ms. Saraswati Roy*** for being my good colleagues and friends. I wholeheartedly thank ***Dr.***

M. Z. K. Baig and ***Dr. G. Pallikonda***, my laboratory seniors, for their immense love and support as my elder brothers.

Apart from these, I thank ***CSIR***, **India**, and ***BITS*** for their financial support. The central analytical lab (***CALAB***) of ***BITS-PIlani Hyderabad Campus*** is highly acknowledged. I also acknowledge departmental staff, central analytical laboratory staff, and all my fellow research scholars, friends, and colleagues for their cordial assistance. I remain thankful to all the officers and staff of ***BITS-Pilani Hyderabad Library*** and my friends from B.Tech. and M.Tech. streams.

I thank and remain unconditionally grateful to my mother, ***Mrs. Malina Bhuin,*** for the uncountable sacrifices she made in her life to raise me. I sincerely thank ***Mr. Mrityunjoy Roy*** for his spontaneous support in my life for years! I also thank my maternal uncle ***Mr. Rajdip Jana,*** and all the family members. I remember my father, ***Late Subrata Kumar Bhuin***, and dedicate this thesis to him. I maintain the motto that ***everything can be achieved if the intention and dedication are pure and honest***.

Guilelessly,
I do remain
Shouvik Bhuin

Abstract

This dissertation is entitled 'Solid-State Emitting Organic Fluorogens with Diverse Associated Photophysical Properties: From Synthesis to Multifarious Optical and Bioimaging Applications.' Organic fluorescent materials and probes are now quite relevant as dependable tools in multifarious applications, starting from optoelectronics, sensing kits, anticounterfeiting, biomedical, and bioimaging pursuits. Designing and developing a new class of commendable SSEOFs with versatile photophysical outputs, such as aggregation-induced emission (AIE), dual-state emission (DSE), stimuli-responsive emission switching and contrast, and viscosity-induced emission (VIE), is a matter of neatness as one single probe/material can be utilized in multitudinous applications from materials and biological concerns. In 'Chapter I', a very rare phenomenon of crystallochromism is explored with four newly developed SSEOFs. The triphenylamine (TPA) containing pair of SSEOFs was proven to be a crystallochromic pair, whereas the phenothiazine (PTZ) containing pair of SSEOFs could not converge with the supposition. The dual-state emission (DSE) phenomenon was also investigated, and real-world applications were envisaged utilizing crystallochromism and DSE. In 'Chapter II' a series of thiophene and toluene-attached anthracenyl fluorophores were investigated, aiming to establish structural-property relation in solid-state acidodfluorochromic (SSAC) emission switching varying the position of 'N'atom in their pyridinyl counterpart. The lead material was further utilized in acid and base vapor sensing with a polymer-appended solid-state emitting matrix, which could even be used for ammonia gas and melamine sensing in milk and water samples. In 'Chapter III' the urge was to develop an SSEOF that is an anticancer agent and a bioimaging agent simultaneously. So, the drug-treated to inhibit the cancer cells, the same compound, can detect the inhibited cancer cells by variation in fluorescence signals through bioimaging. The design was made with a common indolyl-anthracene stature conjugated to a variable donor/acceptor scaffold through a 'diene' extension. The selected non-cytotoxic probes were even proven useful in wash-free cancer cell bioimaging. In 'Chapter IV', two more compounds from the library of molecules of earlier 3rd chapter were investigated as the sole organic material that displays seven photophysical properties and at least three to six different diverse optical applications.

In ‘Chapter V’ a series of tetrasubstituted dicyanoethylenes were designed synthesized, and their photophysical properties were prospected thoroughly. Not only that, the cell permeability and cytotoxicity were scrutinized, and ultimately, the lead dye was employed for wash-free lipid droplet bioimaging of living cancer cells. Moreover, counting the lipid droplet depositions made detecting cancer cells over normal cells in in vitro experimentation possible. In ‘Chapter VI’ a nucleus-specific bioimaging dye was established and applied in multitudinous bioimaging applications, including in vivo tumor imaging in nude mice models. Overall, this thesis successfully establishes- i) a new pair of crystallochromic dyes with real-world application, ii) a new SSAC material that could sense acid vapor, ammonia, and melamine, iii) a new anticancer SSEOF that can itself inhibit and detect cancer cells, iv) a new SSEOF that display seven different photophysical outputs with six different real-world applications including forensic, food-quality sensing, wash-free bioimaging, identifying blood-smeared healthcare-disposals, patent fingerprint comparison, and other related applications, v) a new class of lipid droplet bioimaging dye for wash-free live cancer cell bioimaging and clarification with normal cells, vi) a new nucleus-specific bioimaging dye that was possible to apply in animal body to detect tumor. Hence, this thesis avers a new abstraction to the continued journey of research and development in our country, nay of the broader scientific community across the globe.

❖ Table of Contents:

❖ List of Tables

❖ Figures enlisted

List of Abbreviations/Symbols

δ	:	delta chemical shift value in ppm
η	:	refractive index of a solvent
λ	:	wavelength (usually in nm)
g	:	gram
mg	:	milligram
m. (distance)	:	metre
mm (distance)	:	millimetre
cm (distance)	:	centimetre
nm (distance)	:	nanometre
Lit.	:	litre
mL	:	millilitre
μL	:	microlitre
mol.	:	mole
mmol.	:	millimole
mM	:	millimolar concentration
μM	:	micromolar concentration
μm	:	micrometer
θ	:	radian Theta
τ	:	Lifetime value Tau in ps
ns	:	nanosecond
υ	:	wavenumber (in cm^{-1})
ϕ	:	quantum yield
QY	:	quantum yield
AIE	:	aggregation-induced emission
AIEE	:	aggregation-induced enhanced emission
ACQ	:	aggregation cause quenching
DCM	:	dichloromethane
DCE	:	1,2-dichloroethane
THF	:	tetrahydrofuran
MeCN	:	acetonitrile
DMSO	:	dimethylsulfoxide
DMF	:	*N*,*N*-dimethylformamide
EtOH	:	ethanol
MeOH	:	methanol
$CDCl_3$	:	deuterated chloroform
EtOAc	:	ethyl acetate
m (in NMR)	:	multiplet
quint. (in NMR)	:	quintet
t (in NMR)	:	triplet
d (in NMR)	:	doublet

s (in NMR)	:	singlet
%	:	percentage
α	:	alpha
β	:	beta
γ	:	gamma
^{1}H	:	^{1} proton NMR
^{13}C	:	^{13} carbon NMR
^{31}P	:	^{31} phosphorus NMR
NMR	:	nuclear magnetic resonance
Calcd.	:	calculated
^{o}C	:	centigrade
conc.	:	concentration
J	:	coupling constant
Hz	:	hertz
MHz	:	megahertz
ESI	:	electron spray ionization
MS	:	mass spectrometry
HRMS	:	high resolution mass spectrometry
m.p.	:	melting point
h (time)	:	hour
FT-IR	:	Fourier transform infrared
UV-Vis	:	ultraviolet-visible
min	:	minute
ppm	:	parts per million
rt	:	room temperature
TMS	:	tetramethylsilane
MSA	:	methanesulfonic acid
HCl	:	hydrochloric acid
TLC	:	thin layer chromatography
Vol.	:	volume
Me	:	methyl
$KO^{t}Bu$	:	potassium tert-butoxide
KBr	:	potassium bromide
K_2CO_3	:	potassium carbonate
atm.	:	atmospheric
o-	:	ortho
p-	:	para
m-	:	meta
Pd	:	Palladium
equiv.	:	equivalent
M^{+}	:	metal ion
$[MH]^{+}$	:	molecular weight ion
MTT	:	3-(4,5-dimethylthiazol-2-yl)-2,5-diphenyltetrazolium bromide

IC_{50}	:	Inhibitory concentration
R_f	:	retention factor
m/z	:	mass/charge ratio
TPE	:	tetraphenylethene
RIM	:	restricted intramolecular motion
RIR	:	restricted intramolecular rotation
RIV	:	restricted intramolecular vibration
I	:	Fl. Int. of current solution
I_0	:	initial Fl. Int.
Max.	:	maximum
Min.	:	minimum
N_2	:	Nitrogen
O_2	:	Oxygen
HWE	:	Horner Wadsworth Emmons
2D	:	2-dimensional
Kcal	:	kilocalorie
^{o}	:	degree
f_w	:	fraction of water
f_m	:	fraction of methanol
f_g	:	fraction of glycerol
f_a	:	fraction of acetone
v/v	:	volume/volume
Fl.	:	fluorescence
Int.	:	intensity
ex.	:	excitation
em. or emi.	:	emission
Abs.	:	absorbance
DLS	:	dynamic light scattering
LUMO	:	lowest unoccupied molecular orbital
HOMO	:	highest occupied molecular orbital
Agg.	:	aggregate
TCSPC	:	time correlated single photon count
TBABr	:	tetra-*n*-butylammoniumbromide
OLED	:	organic light emitting diode
DSA	:	distyrylanthracene
ICT	:	intramolecular charge transfer
TICT	:	twisted intramolecular charge transfer
P-XRD	:	powder X-ray diffraction
SC-XRD	:	single crystal X-ray diffraction
Å	:	angstrom

General Introduction

Solid-state emitting organic fluorogens (SSEOFs) have attracted consequential consideration in the last two decades due to their fascinating photophysical outputs and utilities.[1-3] Implementing these emissive compounds is continuously being pursued in myriad applications in optoelectronic devices,[4-7] sensors,[8] security-inks,[9] anticounterfeiting,[10,11] latent fingerprint detection,[12] biosensing and bioimaging,[13,14] and so on. Anyways, there is no established strategy to receive solid-state emissions so far. The stimuli-responsive switching of solid-state emission is again another challenge to understand fundamentally. Maximum reports are case study and generalized predictions is still tricky.[15,16] A fluorophore may stay crystalline or amorphous in solids depending on its non-covalent interactions. Even different crystals have different non-covalent interactions, orientations, planes, and axes.[17,18] Just one change at some point in a molecular structure can alter the whole crystal packing.[19] Hence, it is hard to believe that one similar molecular structure will have a similar crystal packing or similar extent of amorphous nature. Rather, the solid-state emission strongly depends on the intermolecular dipole coupling, orientations of their dipole moments, and, as stated earlier, the non-covalent routes inclusive of polymorphism, phase transition, nano/microcrystal generation, and the formation of multicomponent systems control the fluorescence in the solids. For the multi-stimuli responsive materials, a phase transition takes place either between two separate crystalline states or between a crystalline and an amorphous state.[16, 20,21]

Apart from the emission property in solids, SSEOFs with diverse photophysical properties have drawn the ultimate attention. The design of dual-state emitting fluorogens (DSE-gens) has become a relevant topic of research. A DSE-gen can emit both in solids and solution. The torsion angle between the fluorophore and attached aromatic rings plays a significant role in rendering a twisted structure and this twisted conformation eliminates the π...π stacking to a great extent to favor dual-state emission.[22,23] There are many reports where self-isolation by an alkyl chain or any bulky group helped to receive DSE-genic emission.[24] Apart from suppressing the π...π stacking, these chains can greatly influence crystal packing, regulation of vibration, and internal conversion (IC).[25] In fact, introducing donor (D)-acceptor (A) architecture into

the molecular design results in the formation of a strong dipole that can find intramolecular charge transfer (ICT) based emission.[26,27] Even twisted intramolecular charge transfer (TICT) and quasi-TICT are other important possible phenomena.[28,29] The above-mentioned facts and the dual-state emission can also be explained in terms of the excited-state planarity, root mean square displacement (RMSD), and oscillator strength.[30]

The concept of aggregation-induced emission (AIE) crucially changes the cognition of the scientific community toward the phenomena of classical photophysics and is still a matter of debate.[31] Being opposite to aggregation-caused quenching (ACQ)[32], the AIE feature describes the fluorophores that display better emission or generation of emission at their aggregate states. Many scientists debatably believe that in the aggregate state, the AIE-gen undergoes restriction of intramolecular rotation (RIR), and intramolecular vibration (RIV), and overall, the intramolecular motion (RIM) gets restricted. Like the solid state, the fluorophore's twisted structure helps eliminate π...π stacking among the neighbor molecules and enhances the emission even in the aggregate state.[33] Of note, the aggregate state is believed to be a similar type of solid-state, yet not exactly the solid state. In this regard, it should be noted that there are lot many reports where a fluorophore emits different wavelengths in solid and aggregate states.[34] In those cases, many factors like reorganization energy and different scopes of molecular arrangements may govern these differences.[35] However, many reports are available where a fluorophore emits the same in solid and aggregate states as well.

The molecular arrangement often can adopt a 'pitch and roll' inclination from an 'ideal' co-facial π-stack (*H*-type aggregates) in the aggregate and solid states. 'Pitch' inclination indicates the translation of adjacent molecules in the direction of the long molecular axes (*J*-type aggregates), while the 'roll' inclination indicates the translation along the short molecular axes (herringbone-type aggregates). In *J*-type aggregates, a head-to-tail arrangement with an enhanced delocalization of electronic excitation is likely to be observed. According to the exciton coupling and 'Davydov splitting' theory, the excited states of the aggregates split into two energy levels- one lower and another higher than the monomer.[16] The coupling of the transition dipoles cancels out each other, but for an allowed transition the resulting, the coupling of the dipoles results in

a nonzero transition moment. Again, the vibration relaxation from the upper to lower energy level becomes non-radiative, weakening the fluorescence.[16]

The change in motion, such as in molecular rotation and vibration for a fluorophore, may happen due to its conformational flexibility. These changes in motion have direct implications for the fluorescence properties of the molecular probes. If the probe adopts a rigid molecular structure, the absorbed energy can be released in the form of fluorescence, reducing the dominance of non-radiative relaxation.[36] In the case of viscosity-induced emission (VIE), the molecular motion of a twisted fluorophore is restricted in a viscous medium, and the probe starts to emit. Thus, the VIE becomes another important phenomenon apart from the AIE.[37]

Another fact is that despite significant advances in developing organic solid-state emissive fluorogens, there has been an upsurging quest in the past decade for materials where the emission is preserved not only in solids but also in solvents, aggregated states, and viscous mediums. The photophysical properties are mutually exclusive,[30] and thus, it is a pitfall where one single fluorophore falls short of displaying all the above-mentioned photophysical properties. The facile synthesis, scope of structural modification, and storage of the synthesized fluorophores are also mattering concerns.

Here in this thesis, different synthetic routes have been weaved to reach out to target organic fluorophores with ample scope of structural modifications with decent to excellent synthetic yields. Four types of scaffolds/moieties have been explored: di-cyano-aniline, anthracene, naphthalene, and heterocyclic scaffolds. Moreover, special attention has been given to designing the molecular scaffolds in such a way that one single fluorophore will be able to display emissions in solids, solvents, aggregates, and viscous medium as well. Utilizing multitudinous photophysical properties, the synthesized fluorophores have been used in multifarious optical applications in crystallochromism-based security writing, solid-state acidofluorochromism (SSAC) based security writing and ammonia and melamine sensing, patent fingerprint optical recording and anticounterfeiting of fake fingerprint, hidden stimuli-responsive QR-code based and stamp based anticounterfeiting, self-erasable inkless writing, inkless writing utilizing mechanofluorochromism, data encryption, fluorescent detection of blood-smeared fingerprint for forensic utilities, fluorescent detection of hospital disposed-of biohazards, and food-additive detection.

SSEOFs are emerging as trustworthy tools in biomedicine and biomedicals.[38] This thesis even addresses this perspective and includes the development of an anticancer agent cum bioimaging agent to inhibit and detect cancer cells with a single compound, which is an SSEOF with an indolyl-anthracene conjugated tri methoxy benzene-based structural entity. A few other SSEOFs have been established with the same structural backbone but with certain modifications to achieve wash-free bioimaging of cancer cells and detection of cell distortion as an effect of anticancer agents. Another SSEOF, a naphthalene-based heterocycle conjugated tetrasubstituted dicyanoethylene, has been established for lipid droplet wash-free bioimaging in cancer cells. On the other hand, a twisted triphenylamine-anthracenyl tri methoxy benzene conjugated SSEOF has been developed for wash-free bioimaging of living cancer cells and detection of cancer cells over the normal cells with 8 to 10 times emission enhancement for the cancer cells in confocal microscopy.

Hence, this present thesis has many aspects of adding up and contributing to the already existing athenium of the library of organic fluorophore chemistry with utmost real-world applicability.

References

1 Prof. Dr. M. Shimizu and Prof. Dr. T. Hiyama, ***Chem. Asian, J.***, 2010, **5**, 7, 1516-1531.

2 S. P. Anthony, ***ChemPlusChem***, 2012, **77**, 7, 518-531.

3 Y. Q. Zhang, J. X. Wang, Z. Y. Ji, W. P. Hu, L. Jiang, Y. L. Song and D. B. Zhu, ***J. Mater. Chem.***, 2007,**17**, 90-94.

4 Y. Jiang, Y. Y. Liu, X. Liu, H. Lin, K. Gao, W. Y. Lai and W. Huang, ***Chem. Soc. Rev.***, 2020,**49**, 5885-5944.

5 J. Huang, C. Li, Y. J. Xia, X. H. Zhu, J. Peng and Y. Cao, ***J. Org. Chem.***, 2007, **72**, 22, 8580-8583.

6 Z. Li, X. Hu, G. Liu, L. Tian, H. Gao, X. Dong, T. Gao, M. Cao, C. S. Lee, P. Wang and Y. Wang, ***J. Phys. Chem. C***, 2021, **125**, 3, 1980-1989.

7 T. Zhang, Y. Xiao, H. Wang, S. Kong, R. Huang, Dr. V. K. M. Au, Prof. T. Yu and Prof. W. Huang, ***Angew. Chem. Int. Ed.***, 2023, **62**, 39, e202301896.

8 S. Fan, J. Lai, P. L. Burn and P. E. Shaw, ***ACS Sens.***, 2019, **4**, 1, 134-142.

9 P. Kumar, S. Singh and B. K. Gupta, ***Nanoscale***, 2016,**8**, 14297-14340.

10 D. Wang, J. Gong, Y. Xiong, H. Wu, Z. Zhao, D. Wang and B. Z. Tang, ***Adv. Funct. Mater.***, 2023, **33**, 1, 2208899.

11 T. Pan, S. Liu, L. Zhang, W. Xie and C. Yu, ***Light Sci. Appl.***, 2022, **11**, 59.

12 R. Singh, A. K. Gupta and C. P. Pradeep, ***Cryst. Growth. Des.***, 2021, **21**, 2, 1062-1076.

13 Z. Huang, E. Terpetschnig, W. You and R. P. Haugland, ***Anal. Biochem.***, 1992, **207**, 1, 32-39.
14 S. Kim, H. E. Pudavar, A. Bonoiu and P. N. Prasad, ***Adv. Mater.***, 2007, **19**, 22, 3791-3795.
15 A. Huber, J. Dubbert, T. D. Scherz, and Jun. Prof. Dr. J. Voskuhl, ***Chem. Eur. J.***, 2023, **29**, 2, e202202481.
16 S. Varughese, ***J. Mater. Chem. C***, 2014, **2**, 3499-3516.
17 M. K. Bera, C. Chakraborty, and S. Malik, ***J. Mater. Chem. C***, 2017, **5**, 6872-6879.
18 F. Joy, K. P. Chaithra, A. Nizam, A. Deepti, P. S. B. Chakrapani, A. K. Das, T. P. Vinod and Y. Nair, ***Chem. Eng. J.***, 2023, **453**, 139798.
19 R. Thomas, S. Varghese and G. U. Kulkarni, ***J. Mater. Chem.***, 2009, **19**, 4401-4406.
20 J. Wang, Z. Chai, J. Wang, C. Wang, M. Han, Q. Liao, A. Huang, P. Lin, Prof. C. Li, Prof. Q. Li and Prof. Z. Li, ***Angew. Chem. Int. Ed.***, 2019, **58**, 48, 17297-17302.
21 A. A. Esteban, J. Krumrain, A. Liess, M. Stolte, L. Huang, D. Schmidt, V. Stepanenko, M. Gsanger, D. Hertel, K. Meerholz and F. Wurther, ***J. Am. Chem. Soc.***, 2015, **137**, 42, 13524-13534.
22 L. Zong, Y. Xie, C. Wang, J. R. Li, Q. Li and Z. Li, ***Chem. Commun.***, 2016, **52**, 11496-11499.
23 Y. Liu, Y. Zhang, X. Wu, Q. Lan, C. Chen, S. Liu, Z. Chi, L. Jiang, X. Chen and J. Xu, ***J. Mater. Chem. C***, 2014, **2**, 1068-1075.
24 K. Tanaka, T. Kajiyama, A. Takahara, and S. Tasaki, ***Macromolecules***, 2002, **35**, 12, 4702-4706.
25 S. Qu, Q. Lu, S. Wu, L. Wang and X. Liu, ***J. Mater. Chem.***, 2012, **22**, 24605-24609.
26 N. Venkatramaiah, G. D. Kumar, Y. Chandrasekaran, R. Ganduri and S. Patil, ***ACS Appl. Mater. Interfaces***, 2018, **10**, 4, 3838-3847.
27 F. Yu, Q. Yan, K. Liang, Z. Cong, Q. Shao, Y. Wang, L. Hong, L. Jiang, G. Ye, H. Wang, B. Chi and G. Xia, ***J. Lumin.***, 2021, **233**, 117882.
28 A. M. E. Zohry, E. A. Orabi, M. Karlsson and B. Zietz, ***J. Phys. Chem. A***, 2021, **125**, 14, 2885-2894.
29 J. Li, Y. Qian, L. Xie, Y. Yi, W. Li and W. Huang, ***J. Phys. Chem. C***, 2015, **119**, 4, 2133-2141.
30 J. L. B. Vazquez, Y. A. A. Sanchez, L. A. R. Cortes and B. R. Molina, ***Chem. Mater.***, 2021, **33**, 18, 7160-7184.
31 Y. Hong, J. W. Y. Lam and B. Z. Tang, ***Chem. Commun.***, 2009, 4332-4353.
32 M. Wang, G. Zhang, D. Zhang, D. Zhu and B. Z. Tang, ***J. Mater. Chem.***, 2010, **20**, 1858-1867.
33 Q. Peng and Z. Shuai, ***Aggregate***, 2021, **2**, 5, e91.
34 T. Okawara, Y. Matsufuji, K. Mizuno, K Takehara, T. Nagamura and S. Iwasa, ***RSC Adv.***, 2019, **9**, 22817-22822.
35 Q. Wu, T. Zhang, Q. Peng, D. Wang and Z. Shuai, ***Phys. Chem. Chem. Phys.***, 2014, **16**, 5545-5552.

36 D. Su, C. L. Teoh, L. Wang, X. Liu and Y. T. Chang, ***Chem. Soc. Rev.***, 2017, **46**, 4833-4844.
37 Q. Peng, L. Yang, Y. Li, Y. Zhang, T. Li, Y. Qin, Y. Song, H. Hou and K. Li, ***J. Phys. Chem. C***, 2020, **124**, 41, 22684-22691.
38 K. Li, T. B. Ren, S. Huan, L. Yuan and X. B. Zhang, ***J. Am. Chem. Soc.***, 2021, **143**, 50, 21143-21160.

Materials, General Conditions and Measurements

0.1 Materials and General Conditions

All the experiments were carried out in hot air oven-dried glass-wares. For the work described in **Chapter I**, 4-(diphenylamino) benzaldehyde & 10-pentyl-10H-phenothiazine-3-carbaldehyde were prepared in our laboratory following the procedure reported by Roqouet *et al.*[1] Other reagents were purchased from Aldrich & Thermofischer and used without further purification. Spectroscopic-grade solvents were used for UV-vis and fluorescence spectroscopy, and obtained from Sisco Research Laboratories (SRL).

For the work described in **Chapter II**, all aldehydes were purchased from Sigma Aldrich. KO^{t}Bu was purchased from Sigma Aldrich. Tetrahydrofuran (THF) was distilled with sodium metal and benzophenone. Dry dichloroethane (DCE), dichloromethane (DCM), hexane, ethyl acetate, toluene, acetonitrile, and hydrochloric acid (HCl) were purchased from Sisco Research Laboratories (SRL) and used without further purification.

For the work discussed in **Chapter III**, 1*H*-Indole, 1-bromohexane, 1-bromopentane, anthracene-9-carbaldehyde, diethyl phosphite, and piperazine were obtained from Alfa-aesar, Avra, and Merck and were utilized without further purification. Potassium hydroxide, potassium *tert*-butoxide and methanesulfonic acid (MSA) were procured from Alfa-aesar and Sigma and were used as received. Dry DMSO, DCE and THF were purchased from Finar. The rest of the chemicals were bought from Merck and Alfa-aesar and were taken to use without any further purification. Spectroscopic grade solvents were used for UV-vis and fluorescence spectroscopy studies and procured from Sisco Research Laboratories (SRL).

For the work of **Chapter V**, Thianthrene, phenoxathiine, oxanthrene, dibenzothiophene, dibenzofuran, methane sulfonic acid, dichloroethane, potassium tert-butoxide, $TiCl_4$, malononitrile, other required chemicals, and reagent grade and spectroscopic grade solvents were procured from Alfa Aesar, Merck, SRL, TCI, and Avra Chemicals.

For the work discussed in **Chapter VI**, triphenylamine, methanesulfonic acid (MSA), dichloroethane (DCE), and the respective aldehydes, THF, and potassium tert-butoxide were procured from Alfa Aesar, Merck, SRL, TCI, and Avra Chemicals.

All the column chromatography was performed using 100-200 mesh silica gel. Reactions were monitored by thin-layer chromatography on pre-coated silica gel 60 F254 plates (Merck & co.) & were visualized by a UV lamp. All NMR spectra recordings were performed at ambient temperature (ca. 20 ^{0}C) in $CDCl_3$ solution. The signals were referred to as TMS and solvent used in deuterated chloroform (7.26 ppm in ^{1}H, 77.0 ppm in ^{13}C NMR). The chemical shifts were reported in ppm, the denotation of multiplicities was done by using s (singlet), d (doublet), dd (doublet of doublet), t (triplet), q (quintet), and m (multiplet). All the experiments were performed at room temperature ($298\pm2K$).

0.2 Methods and Measurements

0.2.1 Steady-state absorption and fluorescence measurements

For the work of **Chapter I**, the solution-state absorption spectra were recorded using the dint of a UV-Vis-NIR spectrophotometer (Hitachi F7000, Japan). The solid-state absorption spectra were measured with a JASCO-500 spectrophotometer. The solution-state emission spectra were recorded with FP-6300, JASCO using a 10 mm path length quartz cuvette, while the solid-state emission spectra were recorded with a fluorimeter (Fluorolog, HORIBA). The emission spectra were recorded at their corresponding absorption wavelengths.

The primary methods of the steady-state absorption and fluorescence measurements were the same. Still, additionally, it should be mentioned for the work of **Chapter II**, the stock solutions of 10^{-3} M **AThio4P**, 10^{-3} M **AThio4PH** and 10^{-3} M deprotonated **AThio4P** were prepared in 1,4-dioxane. All the absorbances and emissions were recorded, keeping the probe concentration of 10^{-5} M in acetonitrile as this solvent was used with PMMA. The solution state study revealed that **AThio4P** does not show notable acidochromism in the solution state and is not worthy of finding any application in the solution state. Once the polymer matrix is dried i.e., in solid state, **AThio4P** becomes the best for portable polymer appended dual sensing probe of acid and base vapour simultaneously.

0.2.2 Absolute quantum yield measurement

The absolute quantum yield (Φ_f) was obtained for the solid sample using a calibrated integrating sphere method with a fluorimeter (Fluorolog, HORIBA). The absolute errors of ~2% are mentioned. For the relative quantum yield (relative Φ_f) in the solution state, the error is (±)5 %.

0.2.3 Powder X-ray diffraction and calculations of crystallinity

The PXRD spectra of the pristine, ground, and recovered forms of the compound **SB3** were recorded by using a Rigaku Ultima IV X-ray diffractometer and keeping the parameters constant for all samples, with a step width of 0.21 and a scan rate of 21 min1 from 5–501 (Cu K_α radiation, λ = 1.54 Å).

Calculation of crystallinity from PXRD

Crystallinity is considered as the ratio between the area of crystalline peaks to the area of all peaks. Here, the crystallinity is revealed as a percentage by multiplying the ratio with 100. The deconvolution of the PXRD raw data was completed using origin software (Origin Pro 8.5, student version), having a good increment of peaks. Then, by selecting the plot the 'Analysis' menu should be clicked followed by the 'Peaks and Baseline' and 'Peak Analyzer' to reach the 'Open Dialogue'. Here, the 'Peak Analyzer Window' will be opened to perform 'Integrate Peaks.' Followed by the 'Next' option, the 'Constant Y' should be selected to set up the baseline. Again, 'Next' and 'Find' options should be clicked and 'Untick' to 'Enable Auto Find' should be done. Next 'Add' option should be clicked and all the relevant peaks should be selected accordingly. Next, the 'Done' option should be clicked. In the 'Peak Finding Setting' the 'Direction' should be selected as 'Positive' and 'Next' button should be clicked again. Here 'Adjust ad Preview Graph' should be done. Next the 'Finish' button has to be clicked. From the grown window, 'Select Data' then 'Select Integral Results' should be copied and pasted into a new Excel sheet. It was named as 'Area of crystalline peaks'. Here sum it in excel. The area will be obtained. Therefore, the same process should be undergone again but this time no specific peaks but the 'Total area' should have to be integrated and the total area thus can be calculated using the excel sheet. Finally, the area under relevant crystalline peaks

should be divided by the total area under the PXRD signal and multiplied by 100 to get the percentage of crystallinity.[2]

0.2.4 Differential scanning calorimetry analysis

DSC thermograms were recorded using a Themys One+ (Setaram) instrument keeping the temperature in the 30–300 °C range with a ramp rate of 2 °C min^{-1} under a N_2 atmosphere.

0.2.5 Cyclic-Voltammetry (CV)

For the work of Chapter **IV**, the HOMO/LUMO energy levels were calculated from the oxidation onset/reduction potentials in due course of positive/negative scans. For **SB3** 10^{-5} M of DCM and 10^{-5} M of *N,N*-DMF solutions were used with glassy carbon (GC) electrode as working electrode (WE) along with the Pt-wire and Ag/AgCl were used as counter electrode (CE) and reference electrode (RE) respectively with a 0.1 M tetrabutylammonium perchlorate (TBAP) in the respective solvents as electrolyte in a typical three-electrode system at normal atm,

$E_{HOMO}(DCM) = - (E^{OX}{}_{Onset} - 0.49 + 4.8)$ eV = - (1.2135- 0.49 + 4.8) eV = -5.5235 eV

$E_{LUMO}(DCM) = - (E^{Red}{}_{Onset} - 0.49 + 4.8)$ eV = - (-1.662- 0.49 + 4.8) eV = -2.648 eV

Energy Gap (DCM) = $E_{LUMO} - E_{HOMO}$ = (-2.648 + 5.5235) eV = 2.8755 eV

Again,

$E_{HOMO}(DMF) = - (E^{OX}{}_{Onset} - 0.49 + 4.8)$ eV = - (1.1179- 0.49 + 4.8) eV = -5.4279 eV

$E_{LUMO}(DCM) = - (E^{Red}{}_{Onset} - 0.49 + 4.8)$ eV = - (-1.6374- 0.49 + 4.8) eV = -2.6726 eV

Energy Gap (DCM) = $E_{LUMO} - E_{HOMO}$ = (-2.648 + 5.5235) eV = 2.7553 eV

0.2.6 Single-crystal X-ray measurement

For the single crystals of this thesis, all measurements were performed on a Rigaku XtaLAB P200 diffractometer using multi-layer mirror monochromated Cu-K_α

radiation (λ=1.54184 Å). The data were collected at a temperature of -173±1 °C to a maximum 2θ value of 149.8 and were processed using CrysAlisPro (Rigaku Oxford Diffraction). The linear absorption coefficient (m) for Cu-K_α radiation is 18.391 cm^{-1}. An applied empirical absorption correction resulted in transmission factors ranging from 0.227 to 0.593. The data were corrected for the Lorentz and polarization effects. The structure was solved by direct methods (SIR2011)[3] and expanded by Fourier techniques. The non-hydrogen atoms were refined anisotropically, whether the hydrogen atoms were refined by the riding model. All the calculations were performed using the Olex2 crystallographic software package except for the refinement, which was done using SHELXL Version 2014/7.[4]

0.2.7 Time-resolved fluorescence measurements

Time-resolved fluorescence measurements were measured using a time-correlated single-photon counting (TCSPC) unit (Horiba Deltaflex). The laser used for all the samples was 510 nm. All the measurements were undergone at room temperature. The decay fitting was done by keeping the χ^2 value close to 1.

The average lifetime was obtained by fitting the decay profiles to a tri- or bi-exponential function eq-1. $Fit=A1.exp(-t/\tau1)+A2.exp(-t/\tau2) + A3.exp(-t/\tau3)$ .....(eq-1)

$\alpha1$, $\alpha2$ are the weighted components and $\tau1$, $\tau2$, $\tau3$ are the individual lifetime components of the decay. The qualities of the fit were understood by judging the chi square ($\chi2$) values. The rate constants are calculated by using: $k_r = [\Phi_f / \tau_{avg}]\ s^{-1}$; $k_{nr} = [(1-\Phi_f) / \tau_{avg}]\ s^{-1}$

0.2.8 Density Functional Theory Study

All density functional theoretical (DFT) calculations were done using the ORCA Version 5.0.3 quantum chemical software package.1,2 Ground state (S_0) geometry optimizations were performed using DFT with CAM-B3LYP3 functional and 6-31G* basis set. The excited stats (S_1) geometry optimization was carried on using time-dependent DFT (TDDFT). Root mean square deviation (RMSD) calculations were obtained using the Kabsch algorithm.4. All structural and MOs were visualized using Avogadro software.5.[5-9]

0.2.9 IR

An FT-IR spectrometer (FT/IR-4200, Jasco) was utilized to record the IR spectra of the samples. Solid samples were mixed with KBr to form pellets to record the spectra.

0.2.10 SEM

The FE-SEM (Field Emission Scanning Electron Microscopy) images were taken in the one mM range for all the samples using Apreo S with Leica Ultra Microtome EM UC7 (Sputter Coater).

0.2.11 Molecular docking

Schrodinger suites 2022-1 were employed to prepare the crystal structures of protein obtained from PDB, for ligand preparation and performing molecular docking, respectively.

0.2.12 Cell-culture

The cell lines were purchased from NCCS, Pune, India and ATCC and maintained in DMEM media supplemented 10% FBS with 1% (v/v) penicillin-streptomycin. Cells were incubated at 37 ^{o}C in a humidified atmosphere comprising 05/95 CO_2/air composition. All culture supplies were procured from Thermo Fisher Scientific.

For the work of **Chapter III**, FaDu cells were seeded in a 6-well plate with a density of 5000 cells per well. The cells were allowed to grow overnight to attach, and the next day treatment was done for 1 hour in PBS. The medium was removed for treatment, cells were fixed with 4% pre-chilled PFA for 15 mins, and PBS wash was given three times. Cells were stained with DAPI for 5 mins and rinsed with PBS again 3 times. Cells were stained with **IAT**/**IAP** in PBS for 4h/6 h at 37 ^{o}C and 5% CO_2. Post-treatment with **SB6(IAT)**/**SB7 (IAP)**, coverslips were mounted on slides without PBS wash, and images were captured.

For **Chapter V,** FaDu cells were cultured in RPMI-1640 medium containing L-glutamine (300 mg/L) and sodium bicarbonate (2 g/L) supplemented with 10% (v/v) fetal bovine serum (FBS), and penicillin (100 IU)/ streptomycin (100 mg/mL).

0.2.13 Cytotoxicity-MTT assay

All type of cells was seeded into 96 well-plate at a density of $5X10^3$ cells/well. After proper adhesion cells were incubated with compounds for 24 h. Cells treated with DMSO (less than 1%) were used as a control group. After 24 h, supernatant from the plate was discarded and rinsed with 100 µL of sterile PBS. Freshly prepared 3-(4,5-Dimethylthiazol-2-yl)-2,5-diphenyl tetrazolium bromide) (MTT) (100 μL of 5 mg/mL, in sterile PBS, was added. The 96 well-plate was incubated at 37 °C for 4 h. The supernatant was removed after 4 h, and 100 μL/well of DMSO was added to the individual 96 well-plate. A multi-plate reader was used to read absorbance at a wavelength of 570 nm. The anticancer activities of the synthesized indole-anthracene-based AIE-gens were evaluated against three cell lines-FaDu which is a robust cell line, 4T1 triple-negative breast cancer cell line, and MCF-7 which is a non-TNBC cell line, and one normal cell line-HEK 293 which is a human embryonic cell line using MTT assay. Doxorubicin is a clinical anticancer drug that was used as a positive control.

0.2.14 Cellular uptake (FACS)

Cells were used for quantitative analysis of uptakes of compounds by using flow cytometry. Cell lines were seeded in 12 well cell culture-plate (1×106 cells per well) in DMEM media (Dulbecco's Modified Eagle's Medium) containing 10% FBS with 1% antibiotic. After complete adhesion cells were treated with different AIE-gens using their GI_{50} for 24h. The next day cells were washed with sterile PBS followed by trypsinization of cells. Cells were collected in a 1.5 ml tube and centrifuged at 4 °C at 1000 rpm for 5 minutes. Cells were resuspended in 250 μL of sterile PBS (pH 7.4). A flow cytometer (BD FACS Aria™ III) was used for histogram generation of compound uptake.

0.2.15 Reactive Oxygen Species (ROS) assay

FaDu cells were seeded in 96 well-plate using DMEM media for 24 hrs. Later, cells were treated with AIE-gens for 24 h. Cells were washed with PBS and incubated with 10 μM of 2′, 7′-Dichlorofluorescin diacetate (DCF-DA) solution for 30 min. The cells

were washed 3 times with PBS and fluorescence was taken using a Spectramax instrument excitation wavelength of 485 nm and an emission wavelength of 530 nm.

0.2.16 Haemolysis assay

Rat blood was collected and centrifuged at 2500 rpm for 10 minutes. Red blood cells (RBCs) were carefully separated from plasma, and collected RBCs were washed with PBS and centrifuged at 3000 rpm for 10 minutes. RBCs were resuspended into PBS to obtain a working 5% v/v solution. Triton-X 100 (1%) was used as positive control and PBS treated sample as a negative control. Compounds were incubated with their GI_{50} concentration for 1 h and at 37 °C. Later, RBC's solution was centrifuged at 8000 rpm for 1 minute and the supernatant was collected for absorbance at 576 nm using a Spectramax™ multiplate reader (Molecular Devices, US). The formula used to calculate: Haemolysis (%) $=(A_s-A_o)/(A_{100}-A_o) \times 100$, where A_s is sample absorbance, A_o is the negative control absorbance treated with PBS and A_{100} is (Absorbance of titron X-100).

0.2.17 Fixed cell/Live Cell confocal fluorescence imaging and treatments

Cell lines were seeded on lysine coated sterile coverslip placed in 12 well cell culture plate (1×10^5 cells per well) in DMEM media containing 10% FBS with 1% antibiotic. Cells were allowed to adhere completely. After 24 h cells were treated with different formulation using their GI_{50} for 4 h and 24h. Later, cells were washed with sterile PBS and mounted on a glass slide. Cell imaging was done using a confocal microscope.

For **Chapter V**, Cells were seeded at the density of 5000 cells per well in a 96-well plate in 100 μL of RPMI and allowed to grow and attach overnight. The absorbance was read on a microplate reader (Spectramax M4, Molecular Devices) at 570 nm with a reference wavelength of 620 nm. The percent growth inhibition was calculated based on the absorbance of treated wells relative to control. Based on that, the GI_{50} (the concentration at which 50 % growth reduction is observed) was calculated using the following formula:

% growth inhibition = % (abs of control - abs of treated)/abs of control

FaDu cells were seeded with a density of 0.25 million cells/ well on coverslips in a 6-well plate in 2 mL of medium for imaging experiments. They were allowed to attach and grow overnight. Imaging experiments were performed the next day. The cells were treated with various compounds in DMSO solvent or serum-free medium, and post-treatment the cells were washed and treated with DAPI. Probed FaDu cells on coverslips were fixed with ice-cold methanol for 15 minutes at -20 °C, and used for imaging experiments using a Leica DMi8 laser scanning confocal microscope. The imaging experiments with 3 μM probe and temperature-dependent imaging experiments were performed in live FaDu cells without PBS washes. In comparison, imaging experiments with 10 μM probe were performed in live FaDu cells with PBS washes. The cholesterol depletion and repletion imaging studies were performed in fixed FaDu cells with PBS washes.

Treatments (Chapter V)

For MTT assays, different compound dilutions were added to each well, resulting in a final concentration of 3, 10, 30 and 100 μM in a final volume of 200 μL. After incubating the cells with the compounds for 72 h, 20 μL of 5 mg/mL MTT in PBS was added to each well and incubated for 3.5 h at 37 °C. After that, the medium was removed, and the precipitated formazan crystals were dissolved in 50 μL of DMSO. For imaging experiments, FaDu cells grown on coverslips were treated with 10 mM final concentration of MβCD for 1 h at 37 °C for cholesterol depletion. Cells were washed thrice with serum-free RPMI medium and then treated with 3 μM probe for 1 h. For cholesterol repletion, MβCD-treated FaDu cells were further treated with cholesterol/MβCD (1/10) mixture with 50 μM working concentration of cholesterol for 1 h at 37 °C, washed two times with serum-free RPMI medium and then treated with 3 μM of probe for 1 h. Control FaDu cells treated with 3 μM of **OXNCN** were also treated with 50 μM of oleic acid and incubated for 30 mins.

0.3 References

1 S. Roquet, A. Cravino, P. Leriche, O. Aleveque, P. Frere and J. Roncali, ***J. Am. Chem. Soc.***, 2006, **128**, 3459–3466.

2 R. Rotaru, M. Savin, N. Tudorachi, C. Peptu, P. Samila, L. Sacarescu and V. Harabagiu, ***Polym. Chem.***, 2018, **9**, 860-868.

3 M. C. Burla, R. Caliandro, M. Camalli, B. Carrozzini, G. L. Cascarano, C. Giacovazzo, M. Mallamo, A. Mazzone, G. Polidori, R. Spagna, SIR2011: a new package for crystal structure determination and refinement, ***J. Appl. Crystallogr.***, 2012, **45**, 357-361.

4 G. M. Sheldrick, A short history of SHELX**.** ***Acta Crystallogr. Sect. A: Found. Crystallogr.***, 2008, **64**, 112.

5 Neese, F.; Wennmohs, F.; Becker, U.; Riplinger, C. "The ORCA Quantum Chemistry Program Package." *Journal of Chemical Physics* **2020**, *152*, 224108.
6 F. Neese, "Software Update: The ORCA Program System-Version 5.0." *WIREs Computational Molecular Science* **2022**, *2*, 73-78.
7 Yanai, T.; Tew, D.; Handy, N. "A new hybrid exchange-correlation functional using the Coulomb-attenuating method (CAM-B3LYP)," *Chem. Phys. Lett.* **2004**, *393*, 51-57.
8 Kabsch, W. A solution for the best rotation to relate two sets of vectors, *Acta Crystallogr.* **1976**, *A32*, 922-923. (Code: https://github.com/charnley/rmsd)
9 Hanwell, Marcus D., et al. "Avogadro: an advanced semantic chemical editor, visualization, and analysis platform."*J. Cheminformatics* **2012**, *4*, 1-17.

Chapter I

Triphenylamine and Phenothiazine Conjugated Dicyanoanilines as Stimuli-Responsive Crystallochromic Solid State Emitting Organic Fluorogens (SSEOFs)

Objectives:

- Establish a new one-pot, transition metal-free synthetic route to afford dicayanoaniline system-based crystallochromic fluorogens,
- Investigate other relevant photophysical aspects, such as solid-state stimuli-responsive emission switching of crystallochromic fluorogens.
- Utilize the photophysical aspects in real-world applications to address the practical utilities of such materials

Abstract:

Crystallochromic and stimuli-responsive dual-state emitters are hard to achieve. Again, numerous molecules with donor-acceptor–donor (D–A–D) combinations have been investigated, but the exploitation of A–D–A systems remains at a nascent stage. Herein, we integrate twisted, and electron-rich triphenylamine (TPA) or phenothiazine (PTZ) core into an A–D–A dicyanoaniline (DCA) backbone to attain emissive π-conjugates as small-molecule dual-state emitters (DSEgens). The synthesis of new structurally similar (cousin) molecules is explored judiciously, and this approach provides methylated DCA in triethylamine and nonmethylated DCA through a KO^{t}Bu-mediated synthetic pathway. The influences of methyl and electron-rich bulky groups have created these differences in the stimuli-responsiveness of these cousin molecules. The methylated/nonmethylated **TPADCA** pair displays crystallochromic behavior, with similar emission in solution but dramatic differences in solid form, while the PTZ analogs do not exhibit such behavior. The variations in the stimuli-responsive natures of these analogs are interpreted *via* analyzing molecular conformation data, DFT information, packing motifs, powder/single-crystal X-ray diffraction data, fluorescence lifetime data, and differential scanning calorimetric (DSC) information. Finally, polymer-appended **TPADCA** and **MTPADCA** are employed in auto-reversible and self-erasable secure writing platforms.

1.1 Introduction

Systematic investigations to alter benzene's electronic spectra had begun four decades before, and the dicyanoaniline (DCA) moiety could render great attention as it consists of one electron donor but two electron acceptors .[1] Let us find the reason of our selection of the *2,6-dicyanoanilines system* to explore as organic solid-state emitters. Substituted 2,6-dicyanoanilines constitute an essential group of valuable compounds, with the acceptor-donor-acceptor (A-D-A) systems displaying wide applications.[2] The utility of various substituted DCA molecules has been examined as intermediates for chiral phases in chromatography.[2] Even many DCA-linked compounds have been utilized as heat-resistant polymers.[2] The DCA systems and the related molecules also have been studied for their structural features,[3,4] optical properties,[5-10] applications as potential mimics for photosynthesis.[11] Moreover, substituted DCA compounds connected to 2,6-dicyanoaniline moiety as a part of their molecular structure exhibit various bio-activities such as growth-promoting agents,[12] anti-amyotrophic lateral sclerosis,[13] antileishmanial,[14] antihyperglycemic,[15] and anticancer agents.[16] The aspects of dicyanoaniline moiety in the generation of solution-state fluorescent organic compounds were realized by Cui *et al.*, who synthesized a variety of DCA core-containing molecules and investigated the emission properties of **1A** and **1B** (Fig 1.1) in some selective solvents such as DCM, MeOH, and THF.[17] However, the emission was weak, ranging from fluorescence quantum yield (Φ_f) 0.09% to 0.13 % in solvents. Yi *et al.* again focussed on an efficient and facile synthesis of highly substituted DCA systems, but the real-world applications were still not established.[18]

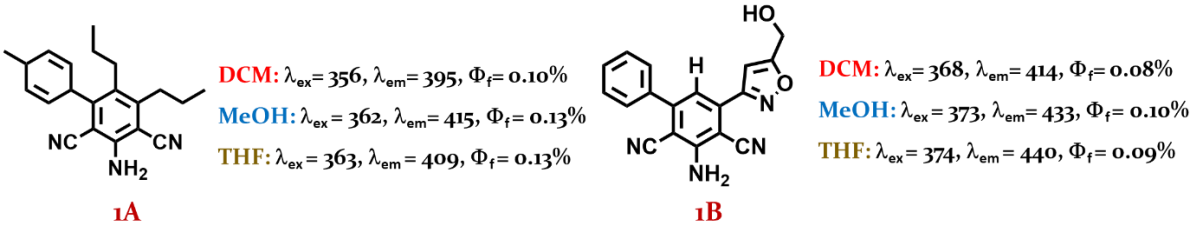

Figure 1.1 Reported dicyanoaniline molecules with their emissions features in various solvents (taken from ref. 17)

Ergo, *Cardozo et al.* established a new class of DCA systems with non-linear optical properties.[19] In 2017, *Aydiner et al.* again established a microwave irradiation-assisted synthetic procedure of 3,5-disubstituted 2,6-dicyanoaniline coumarin derivatives

displaying emissions in the yellow-green region in solvents with low Φ_f. Among those synthesized derivatives, **1C** and **1D** (Figure 1.2) showed the highest emission efficacy in ethanol with a Φ_f of 0.73% and 0.58%.[20]

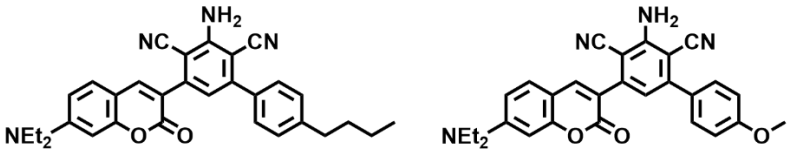

Figure 1.2 Reported coumarin-conjugated dicyanoaniline molecules displaying emissions in ethanol (ref. 20)

In the same year, *Kulkarni et al.* synthesized 2H-chromen-2-One-2,6-Dicyanoanilines and investigated the effects of substituents and pH on their luminous behavior, but the solid-state emission was still unexplored, and the emissions in solution also were not much improved.[21] Back in 2013, *Ramulu et al.* could modify the synthetic route to access the 3,5-disubstituted 2,6-dicyanoanilines *via* domino annulation of α-enolicdithioesters with malononitrile.[22] Still, the applications of DCA systems got improved when, *Pisai et al.* utilized their synthesized DCA molecules in cellular bioimaging, in 2017. They could image THP-1 cells with their synthesized compounds **1E**, **1F**, **1G**, and **1H** (Figure 1.3).[23] *Held et al.* worked on metal-free domino reactions to access potent antiviral quinazoline heterocycles with fluorescence properties, and 2,6-dicyanoanilines were the intermediates in their synthesis.[24] *Nevertheless, DCA core containing smart fluorescent materials remained sporadic, especially the solid-state emission tuning was rarely reported as maximum researchers concentrated on various substrate scopes and synthetic protocols of DCA cores.*

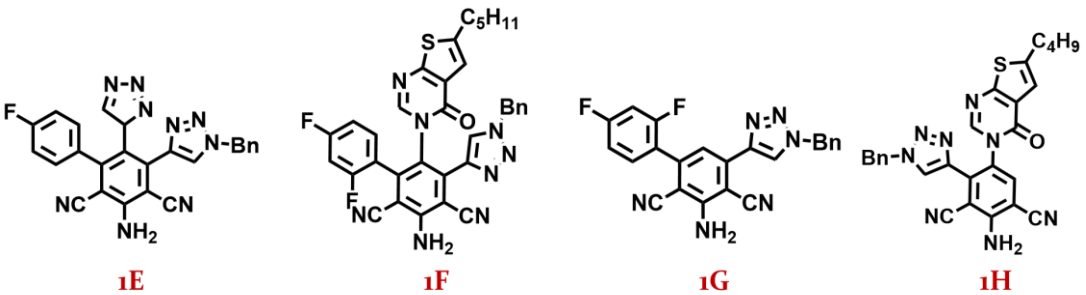

Figure 1.3 Reported fluorescent dicyanoaniline molecules, recognized for cellular imaging (ref. 23)

Why to choose triphenylamine and phenothiazine to conjugate with DCA?

Actually, triphenylamine (TPA) and phenothiazine (PTZ) cores are highly celebrated moieties in the generation of plenty of organic solid-state emitters due to their twisted/non-planar bowel shape conformation and modifiable electronic distributions[25-29] to find a variety of applications as/in optoelectronics,[30-32] data protection and anticounterfeiting,[33] stimuli-responsive smart materials,[34-38] bioimaging[39-41] and so on. To highlight a few noteworthy examples, Li *et al.* invented a quasi-planar deep-red TADF emitter comprising two TPA cores within a molecule **1I**.[42] *Shi et al.* established efficient and color-pure blue electroluminescent molecules **1J** and **1K** having PTZ core as the strong donor.[43] Recently, Zhang et al. discovered a molecule **1L** which is an AIE-gen containing TPA scaffolds with multi-stimuli responsive behavior.[44] Again, an interesting thing was reported when *Suganya et al.* found mechano-fluorochromic gels and solids containing phenothiazine molecules **1M** and **1N** that attire superhydrophobic surface formation and crystal-to-crystal phase transition.[45] A few years back, *Jiang et al.* synthesized a TPA-based dye **1O** that can detect the presence of OCl^- in A549 cancer cells through fluorescence bioimaging[46,] and again *Wang et al.* reported a tiny probe **1P** with existing phenothiazine core to apply for cellular detection of Hg^{2+} through fluorescence bioimaging (Figure 1.4).[47] *Thus, TPA and PTZ cores are extremely well-explored and well-utilized in several solid and solution-state-emitting structural designs. So, conjugating TPA/PTZ (D) to the DCA (A-D-A) system makes sense to generate a new class of organic π-conjugates.*

What is crystallochromism and why to explore?

Crystallochromism is one of the rarest photophysical phenomena. Two cousin organic solid-state emitters with the same molecular structures except one little change at any one design site are required to investigate this phenomenon. Now, if these two fluorophores display different emissions in their solid states but the same emissive behavior in their solution states, then they are crystallochromic fluorophores. To receive such an exciting feature, the design of the molecules should escape from different photophysical pitfalls, which is not an easy task to accomplish, and so the phenomenon is scarce. Notably, crystallochromism is not polymorphism.[48] *Hence, we endeavored to*

establish a DCA-conjugated TPA/PTZ core containing crystallochromic pair of molecules to investigate the relevant photophysical properties to realize their real-world applications.

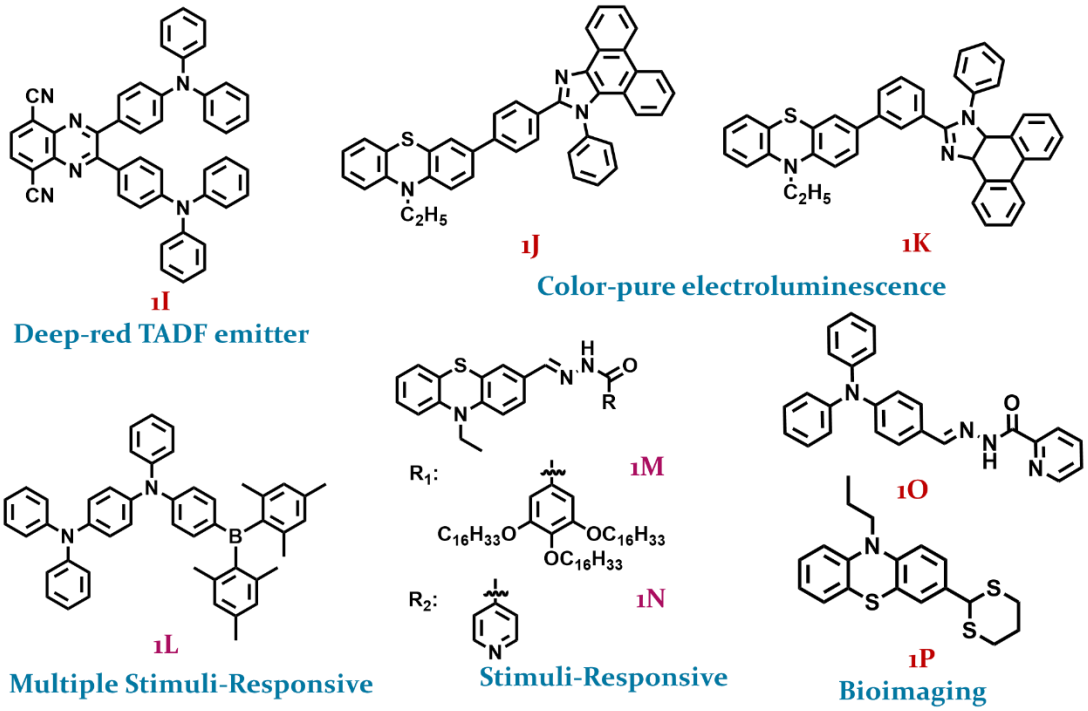

Figure 1.4 Reported TPA and PTZ core-based organic emitters for specific applications (refs. 42-47)

1.2 Literature Review on Crystallochromism

From the beginning of the past decade till the current date, very few reports deal with the phenomenon of crystallochromism. Crystallochromism is correctly defined as the subservience of solid-state emission resulting from a small structural change of the molecule, primarily related to the length, number, shape, pattern of substitutions, and kind of substituent groups. This indicates that different molecules, owning the same backbone structure but different substituents, can display considerably other solid-state emissions, despite presenting very similar emissions in solutions.[48] Nevertheless, a few reports misuse the term 'crystallochromism' as sometimes they describe it as synonymous with color polymorphism.[48] Here, some rare literature is described on the phenomenon of crystallochromism.

1.2.1 Crystallochromism from hydrophilic functionalized aromatic amino ketones consisting of furan and thiophene rings

Twenty years back, in 2003, El-Sayed *et al.* worked on four molecules, **1Q**, **1R**, **1S** and **1T,** where either they had changed the functional group or the heteroatom to produce

slightly different structures with the same backbone intact. They reported the solid-state structures, UV-Vis absorption maxima in 30 different solvents and solid-states for all four compounds. Starting from cyclohexane ethyl acetate to water, all four compounds showed similar absorption values for each solvent. The authors correlated the values with a simplified form of Kamlet-Taft LSErs and justified the observations. Interestingly, the compounds displayed quite different UV/Vis absorption maxima from each other while recorded in their respective solid-state. However, the emission behavior was not explored in their findings. Nevertheless, this report clearly indicated the presence of crystallochromic behavior (Figure 1.5).[49]

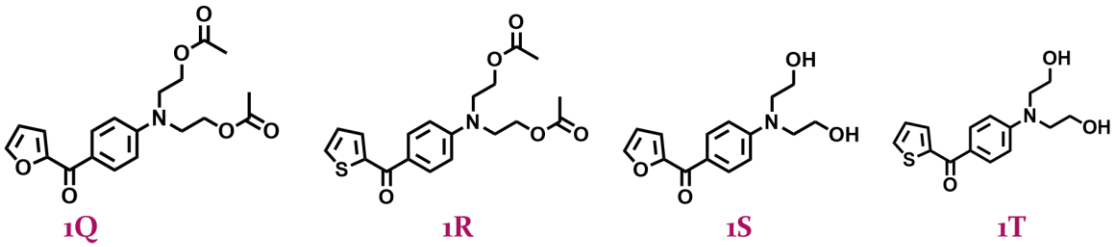

Figure 1.5 Reported crystallochromic pairs consisting of thiophene and furan rings (ref. 49)

1.2.2 Crystallochromism from 1,4,7,10-Tetraalkyltetracenes core-based molecules with tuned alkyl side-chain length

In 2010, Kitamura *et al.* established the concept of crystallochromism most conveniently till that date when they synthesized 1,4,7,10-tetraalkyltetracenes based molecules (**1U-1Z**) varying their alkyl side-chain lengths to investigate the same phenomenon. In compound **1a,** there is a simple methyl group as the chain and then an ethyl group for compound **1b**, and likewise, with a consecutive increment in the chain length, they made six different molecules where compound **1f** consists of a hexyl alkyl chain finally. In the solid state, the emission maxima and the fluorescence quantum yield for the compounds are different, but in solutions, their emission maxima are almost the same as each other with the same extent of their quantum yields. Among them, compound **1d** had two polymorphs-form A and form B. Thus, this report clearly indicates the difference between polymorphism and crystallochromism as well (Figure 1.6).[50]

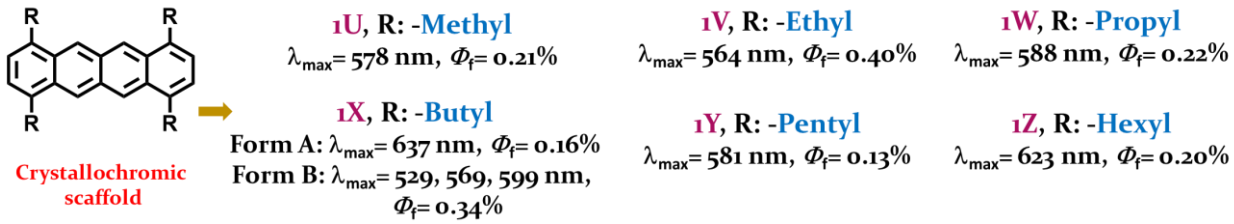

Figure 1.6 Reported crystallochromic tetracene derivatives (ref. 50)

1.2.3 Crystallochromism from diketopyrrolopyrrole-co-thieno[3,2-b]thiophene derivatives by tuning alkyl chains

In 2018, Genevaz *et al.* again tried to tune the effect of crystallochromism with the diketopyrrolopyrrole-co-thieno[3,2-b]thiophene derivatives by changing the alkyl chain length, which is the same strategy as the work of *Kitamura et al.* but of course the molecular system was different. They worked with two diketopyrrolopyrrole-co-thieno[3,2-b]thiophene derivatives which were substituted either with branched ethylhexyl (**1ZA**) or linear hexyl side chains (**1ZB**). Both these derivatives displayed the same kind of emissions in solvents, but in solids, **TTDPP-EH** emits at 650-750 nm and **TTDPP-C6** at 700-850 nm, indicating broad spectra. The major problem was the quenching of the fluorescence in their respective solid states (Figure 1.7).[51]

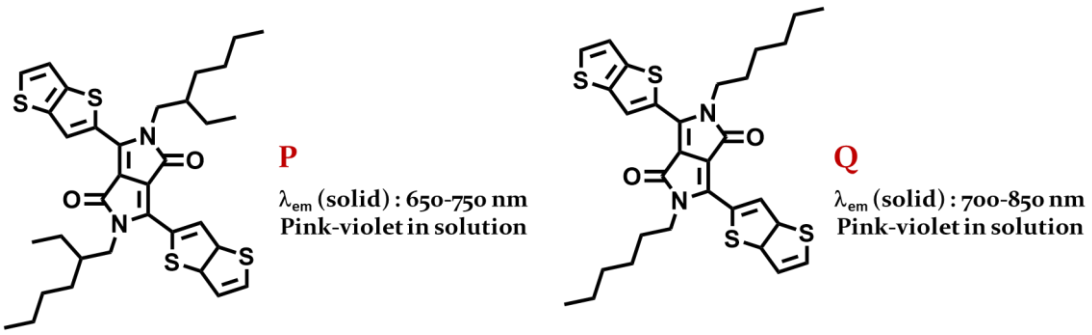

Figure 1.7 Reported crystallochromic diketopyrrolopyrrole-co-thieno[3,2-b]thiophene derivatives (ref. 51)

1.2.4 Synthetic routes of the reported crystallochromic compounds

Not only the photophysical outputs, but it is also convenient to discuss the synthetic routes to produce those reported crystallochromic molecules because the facile synthetic way to generate crystallochromic pairs is also sporadic, as most of them follow coupling reactions utilizing costly metal-based catalysts. El-Sayed *et al.* followed a long

procedure of synthesis[49] whereas Kitamura *et al.* reached their final products after doing three consecutive steps of synthesis. They utilized KF with 18-crown-6 to receive the tetracene moiety, and then in the second step, they had to use 10% Pd/C with *n*BuOH followed by an acidification step (Figure 1.8).[50] Even *Genevaz et al.* could not produce the crystallochromic derivatives in a single one-pot step. For them, it was a two-step procedure where they used di-n-butyl succinate with *t*-BuOK in *t*-amyl alcohol to generate the diketopyrrolopyrrole-co-thieno[3,2-b]thiophene core and then the next step was needed to proceed for the respective alkylation (Figure 1.9).[51]

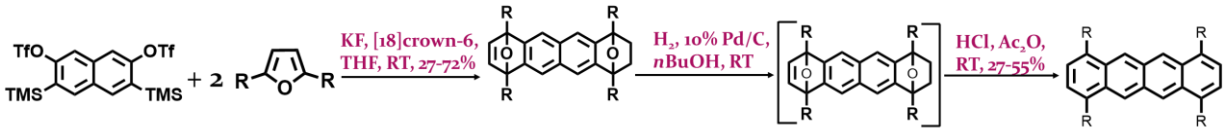

Figure 1.8 Synthetic route for the reported 1,4,7,10-Tetraalkyltetracene-based crystallochromic derivatives (ref. 50)

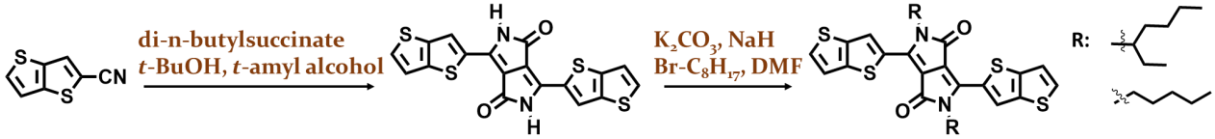

Figure 1.9 Synthetic route for the reported diketopyrrolopyrrole-co-thieno[3,2-b]thiophene derivatives (ref. 51)

1.3 Results and discussion

1.3.1 Synthetic route of newly conceptualized molecules

Unlike the previous reports on crystallochromism, we focussed on one-pot and one-step protocol to synthesize crystallochromic pairs. We utilized the respective aldehydes 4-(diphenylamino)benzaldehyde and 10-pentyl-10H-phenothiazine-3-carbaldehyde to undergo simple Knoevenagel condensation with malononitrile followed by a cyclization step to conjugate dicyanoaniline part with the TPA or PTZ. These reactions behave differently when substrates or bases differ. Et_3N as a base provides a methylated product, **MTPADCA**, whereas K^{t}OBu offers the nonmethylated product **TPADCA** (see Scheme 1). The yield and selectivity for the phenothiazine analog **MPTZDCA** appear better with NEt_3, but KO^{t}Bu produces **PTZDCA** only in 35% yield with excellent selectivity. The product yield is improved to 62% using NaOH with relatively

low selectivity. The possible mechanistic paths are described for both methylated and nonmethylated analogs. Thus, these DCA compounds are sufficiently electron-rich with methyl and TPA or PTZ units. The reaction was optimized using different bases and time points, and here, the optimizing information is tabulated in Table 1.1.

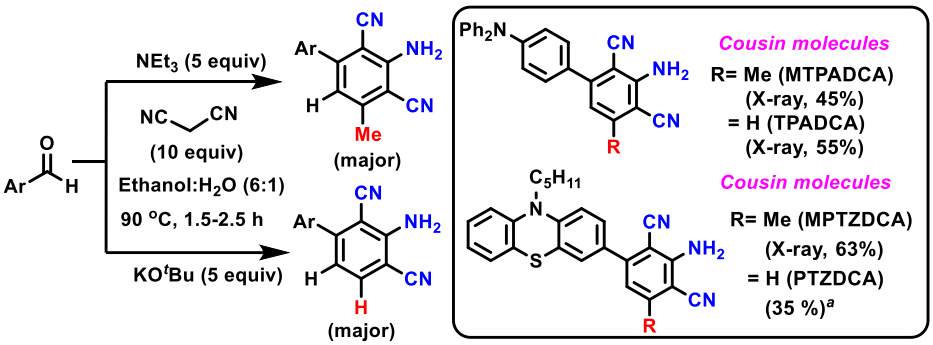

Scheme 1 Synthesis of cousin DCA molecules.[a]The yield becomes 62% while KO^{t}Bu is replaced with NaOH

The IR, NMR, and Mass spectroscopic studies confirmed the molecular structures. Single crystals were grown for all the compounds except **PTZDCA** using a room-temperature solvent evaporation path with several attempts and analyzed using single-crystal X-ray diffraction studies to understand the molecular structure and crystal packing. Thus, the simple A-D-A system had turned into two unique designs such as (i) D'-A-D-A-D" and (ii) D'-A-D-A [D': PTZ or TPA and D": Me; A= -CN; D: -NH_2]. Herein, a new synthetic strategy was employed to access methylated and nonmethylated PTZ or TPA-linked cousin DCA molecules just by varying the nature of the base.

1.3.2 Plausible mechanism

1.3.2.1 Plausible mechanism to receive the methylated product using organic base

The mechanism for getting the methylated product was proposed by *Mohammadi et al.* (Scheme 2).[52] The first step involves the Michael Addition of malononitrile to the arylidenemalononitrile in the presence of organic base Et_3N, with the formation of an adduct that further undergoes elimination of hydrogen cyanide to form α,β-unsaturated nitrile. Michael's addition of a second molecule of malononitrile to this α,β-unsaturated nitrile leads to the formation of a new adduct, which undergoes successive addition of two further molecules of malononitrile to the nitrile triple bonds to form 1:4 adduct by way of imine. All the previously formed adducts were 1:1. However, from that 1:4 adduct,

the elimination of malononitrile followed by a proton shift would culminate into 1-azatriene intermediate. Next, an intramolecular nucleophile attack of the methylene nitrile anion on the imine moiety would generate a highly substituted cyclohexadiene intermediate.

Table 1.1 Reaction optimization

Entry	R	Solvent	Base	Time(h)	**MTPADCA / TPADCA** (%)	**MPTZDCA / PTZDCA** (%)
1	TPA	EtOH:H_2O (6:1)	Et_3N	1.5	45	12
2	TPA	EtOH:H_2O (6:1)	NaOH	1.5	42	52
3	TPA	EtOH:H_2O (6:1)	KO^tBu	1.5	18	55
4	TPA	EtOH:H_2O (6:1)	K_2CO_3	1.5	12	17
5	TPA	EtOH:H_2O (6:1)	NH_4Oac	1.5	Trace	15
6	TPA	EtOH:H_2O (6:1)	Pipyridine	1.5	22	Trace
7	TPA	Toluene	Et_3N	2.5	0	0
8	TPA	Toluene	NaOH	2.5	0	0
9	TPA	Toluene	Pipyridine	2.5	0	0
10	TPA	Toluene	Pyrrolidine	2.5	Trace	20
11	TPA	Acetonitrile	Pyrrolidine	2.5	Trace	Trace
12	PTZ	EtOH:H_2O (6:1)	Et_3N	1	63	Trace
13	PTZ	EtOH:H_2O (6:1)	NaOH	1.5	15	62
14	PTZ	EtOH:H_2O (6:1)	^tBuOK	1.5	Trace	35
15	PTZ	EtOH:H_2O (6:1)	Et_3N	1.5	63	20
16	PTZ	Acetonitrile	Pipyridine	2.5	25	Trace

Again, three consecutive 4-exo-dig cyclizations through the nucleophilic addition of the amine group to the adjacent nitriles and subsequent ring-opening of the spirocyclic intermediates would produce bicycle by way of intermediates. Finally, that may again

undergo ring-opening and elimination of tricyanoamine molecule to afford 3-aryl-2,6-dicyano-5-methylaniline.[52] It is worth mentioning a similar kind of reaction mechanism was proposed by *Yi et al.*[18]

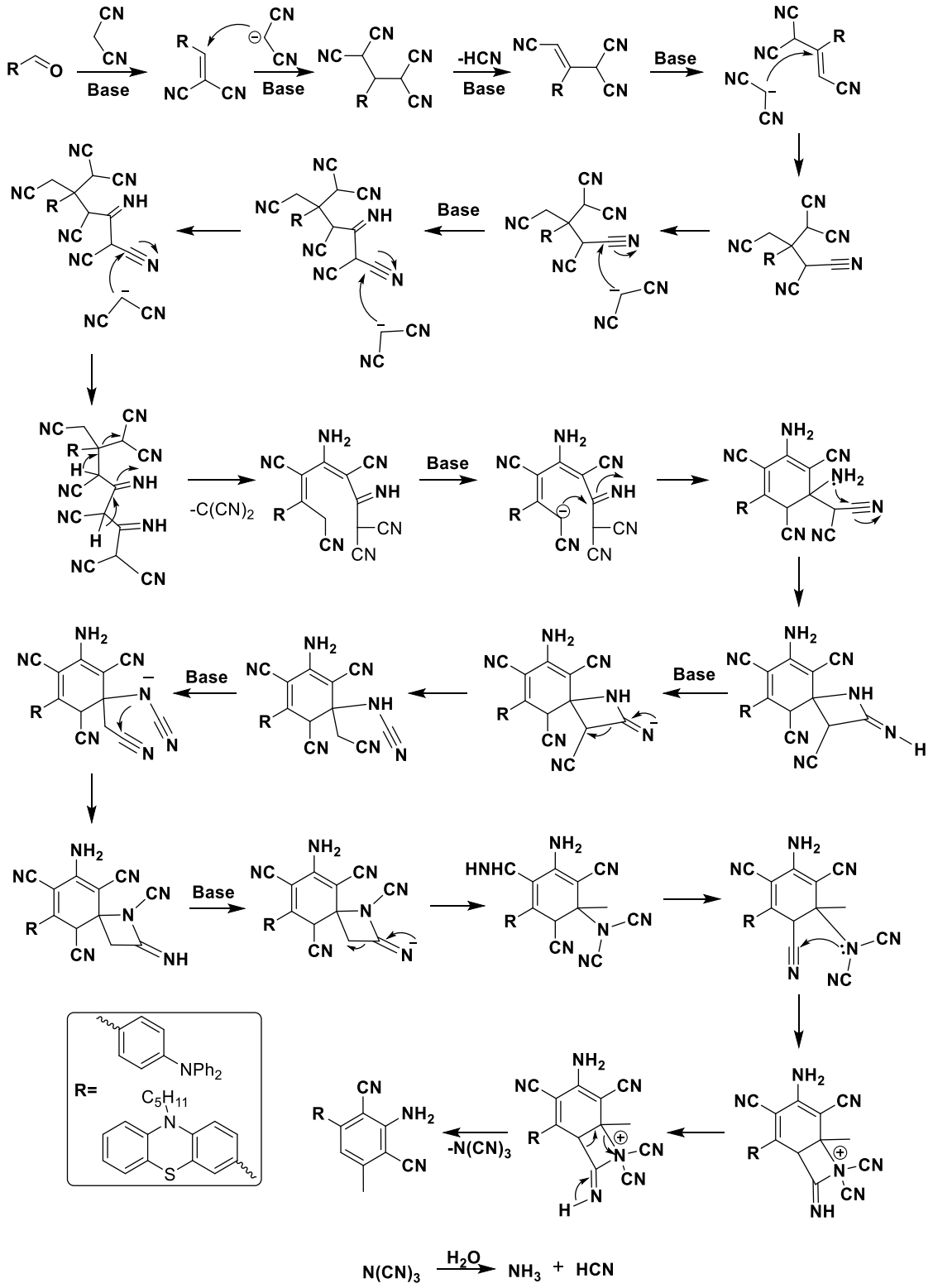

Scheme 2 Reaction mechanism to receive the methylated product

1.3.2.2 Plausible mechanism to receive the non-methylated product using inorganic base

For the nonmethylated product formation, the following mechanism was proposed by us. The first step involves the Michael addition of malononitrile to the arylidenemalononitrile in the presence of organic base K^{t}OBu, with the formation of an adduct that further does not undergo elimination of hydrogen cyanide to form α,β-unsaturated nitrile.

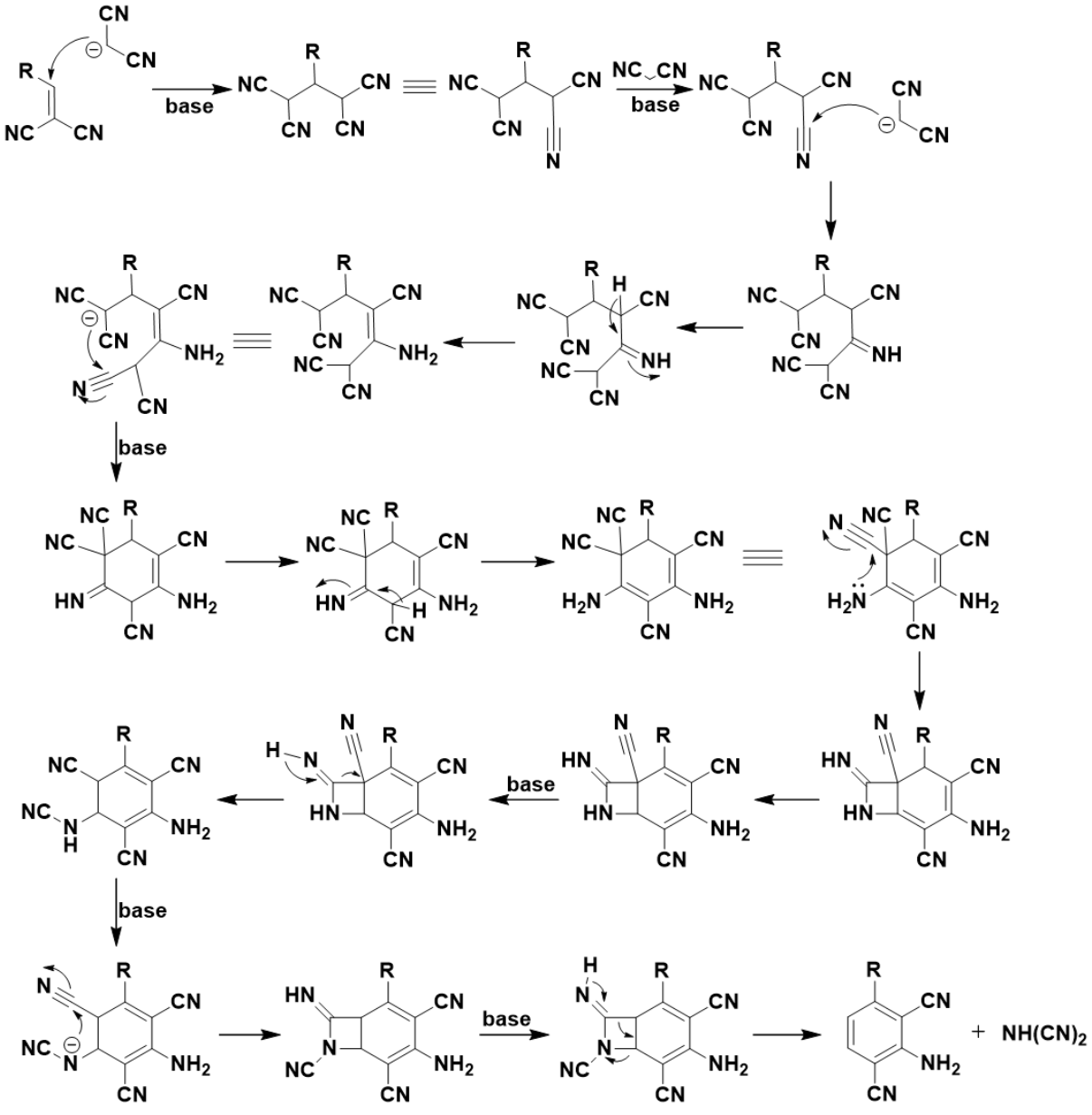

Scheme 3 Reaction mechanism to receive the nonmethylated product

Rather Michael addition of a second molecule of malononitrile happens to alter the reaction pathway, followed by a hydrogen bond shift to create a new type of adducts upon

an intramolecular Michael type of attack to the available nitrile, resulting in a ring closure and hydrogen bond shift. The available lone pair of the amine then attacks another intramolecular nitrile to form a bicycle intermediate followed by other intermediates consecutively. Finally, the tetracycle ring gets opened to create the nonmethylated product.

1.3.3 Structural elucidation

1.3.3.1 NMR spectroscopic analysis of the synthesized compounds

All the synthesized molecules were characterized through $^{1}H/^{13}C$ NMR spectroscopy. In all the ^{1}H NMR data, the chemical shift (in ppm) for the distinguishing -NH_2 peak was received at $\delta \sim$ 5.5-6.7 range. The distinct -CH_3 peak at $\delta \sim$ 2.5 was detected for the methylated products, whereas for the non-methylated products, this peak was absent as expected (representative NMR spectra, Figures 1.10-11).

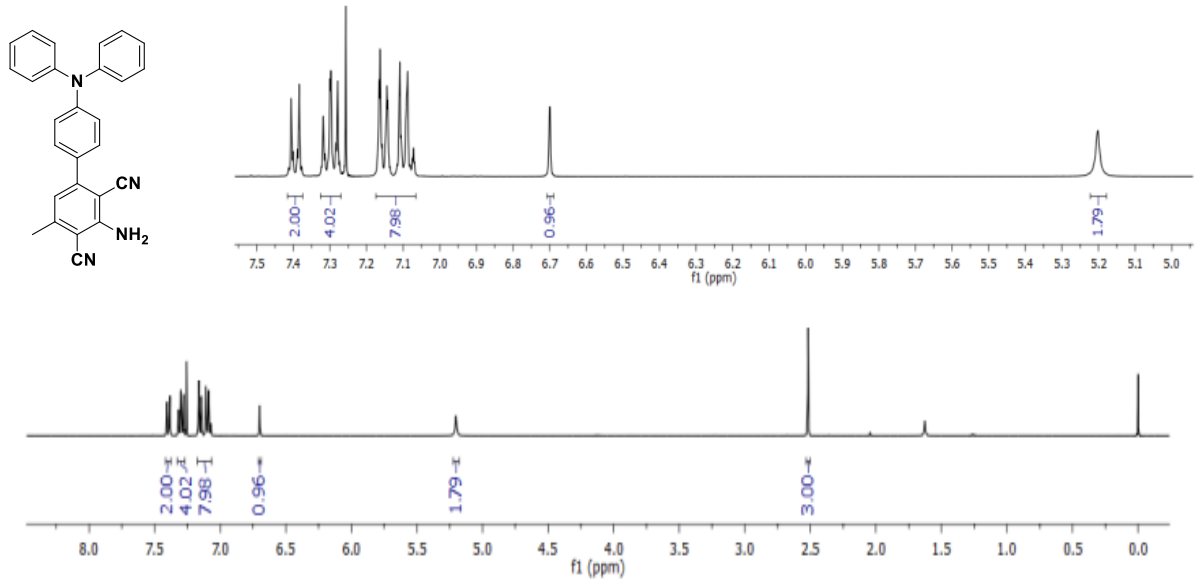

Figure 1.10 ^{1}H NMR spectra of **MTPADCA**

1.3.3.2 Single-crystal X-ray diffraction (SCXRD) studies of the synthesized compounds

We could grow single-crystals for **MTPADCA**, **MPTZDCA** and **TPADCA** from hexane/DCM (3:1) binary solvent medium by slow evaporation of the solvent (Figure 1.12). Both the **MTPADCA** and **TPADCA** crystallize in a monoclinic system ($P2_1/c$ space group) with a twisted molecular conformation and a difference in the significant torsion angle of

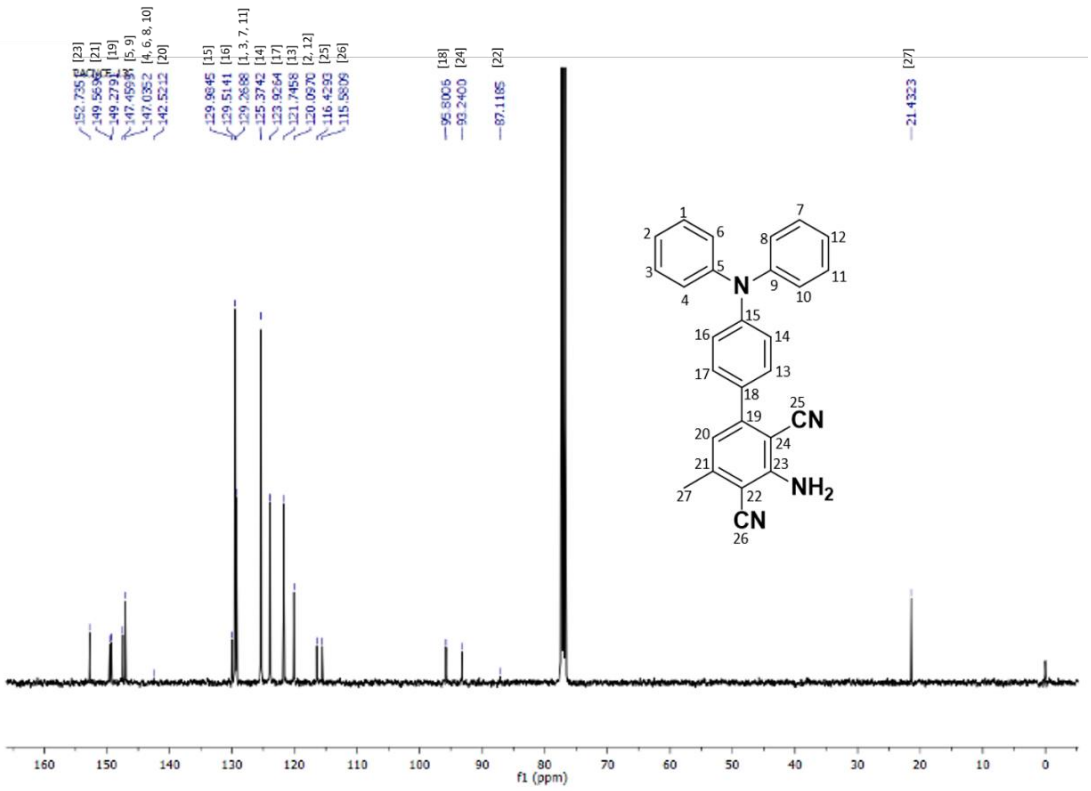

Figure 1.11 ^{13}C-NMR spectrum of **MTPADCA**

~2-4°. In contrast, **MPTZDCA** crystallizes in a triclinic system (*P-1* space group) with a herringbone packing. The details are discussed later.

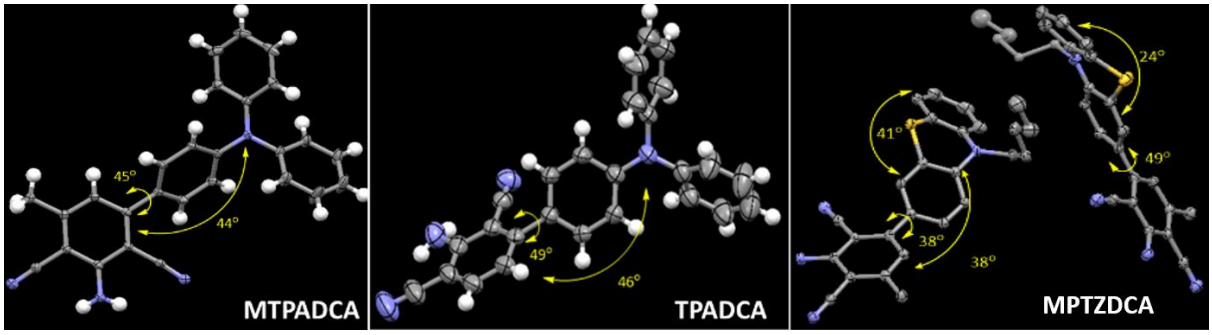

Figure 1.12 Molecular structures (ORTEP presentation with probability level ~40%) of **MTPADCA**, **TPADCA**, and **MPTZDCA**

1.3.4 Investigation of the photophysical properties

1.3.4.1 Crystallochromic behavior and the dual state emission

As mentioned earlier, crystallochromism deals with both solid and solution-state emissive behavior.[48] Again, the compounds displaying commendable emissions in both solid and solution are recognized as dual-state emitting fluorogens or DSE-gens.[49] Hence,

the investigation on crystallochromic and dual-state emissive behavior should go hand in hand.

At first, we investigated the photophysical features of the TPA-based cousin molecules in their solid and solution states. Before studying the solid state, the photophysical properties were investigated in the solution state. The compound **MTPADCA** exhibited two absorption bands at λ_{max} = 290 nm and 380 nm, possibly attributed to π-π* and intramolecular charge transfer (ICT) (Figure 1.13a). The **TPADCA** also displays three absorption bands with major at λ_{max} = 280 nm (π-π*) and 380 nm (ICT) along with a small signature at 330 nm (possibly n- π*) (Figure 1.14a). The emission maximum peaked at λ_{max} ~ 430 nm is noted for both **MTPADCA** and **TPADCA** in hexane as a single relatively narrower band, attributed to the emission from the locally excited (LE) state (Figures 1.13b and 1.14b). A trivial change is observed in the solution state absorption spectra for both **MTPADCA** (Figure 1.13a) and **TPADCA** (Figure 1.14a) upon changing the polarity of solvents, indicating a negligible impact at the ground state. Bathochromic emission shifts of 102 nm for **MTPADCA** (Figure 1.13b) and 133 nm for **TPADCA** (Figure 1.13b) upon the increasing polarity of solvents demonstrate an increase in the molecular dipole moment and conformational change in the excited state.[53] It designates the presence of a twisted-internal charge transfer (TICT) state, as expected from a twisted TPA core.[54-56] The plots of $E_T(30)$ [a solvent-polarity scale] against maximum λ_{em}, Stokes shift, and quantum yield display similar solvatofluorochromic features for both **MTPADCA** and **TPADCA** (Figure 1.15).

The solid-state emission studies revealed the isolated compound **MTPADCA** as a green-emitting solid with λ_{max} = 501 nm (broad absorbance at λ_{max} = 442 nm; Figure 1.16a), and absolute Φ_f 25.1% albeit **TPADCA** solid absorbs maximum at λ_{max} = 471 nm and (Figure 1.16b) emits at longer wavelength λ_{max} = 578 nm (light yellow) with much lower Φ_f (2.8%) (Figures. 1.17a-b). This result specified a better intermolecular π-conjugation in **TPADCA** than in **MTPADCA**. Thus, crystallochromic behavior was established for these cousin molecules by finding almost similar emission behavior for **MTPADCA** and **TPADCA** in the solution state (Figures. 1.17c-d, Figures 1.13 and 1.14 for the emission spectra and Table 1.3). Such a distinct emission variation in the solid state but not in the solution state indicates crystallochromic behavior. Notably, color polymorphism and

Table 1.2 Crystal Data

Compounds	**MTPADCA**	**TPADCA**	**MPTZDCA**
Emp. Formula	$C_{27}H_{20}N_4$	$C_{26}H_{18}N_4$	$C_{26}H_{24}N_4S$
Formula weight	400.47	386.44	424.55
Crystal system	monoclinic	monoclinic	Triclinic
Space group	$P2_1/c$	$P2_1/c$	P -1
a /Å	10.1248(2)	17.0172(3)	8.9131(4)
b /Å	9.8792(2)	14.7978(3)	11.8184(4)
c /Å	21.3435(3)	8.29705(16)	21.8914(9)
α/degree	90	90	91.003(3)
β/degree	97.401(2)	98.9384(18)	95.825(4)
γ/degree	90	90	106.344(4)
V /Å^3	2117.10(7)	2063.96(7)	2198.84(16)
Z	4	4	4
D_{calc} /g cm^{-3}]	1.216	1.244	1.282
μ /mm^{-1}	.626	.589	1.458
F (000)	819.0	808.0	896.0
Data/ restraints/ parameters	4491/0/282	4377/0/272	10060/0/562
S	1.083	1.059	1.061
+R1 [I>2σ(I)]	0.0532(3974)	0.0670(3233)	0.0671(8733)
wR2 [all data]	0.1564(4491)	0.2056(4377)	0.1933(10060)
Max./min. residual electron dens. [eÅ^{-3}]	0.320/ -0.420	0.737/ -0.192	0.785/ -0.984
CCDC No.	2062771	2062770	2041739

crystallochromism are fundamentally different. Polymorphism arises from a single molecule with other conformational structures, while crystallochromic molecules are associated with structurally similar molecules with some atomic or substituent variation.

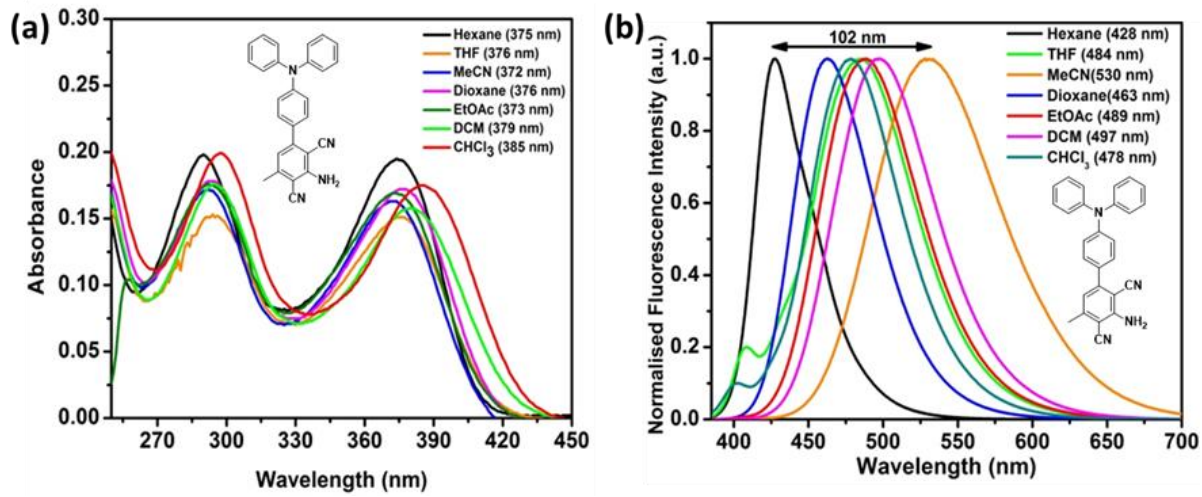

Figure 1.13 Solution state (a) absorption & (b) normalized emission spectra for **MTPADCA** (10^{-5} M)

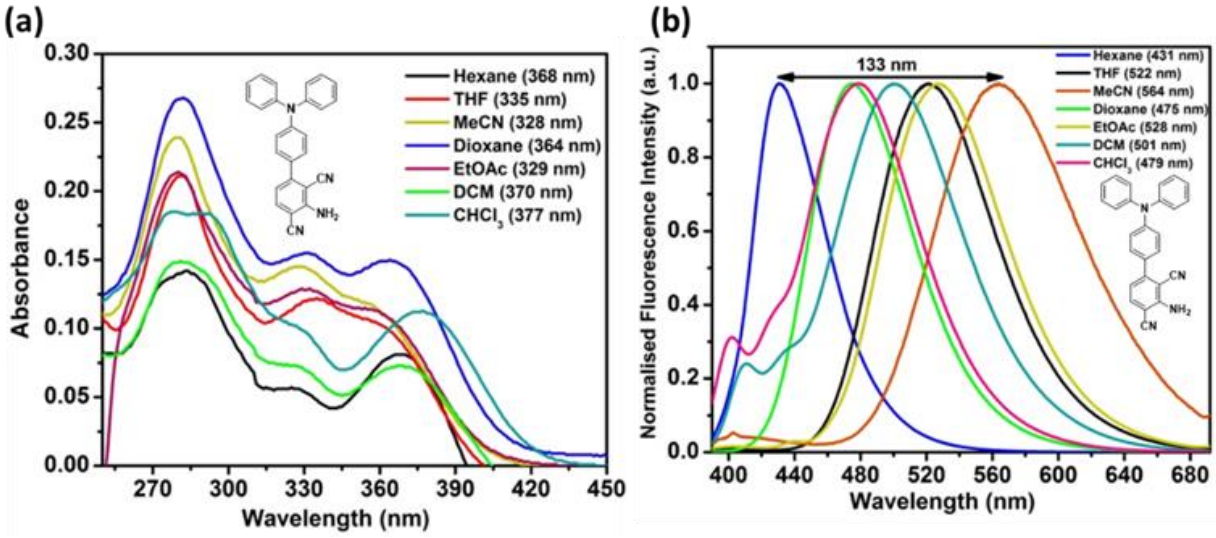

Figure 1.14 Solution state (a) absorption & (b) normalized emission spectra for **TPADCA** (10^{-5} M)

Higher Φ_f for methylated compound happens due to the stabilized excited singlet state, originated *via* C-H σ-π and/or C-C σ-π hyperconjugation.[57]

Next, the crystallochromic feature is examined for the PTZ-linked cousin molecules **MPTZDCA** and **PTZDCA**, which emit in a somewhat different region in the solid state (Figures. 1.18a-b) (see absorbance λ_{max} = 471 nm for **MPTZDCA** and λ_{max} = 520 nm for **PTZDCA** (Figure 1.16b). The maximum absorption at a higher wavelength for **PTZDCA** than **MPTZDCA** reflects a better donor-acceptor property in **PTZDCA**. The

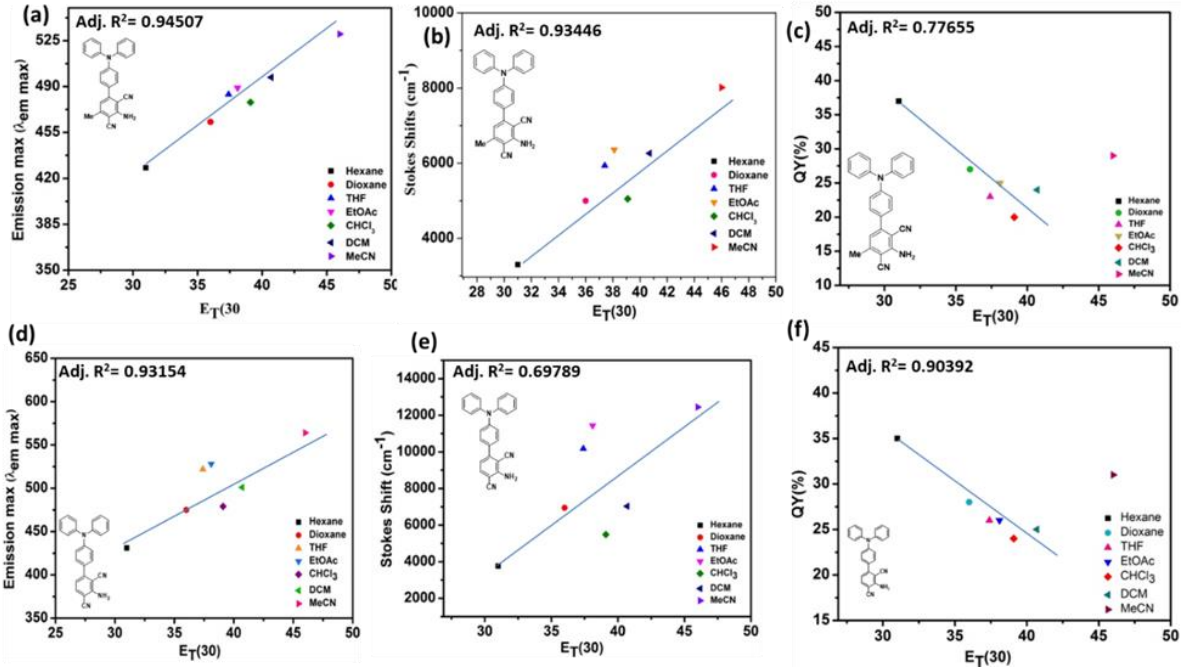

Figure 1.15 Solvatofluorochromic behavior for **MTPADCA**: (a)-(c) and **TPADCA**: (d)-(f)

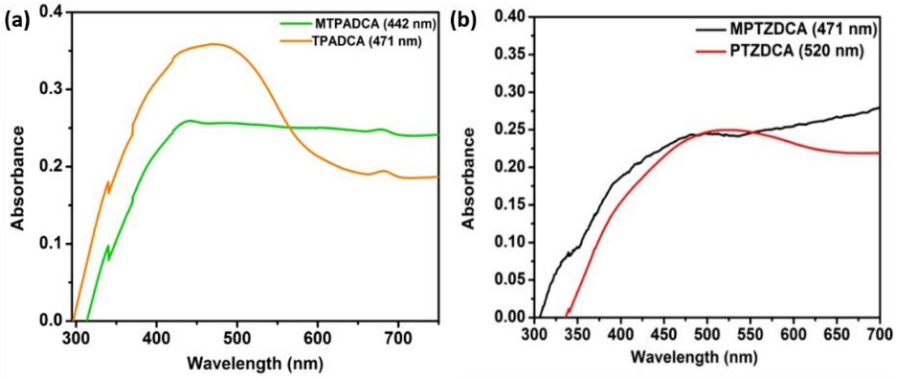

Figure 1.16 Solid state absorption spectra for (a) **TPA** cousin molecules (b) **PTZ** cousin molecules

electron-donating ability of the methyl group reduces the electron-deficient nature of the DCA ring. This effect is more recognized in **PTZ** analogs than **TPA**, even in the solution state. There is a substantial difference in the solvatofluorochromic behavior between these two compounds. Both π-π* and ICT bands are observed in absorption spectra, and the emission spectra appear as vibronic-structured bands (See Figures. 1.19-1.21 and Table 1.4 for details). The polar solvents open both LE and CT states to emit, but no change in the ground state as indicated in the absorption spectra (Figures. 1.19a and 1.20a). Thus, different emissions from both solid and solution states cannot be considered crystallochromic molecules. The weaker Φ_f for these PTZ molecules is possibly due to the

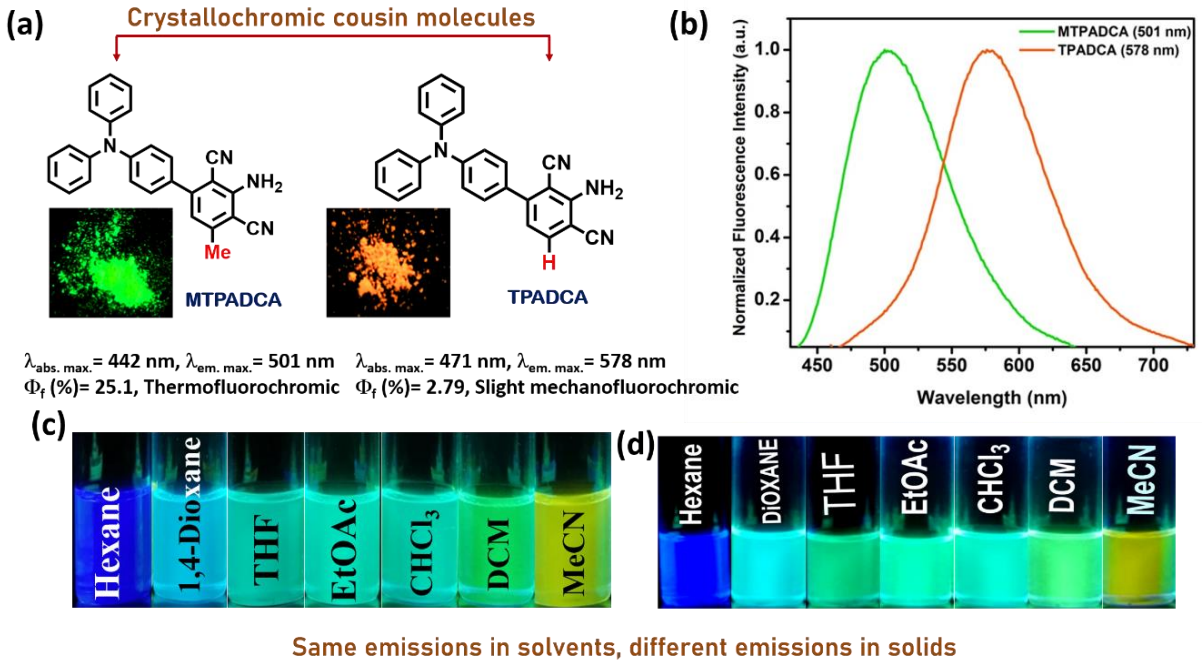

Figure 1.17 (a) High contrast in solid-state emission between **MTPADCA** and **TPADCA** with related emission parameters. (b) The difference in the emission spectra. Solvatofluorochromic similarity between (c) **MTPADCA** and (d) **TPADCA**.

Table 1.3 Comparison Table of emission in solution state for **MTPADCA** & **TPADCA**

Solvent [$E_T(30)$]	λ_{abs} (nm) **TPADCA**	λ_{abs} (nm) **MTPADCA**	$\lambda_{em.}$ (nm) **TPADCA**	$\lambda_{em.}$ (nm) **MTPADCA**	Relative Φ_f (%) **TPADCA**	Relative Φ_f (%) **MTPADCA**
Hexane (31)	368	374	431	428	35	37
1,4-Dioxane (36)	364	376	475	463	28	27
THF (37.4)	335	376	522	484	26	23
EtOAc (38.1)	329	373	528	489	26	25
$CHCl_3$ (39.1)	377	385	479	478	24	20
DCM (39.6)	370	379	501	497	25	24
MeCN (45.6)	328	372	564	530	31	29

heavier sulfur atom and movement of the *N*-substituted long alkyl chain that drives the molecular relaxation from an excited state, preferably through non-radiative channels.[58]

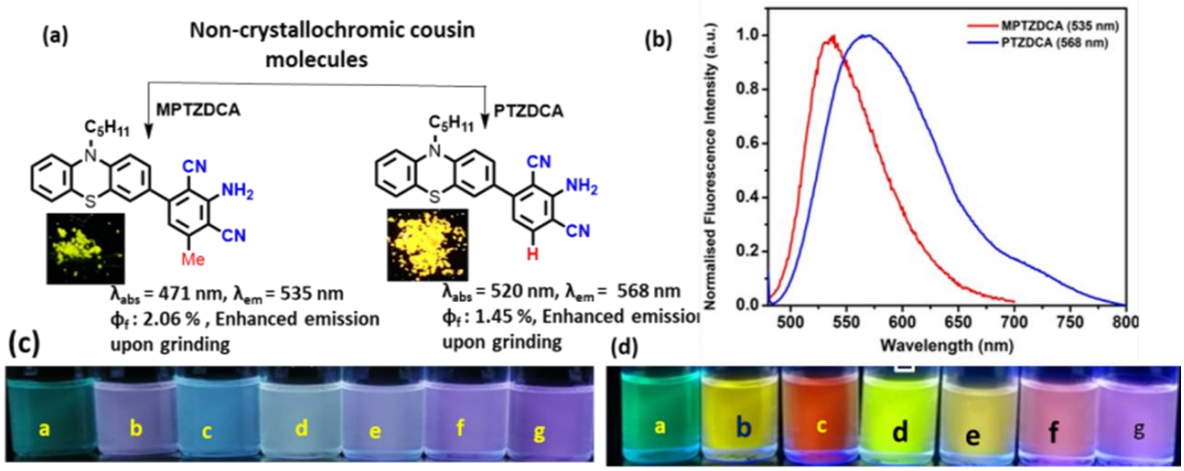

Figure 1.18 (a) Solid-state emission between **MPTZDCA** and **PTZDCA** with related emission parameters. (b) The difference in the emission spectrum. Solvatofluorochromic difference between (c) **MPTZDCA** and (d) **PTZDCA**. Concentration taken (10 μM) (respective absorbances are given in next figures)

Although the enhanced solid-state Φ_f for **MPTZDCA** than that of **PTZDCA** is distinguished as in TPA analogs, the methyl effect is relatively trivial here. However, prominent solvatofluorochromic behavior for nonmethylated analogs (only **PTZDCA**) indicates a somewhat better solvent-polarity-induced change in the dipole moment between excited and ground state, including the excited state orientation (Figure. 1.18d and Figures. 1.19-1.21). Hence, TPA cousins are only crystallochromic but interestingly, all of these TPA and PTZ cousins are good DSEgens[59] owing to their finer ability to emit both in solid and solution state (Figures. 1.17 and 1.18).

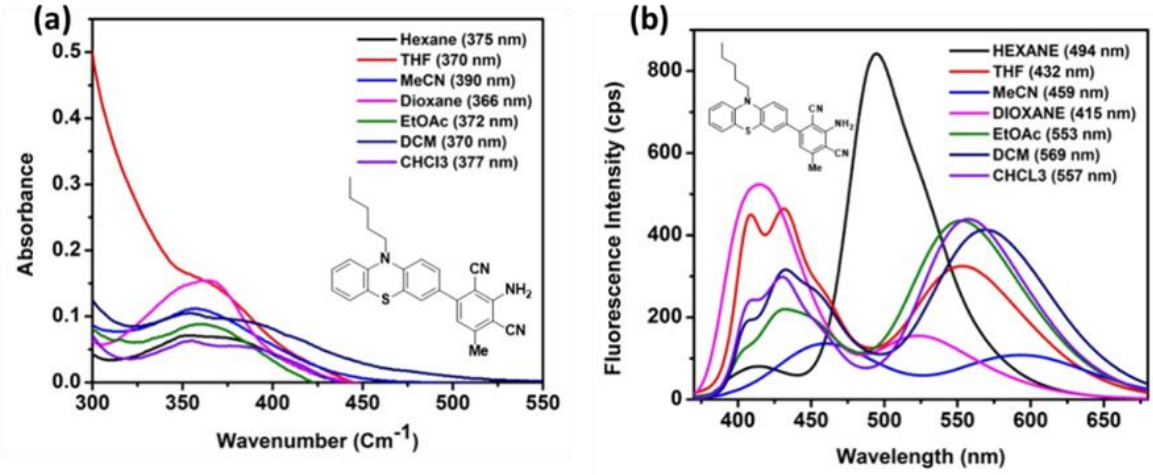

Figure 1.19 Solution state (a) absorbance & (b) emission of **MPTZDCA** (10^{-5} M)

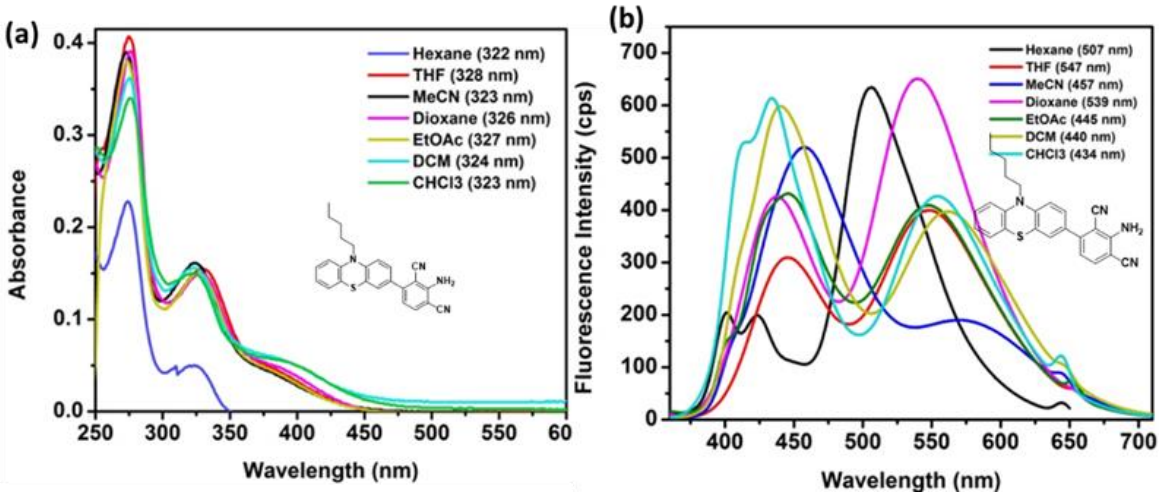

Figure 1.20 Solution state (a) absorbance & (b) emission of **PTZDCA** (10^{-5} M)

1.3.4.2 Stimuli-responsive properties in solids

All the solid-state emitters were individually tested for stimuli-responsive properties. Green-emitting **MTPADCA** crystals displayed a reversible hypsochromic shift of 42 nm (blue-emission, Figure 1.22a) by heating at 180 °C. While monitoring the temperature, the green emission was switched to blue after heating at 155 °C for 3-5 min but immediately regained the green-emitting feature at 30 °C. Finally, heating at 180 °C for the same duration, the change from green to blue-emission became permanent. Green emission could be reverted only after spraying with dichloromethane and subsequent evaporation.

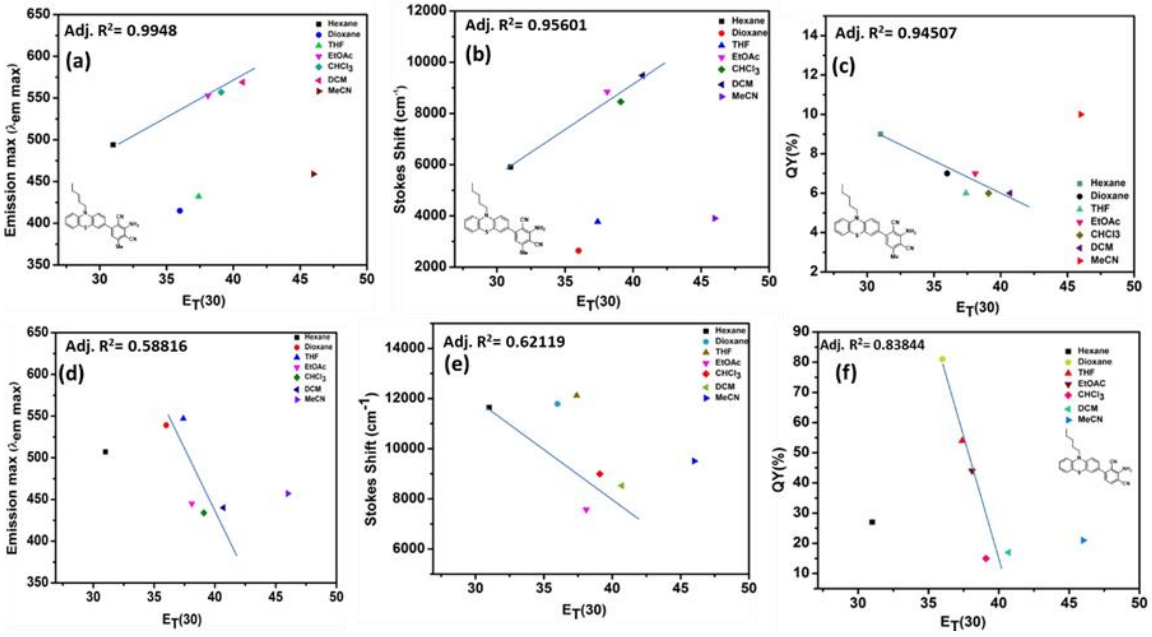

Figure 1.21 Solvatofluorochromic behavior for (a)-(c) **MPTZDCA** and (d)-(f) **PTZDCA**

Only the exposure to DCM fumes did not return the original emission, indicating the requirement of recrystallization after dissolution.

Table 1.4 Comparison table specifying emission in solution state for **MPTZDCA** & **PTZDCA;** the relative quantum yields (Φ_f) are reported here with a standard of coumarin-53B as a reference

Solvent (E_T30)	$\lambda_{abs.}$ (nm) **PTZDCA**	$\lambda_{abs.}$ (nm) **MPTZDCA**	$\lambda_{em.}$ (nm) **PTZDCA**	$\lambda_{em.}$ (nm) **MPTZADCA**	Relative Φ_f (%) **PTZDCA**	Relative Φ_f (%) **MPTZDCA**
Hexane (31)	322	375	507	494	27	9
1,4-Dioxane (36)	326	366	539	415	81	7
THF (37.4)	328	370	547	432	54	6
EtOAc (38.1)	327	372	445	553	44	7
$CHCl_3$ (39.1)	323	377	434	557	15	6
DCM (39.6)	324	370	440	569	17	6
MeCN (45.6)	323	390	457	459	21	10

However, upon intense mechanical grinding in a mortar, there was no emission switching for **MTPADCA** (Figure 1.23a). Based on the literature, we expected conjugated TPA molecules to display MFC behavior.[60-62] Notably, high-contrast blue-shifted TFC (Thermofluorochromic) materials are sporadic.[63-65] Contrarily, **TPADCA** did not exhibit any TFC behavior as it melts at ~70 °C but displayed slightly reversible (upon solvent fuming) mechanofluorochromism (10 nm blue-shift upon grinding, Figure 1.23b) with enhanced FL-intensity (MIEE effect, Figure 1.23b). Thus, we identified the difference in the stimuli-responsive features for these crystallochromic cousin molecules. The methyl group's presence offered a different molecular conformation, electronic effect, and packing pattern (as revealed by crystal structure), and such a small structural change could make this magic.

Interestingly, neither **MPTZDCA** nor **PTZDCA** exhibits impressive fluorescence-switching under thermal or mechanical stimuli. Upon grinding, we find a slight enhancement in the emission (3 times rise in Φ_f; Figure 1.24a) with 5 nm redshift for **MPTZDCA** and two times enhancement in Φ_f for **PTZDCA** with 9 nm blue-shift (Figure 1.24b).

Typically, the fluorescence intensity is quenched under mechanical grinding due to excimer formation.[64] The MIEE effect offers promising optical pressure-sensing devices

and is considered early-stage research.[65] Therefore, all the stimuli-responsive photophysical properties are enclosed in the following table 1.5 for a comparative outlook.

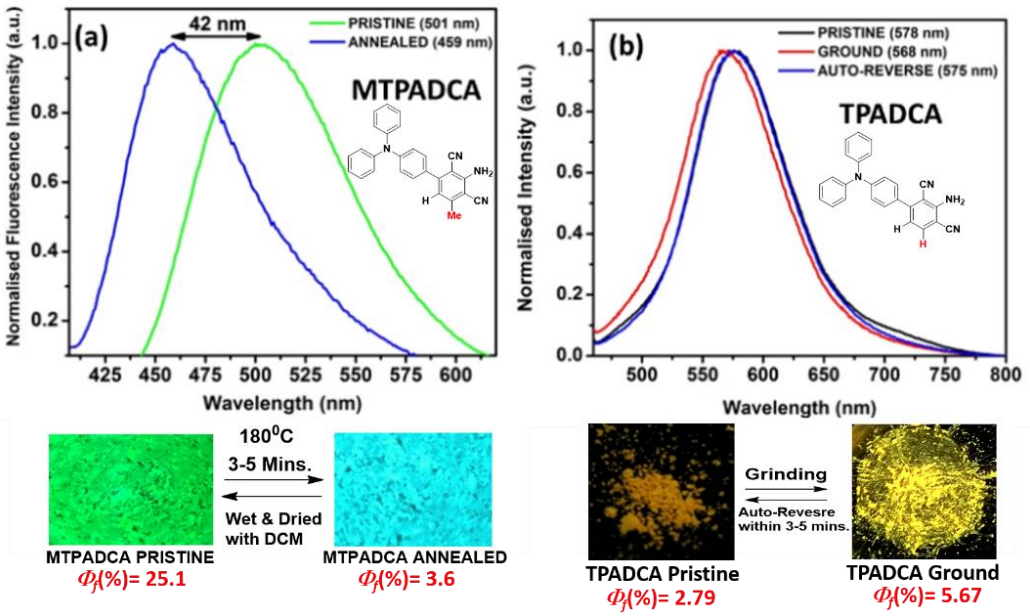

Figure 1.22 (a) TFC behavior of **MTPADCA** (b) MFC behavior of **TPADCA.** The images are taken after irradiation with a 365 nm UV lamp. Error in absolute Φ_f measurement is within ~ (±)2 %. λ_{ex} = 442 nm (**MTPADCA**) and 471 nm (**TPADCA**).

1.3.4.3 Frontier Molecular Orbitals study through DFT (Density Functional Theory)

Frontier molecular orbitals were determined using the density functional theory with a 6-31G(d,p) level for **MTPADCA** and **TPADCA** molecules with an input of crystal information file.

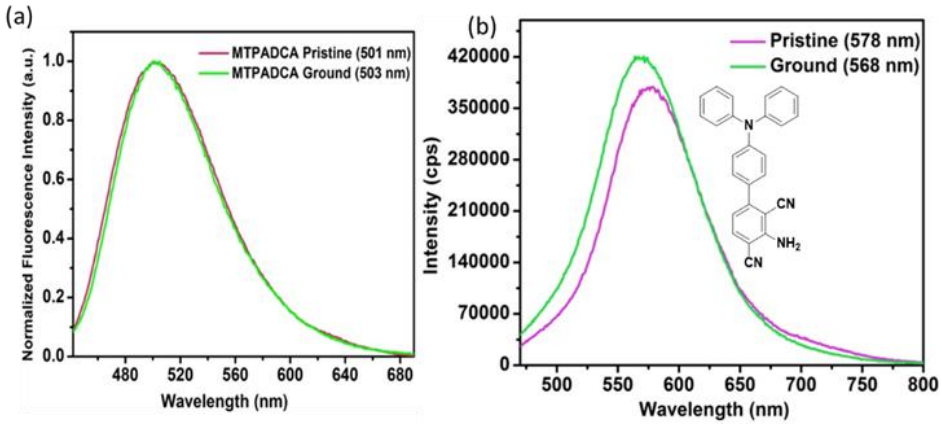

Figure 1.23 Fluorescence spectra of (a) **MTPADCA** under stimuli λ_{ex} = 442 nm (b) MIEE-effect of **TPADCA;** λ_{ex} =471 nm

The highest occupied molecular orbital (HOMO) distribution was mainly associated with the TPA core and partly with DCA moiety (Figure 1.25).

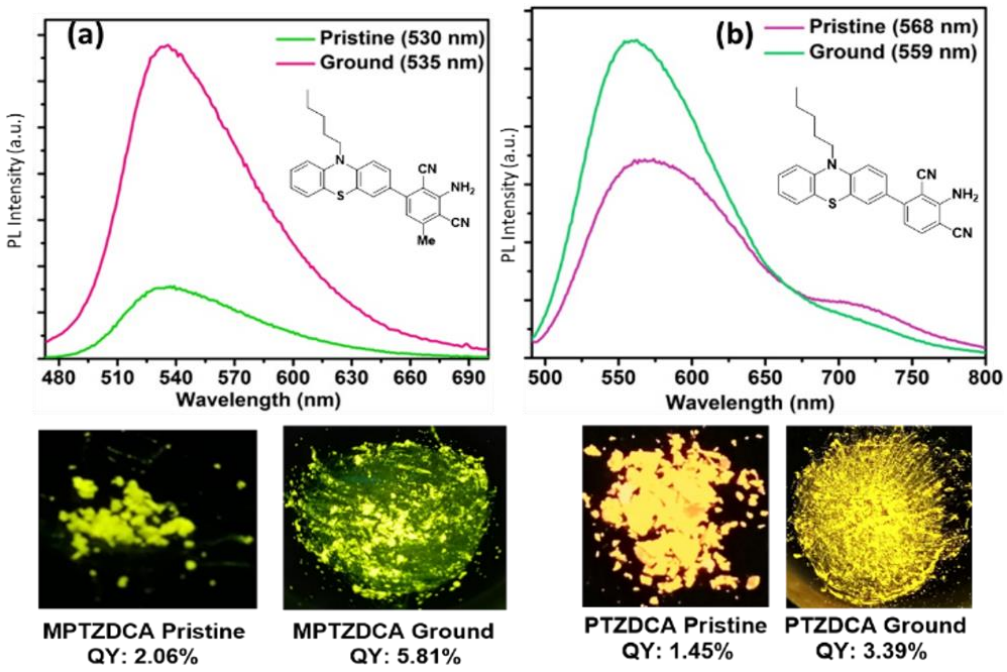

Figure 1.24 Mild MIEE-effect of (a) **MPTZDCA** and (b) **PTZDCA**. The image is taken under a 365 nm UV lamp. Error in absolute [Φ_f measurement is within ~ (±)2 %; λ_{ex} = 471 nm (**MPTZDCA**) and 520 nm (**PTZDCA**)].

The theoretical study revealed that the HOMO-LUMO gap (Table 1.6) is lower for **TPADCA** (5.68 eV) than **MTPADCA** (5.73 eV), and it harmonized well with the observed photophysical properties, especially with the bathochromic shift and weaker Φ_f.

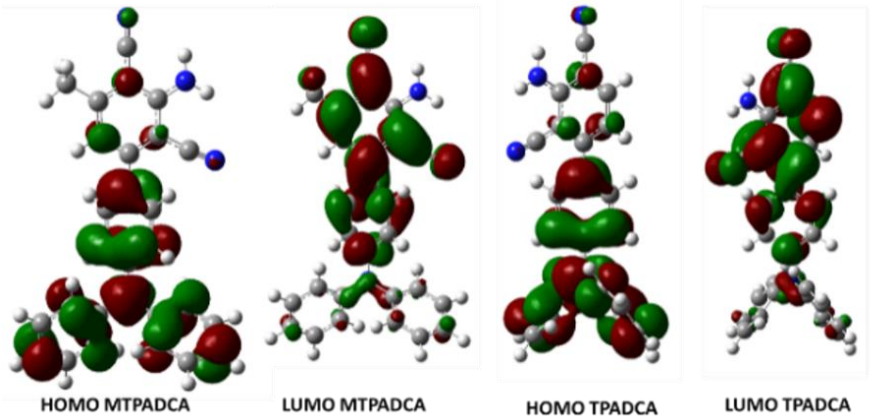

Figure 1.25 HOMO and LUMO for **MTPADCA** and **TPADCA**

The DCA part's contribution to constructing HOMO was slightly better for **MTPADCA** than **TPADCA**, possibly related to an electron-donating methyl group. The lowest

unoccupied molecular orbital (LUMO) is majorly built with an electron-deficient DCA core, but the TPA arms contribution is also noteworthy. For such a twisted molecule, a completely pure CT transition is difficult. An inter-crossed excited state consisting of LE and CT state is anticipated from such a system.[66]

Table 1.5 Stimuli-responsive photophysical properties at a glance

Compounds	λ_{ex}(nm) Pristine	λ_{em}(nm)/ Φ_f(%) (Pristine)	λ_{em}(nm)/ $\Phi_{f(\%)}$ (Ground)	λ_{em} (nm)/ $\Phi_{f(\%)}$ (Annealed)	λ_{em}(nm) Solvent treated and dried
MTPADCA	442	501/25.1	503/25.5	459/3.6	502
TPADCA	471	578/2.79	568/5.67	-	575
MPTZDCA	471	530/2.06	535/5.81	-	531
PTZDCA	520	568/1.45	559/3.39	-	567

1.3.4.4 X-ray diffraction studies: Molecular structure and packing modes

The best way to determine the crystallochromic and MFC behavior is to analyze their molecular structure, including the molecular packing pattern. The powder X-ray diffraction (PXRD) studies can also support the observed difference in the order of molecular arrangement emission-switching for pristine and annealed/ground samples.

Table 1.6 HOMO and LUMO for **MTPADCA** and **TPADCA** obtained from DFT studies with CAMB3LYP 6-31g (d,p) basis set.

Molecules	Dipole moment (D)	HOMO (eV)	LUMO (eV)	Gap (eV)	λ_{abs}	λ_{em}
MTPADCA	4.482	-6.774001926	-1.045733486	5.73	442	501
TPADCA	4.5698	-6.814819002	-1.138252192	5.68	471	578

The PXRD patterns for as-obtained **MTPADCA** and **TPADCA** solids indicated a much higher crystallinity for **MTPADCA** than for **TPADCA** (Figure 1.26a). The non-

crystallinity nature of **TPADCA** created trouble in generating the crystal for SCXRD studies. Before and after thermal stimuli at 180 °C, we found numerous sharp and intense diffractions for **MTPADCA** (Figure 1.26b). However, the disappearance of a few peaks from the pristine and the appearance of new peaks of the heated sample specifies the new facets, possibly formed from a new crystalline state.

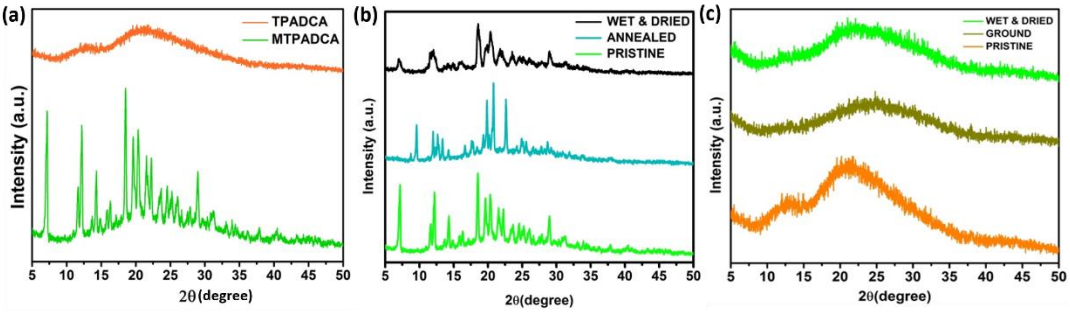

Figure 1.26 The PXRD pattern of (a) **MTPADCA** and **TPADCA;** (b) **MTPADCA** pristine after annealing at 180 °C.

Thus, the change in emission behavior had originated from a newly formed molecular crystalline arrangement developed on annealing at 180 °C. The original diffractions began reappearing after spraying DCM and subsequent drying (Figure 1.26b). It proved the reversible TFC nature of **MTPADCA.** Further, a minor change in the broad PXRD pattern of **TPADCA** could validate slight MFC behavior (Figure 1.26c).

Molecular structures of green and orange-emitting materials are examined in detail to provide a better understanding. The PXRD patterns (Figure 1.26a) reflect the strong diffractions from **MTPADCA** (crystalline nature) but weak and broad diffractions from **TPADCA** (amorphous nature). Thus, the crystals are grown for methylated analogs much easier than the nonmethylated ones. Both the compounds **MTPADCA** and **TPADCA** crystallize in a monoclinic system ($P2_1/c$ space group) with a twisted molecular conformation and a difference in the significant torsion angle of ~2-4°. Such a difference in torsion angle can induce molecular twisting to achieve a different molecular packing and result in diverse emission behavior.[67-69]

The twisted molecular structure of **MTPADCA** with primarily seven weak intermolecular interactions (Figure 1.27a π···π, CH···π, N···H, etc. see Table 1.7) facilitates a strong molecular packing. However, thermal energy can destroy a few weak intermolecular interactions and reorganize the molecular packing to reach a new crystalline state with relatively weaker π- conjugations to favor higher energy light

emission. In contrast, the twisted molecular conformation of **TPADCA** allows mainly two intermolecular interactions (Figure 1.27b CH...π and N...H only, Table S5) to build the crystal structure. All the crystal data and parameters were tabulated in Table 1.2.

These few interactions are accountable for imposing an amorphous nature in this sample and assisting the molecular conformation change upon grinding to emit slightly different wavelengths. This difference in crystal packing was also reflected significantly in the melting point difference of these crystals. With a strong molecular packing, **MTPADCA** melted at ~207 °C, while **TPADCA** melted at ~70 °C because of weaker crystal packing. The methyl group's effect is also detected in the FT-IR -C≡N stretching, which shows a strong **TPADCA** signal at 2217 $cm^{-1,}$ and relatively broad signals appear at 2230 cm^{-1} in **MTPADCA.** Such a difference suggests that the methyl group can enable two cyano groups' vibration at a slightly different frequency. Thus, the variance (Figure 1.28) in cyano groups is more significant in **MTPADCA,** while it is meager for **TPADCA**.

A relatively more substantial N···H interaction in **TPADCA** than **MTPADCA** can also be a result of this methyl effect and subsequent difference in solid-state emission.[70,71] Considering the plane of only DCA moiety, the molecular sheets in **MTPADCA** are arranged in a slip stack (*J*-type herringbone packing) with a pitch angle of 24.8° with interlayer distances ranges from 0.86 Å to 4.27 Å, as shown in Figure 1.29. This slip-stack formation is driven by CN···HN intermolecular interactions.

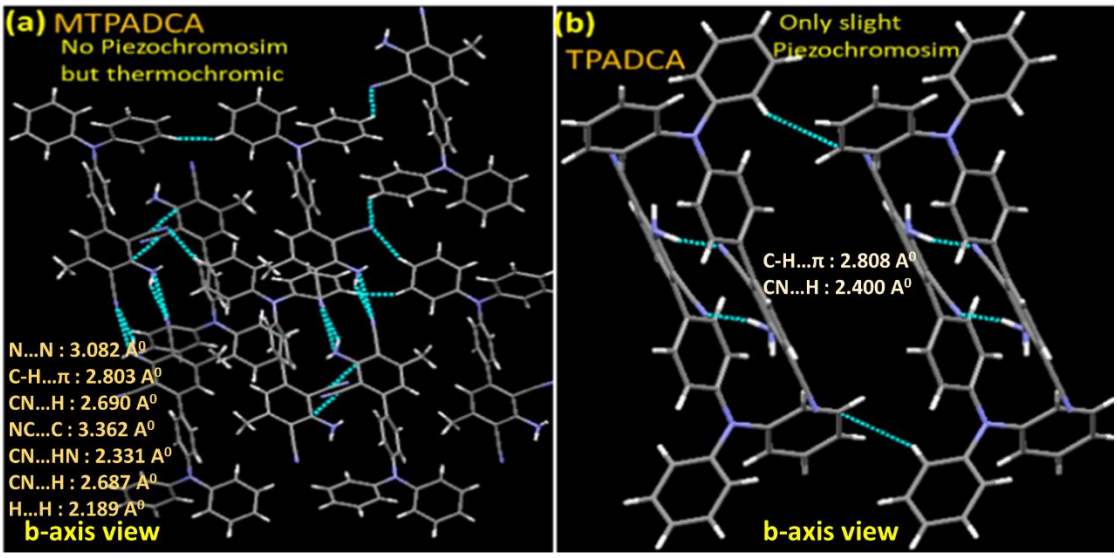

Figure 1.27 Crystal packing modes (b-axis view) of (a) **MTPADCA** and (b) **TPADCA** along with non-covalent interactions in Å.

Thermal annealing of **MTPADCA** must also have induced specific changes to this slip-stack with partial destruction of conjugation, leading to a blue-shifted thermochromism.

Table 1.7 Intermolecular interactions in **MTPADCA**, **TPADCA** & **MPTZDCA** crystals

Compounds	N...N (Å)	C-H...π (Å)	CN...HC (Å)	NC...C (Å)	C≡N...H$_2$N (Å)	H...H (Å)	S...H (Å)
MTPADCA	3.082	2.803	2.690, 2.687	3.362	2.331	2.189	
TPADCA	-	2.808	2.400	-	-	-	
MPTZDCA (19 interactions)	3.013	2.828, 2.882, 2.760 2.883 2.886, 2.876,2.883, 2.803	2.580, 2.706	3.369, 3.381, 3.323	2.422, 2.456	2.371 2.344	2.880

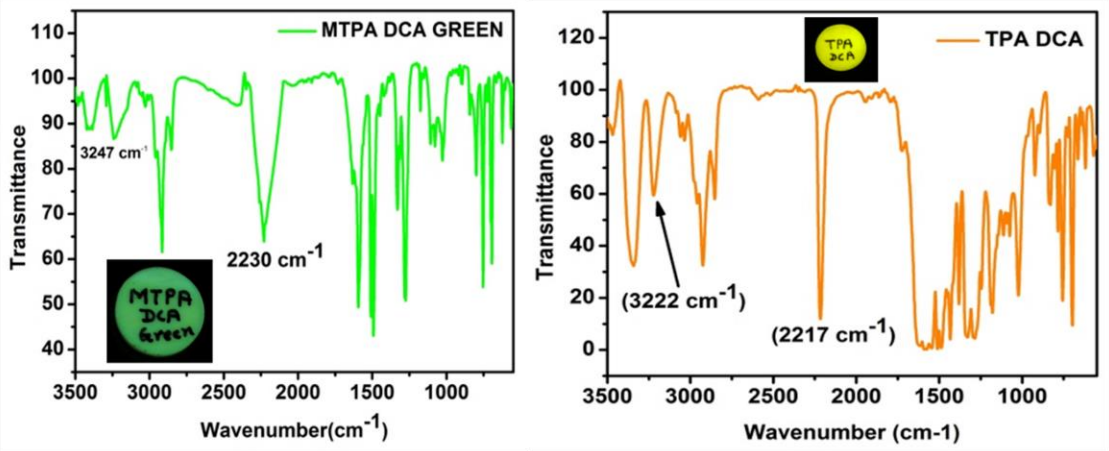

Figure 1.28 IR comparison of **MTPADCA** & **TPADCA** (Pellet of **g**round sample with KBr was photographed under UV-365 nm lamp and kept inset)

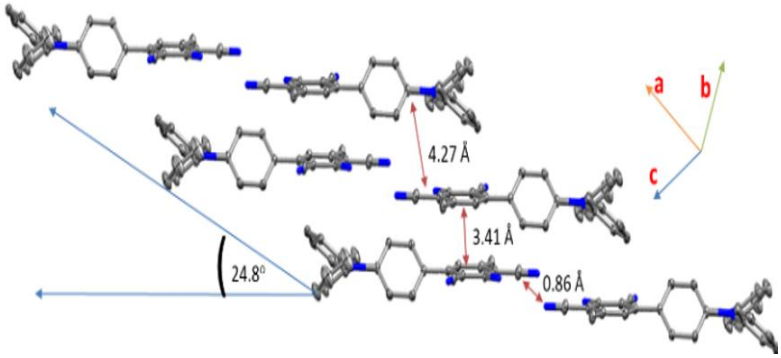

Figure 1.29 Crystal packing of **MTPADCA** with few interlayer distances and pitch angle considering dicyanomethylamine (DCA) core.

In the PXRD patterns, methylated **MPTZDCA** was crystalline, while the nonmethylated **PTZDCA** was amorphous (Figure 1.30a). This fundamental difference in the diffractogram could help understand the slight variation in emission behavior. The PXRD patterns of both **MPTZDCA** and **PTZDCA** remained almost unchanged upon grinding in a mortar (Figure 1.30 b-c). Thus, we found relatively higher solid-state absolute quantum yields for the methylated molecules for both **PTZ** and **TPA** systems due to more crystallinity/rigidity in the design and earlier stated.

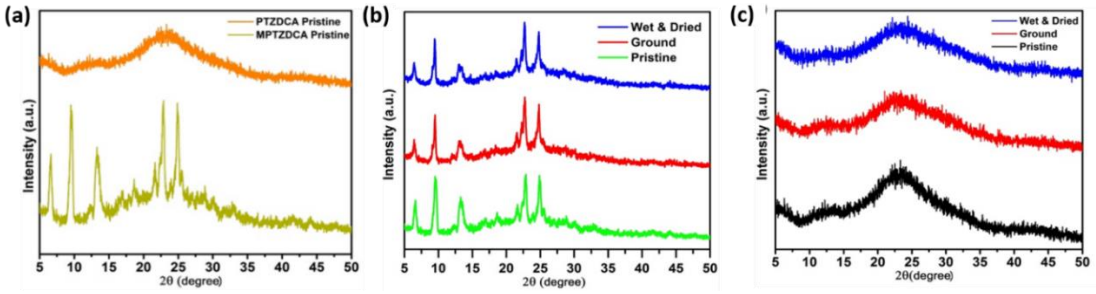

Figure 1.30 (a) PXRD pattern of **MPTZDCA & PTZDCA,** PXRD pattern of (b) **MPTZDCA**, and (c) **PTZDCA** after grinding the sample.

The IR spectrum was recorded as vibrational stretching plays a vital role in emission and crystal packing. A minute difference in the IR-stretching (Figure 1.31) for -C≡N (5 cm^{-1}) and 17 cm^{-1} in the -NH_2 stretching between **MPTZDCA** and **PTZDCA** indicate the difference in the bond strength.

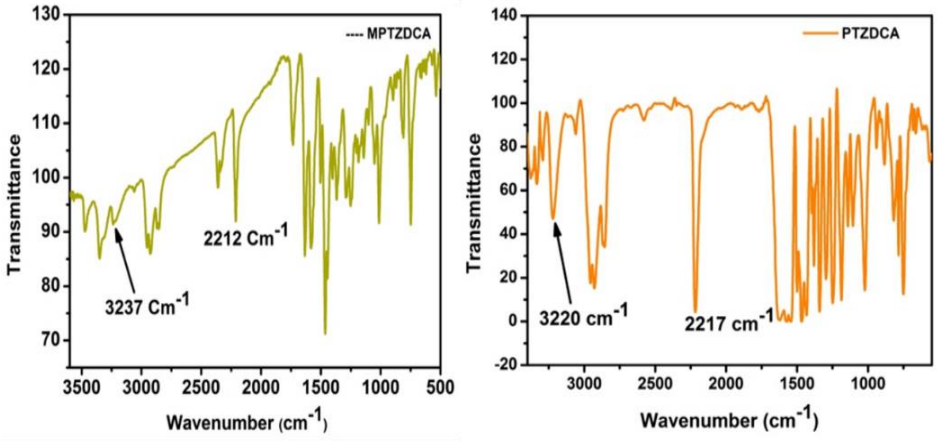

Figure 1.31 IR comparison of **MPTZDCA & PTZDCA**

The crystal structure is also determined for the compound **MPTZDCA,** but the crystal for the **PTZDCA** could not be generated, perhaps due to its highly amorphous nature. The compound **MPTZDCA** crystallizes in a triclinic system with a P1 space group.

Two independent molecules are in an asymmetric unit (Figure 1.32a), and the molecule is very much twisted as expected.

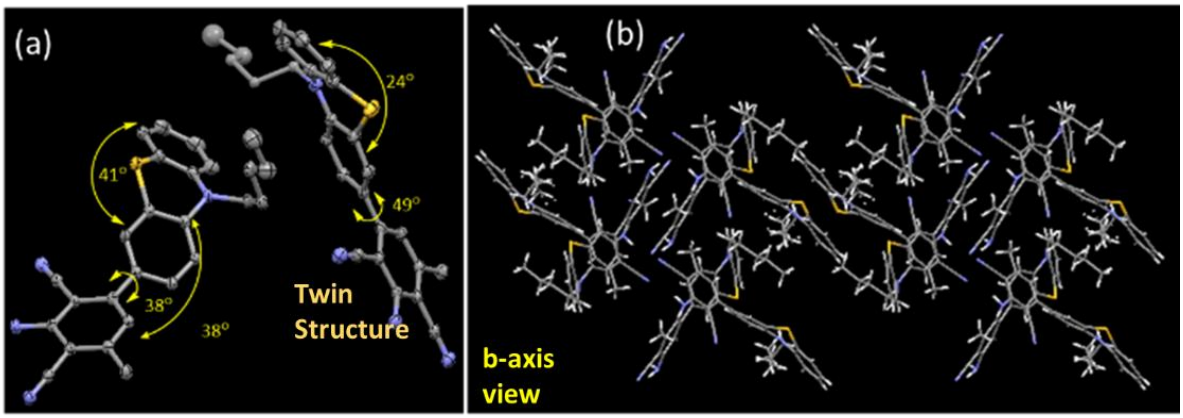

Figure 1.32 Molecular structure of (a) **MPTZDCA** with selected torsion angles and (b) packing diagram (b-axis view).

The DCA ring is titled 38°, and 49° torsion angles, almost similar to the torsion angle found for **MTPADCA**. The crystal packing exhibits a herringbone motif with many (nineteen) intermolecular non-covalent interactions (Figure 1.32b and Table 7). The solid-state fluorescence originated from an adopted twisted molecular structure. Such strong interactions ensure a tight crystal packing that cannot be disrupted *via* thermal or grinding stimuli.

A minute redshift (5nm, Figure 1.24) upon grinding can be ascribed due to the diminution of intermolecular distances upon grinding, increasing strong intermolecular coupling.[72] The grinding force can perhaps restrict intramolecular vibration by creating new interactions by distracting the existing ones from causing the suppression of non-radiative channels to increase the quantum yield.[65]

1.3.4.5 Lifetime measurement

A lifetime of the excited state was determined to estimate the radiative (K_r) and non-radiative rate constant (K_{nr}) for these compounds (Table 1.8, Figure 1.33) before and after applying stimuli to demonstrate the variation in the absolute quantum yield. The effect of a methyl group to enhance Φ_f was identified due to higher lifetime (τ) 1.84 ns with K_r/K_{nr}= 0.335 for **MTPADCA** than **TPADCA** (τ = 0.88 ns, K_r/K_{nr}= 0.029) and similar observation was with **MPTZDCA** (τ = 0.45 ns, K_r/K_{nr}= 0.021) than **PTZDCA** (τ = 0.07 ns; K_r/K_{nr}= 0.015) (Table 1.8, Figure 1.33). The annealed sample of **MTPADCA** had a much shorter lifetime (τ = 0.18 ns), and the K_{nr} value was relatively higher for the annealed sample (53.0×10^8 s^{-1}, K_r/K_{nr}= 0.037) than the pristine solid (4.06×10^8 s^{-1}, K_r/K_{nr} = 0.335).

Thus, the reason for the reduction of quantum yield after annealing was further validated. The lifetime studies revealed a decay component (minor, Table 1.8) with a relatively higher lifetime of ~12.9 ns, indicating the formation of an excimer with relatively better excited-state stability. Further, the MIEE effect of **MPTZDCA** could also be elucidated with a substantial increase in $K_r = 7x10^8\ s^{-1}$ (τ = 0.08 ns, K_r/K_{nr} = 0.062) for ground sample in comparison to the pristine with $K_r = 0.46x10^8\ s^{-1}$ (τ = 0.45 ns, K_r/K_{nr} = 0.021). Similar lifetime parameters were also observed for **PTZDCA,** and the observed MIEE effect was confirmed.

1.3.4.6 DSC Studies

The TFC nature of **MTPADCA** was further supported by capturing the phase transition, as noticed in DSC measurement. As we found a quick emission color change starting at 155°C, we closely observed the DSC feature around the temperature range (Figure 1.34a). A clear endothermic peak at ~160°C is recognized in the DSC thermogram, which indicates a phase transition and is possibly associated with the TFC behavior. The DSC thermogram does not show a sharp melting transition, implying that the compound loses crystallinity after the initial phase transition.

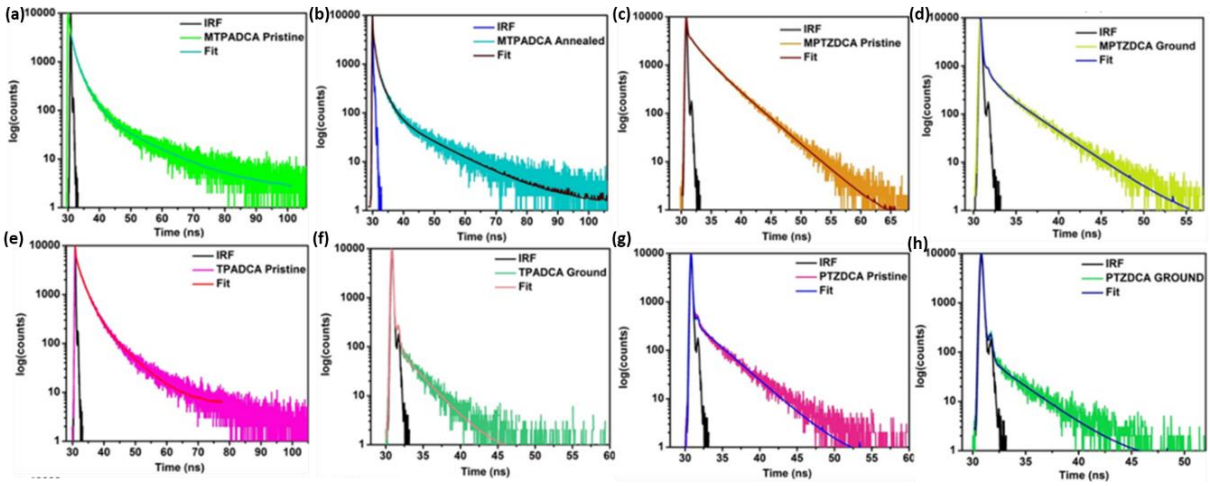

Figure 1.33 Life-time decay profiles for all the compounds as stated in the box.

Although a small signature appears at ~207 °C in the DSC profile, a sharp melting point at 207 °C is detected in the DTA (Differential Thermal Analysis) thermogram (Figure 1.34b).

Table 1.8 Lifetime data (ns) and the related parameters. $K_r = \Phi_f/\tau$; $K_{nr} = (1- \Phi_f)/\tau_f$

Compds	τ_1 (ns)	τ_2 (ns)	τ_3 (ns)	τ_4 (ns)	α_1	α_2	α_3	α_4	χ^2	τ (ns)	Φ_f (%)	$k_r(s^{-1}) \times 10^6$	$k_{nr}(s^{-1}) \times 10^6$
MTPADCA Pristine	2.838	12.993	0.848	-	0.336	0.027	0.637	-	1.173	1.844	25.11	136.171	406.128
MTPADCA Annealed	0.581	2.338	12.704	0.056	0.087	0.024	0.002	0.887	1.151	0.182	3.6	198.000	5300.000
TPADCA Pristine	2.118	0.223	6.821	-	0.239	0.729	0.031	-	1.197	0.883	2.79	31.597	1100.906
TPADCA Ground	0.649	0.039	2.669	-	0.001	.998	0.001	-	1.085	0.0417	5.67	1359.712	22621.103
MPTZDCA Pristine	1.742	4.078	0.081	-	0.059	0.066	0.874	-	1.035	0.445	2.06	46.292	2200.899
MPTZDCA Ground	0.93	3.638	0.049	-	0.011	0.007	0.983	-	1.103	0.083	5.81	700	11348.193
PTZDCA Pristine	0.049	3.222	-	-	0.995	0.005	-	-	1.065	0.067	1.45	216.417	14708.956
PTZDCA Ground	2.842	0.044	-	-	0.001	0.999	-	-	1.014	0.047	3.39	721.277	20555.319

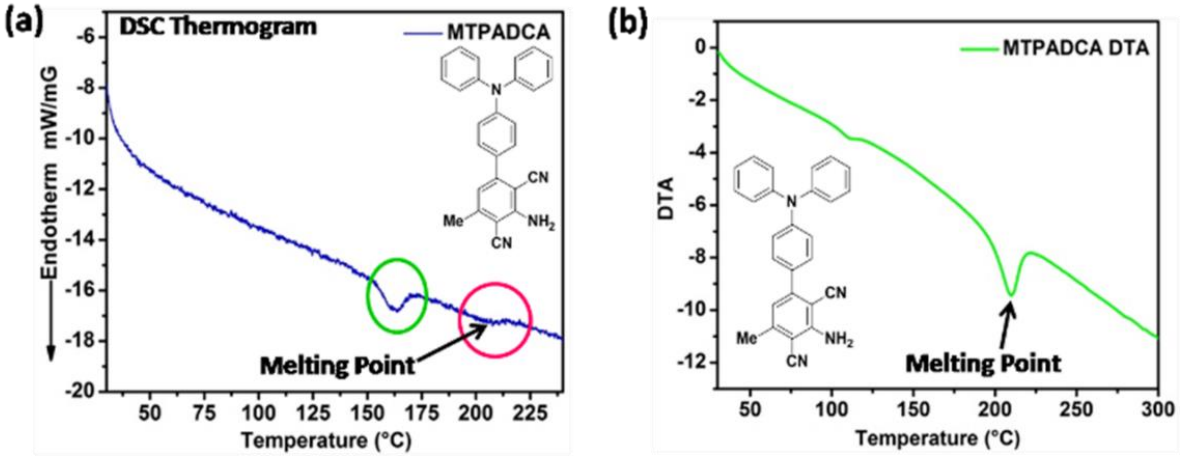

Figure 1.34 (a) DSC and (b) DTA thermogram for **MTPADCA**

The surface appeared to be smooth for **MTPADCA** and perforated for **TPADCA.** The investigation on the crystal surface of **MTPADCA** after heating at 180 °C revealed a rough and cracked surface, signifying a change in the supramolecular interactions in the crystal lattice after heating at 180 °C. It is pretty similar to the observed TFC property recognized by Prof. Park in 2010.[63] The cracked surface made some defects to facilitate fluorescence quenching. For the cracked surface, there will be many non-radiative paths generated to relax *via* a non-radiative pathway. Thus, a TFC behavior can also be anticipated from such surface morphology change.

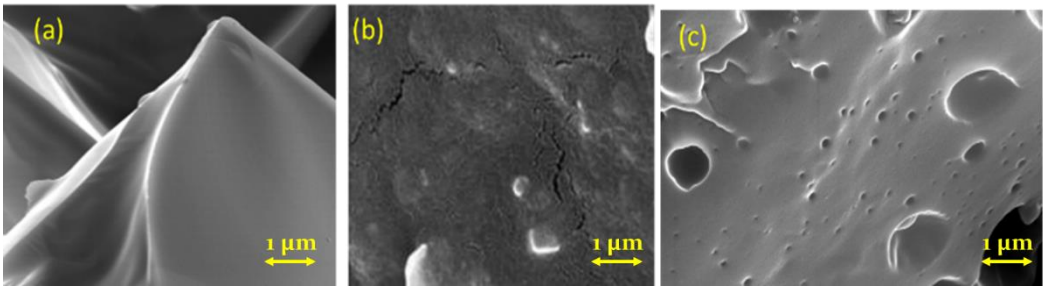

Figure 1.35 SEM images of the crystal surface morphology of (a) pristine **MTPADCA** (b) annealed **MTPADCA** (c) pristine **TPADCA.**

1.3.5 Applications of crystallochromic and dual-state emission behavior

1.3.5.1 Security-writing utilizing the phenomenon of crystallochromism

The crystallochromic nature of **TPADCA** cousins and the dual-state emission property of **TPADCA** were employed for reversible security writing and instant self-erasable writing with solvent on a polymer-blended platform. The **MTPADCA** (1 mg) was blended with 50 mg of **PMMA** (Poly(methyl methacrylate; most accessible and economical polymer), 500 µL of propylene carbonate (binder), and 500 µL of dichloromethane (DCM) and sonicated for half an hour. The resulting solution was allowed to dry on a Whatman paper in the air to afford an intense green-emitting platform (Figure 1.36a). A wooden pen nib was dipped into a DCM solution of **TPADCA** (1 mg in 2 mL) to write a few letters, such as **'CRYS',** on the green-emitting polymer matrix, which was not visible till drying. As **MTPADCA** and **TPADCA** emit different wavelengths in solid, the letters 'CRYS' could be distinguished (Figure 1.36b). The letters became again invisible upon spraying the DCM vapor because they both emit green in DCM (Figure 1.36c). The letters reappear on the DCM vapor's evaporation (Figure 1.36 d).

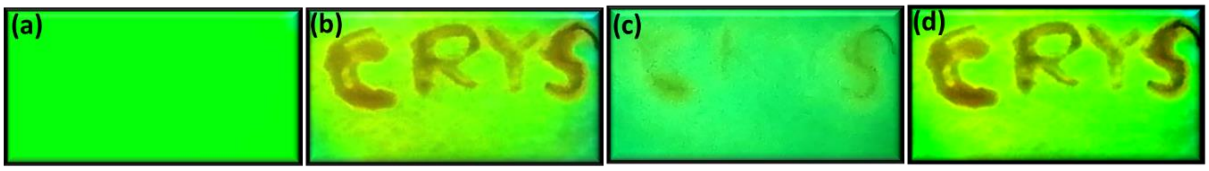

Figure 1.36 Security writing with **TPADCA** cousin molecules on the polymer matrix. (a) **MTPADCA** polymer matrix (b) **'CRYS'** is written with **TPADCA** solution and evaporated to dryness (c) exposed to DCM (d) reappearance of letters after solvent evaporation. Images are taken under 365 nm UV light.

1.3.5.2 Auto-erasable writing utilizing the phenomenon of dual-state emission

In addition, The DSEgen nature of **TPADCA** was employed for fast, auto-erasable security writing using solvent DCM. The Yellow-emitting polymer matrix of **TPADCA** was prepared like **MTPADCA**. Any letters written by DCM solvent were discernible through the naked eye. As **TPADCA** emits green in dichloromethane, the letters "DCM" appear green. The nearby write-up area also turns greenish due to the spreading of solvent, which can be avoided by covering the unwanted part. The letters disappeared as soon as DCM evaporated. Thus, the letters were erased fast and auto-reversible, making the polymer matrix glow with its original color (Figure 1.37).

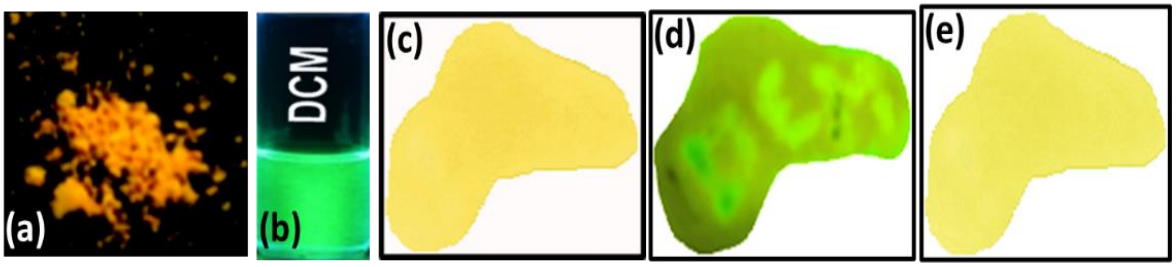

Figure 1.37 (a-b) Dual state emission of **TPADCA** (c) Polymer matrix of **TPADCA** (d) '**DCM**' is written with dichloromethane on the polymer matrix (e) Auto-reverse within 30 seconds.

1.4 Summary

This article provides a new class of stimuli-responsive and crystallochromic A-D-A type DSEgens combined with conformationally twisted, bulky TPA and PTZ-units along with a methyl group. Such cousin DCA molecules with or without methyl substituent are generated using a new protocol by varying the nature of bases. The difference in emission behavior could be identified just by a small structural change associated with the attachment of the methyl group or varying the cores like TPA or PTZ unit. There is a change in crystallinity and crystal packing pattern, resulting in different stimuli responses and the associated emissions. Such a modification of the molecular framework offers crystallochromic behavior for the TPA system only, not for the PTZ analogs, although these molecules' dual state emitting properties are noteworthy.

Moreover, TFC feature is noticed for **MTPADCA,** whereas **TPADCA** provides only slight blue-shifted MFC behavior. This fact is substantiated with variation in the PXRD pattern that indicates a generation of a new crystalline phase for **MTPADCA** upon heating

to enable fluorescence switching. Interestingly the DCA compounds without methyl groups **TPADCA/PTZDCA** appeared amorphous. The SCXRD studies depict the difference in crystal packing between **MTPADCA** and **TPADCA**. Under thermal stimuli, the non-covalent interactions are quickly reorganized and disturb the suitable slip stack to exhibit fluorescence switching. The **PTZDCA** systems do not exhibit stimuli-responsive behavior. However, relatively rare emission enhancement upon grinding for both **MPTZDCA** and **PTZDCA** molecules is recognized, and the strong and closed crystal packing partly supports the observation. Further, the facts are substantiated by DSC, lifetime studies, and also SEM images. The MIEE effect and the difference in fluorescence brightness are supported with K_r/K_{nr} parameters. Methyl plays a crucial role in this state and stimuli-dependent emission switching. Moreover, the demonstrated applications as security-writing have commended their future promises.

1.5. Experimental sections

The experimental methods and measurements or the necessary procedures are described in the '*Materials, General Conditions and Measurements*' part earlier.

1.6 Synthetic procedures with characterization detailing

A common procedure was followed for **MTPADCA**, **TPADCA,** and **PTZDCA**, although the stoichiometry and utilized chemicals were different as per the necessity.

1.6.1 Synthesis of MTPADCA (3-amino-4'-(diphenylamino)-5-methyl-[1,1'-biphenyl]-2,4-dicarbonitrile)

4-(Diphenylamino)- benzaldehyde (100 mg, 0.3658 mmol) was taken first in a round-bottom flask and was allowed to vacuum-dry for 5 min. Later, 10 mL of EtOH:H_2O solution (6:1) was added to it under N_2 atmosphere and this was stirred for another 5 min. Next, malononitrile (242 mg, 3.658 mmol) was introduced to this solution along with the base Et_3N (0.25 mL, 1.829 mmol) under the same inert conditions. The resulting solution was allowed to reflux for 1.5 h. The course of the reaction was monitored *via* checking with TLC, and after completion, the reaction mixture was worked-up three times with EtOAc:H_2O (20 mL, 3:1) solution. The combined organic layer was dried over Na_2SO_4, and the solution was evaporated. The crude product was made into a slurry with silica gel and subjected to column chromatography using 10% EtOAc/hexane (R_f = 0.33), followed by recrystallization

from DCM/hexane (3:1) to provide green crystals in pure form in 45% yield (66 mg). **m.p**.: 207–209°C; **IR** (KBr, in cm^{-1}): 3247, 2915 2230, 1592, 1506, 1493, 1332, 1274, 1107,1077, 1026; **^{1}H NMR** (400 MHz, $CDCl_3$): δ (ppm) 7.41–7.38 (m, 2H), 7.32–7.27 (m, 4H), 7.17–7.04 (m, 8H), 6.69 (s, 1H), 5.20 (s, 2H, –NH_2), 2.52 (s, 3H, CH_3); **^{13}C NMR** (100 MHz, $CDCl_3$): δ(ppm) 152.7, 149.6, 149.3, 147.5, 147.0, 142.5, 129.9, 129.5, 129.3, 125.4, 123.9, 121.7, 120.1, 116.4, 115.6, 95.8, 93.2, 87.2, 21.4; **HR-MS**: calcd. for $C_{27}H_{20}N_4$ 401.1761, found: 401.1751 $[M]^+$. The X-ray crystal structure was determined; **CCDC** 2062771.

1.6.2 Synthesis of TPADCA (3-amino-4o-(diphenylamino)-[1,1o-biphenyl]-2,4-dicarbonitrile)

Requierd chemicals and stoichiometry: 4-(diphenylamino)benzaldehyde (100mg, 0.3658mmol), EtOH:H_2O solution (6:1, 10 mL), malononitrile (242 mg, 3.658 mmol), K^{t}OBu (205 mg, 1.829 mmol); R_f=0.23 (20% EtOAc/hexane); yield: 55% (78 mg), **mp**: 69–72°C; **IR** (KBr, in cm^{-1}): 3222, 2926, 2217, 1623, 1590, 1576, 1543, 1484, 1433, 1382, 1332, 1291, 1181, 1020; **^{1}H NMR** (400 MHz, $CDCl_3$): δ(ppm) 7.42–7.38 (m, 2H), 7.34–7.29 (m, 4H), 7.20-7.17 (m, 4H), 7.14–7.01 (m, 6H), 5.57(s, 2H); **^{13}C NMR** (100 MHz, $CDCl_3$): δ (ppm) 161.0, 160.3, 150.3, 146.7, 129.7, 129.5, 129.4, 129.3, 125.9, 125.2, 124.8, 124.3, 124.2, 120.4, 116.2, 115.1, 86.2, 83.5; **HR-MS**: calcd. for $C_{26}H_{18}N_4$ 386.1651, found: 387.1764 $[M+H]^+$. The X-ray crystal structure was determined; **CCDC** 2062770.

1.6.3 Synthesis of MPTZDCA (2-amino-4-methyl-6-(10-pentyl-10H-phenothiazin-3-yl) isophthalonitrile)

10-pentyl-10H-phenothiazine-2-carbaldehyde (100 mg, .34 mmol, 1 equiv.), malononitrile (118 mg, 1.78 mmol, 5.24 equivalents), were dissolved into 10 ml of ethanol: Water (6:1) medium under N_2 flow and were allowed to stir for 10 minutes. Later the reaction went on reflux at 90°C with continuous stirring up to 45 minutes under this inert condition. The due course of the reaction was monitored by checking TLC by eluting it into 10% Ethyl acetate-hexane medium. Once the aldehyde was consumed fully to form an intermediate 2-((10-pentyl-10H-phenothiazin-3-yl) methylene) malononitrile compound, the reaction was permitted to come down to room temperature. After that triethylamine (TEA, 0.24 ml, 1.7 mmol, 5 equivalent) and malononitrile (118 mg, 1.78 mmol, 5.24 equivalents) were added again to the same reaction mixture without changing

the pot under inert environment and the reaction was let to proceed on refux (90°C) once again for another 15 minutes. Next on TLC checking with 10% the formation of a new yellow fluorescent spot was confirmed at R_f = 0.3. The resulting reaction mixture was quenched with water, extracted with ethyl acetate (15 mL×2), and washed with brine. The organic layer was dried over anhydrous sodium sulphate and was concentrated. The resulting highly fluorescent molecule was separated by performing a 120 mesh silica gel column chromatography with 8% ethyl acetate-hexane solvent mixture. Next the separated compound was dried under a high vacuum and put to grow crystal using 30% ethyl acetate-hexane solvent medium. After completion of crystallization the solution was decanted and the compound was received as orange yellow crystal, **mp.**: (140-142 °C); yield 63% (91 mg); IR (ν cm^{-1}, with KBr): 3237, 2212, 1733, 5 1634, 1582, 1464, 1364, 1014; **^{1}H NMR** (400 MHz, $CDCl_3$): δ 7.37 (1H, dd, *J*=8.2 Hz, *J*=1.8 Hz), 7.24 (1H, d, *J*=2 Hz), 7.18-7.10 (2H, m), 6.95-6.06 (3H, m), 6.64 (1H, s), 5.24 (2H, s), 3.86 (2H, t, *J*= 8.4 Hz), 2.49 (3H, s), 1.82 (2H, q), 1.46-1.34 (4H, m), 0.90 (3H, t, *J*= 8.4 Hz); **^{13}C NMR** (100 MHz, $CDCl_3$): δ 152.7, 148.7, 147.6, 146.6, 144.4, 131.3, 127.6, 127.5, 127.4, 127.0, 125.3, 123.9, 122.9, 119.9, 116.2, 115.6, 115.5, 115.0, 96.0, 93.2, 47.6, 29.3, 29.2, 26.5, 24.5, 22.4; **HR-MS**: m/z: $[M]^+$ calcd. for $C_{26}H_{24}N_4S$, 424.1722, found 424.1714. The X-ray structure is determined for this compound. **CCDC** Number: 2041739.

1.6.4 Synthesis of PTZDCA (2-amino-4-(10-pentyl-10H-phenothiazin-3-yl)isophthalonitrile)

Requierd chemicals and stoichiometry: 10-pentyl-10Hphenothiazine-3-carbaldehyde (100mg, 0.3362 mmol), EtOH:H_2O solution (6:1, 10 mL), malononitrile (222 mg, 3.362 mmol), NaOH (67mg, 1.681 mmol); R_f=0.19 (20% EtOAc/hexane); yield 62% (86 mg, amorphous orange-yellow solid); **mp:** 80–82°C. **IR** (KBr, in cm^{-1}): 3220, 2956, 2928, 2854, 2217, 1622,1576, 1545, 1467, 1432, 1343, 1250, 1184, 1025; **^{1}H NMR** (400 MHz, $CDCl_3$): δ (ppm) 7.35 (dd, *J*=8.4, 1.6Hz), 7.29(d, *J*= 1.6Hz), 7.17-7.09 (m, 3H), 6.95–6.85 (m, 4H), 5.58 (s, 2H), 3.88 (t, *J*= 7.3Hz, 2H), 1.87 (quin, *J*= 7.2Hz, 2H), 1.39–1.30 (m, 4H), 0.93 (t, *J*= 7.2Hz, 3H); **^{13}C NMR** (100 MHz, $CDCl_3$): δ(ppm) 160.9, 159.5, 152.5, 147.8, 144.0, 127.9, 127.6, 127.4, 127.2, 127.0, 125.2, 123.9, 123.0, 115.9, 115.6, 114.9, 114.8, 86.2, 83.6, 83.5, 47.7, 29.1, 26.5, 22.4, 14.3; **HR-MS**: calcd. for $C_{25}H_{22}N_4S$ 410.1565, found: 411.1638 $[M+H]^+$.

1.7 References

1 J. Griffiths, M. Lockwood and B. Roozpeikar, ***J. Chem. Soc., Perkin Trans. 2***, 1977, 1608-1610.

2 H. B. Borate, A. S. Kudale and S. G. Agalave, ***Org. Prep. Proced. Int.***, 2012, **44**, 467-521.

3 V. D. Dyachenko and A. N. Chernega, ***Russian J. Org. Chem.***, 2006, **42**, 567-576.

4 J. Carlsson, L. Yoo, Z. G. Gao, J. J. Irwin, B. K. Shoichet and K. A. Jacobson, ***J. Med. Chem.***, 2010, **53**, 3748-3755.

5 C. X. Hang, Z. Zujin, L. Yang, L. Ping and W. Y. Guang, ***Chemistry Lett.***, 2008, **37**, 570-571.

6 P. Kolek, K. Pirowska, M. Gora, B. Kozik and J. Najbar, ***Chem. Phys.***, 2002, **285**, 55-72

7. M. Jozefowicz, M. Aleksiejew, J. R. Heldt, A. Bajorek, J. Paczkowski and J. Heldt, ***Chem. Phys.***, 2007, **338**, 53-61.

8 G. Angulo, G. Grampp, J. Grilz, P. Jacques, S. Landgraf and A. Rosspeintner, ***J. Photochem.Photobiol., A: Chemistry***, 2008, **199**, 204-210.

9 M. Jozefowicz, J. R. Heldt, A. Bajorek and J. Paczkowski, ***J. Photochem. Photobiol., A: Chemistry***, 2008, **196**, 38-43.

10 M. Zahid, A. Rosspeintner, G. Angulo, G. Grampp, P. Jacques and A. Mansha, ***J. Photochem.Photobiol., A: Chemistry***, 2011, **220**, 54-63.

11 Prof. Dr. H. Kurreck and Dr. M. Huber, ***Angew. Chem. Int. Ed.***, 1995, **34**, 849-866.

12 G. Asato, P. K. Baker, R. T. Bass, T. J. Bentley, S. Chari, R. H. Dalrymple, D. J. France, P. E. Gingher, B. L. Lences, J. J. Pascavage, J. M. Pensack and C. A. Ricks, ***Agri. Biol. Chem.***, 1984, **48**, 2883-2888.

13 W. J. Broom, K. E. Auwarter, J. Ni, D. E. Russel, L.-A. Yeh, M. M. Maxwell, M. Glicksman, A. G. Kazantsev and R. H. Brown Jr., ***J. Biomol. Screen.***, 2006, **11**, 729-735.

14 F. V. Singh, R. Vatsyayan, U. Roy and A. Goel, ***Bioorg. Med. Chem. Lett.***, 2006, **16**, 2734-2737.

15 F. V. Singh, A. Parihar, S. Chaurasia, A. B. Singh, S. P. Singh, A. K. Tamrakar, A. K. Srivastava and A. Goel, ***Bioorg. Med. Chem. Lett.***, 2009, **19**, 2158-2161.

16 F. Saleem, Kanwal, K. M. Khan, S. Chigurupati, Y. Andriani, M. Solangi, S. Hameed, A. A. M. A. Hafez, F. Begum, M. A. Lodhi, M. Taha, F. Rahim, T. S. bin T. Muhammad and S. Perveen, ***Arab J. Chem.***, 2022, **15**, 103651.

17 S. L. Cui, X. F. Lin and Y. G. Wang, ***J. Org. Chem.***, 2005, **70**, 2866-2869.

18 C. Yi, C. Blum, S. X. Liu, G. Frei, A. Neels, P. Renaud, S. Leutwyler and S. Decurtins, ***J. Org. Chem.***, 2008, **73**, 3596-3599.

19 T. M. Cardozo and M. A. C. Nascimento, ***J. Mater. Sci.***, 2005, **40**, 3549-3551.

20 B. Aydiner, E. Yalcin, V. Korkmaz and Z. Seferoglu, ***Synth. Commun.***, 2017, **47**, 2174-2188.

21 R. C. Kulkarni, S. Samundeeswari, F. Shaikh, N. S. Naik, J. M. Madar, L. A. Shastri and V. A. Sunagar, ***J. Fluoresc.***, 2017, **27**, 1613-1619.

22 B. J. Ramulu, T. Chanda, S. Chowdhury, G. C. Nandi and M. S. Singh, ***RSC Adv.***, 2013, **3**, 5345-5349

23 M. M. Pisal, R. A. Annadate, M. C. Athalye, D. Kumar, S. P. Chavan, D. Sarkar and H. B. Borate, ***Bioorg. Med. Chem. Lett.***, 2017, **27**, 979–988.

24 F. E. Held, A. A. Guryev, T. Frohlich, F. Hampel, A. Kahnt, C. Hutterer, M. Steingruber, H. Bahsi, C. V. B. Kninski, D. S. Mattes, T. C. Foertsch, A. N. Mueller, M. Marschall and S. B. Tsogoeva, ***Nat. Commun.***, 2017, **8**, 15071.

25 P. Gayathri, M. Pannipara, A. G. Al-Sehemi and S. P. Anthony, ***New J. Chem.***, 2020, **44**, 8680-8696.

26 W. Z. Yuan, Y. Gong, S. Chen, X. Y. Shen, J. W. Y. Lam, P. Lu, Y. Lu, Z. Wang, R. Hu, N. Xie, H. S. Kwok, Y. Zhang, J. Z. Sun and B. Z. Tang, ***Chem. Mater.***, 2012, **24**, 8, 1518–1528.

27 E. Ramachandran, Dr. S. A. A. Vandarkuzhali, Dr. G. Sivaraman and Prof. R. Dhamodharan, ***Chem. Eur. J.***, 2018, **24**, 11042-11050.

28 T. Sachdeva and M. D. Milton, ***Dyes Pigm.***, 2019, **164**, 305-318.

29 Y. Rout, A. Ekbote and R. Mishra, ***J. Mater. Chem. C***, 2021, **9**, 7508-7531.

30 B. Zhao, H. Wang, Dr. C. Han, P. Ma, Z. Li, P. Chang and Prof. H. Xu, ***Angew. Chem. Int. Ed.***, 2020, **59**, 19042-19047.

31 S. Revoju, A. Matuhina, L. Canil, H. Salonen, A. Hiltunen, A. Abate and P. Vivo, ***J. Mater. Chem. C***, 2020, **8**, 15486-15506.

32 F. Khan and R. Mishra, ***J. Mater. Chem. C***, 2023, **11**, 2786-2825.

33 J. Wu, C. Li, Q. Chen, L. Xu, M. Jian and J. Zhao, ***J. Mater. Chem. C***, 2022, **10**, 10595-10608.

34 F. Khan, M. Mahmoudi, D. Volyniuk, J. V. Grazulevicius and R. Mishra, ***J. Phys. Chem. C***, 2022, **126**, 37, 15573–15586.

35 X. Hu, Y. Zhou, X. Wang, Y. Ge and Y. Zhan, ***J. Lumin.***, 2022, **251**, 119259.

36 J. Zhang, M. Zhu, Dr. Y. Lu, X. Zhang, Dr. S. Xiao, Dr. H. Lan and Prof. Dr. T. Yi, ***Chem. Eur. J.***, 2022, **28**, e202200458.

37 X. Du, X. Liu, S. Lv, H. Ding, X. Cheng, H. Gu, D. Qiu and H. Hao, ***J. Mol. Struct.***, 2023, **1286**, 135587.

38 A. Ekbote, S. H. Han, T. Jadhav, S. M. Mobin, J. Y. Lee and R. Mishra, ***J. Mater. Chem. C***, 2018, **6**, 2077-2087.

39 R. Chennoufi, H. Bougherara, N. G. Eilstein, B. Dumat, E. Henry, F. Subra, S. B. Mone, F. M. Betzer, P. Tauc, M. P. T. Fichou and E. Deprez, ***Sci. Rep.***, 2016, **6**, 21458.

40 Y. Zheng, P. Hou, Y. Li, J. Sun, H. Cui, H. Zhang and S. Chen, ***Molecules***, 2021, **26**(8), 2337.

41 B. Stoean, D. Rugina, M. Focsan, A. M. Craciun, M. Nistor, T. Lovasz, A. Turza, I. D. Porumb, E. Gal, C. Cristea, L. S. Dumitrescu, S. Astilean and L. I. Gaina, ***Int. J. Mol. Sci.***, 2021, **22**(6), 2985.

42 Z. Li, Dr. D. Yang, Dr. C. Han, B. Zhao, H. Wang, Y. Man, P. Ma, P. Chang, Prof. D. Ma and Prof. H. Xu, ***Angew. Chem. Int. Ed.***, 2021, **60**, 14846-14851.

43 J. Shi, L. Xu, C. Chen, X. Lv, Q. Ding, W. Li, S. Xue and W. Yang, ***Dyes Pigm.***, 2019, **160**, 962-970.

44 J. Zhang, A. Li, H. Zou, J. Peng, J. Guo, W. Wu, H. Zhang, J. Zhang, X. Gu, W. Xu, S. Xu, S. H. Liu, A. Qin, J. W. Y. Lam and B. Z. Tang, ***Mater. Horiz.***, 2020, **7**, 135-142.

45 S. Suganya, K. Debsharma, E. Ravindran, M. K. Mahato and E. Prasad, ***ACS Appl. Polym. Mater.***, 2020, **2**, 3, 1222–1233.

46 Y. Jiang, S. Zhang, B. Wang, T. Qian, C. Jin, S. Wu and J. Shen, ***Tetrahedron***, 2018, **74**, 5733-5738.

47 J. Wang, Q. Niu, T. Hu, T. Li and T. Wei, ***J. Photochem. Photobiol., A: Chemistry***, 2019, **384**, 112036.

48 B. A. Nogueira, C. Castiglioni and R. Fausto, ***Commun. Chem.***, 2020, **3**, 1-12.

49 M. El-Sayed, H. Muller, G. Rheinwald, H. Lang and S. Spange, ***Chem. Mater.***, 2003, **15**, 3, 746-754.

50 C. Kitamura, Y. Abe, T. Ohara, A. Yoneda, T. Kawase, T. Kobayashi, H. Naito and T. Komatsu, ***Chem. Eur. J.***, 2010, **16**, 890–898.

51 N. Genevaz, P. Chavez, V. Untilova, A. Boeglin, C. Bailly, L. Karmazin and L. Biniek, ***J. Mater. Chem. C***, 2018, **6**, 9140-9151.

52 B. Mohammadi, H. Kazemi and M. Shafieey, ***Montash. Chem.***, 2014, **145**, 1649-1652.

53 Z. H. Guo, Z. X. Jin, J. Y. Wang and J. Pei, ***Chem. Commun.***, 2014, **50**, 6088-6090.

54 M. Fang, J. Yang, Q. Liao, Y. Gong, Z. Xie, Z. Chi, Q. Peng, Q. Li and Z. Li, ***J. Mater. Chem. C***, 2017, **5**, 9879–9885.

55 R. Hu, E. Lager, A. A. Aguilar, J. Liu, J. W. Y. Lam, H. H. Y. Sung, I. D. Williams, Y. Zhong, K. S. Wong, E. P. Cabrera and B. Z. Tang, ***J. Phys. Chem. C***, 2009, **113**, 36, 15845–15853.

56 S. Sasaki, G. P. C. Drummen and G. Konishi, ***J. Mater. Chem. C*** , 2016, **4**, 2731-2743.

57 Prof. Dr. T. Iwasaki, S. Murakami, Prof. Dr. Y. Takeda, Prof. Dr. G. Fukuhara, Prof. Dr. N. Tohnai, Prof. Dr. Y. Yakiyama, Prof. Dr. H. Sakurai and Prof. Dr. N. Kambe, ***Chem. Eur.J.***, 2019, **25**, 14817–14825.

58 N. Nijegorodov, P. V. C. Luhanga, J. S. Nkoma and D. P. Winkoun, ***Spectrochim. Acta A Mol. Biomol. Spectrosc.***, 2006, **64**, 1–5.

59 W. Xi, J. Yu, M. Wei, Q. Qiu, P. Xu, Prof. Z. Qian and Prof. H. Feng, ***Chem. Eur. J.***, 2020, **26**, 3733-3737.

60 B. Fang, M. Chu, Z. Wu, Y. Shi, Y. S. Zhao and M. Yin, ***J. Mater. Chem. C***, 2019, **7**, 4434–4440.

61 P. S. Hariharan, N. S. Venkataramanan, D. Moon and S. P. Anthony, ***J. Phys. Chem. C***, 2015, **119**, 9460–9469.

62 C. Qi, Prof. H. Ma, H. Fan, Z. Yang, H. Cao, Q. Wei and Prof. Z. Lei, ***Chempluschem***, 2016, **81**, 637–645.

63 S. J. Yoon, J. W. Chung, J. Gierschner, K. S. Kim, M. G. Choi, D. Kim and S. Y. Park, ***J. Am. Chem. Soc.***, *2010*, **132**, 13675–13683.

64 K. Nagura, S. Saito, H. Yusa, H. Yamawaki, H. Fujihisa, H. Sato, Y. Shimoikeda and S. Yamaguchi, ***J. Am. Chem. Soc.*** , 2013, **135**, 10322-10325.

65 H. Liu, Y. Gu, Y. Dai, K. Wang, S. Zhang, G. Chen, B. Zou and B. Yang, ***J. Am. Chem. Soc***,. 2020, **142**, 1153-1158.

66 W. Li, D. Liu, F. Shen, D. Ma, Z. Wang, T. Feng, Y. Xu, B. Yang and Y. Ma, ***Adv. Funct. Mater.***, 2012, **22**, 2797-2803.

67 K. Wang, H. Zhang, S. Chen, G. Yang, J. Zhang, W. Tian, Z. Su and Y. Wang, ***Adv. Funct. Mater.***, 2014, **26**, 6168-6173.

68 Q. Li and Z. Li, ***Acc. Chem. Res.***, 2020, **53**, 4, 962–973.

69 C. Kanimozhi, M. Naik, N. Y. Gross, E. K. Burnett, A. L. Briseno, T. D. Anthopoulos and S. Patil, ***J. Phys. Chem. C***, 2014, **118**, 22, 11536–11544.

70 J. Peng, J. Zhao, L. Zheng, K. Ye, J. Sun and R. Lu, ***New J. Chem.***, 2018, **42**, 18269-18277.

71 B. Kupcewicz and M. Malecka, ***Cryst. Growth Des.***, 2015, **15**, 3893-3904.

72 C. Feng, K. Wang, Y. Xu, L. Liu, B. Zou and P. Lu, ***Chem. Commun.***, 2016, **52**, 3836–3839.

Chapter II

Solid-State Acidofluoro-Chromism (SSAC) from Thiophene/Toluene Attached Anthracene-Based Pyridyl SSEOFs: Structure-Property Investigation with Multiple Real-World Applications

Objectives :

- Establish a new series of anthracene-based asymmetrical pyridyl isomers as efficient reversible SSAC dyes.
- Develop SSAC dyes of different region emission displays.
- Investigate the governing factors of SSAC property by molecular level understanding.
- To understand the design concept to receive photostable efficient SSAC displaying structure.
- To extend the applications in practical utilities with the lead compound.

Abstract:

Reversible solid-state acidochromic (SSAC) behavior basically depends on the pyridine-based linkers in the solution state but remains ill-defined in the solid-state. This work describes the degree of emission responses, primarily in the solid state, if the N-atom of the pyridyl ring alters the position. The role of N-atom at the 4th position is more sensitive against acid fumes, especially in the thiophene-linked analog that displays 108 nm redshift, compared to the toluene analog (85 nm). The crystal structure and molecular packing analyses dictate that the rotors are significantly twisted with multiple noncovalent interactions, crucially responsible for the admirable solid-state emission. The gained planarity of the molecules, stronger H-bonding, and excited state stabilization for a few pyridinium salts may be accountable for reducing the emission intensity and redshifted emission, respectively. High-contrast emission color variation on protonation-deprotonation has been employed as a handy polymer-blended emitting platform for convenient and reusable security writings.

2.1 Introduction

Stimuli-responsive solid-state emitting organic fluorogens (SSEOFs) offer ample scopes of various reversible emission switchovers from a single entity (read compound).[1-4] Concerning the different applied stimuli that result in the emission change, we name those compounds differently such as a mechanofluorochromic SSEOF can change its emission to respond to the applied mechanical force[5], a thermofluorochromic SSEOF can change its emission to respond against different temperatures[6], and again an SSEOF that can switch its emission on exposure to acid or base vapor is called a Solid-State Acido-Fluorochromic (SSAC) material.[7] SSAC displaying SSEOFs is of great utility as the material exhibits reversible dual-color switching in a solid-state switch on exposure to an acid stimulus and a base stimulus.[7] This emission change can help SSAC materials find real-world applications like inkless security writing, stimuli-responsive QR-code-based anticounterfeiting9-10, solid-state halochromic sensing11, and even cellular pH measurements.[8-12] In this regard, the pyridyl core attached organic fluorogens have snatched the spotlight to generate a lot of SSAC materials[1,12-16] due to their rigid framework and capability of accepting hydrogens, using an energetically available lone pair of electrons on the nitrogen atom. In their crystalline state, such molecules pack in a manner that ensures solid-state emission.[1] To mention a few commendable SSAC organic materials, Wang *et al.* developed TPE (tetraphenylethylene)-based pyridyl stereo-isomers with ethynylene-bridge. The (*E*)-isomer (**2A**) could switch its solid-state emission from being exposed to HCl vapor from 495 nm to 537 nm and retain its original emission after getting fumed with a base.[17]

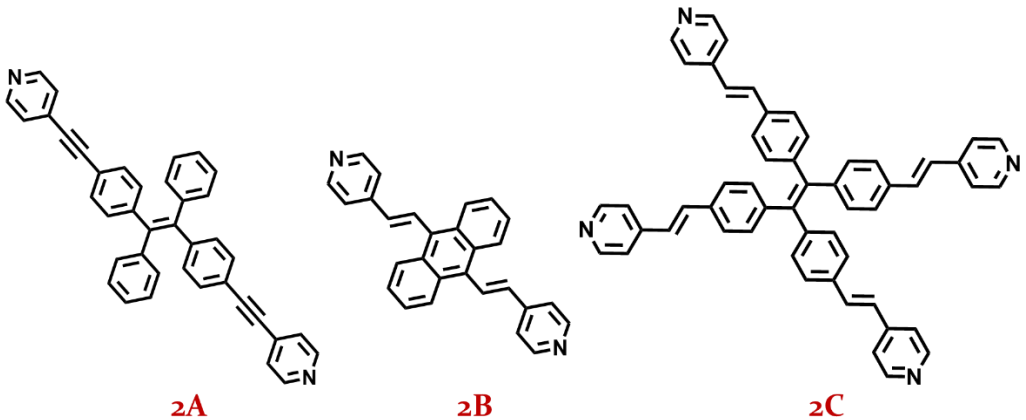

Figure 2.1 Reported SSAC displaying pure organic smart materials (taken from refs. 17, 18 and 1)

Liu *et al.* could decipher the acidofluorochromic emission switching behavior with a normal pyridyl compound **2B** and its co-crystal.[18] Another interesting SSAC material **2C** was developed by Xiong *et al.* when they introduced tetra pyridyl moiety into the TPE framework (Figure 2.1).[1]

What is the need to investigate the structure-property relationship for SSAC?

The real challenge is predicting the design of an SSAC material as most of the reports were on case studies; *rather, almost no effort has been made so far to build the structure-property relationships to analyze the SSAC governing factors at the molecular level. Another technical issue is the acid-fumed or protonated salts, as they are stubborn to produce their single crystals. Hence, most researchers were compelled to rely on theoretically optimized structures that cannot predict the actual non-covalent interactions within a single protonated crystal*. For instance, Li *et al.* developed a diphenylamine-pyridine conjugated acrylonitrile type of compound **2D** with SSAC feature and applied it as a security ink but could not report the crystal structure of protonated **2D**, and hence the molecular level understanding for the protonated form remained unknown.[19] Wang *et al.* reported TPA-based SSAC material **2E** but again could not generate the single crystals to understand the non-covalent interactions (Figure 2.2).[20]

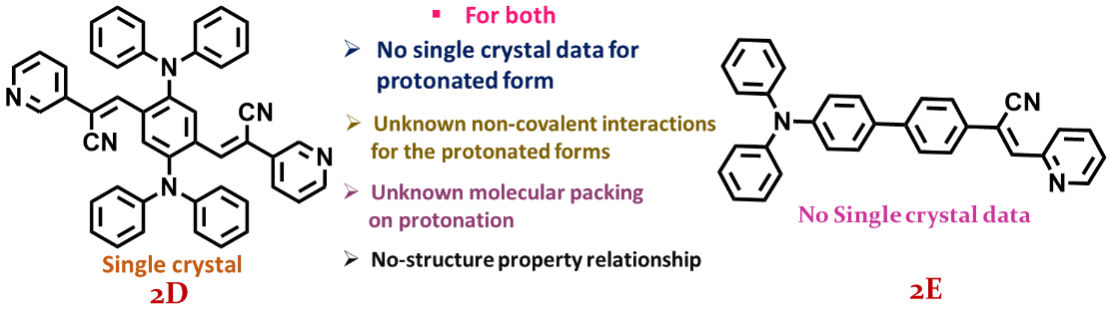

Figure 2.2 Reported SSAC displaying pure organic smart materials that give no idea about crystal-packing of the protonated form to understand the molecular level interactions (refs. 19, 20)

The problem continued when a few more SSAC materials were reported without addressing the solution.[21-24] Doubtlessly, there was an urgent need to investigate the SSAC feature at the molecular level to understand the design concept and the underlying governing factors.

Why do we choose the anthracene-conjugated pyridyl system?

As stated earlier, although there were various SSAC materials established already, the anthracene-linked pyridyl compounds were less identified as a source of smart SSAC displays as maximum reports were on solid and solution state acidofluorochromic materials that consist of pyridinyl moieties conjugated with a system like TPE (tetraphenylethylene), TPA (triphenylamine), naphthalene, quinoxaline, carbazole, pyrazoquinoline, pyrazolopyridine, spiro borates, pyrene, and pyrazine.[14,20-24,25-29] So, establishing a structure-property relation on the anthracene-pyridyl system was an existing research gap, and we focussed there. Again, finding various real-world applications was also a concern for us.

2.2 Literature Review on anthracene-pyridine-based SSAC displaying SSEOFs

2.2.1 Symmetrical and asymmetrical protonation-based emission tuning from pyridinyl vinyl anthracene type of material

In 2017, Ma *et al.* realized the symmetrical and asymmetrical protonation states through the formation of intermolecular H-bonds inside 9,10-bis((*E*)-2-(pyridin-4-yl)vinyl)-anthracene **2F** (**BP4VA**) molecular crystals. Surprisingly, **2H** was asymmetrically protonated on exposure to HCl but was symmetrically protonated by H_2SO_4. They figured out that the different protonation states of the **2H** crystals resulted in diverse supramolecular interactions to display emission tuning (Figure 2.3).[30]

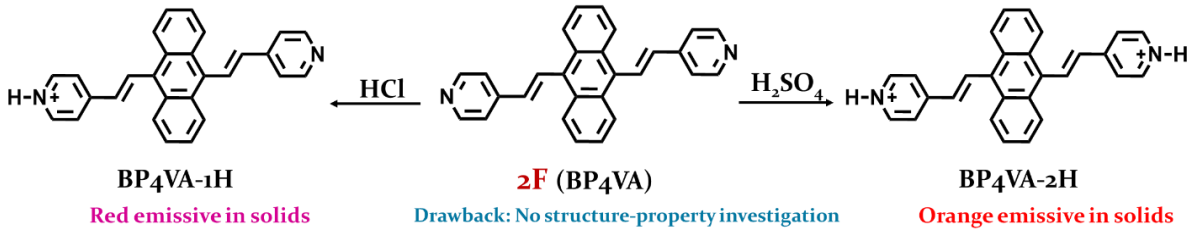

Figure 2.3 Symmetrical and asymmetrical protonation-based SSAC displaying reported pure organic smart materials (ref. 30)

2.2.2 Pyridinyl vinyl anthracene-based triaryls for SSAC displays with different acid fumes and volatile amines

In 2018, Sun *et al.* synthesized another pyridinyl vinyl anthracene type of compound, **2G**, that could sense different acids and bases, tuning its emission between

500 nm and 577 nm. The fast SSAC feature of this material could sense volatile amines as well. The ground form of **2G** also could display the SSAC characteristics (Figure 2.4).[31]

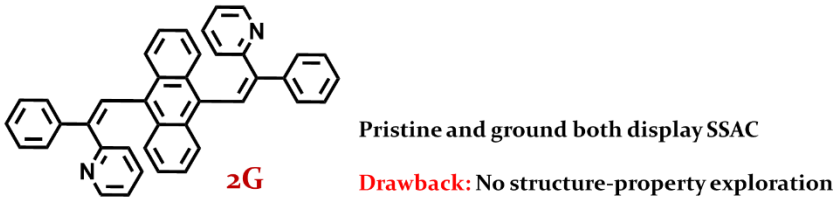

Figure 2.4 Symmetrical and asymmetrical protonation-based SSAC displaying reported pure organic smart materials (ref. 31)

2.2.3 Co-crystallization mediated SSAC improvement from pyridinyl vinyl anthracene-based compounds

Liu *et al.* developed an SSAC showing a co-crystal system that could improve the SSAC outputs of the previously reported **2H** compound. The co-crystal **2I** could shift the emission towards the deep red region on protonation, while normal **2H** emitted orange (Figure 2.5).[18]

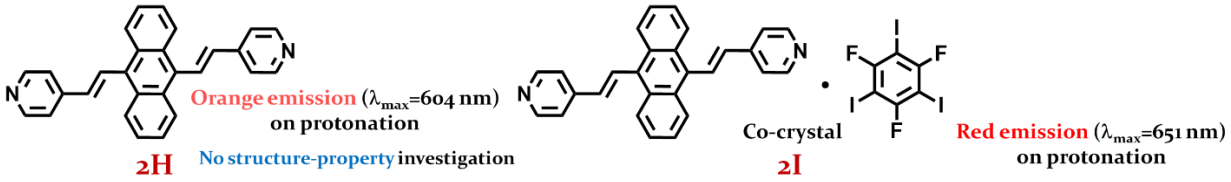

Figure 2.5 Symmetrical and asymmetrical protonation-based SSAC displaying reported pure organic smart materials (ref. 18)

2.2.4 Thiophene conjugated anthracenyl-pyridine as SSAC material with massive emission switchover upon protonation

Baig *et al.* conceptualized a monopyridyl-linked unsymmetrical anthracenyl π-conjugate **2J** where toluene-linked anthracene was conjugated with 2-pyridinyl moiety. This compound displayed a massive 129 nm emission switching upon acid fumigation, and the pristine emission was also recovered, by base fumigation. However, no structure-property relationship was established (Figure 2.6).[8]

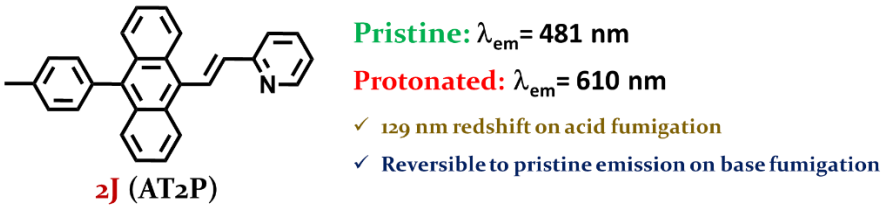

Figure 2.6 SSAC display from asymmetrical π-conjugate (ref. 8)

2.2.5 Carbazole and diphenylamine conjugated unsymmetrical anthracenyl-pyridine as SSAC material with the brightest emission of the protonated form

Prusti *et al.* reported carbazole and diphenylamine conjugated anthracenyl pyridine structures **2K** and **2L** that displayed noteworthy SSAC features. In particular, the DPA4Py increased its emission upon acidification, an unusual phenomenon. However, they did not investigate the effect of different positions of the 'N' atom in the pyridine ring. Rather, their focus was on the contributed effect of carbazole and diphenylamine (Figure 2.7).[32]

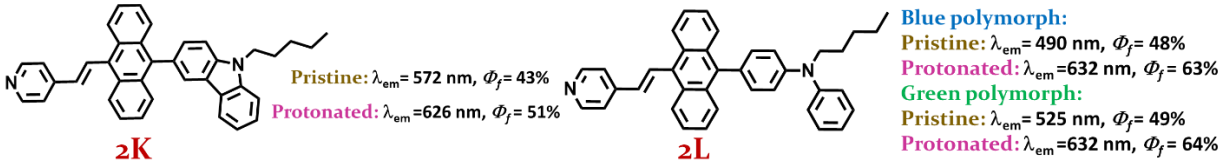

Figure 2.7 Symmetrical and asymmetrical protonation-based SSAC displaying reported pure organic smart materials (ref. 32)

2.3 Results and discussion

2.3.1 Synthetic route for thiophene/toluene attached anthracenyl pyridine derivatives

Diethyl ((10-(p-tolyl) anthracen-9-yl) methyl) phosphonate and diethyl ((10-(thiophen-2-yl) anthracen-9-yl) methyl) phosphonate were synthesized in a transition-metal free Friedel-Crafts arylation pathway following our earlier report.[33] The suitable phosphonates are utilized in economical but effective Horner-Wadsworth-Emmons (HWE) reactions with *N*-positional isomeric pyridyl carboxaldehyde to afford a variety of isomeric pyridyl π-conjugates.[34] The protonated salts were crystallized from the respective acidic solutions of pyridyl π-conjugates from diverse solvent combinations as

appropriate. Again, the protonated and de-protonated versions can be prepared by simple uniform fumigation with acid and base vapors (Scheme 1).

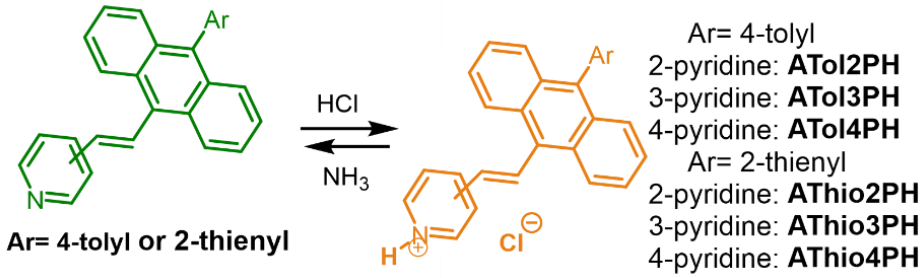

Scheme 1 Synthesis of pyridyl isomers through HWE reactions

2.3.2 Structural elucidation

2.3.2.1 NMR spectroscopic analysis of the synthesized compounds

The acidochromic behavior of these compounds was further verified by the ^{1}H-NMR spectroscopy in the solution state. The protonation-driven change in chemical shift (ppm) of associated protons for **AThio2P** is discussed here due to its better clarity, and almost similar δ shifts are found for other emitters (Figure 2.8). The aromatic protons of representative compound **AThio2P** resonate at δ 7.03–8.76, which are shifted to downfield δ 6.78–9.41 upon protonation (Figure 2.8). Some of the protons in the pyridyl ring are also de-shielded. Moreover, the protonation of pyridyl nitrogen is visible as a broad signal at δ 8.85 in the ^{1}H NMR spectrum. The effect related to polarity change and ionic strength of the medium may also contribute to the shifts of the proton signals of these compounds.[35] All the protonated crystals were characterized by ^{1}H NMR and ^{13}C NMR spectroscopy.

2.3.2.2 Single-crystals of the compounds

The single-crystals of **ATol3p**, **ATol3PH**, **ATol4PH**, **AThio2PH**, **AThio3PH** and **AThio4PH** were grown, solved, and analysed. The crystallographic parameters of the crystallized pyridinium salts are summarized in Table 1.

2.3.3 Photophysical studies in solid-state

The twisted molecular conformations of the molecules are advantageous to exhibit the AIE properties due to the excited state relaxation *via* a radiative pathway. They are competent enough to emit in a solid state.[36-40] The compound **ATol2P** was earlier

established as an effective reversible FL-switching with a maximum redshift of 129 nm in the solid state with reduced quantum yield after protonation and employed in reusable security writing.[8]

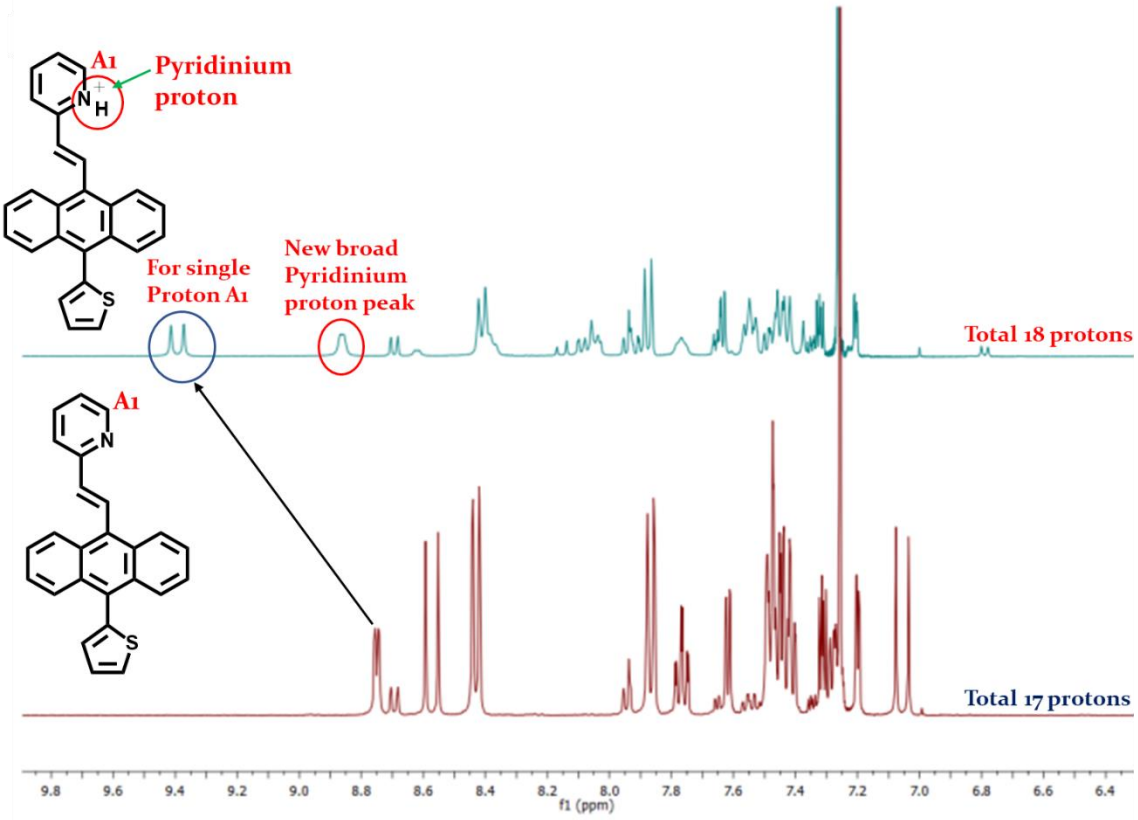

Figure 2.8 Representative NMR of **AThio2P** and its protonated version

This result drives us to find the structure-property relationship in SSAC properties within these series of π-conjugates. Therefore, we start herein with the solid-state FL behavior of **ATol3P** that emits at 496 nm and shifts to 544 nm upon protonation. Thus, FL-switching from green to yellow (48 nm redshift) is visible through the naked eye upon illuminating with a 365 nm UV lamp (Figure 2.10**).**

The original color returns with almost the same wavelength and efficiency upon further deprotonation with a base such as Et_3N. After protonation, the Φ_f is marginally reduced from 2.44 % to 2.36 %. However, there was no impressive variation in the solid-state absorption spectra (Figure 2.9) under similar conditions; the protonation-deprotonation process signified no change in the ground-state energy levels. The reversible 85 nm redshifted emission (Figure 2.9 and 2.10) on the protonation-deprotonation process is relatively more sensitive with **ATol4P,** even though it is weakly emissive due to the facial π···π stacking in the molecular crystal packing (*vide infra*). The

red-shifting designates a better molecular coplanarity that facilitates π-electronic conjugation within the molecule and stabilizes the TICT state to a greater extent. Such stability also reduces the energy gap between the ground and excited state resulting from the emission through a nonradiative channel, and hence, the quantum yield reduces significantly.

Table 2.1 Crystal parameters of the crystallized pyridinium salts

Compounds	**ATol3P**	**ATol3PH**	**ATol4PH**	**AThio2PH**	**AThio3PH**	**AThio4PH**
Emp. Formula	$C_{28}H_{21}N$	$C_{28}H_{24}ClNO$	$C_{28}H_{24}ClNO$	$C_{25}H_{18}ClNS$	$C_{25}H_{18}ClNS$	$C_{25}H_{20}ClNOS$
Formula weight	371.46	425.93	425.93	399.91	399.91	417.93
Crystal system	triclinic	triclinic	triclinic	triclinic	monoclinic	triclinic
Space group	$P\bar{1}$	$P\bar{1}$	$P\bar{1}$	$P\bar{1}$	$P2_1/c$	$P\bar{1}$
a /Å	9.4494(4)	7.25657(16)	7.26890(14)	5.77152(16)	10.07317(18)	9.2006(3)
b /Å	10.0848(3)	7.38608(16)	7.74010(16)	7.65617(15)	8.13563(15)	9.2738(4)
c /Å	11.3291(4)	21.0326(4)	20.5702(5)	22.1252(5)	46.9321(7)	13.5775(5)
α/degree	92.049(3)	91.6421(16)	80.4877(18)	98.3428(18)	90	95.796(3)
β/degree	106.583(3)	98.4875(17)	83.6516(17)	93.419(2)	94.1811(15)	98.796(3)
γ/degree	110.456(3)	102.6366(18)	75.2413(17)	97.640(2)	90	114.474(4)
V /Å^3	958.36(6)	1085.77(4)	1100.90(4)	955.62(4)	3835.93(11)	1024.47(7)
Z	2	2	2	2	8	2
D_{calc} /g cm^{-3}]	1.287	1.303	1.285	1.390	1.385	4293/3/280
μ /mm^{-1}	0.564	1.704	1.680	2.855	2.845	2.723
F (000)	392.0	448.0	448.0	416.0	1664.0	436.0
Data/ restraints/ parameters	4002/0/263	4558/3/293	4636/3/293	4003/1/253	8042/2/505	4293/3/280
GOOF	1.058	1.091	1.066	1.072	1.027	1.043
+R1 [I>2σ(I)]	0.0448	0.0399	0.0418	0.0601	0.0932	0.0518
wR2	0.1273	0.1326	0.1200	0.1618	0.2588	0.1397
Max./min. residual electron dens. [eÅ^{-3}]	0.29/-0.27	0.28/-0.32	0.30/-0.27	0.63/-1.19	0.94/-1.09	0.47/-0.34
CCDC No.	2107221	2107222	2107223	2107224	2107225	2107226

The replacement of the tolyl group with a much smaller thiophene ring demonstrates comparatively better emission efficiency of the pyridyl π-conjugates due to favorable twisting of the thiophene group, preventing π···π stacking and facilitating its emission in the solid state before protonation.

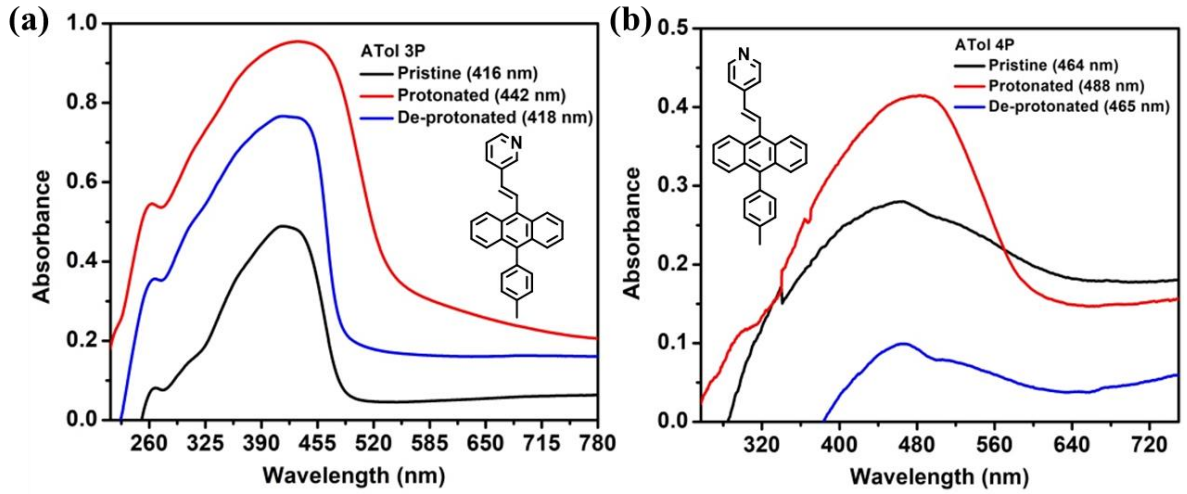

Figure 2.9 Solid state absorption spectra of protonated and de-protonated **ATol3P** and **ATol4P**

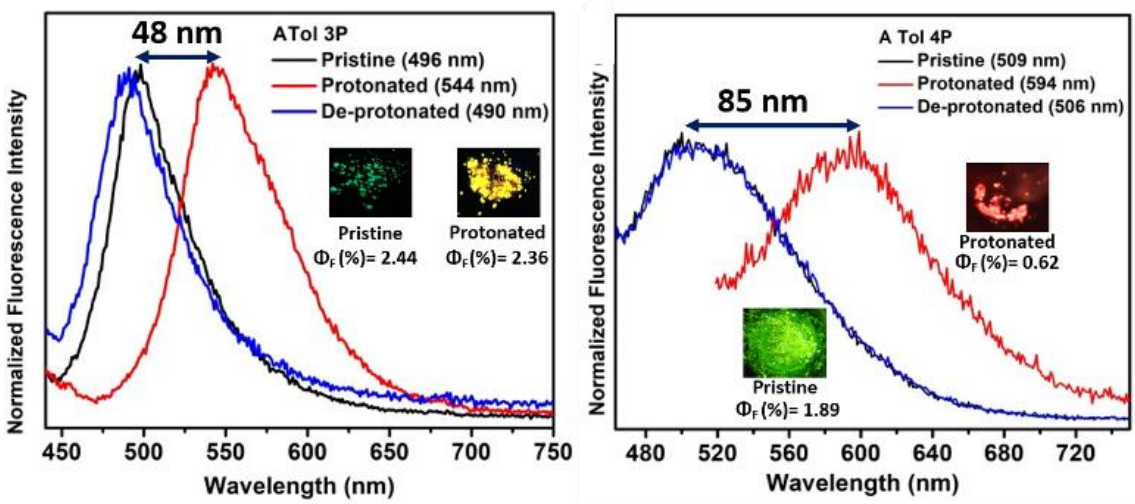

Figure 2.10 Normalized FL- spectra of **ATol3P** and **ATol4P**. (**ATol3P**: λ_{ex}(Pristine) = 416 nm, λ_{ex}(Protonated) = 442 nm; **ATol4P**: λ_{ex}(Pristine) = 464 nm, λ_{ex}(Protonated) = 488 nm); Instrument generated absolute error for calculating Φ_f: **ATol3P** Pristine ±0.059, **ATol3P** Protonated ±0.047; **ATol4P** Pristine ±0.051, **ATol4P** Protonated ±0.059.

Further, *unsubstituted* thiophene is more rigid and encourages better solid-state emission than toluene. The presence of the methyl group might assist a nonradiative relaxation due to its vibrational and rotational degrees of freedom. Additionally, variations in the position of pyridinyl nitrogen-atom offer a crucial role in exhibiting a diverse SSAC behavior.

Unlike **ATol2P** (129 nm redshift)[8], **AThio2P** shows only 38 nm redshift upon protonation, which does not offer a notable change in emission color during the protonation-deprotonation process. Thus, this **AThio2P** (Figure 2.12) is not a promising

emitter compared to **ATol2P.** More strikingly, **AThio3P** undergoes only a 14 nm redshift within the same green emissive range (Figure 2.12) upon protonation, which is considered an almost negligible change. Of note, there were slight changes in absorption λ_{max} for **AThio2P** (28 nm) and **AThio3P** (6 nm) after protonation (Figure 2.11).

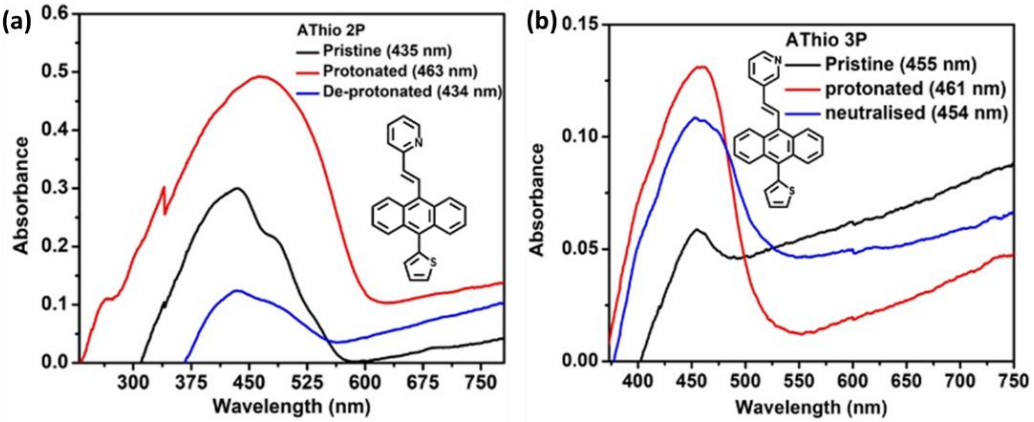

Figure 2.11 Solid state absorption spectra of protonated and de-protonated forms of **AThio2P** and **AThio3P**

Nevertheless, the SSAC effect is highly noticeable with **AThio4P**, which displays a remarkable 108 nm redshift from green to red (Figure 2.13b), indicating a substantial coplanarity gained upon protonation. The deprotonation process by Et_3N (TEA) fuming brings back the original green emission color, and such reversible color change remains intact even after the 10th cycle of the protonation-deprotonation process (Figure 2.14). A notable redshift of 71 nm was observed for **AThio4P** (Figure 2.13a) in the absorbances, indicating even a change in the ground state due to better electronic conjugation governed by the protonation effect.

Meanwhile, the reversible FL-switching of various pyridyl fluorophores studied herein is suitable for fast reversible dual detection of acid and base fumes successively (Figure 2.15). The fluorescence lifetime (ns) was attempted to measure some of these compounds (Table 2). Most of these lifetime decay profiles were fitted triexponentially, and the excited state lifetime is considerably poor (Table 2).

After protonation, a much faster decay was found for the protonated samples and was difficult to measure on the nanosecond scale. The faster-excited state decay for the protonated samples supports the reduced quantum yield.

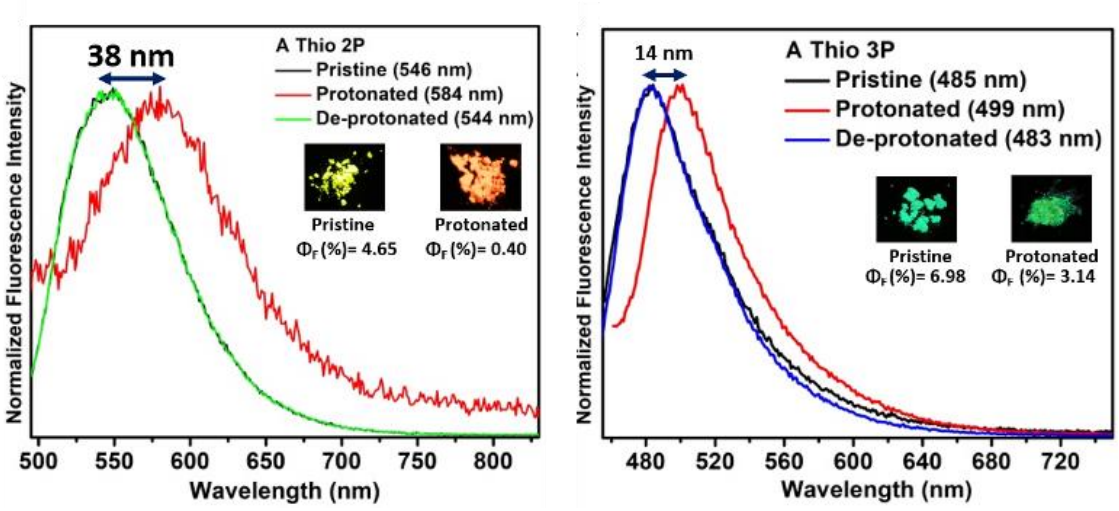

Figure 2.12 Normalized Fl- spectra of **AThio2P** and **AThio3P**. (**AThio2P**: λ_{ex}(Pristine) = 435 nm, λ_{ex} (Protonated) = 463 nm; **AThio3P**: λ_{ex} (Pristine) = 455 nm, λ_{ex} (Protonated) = 461 nm); Instrument generated absolute error for calculating Φ_f: **AThio2P** Pristine ±0.06, **AThio2P** Protonated ±0.072; **AThio3P** Pristine ±0.032, **AThio3P** Protonated ±0.052.

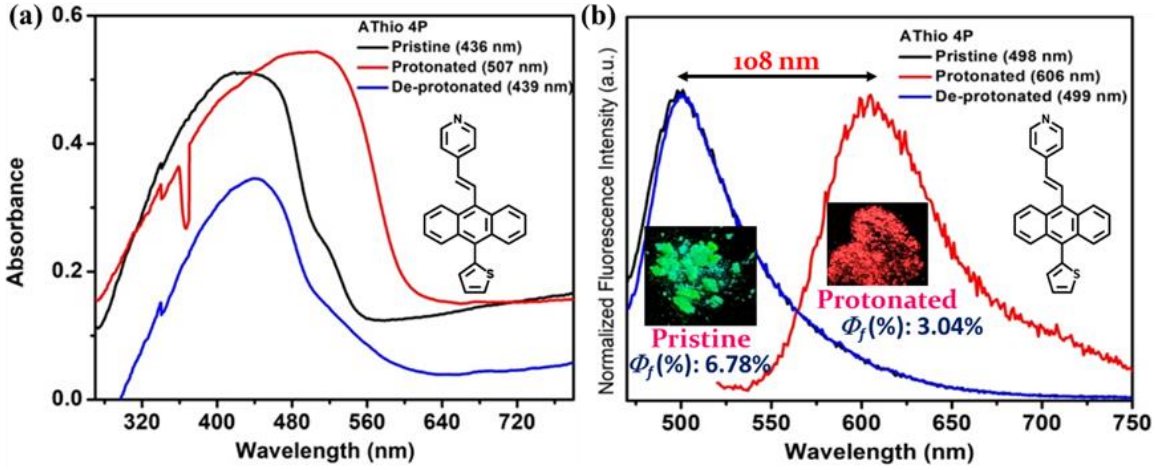

Figure 2.13 (a) Absorption and (b) emission spectra **of AThio4P**. (**AThio4P**: λ_{ex}(Pristine) = 436 nm, λ_{ex}(Protonated) = 507 nm; Instrument generated absolute error for calculating Φ_f: **AThio4P** Pristine ±0.038, **AThio4P** Protonated ±0.039.

2.3.4 Crystal Structure Analysis

Except for **ATol4P** and **AThio2P,** all other structures for the protonated and deprotonated molecules were determined by single-crystal X-ray diffraction. We commenced examining the molecular structure of the fluorophores before and after the protonation. The observed redshift upon protonation is explained by the coplanarity developed within the molecule (Figure 2.16). There are two different types of torsion

angles measured between (a) anthracene and flanking donors (thiophene/toluene) and (b) anthracene and pyridine. Coplanarity is developed upon protonation because the torsion angles of the salts are reduced significantly except for **AThio3P**, supporting its almost unresponsive nature against protonation.

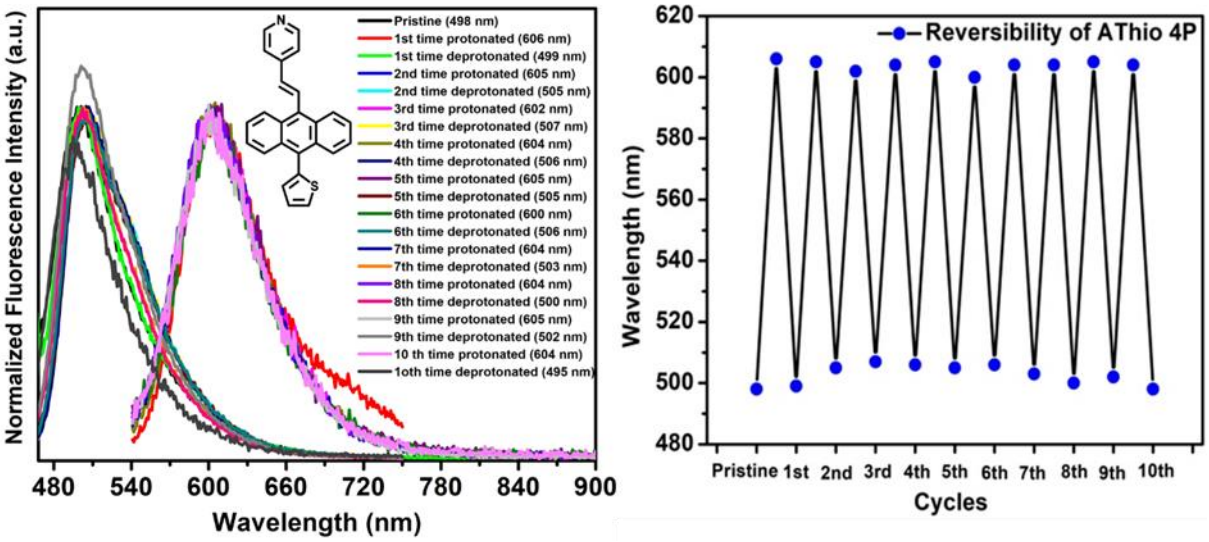

Figure 2.14 Multiple reversible acidochromic sensing using **AThio4P**

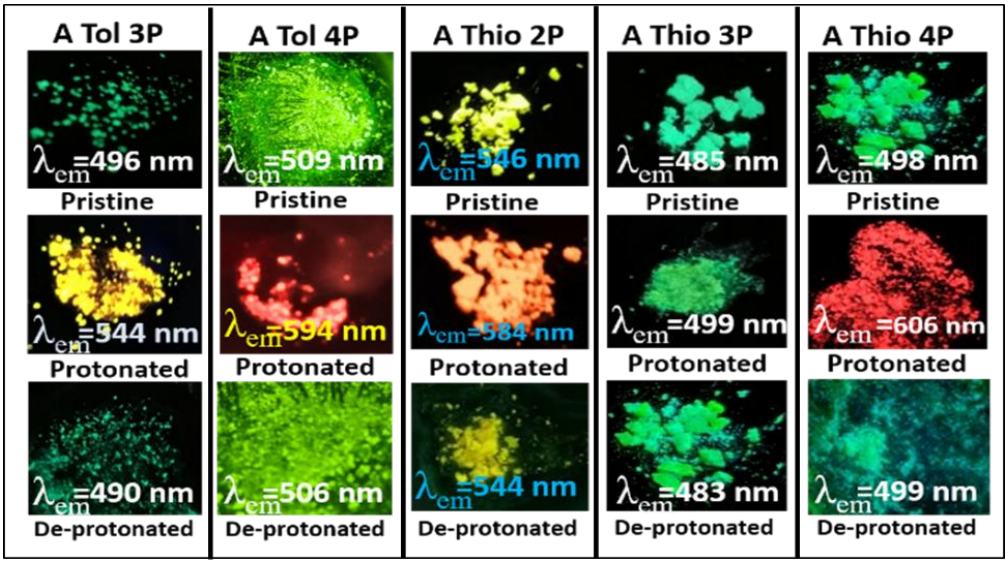

Figure 2.15 Reversible FL switching upon protonation (acidification) and deprotonation (using base) of all the pyridyl isomers of toluene and thiophene series: A detection of acid and bases

For tolyl as flanking donors (needs to be clarified), **ATol4P** exhibited a relatively larger redshift of 80 nm than **ATol3P** due to the preferred position of a nitrogen atom that can

stabilize the resonating structure with a negative charge on the electronegative nitrogen atom.

Table 2.2 Photophysical parameters for the solid-state emitters

Compounds	Pristine Abs λ_{max}(nm)	Pristine Em λ_{max}(nm)	Salt Abs λ_{max}(nm)	Salt Em λ_{max}(nm)	Shift in emission	Φ_f (%) Pristine/salt	Lifetime (ns): Pristine/salt
ATol 3P	416	496	442	544	48	2.44/2.36	0.01/n.r.
ATol 4P	464	498	488	578	80	1.89/0.62	2.54/0.01
AThio 2P	435	536	463	567	31	4.65/0.4	-
AThio3P	455	491	461	499	08	6.98/3.14	-
AThio 4P	436	498	507	606	108	6.78/3.04	0.42/0.03

From the molecular structure, we found planarity gained by protonated **ATol3P** molecules.

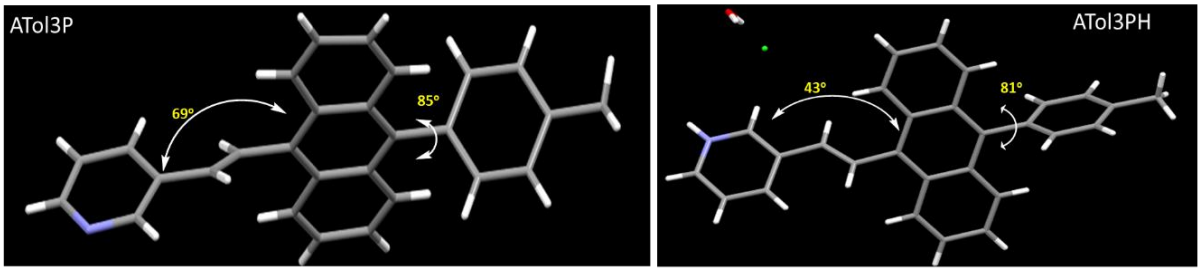

Figure 2.16 Crystal structure of **ATol3P**and **ATol3PH** (a protonated form of **ATol3P;** Chloride salt crystalized with water molecule)

AThio2P displays only 38 nm redshift (entry 3, Table 3), while **AThio3P** exhibits a poor redshift (entry 4, Table 3), and the changes in solid-state emission color are not impressive. We were not able to compare the coplanarity effect between **AThio2P** and **AThio2PH** (as chloride salt) as a suitable single crystal could not be grown for **AThio2P**. However, coplanarity after protonation was not achieved in **AThio3P**. Notably, there are two independent molecules in one asymmetric unit for **AThio3P** (Figure 2.17). These thiophene-linked pyridyl π-conjugates are relatively more planar than toluene-linked analogs, and therefore, thiophene-linked molecules possess somewhat better conjugation, an influential driving force to enhance planarity. The accessible lone pair of

pyridinyl nitrogen gets protonated by its virtue. Still, the impact in emission looks feeble because the electron flow from anthracene to the pyridyl part does not hamper the molecular orientation of **AThio3P** and its salt.

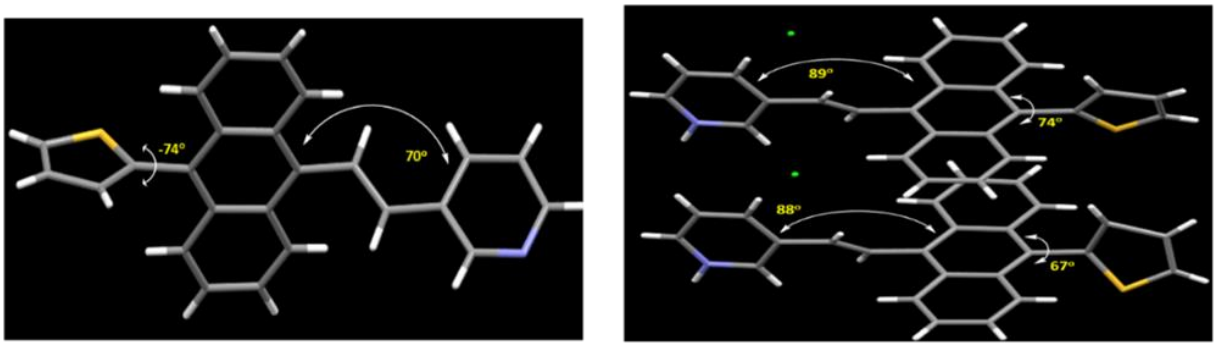

Figure 2.17 Crystal structure of **AThio3P** and **AThio3PH** (protonated chloride salt)

The maximum redshift of 108 nm is observed in **AThio4P** when the pyridyl nitrogen atom is suitably placed away from the anthracene-olefinic electron clouds. Electronic conjugation is also favored in this molecule. In contrast to other analogs, significant planarity is established in the **AThio4P** molecule upon protonation. Both types of torsional angles are reduced to the extent of ~10° and that makes the molecules significantly planar and electronically better conjugated (Figure 2.18). Reducing torsion angles and suitably placed nitrogen atoms can elicit this redshift compared to other analogs discussed herein. The related torsion angles and the emission switching are summarized in **Table 3.**

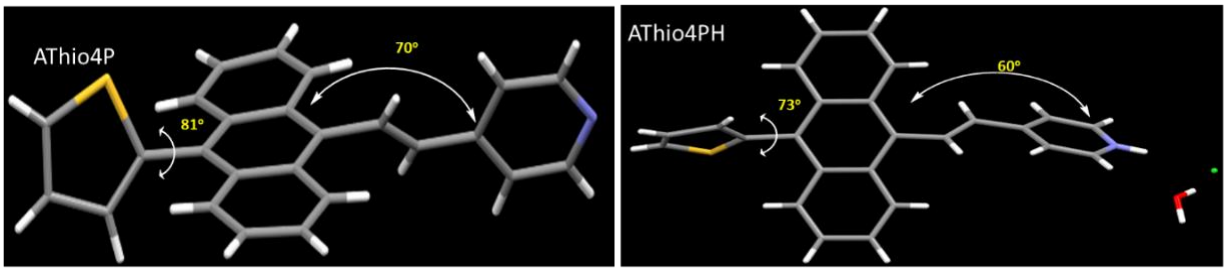

Figure 2.18 Crystal structure of **AThio4P** and its protonated salt

Table 2.3 The torsion angles for the selected probes before and after protonation

Entry	Compounds	Torsion angle (°) type a	Torsion angle (°) type b	Solid-state emission shift (nm)
1	**ATol3P/3PH**	85/81	69/43	48
2	**ATol4P/4PH**	-/87	-/54	85
3	**AThio2P/2PH**	-/69	-/69	38
4	**AThio3P/3PH**	74/67	70/88	14
5	**AThio4P/4PH**	81/73	70/60	108

2.3.5 Analysis of molecular packing

The structures of the five pyridinium chloride salts are sustained by numerous intermolecular interactions due to the presence of Cl^- and water molecules present in the crystal lattice. Both Cl^- and the water molecules formed several intermolecular interactions involving heavy atoms, e.g., Cl···H, S···H, O···C, Cl···C, S···C, O···Cl, N···H, N···Cl and O···H along with the typical C-H···π and π···π interactions (Table 4) and (Figure 2.19-2.22). The diminution of FL intensity could be attributed to the formation of numerous noncovalent interactions that facilitate the formation of the crystals. Despite the presence of many intermolecular interactions, all the salts are twisted significantly, and that avoids forming multiple strong π···π interactions. As anthracene (anth) rings incline to form π···π interactions, anth···anth centroid distances (Å) are calculated and appear to be more than 4.5 (See Table 5 and Figure 2.19-2.22), and it prevents efficient overlap between two anthracenyl cores.

Table 2.4 Crystal interactions of the crystallized pyridinium salts

Comp.	C-H... π (Å)	C...C (π...π, (Å)	H...H (Å)	Anth-Anth (Å)	X...H (Å)	X...C (Å)	N...X (Å)	O...H
ATol3P (4)	2.838, 2.878,	3.387	NA	5.645, 4.607	NA	NA	(X=H) 2.722	
AT3PH.H_2O (17)	2.879, 2.841	3.387,	2.390, 2.373, 2.343	7.257	(X= Cl): 2.851, 2.880, 2.616, 2.809, 2.260, 2.242	(X=O) 3.359	2.658 (X=O)	2.482, 1.790
AT4PH.H_2O (17)	2.892, 2.828, 2.865		2.124, 2.151	7.269	(X= Cl) 2.637, 2.825, 2.929, 2.871, 2.254, 2.192; Cl...O: 3.091	3.198 (X=O)	2.693 (X=O)	2.395, 1.812

AThio2PH	2.862, 2.692, 2.832, 2.842	3.398		5.772	(X=Cl): 2.823,2.095, 2.655, 2.651 (X= S) : 2.919, 2.996	(X=Cl): 3.424, (X=S): 3.436	(X=Cl) 2.965	
AThio3P	2.891, 2.892	3.315	2.310	5.037	(X= S) 2.985, 2.989, 2.651,	(X=S) 3.435	-	
AThio3PH 29 interactions	2.710, 2.875, 2.546, 2.883, 2.861, 2.836, 2.866, 2.717	3.209, 3.175	2.291, 2.168, 2.325	5.061	(X=Cl): 2.576, 2.824, 2.059, 2.855, 2.942. 2.930, 2.577, 2.807, 2.046 (X=S): 2.867	(X=Cl) 2.988, 3.397, 2.974; (X=S): 3.380, 3.387, 3.464,		
AThio4PH (17)	2.835, 2.842, 2.813, 2.651, 2.897	3.309, 3.347, 3.170	-	4.852	(X= S) 2.802, (X=Cl): 2.770, 2.152, 2.734, 2.438, 2.345; (Cl...O): 3.206		X=Cl 3.008	2.376

Thus, we find a decent detectable emission from all these salts. Notably, there is only a subtle change in centroid···centroid distances for a protonated and deprotonated **AThio3P,** and such an observation can describe the unresponsiveness feature. For 4-pyridyl analogs, the centroid···centroid distances of the protonated form are shortened, resulting in a quenching of emission.

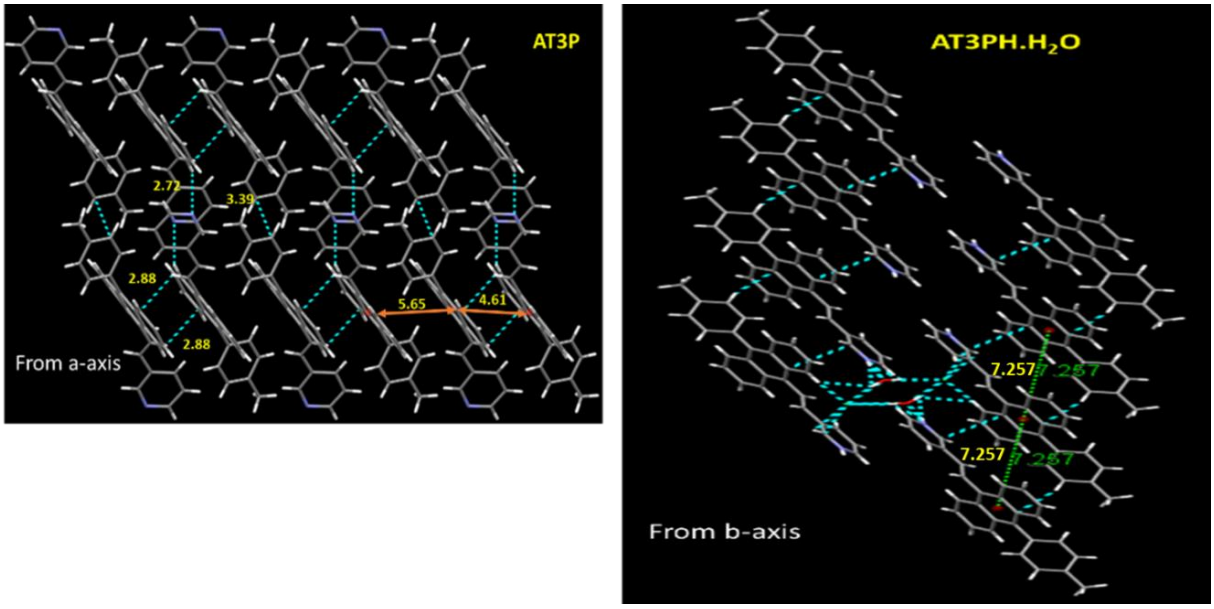

Figure 2.19 Crystal packing with centroid...centroid distances a few noncovalent interactions for **ATol3P** and **ATol3PH**.

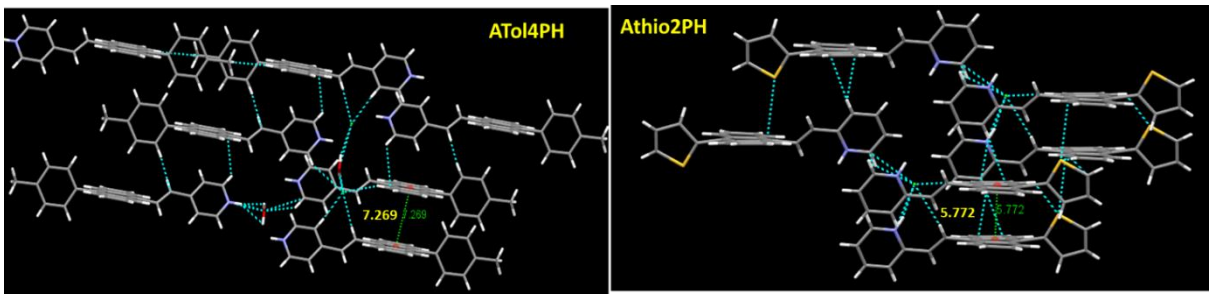

Figure 2.20 Crystal packing with centroid...centroid distances and interactions of **ATol4PH** and **AThio2PH** protonated salt.

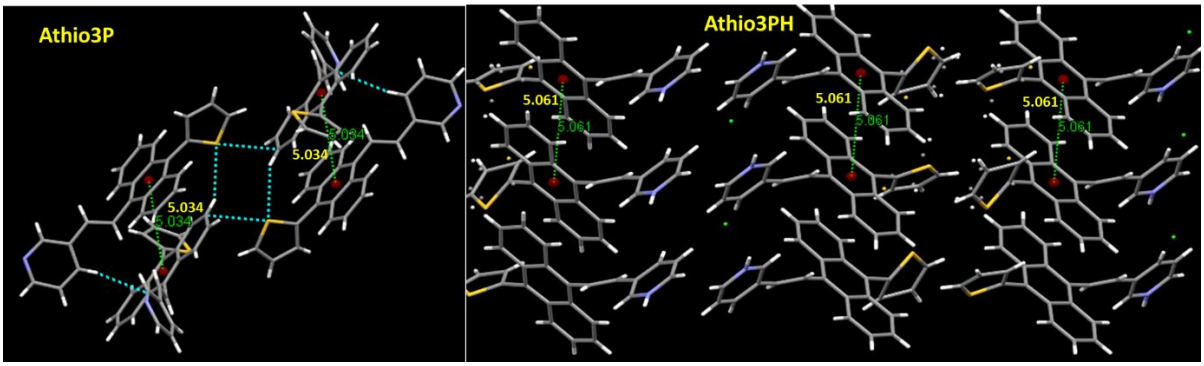

Figure 2.21 Crystal packing with centroid···centroid distances and interactions of **AThio3P** and **AThio3PH** protonated salt.

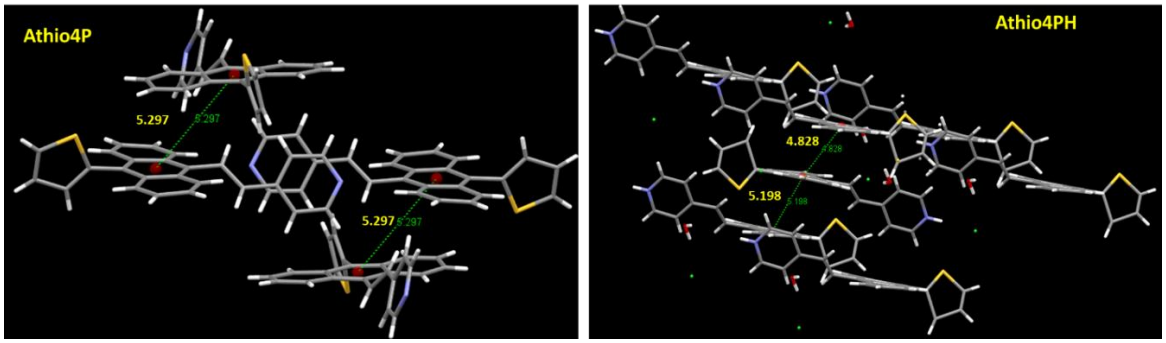

Figure 2.22 Crystal packing with centroid...centroid distances and interactions of **AThio4P** and **AThio4PH**.

Table 2.5 anth···anth centroid distances for the obtained crystals

Compounds	Anthracene Centroid···centroid (Å)	Salt	Anthracene Centroid···centroid (Å)
ATol3P	5.65 and 4.61	**ATol3PH**	7.257
ATol4PH	7.269	**AThio2PH**	5.772
AThio3P	5.034	**AThio3PH**	5.061
AThio4P	5.297	**AThio4PH**	5.198 and 4.828

To decipher the highest sensitivity in the solid-state emission shifting on protonation-deprotonation, the crystal structure and the packing of most acid-sensitive salts **ATol4PH** and **AThio4PH** are further elaborated (Figure 2.23). The **ATol4PH** salt is crystallized in the $P\bar{1}$ space group with one **ATol4P** cation, a chloride anion, and a water molecule in the asymmetric unit with 17 noncovalent interactions (Table 4). The structure is primarily sustained by the five hydrogen bonds, N1—H1···O2 (2.693(2), 1.812(1), 172.69(1)^0), O2—H2B···Cl1 (3.091(1), 2.254(2), 166.81(1)^0), O2—H2A···Cl1 (3.082(1), 2.192(1), 174.03(1)^0), C7—H7···Cl1(3.754(2), 2.825, 176.27^0), C4—H4···Cl1(3.559(2), 2.637, 171.37(1)^0) and C5—H5···Cl1(3.697(1), 2.871, 148.6^0). There are no face-to-face π···π interactions between the anthracene moiety inside the lattice, instead C9—H1A···π(C1) (3.461(1), 2.828, 126.33^0) and C27—H27···π(C6) (3.694(1), 2.892, 145.25^0) supports the crystal packing. The absence of co-facial strong π···π interactions makes the anthracene rings far apart (7.269 Å). The presence of a tolyl group would create more vibration/rotational motion, and a greater number of very strong H-bonding plays a major role in reducing the quantum yield.

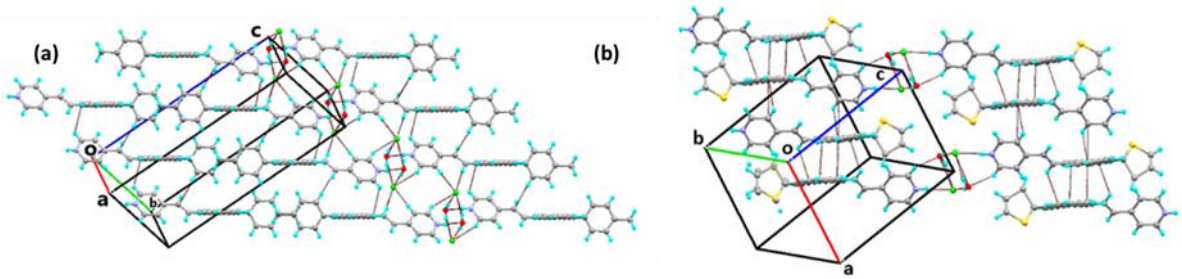

Figure 2.23 Crystal packing sustained by hydrogen bond and π interactions (a) **ATol4PH** (b) **AThio4PH**

Compound **AThio4PH** was also crystallized in the $P\bar{1}$ space group with one **AThio4P** cation, a Cl^- anion, and a water molecule in the asymmetric unit with 17 noncovalent interactions, similar to the tolyl analog. The thiophene moiety of the **AThio4PH** cation is disordered over two positions and has been modeled with 0.63(1) and 0.47(1) occupancies. The structure is sustained primarily by three hydrogen bonds O1—H1C···Cl1 (3.206(1), 2.354(1), 173.49(2)^0), O1—H1B···Cl1(3.278(1) Å, 2.436(2) Å, 162.70(1)^0), N1—H1···Cl1 (3.007(2), 2.146(2), 175.18(1)^0) and face-to-face π···π interactions C9···C12 (3.309 Å) between the anthracene moiety of the **AThio4PH** cations. However, the centroid-centroid distances between two anthracene ring is measured to be 4.852 Å. Weaker hydrogen bonds C5—H5···Cl1 (3.645(3), 2.734, 166.6^0), C1—H1A···O1 (3.226(2), 2.376, 151.92^0), C12—H12···Cl1 (3.507(2), 2.770, 136.82^0), C4—H4···π (3.347(2), 2.897, 111.17^0) renders further stability to the packing. Thus, the presence of small unsubstituted thiophene moiety in **AThio4PH** and fewer H-bonding interactions in the molecular packing facilitate emitting significantly better than **ATol4PH**. It is well established that H-bonding plays a substantial role in controlling emissions.[41,42] The H-bonding has both adverse and beneficial effects on FL intensity; however, we found a reduction in FL intensity for these analogs.[41]

Thus, fluorescence in the solid state is mainly instigated by molecular conformation and intermolecular interactions in the crystals. To clarify the contribution of the factors, fluorescence in the solution state for **AThio4P** and **AThio4PH** is also examined. Both compounds are found to be almost non-emissive in acetonitrile with Φ_f < 1% (Figure 2.24). It indicates that molecular conformation and supramolecular interactions play a significant role in solid-state emission.

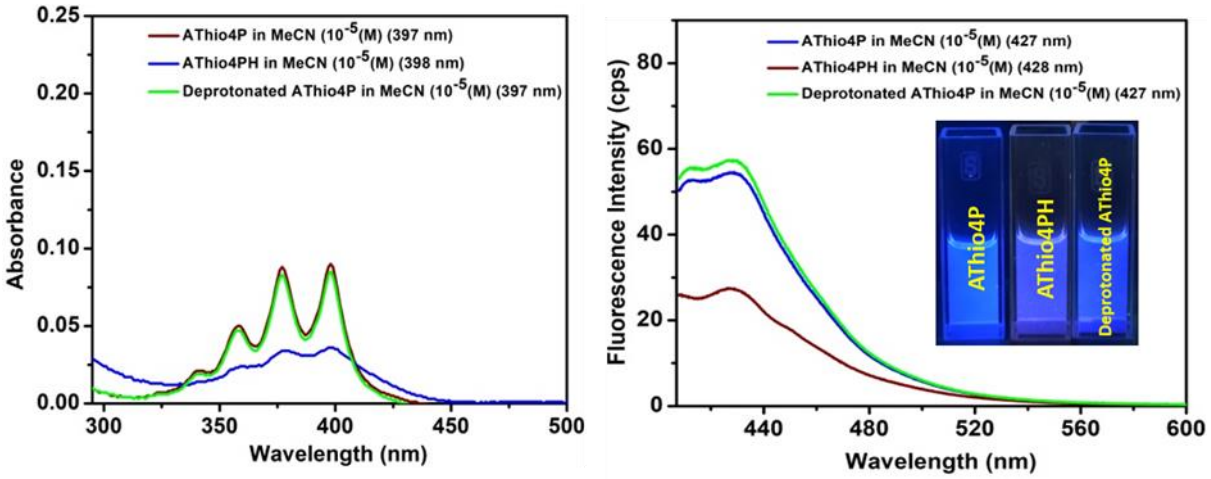

Figure 2.24 Absorbance and emission of **AThio4P**, **AThio4PH** and deprotonated **AThio4P** in acetonitrile.

2.3.6 Powder X-ray diffraction studies

The SSAC behaviors of mainly **ATol4P**, **AThio3P,** and **AThio4P** are further investigated through PXRD studies. In response to acid exposure within a few seconds (3-5), an immediate FL-switching of the crystal is observed, and the question arises if the whole crystal is protonated. The acid vapor was continuously exposed for 5- 10 min to complete the protonation process. A distinct emission at 606 nm indicates a complete protonation. The presence of acidic water vapor might cause partial dissolution on the crystal surfaces through the condensation process. When dissolution and crystallization of the protonated species mediated by condensed water are continued, the conversion may be initiated and achieved fully within 5-10 min. Similar processes could also be perceived in response to TEA exposure. In such a case, changes in crystallinity are anticipated. Thus, PXRD was recorded for each pristine, protonated, and deprotonated sample only for selected probes (Figure 2.25).

The PXRD patterns reflect a loss of crystallinity of the probes upon exposure to acid vapor for 5-10 min. Notably, the sharp diffraction peaks of pristine almost disappeared upon protonation for **ATol4P,** whereas **AThio3P/AThio4P** still displayed some sharp and broad diffractions (Figure 2.25). In addition, a few new diffractions also appeared for the protonated samples, indicating the generation of new facets, and the changes in the PXRD patterns were relatively prominent for both **ATol4P** and **AThio4P**, compared to **AThio3P**.

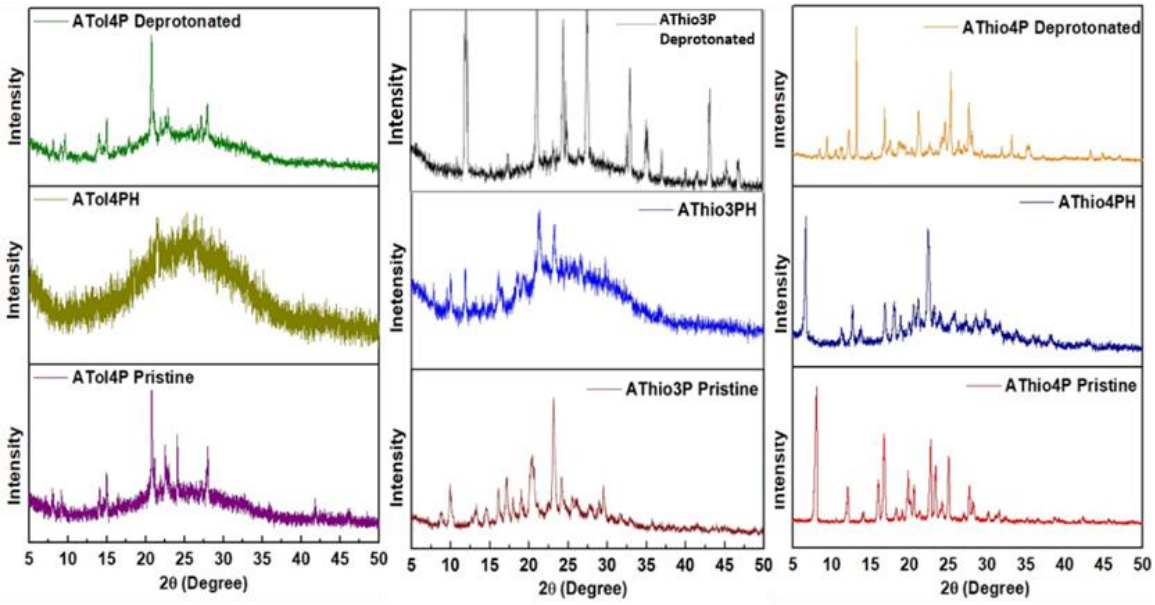

Figure 2.25 Powder X-ray diffraction pattern

This difference in the PXRD pattern can further validate a significant FL-shift of 108 nm and 85 nm consecutively for **AThio4PH** and **ATol4PH** compared to **AThio3P** with a subtle shift of 14 nm. During the deprotonation process (exposure to TEA for 5-10 min), the crystallinity of all the samples was almost regained, however, with a few more new diffractions. Therefore, the emission color was almost recovered to its originality with a slight difference in the fluorescence spectra. The variance between pristine and deprotonated forms can further be substantiated by the PXRD pattern revealed by the deprotonated samples. The deprotonated forms appear to be more amorphous than the pristine samples. Such differences in emission and PXRD patterns for pristine and deprotonated samples can be attributed to the deposition of the triethylamine hydrochloride salt. This salt will persist in a solid state and is hard to remove by the fumigation process. The salt accumulation also can gradually reduce the efficiency in FL-switching recyclability.[42]

2.3.7 Conjugation pathways

The extent of conjugation and its interaction between donor-acceptor (D-A) groups are the utmost factors in determining the emission properties of molecules. Here all the reported salts are sufficiently twisted, and the admirable bathochromic shifts (except for **AThio3PH**) might be the circumstances of an increased conjugation. The location of pyridyl *N*-atom at the 4th position brings far better conjugation than the 3rd

position. Moreover, the pK_a of pyridyl *N*-atom at the 4th / 2nd position will be much greater (higher basicity) than the 3rd position due to the significant negative charge accumulation on nitrogen at the 4th / 2nd position. In comparison between 4th and 2nd, lone pair of nitrogen for 4th pyridyl would be more accessible, exhibiting more basicity than the 2nd position. Such an effect can clarify the observed difference in emission shift for the regioisomers.[43] Therefore, **ATol4P or AThio4P** produces a much higher redshift (> 80 nm) than **ATol3P** or **AThio3P** (< 40 nm) (Figure 2.26). The type of noncovalent interactions, originated by these salts with a preferred orientation also enforces a crucial role in the crystal packing and the emission. The variation in absorption spectra of a few salts further supports the molecular geometries and existing conjugation pathways in them.[26]

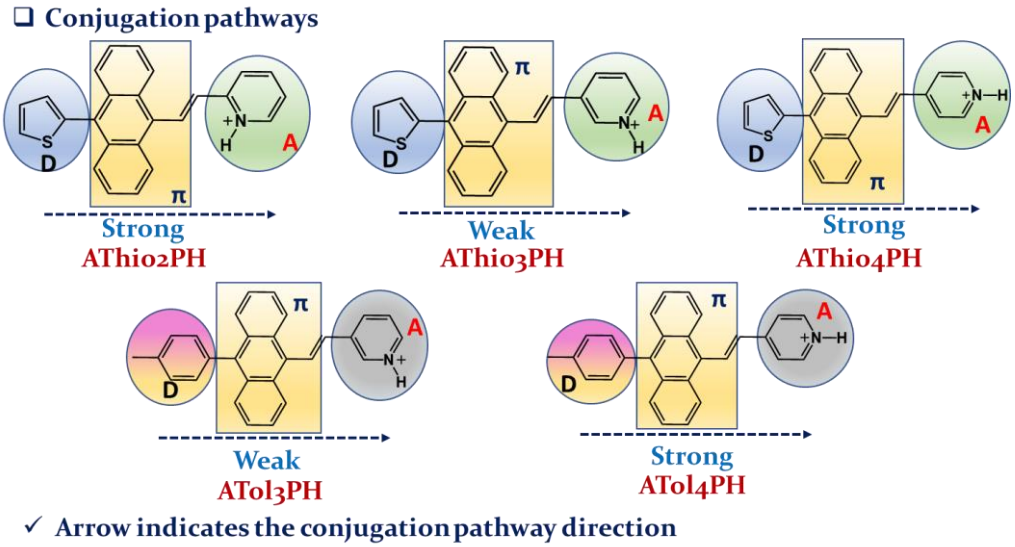

Figure 2.26 Pathway of conjugation in the protonated salts; here, donor (D) is shown as tolyl or thiophene group. However, anthracene core is also added as a part of the donor. Strong and weak π-conjugation systems are presented with different color combinations.

2.3.8 Photostability of ATol4PH and AThio4PH salts

As the protonated salts like **AThio4PH** and **ATol4PH** have the maximum spectral shift from their corresponding pristine forms, the photostability of these two salts was examined under continuous exposure of UV light (at their absorption λ_{max}) for a time span of 4 h continuously. An admirable photostability with almost unchanged intensity was found for **AThio4PH** (Figure 2.27b), while a slight reduction is noticed in **ATol4PH** (Figure 2.27a).

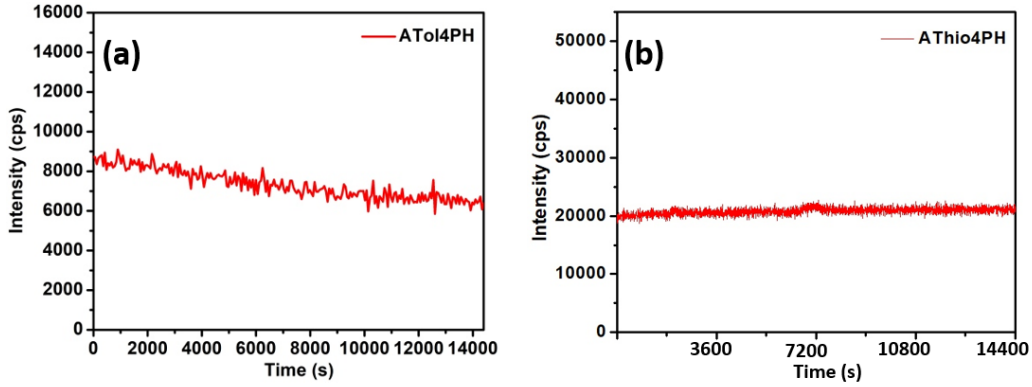

Figure 2.27 Photostability comparison between (a) **ATol4PH** and (b) **AThio4PH**

2.3.9 Scanning Electron Microscope (SEM) studies

The surface morphology of organic solids may change after exposure to certain stimuli.[44] In this connection, the SEM images are taken only for the most sensitive probe **AThio4P** upon exposure to acid and base vapor stimulus. The surface of the pyridyl emitter appears to be smoother, which displays a wrinkling pattern after protonation, and the smoothness is almost returned after exposure to base vapor (Figure 2.28). However, crystal packing and intermolecular interactions lead to the essential roles for the reversible SSAC features.

2.3.10 Theoretical studies

The most and least SSAC-sensitive molecules **AThio4P** and **AThio3P** are selected to calculate the difference in transition dipole moment and molecular orbitals before and after protonation using CAM-B3LYP/6-31G(d) level of theory (Table 6). The calculated lowest transition energy for **AThio3P** and **AThio4P** are 358.66 nm and 360.84 nm, respectively.

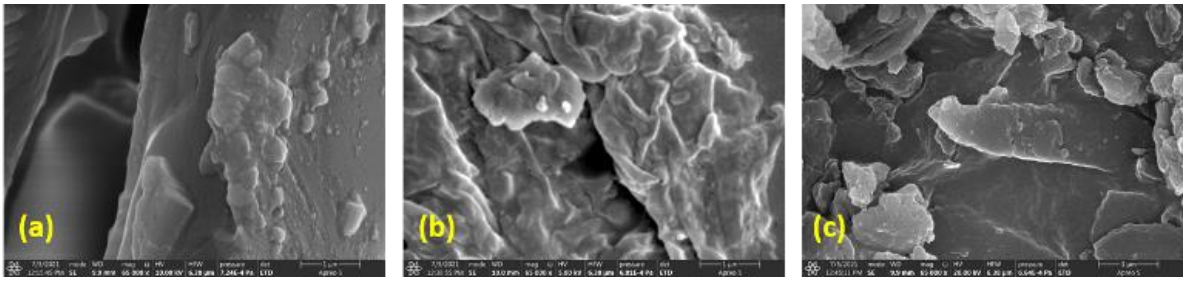

Figure 2.28 (a) **AThio4P** Pristine (b) **AThio4PH** Protonated (fumed by acid vapor) (c) **AThio4P** (after exposing base vapor to **AThio4PH**). All the images were captured on a 1 μm scale.

The corresponding transition dipole moment for **AThio3P** (μ=6.732 D) is comparable with **AThio4P** (μ=6.702 D). This can be ascribed to the lowest energy optical transition for both the molecules, involving mainly HOMO→LUMO (~94%, HOMO and LUMO are the highest occupied molecular orbital and lowest unoccupied molecular orbital, respectively). Both HOMO and LUMO are primarily localized on anthracene moiety before protonation (Figure 2.29). However, the energy of LUMO is considerably stabilized by ~3.8 eV for both **AThio3PH** and **AThio4PH** by gaining a positive charge after protonation. Hence, the lowest energy optical transition (which is also mainly HOMO→LUMO transition) is redshifted. Notably, weak conjugation in **AThio3PH** offers a profound donor-acceptor property (Figure 2.28) and exhibits a lower transition dipole moment (5.998 D, **Table 6**) than **AThio3P**. In contrast, the strongly favorable conjugation in **AThio4PH** reveals a much higher transition dipole moment of 9.923 D due to local excitation.

Table 2.6 Lowest energy optical absorption along with corresponding transition dipole moment (μ) and oscillator strength (f) calculated using CAM-B3LYP/6-31G(d) Level of Theory

Molecule	State	Energy (nm)	Trans. Dip. (μ)	Osc. Strength (f)	Orbital contribution
AThio3P	S_1	358.66	6.732 D	0.594	H→L (94%)
ATh3PH	S_1	548.85	5.998 D	0.308	H→L (96%)
AThio4P	S_1	360.84	6.702 D	0.585	H→L (94%)
ATh4PH	S_1	532.81	9.923 D	0.869	H→L (95%)

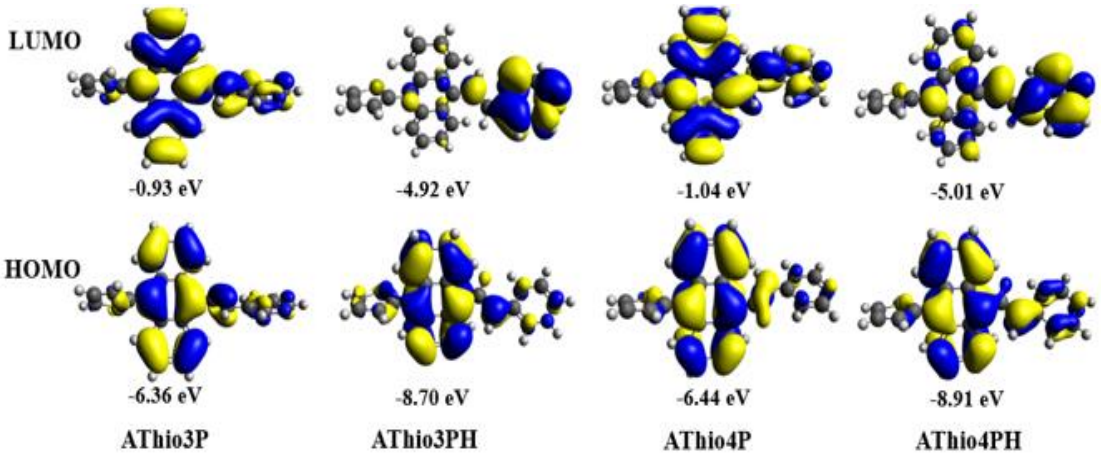

Figure 2.29 Frontier Molecular Orbital (FMO) for **AThio3P**, **AThio3PH**, **AThio4P,** and **AThio4PH** using CAM-B3LYP/6-31G(d) level of theory.

2.3.11 Real-world application of SSAC feature

2.3.11.1 Reversible security writing on polymer appended platform

A high-contrast 108 nm redshift in solid-state emission upon protonation of the **AThio4P** compound has motivated us to generate an easily accessible, stable platform for security-based writing. A fluorophore-blended polymer matrix was generated to afford a steady, economical, and bright platform. The polymer blend was easily prepared by mixing 5 mg fluorophore **AThio4P**, 50 mg of poly (methyl methacrylate) [PMMA, cheapest polymeric material], and 500 µL of propylene carbonate (as plasticizer) in 1-2 mL of acetonitrile and followed by sonication for 30 min. This solution was drop-casted on a glass surface and allowed to dry in the air at room temperature for a day. Thus, the green emissive fluorescent platform (Figure 2.30a) becomes ready for security writing/drawing, visible only after illuminating with a 365 nm UV-lamp. The pen nib was dipped in a 0.1 M HCl solution and used to write the letters emitting a brilliant red color (Figure 2.30b). Initially, care should be taken to avoid the acid vapor that can spread and change the color of this entire platform from green to red. The original green-emitting platform can further be generated by exposing triethylamine (TEA) vapor. Good recyclability could help us to use the same materials multiple times. Thus, letters/drawings are marked on such a green-emitting solid platform using an acid pen and erased with a base. The polymer blend is dried over glass slides and lifted as a green-emitting film. It can be given a shape of our choice by trimming the polymer and employed as a portable and reusable writing pad (Figure 2.30d). Such a polymer matrix can be prepared with all the emitters mentioned herein. We have verified with **ATol3P** as another platform; however, the color change was not impressive (Figure 2.30e). This whole system would be prominent only under 365 nm UV light and, therefore, would be a potential substrate for anti-counterfeiting applications in solid-state.

2.3.11.2 Fluorescent optical detection of ammonia vapor and melamine in water using AThio4Ph appended PMMA matrix

Ammonia is highly toxic and corrosive to the environment.[45-47] Inhalation of hazardous ammonia, even in lower concentrations, can cause severe damage to the eyes and respiratory systems.[48] Thus, easy detection of ammonia leakage is a pressing need.

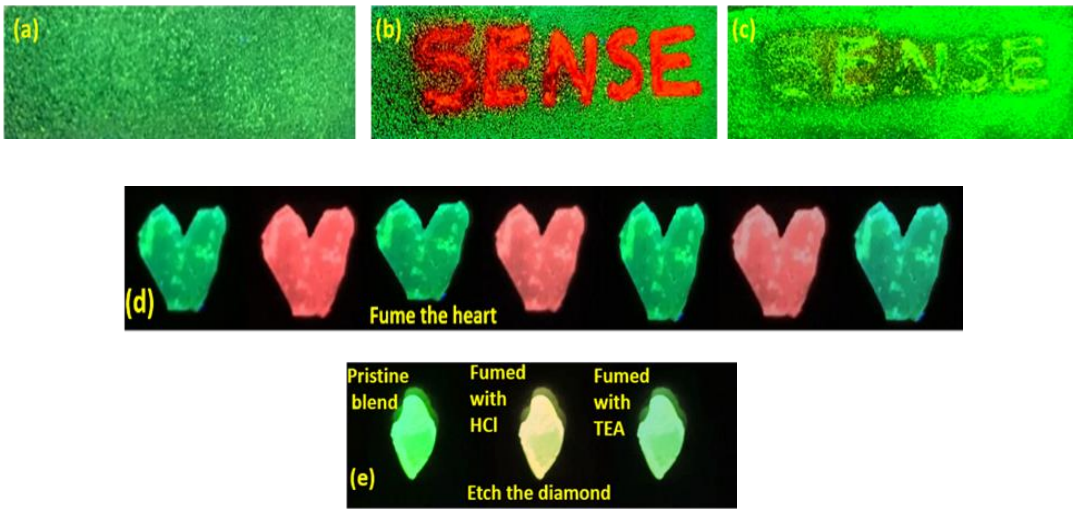

Figure 2.30 (a) Polymer Blended Pristine sample (b) pen was dipped into HCl and then used to write the letters (c) after exposure to TEA vapor**.** (d) Simultaneous reversible dual sensing of acid and base vapor with the portable heart-shaped **AThio4P** polymer matrix. (e) Reversible sensing of acid and base vapor with the diamond-shaped **ATol3P** polymer matrix.

On the other hand, high nitrogen-containing amine and melamine (2,4,6-triamino-1,3,5-triazine) are used in paint, plastic, and adhesive industries.[49] Because of its high nitrogen contents, melamine is illegally used in milk powder and other protein-containing foodstuffs. Melamine is also toxic to humans on long-term consumption due to the formation of cyanuric acid *via* hydrolysis of melamine.[50] Hence, the recognition of melamine in food is essential. Although there are various techniques to detect such analytes, most are time-consuming and expensive.[51]

2.3.11.2.1 Preparation and characterization of AThio4Ph appended PMMA matrix

The synthesized compound **AThio4P** is a solid-state green emitter under 365 nm UV lamp illumination. The alkaline nature of the pyridyl core with pK_b = 8.8 can readily accept the proton and release it under a suitably sensitized chemical environment. Among many variations on pyridinyl *N*-atom position and (hetero) aryl substituents, we realized reversible **AThio4P** to **AThio4PH** (in response to acid vapor) as a quick and sensitive solid platform to display FL-switching with a high color contrast from green (λ_{em}= 498 nm) to orange (λ_{em}= 606 nm). Thus, the reversible nature could identify the amine analytes instantly by a visible naked-eye FL-switching under 365 nm light.

The solid-state emitting **AThio4P** [5 mg, quantum yield (Φ_f) = 6.78 %] is mixed with PMMA (30 mg or 60 mg) in 300 µL MeCN + 500 µL propylene carbonate (binder) and sonicated for 20-30 mins. Next, the solution was laid down on a glass slide and allowed to dry at room temperature (27°C). After 2-3 days, the dried polymer-appended fluorophore matrix was given a different shape for attractive usage. The fluorophore–blended polymer exhibits green emission at λ_{em}= 493 nm with Φ_f = 5.76 %. Notably, both **AThio4P: PMMA** 1:6 and 1:12 mixing provided the green-emitting solid and durable platform. To use a small amount of probes, we preferred a 1:12 ratio for such detection studies. We have investigated the ^{1}H NMR spectrum for this composite sample and compared it with the PMMA + propylene carbonate mixture and the pure probe. The ^{1}H-NMR reveals unchanged chemical shifts of the probe after the blending, indicating a weak van der Waals force involvement between the probe and the polymer. In addition, the SEM (Scanning electron microscopic)-images are captured before and after adding the probe to the polymer (Figure 2.31-32). The surface of the polymer-blended fluorophore becomes more homogeneous and cleaner for the 1:12 ratio than for the 1:6 ratio (Figures 2.31B, 2.32B). The fluorophores are segregated (Figures 2.31c-2.32C) on the surface after fuming with acid (*vide infra*). Thus, the probe is embedded with the polymer *via* various intermolecular weak noncovalent interactions. The green-emitting pristine **AThio4P** (Φ_f = 6.78 %) is converted to **AThio4P.HCl** (**AThio4PH**) on HCl exposure and results in red emission (λ_{em}= 606 nm) with reduced Φ_f (3.04 %). In response to acid exposure, green-emitting polymer emits at 600 nm (Φ_f=1.38%).

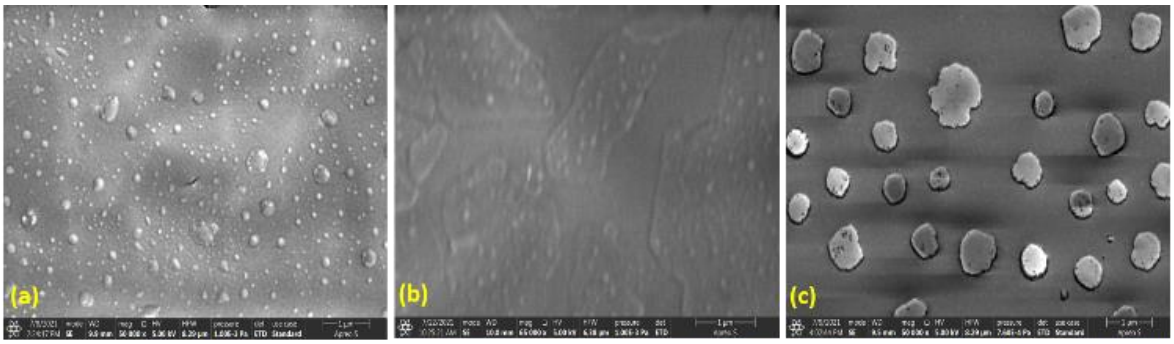

Figure 2.31A Surface morphology of (a) only **PMMA** (b) **AThio4P polymer matrix** (1:6) (c) acid-fumed **AThio4P polymer matrix** (1:6). All the images have been captured at the same scale of 1µm.

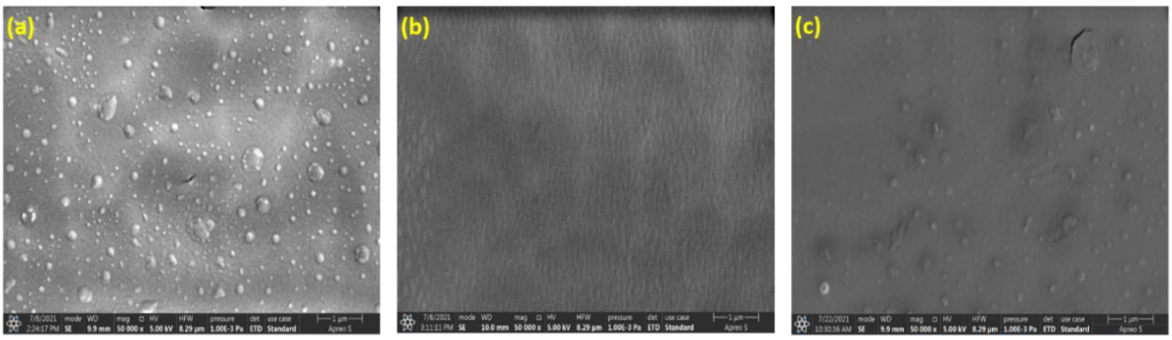

Figure 2.32B Surface morphology of (a) only **PMMA** (b) **AThio4P polymer matrix** (1:12) (c) acid-fumed **AThio4P polymer matrix** (1:12). All the images have been captured at the same scale of 1μm.

2.3.11.2.2 Photophysical studies with the AThio4P appended PMMA solid-matrix for ammonia and melamine detection

This red-emitting polymer (Φ_f =1.38%) is utilized to detect ammonia (pK_b = 4.75) vapor and 10^{-5} M aq. melamine (pK_b = 9.0) solution. An immediate blue-shifted emission (107 nm switch) with an increment in the emission of the polymer matrix (Φ_f =2.77%) is detected by exposing ammonia gas to the acid-fumed polymer platform because the ammonia is capable of deprotonating the probe and bringing back the original form (Figure 2.33a). As the pyridyl core is attached to electron-rich anthracenyl π-conjugate, a higher electron density on the pyridyl ring is speculated and, thus, becomes relatively more basic. Hence, this probe will be a stronger base than melamine, which disfavors deprotonation from the probe. However, amine groups and pyridyl nitrogen could interact with the probe's pyridyl proton and alter the emission. Thus, upon dipping the red-emitting polymer into 10^{-5} M aq melamine solution, a shift of 24 nm is noticed with a resulting λ_{em}= 576 nm and Φ_f =2.33%. However, the emission color can be easily distinguished from red to orange, as demonstrated in Figure 2.33b.

Next, we made a simple strategy to recognize NH_3 vapor and examine the leakage detection. Commercially available NH_3 [~2.5 ppm; 5% in Helium (balance gas, *v*/*v*)] was taken in a large size balloon and attached with a 1 mL syringe with a tiny needle of 0.60 mm diameter. The ammonia passing from a balloon was controlled by releasing the gas flow from a balloon. The green-emitting polymer (Figure 2.34a) is initially converted to a red-emitting one (Figure 2.34b) under acid vapor.

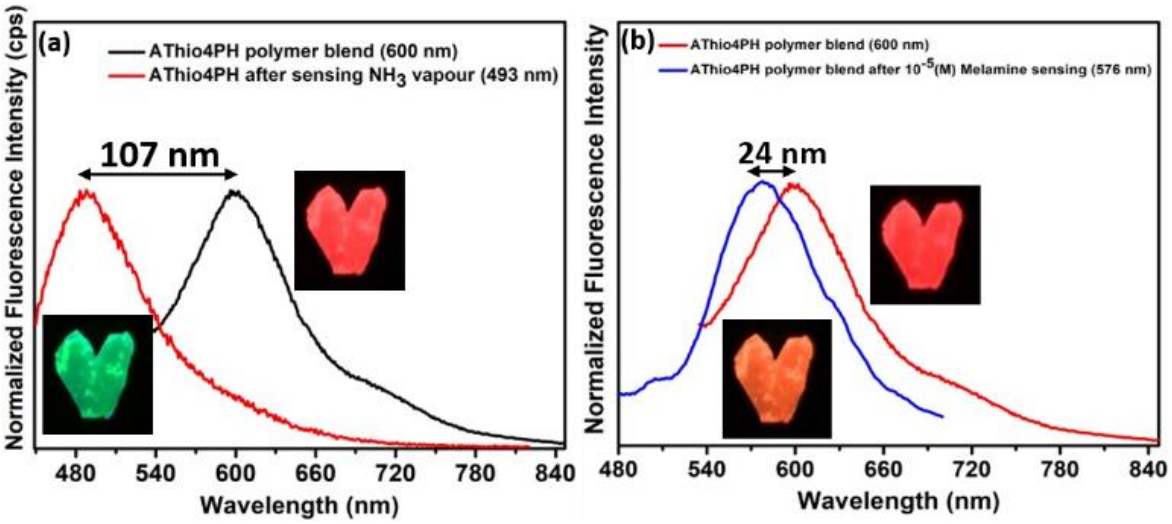

Figure 2.33 Sensing by acid-fumed **AThio4P polymer matrix** (a) Ammonia gas (b) Aq. melamine. (λ_{ex}= 498 nm)

Subsequently, we allowed passing NH_3 through the syringe on the red-emitting polymer, rapidly resulting in a green-emitting solid (Figure 2.34c), which was detected visually by illuminating a 365 nm UV lamp. When we exposed NH_3 on one surface of a diamond-shaped polymer, an immediate change in emission was observed, while the other side was the original red color. The SEM image of the acidified polymer revealed a microphase separation, which possibly occurred due to the formation of relatively polar hydrophilic pyridinium salt. Thus, the emission is also shifted, and the protonation enhances the molecular π-conjugation, generating a red emission.

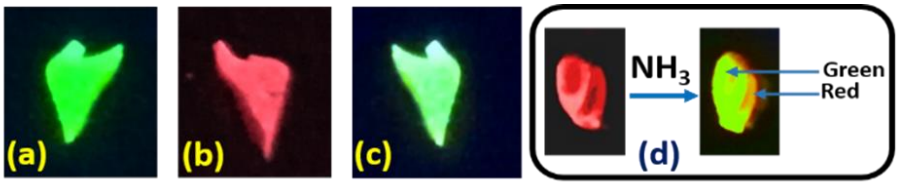

Figure 2.34 (a) **AThio4P** polymer matrix (b) **AThio4PH** polymer matrix (after exposure to acid) acid fumed (c) after NH_3 vapor exposure on b. (d) NH_3 exposed to one surface and the contrast.

It is pertinent to mention that **AThio4PH** powder could instantly recognize ammonia vapor with a 104 nm spectral blue shift (Figure 2.35a). This color change is also dictated by the Commission Internationale d'Elcairage (CIE-1931) chromaticity diagram (Figure 2.35b-c).

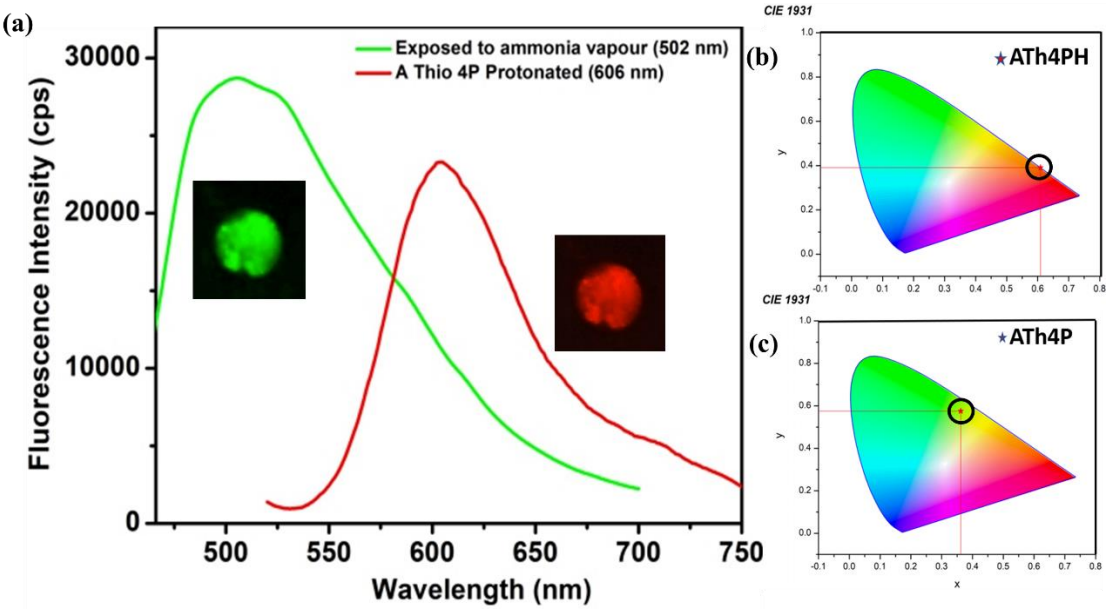

Figure 2.35 (a) Reversible detection of ammonia gas by **AThio4P** protonated solid (**AThio4PH** powder) (b-c) CIE-diagram of emission swithing due to reversible sensing of ammonia.

Next, the red-emitting polymer was explored to detect dilute ammonia solution with a control experiment using 100% water. No significant FL-switching was observed in water (Figure 2.36a), but the floated polymer matrix (Figure 2.36b) could recognize 11.3 ppm aqueous ammonia solution (Figure 2.36c). The polymer matrix exhibited visually recognizable emission switching once dipped into the solution for 1-2 min (Figure 2.36d-f). Thus, this polymeric system is superior to the typical fluorophore-coated paper strips in detecting these important analytes in water.

Subsequently, the polymer probe was tested to detect melamine of different strengths. Upon treatment with 10^{-5} M aq. melamine solution, a 24 nm blue shift (red to orange; 600 to 576 nm, Figure 2.37) occurred to signify a sort of interaction of the probe with melamine. Being a weaker base, melamine won't be able to snatch the proton from the probe, but other supramolecular interactions can change the position of the proton and, thus, the emission property. Numerous weak noncovalent interactions can alter the conformational behavior of a molecule. If there is any lack of coplanarity, a blue-shifted emission would result. A quantitative analysis of the response of melamine was performed with **AThio4PH** powder by adding a few drops of 10^{-5} M aq. melamine solution onto the **AThio4PH** powder. It turns into yellowish orange (606 to 572 nm) within 1-2

min, and such color-contrasting behavior gradually diminishes while decreasing the concentration of melamine. Thus, the solid **AThio4PH** powder could detect 10^{-5} M aq melamine solution with 34 nm spectral blue shift and switch the powder's color from red to yellowish orange with Φ_f =2.70 %.

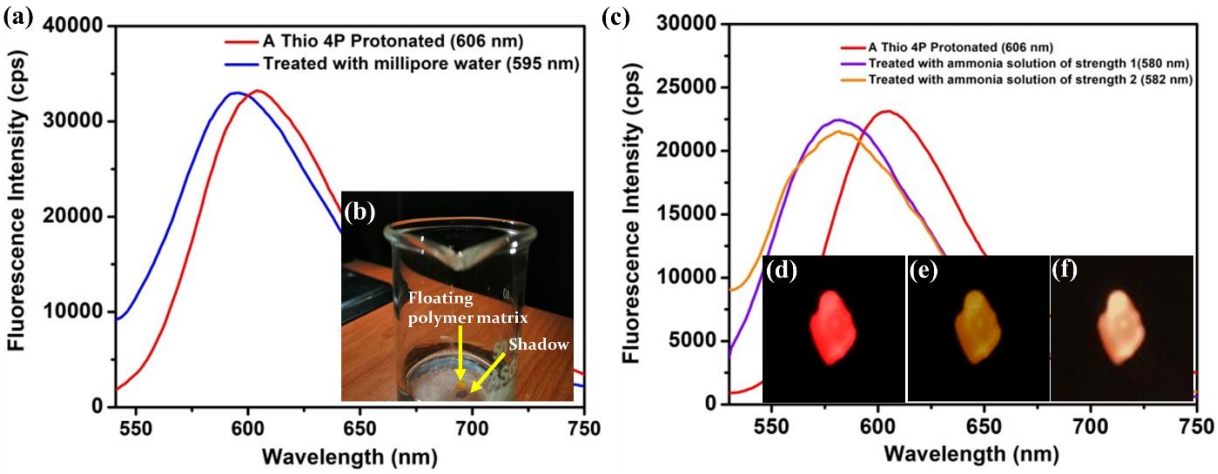

Figure 2.36 (a) Acid-fumed **AThio4P** polymer matrix to cross-check if can change color only being dipped into millipore water, (b) The polymer matrix floats on solution or partially submerges sometimes and so the shadow is there in normal room light, (c) **AThio4PH** powder (**AThio4P** protonated) to detect different strengths of aq. ammonia solution (**Solution of strength 1:** 10 µL of 25% ammonia solution in 100 mL of Millipore water, **solution of strength 2:** 10 µL of 25% ammonia solution in 200 mL of Millipore water, (d) Acid-fumed **AThio4P** polymer matrix to sense different strengths of aq. ammonia solution, (e) **Solution of strength 1:** 10 µL of 25% ammonia solution in 100 mL of millipore water, (f) **solution of strength 2:** 10 µL of 25% ammonia solution in 200 mL of millipore water.

The color change was still discernible at 10^{-6} M and 10^{-7} M aq melamine solution with 28 nm and 25 nm spectral blue shift (Figure 2.38). However, the spectral shift was not impressive for 10^{-8} M aq melamine solution, and the reason was stated before. Hence, melamine could be detected by **AThio4PH** powder through the naked eye from 1.3 - 0.126 ppm. Notably, the food safety authorities of different countries have set certain limits of melamine content in foods varying from 50 ppb to 5 ppm to avoid health risks to their citizens.[52] The polymer blended **AThio4P** was acid-fumed, and the resulting red-emitting polymer matrix was tested to sense melamine in milk samples for real applications.

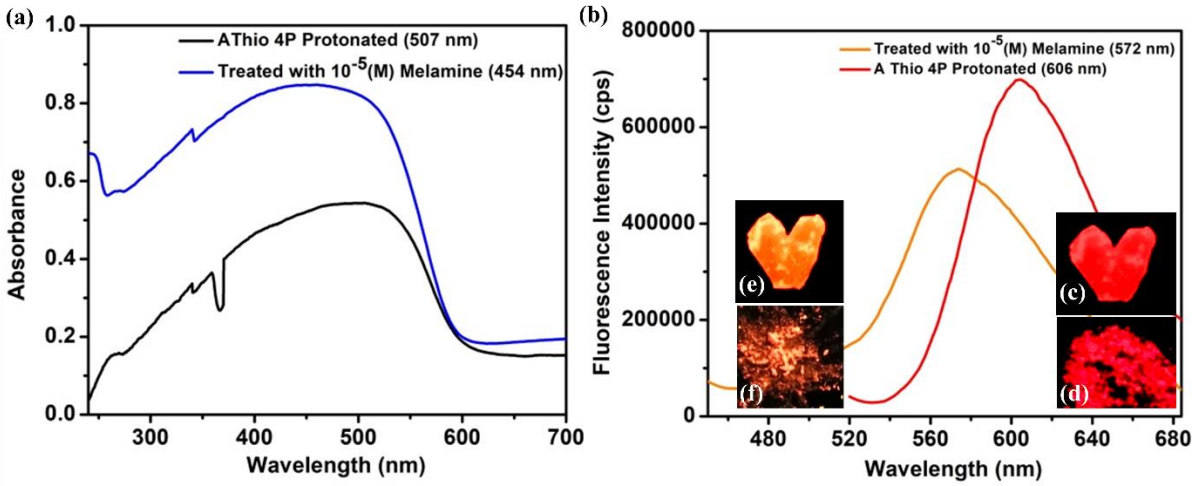

Figure 2.37 Sensing of 10^{-5} M aq. melamine solution by **AThio4PH** powder in solid-state and with the polymer matrix, (a) absorbances (b) emissions (c) **AThio4PH** powder (d) **AThio4PH**-PMMA matrix (e) **AThio4PH** powder after sensing of 10^{-5} M aq. melamine solution (f) **AThio4PH**-PMMA matrix after sensing of 10^{-5} M melamine aq. solution

Further, the emission color remained unchanged upon dipping the red-emitting polymer matrix into market-available milk (Figure 2.39). However, different concentrations of 10^{-5} M, 10^{-6} M, and 10^{-7} M melamine-containing milk sources were prepared, and the polymer matrix was dipped into this contaminated milk. The color change was observed within a few min (2-7 min, Figure 2.40) under UV light with naked eyes, but the color change was not much exciting at 10^{-6} M and 10^{-7} M solution. Thus, this polymeric probe became helpful in detecting melamine in food items in a convenient and economical route, avoiding expensive methods.[53]

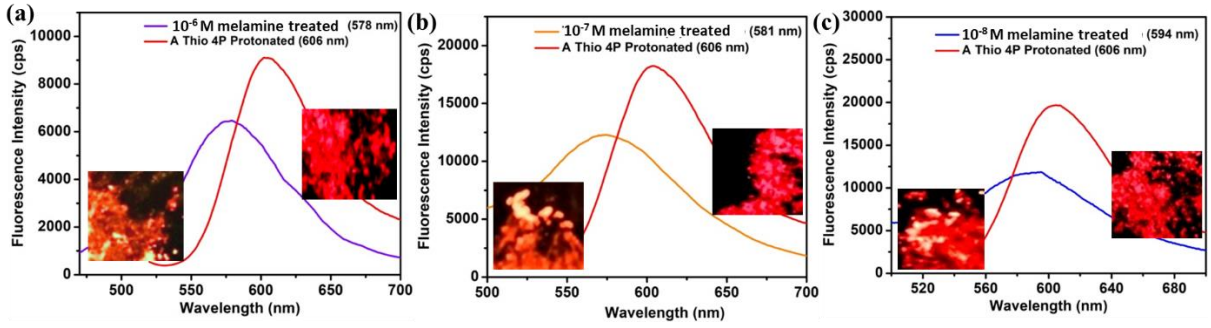

Figure 2.38 Sensing of different strengths of aq. melamine solution by **AThio4PH** powder in solid-state

Most fluorescence-based techniques are reported in the solution state, and they need a fluorimeter to identify. This solid-state emitting polymer matrix is portable and

reusable to distinguish the FL-switching easily after dipping into the solution or holding against the gas/vapor with the help of a portable UV lamp.

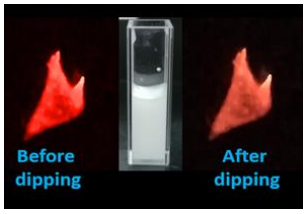

Figure 2.39 Sensing of milk with no melamine content with the acid-fumed **AThio4P** polymer matrix

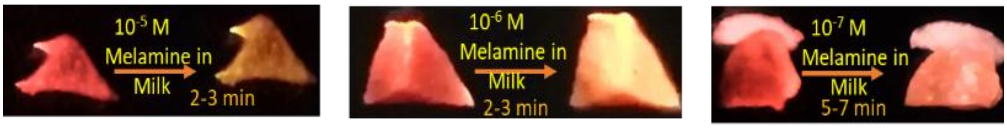

Figure 2.40 Acid-fumed **AThio4P** polymer matrix with different shapes for melamine sensing in an actual milk sample

Precisely, the melamine contains three $-NH_2$ groups linked to a triazine core. To understand the role of these functionalities in melamine recognition, a few more compounds with electronic diversities are screened with a powder **AThio4PH** probe. Only pyridine (pK_b = 8.8) and aniline (pK_b = 9.38) (10^{-5} M solution) were initially tested and showed a similar effect of ~26 nm blue shifts as melamine (pK_b = 9.0). When 2-aminopyridine (pK_b = 7.20) solution was exposed, only 13 nm switching was noticed. The interactions between nitrogen lone pair of pyridines and the hydrogens of the $-NH_2$ group would possibly cause this outcome. Further, weaker base 4-nitroaniline (pK_b = 12.99) brings the effect of a 21 nm shift. (Table 7). This study demonstrates that the change in the blue shift for melamine detection is not only guided by the basicity of the analytes. It is more likely directed through a reversible proton exchange and weak noncovalent interactions, and therefore the shifts are not that prominent compared to the response from ammonia.

The almost auto-reversible emission from powder **AThio4PH** can further support the effect while sensing 10^{-5} M aq melamine solution. The FL-switching from 606 to 572 nm was noticed immediately, but gradually, the emission λ_{max} started regaining its original position and reached 585 nm within 5 min. Thus, the actual red emission can be retrieved within a day (Figure 2.42).

Table 2.7 Spectral shifts of analytes structurally similar to melamine, by **AThio4PH** powder at 10^{-5} (M) concentration of each analyte

Probe	Analytes	pK_b	Concentration of analytes (M)	Spectral blue shift (nm) from 606 nm
AThio4PH powder	Melamine	9.0	10^{-5}	34
AThio4PH powder	Pyridine	8.8	10^{-5}	26
AThio4PH powder	2-aminopyridine	7.20	10^{-5}	13
AThio4PH powder	Aniline	9.38	10^{-5}	27
AThio4PH powder	4-nitroaniline	12.99	10^{-5}	21

Therefore, such weak interactions are highly reversible and can be regenerated. As reported earlier, melamine can exist in two isomeric forms, where the aromatic form is relatively more stable, as shown in Figure 2.41.[54] In melamine, nitrogen atoms possess superior basicity in azine (C= N) than $-NH_2$ groups. The lone-pair on $-NH_2$ is delocalized within the ring, resulting in a dense negative charge on the triazine nitrogen atoms. Thus, the pyridyl protons from the fluorescent probe would have a significant tendency to interact with azine N-atoms (See the graphics Figure 2.41). Such interactions would perhaps enable a partial proton transfer between the probe and melamine through a dynamic equilibrium, leading to a display of a blue-shifted switching. The H-bonding interactions between the probe and $-NH_2$ functionality can also play a crucial role. However, only 34 nm reversible blue-shift indicates the presence of mostly weak to moderate interactions. The word "mine" is drafted on the red-emitting platform using an aq melamine solution (10^{-5} M) with the help of a wooden nib. It was visible with a slightly different orange coloration, which turned into the original red emission after a day (Figure 2.42).

2.4 Summary

In conclusion, this study reveals that the variation of the pyridyl nitrogen atom's position causes a different response in the reversible SSAC behavior for structurally twisted anthracenyl π-conjugates. In addition, the efficiencies of the SSAC feature also differ from the substituents attached as a part of π-conjugations. In these investigations, the maximum redshift on protonation has mainly occurred for the 4-pyridyl isomer attached to thiophene, not toluene. The toluene-linked 3-pyridyl analog switches its FL

reversibly with 48 nm redshift, but the thiophene-linked analog does not respond reasonably.

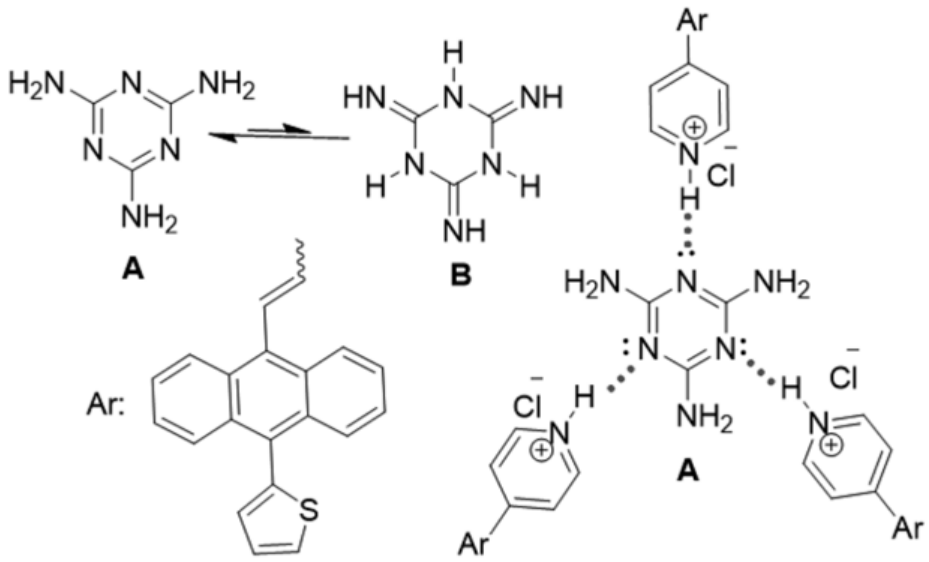

Figure 2.41 Possible interactions of melamine with the probe (a pictorial illustration)

Figure 2.42 (a) acid-fumed **AThio4P+PMMA** polymer matrix (b) a word called 'mine' is written with 10^{-5} M aq. melamine solution on acid-fumed **AThio4P+PMMA** polymer matrix (c) after 1 day

For thiophenyl π-conjugates, apart from the 4-pyridyl linker, other analogs are relatively unresponsive than tolyl analogs. However, thiophene-linked analogs are more intense emitters than toluene-linked analogs, and therefore FL-switching can be easily detected. These diversities are well documented with a detailed analysis of protonated and deprotonated probes' molecular structure and crystal packings. Few other supports such as lifetime, SEM-images are also elucidated for SSAC properties.

Finally, rewritable security writing is demonstrated using fluorophore-appended polymer matrix using acid and base. Thus, we have established a structure-property relationship on reversible acidochromism. Such a study will guide selecting a particular combination to achieve the best result on solid-state acidochromism. Moreover, the best SSAC-displaying pyridyl-based solid-state emitting probe **AThio4P** is blended with

PMMA to afford a sturdy and handy platform to respond against acid vapor by fluorescing a decent red color.

Such a red-emitting polymeric probe is identified to detect ammonia vapor and aqueous melamine. The visible color change is very much prominent for ammonia, and this red-emitting probe would be reusable for ammonia gas leakage detection, even during the rainy season. Melamine detection could also be carried out using this probe with a detectable color change. The weak noncovalent and acid-base interactions mainly govern this discernible detection.

2.5. Experimental Section

The general experimental methods are detailed earlier in '*Materials, General Conditions and Measurements*'.

2.6 Synthetic procedures with detailed characterizations

Most of the isomeric pyridyl conjugates are prepared using an earlier-reported procedure.[33,34] .

2.6.1 Synthesis of ATol3PH [as chloride salt] ((E)-3-(2-(10-(p-tolyl) anthracen-9-yl) vinyl) pyridin-1-ium) chloride salt

Protonated crystals were grown by the following procedure. 5 mg of pure **ATol3P**[33] was dissolved in 10 mL of 3:1 Hexane:EtOAc mixture by slight heating. To the solution, 2 drops of conc HCl (~0.1 mL) were added and the mixture was shaken for 1 min. The solution was gently heated for 5 min and undisturbed for slow cooling and evaporation of the solvent. Diffraction-quality single crystals were obtained after 5 days, characterized as **ATol3PH.Cl.H$_2$O** by single-crystal diffraction**. m.p.** 218-220 ^{0}C; **IR** (with KBr in cm^{-1}): 3437, 1730, 1648, 1631, 1555, 1289, 1121, 1071; **^{1}H NMR** (400 MHz, $CDCl_3$): δ 8.71 (s, br, 1H), 8.43 (s, br, 1H), 8.32 (s, br, 1H), 8.14-7.65 (m, 3H), 7.64-7.34 (m, 6H), 7.36-7.27 (m, 2H), 7.24-7.04 (m, 4H), 6.99 (s, 1H), 2.54 (s, 3H); **^{13}C NMR** (100 MHz, $CDCl_3$): δ 136.5, 136.4, 134.3, 130.1, 130.0, 129.9, 129.2, 129.1, 129.0, 128.3, 128.2, 128.1, 127.2, 126.9, 124.6, 124.3, 119.7, 114.1, 95.1, 20.4; **LC-MS** (ESI): calc. $C_{25}H_{22}N^+$ 372.17, found 372.20; X-ray structure is determined for this sample [**CCDC** No: 2107222].

2.6.2 Synthesis of ATol4PH [as chloride salt] ((E)-4-(2-(10-(p-tolyl) anthracen-9-yl) vinyl) pyridin-1-ium) chloride salt

A similar procedure is followed as applied in ***ATol3PH***. However, the solvent system is replaced with Hexane:DCM (3:1) solvent mixture; **m.p.** 228-230 °C; IR (with KBr in cm^{-1}): 3441, 2916, 1735, 1653, 1554, 1363, 1285, 1119, 1064, 1038; **^{1}H NMR** (400 MHz, $CDCl_3$): δ 9.05-8.43 (m, 2H), 8.31-7.88 (m, 3H), 7.82-7.63 (m, 3H), 7.58-7.30 (m, 7H), 7.04-6.73 (m, 4H), 2.55 (s, 3H); **^{13}C NMR** (100 MHz, $CDCl_3$): δ 131.0, 130.9, 130.1, 130.0, 129.4, 129.2, 128.2, 128.1, 126.9, 126.7, 125.7, 125.4, 124.9, 124.4, 123.4, 115.1, 96.1, 22.7; **LC-MS** (ESI): calc. $C_{25}H_{22}N^+$ 372.17, found 372.20. Diffraction-quality single crystals were obtained after 7 days, characterized as **ATol4PH.Cl.H_2O** by single-crystal diffraction; X-ray structure is determined for this sample [**CCDC** No: 2107223].

2.6.3 Synthesis of AThio2PH [as chloride salt] ((E)-2-(2-(10-(thiophen-2-yl) anthracen-9-yl) vinyl) pyridin-1-ium) chloride salt

A similar procedure is followed as applied to ***ATol3PH***. **m.p.** 164-166 °C; **IR** (with KBr in cm^{-1}): 3118, 3067, 1722, 1602, 1450, 1435, 1373, 1284, 1121, 1071; **^{1}H NMR** (400 MHz, $CDCl_3$): δ 9.41 (d, J= 16 Hz, 1H), 8.87 (s, br, 1H), 8.70-8.63 (m, 1H), 8.49-8.33 (m, 2H), 8.20-7.99 (m, 2H), 7.97-7.84 (m, 2H), 7.81-7.74 (m, 1H), 7.67-7.62 (m, 1H), 7.59-7.51 (m, 2H), 7.50-7.40 (m, 3H), 7.39-7.31 (m, 1H), 7.24-6.76 (m, 1H); **^{13}C NMR** (100 MHz, $CDCl_3$): δ 150.2, 149.6, 144.9, 144.3, 141.7, 141.0, 140.6, 140.4, 138.6, 131.6, 129.7, 129.3, 127.3, 126.9, 126.6, 125.9, 125.3, 124.7, 124.1; **LC-MS** (ESI): calc. $C_{25}H_{18}NS^+$ 364.12, found 364.15; Diffraction quality single crystals were obtained after 5-6 days, characterized as **AThio2PH.Cl** by single-crystal diffraction; X-ray structure is determined for this sample [**CCDC** No: 2107224].

2.6.4 Synthesis of AThio3PH [as chloride salt] ((E)-3-(2-(10-(thiophen-2-yl) anthracen-9-yl) vinyl) pyridin-1-ium) chloride salt

Crystals were grown following a route similar to **ATol3PH**, using Toluene: Acetonitrile (3:1) medium. **m.p**. 201-203 °C; **IR** (with KBr in cm^{-1}): 3441, 2992, 1731, 1650, 1537, 1469, 1363, 1285, 1121, 1072; **^{1}H NMR** (400 MHz, $CDCl_3$): δ 9.12 (s, br, 1H), 8.74-6.67 (m, 2H), 8.43-7.96 (m, 4H), 7.92 (d, J= 8.8 Hz, 2H), 7.65 (d, J= 6.4 Hz, 1H), 7.59-7.37 (m, 5H), 7.36-7.30 (m, 1H), 7.23-7.18 (m, 1H), 7.15-6.98 (m, 1H); **^{13}C NMR** (100 MHz, $CDCl_3$): δ 141.8, 139.5, 139.4, 138.5, 137.4, 134.2, 131.6, 130.8, 130.7, 129.8, 129.7, 129.1, 127.5, 127.3, 127.0, 126.5, 125.8, 125.5, 125.1; **LC-MS** (ESI): calc. $C_{25}H_{18}NS^+$ 364.12, found 364.15. Diffraction-

quality single crystals were obtained after 5-6 days, characterized as **AThio3PH.Cl** by single-crystal diffraction; X-ray structure is determined for this sample [**CCDC** No: 2107225].

2.6.5 Synthesis of AThio4PH [as chloride salt] ((E)-4-(2-(10-(thiophen-2-yl) anthracen-9-yl) vinyl) pyridin-1-ium) chloride salt

Crystals were grown by following the route similar to **ATol3PH**, using Hexane:EtOAc (3:1) mixture **m.p.** 245-247 ^{0}C; **IR** (with KBr in cm^{-1}): 3449, 1730, 1626, 1559, 1507, 1283, 1123, 1074; **^{1}H NMR** (400 MHz, $CDCl_3$): δ 8.74-8.55 (m, 2H), 8.22 (s, 1H), 8.21-8.05 (m, 2H), 7.96-7.84 (m, 3H), 7.59-7.57 (m, 1H), 7.49-7.37 (m, 4H), 7.28-7.26 (m, 2H), 7.20-7.18 (m, 2H), 7.14-7.07 (m, 1H); **^{13}C NMR** (100 MHz, $CDCl_3$): δ 150.1, 149.3, 138.9, 135.2, 132.7, 131.7, 130.3, 129.6, 129.2, 128.0, 127.2, 126.9, 125.9, 125.8, 125.6, 123.0, 121.1; LC-MS (ESI): calc. $C_{25}H_{18}NS^{+}$ 364.12, found 364.15; X-ray structure is determined for this sample [**CCDC** No: 2107226].

2.7 References

1 J. Xiong, K. Wang, Z. Yao, B. Zou, J. Xu and X. H. Bu, ***ACS Appl. Mater. Interfaces***, 2018, **10**, 6, 819–5827.

2 X. Lin, X. Wang, R. Li, Z. Wang, W. Liu, L. Chen, N. Chen, S. Sun, Z. Li, J. Hao, B, Lin and L. Xie, ***ACS Omega***, 2022, **7**, 13, 10994–1100.

3 V. Thanikachalam, U. Karunakaran, J. Jayabharathi, J. Anudeebhana and S. Thilagavathy, ***J. Photochem. Photobiol. A***, 2022, **428**, 113852.

4 Y. Ma, Y. Li, L. Chen., Y. Xiong and G. Yin, ***Dyes Pigm.***, 2016, **126**, 194-201.

5 J. Zhao, Z. Chi, Y. Zhang, Z. Mao, Z. Yang, E. Ubba and Z. Chi, ***J. Mater. Chem. C***, 2018, **6**, 6327-6353.

6 S. Ying, M. Chen, Z. Liu, M. Zheng, H. Zhang, S. Xue and W. Yang, ***J. Mater. Chem. C***, 2017, **5**, 5994-5998.

7 M. Wang, L. Qian, Y. Guo, H. Wu, M. Liu, W. Gao, G. Li, J. Ding and X. Huang, ***Dyes Pigm.***, 2019, **160**, 378-385.

8 M. Z. K. Baig, B. Prusti and M. Chakravarty, ***J. Mater. Chem. C***, 2019,**7**, 3735-3739.

9 S. Md. Pratik, V. Coropceanu and J. L. Bredas, ***ACS Materials Lett.***, 2022, **4**, 440-447.

10 D. Devadiga and T. N. Ahipa, ***Soft Matter.***, 2022, **18**, 8008-8016.

11 S. Ito, C. Nishimoto and S. Nagai, ***CrystEngComm***, 2019, **21**, 5699-5706.

12 L. Li, A. V. Zhdanov and D. B. Papkovsky, ***Sens. Actuators B: Chem.***, 2022, **371**, 132486.

13 Y. Xie, Y. Pan, F. Xiao, Y. Lei, Y. Zhou, M. Liu, W. Gao, X. Huang and H. Wu, ***Dyes Pigm.***, 2021, **188**, 109217.

14 K. Li, J. Cui, Z. Yang, Y. Huo, W. Duan, S. Gong and Z. Liu, ***Dalton Trans.***, 2018, **47**, 15002-15008.

15 Y. Wang, M. Liu, Prof. W. Zhang, Dr. Y. Lei, Dr. Y. Zhou, Prof. W. Gao, Prof. Q. Ding, Prof. H. Wu and Prof. X. Huang, ***Chem. Asian J.***, 2023, 18, e202300213.

16 A. Kathiravan, A. Gowri, T. Khamrang, M. D. Kumar, N. Dhenadhayalan, K. C. Lin, M. Velusamy and M. Jaccob, ***Anal. Chem.***, 2019, **91**, 20, 13244–13250.

17 Z. Wang, X. Cheng, A. Qin, H. Zhang, J. Z. Sun and B. Z. Tang, ***J. Phys. Chem. B***, 2018, **122**, 7, 2165–2176.

18 Y. Liu, A. Li, Prof. Dr. S. Xu, Prof. Dr. W. Xu, Prof. Dr. Y. Liu, Prof. Dr. W. Tian and Prof. Dr. B. Xu, ***Angew. Chem. Int. Ed.***, 2020, **59** (35), 15098-15103.

19 Y. Li, X. Wang, L. Zhang, L. Liu, Q. Wang, H. Lu and X. Zhao, ***Mater. Chem. Front.***, 2020, **4**, 3378-3383.

20 B. Wang and C. Wei, ***RSC Adv.***, 2018, **8**, 22806-22812.

21 S. Kothavale and N. Sekar, ***Dyes Pigm.***, 2017, **136**, 31-45.

22 S. Gupta and M. D. Milton, ***Dyes Pigm.***, 2019, **165**, 474-487.

23 S. B. Yadav, S. Kothavale and N. Sekar, ***J. Photochem. Photobiol. A***, 2019, **382**, 111937.

24 S. Manickam, U. Balijapalli and K. I. Sathiyanarayanan, ***New J. Chem.***, 2018, **42**, 860-871.

25 V. Kumar, P. Kumar, P. Kaur and K. Singh, ***Anal. Chim. Acta***, 2021, **1178**, 338807.

26 H. H. Park, P. Meti and Y. D. Gong, ***Dyes Pigm.***, 2021, **190**, 109320.

27 J. Jia and L. Wu, ***J. Photochem. Photobiol. A***, 2020, **399**, 112640.

28 M. Medved, M. W. H. Hoorens, M. D. Donato, A. D. Laurent, J. Fan, M. Taddei, M. Hilbers, B. L. Feringa, W. J. Buma and W. Szymanski, ***Chem. Sci.***, 2021, **12**, 4588-4598.

29 T. Sachdeva, S. Bishnoi and M. D. Milton, ***ChemistrySelect***, 2017, **2**, 11307-11313.

30 S. Ma, J. Zhang, Y. Liu, J. Qian, B. Xu and W. Tian, ***J. Phys. Chem. Lett.***, 2017, **8**, 3068-3072.

31 Q. Sun, H. Wang, X. Xu, Y. Lu, S. Xue, H. Zhang and W. Yang, ***Dyes Pigm.***, 2018, **149**, 407-414.

32 B. Prusti, P. Sarkar, S. K. Pati and M. Chakravarty, ***J. Mater. Chem. C***, 2021, **9**, 9555–9570.

33 M. Z. K. Baig, B. Prusti, D. Roy and M. Chakravarty, ***ACS Omega***, 2019, **4**, 3, 5052-5063.

34 M. Z. K. Baig, S. Pawar, R. N. P. Tulichala, A. Nag and M. Chakravarty, ***Sens. Actuators B: Chem.***, 2017, **243**, 226-233.

35 V. D. Singh, A. K. Kushwaha and R. S. Singh, ***Dyes Pigm.***, 2021, **187**, 109117.

36 Dr. S. Suzuki, Dr. S. Sasaki, A. S. Sairi, R. Iwai, Prof. Dr. B. Z. Tang and Prof. Dr. G. Konishi, ***Angew. Chem. Int. Ed.***, 2020, **59** (25), 9856-9867.

37 S. Sasaki, S. Suzuki, K. Igawa, K. Morokuma and G. Konishi, ***J. Org. Chem.***, 2017, **82**, 13, 6865–6873.

38 N. L. C. Leung, Dr. N. Xie, Dr. W. Yuan, Dr. Y. Liu, Dr. Q. Wu, Prof. Q. Peng, Prof. Q. Miao, Dr. J. W. Y. Lam and Prof. B. Z. Tang, ***Chem. Eur. J***, 2014, **20**, 15349-15353.

39 S. Sasaki, K. Igawa and G. Konishi, ***J. Mater. Chem. C***, 2015, **3**, 5940-5950.

40 S. Redon, G. Eucat, M. Ipuy, E. Jeanneau, I. G. Luneau, A. Ibanez, C. Andraud and Y. Bretonniere, ***Dyes Pigm.***, 2018, **156**, 116-132.

41 Dr. S. Xie, S. Manuguri, Prof. Dr. O. Ramstrom and Prof. Dr. M. Yan, ***Chem. Asian J***, 2019, **14**, 6, 910-916.

42 J. Zhang, J. Chen, B. Xu, L. Wang, S. Ma, Y. Dong, B. Li, L. Ye and W. Tian, ***Chem. Commun.***, 2013, **49**, 3878-3880.

43 X. Feng, Y. Li, X. He, H. Liu, Z. Zhao, R. T. K. Kwok, M. R. J. Elsegood, J. W. Y. Lam and B. Z. Tang, ***Adv. Funct. Mater.***, 2018, **28**, 1802833.

44 S. J. Yoon, J. W. Chung, J. Gierschner, K. S. Kim, M. G. Choi, D. Kim and S. Y. Park, .***J. Am. Chem. Soc.***, 2010, **132**, 39, 13675–13683.

45 Y. Hu, X. Ma, Y. Zhang, Y. Che and J. Zhao, ***ACS Sens.***, 2016, **1**, 1, 22–25.

46 D. Kwak, Y. Lei and R. Maric, ***Talanta***, 2019, **204**, 713-730.

47 T. N. Ly and S. Park, ***Sci. Rep.***, 2018, **8**, 18030.

48 Y. Tu, C. Kyle, H. Luo, D. W. Zhang, A. Das, J. Briscoe, S. Dunn, M. M. Titirici and S. Krause, ***ACS Sens.***, 2020, **5**, 11, 3568–3575.

49 C. H. Lei, X. E. Zhao, S. L. Jiao, L. He, Y. Li, S. Y. Zhu and J. M. You, ***Anal. Methods.***, 2016, **8**, 4438-4444.

50 Toxicological and health aspects of melamine and cyanuric acid: report of a WHO expert meeting in collaboration with FAO, supported by Health Canada, Ottawa, Canada, 1-4 December 2008. ISBN 9789241597951. https://apps.who.int/iris/handle/10665/44106.

51 A. Kim, S. J. Barcelo, R. S. Williams and Z. Li, ***Anal. Chem.***, 2012, **84**, 21, 9303–9309.

52 Y. C. Tyan, M. H. Yang, S. B. Jong, C. K. Wang and J. Shiea, ***Anal. Bioanal. Chem.***, 2009, **395**, 729-735.

53 J. Zhang, C. Ou, Y. Shi, L. Wang, M. Chen and Z. Yang, ***Chem. Commun.***, 2014,**50**, 12873-12876.

54 S. Mukherjee and J. Ren, ***J. Am. Soc. Mass. Spectrom.***, 2010, **21**, 10, 1720–1729.

Chapter III

Indolyl Anthracene Conjugated Solid-State Emitting Organic Fluorogens (SSEOFs) as AIE-active DSE-gens: *in vitro* Anticancer Property and Detection of Dead Cancer Cells through On-Off Fluorescent Bioimaging

Objectives:

- Develop an SSEOF that is emissive in solids, solutions, aggregates, and viscous environment
- Introduce such SSEOF in studying anticancer property
- Establish an SSEOF with biocompatibility and bioimaging ability.
- Ultimately, to develop an SSEOF that can inhibit the cancer cells selectively and differentiate dead cancer cells from the normal cells.

Abstract:

Dual-state emissive fluorogens (DSE-gens) are currently defining their importance as a transpiring tool in biological and biomedical applications. This work focuses on designing and synthesizing indole anthracene-based solid-state emitting twisted p-conjugates using a metal-free protocol to achieve AIEactive DSE-gens, expanding their scope in biological applications. Here, the lead DSE-gen initially detects cancer and normal cells by bioimaging; however, it could also confirm and distinguish cancer cells from normal cells by its abated fluorescence signal after killing cancer cells. In contrast, the fluorescence signals for a normal cell remain unscathed. Surprisingly, these molecules displayed decent anticancer properties against FaDu and 4T1 but not MCF-7 cell lines. From a series of newly designed indole-based molecules, we report one single 2,3,4-trimethoxybenzene-linked DSE-gen (the lead), exhibiting high ROS generation, less haemolysis, and less cytotoxicity than doxorubicin (DOX) for normal cells, crucial parameters for a biocompatible in vitro anticancer probe. The primary mechanism behind the identified outcomes is deciphered with the support of experimental (steady-state and time-resolved fluorescence, biological assays, cellular uptake) and molecular docking studies.

3.1 Introduction

The dual-state emission (DSE) feature of aggregation-induced emission (AIE) active solid-state emitting organic fluorogens (SSEOFs) unveils their effectiveness in biotechnology and biomedical applications due to their presence of emission in all states like solutions, aggregates, and solids.[1-4] Besides, simple administration into the cells and flexibility in the structural modification are the main benefits of organic fluorescent molecules for their versatile use in biomedical applications avoiding the ACQ effects that limit their ultimate utility for image-guided treatment.[1,5] Hence, biologically non-toxic dual-state emitting AIE-active SSEOFs claim high importance in bioimaging, biosensing, and image-guided therapy systems (IGTs).[1,6-7] Moreover, small but efficient π-conjugated organic fluorogens are primarily desired in comparison to various inorganic-organic hybrid materials due to the easy synthesis/modifications, high thermo/photostability, and cost-effectiveness.[8-13]

Cancer cell detection by simple bio-imaging techniques using AIE-gens and DSE-gens has recently become a dependable, convenient, and cost-effective technique in cancer treatment.[7b,14-16] Notably, molecular imaging techniques can detect cancer mass based on the photophysical properties, enabling cell visualization in living organisms at the cellular and molecular level without any disorder. Some earlier identified molecular probes for *in vitro* and *in vivo,* bio-imaging agents remain with inadequate effectivity due to their photobleaching tendency, acute toxicity, and low-fluorescent efficacy.[17] Highly active commercial drugs are known to treat several types of cancers but with severe side effects.[18-21] Nevertheless, many admirable anticancer drugs are available, but with no bioimaging ability[22-23] while, numerous bioimaging agents are known without anticancer properties.[24] Hence, the discovery of an anticancer agent owning bioimaging ability is a looming challenge but a surging need of the time.[25]

To address this necessity, we herein focus on designing an indole-based fluorophore by incorporating anthracene and indole as the primary scaffold. Of note, typical ACQ-fluorophore anthracene becomes emissive in solutions, aggregate, and solid states with our thoughtful design. An additional conjugation was needed to enhance the emission intensity. The newly designed indole-anthracene-based dyes could be easily accessed economically and mainly established as efficient AIE-active DSE-gens. Here, a few

aggressive and obdurate cell lines are picked up: (i) FaDu (one of the most aggressive hypopharyngeal carcinoma cell lines),[26-28] (ii) 4T1 (highly destructive triple-negative mouse breast cancer cell line (TNBC), showing a lack of treatment scope)[29-33], (iii) MCF-7 (a breast cancer cell line, but not triple negative)[34] and (iv) non-cancerous human kidney embryonic cell line HEK-293 to investigate normal cell cytotoxicity and comparison in bioimaging. Most of the approved marketed therapeutic drugs used for breast cancer (sporadic for 4T1) are not emissive and hold diversified side effects.[31]

3.2 Literature review on indole-based anticancer derivatives without bioimaging ability

3.2.1 Design, synthesis, and biological evaluation of 5-chloro-3-hydroxymethyl-indole-2-carboxamide scaffolds as EGFR inhibitors

Mohamed *et al.* designed and synthesized 5-chloro-3-hydroxy-methyl-indole-2-carboxamide based several derivatives, which displayed promising antiproliferative effects on cancer cell lines, and the EGFR inhibitory assay revealed commendable inhibitory effects on EGFR TK for the synthesized compounds. Reported **3A** and **3B** are representative examples, but the authors did not concentrate on investigating the emissive properties of the molecules. Instead, the multistep synthesis of the reported compounds is another concern (Figure 3.1).[35]

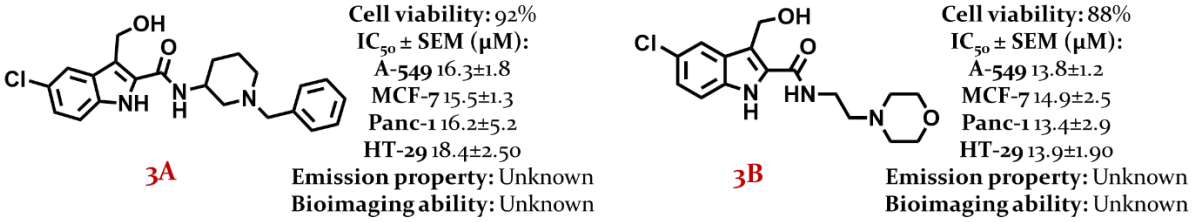

Figure 3.1 Reported 5-chloro-3-hydroxy-methyl-indole-2-carboxamide-based representative derivatives with good anticancer activity and unexplored bioimaging ability (taken from ref. 35)

3.2.2 *N*-Hydroxycinnamamide-based histone deacetylase inhibitors with an indole-containing cap group

Zhang *et al.* developed a novel series of deacetylase inhibitors containing indole bioactive fragment and *N*-hydroxycinnamamide bioactive core, and their synthesized

derivatives displayed comparable to superior HDACs inhibitory activity and in vitro antiproliferative activities to the approved SAHA drug (vorinostat). However, their group also did not focus on the bioimaging capability of their drugs or any related conjugates to monitor the anticancer effectivity (Figure 3.2).[36]

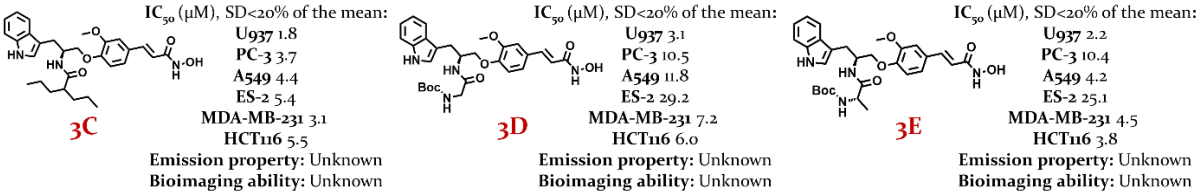

Figure 3.2 Reported indole and *N*-hydroxycinnamamide bioactive core containing derivatives with good anticancer activity and unexplored bioimaging ability (ref. 36)

3.2.3 Arylthioindole class of tubulin polymerization inhibitors as potential anticancer agents

Regina *et al.* synthesized arylthioindole derivatives with different cyclic substituents at position 2 of the attached indole and set up a perfect structural-property relationship. *Their work included MRI imaging*, and the compounds' bioactivity was appreciable. Again, they did not focus on low-cost fluorescent bioimaging to detect cancer cells (Figure 3.3).[37]

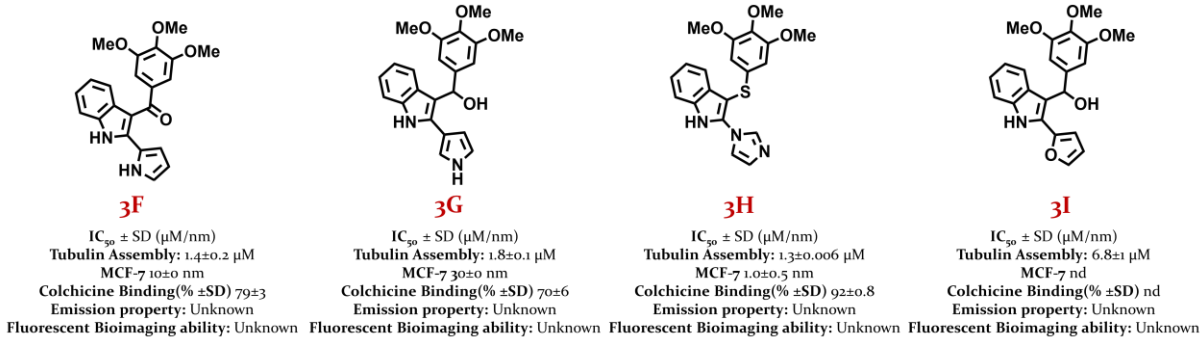

Figure 3.3 Reported arylthioindole class of representative derivatives with MRI imaging ability (unexplored fluorescent bioimaging, ref. 37)

3.2.4 Indole-sulfonamide derivatives as anticancer drugs

Pingaew et al. synthesized many indole-sulfonamide derivatives, investigated their cytotoxic activities against several cancer cell lines, and scrutinized their antimalarial effect. They were able to receive some convincing bioactive molecules, but

as a common trend, they still did not explore the bioimaging ability of their bioactive compounds (Figure 3.4).[38]

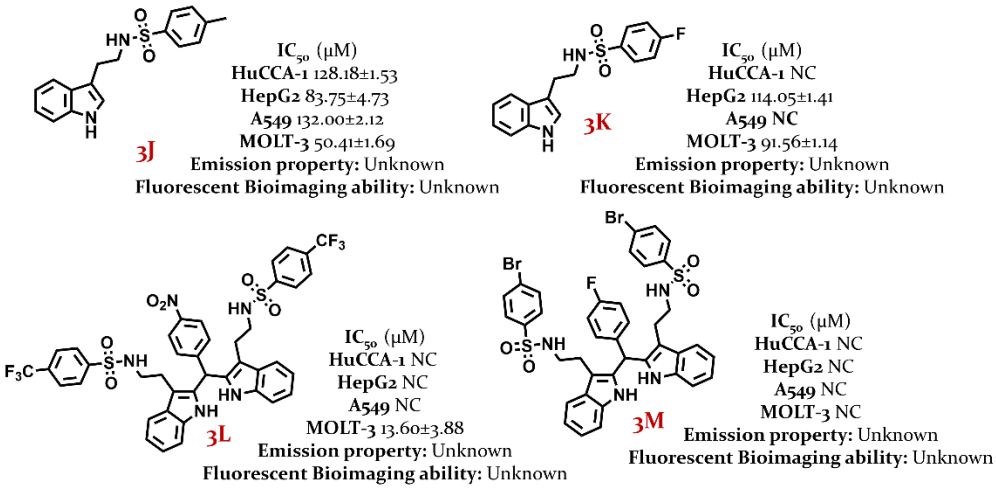

Figure 3.4 Reported representative indole-sulfonamides as anticancer derivatives (unexplored fluorescent bioimaging, ref. 38)

3.2.5 Indole-thiazole derivatives as inhibitors of breast cancer cell growths

O'Dea *et al.* showed how indole-thiazole derivatives act as GPER agonists to inhibit breast cancer cell growth. In their study, the indole ring is required for activity because the pyrimidine ring is not tolerated (**3N**). Again, the diminished activity for **8** indicated that lack of substitution of the benzyl group or indole substitution negatively affected GPER activity. The nitrile group (**3O**) also negatively affected GPER activity as **3O** and **3Q** differed by only one substitution. However, the bioimaging capability still was unexplored (Figure 3.5).[39]

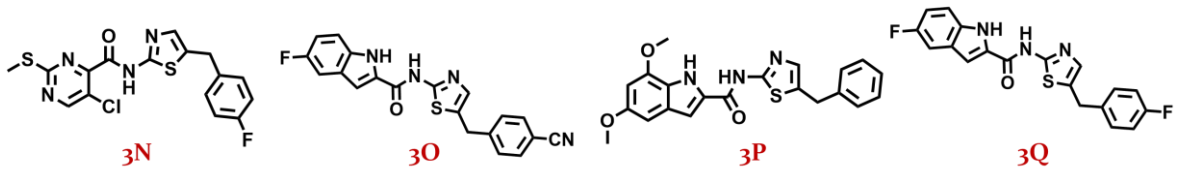

Figure 3.5 Reported representative indole-thiazole derivatives act as GPER agonists and inhibitors of breast cancer cell growth (unexplored fluorescent bioimaging, ref. 39)

3.3 Results and discussion

3.3.1 Molecular enigineering

We have intended to access indole-anthracene-based molecules to develop an anticancer compound that can kill cancer cells and detect them by bioimaging. In earlier reports, indole and anthracene cores are individually realized as potential anticancer agents.[40-44] We designed indole-anthracene-based twisted organic molecules, accessing donor(D)-π-acceptor(A) and D-π-D combinations. Thus, the flat indole (an established motif with anticancer property) with a moderately long alkyl chain has been tagged onto the flat anthracene ring. These two indole and anthracene cores don't prefer occupying the same plane. Such a twisted structure would prohibit π-π stacking in aggregates, resulting in relaxation through a radiative channel and emitting strongly.

The extended conjugation with the core consisting of pyridine, TMB (tri-methoxy benzene), phenothiazine, and triphenylamine is conveniently created because these are well-known motifs for bioimaging and anticancer applications.[45-49] Unlike, many previous reports, all synthesized molecules are intended to be non-charged, not to compromise with the fluorescent quantum yield [50] despite a possible reduction in cellular permeability.[51] Nevertheless, the long alkyl chain and many hydrophobic units in our synthesized probes assist in displaying commendable cellular uptake capacity. The twisted structure and extended π-conjugation even favorably contribute to their fluorescence efficiency in solid and solution states. Introducing a conventional 'spacer' is also escaped to keep the fluorescence efficacy intact because it might disrupt the π-conjugation and introduce molecular motion, leading to quenched emission.[51] Designing complex organic molecules with chiral/spiro center or complex functionalization is also avoided to make the compounds stable and storable at room temperature.[52,53]

3.3.2 Synthetic route of the compounds

The compounds were synthesized through an easy electrophilic aromatic substitution reaction[54] using freshly prepared alkylated (*n*-hexyl) indole[55] as a nucleophile. The designed D-π-A (**SB1-SB3**) and D-π-D combinations (**SB4-SB7,** Figure 3.6) could be generated by Horner-Wadsworth-Emmons (HWE)-reactions of indole-anthracenyl phosphonates at room temperature through a metal/ligand-free protocol.[56]

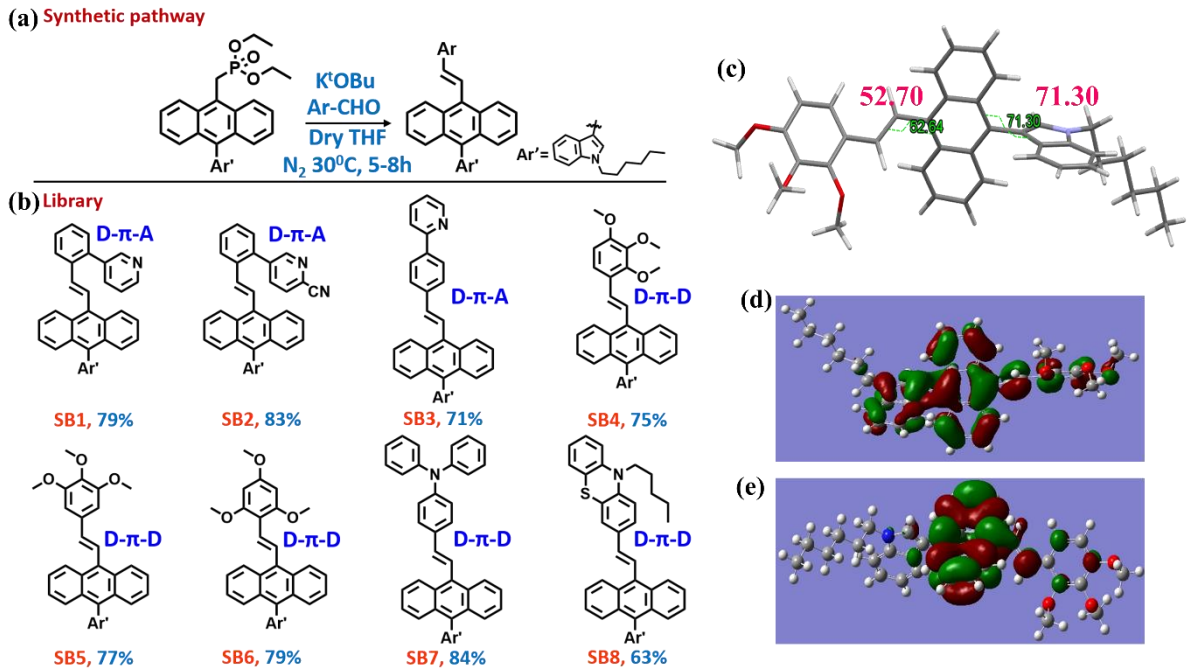

Figure 3.6 (a) Reaction pathway to synthesize indole-anthracenyl derivatives (b) library of the synthesized molecules. ('D' stands for 'Donor' and 'A' stands for 'Acceptor') (c) optimized structure of one representative twisted π-conjugate **SB4** in the gas phase (d) gas-phase HOMO (e) LUMO distribution of **SB4**

3.3.3 Structural elucidation

3.3.3.1 NMR spectroscopic analysis of the synthesized compounds

The formation of precursor diethyl ((10-(1-hexyl-1H-indol-3-yl)anthracen-9-yl)methyl)phosphonate was confirmed with single ^{31}P-NMR signal at $\delta \sim 26.08$, and the aliphatic part proton counts (total 25) from ^{1}H NMR signals with P-CH2 peak at $\delta \sim 4.33$ (d, J= 24.84 Hz), and nine distinctive peaks at the aliphatic part of the ^{13}C NMR with a characteristic P-CH2 peak at $\delta \sim 27.9$ (d, J= 121.64 Hz). The formation of other precusors, 2-(pyridin-3-yl)benzaldehyde and 5-(2-formylphenyl)picolinonitrile were confirmed from the signal of aldehyde proton in ^{1}H NMR near $\delta \sim 9.98$ and $\delta \sim 190$-191 in ^{13}C NMR.

3.3.4 Photophysical studies

3.3.4.1 Photophysical studies in solid state

The photophysical studies in solid-state were carried on to investigate and establish the synthesized indole-anthracenyl π-conjugates as SSEOFs. Our actual aim

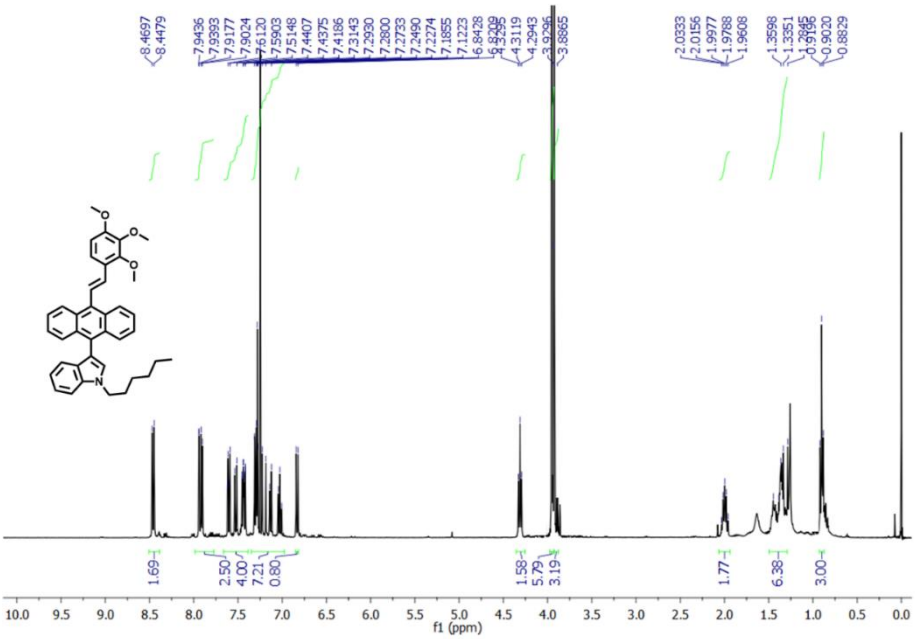

Figure 3.7 ^{1}H NMR spectra of (E)-1-hexyl-3-(10-(2,3,4-trimethoxystyryl)anthracen-9-yl)-1H-indole (**SB4**)

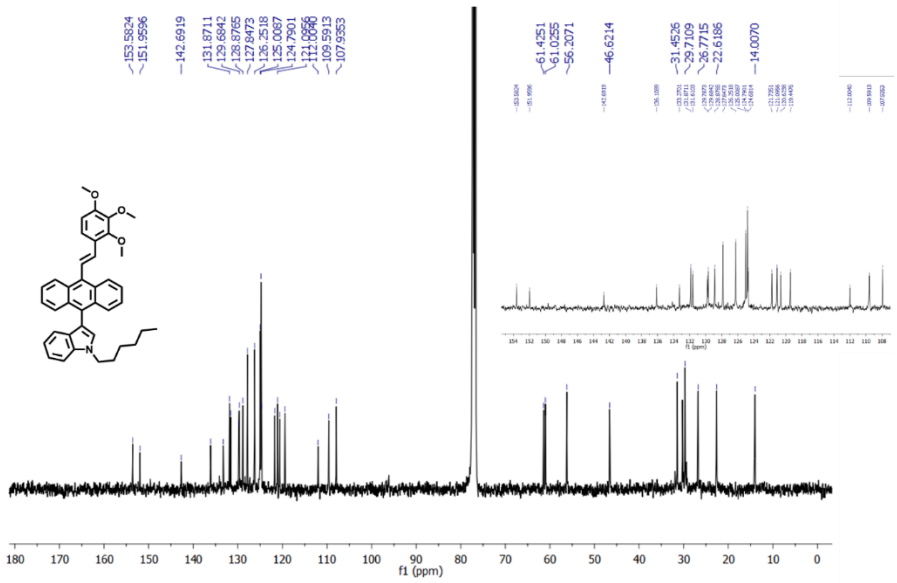

Figure 3.8 ^{13}C NMR spectra of (E)-1-hexyl-3-(10-(2,3,4-trimethoxystyryl)anthracen-9-yl)-1H-indole (**SB4**)

was to get emissions in solutions, aggregates, and solid-states for all these synthesized D-π-A (**SB1-SB3**) and D-π-D (**SB4-SB7**) molecules to amplify the biological applications. To say about their solid-state emission efficacy, all of those synthesized π-conjugates exist as SSEOFs and exhibit green/greenish-yellow emission in the solid state under 365 nm UV light except **SB7,** which emitted orange (Figure 3.9).

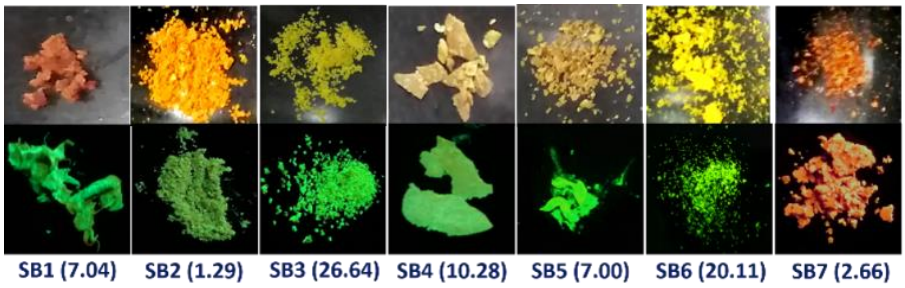

Figure 3.9 The lower row pictures are the solid-state fluorescence images (under 365 nm UV lamp) of indole-anthracenyl derivatives with their respective solid-state fluorescent quantum yield (Φ_f%) with absolute error range: (±) 0.005-0.007. The upper row pictures are taken under ambient room light in the daytime

The solid-state absorbance, emission, and other related parameters are tabulated elsewhere. In solid-state UV-Vis studies, **SB1** shows maximum λ_{abs} at 426 nm with the bent phenyl-pyridinyl core, while **SB2** absorbs maximum λ_{abs} at 458 nm due to the suitably placed cyano group, improving π-conjugation in the ground state (Figure 3.10a). In the emission profile, **SB1** displays emission at 510 nm with higher brightness (absolute quantum yield Φ_f = 7.04%), but **SB2** is feebly emissive (Φ_f = 1.29%) with λ_{em} 505 nm.

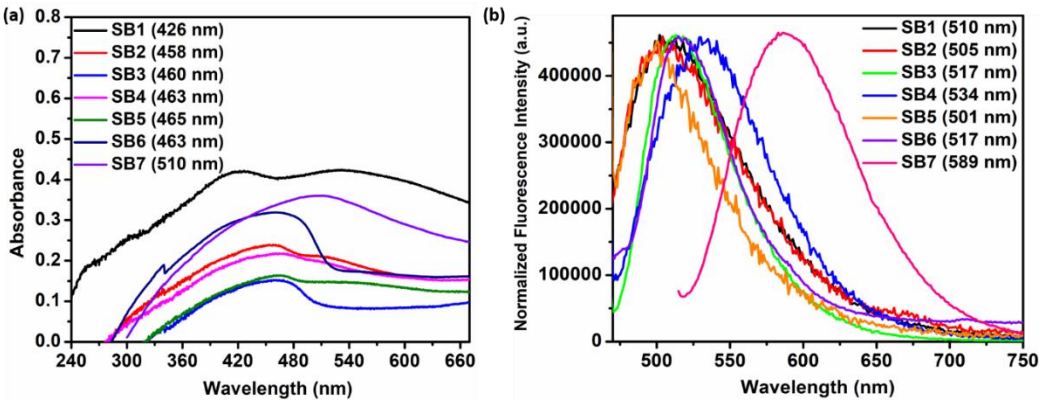

Figure 3.10 Solid-state (a) absorbance and (b) emission of indole-anthracenyl derivatives

Another pyridinyl-conjugated dye **SB3,** has appeared as an intense solid-state emitter (Φ_f = 26.64%) with λ_{em} at 517 nm. Out of the two TMB-linked isomeric D-π-D systems, **SB4** with 2,3,4-TMB emits at $\lambda_{max.}$=534 nm (Φ_f = 10.28%) with 33 nm red-shift compared to its 3,4,5-TMB analog **SB5** ($\lambda_{max.}$ =501 nm, Φ_f = 7.00%), possibly due to the presence of –OMe in both *ortho* and *para* position. The presence of bulky and conformationally twisted triphenylamine assisted in offering intense emission for **SB6** ($\lambda_{max.}$ =517 nm, Φ_f = 20.11%), but the bowl-shaped phenothiazine moiety introduced a

weak red emission in **SB7** ($\lambda_{max.}$ =589 nm, Φ_f= 2.66%). So among all the seven molecules, D-π-D family members display more red-shifted emission as compared to D-π-A family members (Figure 3.10b, Table 3.1).

Table 3.1 Solid-state fluorescence properties of the synthesized indole-linked anthracenyl π-conjugates

Compound	$\lambda_{abs\ max}$ (nm)	$\lambda_{em\ max}$ (nm)	$\Phi_{f\ solid}$ (%) (± absolute error)
SB1	426	510	7.04(±0.008)
SB2	458	505	1.29 (±0.011)
SB3	460	517	26.64 (±0.010)
SB4	463	534	10.28 (±0.017)
SB5	465	501	7.00 (±0.015)
SB6	463	517	20.11 (±0.229)
SB7	510	589	2.66 (±0.005)

3.3.4.2 Dual-state emission (DSE) property of the SSEOFs

To investigate the solution state emission property of the SSEOFs, DMSO was selected as a solvent due to its numerous applications in biology and medicinal fields.[57] Even MeCN is considered with DMSO from the chemistry perspective, as both of them have very close relative polarity. All the synthesized SSEOFs (**SB1**-**SB7**) were found to be dual-state emitters as they displayed commendable emissions in solids (Figure 3.10, Table 1), and both of the solvents-MeCN and DMSO (Figures 3.11 and 3.12, Table 3.2).

3.3.4.2.1 Time-dependent density functional theory (TD-DFT) studies

The observed DSE-genic behaviors were well-supported by the TD-DFT calculations done with **SB2** as a representative molecule of the D-π-A family and **SB4** as a representative molecule of the D-π-D family. The excited S_1 state attains greater planarity than the So state for SB2 and SB4 in both solvents, which may contribute to their emissions in solutions (Figures 313-3.15, Table 3). **SB2** and **SB4** both have lower fluorescence quantum yields in DMSO than in MeCN, possibly due to their greater extent increment of RMSD (Root Mean Square Displacement) than that of emission oscillator strength in DMSO.[58] The HOMO-LUMO energy gap in both solvents was larger for **SB4** than **SB2** (Figure 3.16, Table 3.3).

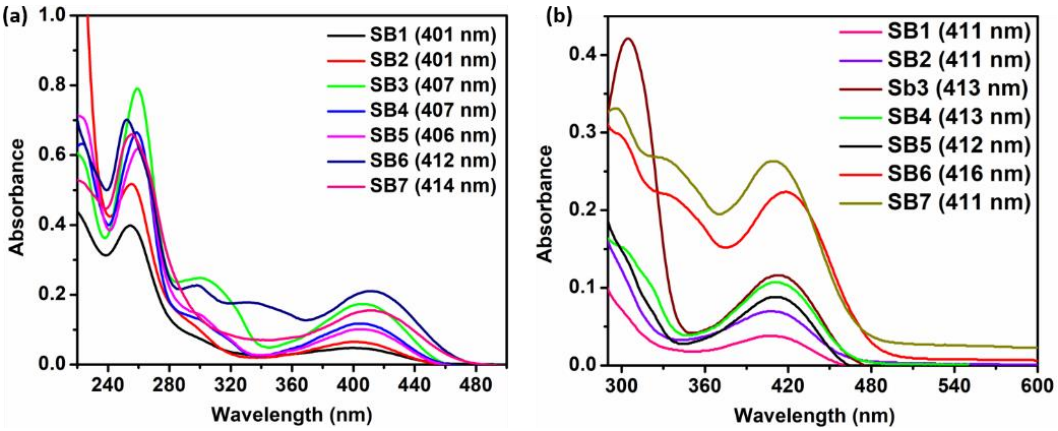

Figure 3.11 (a) Absorbance in MeCN and (b) absorbance in DMSO of indole-anthracenyl derivatives (corresponding Abs $\lambda_{max.}$ have been mentioned)

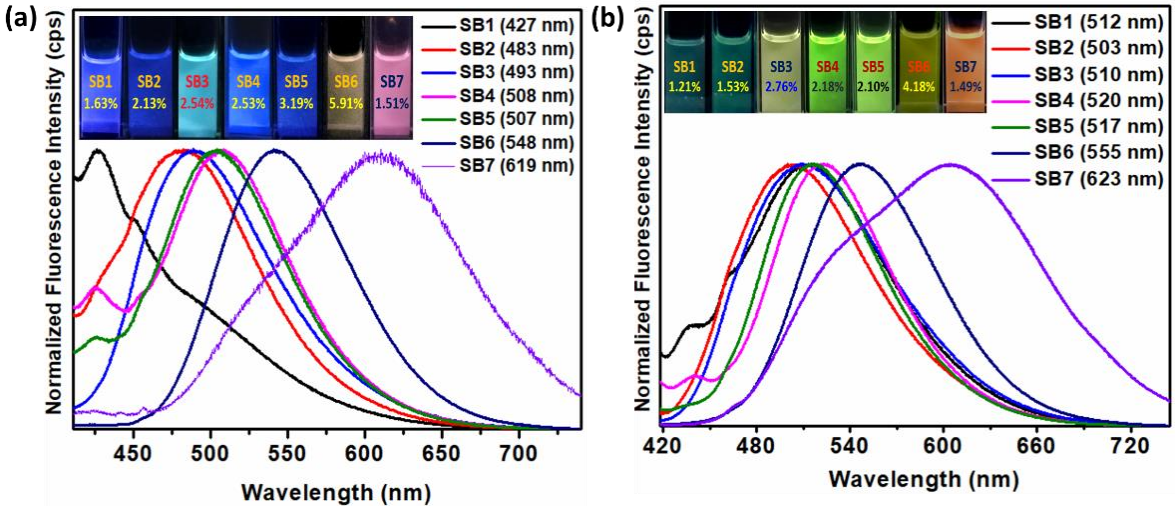

Figure 3.12 Solution-state fluorescence emissions with images (under 365 nm UV lamp) of indole-anthracenyl derivatives with their respective relative fluorescent quantum yields (Φ_f%), (Error range: (±) 5%) with respect to 10^{-5} M quinine sulfate solution) (a) Emissions in MeCN (b) Emissions in DMSO

Some of these molecules have other shoulder emissions peaks in a different region from the maxima. **SB3** in DMSO has a very broad spectrum covering from 427 nm to 720 nm, almost with a max (maximum) at 510 nm without any shoulder emission.

3.3.4.3 Aggregation-induced emission (AIE) property of the DSE-genic SSEOFs

We targeted verifying the AIE activity of the synthesized DSE-gens as those are SSOF-gens also and expected to emit in aggregates. DSE-gens and SSOF-gens with AIE-property are more valuable in illumining biological information.[4b,4g,59,60]

Table 3.2 Steady-state photophysical parameters of DSEgens

Compound	Solvent	$\lambda_{max.abs}$ (nm)	$\lambda_{.em}$ (nm)	Stokes shift (nm) with respect to the $\lambda_{.em\ max}$	Φ_f (%)
SB1	MeCN	401	427 (max), 450	26	1.63
SB2	MeCN	401	483	82	2.13
SB3	MeCN	407	493	86	2.54
SB4	MecN	407	427, 508 (max)	101	2.53
SB5	MeCN	406	428, 507 (max)	101	3.19
SB6	MeCN	412	548	136	5.91
SB7	MeCN	414	457, 619 (max)	205	1.51
SB1	DMSO	411	436, 512 (max)	101	1.21
SB2	DMSO	411	503	92	1.53
SB3	DMSO	413	510	97	2.76
SB4	DMSO	413	441, 520 (max)	107	2.18
SB5	DMSO	412	517	105	2.10
SB6	DMSO	416	555	139	4.18
SB7	DMSO	411	531, 623 (max)	92	1.49

Initially, the AIE-activity of all the DSE-gens was tested in an acetonitrile/water medium (fraction of water in acetonitrile f_w: *v*/*v*%). All of these DSE-gens discussed here were not AIE-active. Especially, commendable solid-state fluorophore **SB1** undergoes the ACQ effect (Figure 3.17) with a gradual increment of water fraction (f_w), possibly due to the π-stacking of the phenyl/pyridine rings in the aggregate state.[61,62]

The AIE characteristic of **SB3** is more pleasing (Figure 3.19), with 11 times fluorescent boosting in f_w = 80%. The aggregate formation was also verified from the DLS (dynamic light scattering) studies, and the particle size was found to be 194.5 nm for **SB3** aggregates (Table 4). An introduction of the cyano group in **SB2** might relinquish π-stacking to a small extent, and the AIE-property of **SB2** was somewhat better but not promising (Figure 3.18). A commendable AIE feature (7 times increment, Figure 3.22) was noticed at f_w of 70% with **SB4,** holding three methoxy groups in an unsymmetrical fashion. The indole with a long alkyl chain, twisted structure, and lack of symmetry may significantly restrict π-stacking formation and facilitate exhibiting AIE

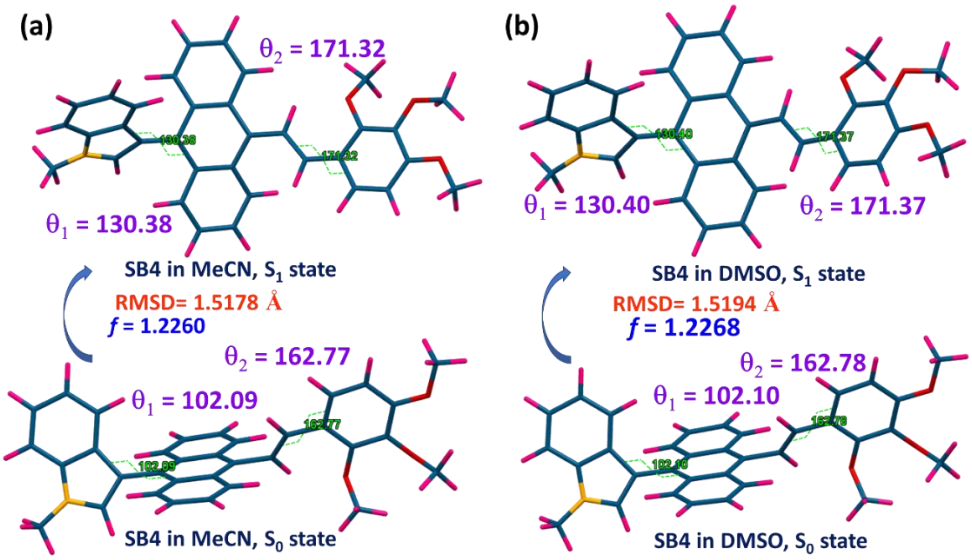

Figure 3.13 TD-DFT optimized structures for **SB4** presentations ('b' axis. (Only the emission maxima for each of the molecules in each of the solvents are written in (a) MeCN and (b) DMSO. θ_1 is the dihedral angle between indole and anthracene parts whereas θ_2 is the dihedral angle in degree between the 'diene' and the substituted benzene ring.)

features (Figures 3.20a, 3.21a-b). A simple viscofluorochromism study further supports this speculation.

In MeOH, **SB4** is little emissive, and upon consecutive addition of glycerol into MeOH, the overall viscosity of the medium is gradually increased and would help restrict the molecular motion, resulting in enhanced emission. To our delight, the emission efficacy of **SB4** has progressively enhanced with the increasing viscosity up to f_G of 70% (Figures 3.20b, 3.20c-d), indicating the viscofluorochromism in **SB4.**

Another symmetrically different analog, **SB5** is also identified as a good AIE-gen (Figure 3.21). The non-planar conformation of TPA in **SB6** and bowel-shaped-phenothiazine in **SB7** induce molecular twisting in the aggregate form, enabling the destruction of the ACQ effect and experience of AIE-property (Figure 3.22).

The emission enhancement efficiency (I/I_o) comparison (Figure 3.23) for all the synthesized molecules is also highlighted to have a clear view, and their AIE-genic

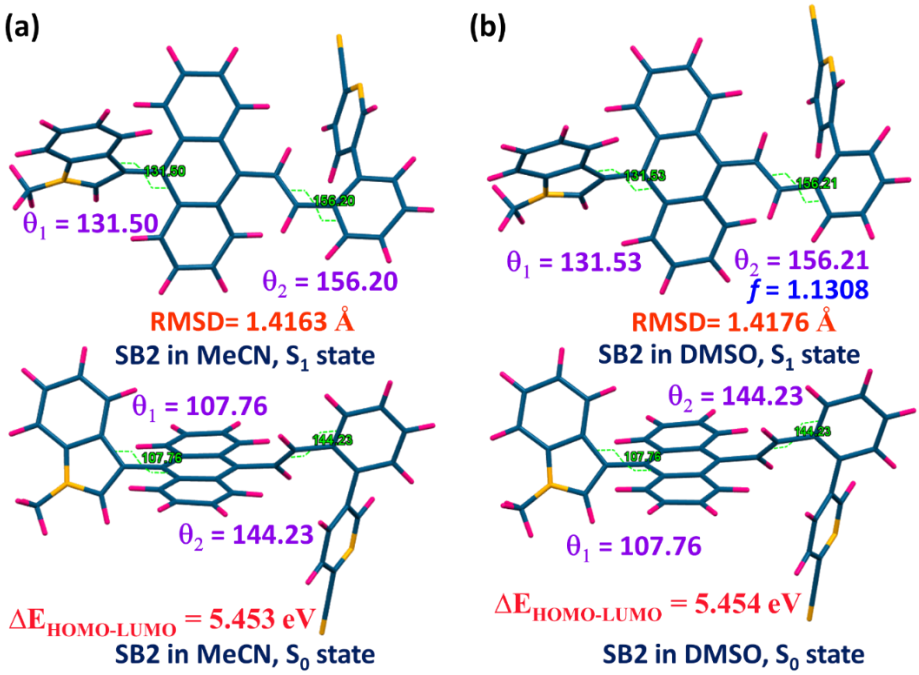

Figure 3.14 TD-DFT optimized structures of **SB2** in MeCN and DMSO with capped sticks presentations from 'b' axis

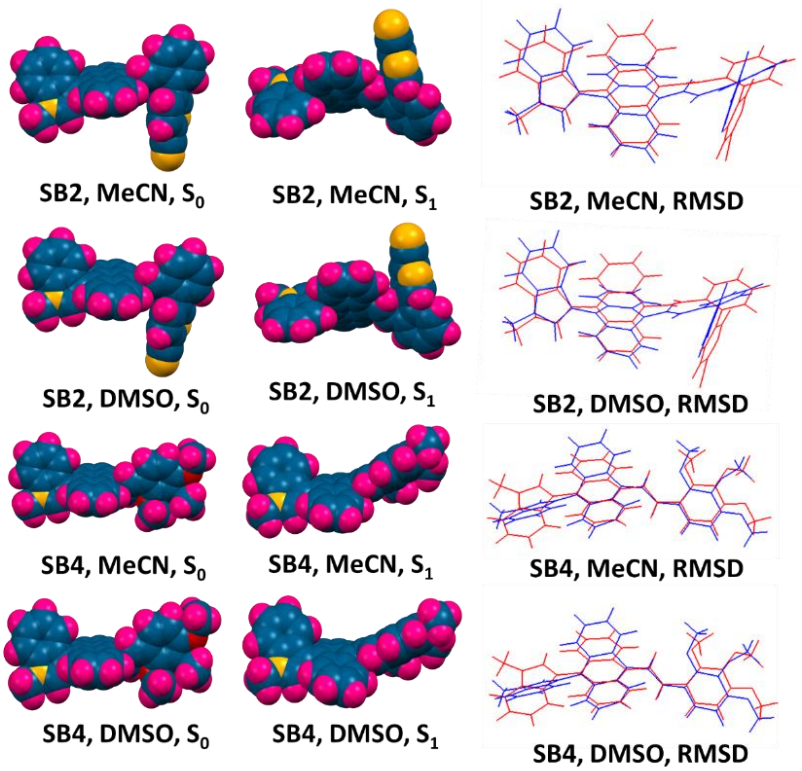

Figure 3.15 Space fill presentations from the 'b' axis view of the TD-DFT optimized structures with the probable RMSD orientation

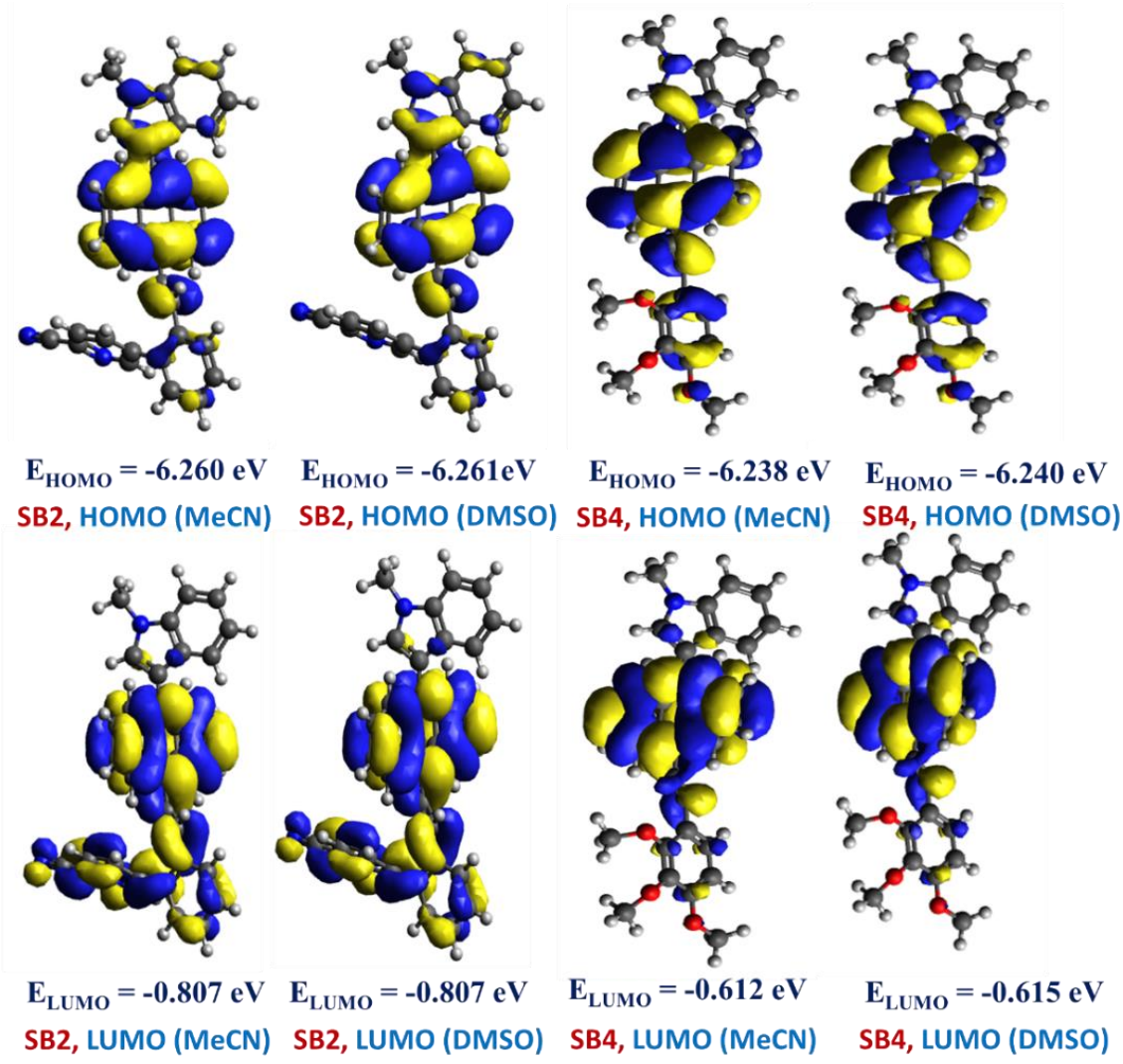

Figure 3.16 HOMO-LUMO distribution of **SB2** and **SB4** in MeCN and DMSO

Table 3.3 TD-DFT calculation results for **SB2** and **SB4** in MeCN and DMSO

Compound	Solvent	Absorbance Oscillator strength (*f'*)	Emission oscillator strength (*f*)	θ_1 (degree) in S_0 state	θ_2(degree) in S_0 state	θ_1(degree) in S_1 state	θ_2 (degree) in S_1 state	RMSD (Å)	$\Delta E_{HOMO-LUMO}$ (eV)
SB2	MeCN	0.6546	1.1298	107.76	144.23	131.50	156.20	1.4163	5.453
SB2	DMSO	0.6726	1.1308	107.76	144.23	131.53	156.21	1.4176	5.454
SB4	MeCN	0.6522	1.2260	102.09	162.77	130.38	171.32	1.5178	5.626
SB4	DMSO	0.6691	1.2268	102.10	162.78	130.40	171.37	1.5194	5.625

properties are tabulated at a glance (Table 3.4). The photostability of **SB4** (Figure 3.23) was investigated at its aggregated state (f_w of 70%). To be noted, the AIE property was even investigated in the DMSO/water medium as well for the synthesized DSE-genic compounds (Figure 3.24).

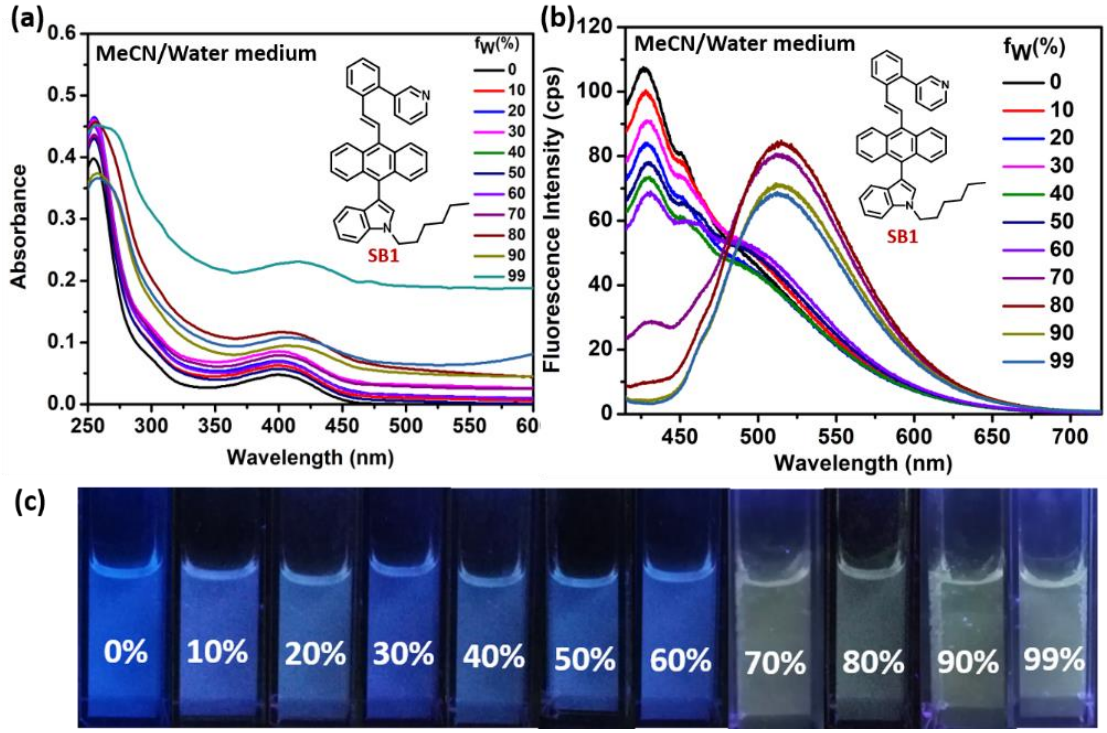

Figure 3.17 Non-AIE-property of **SB1** in MeCN/Water medium (a) absorbance (b) emission (c) visualization under 365nm UV-lamp

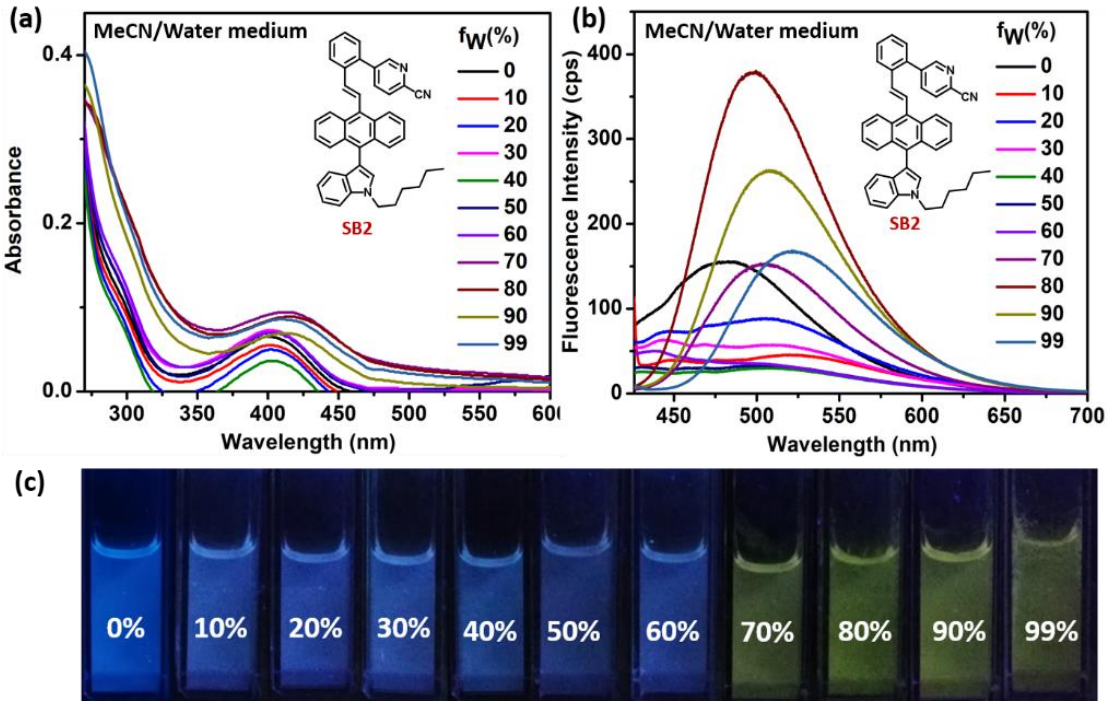

Figure 3.18 non-AIE-property of **SB2** in MeCN/Water medium (a) absorbance (b) emission (c) visualization under 365nm UV-lamp

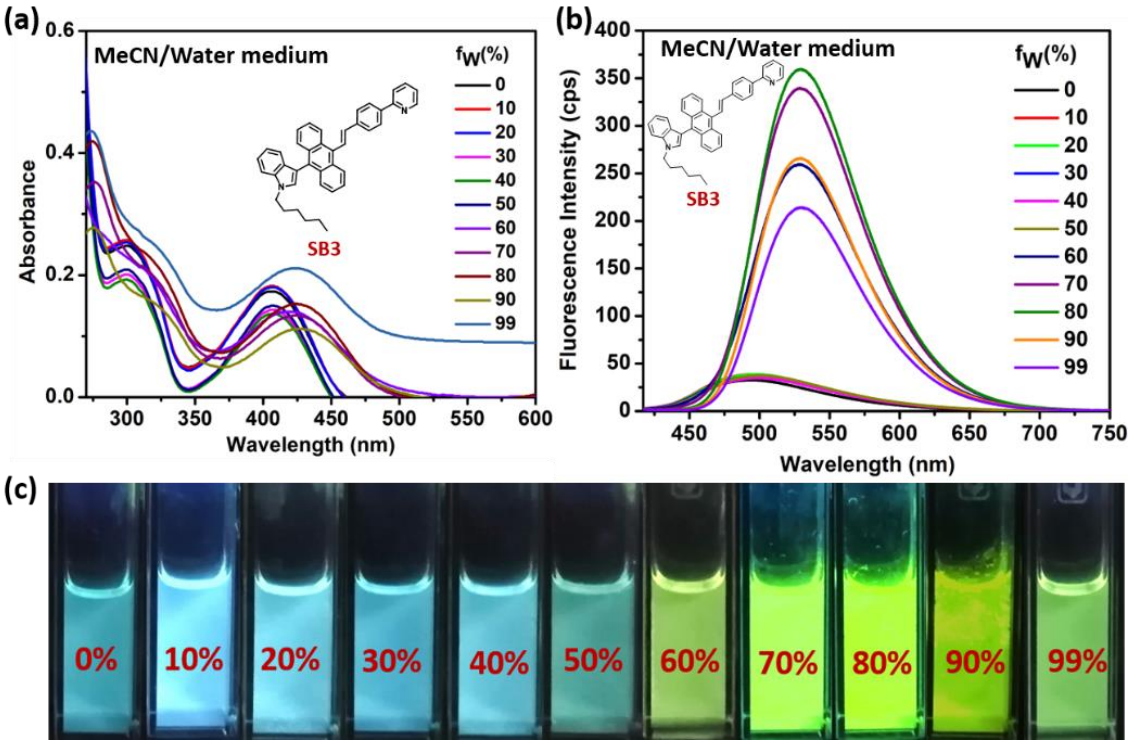

Figure 3.19 AIE-property of **SB3** in MeCN/Water medium (a) absorbance (b) emission (c) visualization under 365nm UV-lamp

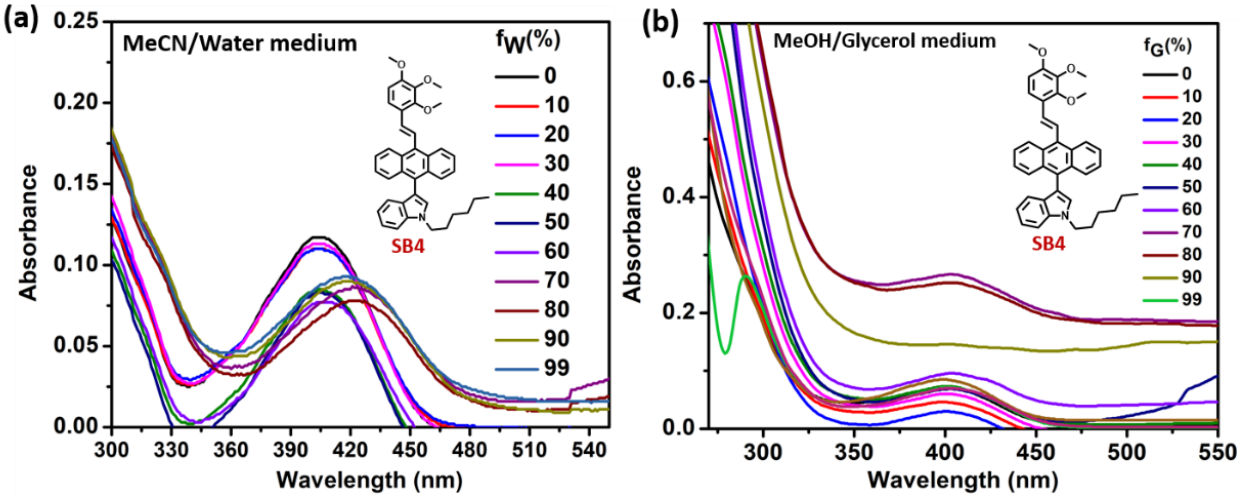

Figure 3.20 (a) **SB4** absorbance in MeCN/water medium in different water fractions (b) **SB4** absorbance in MeOH/glycerol medium in different glycerol fraction

3.3.4.4 Time-resolved fluorescence study

We were interested in measuring the nanosecond scale excited state lifetime of one of the molecules, **SB4** (as it proved to be the lead compound after undergoing the

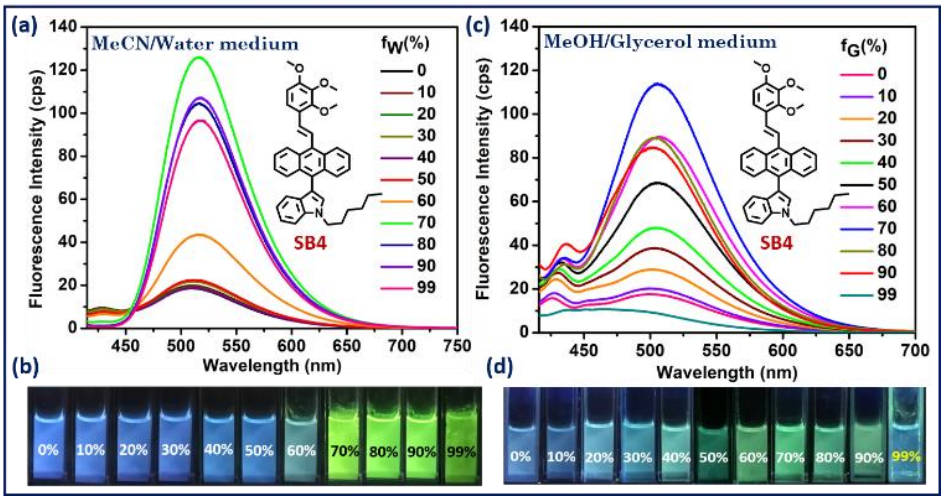

Figure 3.21 AIE-property (a-b) and viscofluorochromism (c-d) of **SB4**; f_w is the fraction of water (*v/v %)* in MeCN and f_G is the fraction of glycerol (*v/v %)* in MeOH

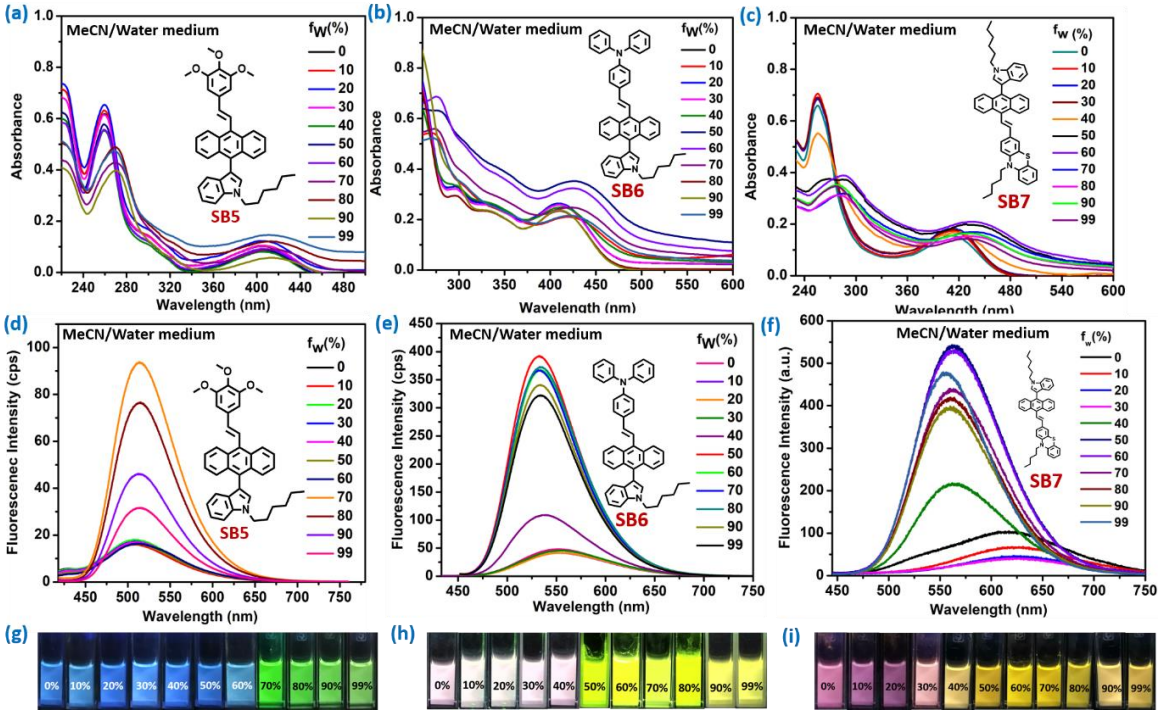

Figure 3.22 AIE-properties of **SB5** (a,d,g), **SB6** (b,e,h) and **SB7**(c,f,i) in MeCN/water medium

biocompatibility and cytotoxicity investigation) in the solution, aggregate, and solid states. But, we noticed that it was hard to measure the lifetime on a nanosecond scale due to its quick decay from the excited state. However, the decay profiles were fitted better into bi or triexponential forms.

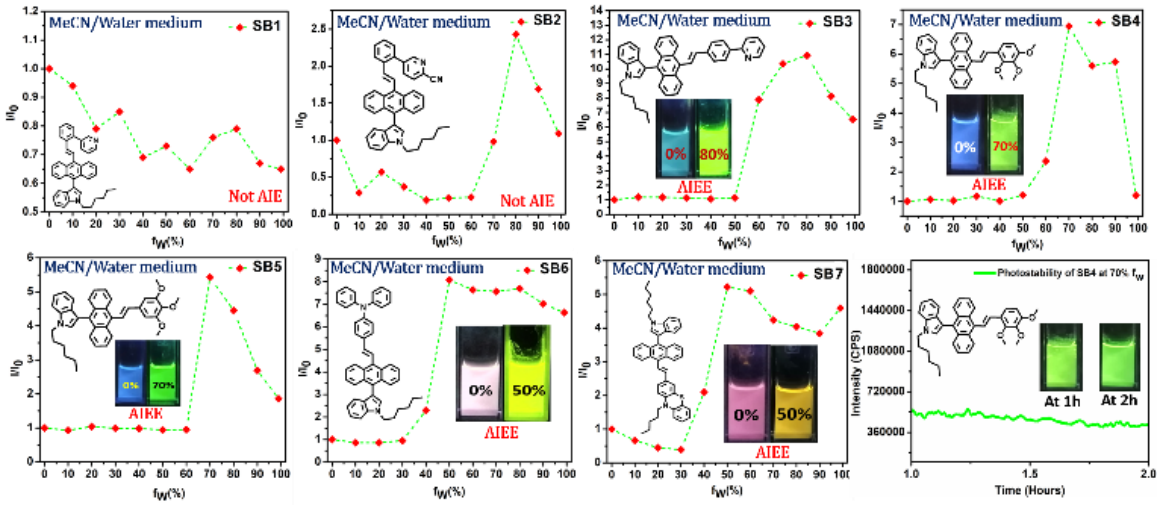

Figure 3.23 Efficiency of AIE-property of indole-anthracenyl derivatives and photostability of **SB4** at f_w(%) =70

Table 3.4 AIE/E-genic properties in a nutshell

SSOF-gen with AIE-property	$\lambda_{max.\ abs.}$ (nm) in agg. state	$\lambda_{max.\ em.}$ (nm) in agg. state	α-factor	Z-avg. (d.nm) in agg. state	PDI	Life-time in agg. state (ps)
SB3	425	530	3.52	194.5	0.296	64
SB4	423	517	1.61	186.1	0.178	66
SB5	418	514	1.12	190.4	0.197	48
SB6	428	533	2.64	219.9	0.295	51
SB7	440	565	1.18	190.7	0.185	49

(Here α-factor is the ratio of an SSEOF in Φ_f in the water fraction of aggregation and of its Φ_f in 100% MeCN. DLS particle size is presented as 'Z-avg.' in the 'nm' unit with the PDI value. Here 'agg' stands for 'aggregated', 'avg.' stands for 'average', and 'PDI' is the polydispersity index.)

As observed in the emission intensity, the lifetime (ns) was enhanced in the aggregated/solid state, as reported for other relevant molecules previously.[62] The radiative (k_r) and nonradiative (k_{nr}) rate constants were measured (Table 3.5), and the large nonradiative rate constant in the solution explains the weak emission. The gradually improving k_r in the aggregate and solid state explains the emission enhancement.

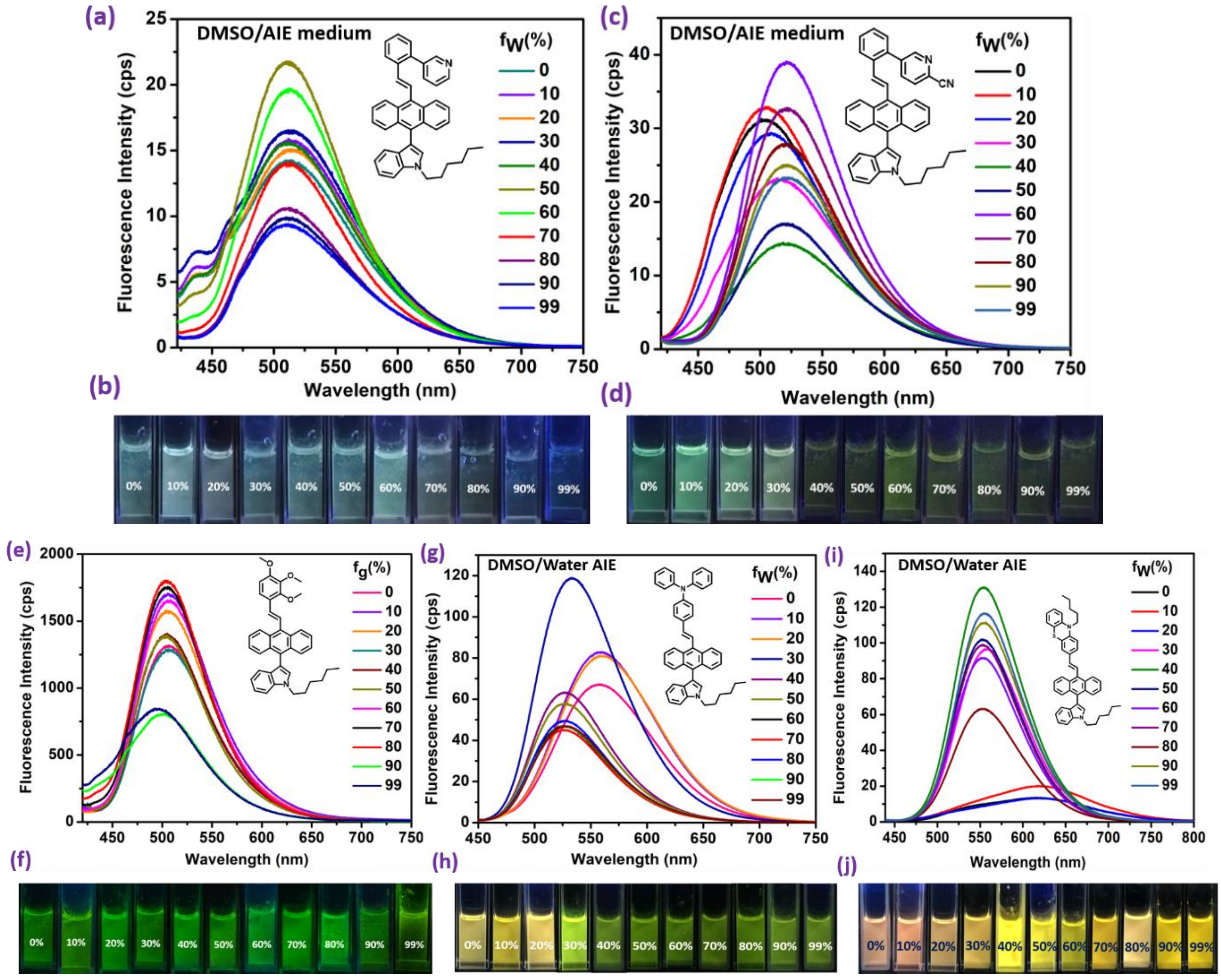

Figure 3.24 Aggregation-induced enhanced emission property of **SB1** (a-b), **SB2** (c-d), **SB4** (e-f), **SB6** (g-h) and **SB7** (i-j) in DMSO/Water medium. The pictures had been taken by keeping the containers under 365nm UV lamp. The excitation wavelengths were in between 408 nm to 424 nm for them

3.3.4.5 Field-Emission Scanning Electron Microscopy (FE-SEM) Studies

The SEM images of the aggregate states of the AIE-gens had been captured, and it was noticed that in their respective water fractions except **SB3,** the rest of the compounds, say **SB4**, **SB5**, **SB6,** and **SB7,** displayed a block kind of pattern in a very synchronized way. Even **SB3** displayed very good aggregated morphology (Figure 3.25).

Table 3.5 Time-resolved fluorescence parameters for **SB4** as an SSEOF-gen, DSE-gen, and AIEE-gen

Form	χ 2	τ_1	τ_2	τ_3	α1	α2	α3	$\tau_{avg.}$ (ns)
In MeCN	1.0351	0.0277	0.3848	-	0.9995	0.0005	-	0.0279
Aggregate in MeCN/Water medium	0.9909	0.0614	0.4265		0.9866	0.0134	-	0.0663
In DMSO	1.0282	0.0907	0.0432	0.6831	0.0555	0.9436	0.0009	0.0464
Aggregate in DMSO/Water medium	1.0206	0.0787	0.0466	-	0.1052	0.8948	-	0.0500
Solid-state	0.9915	0.7666	3.004	0.0509	0.0176	0.0004	0.9779	0.0766

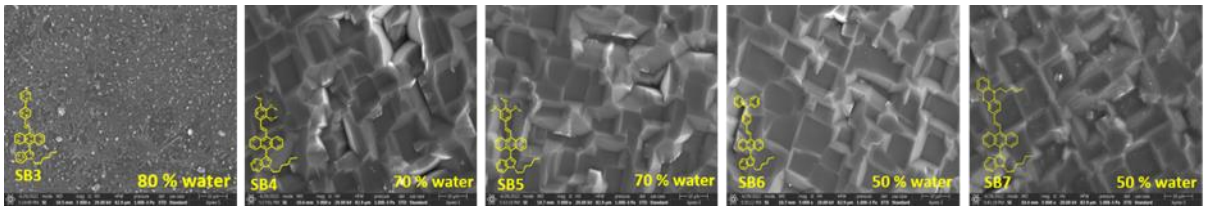

Figure 3.25 Drop-casted SEM images of the AIE-gens at their respective water fraction for aggregation

3.3.5 Biological applications

3.3.5.1 Cytotoxicity of synthesized compounds against different cell lines

The evaluation of *in vitro* cytotoxicity for all the SSEOFs with DSE nature was conducted against FaDu (a robust and aggressive cell line), 4T1 triple-negative breast cancer cell line (TNBC), and MCF-7 non-TNBC cancer cell lines. After incubation with different concentrations of these dyes for 24 h, the cell viability was determined with the standard MTT assay. GI_{50} values for the individual cell lines were defined as the concentration of the compounds at 50% survival of cells. Doxorubicin was utilized as the standard drug. The anticancer activities of these dyes are tabulated below (Table 3.6). From the cytotoxicity assay results against the cancer cell lines, five active SSEOFs with DSE characteristics were only selected to check their cytotoxicity against the non-cancerous human kidney embryonic cell line HEK-293. Notably, DSE-gen **SB4** shows the best anti-cancer activity against both FaDu and 4T1 and is less cytotoxic than

doxorubicin for HEK-293 normal cells. Surprisingly, it was inactive against a comparative cell line MCF-7.

Table 3.6 GI_{50} values of all the AIE-gens in various cancer cell lines

GI_{50}(μM) for each cell-line	Doxorubicin	SB1	SB2	SB3	SB4	SB5	SB6	SB7
FaDu	0.24-0.3	39.27	37.53	>100	**24.94**	>100	27.21	69.27
4T1	0.85-2.2	49.75	32.99	>100	**20.76**	82.11	>100	>100
MCF-7	1.07-2.57	88.7	>100	>100	>100	>100	>100	>100
HEK-293	3.3	35.63	33.72	-	>100	-	>100	>100

This table also indicates good responses from **SB1** and **SB2** against FaDu and 4T1, but these are acutely toxic against HEK-293 and, thus, inappropriate for further use. The TPA-analog **SB6** also possesses favorable anti-cancer activity against FaDu but not 4T1.

3.3.5.2 Reactive oxygen species (ROS) generation and *in vitro* Haemolysis study

Reactive Oxygen Species (ROS) is a phrase used to indicate several reactive molecules and free radicals derived from molecular oxygen. ROS dynamically influences the tumor microenvironment and is known to initiate cancer angiogenesis, metastasis, and survival at different concentrations.[63] At moderate concentrations, ROS activates the cancer cell survival signaling cascade. At high concentrations, ROS can cause cell apoptosis. Thus, it shows the potential as an effective anti-tumor modality and therapeutic target for treating malignancies.[63] To evaluate the ROS generation ability of SSEOFs with DSE-characteristics[7c] against a rigid and aggressive cell line like FaDu, we selected an oxidant-sensitive fluorescent dye named dichlorofluorescein diacetate (DCF-DA). Since DCF-DA has a high fluorescence quantum yield, the interference from the DSE-gens was minimized while evaluating the ROS generation ability. The efficiency of the lead molecule **SB4** was almost identical to that of the standard drug doxorubicin (**Figure 3.26a**).

In addition, we treated the red blood cells with these DSE-genic SSEOFs at their respective GI_{50} concentrations and then analyzed the treated cells by the haemolysis (rupture of red blood cells) assay. For standard titron X, 100% hemolysis was considered, whereas doxorubicin showed 40% haemolysis, a destructive impact. Interestingly,

AIEgens **SB1**, **SB2**, **SB4**, **SB6,** and **SB7** disclosed an inferior haemolyzing effect than doxorubicin (Figure 3.42b). It is noteworthy that **SB1**, **SB2**, **SB4**, **SB6**, and **SB7** are less cytotoxic than doxorubicin. Thus, the prime molecule **SB4** offers a decent anticancer property against FaDu and 4T1 with excellent ROS generation and less haemolysing effect, while relating with doxorubicin (Figure 3.26b).

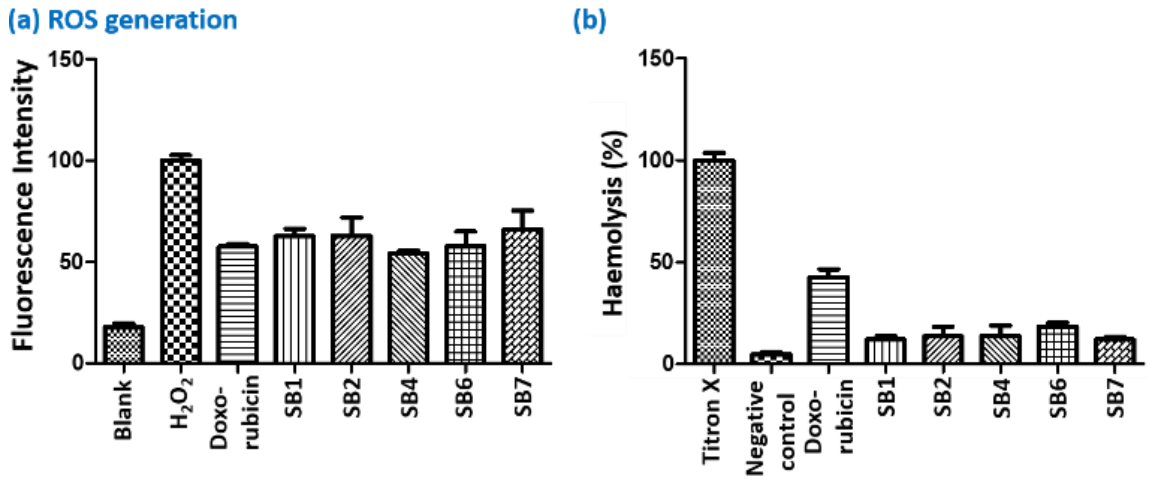

Figure 3.26 (a) ROS study of DSE-gens (b) Haemolysis study of DSE-genic SSEOFs

3.3.5.3 Cellular uptake

The cellular uptakes of the DSE-genic SSEOFs like **SB1**, **SB2**, **SB4**, **SB6,** and **SB7** were investigated by Fluorescence-Activated Cell Sorting (FACS) analysis against the FaDu cell line to understand the nature of the single-cell population. All the synthesized compounds displayed excellent cellular uptake (Figure 3.27). Later, the cellular uptake of lead molecule **SB4** was investigated against other cell lines 4T1, MCF-7, and HEK-293 and displayed an excellent cellular uptake capacity for all. Hence, it is persuaded that the dyes can penetrate 4T1 and MCF-7 cells, and their specificity toward 4T1 is not due to any variances in cellular uptake capacity (Figure 3.27).

3.3.5.4 Utilizing anticancer agent SB4 in bioimaging of FaDu and 4T1 cell lines: Inhibition and detection of cancer cells with the help of the same agent SB4

As DMSO is a preferable solvent in a biological experiment regarding cell culture, the emission properties of the biologically active molecules **SB1, SB2, SB4, SB6,** and **SB7** were also checked for aggregates in DMSO/water medium. To our satisfaction, they increased their emissive efficacy in this solvent medium also (Figure 3.24).

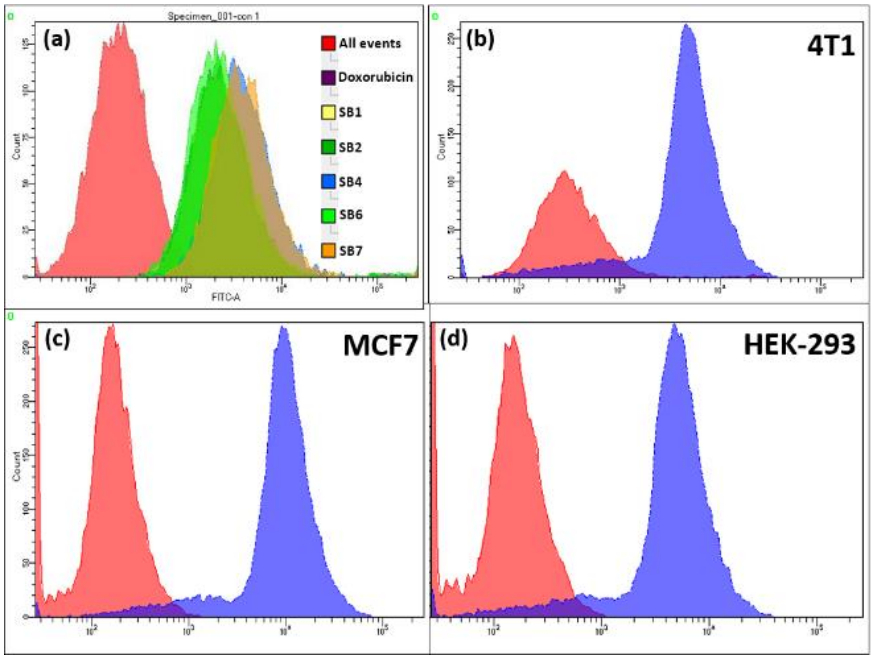

Figure 3.27 (a) Cellular uptake capacity of DSE-gens into FaDu; cellular uptake capacity of lead DSE-gen **SB4** into (b) 4T1 (c) MCF-7, and (d) HEK-293 cell lines

All the above results convincingly introduce **SB4** as a bioimaging agent to visualize the cancer cells FaDu, 4T1, and HEK-293 before and after inhibition. After four hours of **SB4** treatment in both the cell lines FaDu and 4T1 with GI_{50} concentration, the confocal experiment was performed, keeping the cells fixed, and the image was captured. The intense green fluorescence was noticed by staining cells with **SB4** with its GI_{50} concentration**.** As the cytotoxicity assay against cancer cell lines was conducted at a 24h time-point, confocal images were again captured after 24 h of treatment using the same cell lines. For the anticancer properties, **SB4** will inhibit the cells and won't provide any intense fluorescent signal in confocal at 24h time-point. But for HEK-293 strong green fluorescence signal can be received at 4 h and at 24 h timepoint because **SB4** does not inhibit HEK-293 normal cells. Thus, **SB4** can not only kill but also detect cancer cell death with its scathed fluorescence signal (Figure 3.28). The utility of **SB4** as a bioimaging probe for both the cancer cells (Fadu and 4T1) a comparative study was carried on with the standard drug doxorubicin taking DAPI as an already known reference stain.[64-66] As observed from the experiments, DAPI and doxorubicin could stain FaDu and 4T1 at both the time points of 4h and 24h. But as stated earlier, **SB4** could stain cancer cells initially at the 4h time-point only, but a scathed fluorescence signal was observed at the 24h time-point for FaDu and 4T1 (Figures 3.29-3.30).

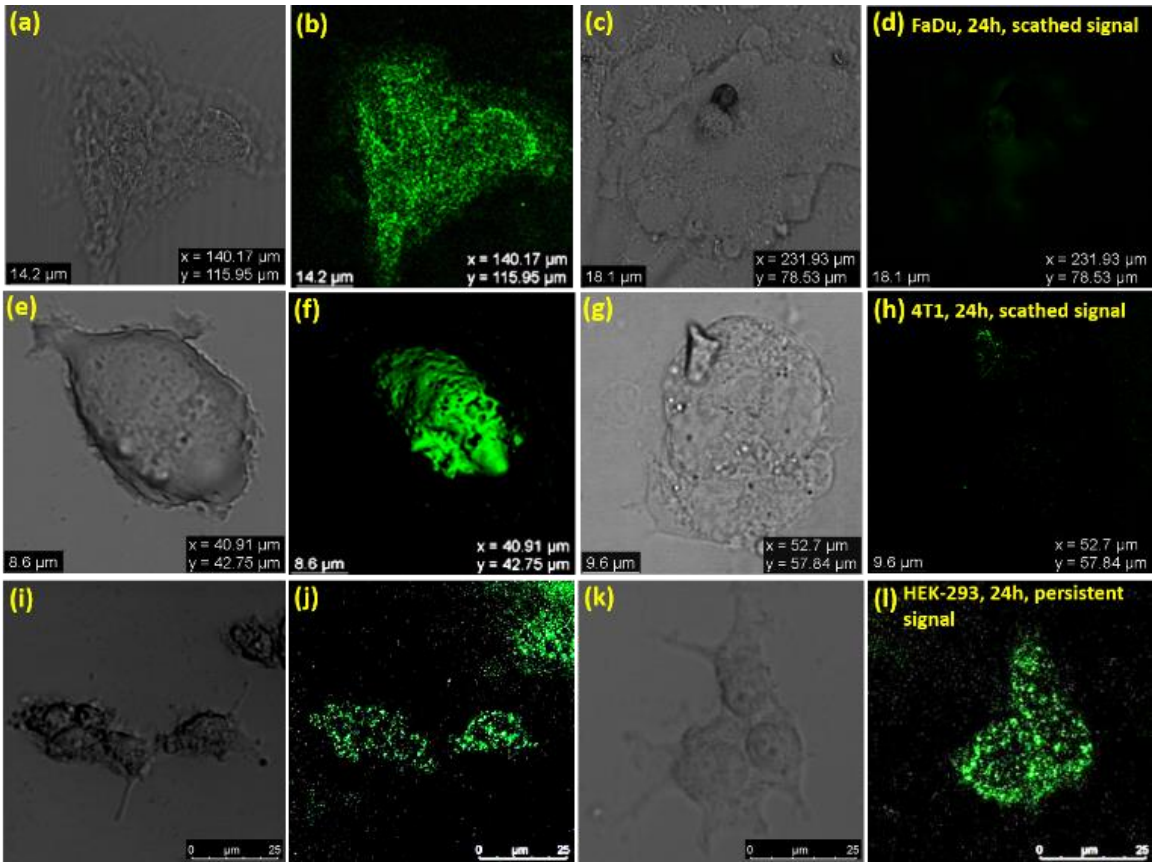

Figure 3.28 (a) Bright-field of FaDu cell after 4 h to staining with **SB4** (b) Fluorescent image of FaDu cell after 4 h to staining with **SB4** (c) Bright-field of FaDu cell after 24h to staining with **SB4** (d) Diminished fluorescence of FaDu cell after 24 h to staining with **SB4** (e) Bright-field image of 4T1 cell after 4 h to staining with **SB4** (f) Fluorescent image of 4T1 cell after 4 h to staining with **SB4** (g) Bright-field image of 4T1 cell after 24h to staining with **SB4** (h) Reduced fluorescent signal of 4T1 cell after 24 h to staining with **SB4** (i) Bright-field image of HEK-293 after 4 h to **SB4** treatment (j) Fluorescent signal given by HEK-293 after 4 h to **SB4** treatment (k) Bright-field image of HEK-293 after 24 h to **SB4** treatment (l) Persistent fluorescence of HEK-293 cell after 24 h of **SB4** treatment

The used concentration of DAPI was 1μG/mL, and here also, the GI_{50} concentration of doxorubicin was used for bioimaging. DAPI is a well-known bis-intercalator with DNA and a minor groove binder.[67] It can stain live cells as well as dead

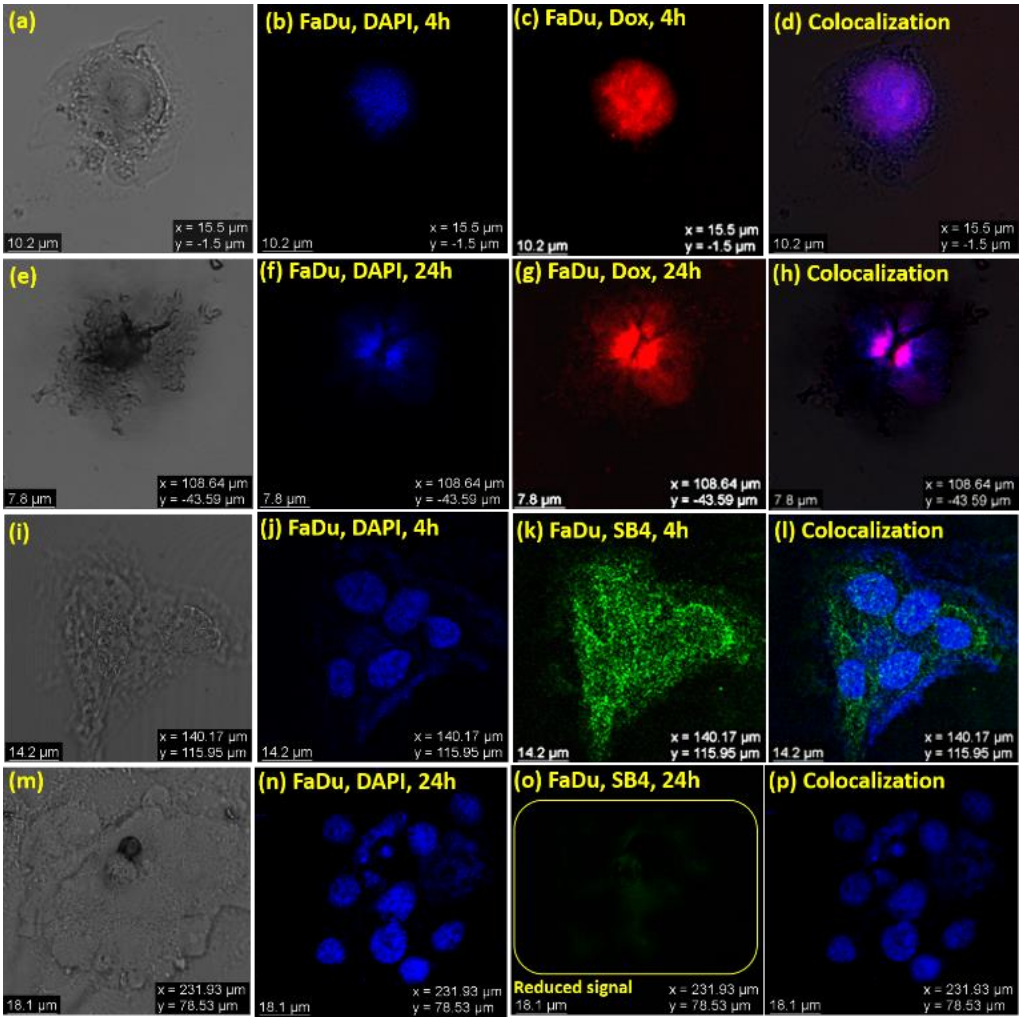

Figure 3.29 (a) Bright-field of FaDu cell at 4h (b) Fluorescent image of FaDu cell after 4 h to staining with **DAPI** (c) Fluorescent image of FaDu cell after 4 h to staining with **doxorubicin** (d) Merged image of a, b, and c to understand colocalization (e) Bright-field of FaDu cell at 24h (f) Fluorescent image of FaDu cell after 24 h to staining with **DAPI** (g) Persistent fluorescent image of FaDu cell after 24 h to staining with **doxorubicin** (h) Merged image of e, f, and g to understand colocalization (i) Bright-field of FaDu cell at 4h (j) Fluorescent image of FaDu cell after 4 h to staining with **DAPI** (k) Fluorescent image of FaDu cell after 4 h to staining with **SB4** (l) Merged image of i, j, and k to understand colocalization (m) Bright-field of FaDu cell at 24h (n) Fluorescent image of FaDu cell after 24 h to staining with **DAPI** (o) Scathed fluorescent image of FaDu cell after 24 h to staining with **SB4** (p) Merged image of m, n, and o to understand colocalization. 'Dox' stands for doxorubicin. 'DAPI' stands for 4',6-diamidino-2-phenylindole

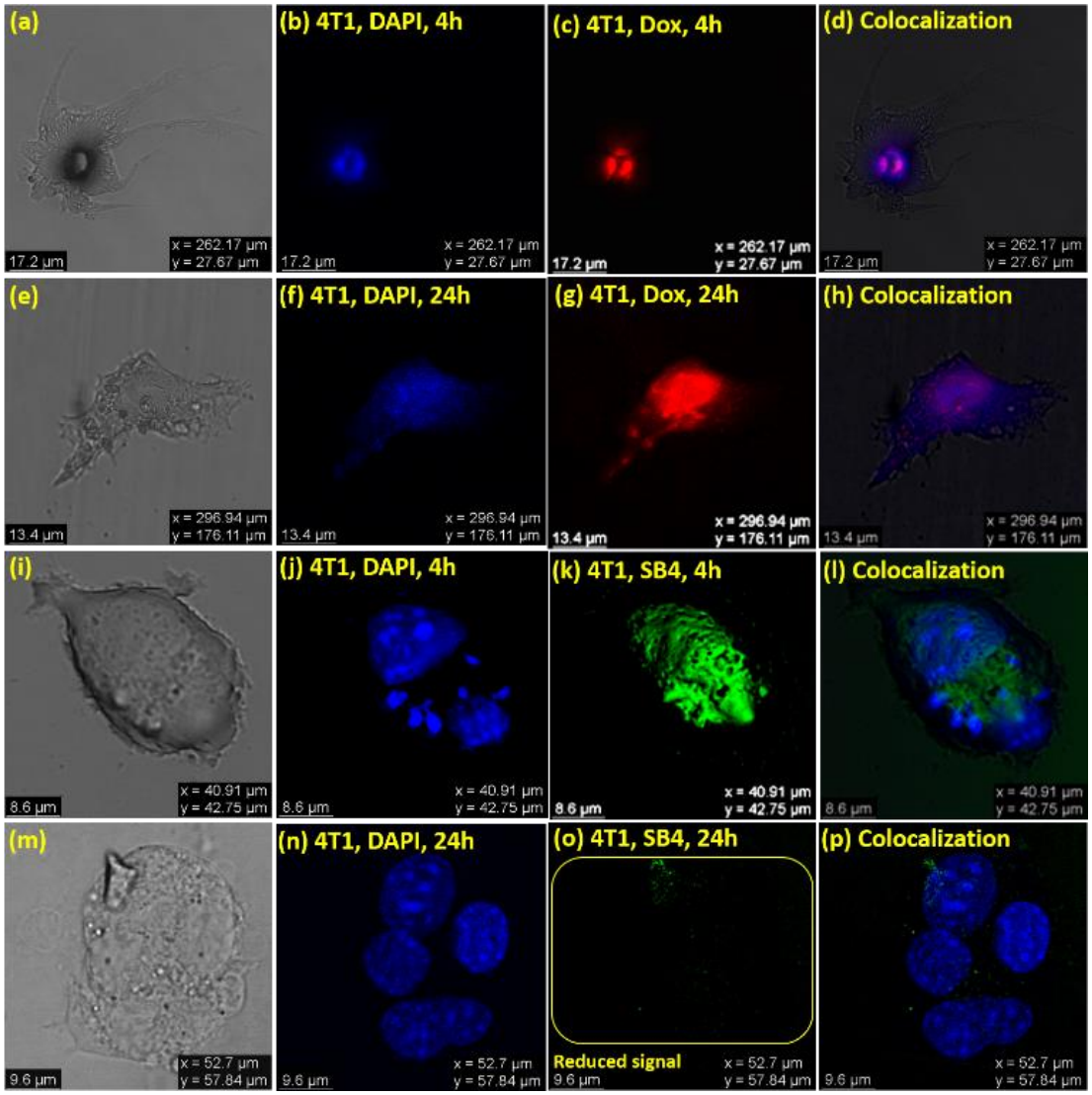

Figure 3.30 (a) Bright-field of 4T1 cell at 4h (b) Fluorescent image of 4T1 cell after 4 h to staining with **DAPI** (c) Fluorescent image of 4T1 cell after 4 h to staining with **doxorubicin** (d) Merged image of a, b, and c to understand colocalization (e) Bright-field of 4T1 cell at 24h (f) Fluorescent image of 4T1 cell after 24 h to staining with **DAPI** (g) Persistent fluorescent image of 4T1 cell after 24 h to staining with **doxorubicin** (h) Merged image of e, f, and g to understand colocalization (i) Bright-field of 4T1 cell at 4h (j) Fluorescent image of 4T1 cell after 4 h to staining with **DAPI** (k) Fluorescent image of 4T1 cell after 4 h to staining with **SB4** (l) Merged image of i, j, and k to understand colocalization (m) Bright-field of 4T1 cell at 24h (n) Fluorescent image of 4T1 cell after 24 h to staining with **DAPI** (o) Scathed fluorescent image of 4T1 cell after 24 h to staining with **SB4** (p) Merged image of m, n, and o to understand colocalization

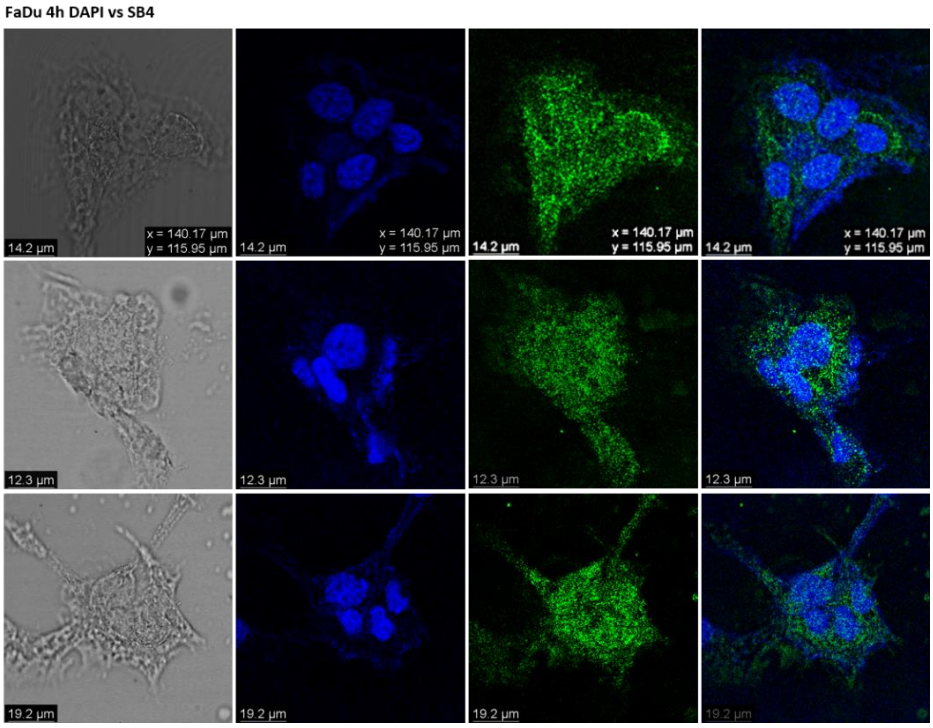

Figure 3.31a Confocal images (FaDu cells) utilized for quantification (DAPI vs SB4, 4h); DAPI displays the blue color, and green by **SB4**, and the mixed color appears by colocalization

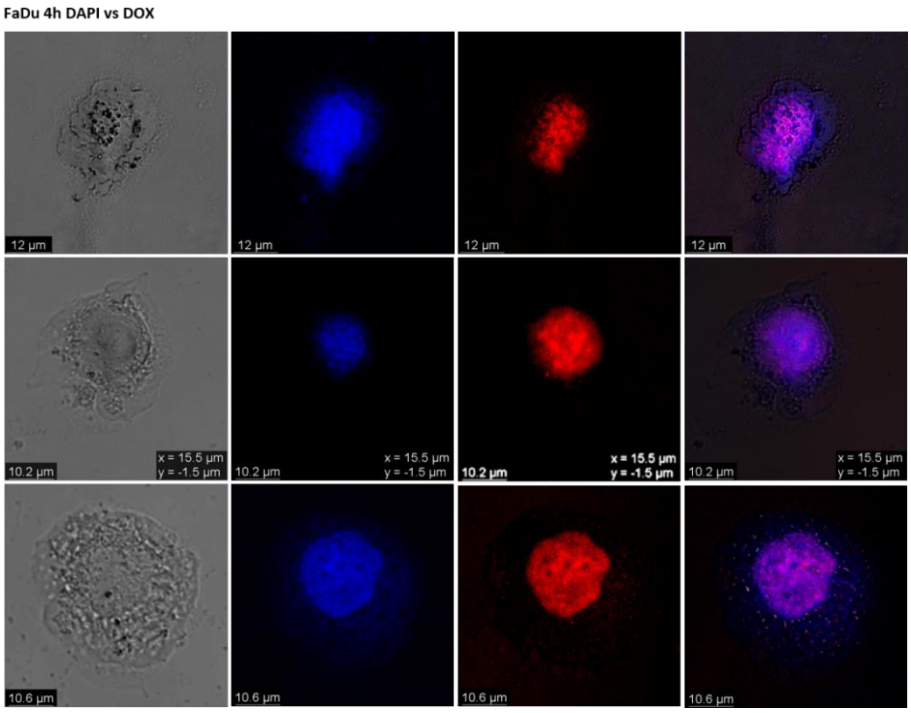

Figure 3.31b Confocal images (FaDu cells) utilized for quantification (DAPI vs Doxorubicin, 4h); DAPI displays the blue color, and red by doxorubicin, and the mixed color appears by colocalization

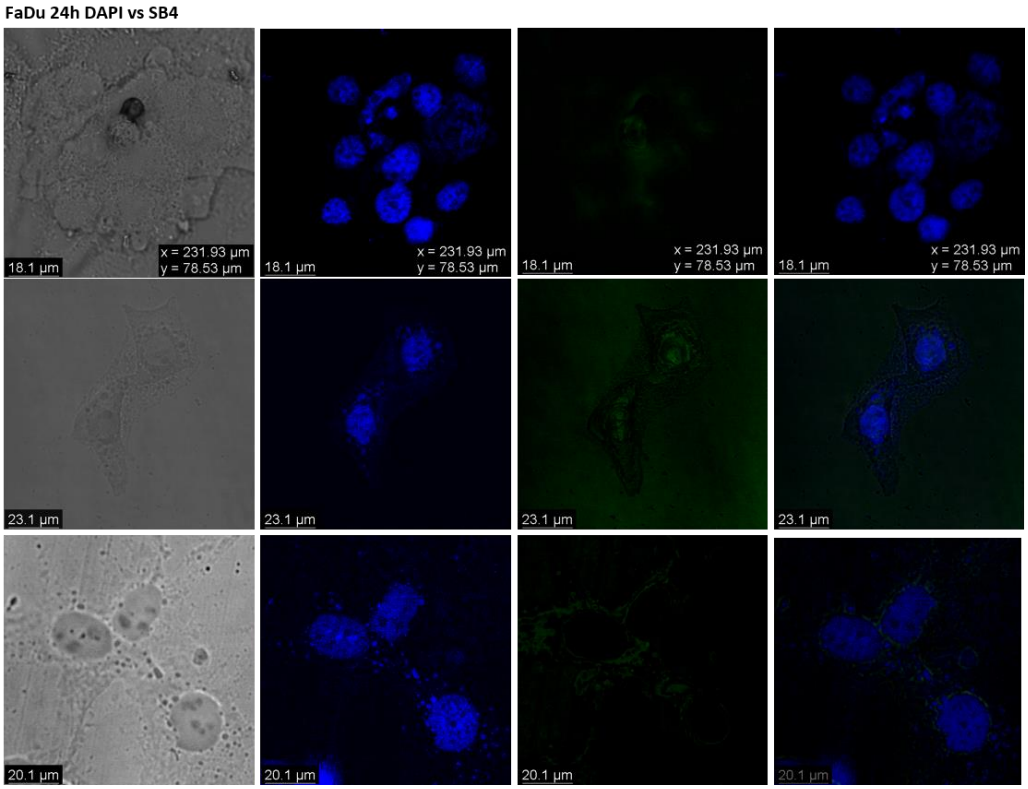

Figure 3.31c Confocal images (FaDu cells) utilized for quantification (DAPI vs SB4, 24h)

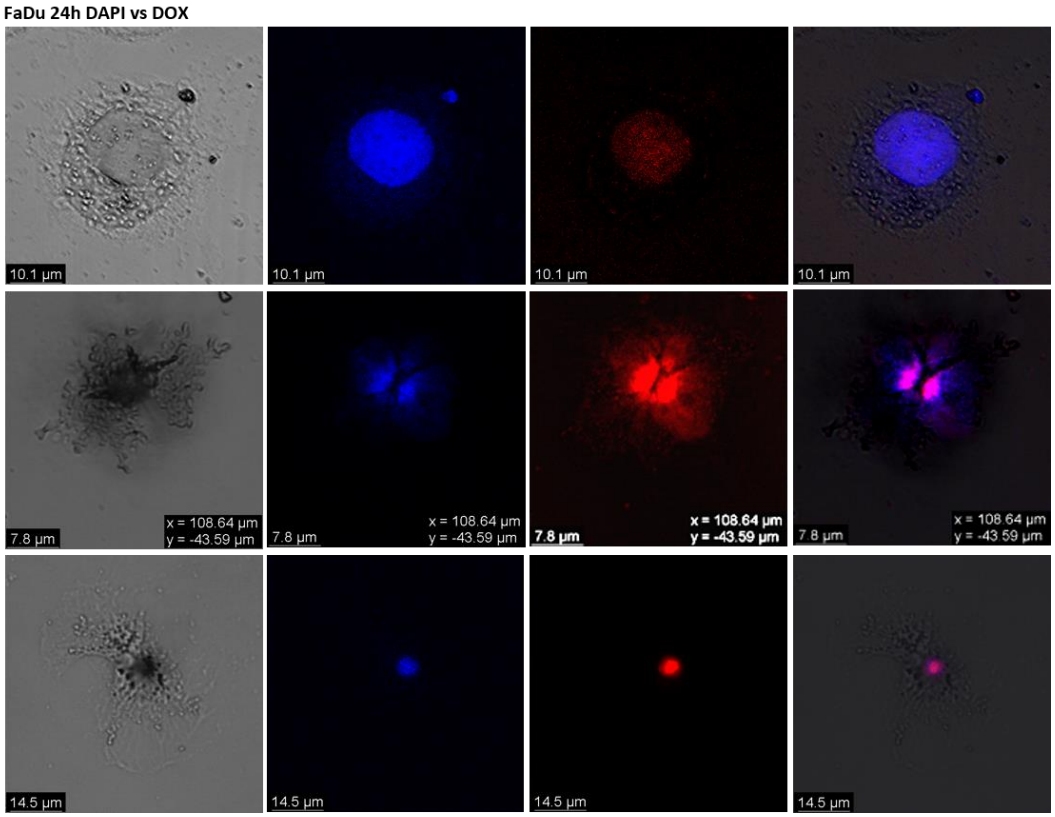

Figure 3.31d Confocal images (FaDu cells) utilized for quantification (DAPI vs Doxorubicin, 24h)

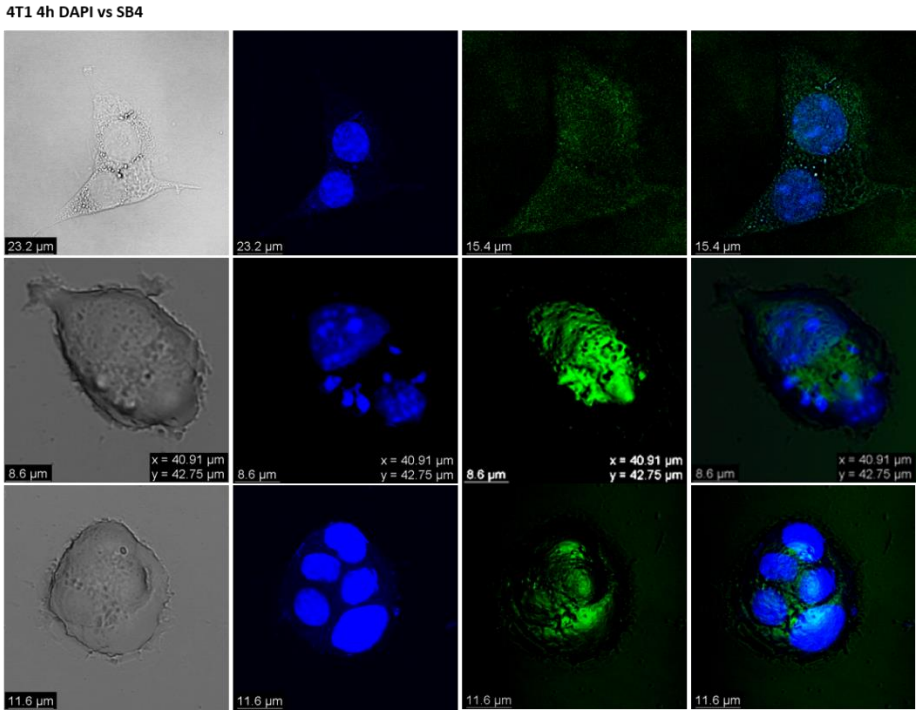

Figure 3.31e Confocal images (4T1 cells) utilized for quantification (DAPI vs SB4, 4h); DAPI displays the blue color, and green by **SB4**, and the mixed color appears by colocalization

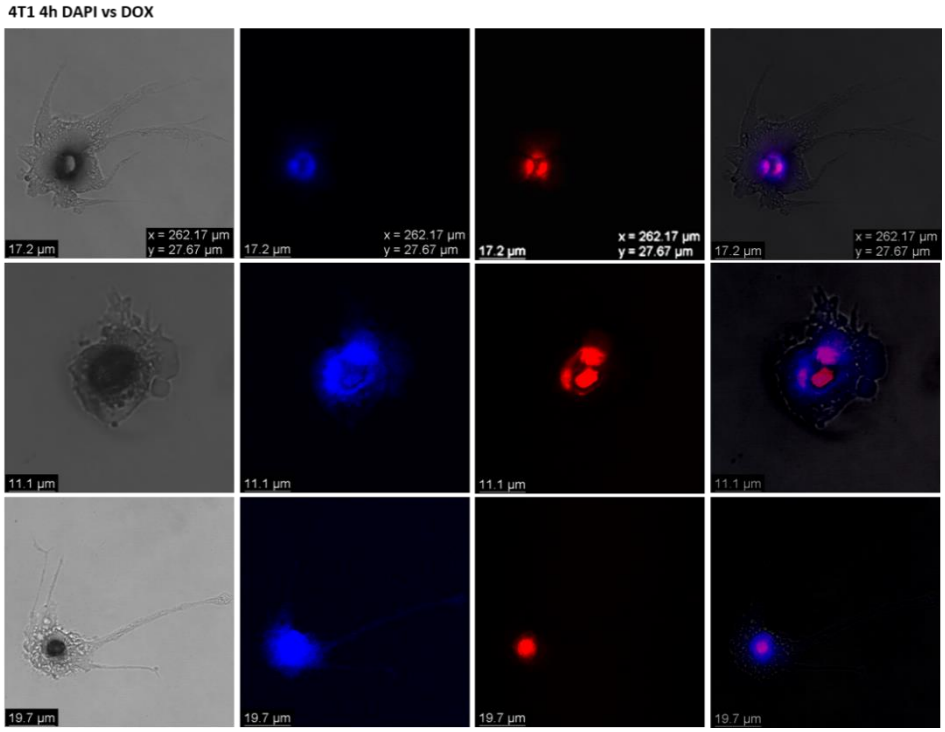

Figure 3.31f Confocal images (4T1 cells) utilized for quantification (DAPI vs Doxorubicin, 4h); DAPI displays the blue color, and red by doxorubicin, and the mixed color appears by colocalization

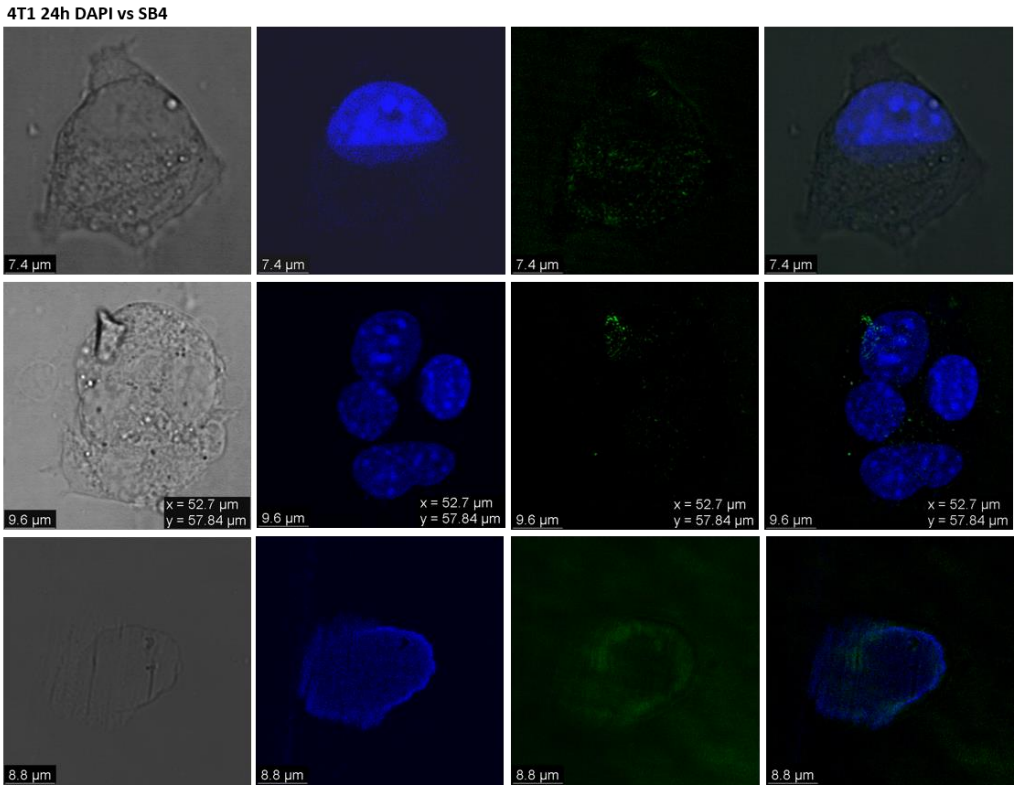

Figure 3.31g Confocal images (4T1 cells) utilized for quantification (DAPI vs SB4, 24h)

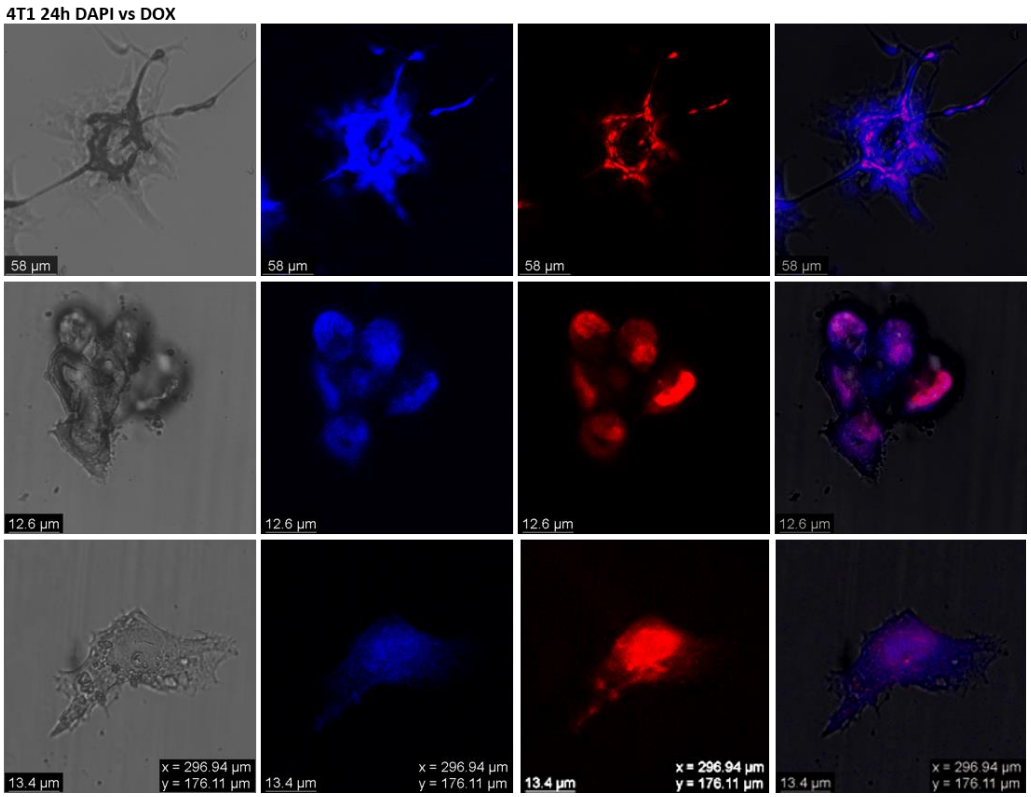

Figure 3.31h Confocal images (4T1 cells) utilized for quantification (DAPI vs Doxorubicin, 24h)

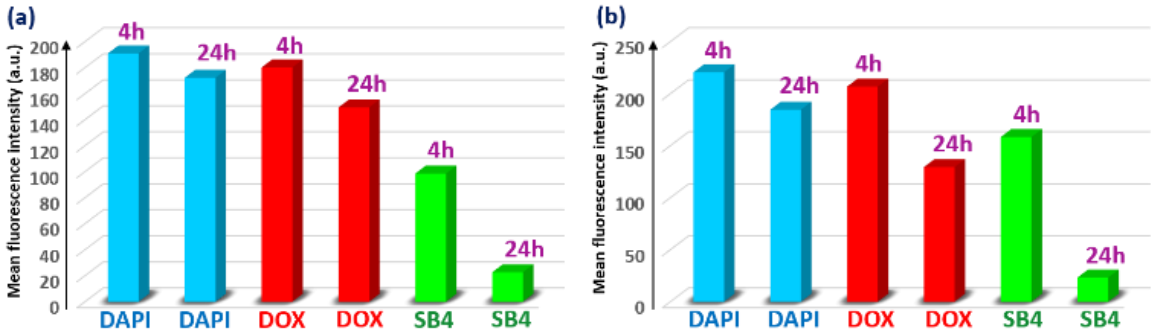

Figure 3.32 Comparison of the mean fluorescent intensity in confocal images using '*ImageJ*' for (a) FaDu and (b) 4T1

cells because after the cell death also, the nucleus is not ruined instantly. Interestingly, doxorubicin also forms complexes by intercalation between DNA-base pairs and it can stain live cells as well as dead cells just like DAPI.[68,69] These may be the reasons to receive fluorescence signals with both DAPI and doxorubicin before and after the death of the cancer cells respectively at 4h and 24h. But the consequence is different for **SB4** from the standard drug doxorubicin. From the colocalization study, it is understood that **SB4** is not nucleus specific and it stains the whole cell. And with **SB4** this staining characteristic remains the same for FaDu, 4T1, and HEK-293 as well. As **SB4** does not inhibit HEK-293, the cell is not ruptured and hence probably **SB4** can stay within the cell to offer a fluorescence signal even at 24h time-point as well as at 4h. On the other hand, aggregates may form ROS[7c],and in our case also it has been noticed that AIE-active DSEgenic SSEOF **SB4** generates ROS and shows more affinity towards the HER2 protein, and eventually inhibits cancer cells. Meanwhile, the dead cells may rupture the cell membranes to become leaky. Hence there is a chance that **SB4** will leak out of the cell, and the fluorescence signal will be reduced due to the scarcity of a sufficient amount of probes inside the cell (Figures 3.29-3.30). Although as a drug, the action of the mechanism for **SB4** needs to be investigated in detail as a next target. To understand a comparative view different confocal images (Figure 3.31) were analyzed through 'ImageJ'[70] and the quenching of the mean fluorescent intensity of **SB4** at a 24h time-point is clearly indicated in the bar graph (Figure 3.32).

3.3.5.5 Utilizing AIE-active DSE-genic SSEOFs in wash-free bioimaging of cancer cells

Whether **SB4** was proven to be a smart anticancer active bioimaging agent to inhibit and detect cancer cells, we even tried to find bioimaging applications of other non-cytotoxic AIE-active, DSE-genic SSEOFs too. As we know, fluorescence imaging of cancer cell lines has become a dependable tool in biomedical research[71,72], especially the wash-free cancer cell imaging is considerably rare and challenging due to the appearance of unwanted background signals. However, wash-free imaging can simplify the analytical procedure, shorten the detection time, and reduce the cost.[72] Again, red and green are the most-preferable dyes from the entire chromatic spectrum, as those are widely used in biochemistry, immunohistochemistry, immune-staining, and nanochemistry applications.[73-76]

In this context, we attempted to investigate the wash-free bioimaging capabilities of **SB6** and **SB7** with FaDu cells. The reason coincides with our future planning. We aim to develop a bioimaging probe that can be useful to detect distortion of cancer cells through wash-free bioimaging. Although not effective like **SB4**, as both **SB6** and **SB7** have anticancer properties (Table 6), and **SB3** is not a bioactive compound. So, we did some preliminary studies in this regard and opted for **SB6** as a green emitter and **SB7** as a red emitter. Initially, the cellular uptake of all of them was investigated by Fluorescence-Activated Cell Sorting (FACS) analysis against the FaDu cell line to understand the nature of the single-cell population. Both displayed commendable cellular uptake (Figure 3.27). Herein, **SB7** propounds wash-free bioimaging of FaDu in the near red region (Figure 3.34) and **SB6** in the green region (Figure 3.33) with commendable efficacy of cell visualization without major background glitches. After 4 h of staining with **SB6**/**SB7** at 10 μM concentration, the images of FaDu cells were captured.

3.3.5.6 Utilizing AIE-active DSE-genic SSEOF in the detection of cancer cell distortion through wash-free bioimaging

The compound **SB6** killed FaDu effectively with a GI_{50} concentration of 27.21 μM at a 24 h time-point by keeping the normal cells intact (as the GI_{50} concentration for the normal cell is more than 100 μM). Now, we attempted to visualize if this dye could

monitor cell deformation as an effect of its anticancer activity. So, after 6 h of staining with **SB6**, the images of FaDu cells were captured. As **SB6** is cytotoxic to FaDu, the probably deformed cells can be captured through bioimaging. To our delight, it was possible to observe the initiation of cell deformation 6 h post-treatment with **SB6** at the GI_{50} concentration (Figure 3.35).

Furthermore, colocalization quantification was done, and the results are tabulated (Table 3.7) here. Pearson's correlation (PC), overlap coefficient (OC), colocalization rate (CR) percentage, and mean intensity colocalization (MIC) with respect to DAPI and **SB6**/**SB7** were investigated, and the results were satisfying. Representative 'scat' profile images are placed for better understanding (Figure 3.36).

3.3.5.7 Utilizing AIE-active DSE-genic SSEOF SB3 in wash-free bioimaging of cancer cell

Although **SB3** was not found to exhibit anticancer property but as a bioimaging dye it performed well because we received good wash-free bioimages of FaDu cells while utilizing **SB3** for the same. With >100 µM GI_{50} concentration of **SB3** against the FaDu cell line, the cells were safely stained with 10 µM (ten times lesser concentration) solution without major background glitches (**Figure 3.37**). For **SB3** also, DAPI (4',6-diamidino-2-phenylindole) was utilized as a standard cellular imaging dye with 3 µM concentration, but PBS-washed bioimaging was performed with DAPI. We intended to match up normal PBS-washed bioimaging with DAPI and PBS-wash-free bioimaging with **SB3**.

To our delight, for **SB3** we found commendable colocalization with DAPI (Figure 3.37). These merged images between DAPI and **SB3** stained ones indicate that **SB3** has the ability to visualize the cell nucleus although the cytoplasmic area is also visible with a very lower intensity. The same thing was even noticed for **SB6** and **SB7**. The cause of this selective bioimaging needs a detailed investigation and is currently undergoing as our next target.

3.3.6 Molecular docking

Molecular docking is a methodology applied to study molecular behavior target proteins binding. Indeed, it is a tool that is used extensively in drug discovery. We have

initiated inspection with our molecules, and further investigation will be carried on as our future perspectives.

From the existing literature, it can be easily understood that Epidermal Growth Factor Receptor (EGFR) is believed to play an essential role in oral, oropharyngeal, and triple-negative breast cancer (TNBC).[77,78] Human epidermal growth factor receptor 2 (HER2) is a member of the epidermal growth factor receptor family having tyrosine

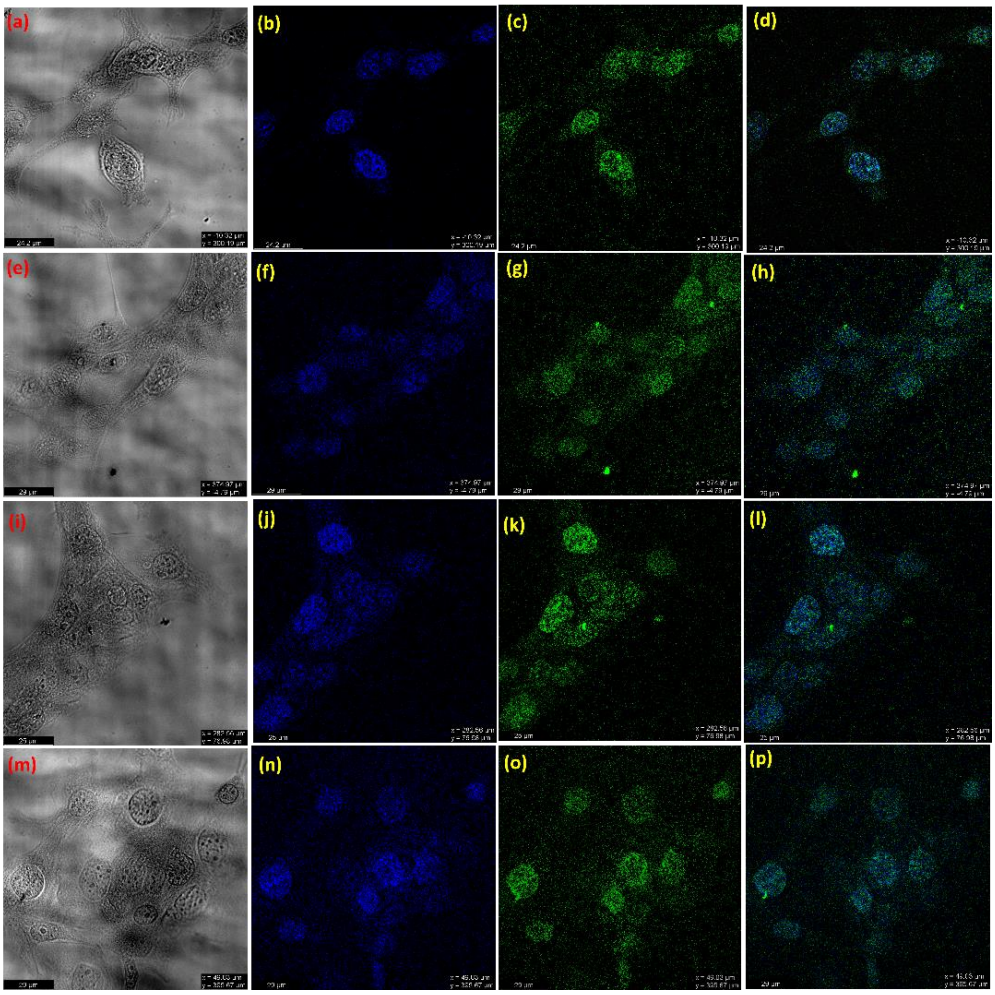

Figure 3.33 FaDu cells in bright-field (a, e, i, m); FaDu cells stained with DAPI (b, f, j, n); FaDu cells stained with **SB6** (c, g, k, o) and the respective colocalization studies taking DAPI stained and **SB6** stained images (d, h, I, p)

kinase activity. Amplification or overexpression of HER2 occurs in approximately 15-30% of breast cancers, and HER2 testing and HER2-directed therapies are recommended only in breast and gastroesophageal cancers.[79,80] Here, the Protein Preparation Wizard module, LigPrep module, and Glide module from Schrodinger suites 2022-1 were employed to prepare the crystal structures of protein obtained from

PDB (PDB IDs: 7JXH, 3RCD, and 3PP0 for HER2 protein and 5X2C and 4I22 for EGFR protein), for ligand preparation and for performing molecular docking, respectively. The crystal structures were chosen based on the availability of inhibitor ligands at the tyrosine kinase binding site and their resolutions. For HER2/ ErbB2 protein, the resolution of structures was: 3PP0 with 2.25 Å, 7JXH with 3.27 Å, and 3RCD with 3.21 Å. For EGFR protein, the resolution of structures was: 5X2C with 2.05 Å and 4I22 with 1.71 Å. Post-protein preparation, the co-crystal ligands and inhibitor ligands were prepared using the LigPrep module.

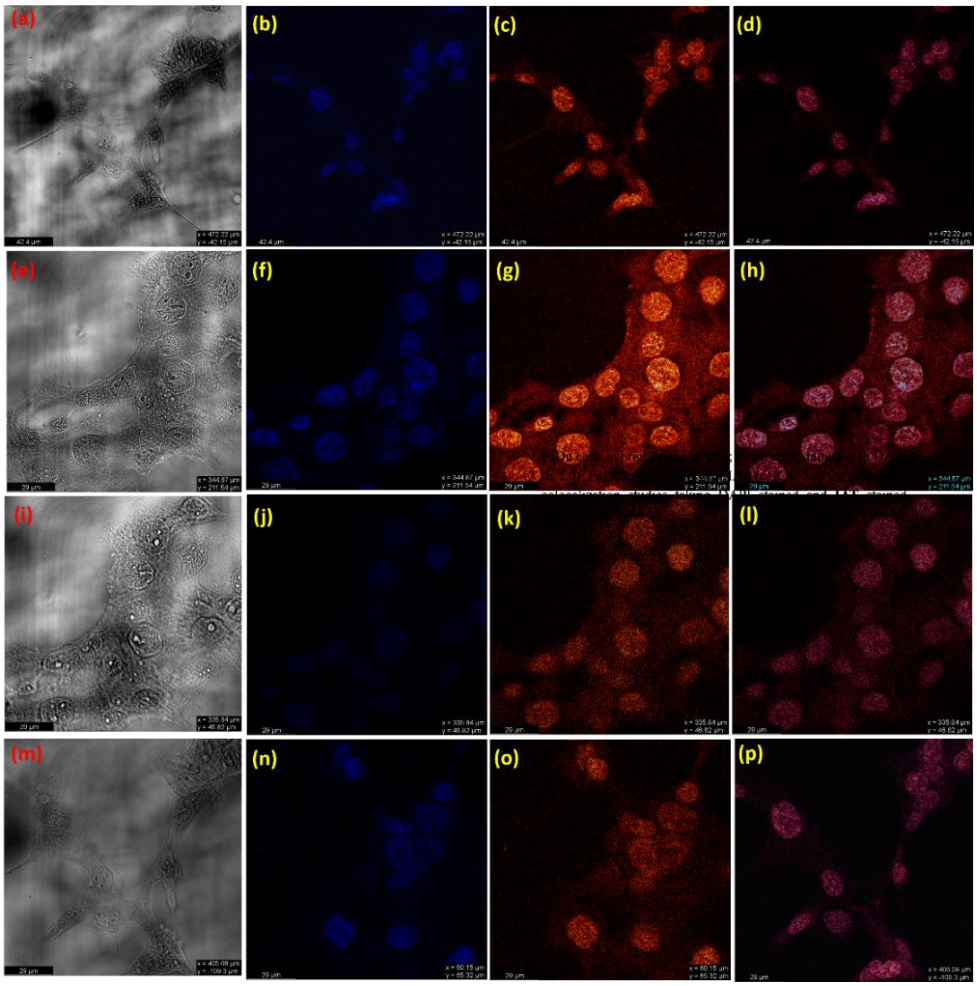

Figure 3.34 FaDu cells in bright-field (a, e, i, m); FaDu cells stained with DAPI (b, f, j, n); FaDu cells stained with **SB7** (c, g, k, o) and the respective colocalization studies taking DAPI stained and **SB7** stained images (d, h, I, p)

The crystal structures were analyzed to find the active site of the kinase domain where the inhibitor binds. For all the proteins 20X20X20 Å size grid was generated at

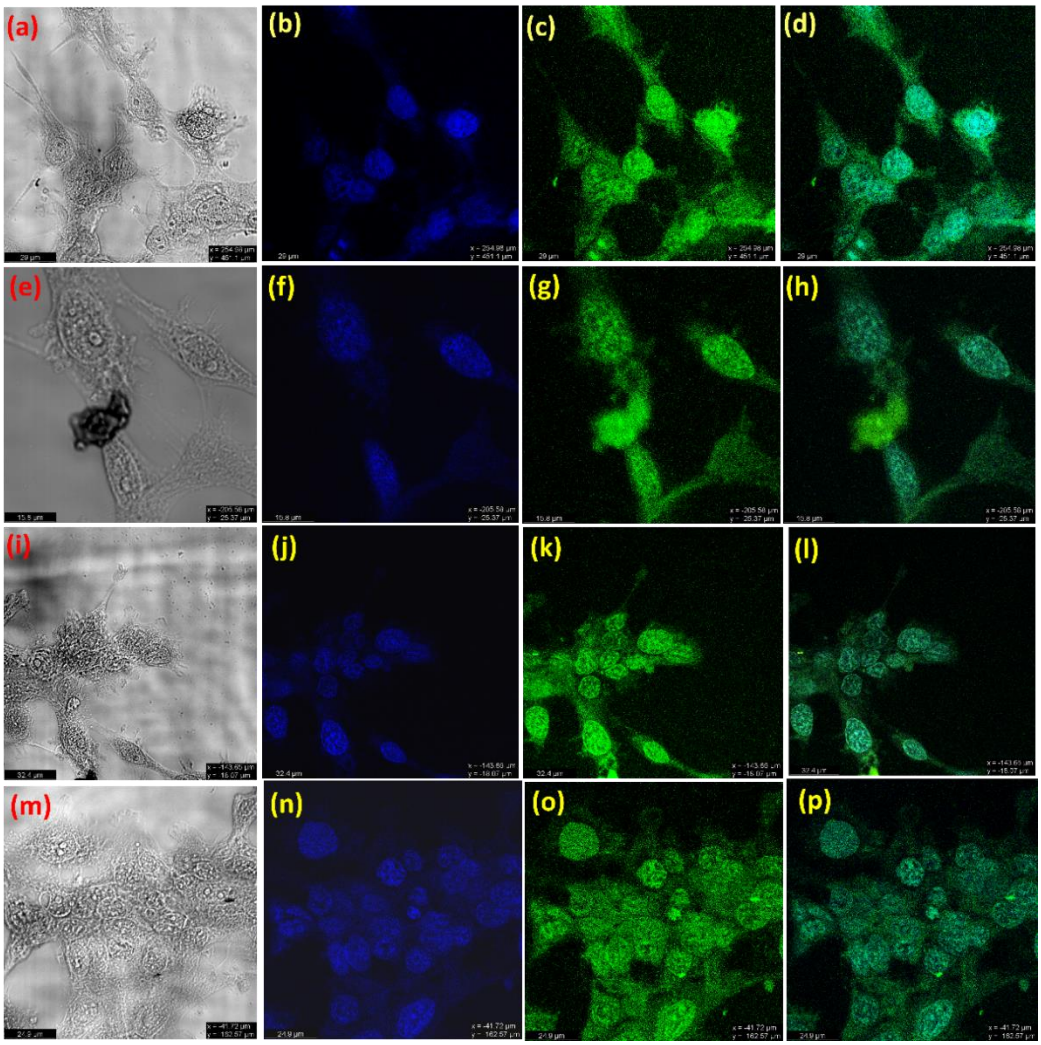

Figure 3.35 Distorting FaDu cells in bright-field (a, e, i, m); FaDu cells stained with DAPI (b, f, j, n); FaDu cells stained with **SB6** (c, g, k, o) and the respective colocalization studies taking DAPI stained and **SB6** stained images (d, h, I, p)

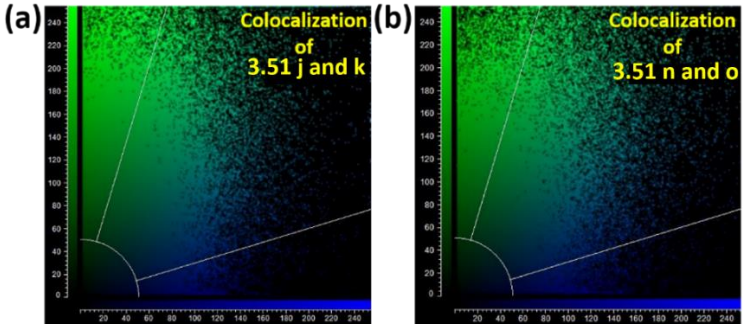

Figure 3.36 Representative 'Scat' profile images for colocalization quantification

the ligand binding site of the protein before docking, and the ligand was docked to the active site of all the proteins. Post-docking ligand protein interactions were analyzed.

For the indole compound docked to the EGFR and HER2 proteins, the interacting amino acid residues have been mentioned in Table 3.8. A comparison has been made with the interacting residues of the co-crystal ligands, suggesting the indole compound's affinity towards HER2 protein compared to EGFR protein (Figures 3.38-3.41, Table 3.8). However, a further detailed investigation is highly needed for our future work.

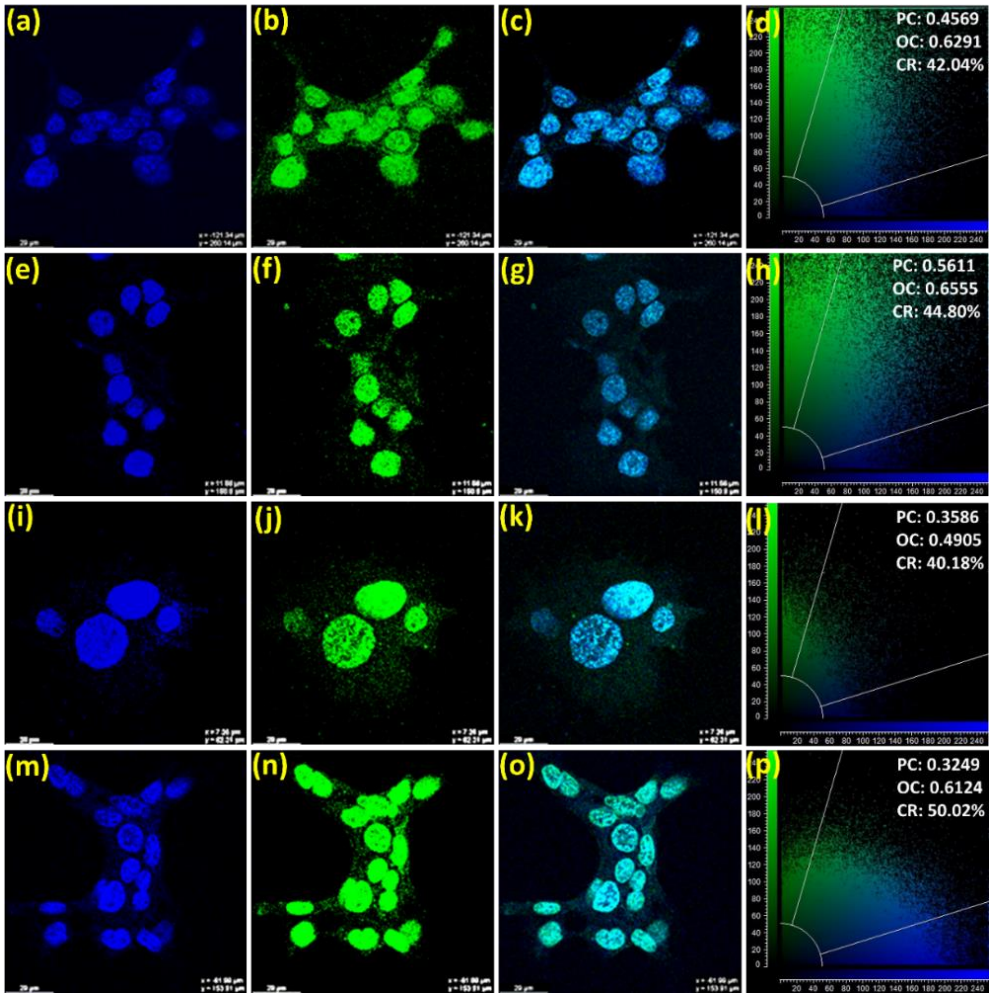

Figure 3.37 Wash-free bioimaging of FaDu with **SB3** (10 μM): a,e,i,m are for staining with DAPI, (b,f,j,n) are for staining with **SB3**, merged images (of DAPI and **SB3** stained) comparison between (c) a and b (g) e and f (k) i and j (o) m and n; colocalization analysis between (d) a and b (h) e and f (l) i and j (p) m and n. 'PC' stands for Pearson's Correlation, 'OC' for Overlap Coefficient, and 'CR' for Colocalization Rate. During confocal imaging, λ_{ex} (DAPI)= 405 nm, λ_{em} (DAPI)= 458-488 nm; λ_{ex} (**SB3**) = 458 nm, λ_{em} (**SB3**) = 514-561 nm (images can be captured in both the channels of 514 nm and 561 nm laser sources)

Table 3.7 Results of colocalization quantification

Image No	Colocalization between images	PC	OC	CR (%)	MIC (DAPI)	MIC (SB6/SB7)
3.49 d	3.49 b and 3.49 c	0.4569	0.6291	42.04	57.92	70.01
3.50 h	3.50 f and 3.50 g	0.3311	0.4807	44.20	57.57	88.17
3.51 d	3.51 b and 3.51 c	0.5850	0.6405	42.66	60.41	112.29
3.51 h	3.51 f and 3.51 g	0.5611	0.6555	44.80	67.30	97.77

Table 3.8 Interactions and scores obtained from the docking study

PDB ID	Crystal ligand interacting residues and Glide docking score	Indole compound interacting residues and Glide docking score
3PP0	Lys753, Leu796, Met801, Asp863, Phe864 -14.784	Arg811 -5.931
7JXH	Ser783, Cys805, Asp808 -10.752	Lys736 -6.058
3RCD	Lys753, Leu796, Met801, Asp863 -11.277	Phe1004 -5.597
5X2C	Met793 -9.854	NA -6.502
4I22	Leu788, Met793 -10.065	NA -7.519

3.3.7 Summary

This work introduces a new class of *N*-alkyl indole-linked anthracenyl twisted π-conjugates as efficient AIE and DSE-active SSEOFs. All these emitters were tested for anticancer studies, especially with aggressive and robust FaDu and TNBC 4T1 cell lines. Among all these molecules, 2,3,4-TMB substituted probe **SB4** has appeared as a potential and convincing AIE-active DSE-gen that not only inhibited both FaDu and 4T1

(not MCF-7 and HEK-293) at 24 h but also could detect cell death by its diminished fluorescence signal. The normal and cancer cells could be easily distinguished by

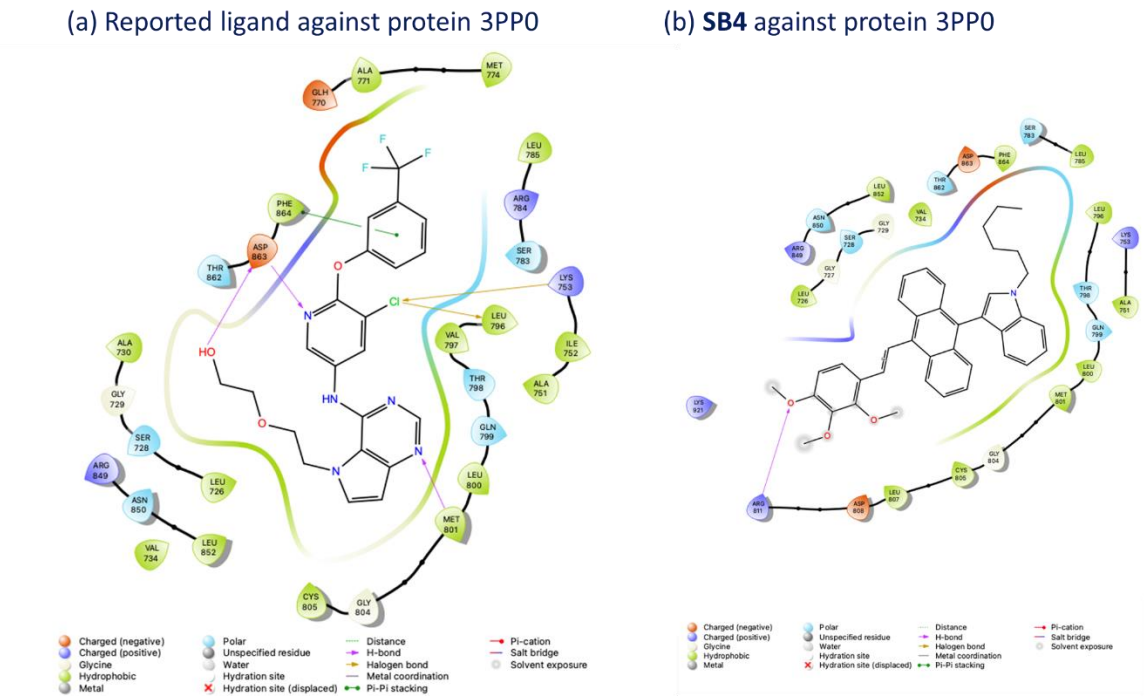

Figure 3.38 2D view of interactions of (a) reported ligand against protein 3PP0, (b) **SB4** against protein 3PP0

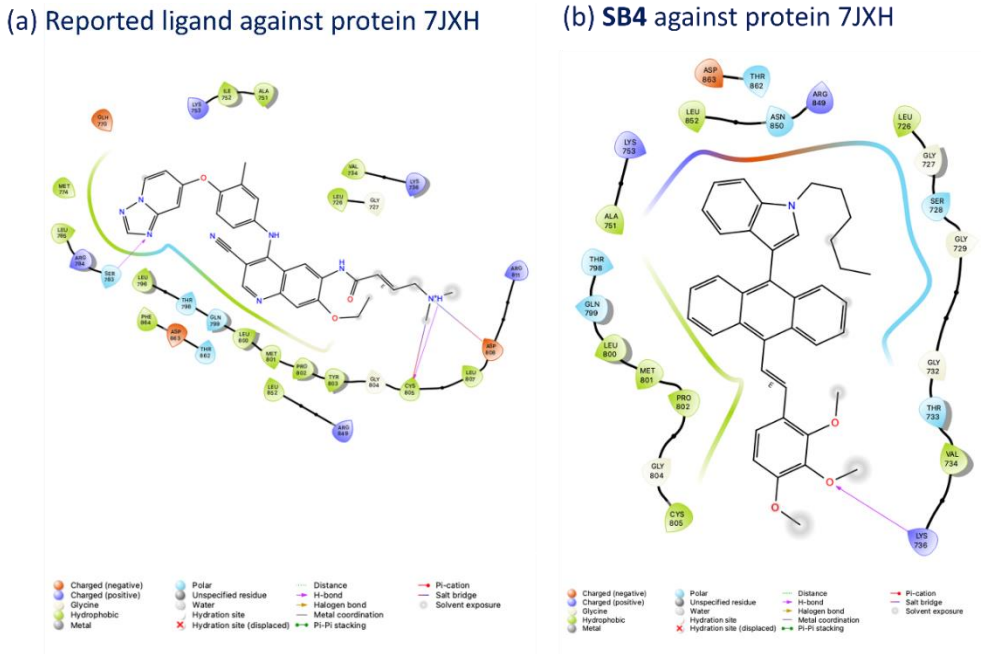

Figure 3.39 2D view of interactions of (a) reported ligand against protein 7JXH, (b) **SB4** against protein 7JXH

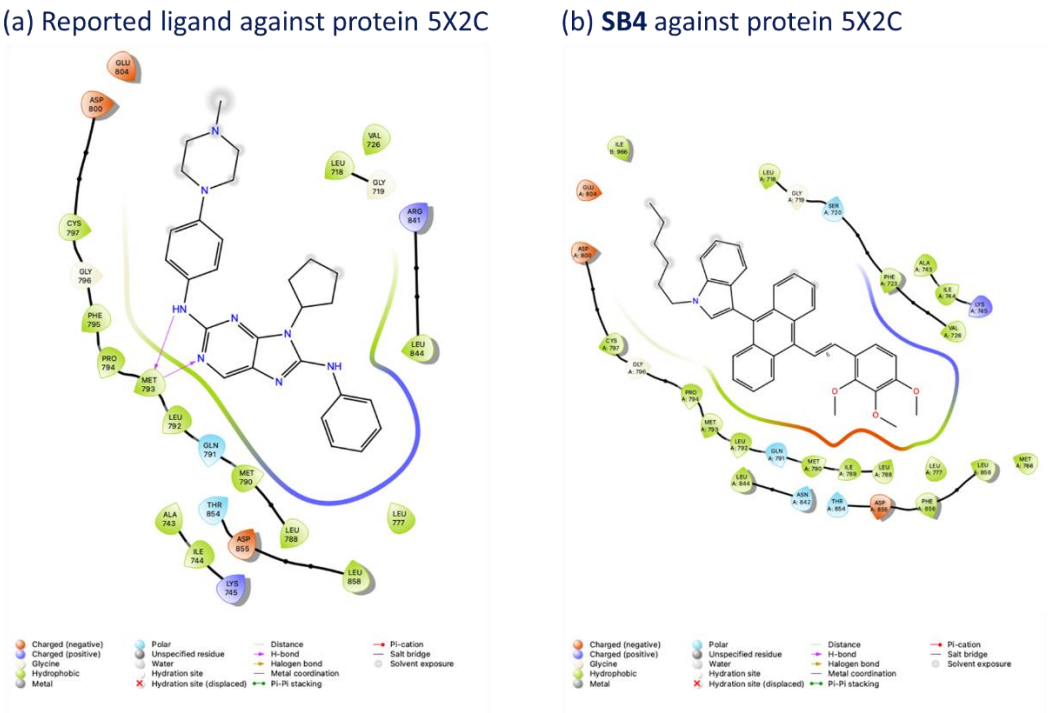

Figure 3.40 2D view of interactions of (a) reported ligand against protein 5X2C, (b) **SB4** against protein 5X2C

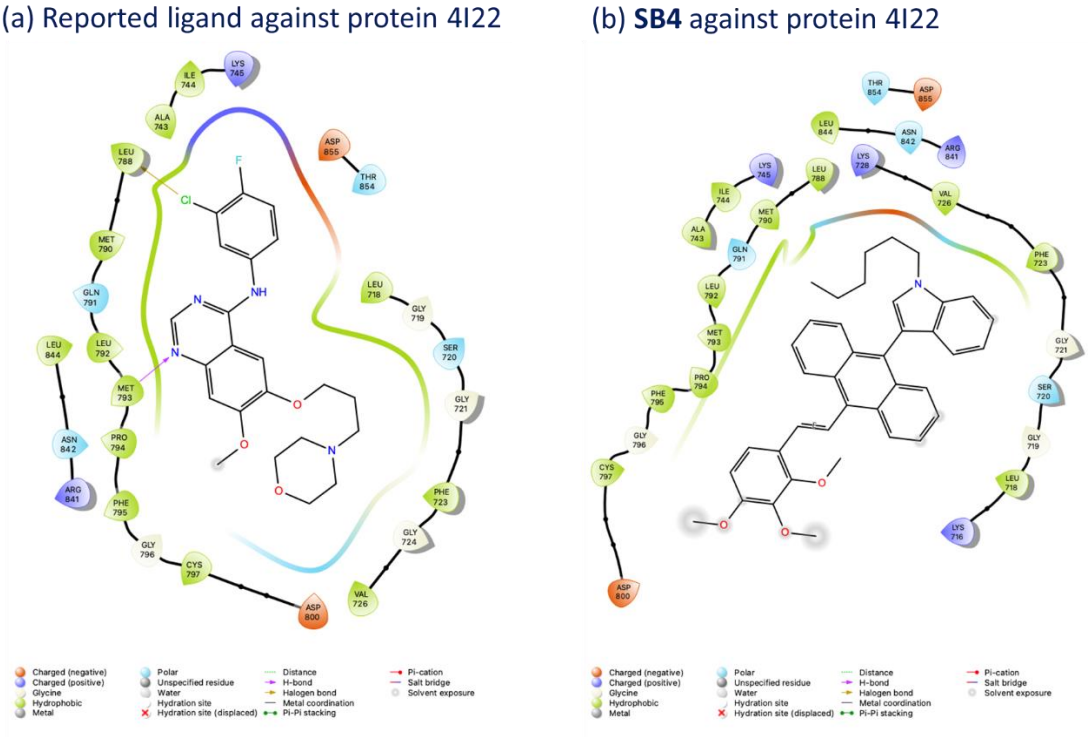

Figure 3.41 2D view of interactions of (a) reported ligand against protein 4I22, (b) **SB4** against protein 4I22

comparing the intensity of intact fluorescence signals for the normal cell HEK-293. The noncytotoxic nature, high ROS, and less haemolysis make **SB4** a commendable biocompatible drug with imaging capability, even in comparison to doxorubicin. The intrinsic anticancer features of indole and anthracene play a crucial role in exhibiting anticancer features with their affinity towards HER2 protein, as suggested by the primary docking studies. The hydrophobicity of the lead probe may have assisted in penetrating the cell membrane (validated by FACS) to have a closer interaction and capture an image of the cells with its DSE properties. Hence, a new class of easily accessible indole-anthracenyl π-conjugate offers a promising solution to kill the cancer cells selectively and detect the damaged cells through its diminished fluorescence signals. This research would ensure a potential prospect of such newly designed AIE-active, DSE-genic SSEOFs in challenging cancer research.

Furthermore, **SB7** was revealed as a potential dye in wash-free cancer cell imaging in near-red regions. **SB6** was also identified as an anticancer agent that assists in green emitting bioimaging of FaDu cells. Additionally, the distortion of FaDu cells was successfully monitored using **SB6** dye. All of these were possible with the designed D-π-D′ systems, which are rarely reported for wash-free bioimaging. However, **SB3** was found to be inactive to be considered as an anticancer agent but was proven to be useful for wash-free cancer cell imaging, and notably, unlike **SB6** and **SB7**, **SB3** is a D-π-A system. Of note, finding a detailed mechanistic path to decipher the selectivity of 4T1 and modification of the probe to improve the sensitivity and specificity are currently undergoing in our laboratory.

3.3.8 Experimental sections

The general procedures are mentioned earlier in '*Materials, General Conditions and Measurements*'.

3.3.9 Detailed synthetic procedures and characterizations

The reaction procedures are discussed herein. To be noted, the general reaction procedure for **SB2**-**SB7** was as same as for **SB1**. Again, the reaction procedure of 5-(2-formyl phenyl)picolinonitrile was as same as for 2-(pyridin-3-yl)benzaldehyde.

3.3.9.1 *Synthesis of diethyl ((10-(1-hexyl-1H-indol-3-yl)anthracen-9-yl)methyl)phosphonate*

Diethyl (anthracen-9-yl(hydroxy)methyl)phosphonate (1.45 mmol, 1 equiv, 0.5 gm) was taken into one 100 mL round bottom flask and subjected to a vacuum drying for 10 mins. Next, under the N_2 environment, dichloroethane (15 mL) was poured into it and stirred for 5 mins in an ice bath. Later methanesulphonic acid (MSA) (5.05 mmol, 3.48 equiv, 0.33 mL) was added to it under the N_2-environment and allowed to stir for another 15 mins. Next, the ice bath was taken away, the reaction mixture was brought back to room temperature, and the solution turned into marron. Now the freshly prepared alkylated indole (2.59 mmol, 1.79 equiv, 0.52 gm) was added into it slowly under the N_2-environment and allowed to stir for 15 mins until it finally changed from marron to green to blue coloration. The alkylation of indole was done following a reported procedure.[55] Next was refluxed for 3 h at 90°C and then cooled to room temperature. The completion of the reaction can be monitored by observing the formation of a cyan color fluorescent product spot at R_f = 0.17 while eluting the TLC (Thin Layer Chromatography) plate into Hexane/EtOAc medium (40% EtOAc into Hexane (v/v). The reaction mixture was subjected to work up with 30 mL of EtOAc and brine water mixture with EtOAc:H_2O (1:2) ratio. The maroon color organic layer was separated and made into a slurry with silica gel (60-120 mesh) to perform column chromatography (30% EtOAc into Hexane (v/v), which yielded (50%, 0.38 gm) of the gummy cyan fluorescent compound; **IR** (KBr, cm^{-1}): 3057, 2930, 2854, 2355, 1586, 1462, 1390, 1254, 1161, 1057, 1021; **m.p.**: 79-81°C; **^{1}H NMR** (400 MHz, $CDCl_3$, 25°C, δ): 8.39 (d, *J* = 8.92 Hz, 2H), 7.92 (d, *J* = 8.76 Hz, 2H), 7.54-7.45 (m, 3H), 7.29-7.21 (m, 4H), 7.05-6.98 (m, 2H), 4.33(d, *J*= 24.84 Hz, P-CH2, 2H), 4.28-4.25 (m, 2H), 4.01-3.85 (m, 4H), 2.00-1.93 (m, 2H), 1.42-1.26 (m, 6H), 1.13 (t, *J* = 7.04 Hz, 6H), 0.90 (t, *J* = 6.48 Hz, 3H); **^{13}C NMR** (100 MHz, $CDCl_3$, 25°C, δ): 136.1, 131.7, 130.8, 130.5, 129.8, 128.9, 128.3, 125.7, 125.1, 124.7, 123.3, 121.8, 120.5, 119.5, 111.9, 109.7, 62.4, 46.6, 31.5, 27.9 (d, *J*= 121.64 Hz, P-CH2), 22.6, 16.4, 16.3, 14.0; **^{31}P NMR** (162 MHz, $CDCl_3$, 25°C, δ): 26.08; **HRMS** (ESI) m/z: calcd. for $C_{33}H_{38}NO_3P$ 527.2589, found: 528.2445 $[M+H]^+$.

3.3.9.2 Synthesis of 2-(pyridin-3-yl)benzaldehyde

2-Bromobenzaldehyde (1.08 mmol, 1 equiv, 0.2 gm) and pyridin-3-ylboronic acid (2.16 mmol, 2 equiv, 0.27 gm) were taken in a two-neck round bottom flask and subjected to a vacuum drying for 5 mins. Later under the N_2 environment 15 ml of dioxane/water (9:1, (v/v) was poured into it and stirred for 5 mins again. Next $Pd(PPh_3)_4$ (0.09 mmol, 0.08 equiv, 0.09 gm), K_2CO_3 (1.63 mmol, 1.5 equiv, 0.22 gm) and tetrabutylammonium bromide (0.09 mmol, 0.08 equiv, 0.03 gm) were added into the reaction solution, stirred for 15 mins and N_2-environment was maintained. Then the reaction mixture was allowed to be refluxed at 90 ^oC for 18 h. The occurrence of the reaction was monitored by eluting the TLC into a Hexane/EtOAc [20% EtOAc into Hexane (v/v)] medium to observe an intense product spot formed at R_f = 0.32. The reaction mixture was worked up with 30 mL of EtOAc and brine water mixture with EtOAc:H_2O (1:2) ratio. The organic layer was separated, passed through the Na_2SO_4 layer and made into a slurry with silica gel (60-120 mesh) to perform column chromatography (12% EtOAc into hexane (v/v), which yielded 81% (0.16 gm) of the solid whitish compound. **IR** (KBr, cm^{-1}): 3055, 2898, 2768, 1677, 1599, 1469, 1252, 1191, 836; **M.p.**: 60-62^oC; NMR spectroscopy: **^{1}H NMR** (400 MHz, $CDCl_3$, 25^oC, δ): 9.98 (s, 1H), 8.72-8.67 (m, 2H), 8.09 (t, J = 8.33 Hz, 1H), 7.75-7.56 (m, 3H), 7.46-7.29 (m, 2H); **^{13}C NMR** (100 MHz, $CDCl_3$, 25^oC, δ): .191.3, 150.1, 149.3, 141.8, 137.2, 133.9, 133.8, 133.7, 131.0, 128.7, 128.5, 123.2; **LCMS** (ESI) m/z: calcd. for $C_{12}H_9NO$ 184.0684, found: 184.1500 $[M]^+$.

3.3.9.3 Synthesis of 5-(2-formyl phenyl)picolinonitrile

Required chemicals and stoichiometry: 5-Bromopicolinonitrile (1.09 mmol, 1 equiv. 0.2 gm), (2-formyl phenyl)boronic acid (2.19 mmol, 2 equiv, 0.33 gm), dioxane/water [9:1, (v/v), 15 mL], $Pd(PPh_3)_4$ (0.09 mmol, 0.08 equiv, 0.1 gm), K_2CO_3 (1.64 mmol, 1.5 equiv, 0.23 gm). and Tetrabutylammonium bromide (0.09 mmol, 0.08 equiv, 0.03 gm); R_f = 0.36 (20% EtOAc into Hexane (v/v) medium); column chromatography [12% EtOAc into hexane (*v/v*)]; yield 71 % (0.16 gm, solid whitish compound); **IR** (KBr, cm^{-1}): 3040, 2925, 2782, 2232, 1688, 1595, 1462, 1260, 1197, 992; **M.p.**: 120-122^oC; **^{1}H NMR** (400 MHz, $CDCl_3$, 25 ^oC, δ): 9.98 (s, 1H), 8.75-8.74 (m, 1H), 8.08-8.06 (d, J = 7.68 Hz, 1H), 7.87-7.65 (m, 4H), 7.42 (d, J = 7.58 Hz); **^{13}C NMR** (100 MHz, $CDCl_3$, 25^oC, δ): .190.6, 151.3,

139.6, 137.8, 134.1, 133.9, 133.7, 133.2, 131.1, 130.7, 129.8, 127.8, 117.0; **LCMS** (ESI) m/z: calcd. for $C_{13}H_8N_2O$ 208.0637, found: 209.2000.$[M+H]^+$.

3.3.9.4 Synthesis of (*E*)-1-hexyl-3-(10-(2-(pyridin-3-yl)styryl)anthracen-9-yl)-1H-indole (SB1)

Diethyl ((10-(1-hexyl-1H-indol-3-yl)anthracen-9-yl)methyl)phosphonate (0.37 mmol, 1 equiv, 0.2 gm) and 2-(pyridin-3-yl)benzaldehyde (0.82 mmol, 2.2 equiv, 0.15 gm) and K^tOBu base (0.93 mmol, 2.5 equiv, 0.1 gm) were taken in a two-neck round bottom flask and subjected to a vacuum drying for 5 mins. Later N_2 was purged throughout the flask and sealed with silicon septum. On one end N_2-containing balloon was placed and from the other neck dry THF (15 mL) was injected into the flask and set to stir for 4h. The progress of the reaction was monitored by eluting the TLC into Hexane/EtOAc (20% EtOAc into hexane (v/v) medium to observe an intense product spot formed at R_f = 0.35. The reaction mixture was worked up with 30 mL of EtOAc and brine water mixture with EtOAc: H_2O (1:2) ratio. The organic layer was separated, passed through the Na_2SO_4 layer and made into a slurry with silica gel (60-120 mesh) to perform column chromatography (12% EtOAc into hexane (v/v), which yielded 79 % (0.16 gm) of the maroon sticky solid compound in room light but green fluorescent under UV-365 nm lamp; **IR** (KBr, cm^{-1}): 3452, 3178, 2966, 2852, 1728, 1597, 1453, 1429, 1380, 1328, 1190, 1119, 1062, 1015; **^{1}H NMR** (400 MHz, $CDCl_3$, 25°C, δ): 8.73 (s, 1H), 8.53-8.51 (m, 1H), 8.35 (d, *J* = 8.76 Hz, 2H), 8.15-8.13 (d, *J* = 7.56 Hz, 1H), 7.99-7.89 (m, 3H), 7.79-7.76 (m, 1H), 7.61-7.39 (m, 6H), 7.30-7.25 (m, 5H), 7.11-6.89 (m, 3H), 4.29 (t, *J* = 7.04 Hz, 2H), 2.02-1.95 (m, 2H), 1.39-1.28 (m, 6H), 0.89 (t, *J* = 7.02 Hz, 3H); **^{13}C NMR** (100 MHz, $CDCl_3$, 25°C, δ): 150.2, 148.3, 137.4, 137.1, 136.5, 136.1, 136.0, 135.4, 132.3, 131.5, 130.5, 130.3, 129.7, 129.5, 128.8, 128.6, 128.1, 127.9, 127.7, 126.5, 125.8, 125.2, 124.8, 123.0, 121.8, 120.6, 119.5, 111.8, 109.6, 46.6, 31.4, 29.7, 26.8, 22.6, 14.0; **HRMS** (ESI) m/z: calcd. for $C_{41}H_{36}N_2$ 556.2878, found: 557.2743 $[M+H]^+$.

3.3.9.5 Synthesis of (*E*)-5-(2-(2-(10-(1-hexyl-1H-indol-3-yl)anthracen-9-yl)vinyl)phenyl)picolinonitrile (SB2)

Required chemicals and stoichiometry: Diethyl ((10-(1-hexyl-1H-indol-3-yl)anthracen-9-yl)methyl)phosphonate (0.37 mmol, 1 equiv, 0.2 gm), 5-(2-

formylphenyl)picolinonitrile (0.82 mmol, 2.2 equiv, 0.17 gm), K^{t}OBu base (0.93 mmol, 2.5 equiv, 0.1 gm), dry THF (15 mL); R_f = 0.27 [20% EtOAc into Hexane (*v*/*v*)]; yield 83 % (0.18 gm, solid yellowish in room light, green fluorescent); **IR** (KBr, cm^{-1}): 3436, 3123, 2924, 2848, 1690, 1569, 1464, 1419, 1364, 1021; **mp**: 168-170^{o}C; **^{1}H NMR** (400 MHz, $CDCl_3$, 25^{o}C, δ): 8.67 (s, 1H), 8.33 (d, *J* = 8.76 Hz), 8.21-8.15 (m, 2H), 8.0-7.97 (m, 3H), 7.82-7.60 (m, 2H), 7.53-7.40 (m, 5H), 7.30-7.27 (m, 2H), 7.24 (s, 1H), 7.10-6.86 (m, 3H), 5.51 (s, 1H), 4.30 (t, *J* = 7.04 Hz, 2H), 1.98 (quint, *J* = 7.36 Hz, 2H), 1.45-1.26 (m, 6H), 0.89 (t, *J* = 7.1 Hz, 3H); **^{13}C NMR** (100 MHz, $CDCl_3$, 25^{o}C, δ): 148.9, 148.1, 139.5, 138.3, 136.5, 136.2, 136.1, 135.1, 131.9, 131.5, 130.5, 130.4, 129.7, 129.6, 129.5, 129.3, 129.1, 128.9, 128.3, 128.2, 127.9, 126.7, 125.7, 125.3, 124.8, 121.9, 121.8, 120.6, 119.5, 109.6, 46.6, 31.4, 30.2, 26.8, 22.6, 13.9; **HRMS** (ESI) m/z: calcd. for $C_{42}H_{35}N_3$ 581.2831, found: 582.2720 $[M+H]^+$.

3.3.9.6 Synthesis of (*E*)-1-hexyl-3-(10-(4-(pyridin-2-yl)styryl)anthracen-9-yl)-1H-indole (SB3)

Required chemicals and stoichiometry: Diethyl ((10-(1-hexyl-1H-indol-3-yl)anthracen-9-yl)methyl)phosphonate (0.37 mmol, 1 equiv, 0.2 gm), 4-(pyridin-2-yl)benzaldehyde (0.82 mmol, 2.2 equiv, 0.15 gm), KO^{t}Bu base (0.93 mmol, 2.5 equiv, 0.1 gm), dry THF (15 mL); R_f = 0.29 [12% EtOAc into Hexane (v/v)]; yield 71 % (0.15 gm, solid yellowish in room light, bright yellowish-green fluorescent); **IR** (KBr, cm^{-1}): 3445, 3048, 2944, 2849, 1580, 1467, 1431, 1345, 1322, 1233, 1147, 1017; **m.p.**: 154-156^{o}C; **^{1}H NMR** (400 MHz, $CDCl_3$, 25^{o}C, δ): 8.74 (s, 1H), 8.46 (d, *J* = 8.76 Hz, 2H), 8.13-7.93 (m, 5H), 7.82-7.75 (m, 4H), 7.53-7.43 (m, 3H), 7.32-7.23 (m, 5H), 7.14-7.01 (m, 3H), 4.30 (t, *J* = 7.04 Hz, 2H), 1.99 (quint, *J* = 7.32 Hz, 2H), 1.46-1.23 (m, 6H), 0.90 (t, *J* = 7.04 Hz, 3H); **^{13}C NMR** (100 MHz, $CDCl_3$, 25^{o}C, δ):156.9, 149.8, 138.8, 138.1, 136.9, 136.1, 132.4, 131.6, 130.2, 129.8, 129.7, 128.9, 127.9, 127.3, 127.2, 127.0, 126.2, 126.1, 125.3, 124.9, 122.2, 121.8, 120.6, 120.5, 119.5, 111.9, 109.6, 46.6, 31.5, 30.3, 26.8, 22.6, 14.0; **HRMS** (ESI) m/z: calcd. for $C_{41}H_{36}N_2$ 556.2878, found: 557.2674 $[M+H]^+$.

3.3.9.7 Synthesis of (*E*)-1-hexyl-3-(10-(2,3,4-trimethoxystyryl)anthracen-9-yl)-1H-indole (SB4)

Required chemicals and stoichiometry: Diethyl ((10-(1-hexyl-1H-indol-3-yl)anthracen-9-yl)methyl)phosphonate (0.37 mmol, 1 equiv, 0.2 gm), 2,3,4-

trimethoxybenzaldehyde (0.82 mmol, 2.2 equiv, 0.16 gm), K^{t}OBu base (0.93 mmol, 2.5 equiv, 0.1 gm), dry THF (15 mL); R_f = 0.33 [12% EtOAc into Hexane (v/v)]; yield 75% (0.16 gm, solid yellowish in room light, green fluorescent); **IR** (KBr, cm^{-1}): 3447, 3401, 2959, 2934, 2854, 1596, 1465, 1378, 1324, 1287, 1091; **mp**: 125-127^{o}C; **^{1}H NMR** (400 MHz, $CDCl_3$, 25^{o}C, δ): 8.47 (d, *J* = 8.72 Hz, 2H), 7.94-7.90 (m, 3H), 7.62-7.42 (m, 4H), 7.31-7.00 (m, 7H), 6.84 (d, *J* = 8.76 Hz, 1H), 4.31 (t, *J* = 7.06 Hz, 2H), 3.92 (s, 6H), 3.88 (s, 3H), 1.99 (quint, *J* = 7.36 Hz, 2H), 1.45-1.28 (m, 6H), 0.90 (t, *J* = 7.34 Hz, 3H); **^{13}C NMR** (100 MHz, $CDCl_3$, 25^{o}C, δ): 153.6, 151.9, 142.7, 136.1, 133.3, 131.9, 131.6, 129.8, 129.7, 128.9, 127.8, 126.3, 125.0, 124.8, 124.7, 121.7, 121.1, 120.6, 119.4, 112.0, 109.6, 107.9, 61.4, 61.0, 56.2, 46.6, 31.5, 29.7, 26.8, 22.6, 14.0; **HRMS** (ESI) m/z: calcd. for $C_{39}H_{39}NO_3$ 569.2930, found: 570.2792 $[M+H]^+$.

3.3.9.8 Synthesis of (*E*)-1-hexyl-3-(10-(3,4,5-trimethoxystyryl)anthracen-9-yl)-1H-indole (SB5)

Required chemicals and stoichiometry: Diethyl ((10-(1-hexyl-1H-indol-3-yl)anthracen-9-yl)methyl)phosphonate (0.37 mmol, 1 equiv, 0.2 gm), 3,4,5-trimethoxybenzaldehyde (0.82 mmol, 2.2 equiv, 0.16 gm), K^{t}OBu base (0.93 mmol, 2.5 equiv, 0.1 gm), dry THF (15 mL); R_f = 0.24 [12% EtOAc into Hexane (*v/v*)]; yield 77% (0.17 gm, solid yellowis in room light, green fluorescent); **IR** (KBr, cm^{-1}): 3417, 3064, 2955, 2930, 2359, 1580, 1504, 1461, 1417, 1319, 1231, 1128, 1013; **mp**: 108-110^{o}C; **^{1}H NMR** (400 MHz, $CDCl_3$, 25^{o}C, δ): 8.43 (d, *J* = 8.76 Hz, 2H), 7.9-7.89 (m, 3H), 7.54-7.43 (m, 3H), 7.32-7.28 (m, 4H), 7.13-6.91 (m, 5H), 4.32 (t, *J* = 7.04 Hz, 2H), 3.99 (s, 6H), 3.94 (s, 3H), 2.00 (quint, *J* = 7.38 Hz, 2H), 1.45-1.24 (m, 6H), 0.91 (t, *J* = 7.1 Hz, 3H); **^{13}C NMR** (100 MHz, $CDCl_3$, 25^{o}C, δ): 153.6, 138.3, 137.3, 136.1, 134.3, 133.2, 132.3, 131.6, 130.1, 129.8, 129.7, 128.9, 127.9, 126.1, 125.2, 124.8, 121.8, 120.6, 119.5, 111.9, 109.6, 103.7, 61.1, 56.3, 46.6, 31.5, 30.3, 26.8, 22.6, 14.0; **HRMS** (ESI) m/z: calcd. for $C_{39}H_{39}NO_3$ 569.2930, found: 570.2744 $[M+H]^+$.

3.3.9.9 Synthesis of ((*E*)-4-(2-(10-(1-hexyl-1H-indol-3-yl)anthracen-9-yl)vinyl)-N,N-diphenylaniline (SB6)

Required chemicals and stoichiometry: Diethyl ((10-(1-hexyl-1H-indol-3-yl)anthracen-9-yl)methyl)phosphonate (0.37 mmol, 1 equiv, 0.2 gm), 4-(diphenylamino)benzaldehyde (0.82 mmol, 2.2 equiv, 0.22 gm), K^{t}OBu base (0.93 mmol,

2.5 equiv, 0.1 gm), dry THF (15 mL); R_f = 0.38.[8% EtOAc into Hexane (v/v)]; yield 84% (0.20 gm, solid greenish in room light, bright green fluorescent); **IR** (KBr, cm^{-1}): 3029, 2928, 2860, 2351, 2323, 1588, 1505, 1494, 1326, 1280, 1173; **mp**: 190-192°C; **^{1}H NMR** (400 MHz, $CDCl_3$, 25°C, δ): 8.46 (d, *J* = 8.72 Hz, 2H), 7.93-7.87 (m, 3H), 7.60-7.42 (m, 5H), 7.32-7.28 (m, 8H), 7.19-7.16 (m, 6H), 7.13-6.93 (m, 5H), 4.31 (t, *J* = 7.04 Hz, 2H), 1.99 (quint, *J* = 7.34 Hz, 2H), 1.49-1.26 (m, 6H), 0.90 (t, *J* = 7.12 Hz, 3H); **^{13}C NMR** (100 MHz, $CDCl_3$, 25°C, δ): 147.7, 147.6, 139.9, 136.8, 136.1, 132.8, 131.7, 131.6, 129.8, 129.7, 129.6, 129.3, 128.9, 127.9, 127.5, 126.2, 125.0, 124.8, 124.5, 123.8, 123.6, 123.1, 121.7, 120.6, 119.5, 113.1, 113.0, 112.9, 111.9, 109.6, 46.6, 31.5, 30.3, 26.8, 22.6, 14.0; **HRMS** (ESI) m/z: calcd for $C_{48}H_{42}N_2$ 646.3348, found: 647.3156 $[M+H]^+$.

3.3.9.10 Synthesis of (*E*)-3-(2-(10-(1-hexyl-1H-indol-3-yl)anthracen-9-yl)vinyl)-10-pentyl-10H-phenothiazine (SB7)

Required chemicals and stoichiometry: Diethyl ((10-(1-hexyl-1H-indol-3-yl)anthracen-9-yl)methyl)phosphonate (0.37 mmol, 1 equiv, 0.2 gm), 10-pentyl-10H-phenothiazine-3-carbaldehyde (0.82 mmol, 2.2 equiv, 0.25 gm), K^{t}OBu base (0.93 mmol, 2.5 equiv, 0.1 gm), dry THF (15 mL); R_f = 0.37 [8% EtOAc into Hexane (v/v)]; yield 63% (0.19 gm, orange gummy compound becomes solid after 2-3 days, orange-red fluorescent); **IR** (KBr, cm^{-1}): 3441, 3061, 2953, 2927, 2856, 1573, 1463, 1334, 1247; **mp**: 119-121°C; **^{1}H NMR** (400 MHz, $CDCl_3$, 25°C, δ): 8.41 (d, *J* = 8.76 Hz, 2H), 7.93-7.83 (m, 3H), 7.64-7.37 (m, 5H), 7.31-7.23 (m, 4H), 7.17-7.00 (m, 4H), 6.96-6.85 (m, 4H), 4.29 (t, *J* = 7 Hz, 2H), 3.87 (quint, *J* = 6.28 Hz, 2H), 1.99 (quint, *J* = 7.12 Hz, 2H), 1.86 (quint, *J* = 7.14 Hz, 2H), 1.45-1.26 (m, 10H), 0.94-0.86 (m, 6H); **^{13}C NMR** (100 MHz, $CDCl_3$, 25°C, δ): 145.1, 144.9, 136.1, 132.7, 132.0, 131.6, 129.9, 129.8, 129.7, 128.9, 127.9, 127.5, 127.3, 126.2, 125.9, 125.4, 125.1, 124.8, 124.4, 123.6, 122.5, 121.8, 120.6, 119.5, 115.9, 115.5, 115.4, 114.8, 111.9, 109.6, 47.9, 47.6, 46.6, 31.5, 30.3, 29.2, 26.8, 26.7, 22.7, 22.5, 14.1; **HRMS** (ESI) m/z: calcd for $C_{47}H_{46}N_2S$ 670.3382, found: 671.3252 $[M+H]^+$.

3.3.10 References

1 K. Li, T. B. Ren, S. Huan, L. Yuan and X. B. Zhang, ***J. Am. Chem. Soc.***, 2021, **143**, 21143-21160.

2 (a) J. Luo, Z. Xie, J.W.Y. Lam, L. Cheng, H. Chen, C. Qiu, H. S. Kwok, X. Zhan, Y. Liu, D. Zhu and B. Z. Tang, ***Chem. Commun.***, 2001, **18**, 1740-1741. (b) J. Mei, N. L. C. Leung, R. T. K. Kwok, J. W. Y. Lam and B. Z. Tang, ***Chem. Rev.***, 2015, **115**, 11718-11940.

3 (a) Q. Peng and Z. Shuai, ***Aggregate***, 2021, **2(5)**, e91. (b) Y. Hong, J. W. Y. Lam and B. Z. Tang, ***Chem. Soc. Rev.***, 2011, **40**, 5361-5388.
4 (a) J. L. B. Vazquez, Y. A. A. Sanchez, L. A. R. Cortes and B. R. Molina, ***Chem. Mater.***, 2021, **33**, 7160-7184. (b) F. Yu, H. Zhao, Y. Li, G. Xia and H. Wang, ***Mater. Chem. Front.***, 2022, **6**, 155. (c) S. K. Behera, S. Y. Park and J. Gierschner, ***Angew. Chem. Int. Ed.***, 2021, **60**, 22624-22638. (d) C. Han, S. B. Sun, X. Ji and J. W. Wang, ***Spectrochim. Acta-A: Mol. Biomol. Spectrosc.***, 2023, **285**, 121884. (e) H. V. Humeniuk, A. Rosspeintner, G. Licari, V. Kilin, L. Bonacina, E. Vauthey, N. Sakai and S. Matile, ***Angew. Chem. Int. Ed.***, 2018, **57**, 10559-10563. (f) J. Lao, J. Li and H. Zou, ***Chem. Eur. J***, 2022, e202202179. (g) M. Tan, Y. Li, W. Guo, Y. Chen, M. Wang, Y. Wang, B. Chi, H. Wang, G. Xia and H. Wang, ***Dyes Pigm.***, 2022, **201**, 110243.
5 X. Ren, S. Zhang, L. Liu, B. Xu and W. Tian, ***Nanotechnology***, 2021, **32**, 502008.
6 (a) W. Yu, H. Zhang, P. A. Yin, F. Zhou, Z. Wang, W. Wu, Q. Peng, H. Jiang and B. Z. Tang, ***iScience***, 2020, **23**, 101587. (b) Y. Zhang, Y. Qu, J. Wu, Y. Rui, Y. Gao and Y. Wu, ***Dyes Pigm.***, 2020, **179**, 108431.
7 (a) F. Yin, B. Gu, J. Li, N. Panwar, Y. Liu, Z. Li, K. T. Yong and B. Z. Tang, ***Biomater. Sci.***, 2019, **7**, 3855. (b) W. Dai, P. Liu, S. Guo, Z. Liu, M. Wang, J. Shi, B. Tong, T. Liu, Z. Cai and Y. Dong, ***ACS Appl. Bio Mater.***, 2019, **2**, 3686-3692. (c) Z. Huang, F. Tang, F. He, L. Kong, J. Huang, J. Yang and A. Ding, ***Org. Chem. Front.***, 2022, **9**, 5118. (d) H. Lv, L. Wei, S. Guo, X. Zhang, F. Chen, X. Qin, C. Wei, B. Jiang and Y. Gong, ***Front. Chem.***, 2022, **10**, 807088. (e) Y. Liu, L. Teng, C. Xu, T. B. Ren, S. Xu, X. Lou, L. Yuan and X. B. Zhang, ***CCS Chem.***, 2022, **4**, 2153-2164.
8 W. Liu, Y. M. Wang, Y. H. Li, S. J. Cai, X. B. Yin, X. W. He and Y. K. Zhang, ***Small***, 2017, **13(17)**, 1603459.
9 M. Dulski, K. Malarz, M. Kuczak, K. Dudek, K. Matus, S. Sulowicz, A. M. Wilczkiewicz and A. Nowak, ***Nanomaterials***, 2020, **10**, 2551.
10 E. I. Ayisigi and O. Y. Celiktas, ***Eng. Life Sci.***, 2018, **18**, 882-892.
11 F. Duan, M. Hu, C. Guo, Y. Song, M. Wang, L. He, Z. Zhang, R. Pettinari and L. Zhou, ***Chem. Eng. J.***, 2020, **398**, 125452.
12 J. W. M. Osterrieth and D. F. Jimenez, ***Biotechnol. J.***, 2020, **16(2)**, 2000005.
13 W. A. Shakarchi, A. Alsuraifi, A. Curtis and C. Hoskins, ***Pharmaceutics***, 2018, **10**, 63.
14 D. M. J. Seema, B. Saifullah, M. Selvanayagam, S. Gothai, M. Z. Hussein, S. K. Subbiah, N. M. Esa and P. Aruselvan, ***Pharmaceutics***, 2018, **10**, 109.
15 R. S. Bhosale and V. Sing, Advances in Aggregation Induced Emission Materials in Biosensing and Imaging for Biomedical Applications- Part B. *Progress in Molecular Biology and Translational Science, Book Series*, 2021, **185**, 1-234.
16 (a) C. Zhang, S. Jin, S. Li, X. Xue, J. Liu, Y. Huang, Y. Jiang, W. Q. Chen, G. Zou and X. J. Liang, ***ACS Appl. Mater. Interfaces.***, 2014, **6**, 5212-5220. (b) B. Muthuraj, S. Mukherjee, C. R. Patra and P. K. Iyer, ***ACS Appl. Mater. Interfaces***, 2016, **8**, 47, 32220-32229.
17 N. H. Ly and S. W. Joo, ***J. Mater. Chem. B***, 2020, **8**, 186.

18 S, Thangudu, P. Kalluru and R. Vankayala, ***Bioengineering***, 2020, **7**, 20.
19 J. Dhuguru and R. Skouta, ***Molecules***, 2020, **25**, 1615.
20 R. Oun, Y. Moussa and N. Wheate, ***Dalton Trans.***, 2018, **47**, 6645-6653.
21 C. Carvalho, R. X. Santos, S. Cardosa, S. Correia, P. J. Oliveira, M. S. Santos and P. I. Moreira, ***Curr. Med. Chem.***, 2009, **16**, 3267-3285.
22 Y. Qin, T. Guo, Z. Wang and Y. Zhao, ***J. Mater. Chem. B***, 2021, **9**, 4793-4803.
23 H. Cong, X. Zhao, B. T. Castle, E. J. Pomeroy, B. Zhou, J. Lee, Y. Wang, T. Bian, Z. Miao, W. Zhang, Y. Y. Sham, D. J. Odde, C. E. Eckfeldt, C. Xing and C. Zhuang, ***Mol. Pharmaceutics.***, 2018, **15**, 3892-3900.
24 (a) H. Kobayashi, M. Ogawa, R. Alford, P. L. Choyke and Y. Urano, ***Chem. Rev.***, 2010, **110(5)**, 2620-2640. (b) H. C. Hao, G. Zhang, Y. N. Wang, R. Sun, Y. J. Xu and J. F. Ge, ***J. Mater. Chem. B***, 2022, **10**, 5796.
25 S. Liu, W. Song, X. Gao, Y. Su, E. Gao and Q. Gao, ***Anal. Chem.***, 2019, **91**, 1507-1515.
26 S. R. S. Rangan, ***Cancer***, 1972, **29**, 117-121.
27 J. Ma, S. Lu, L. Yu, J. Tian, J. Li, H. Wang and W. Xu, ***Oncol. Rep.***, 2011, **26**, 1189-1195.
28 A. S. M. Noman, R. R. Parag, M. I. Rashid, S. Islam, M. Z. Rahman, A. A. Chowdhury, A. Sultana, C. Jerin, A. Siddiqua, L. Rahman, J. Nayeem, S. Akther, S. Baidya, R. K. Shil, M. Rahman, A. Shirin, R. Mahmud, S. M. I. Hossain, S. A. Sumi, A. Chowdhury, S. B. Basher, A. Hasan, S. Bithy, J. Aklima, N. Chowdhury, M. N. Hasan, T. Banu, S. Chowdhury, M. M. Hossain, H. Yeger, W. A. Farhat and S. S. Islam, ***Cell Death Dis.***, 2020, **11**, 663.
29 H. Wang, H. Bai, J. Wang, X, Zhou, H. Chen, L. Wang, H. Ren, Z. Liu, W. Zhuo, Z. Zhou, J. Tang, Z. Li, J. Wang, Y. Shen, T. Zhou and X. Liu, ***Biomaterials***, 2022, **283**, 121458.
30 B. Schrors, S. Boegel, C. Albrecht, T. Bukur, V. Bukur, C. Holtstrater, C. Ritzel, K. Manninen, A. D. Tadmor, M. Vormehr, U. Sahin and M. Lower, ***Front. Oncol.***, 2020, **10**, 1195.
31 R. Acharya, S. Chacko, P. Bose, A. Lapenna and P. Pattanayak, ***Sci. Rep.***, 2019, **9**, 15743.
32 S. Nagini, ***Anti-Cancer Agents in Med. Chem.***, 2017, **17(2)**, 152-163.
33 Q. Li, M. Li, K. Zheng, S. Tang and S. Ma, ***Trans. Oncol.***, 2021, **14**, 100891.
34 S. Comsa, A. M. Cimpean and M. Raicia, ***Anticancer Res.***, 2015, **35**, 3147-3154.
35 F. A. M. Mohamed, H. A. M. Gomma, O. M. Hendawy, A. T. Ali, H. S. Farghaly, A. M. Gouda, A. H. Abdelazeem, M. H. Abdelrahman, L. Trembleau and B. G. M. Youssif, ***Bioorg. Chem.***, 2021, **112**, 104960.
36 Y. Zhang, P. Yang, C. J. Chou, C. Liu, X. Wang and W. Xu, ***ACS Med. Chem. Lett.***, 2013, **4**, 235-238.
37 G. L. Regina, R. Bai, W. M. Rensen, E. D. Cesara, A. Coluccia, F. Piscitelli, V. Famiglini, A. Reggio, M. Nalli, S. Pelliccia, E. D. Pozzo, B. Costa, I. Granata, A. Porta, B. Maresca, A. Soriani, M. L. Iannitto, A. Santoni, J. Li, M. M. Cona, F. Chen, Y. Ni, A. Brancale, G. Dondio, S. Vultaggio, M. Varasi, C. Mercurio, C. Martini, E. Hamel, P. Lavia, E. Novellino and R. Silvestri, ***J. Med. Chem.***, 2013, **56**, 123-149.

38 R. Pingaew, P. Mandi, V. Prachayasittikul, A. Thongnum, S. Prachayasittikul, S. Ruchirawat and V. Prachayasittikul, ***ACS Omega***, 2021, **6**, 31854-31868.
39 A. O'Dea, C. Sondergard, P. Sweeney and C. K. Arnatt, ***ACS Med. Chem. Lett.***, 2018, **9**, 901-906.
40 D. H. Hua, K. Lou, J. Havens, E. M. Perchellet, Y. Wang, J. P. Perchellet and T. Iwamoto, ***Tetrahedron***, 2004, **60**, 10155-10163.
41 R. B. Weiss, ***Semin Oncol.***, 1992, **19(6)**, 670-686.
42 D. W. Fry, ***Pharmacol Ther.***, 1991, **52(1)**, 109-125.
43 J. Yan, J. Chen, S. Zhang, J. Hu, L. Huang and X. Li, ***J. Med. Chem.***, 2016, **59(11)**, 5264-5283.
44 A. Andreani, S. Burnelli, M. Granaiola, A. Leoni, A. Locatelli, R. Morigi, M. Rambaldi, L. Varoli, L. Landi, C. Prata, M. V. Berridge, C. Grasso, H. H. Fiebig, G. Kelter, A. M. Burger and M. W. Kunkel, ***J. Med. Chem.***, 2008, **51**, 4563-4570.
45 M. El-Naggar, H. Almahli, H. S. Ibrahim, W. M. Eldehna and H. A. Abdel-Aziz, ***Molecules***, 2018, **23**, 1459.
46 M. Yousuf, S. Jinka, S. S. Adhikari and R. Banerjee, ***Bioorg. Chem.***, 2020, **98**, 103719.
47 S. I. Omoruyi, O. E. Ekpo, D. M. Semenya, A. Jardine and S. Prince, ***Apoptosis***, 2020, **25**, 261-274.
48 M. Arulkumar, K. Yang, N. Wang, S. Penislusshiyan, T. Palvannan, K. Ramalingam, F. Chen, S. H. Luo, Y. J. Zhou and Z. Y. Wang, ***New J.Chem.***, 2022, **46**, 675-685.
49 J. Qian and B. Z. Tang, ***Chem.***, 2017, **3**, 56-91.
50 S. A. Tucker and W. E. Jr. Acree, ***Polycyclic Aromat. Compd.***, 1993, **3**, 221-229.
51 Y. Yamaguchi, Y. Matsubara, T. Ochi, T. Wakamiya and Z. Yoshida, ***J. Am. Chem. Soc.***, 2008, **130(48)**, 16442.
52 W. H. Brooks, W. C. Guida and K. G. Daniel, ***Curr. Top. Med. Chem.***, 2011, **11**, 760-770.
53 Y. J. Zheng and C. M. Tice, ***Expert Opin. Drug Deliv.***, 2016, **11(9)**, 831-834.
54 M. Z. K. Baig, G. Pallikonda, P. Trivedi, R. N. P. Tulichala, B. G. Ghosh and M. Chakravarty, M. ***ChemistrySelect***, 2016, **1(14)**, 4332-4339.
55 E. Grenet and J. Waser, ***Org. Lett.***, 2018, **20(5)**, 1473-1476.
56 M. Z. K. Baig, B. Prusti, D. Roy, P. K. Sahu, M. Sarkar, A. Sharma and M. Chakravarty, ***ACS Omega***, 2018, **3(8)**, 9114-9125.
57 B. Gironi, Z. Kahveci, B. McGiill, B. D. Lechner, S. Pagliara, J. Metz, A. Morresi, F. Palombo, P. Sassi and P. G. Petrov, ***Biophys. J.***, 2020, **119**, 274-286.
58 L. Zou, S. Guo, H. Lv, F. Chen, L. Wei, Y. Gong, Y. Liu and C. Wei, ***Dyes Pigm.***, 2022, **198**, 109958.
59 X. C. Cai and B. Liu, ***Angew. Chem.***, 2020, **59(25)**, 9868-9886.
60 Y. Huang, J. Xing, Q. Gong, L. C. Chen, G. Liu, C. Yao, Z. Wang, H. L. Zhang, Z. Chen and Q. Zhang, ***Nat. Commun.***, 2019, **10**, 169.
61 Q.Li and Z. Li, ***Adv. Sci.***, 2017, 1600484.

62 Y. Dai, H. Liu, T. Geng, F. Ke, S. Niu, K. Wang, Y. Qi, B. Zou, B. Yang, W. L. Mao and Y. Lin, ***J. Mater. Chem. C***, 2021, **9**, 934-938.
63 V. Aggarwal, H. S. Tuli, A. Varol, F. Thakral, M. B. Yerer, K. Sak, M. Varol, A. Jain, M. A. Khan and G. Sethi, ***Biomolecules***, 2019, **9**, 735.
64 J. Phuchareon, A. van Zante, J. B. Overdevest, F. McCormick, D. W. Eisele and O. Tetsu, ***Transl. Oncol.***, 2014, **7(5)**, 537-545.
65 Y. Zhou, R. Sridhar, L. Shan, W. Sha, X. Gu and S. Sukumar, ***Cancer Invest.***, 2012, **30**, 119-125.
66 J. G. Rosch, A. L. Brown, A. N. DuRoss, E. L. DuRoss, G. Sahay and C. Sun, ***Nanoscale Res. Lett.***, 2018, **13**, 350.
67 F. A. Tanious, J. M. Veal, H. Buczak, L. S. Ratmeyer and W. D. Wilson, ***Biochemistry***, 1992, **31(12)**, 3103-3112.
68 P. C. Lyon, V. Suomi, P. Jakeman, L. Campo, C. Coussios and R. Carlisle, ***Sci. Rep.***, 2021, **11**, 4404.
69 O. Tacar, P. Sriamornsak and C. R. Dass, ***J. Pharm. Pharmacol.***, 2012, **65**, 157-170.
70 V. Vangala, N. V. Nimmu, S. Khalid, M. Kuncha, R. Sistla, R. Banerjee and A. Chaudhuri, ***Mol. Pharmaceutics***, 2020, **17**, 1859-1874.
71 Drummen, G. P. C., ***Molecules***, 2012, **17**(12), 14067-14090.
72 Huang, X.; Zhang, R.; Chen, C.; Kwok, R. T. K.; Tang, B. Z., ***Mater. Chem. Front.***, 2021, **5**, 723-743.

73 Xu, Z.; Huang, X.; Han, X.; Wu, D.; Zhang, B.; Tan, Y.; Cao, M.; Liu, S. H.; Yin, J.; Yoon, J. A, ***Chem***, 2018, **4**, 1609-1628.

74 Schnermann, M., ***Nature***, 2017, **551**, 176-177.

75 Wu, J.; Shi, Z.; Zhu, L.; Li, J.; Han, X.; Xu, M.; Hao, S.; Fan, Y.; Shao, T.; Bai, H.; Peng, B.; Hu, W.; Liu, X.; Yao, C.; Li, L.; Huang, W, ***Adv. Opt. Mater.***, 2022, **10(8)**, 2102514.

76 Li, D. H.; Schreiber, C. L.; Smith, B. D., ***Angew. Chem. Int. Ed.***, 2020, **59**(29), 12154-12161.

77 P. Chakraborty, S. B. Ahil, T. Jamma and P. Yogeeswari, ***Future Med. Chem.***, 2022, **14**, 463-478.
78 R. Pola, E. Bohmova, M. Filipova, M. Pechar, J. Pankrac, D. Vetvicka, T. Olejar, M. Kabesova, P. Pouckova, L. Sefc, M. Zábrodský, O. Janoušková, J. Broucek and T. Etrych, ***Pharmaceutics***, 2020, **12**, 31.
79 N. Iqbal and N. Iqbal, ***Mol. Biol. Int.***, 2014, Article ID: 852748.
80 K. Aertgeerts, R. Skene, J. Yano, B. C. Sang, H. Zou, G. Snell, A. Jennings, K. Iwamoto, N. Habuka, A. Hirokawa, T. Ishikawa, T. Tanaka, H. Miki, Y. Ohta and S. Sogabe, ***J. Biol. Chem.***, 2011, **286**, 18756-18765.

Chapter IV

Indole Conjugated Anthracene Based *D-π-D′* and *D-π-A* Solid State Emitting Organic Fluorogens (SSEOFs): Quest to Transcend the Limits of Photophysical Properties with Real-World Optical Applications

Objectives:

- To develop an SSEOF with multi-state (solids, solutions, aggregates, and viscous mediums) emission features
- Have an insight into the fundamental understanding of emission diversities
- Grow *D-π-D′* and *D-π-A* SSEOF systems to aggravate the structural scopes of smart materials
- Find out multiple fluorescent-based real-world applications

Abstract:

It is still a conundrum to design a single but simple organic molecule possessing numerous realistic photophysical properties such as solid-state emission and stimuli-responsive emission switching, aggregation-induced emission (AIE) properties, solvatochromic DSE-gens (dual-state emissive fluorogens), and viscofluorochromism. Unlike D-π-A, D-π-D′ systems are seldom explored with various applied features. Despite many reports on organic D–π–A fluorescent materials, the ardent realization of seven different photophysical features in a single material remains obstinate to attain six multitudinous real-world applications. Herein, we discussed how a single D-π-D′ indole-anthracene conjugate displays all these properties with real-world applications. Especially, an indole-anthracene-π-phenothiazine conjugate (**IAP**) appears as a solvatochromic (91 nm shift) DSE-gen that shows the longest 62 nm blue-shifted enhanced emission on aggregation and the longest 45 nm blue-shifted viscofluorochromic features. Furthermore, **IAP** adopts a fingertip-pressure-sensitive 35 nm blueshift, while a triphenylamine-linked analogue **IAT** demonstrates a 23 nm mechanofluorochromic redshift. For indole-anthracene-π-pyridine (**IAPY**), novelty aligns with the judicious design where each molecular part is in a different plane with a well-organized '*V*' shape herringbone crystal packing with a centrosymmetric *C*2/*c* space group. Various anticounterfeiting, forensic, and other relevant optical applications are envisaged and performed with this dye.

4.1 Introduction

The emergence of pure organic emitters has ensnared researchers around the globe due to their continuous contemplation and advancement as smart materials with practical and versatile applications in optoelectronics[1-3] that include luminescent sensors[4], supramolecular encryption systems[5], and many more relevant fields.[6] Despite many exemplary discoveries, the foundation for novel, innovative materials still appreciates exigency. An organic molecule, capable of fine-tuning its emissive properties in different states, and responding to external stimuli, would be a material of neatness by performing all the tasks alone! Achieving such molecular design is a challenging task and needs a critical approach.[7-10] Mostly, the photophysical properties of molecules become mutually exclusive depending on twisted molecular conformation, intramolecular steric hindrances, amorphous and crystalline state, triplet excitons, and several quantum chemical descriptors, such as excited-state planarity, root-mean-square displacement (RMSD), reorganization energy and emission/absorption oscillator strength.[7,11] On a systematic strategy, many donor-π-acceptor (D-π-A) molecular models with twisted conformations have endeavored to alter the electronic density and regulate the extent of π-conjugation within the molecule. This concept is confirmed by earlier reports where the molecules can act as solid-state emitters (SSE), respond to the applied external stimuli, and display aggregation-induced emission (AIE).[12,13] Apart from the stimuli-responsive AIE-gens, of late, seeking dual-state emission (DSE) has primarily been signified due to their ability to emit in nonpolar and polar solvents.[14,15] DSE-gens luminescence originates inherently while relaxing from a locally excited state.[7,11]So, a compound with suitable electronic transition energy, a shorter emitting wavelength, large stokes shift, high oscillator strength, smaller root mean square displacement (RMSD) between S_0 and S_1, and restricted intramolecular rotation facilitate intense emission in both solid and solution by opening up radiative channels.[7,11] Further, attaining planarity in the S_1 state is another essential need to emit in a particular solvent.[14] Notably, AIE-gens don't typically offer dual-state emission efficacy. Hence, *the development of AIE-active DSE-gen is a new thrust area of research* with their emission ability in all the phases like solutions, aggregates, and solids, and perceives suave applications as optical and biomaterials.[16,17] Molecular rotors with

viscosity-sensitive emissions are of advanced priority due to their success in studying protein environments in biological systems, organelle imaging, and even sensing liquid food spoilage.[18-26]Most significantly, earlier reported relevant single molecules failed to display such diverse photophysical properties (See Figure S1 for a few examples and comparison with this report).[27-31] Although multitasking D-π-A systems with a precise transient dipole moment and charge separation are well recognized by others,[32,33] useful D-π-D′ systems are merely explored in the literature. *Especially, indole conjugated anthracene-based π-conjugates are extremely rare, although there are materials on indole [34,35] and anthracene cores separately*.[36,37] Hence, the investigation and development of indole-anthracene-based smart organic SSEOFs makes sense.

4.2 Literature review on organic π-conjugates with multiple photophysical properties and applications

4.2.1 Literature review on *indole scaffold* -linked organic π-conjugates displaying optical properties

4.2.1.1 Four-winged propeller-shaped indole-substituted AIEgens as blue-emitting OLEDs

Lafzi *et al*. recently reported a series of indole-based four-winged SSEOFs with a common TPE (tetraphenylethylene) core. For example, compound **4A** can emit blue in solid film and is utilized as a blue-emitting OLED. Compound **4B** also displays the same emission and isused as an OLED. Both compounds are AIE-gens, but **4A** displays mechanofluorochromism as well. The focus of the work was to establish conventional OLEDs, but these molecules are not smart enough to exhibit plenty of photophysical properties and applications (Figure 4.1).[34]

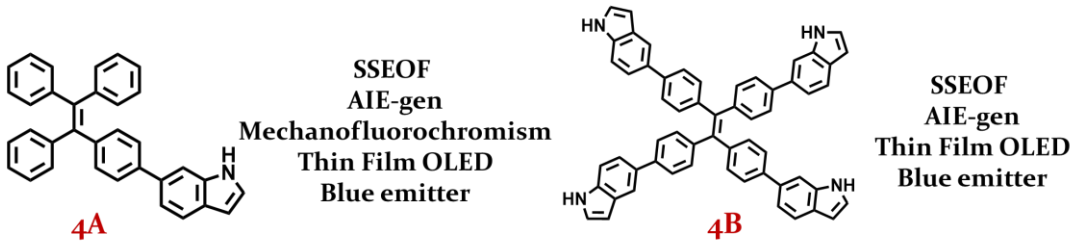

Figure 4.1 Reported representative propeller-shaped indole-substituted AIEgens for OLED applications (taken from ref. 34)

4.2.1.2 Double indolo[3,2-b]indole electron-donors based emitter for OLED applications

Tongsuk et al. reported double indolo[3,2-b]indole electron-donors-based solid film-emitters **4C** and **4D** where the compounds are only different in terms of alkyl chain length from each other and exhibit emission as solid-films and applied as OLEDs. Moreover, those molecules have the potency to display electroluminescence as well (Figure 4.2).[35]

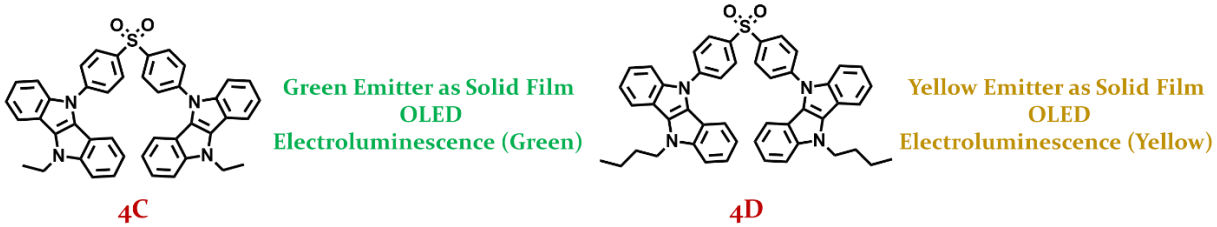

Figure 4.2 Reported double indolo[3,2-b]indole electron-donors based emitters (ref. 35)

4.2.1.3 Dicyanomethylene-4H-pyran conjugated indole derivatives as mechanofluorochromic SSEOFs

Qian *et al.* synthesized dicyanomethylene-4H-pyran conjugated indole derivatives that displayed moderate mechanofluorochromism as SSEOFs, and yet the other photophysical properties like AIE, DSE, VIE were not explored. **4F** exhibited a 27 nm emission shift, whereas **4G** displayed only a 10 nm emission shift. None of the results was convincing enough to consider them as smart materials (Figure 4.3).[38]

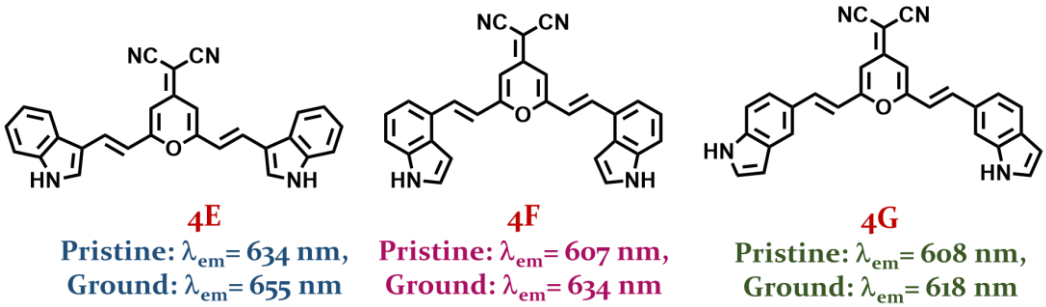

Figure 4.3 Reported representative dicyanomethylene-4H-pyran conjugated indole derivatives (ref. 38)

4.2.1.4 Cyano-functionalized1,4-bis((E)-2-(1H-indol-3-yl)vinyl)benzenes as AIE-active thermofluorochromic dyes

Ma *et al.* reported cyano-functionalized1,4-bis((E)-2-(1H-indol-3-yl)vinyl)benzenes that display thermofluorochromic behavior only when they contain long alkyl chains, this effect is absent for the short alkyl chain lengths for their system. Apart from that, compounds like **4H** and **4I** exhibit TICT and aggregation-induced emission (AIE) dependent emission switching (Figure 4.4).[39]

Figure 4.4 Reported representative thermofluorochromic and AIE-active cyano-functionalized1,4-bis((E)-2-(1H-indol-3-yl)vinyl)benzenes (ref. 39)

4.2.2 Literature review on *anthracene-connected* organic π-conjugates displaying optical properties

4.2.2.1 Trimethoxybenzene-anthracene-phenothiazine conjugated organic compound with multiple photophysical outputs

In consecutive attempts, Prusti *et al.* synthesized and explored the photophysical properties of a trimethoxybenzene-anthracene-π-phenothiazine conjugated organic compound that displays AIE-active solid-state emission, commendable solvatochromism, vapochromism and is suitable for volatile organic solvent vapor sensing and TNT explosive sensing (Figure 4.5).[37,40]

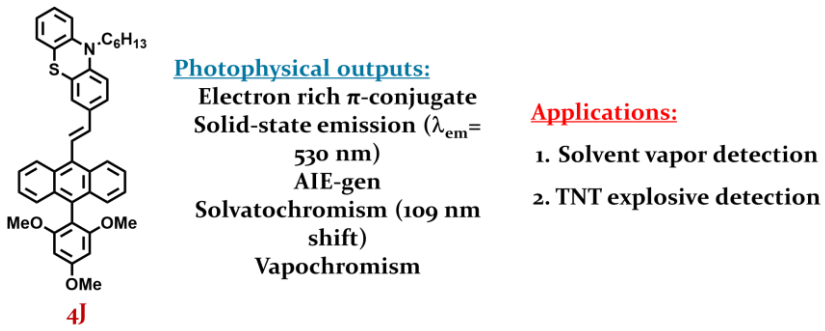

Figure 4.5 Reported representative thermofluorochromic and AIE-active cyano-functionalized1,4-bis((E)-2-(1H-indol-3-yl)vinyl)benzenes (refs. 37, 40)

4.2.2.2 Twisted anthracenyl π-conjugate with interchanged electron-rich substituents exhibiting disparity in AIE-activity and mechabofluorochromism

Prusti *et al.* reported another exciting pair of organic π-conjugates that exhibit disparity in AIE-activity and mechanofluorochromism. The effect of coplanarity on the π-conjugates is explored here. Surprisingly, the better AIE showing conjugate **4K** is not mechanofluorochromic. On the other hand, moderately AIE active**4L** exhibits 62 nm emission redshift on being ground with mortar and pestle (Figure 4.6).[37,40-41]

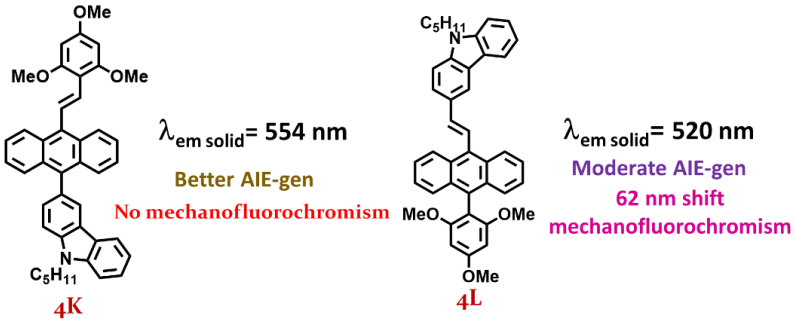

Figure 4.6 Reported AIE-active mechanofluorochromic π-conjugate and its disparity (refs. 37, 40, 41)

4.2.2.3 Anthracene-TPE based π-conjugate for AIE-activity and pressure-induced enhanced emission (PIEE)

Liu *et al.* observed an abnormal blue-shifted pressure-induced enhanced emission phenomenon when two compounds **4M** and **4N** exhibited two different molecular conformations with varying AIE and PIEE properties. The meta linkage was found to have an excimer forming anthracene core while the suppressed energy transfer from TPE to anthracene core induced the appearance of a blue-shifted band from 1.23 to 4.28 GPa. (Figure 4.7).[42]

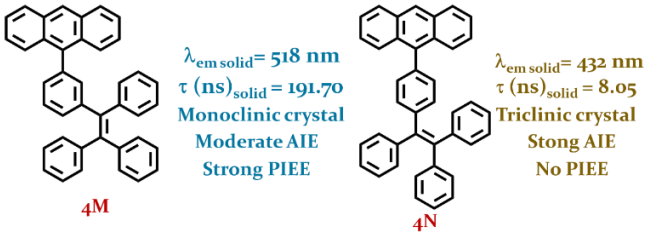

Figure 4.7 Reported AIE-active PIEE/non-PIEE displaying pairs (ref. 42)

4.2.2.4 Anthracene-thianthrene based π-conjugate for pressure-induced quenched emission in solid-state

Liu *et al*. investigated and found that **4O** crystal displayed the constant excimer fluorescence peak from 0.12-1.70 GPa of pressure but later got redshifted (1.70-9.41 GPa), but **4P** exhibited normal redshifted fluorescence emission with increasing pressure. For their case, the monodisperse π-π stacking of anthracene dimer causes quenching of emission under pressure although (Figure 4.8).[43]

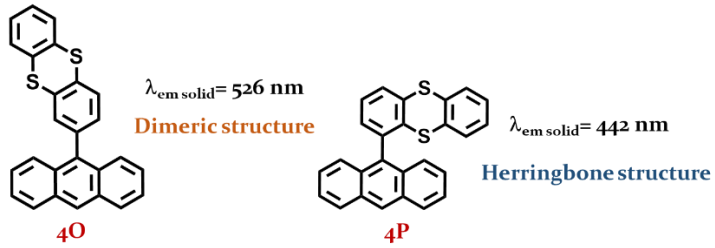

Figure 4.8 Reported non-PIEE displaying pairs (ref. 43)

4.2.2.5 D-π-A system '*N*'-containing heterocyclic chromophores with anthracene moiety with mechanofluorochromism and acidofluorochromism

Zhan reported **4Q** and **4R** compounds that are anthracene conjugated luminophores with moderate mechanofluorochromic response from **4Q** and **4R** depending on the significant distortion of their respective single-crystal packing. Due to the alkalinity of present 'N' atom the **4Q** and **4R**, the compounds display acidofluorochromism in solution and film state through emission quenching upon addition or exposure towards acid/acid vapor.[44]

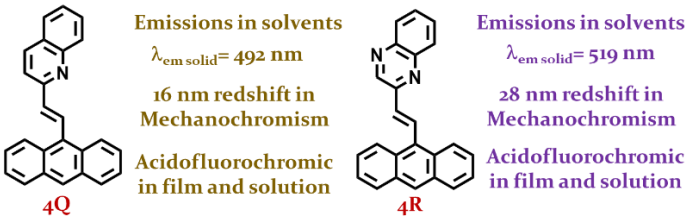

Figure 4.9 Reported mechanofluorochromic and acidofluorochromic anthracene conjugates (ref. 44)

4.3 Results and discussion

Basically, we discuss the photophysical properties of **SB3**, **SB6**, and **SB7** separately here in this chapter, as these compounds were found to display multiple fluorescence-based photophysical outputs to realize many optical applications apart from bioimaging exploration, which is discussed in the previous chapter.

4.3.1 Design strategy

Two kinds of molecular designs have been envisaged based on D-π-D′ [**IAT** (**SB6**) and **IAP** (**SB7**)] and D-π-A [**IAPY** (**SB3**)] systems (Figure 4.10). Several strategies

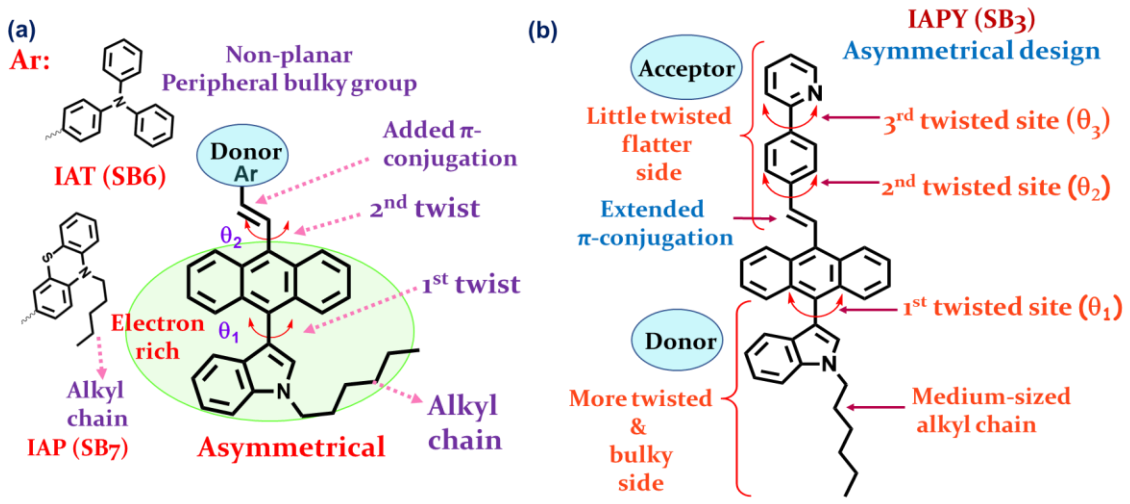

Figure 4.10 Design strategy for (a) D-π-D′ and (b) D-π-A systems

have been considered while designing the *D-π-D′* molecules to achieve multiple photophysical properties from a single organic π-conjugate.[7] These approaches include- *(i)* incorporation of different twisted sites in a molecule, *(ii)* introduction of propeller-shaped bulky, electron-rich triphenylamine (TPA) as a donor and phenothiazine (PTZ) as a bowl-shaped and electron-rich donor, and both these alkylated units create adequate steric crowding, leading to adopt head to tail arrangement[7] *(iii)* moderately long alkyl chain produce severe van der Waals interactions and influence self-isolation effect'[45,46], and *(iv)* asymmetric donor-π-donor (D-π-D′) architecture, expected to monitor the distribution from molecule to build up HOMO and LUMO in the excited state and achieve various photophysical features and exciting applications.[7] However, rigidification from the attached core might change the scenario of the whole system. The reason behind such deliberations is to gain a twisted structure, enabling it to face a

significant barrier to create a close stacked packing. It can block the generation of triplet excitons in the solid state, resulting in an efficient emission.[11] Further, double-site twisted conformation with D-π-D′ architecture becomes crucial to form a solid-state emitter with AIE-gen feature. The conformational flexibility and extended π-conjugation facilitate displaying mechano-responsive fluorescence switching.[47] With increasing viscosity, the molecular motion of double-site twisted π-conjugate would be restricted to a reasonable extent to qualify VIBSEE behavior.[48] An *n*-hexyl chain length (medium) has been introduced as the insightful chain length to enhance the solubility /solution processability. However, an efficient, optimized emission is maintained by tuning the fluorescence quenching, originated by amplified vibrations of the alkyl chain.[46] On the other hand, highly twisted structures and medium-sized alkyl chains facilitate emitting brightly in the aggregated state due to certain structure rigidification.[49,50] Nonetheless, generating emissions in the solution state from an AIE-gen is typically challenging.[51] Again, the alkyl chain may create rigidification and provide commendable fluorescence quantum yield (Φ_f) in solutions.[52,53]

For the *D-π-A* system **SB3**, the design concept includes more logic than the already mentioned ones. It is a three-site twisted asymmetrical *D-π-A* system where 2-phenyl pyridine is conjugated with alkylated indolyl anthracene.

The designs mentioned above were expected to display favorable quantum chemical descriptors. Achievement of favorable planarity, emission oscillator strength, and root-mean-square displacement (RMSD) in the excited state with suitable twisting and packing modification scopes could help them display multiple photophysical outputs and emission switching.

4.3.2 Synthetic route

The synthetic route has been discussed in the previous chapter.

4.3.3 Structural elucidation

4.3.3.1 NMR spectroscopic analysis of the synthesized compounds

The structural elucidation from NMR spectroscopy has been discussed and explained in the previous chapter.

4.3.3.2 Single-crystals of the synthesized compounds

After several attempts, a suitable single-crystal of **SB6** and **SB7** could not be generated. However, for **SB3**, the compound was crystallized from a 3:1 $CHCl_3$/dimethylsulfoxide (DMSO) medium by a slow evaporation process. It crystallizes with a centrosymmetric C2/c space group (CCDC No: 2261976) with the shortest axis of 8.56 Å and only one molecule (Z′=1) in an asymmetric unit.

4.3.4 Investigation of the photophysical properties

4.3.4.1 Solid-state emission and stimuli-responsive emission switching

4.3.4.1.1 Solid-state emission and mechano-force induced enhanced emission (MIEE) from *D-π-A* system SB3 (IAPY)

An emission enhancement for organic molecules by applying a tiny mechano-force/pressure is sporadic.[42,54] Even relevant anthracene-based organic emitters are reported to quench their emissions with increased pressure[43], whereas unique MIEE behavior was identified with this suitably designed **SB3**. To our delight, highly intense green emission from pristine **SB3** ($\lambda_{em.}$ =517 nm, Φ_f =26.64%) was identified, and surprisingly, on being mechanically ground with a mortar and pestle, a meager 17 nm emission redshift *with remarkable emission intensity enhancement* [pristine **SB3** (Φ_f =26.64%); ground **SB3** (Φ_f=53.32%)] (Figures 4.12a, 4.12d), confirming the unique MIEE feature in **SB3**. The original emission was recovered with a marginal reduction in Φ_f =25.72% by treating with 2-3 drops of dichloromethane (DCM) to the ground **SB3** and dried subsequently (Figures 4.12b, 4.11a). Additionally, on applying the mechanical force (mortar/pestle) on this recovered sample, the enhancement in Φ_f =53.27% was impressive. The single-crystal packing analysis with other relevant studies could explain the cause. To mention more, the photostability of **SB3** under continuous UV projection was noteworthy (Figure 4.13).

The compound **SB3** has a three-site twisted asymmetrical structure, and it crystallizes with a centrosymmetric C2/c space group (CCDC No: 2261976) with the shortest axis of 8.56 Å and only one molecule (Z′=1) in an asymmetric unit. The single crystal analysis of **SB3** revealed the distortion of the alkylated indole part by ~66.30° (θ_1) to the plane of

anthracene, while 2-phenyl pyridine moiety is more planarized with anthracene ring (θ_2 ~20.29° and θ_3 ~15.22°) (Figures 4.14, 4.15).

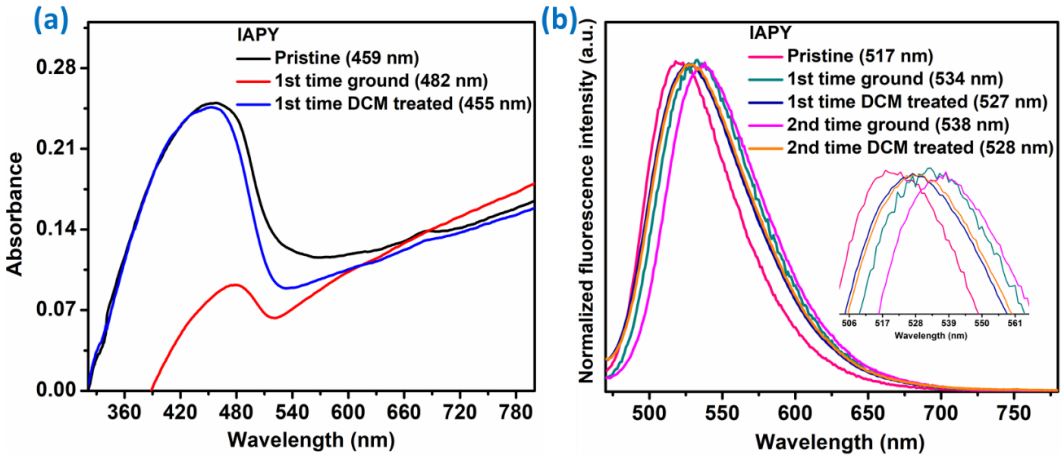

Figure 4.11 Solid-state (a) absorbances (b) emission and MIEE properties of **SB3**

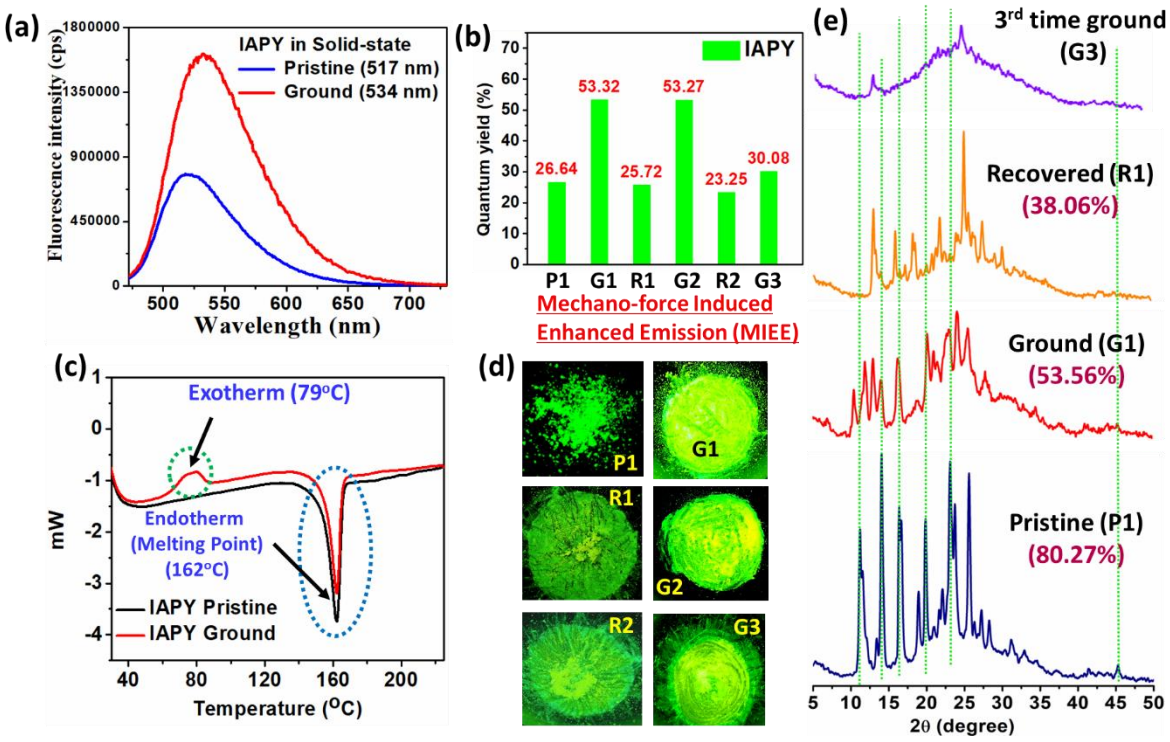

Figure 4.12 *For MIEE property of **SB3*** (a) emissions (b) reversibility (c) DSC curves (d) pictures taken under UV-365 nm bulb; 'P', 'G' and 'R' stand for pristine, ground and recovered and '1' means 1st time, '2' for the second time and '3' means the third time (e) PXRD patterns

The molecular packing of **SB3** shows a characteristic herringbone '*V*'-shaped packing (Figure 4.16) with a total of 22 intra and intermolecular non-covalent interactions

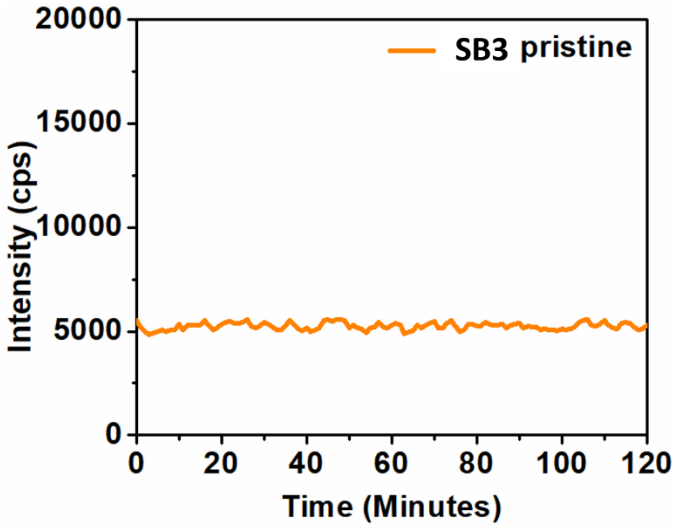

Figure 4.13 Photostability of **SB3** pristine

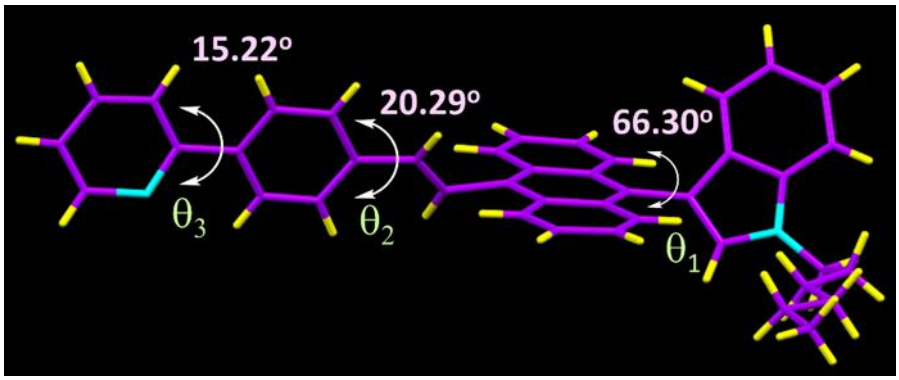

Figure 4.14 Single-crystal with the dihedral angles in three different twisted sites

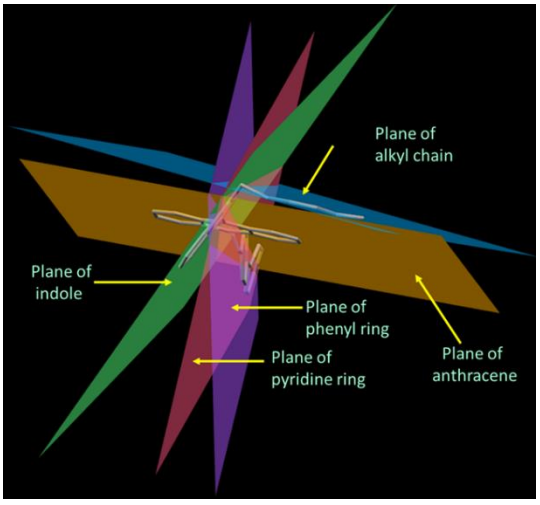

Figure 4.15 Different planes of **SB3**

(C...C, C...H, H...H, and N...H), creating highly ordered and stable arrangement (Figures 4.17, 4.18, Table 4.1). The alkyl chain is placed between two anthracene rings of two

nearby molecules with an alternative head-to-tail sequence. A molecular column interacts with little translated non-parallel neighboring molecules (Figure 4.17).

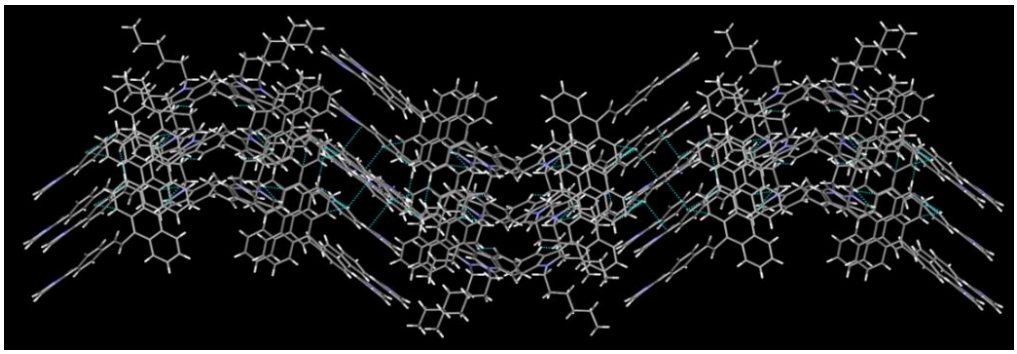

Figure 4.16 '*V*'-shaped herringbone packing of **SB3**

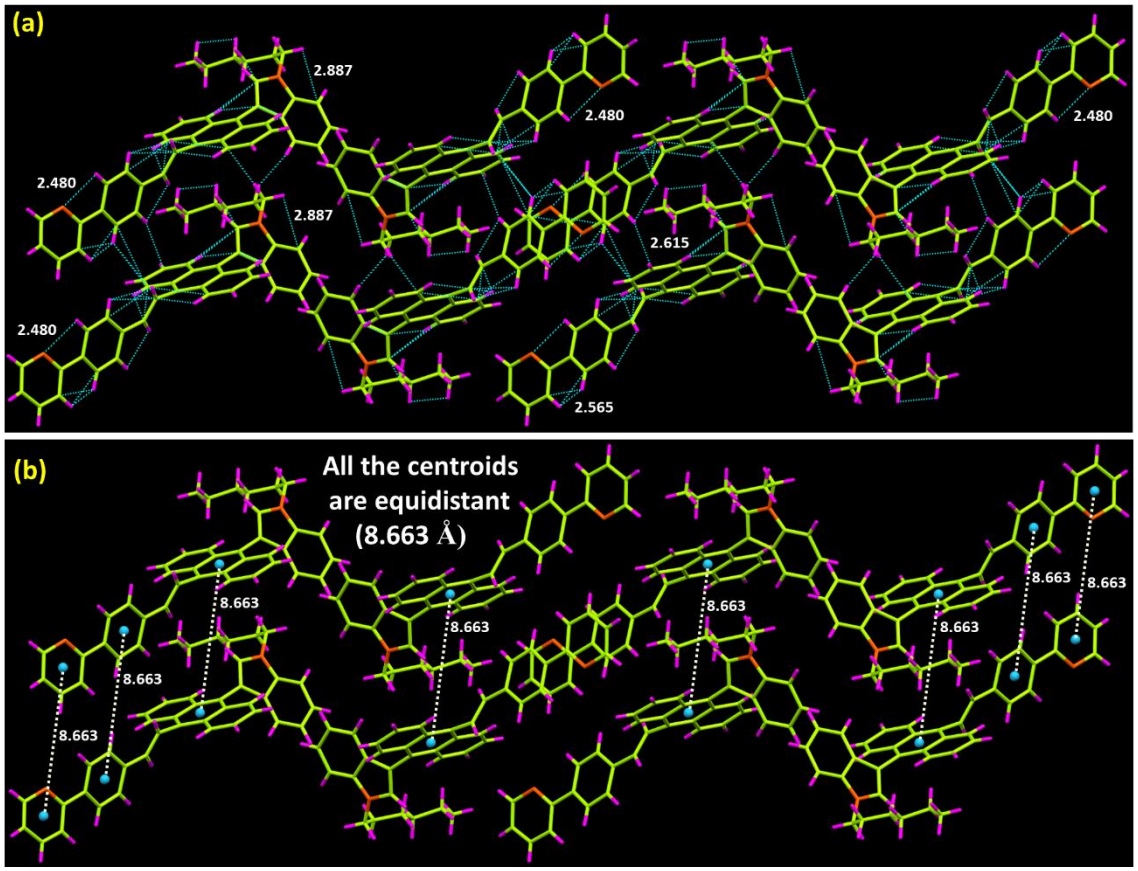

Figure 4.17 (a) Crystal packing for **SB3** pristine with a few selected intermolecular interactions (Å) (b) centroid to centroid distances (Å)

Further, **SB3** has two-fold rotation axes, and as one consequence of the C-centred lattice, there is an equal number of two-fold rotation axes and two-one screw axes (Figure 4.19). Indeed, the rotational flexibility of the herringbone packing along its

principal axis has been reported with a limitation up to a certain angle. Notably, puckered conical intersections are inherently less stable[55], but it does not suffer from an increased instability in herringbone, which is prevalent in luminescent organic molecular crystals. And the extensive conjugation perhaps allows them for low reorganization energy.[55]

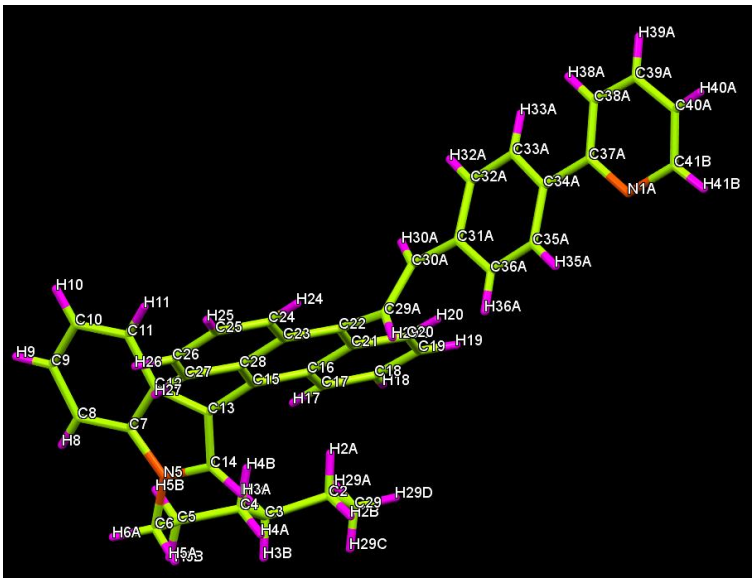

Figure 4.18 Label atom for **SB3** (single-crystal structure)

Table 4.1 Short-contacts

No	Atom1	Atom2	Length (Å)
1	C13	H27	2.60
2	C13	H17	2.55
3	C12	C27	3.34
4	C12	H27	2.76
5	N1A	H35A	2.48
6	C14	C17	3.22
7	C14	H17	2.64
8	C14	C4	3.33
9	C8	H6A	2.89
10	C24	H29E	2.89
11	H24	C29A	2.46
12	C20	C30A	3.22
13	H20	C30A	2.63
14	H20	C29A	2.72
15	C38A	H33A	2.57
16	H38A	C33A	2.55
17	H38A	H33A	1.97
18	H3B	H29C	2.36

19	H30A	H32A	2.37
20	C36A	H29E	2.86
21	H36A	C29A	2.85
22	H36A	H29E	2.39

Two parallel molecules are stacked in a glide fashion (Figure 4.19), and numerous (14) C···H interactions contribute the primary interactions. Such molecular stacking for the C2/c space group was previously documented.[56] Multiple H···H and C···C π-interactions might contribute to emission quenching.[57,58]

However, a remarkable observation between anthracene-anthracene and phenyl-pyridine centroid distances have appeared to be exactly the same i.e., 8.663 Å, facilitating the generation of large void spaces (Figures 4.17b, 4.21), favorable for SSE associated with MIEE. Twenty-two inter and intra-molecular non-covalent interactions with a '*V*'-type packing mode and molecular twisting would reduce molecular vibration and depletion of molecular vibration can enhance emission.[59]

The single crystal analysis using contact surface infers that **SB3** has 8.9% (565.09 Å^3) of void space of total unit cell volume (Figure 4.21), and this void space may allow the molecule to take different metastable energy states under applied mechanical force.

The PXRD study (Figure 4.12e) shows that **SB3** transforms from a highly crystalline pristine state (approx. crystallinity = 80.27 %; calculated from PXRD pattern[60] to a new less crystalline state (approx. crystallinity = 53.56 %) upon grinding (Figure 4.12e). The indication of a crystal-to-crystal transition for a ground sample implies that the pristine has a well-ordered microcrystalline structure, but the ground state seems to possess a semicrystalline (mixture of crystalline and a metastable amorphous) state, which was validated by the DSC profile of the **SB3** ground form that disclosed an exothermic hump at 79 °C (Figure 4.12c). The PXRD pattern of the ground form indicates the arrival of new diffractions and the loss of existing diffractions (Figure 4.12e, Tables 4.2-4.3).

Most possibly, the twisting stress of the molecule is released with a more planar S_1 geometry to raise electronic delocalization between the donor and acceptor, causing a small redshifted (17 nm) emission in the ground sample. At the same time, a few detrimental H···H and C···C interactions will be destroyed to intensify the quantum

yield. In the recovered sample (after grinding → DCM fumed and dried), the PXRD signals are again shifted to the higher angle, indicating a new molecular periodic arrangement with smaller interplanar distances (Figure 4.12e). The **SB3** crystal has solvent-accessible void space, estimated at 1.6% (104.99 Å^3) of unit cell volume (Figure 4.22).

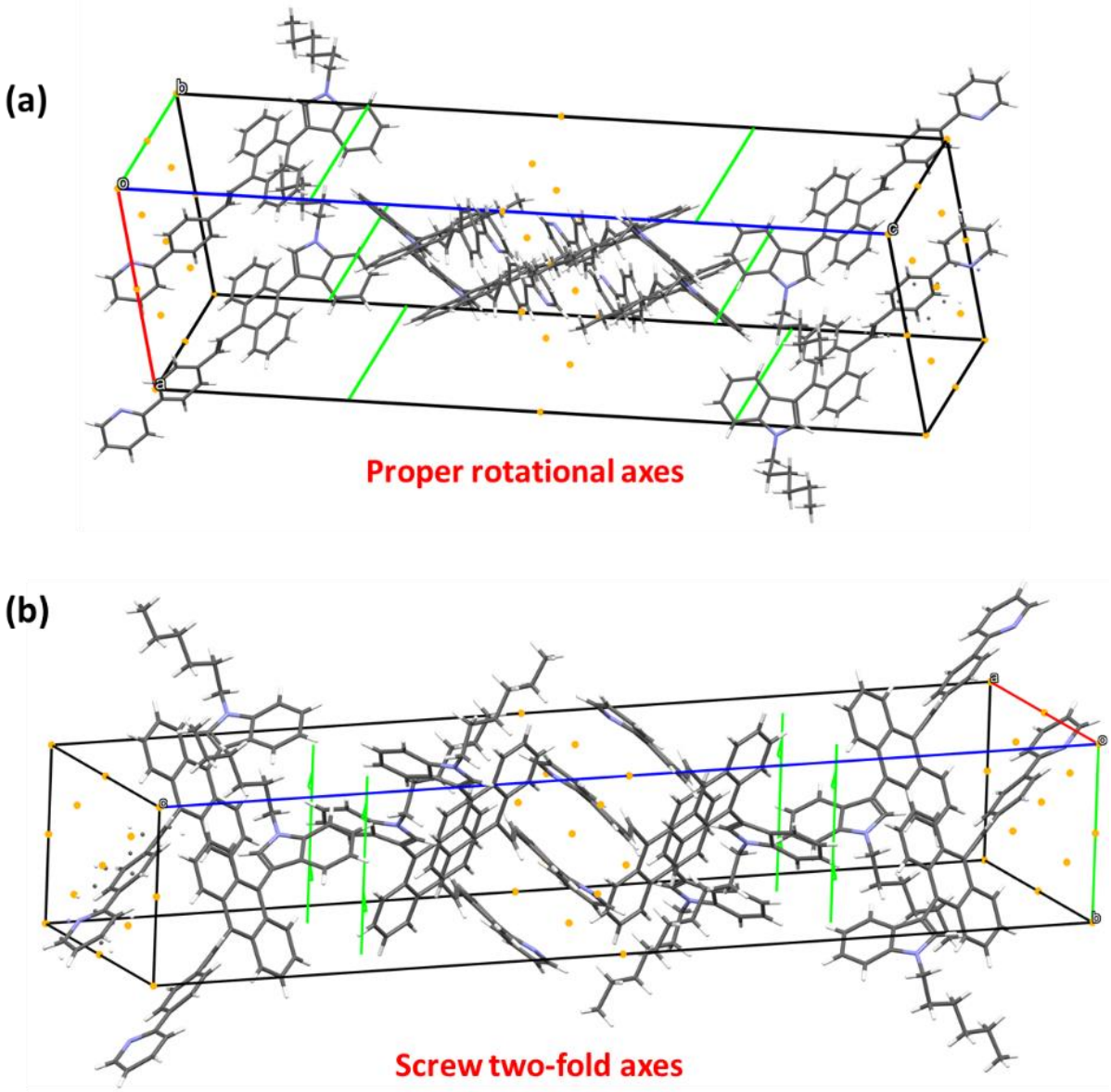

Figure 4.19 Rotational and screw-axes of **SB3**

This available void space is also accountable for MIEE behavior because the molecules can partly /fully occupy this space while applying the force and alter the supramolecular interactions, leading to a new molecular packing pattern. The remaining solvent-accessible void may allow DCM solvent to occupy the space and facilitate recovering a close molecular arrangement, similar to the pristine state. Thus, the 10 nm emission

shift from pristine and unequal Φ_f of the recovered sample concludes that the original pristine packing could not be regenerated upon DCM treatment.

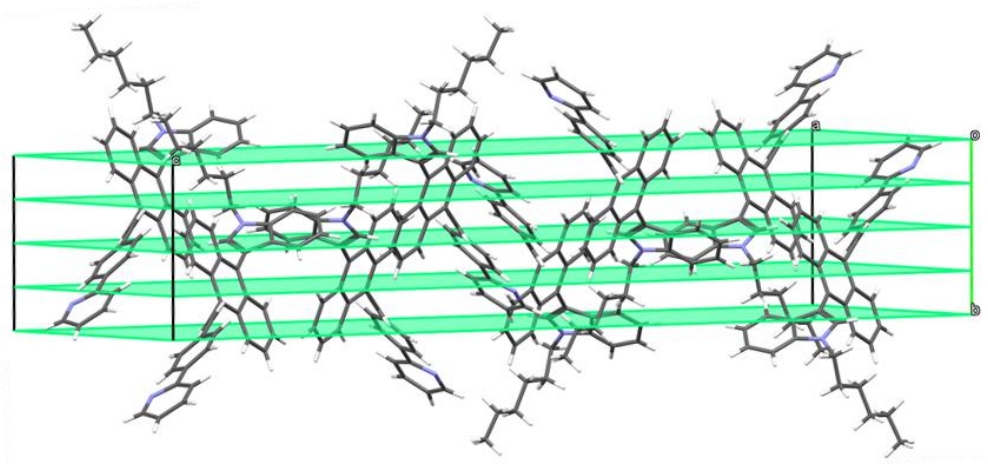

Figure 4.20 Glide plains in packing of **SB3**

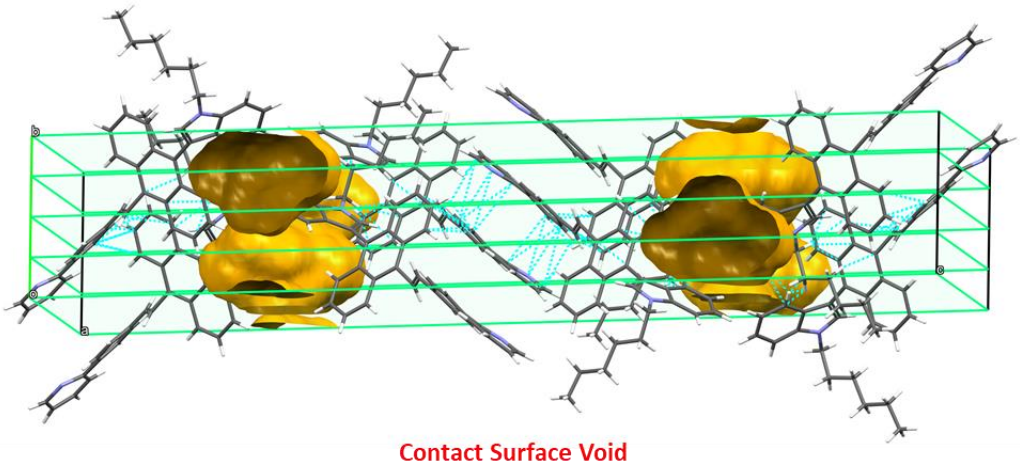

Figure 4.21 Contact surface void of **SB3**

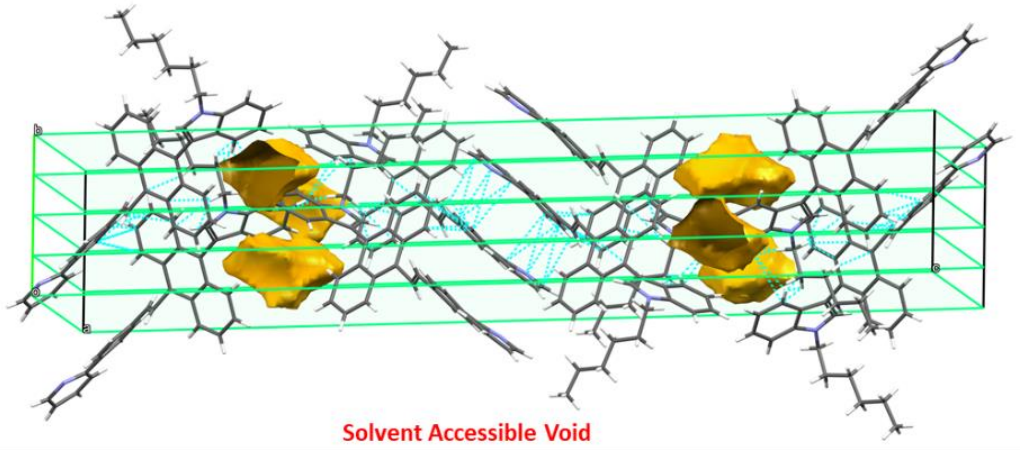

Figure 4.22 Solvent accessible void space of **SB3**

Table 4.2 Peak list for **SB3** pristine PXRD

No.	2θ (deg)	d(ang.)	Height(cps)	FWHM(deg)	Int. I(cps deg)	Int. W(deg)	Asym. factor
1	11.182(5)	7.907(3)	573(24)	0.166(10)	133(11)	0.23(3)	2.2(2)
2	11.584(13)	7.633(8)	453(21)	0.64(2)	404(11)	0.89(7)	2.2(2)
3	13.366(10)	6.619(5)	135(12)	0.26(3)	41(4)	0.30(6)	0.58(6)
4	14.016(2)	6.3136(11)	1044(32)	0.342(7)	420(8)	0.40(2)	0.58(6)
5	16.309(6)	5.430(2)	899(30)	0.177(11)	217(13)	0.24(2)	0.53(11)
6	16.606(8)	5.334(3)	727(27)	0.291(15)	288(14)	0.40(3)	0.53(11)
7	18.881(5)	4.6962(11)	349(19)	0.254(18)	134(5)	0.38(3)	0.6(2)
8	19.836(3)	4.4723(7)	678(26)	0.255(9)	221(6)	0.33(2)	1.1(2)
9	21.62(2)	4.106(4)	120(11)	0.20(5)	26(4)	0.22(6)	0.7(4)
10	22.03(3)	4.031(6)	199(14)	0.26(3)	57(7)	0.29(6)	0.7(4)
11	23.028(7)	3.8591(12)	821(29)	0.26(2)	285(19)	0.35(3)	0.61(9)
12	23.309(12)	3.8132(19)	372(19)	0.16(2)	79(13)	0.21(5)	0.61(9)
13	23.665(12)	3.7565(18)	624(25)	0.382(17)	323(13)	0.52(4)	0.61(9)
14	25.567(8)	3.4813(11)	827(29)	0.325(7)	306(7)	0.37(2)	0.87(9)
15	26.267(14)	3.3901(17)	89(9)	0.17(4)	17(3)	0.19(5)	0.87(9)
16	27.186(8)	3.2775(10)	170(13)	0.28(2)	63(4)	0.37(5)	0.8(4)
17	28.22(3)	3.160(3)	140(12)	0.29(3)	51(4)	0.36(6)	0.7(3)
18	31.12(2)	2.872(2)	72(8)	0.44(6)	36(6)	0.50(14)	0.5(4)
19	45.21(9)	2.004(4)	52(7)	0.31(6)	17(4)	0.33(12)	0.7(8)

Table 4.3 Peak list for **SB3** ground PXRD

No.	2θ (deg)	d(ang.)	Height(cps)	FWHM(deg)	Int. I(cps deg)	Int. W(deg)	Asym. factor
1	10.540(14)	8.387(11)	165(13)	0.52(3)	104(5)	0.63(8)	1.48(15)
2	11.94(2)	7.405(13)	252(16)	0.84(3)	260(7)	1.03(9)	1.48(15)
3	13.062(12)	6.773(6)	278(17)	0.488(19)	167(5)	0.60(5)	1.48(15)
4	14.057(17)	6.295(8)	193(14)	0.62(4)	148(7)	0.77(9)	1.48(15)
5	16.309(7)	5.431(2)	253(16)	0.546(18)	152(6)	0.60(6)	0.96(15)
6	20.145(13)	4.404(3)	244(16)	0.43(2)	111(8)	0.46(6)	0.78(9)
7	21.12(3)	4.204(6)	142(12)	1.12(9)	170(10)	1.19(17)	0.78(9)
8	22.81(3)	3.896(5)	238(15)	1.15(5)	291(11)	1.22(12)	0.78(9)
9	24.113(13)	3.688(2)	294(17)	0.57(2)	180(8)	0.61(6)	0.78(9)
10	25.40(3)	3.504(4)	202(14)	1.21(6)	261(9)	1.29(14)	0.78(9)
11	27.79(3)	3.208(4)	69(8)	0.67(8)	50(5)	0.72(16)	0.78(9)
12	44.45(13)	2.037(6)	16(4)	1.8(4)	30(9)	1.9(10)	0.7(7)

However, a similar crystal packing close to the original can be speculated. *For the third time ground sample, the material becomes amorphous and thus loses the balance between its more and less crystalline state, resulting in weak reversible nature.* Notably, the sample, after 3rd-time grinding, occupies a new phase compared to the pristine, as

observed in DSC (Figure 4.23). Moreover, a significant 23 nm redshift in absorption spectra after mechanical grinding of **SB3** (Figure 4.11a) possibly indicates a '*J*' type arrangement in the ground form.[61]

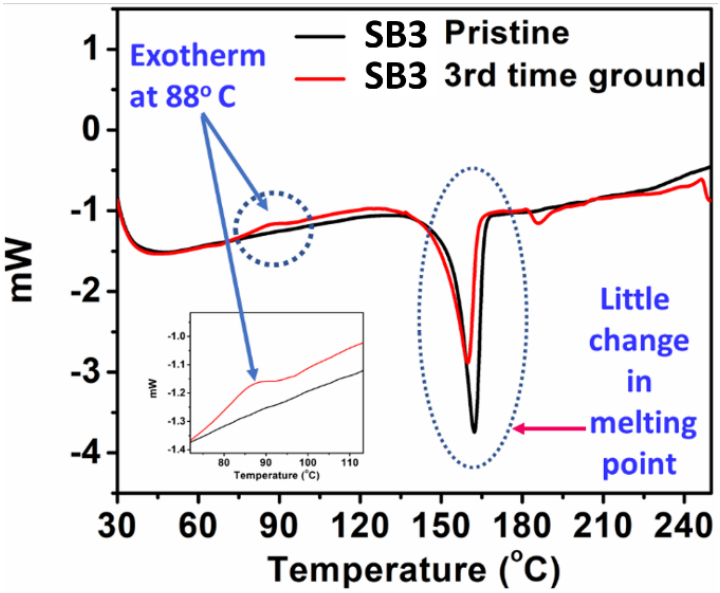

Figure 4.23 DSC for the 3rd time ground form of **SB3**

In addition, the specific contribution of non-covalent interactions to the packing could be quantitatively understood from the Hirshfeld surface analysis (Figure 4.24). The ratio of the % of C...H π and % of π-π (*p*) is 6.04, and the C...H π interactions contribute 30.2% of noncovalent interactions (Figure 4.24). Although the van der Waals (H···H) interaction is 63.8 % (Figure 4.24h), their contribution to the stabilization of the crystal packing may be small due to a low enthalpy of stabilization (~0.4-4 kJ/mol), but the fourteen C...H π interactions should be considered due to their high enthalpy (~10 kJ/mol).[55] Additionally, the total crystal packing energy of **SB3** is -444.7 kJ mol^{-1} (calculated from Mercury 2020.3.0), which is substantial enough to retain the molecular packing, and mortar/pestle grinding is inadequate to destroy the molecular packing completely. Rather, it rearranges to hold another molecular packing.

The MIEE property was even investigated through time-resolved spectroscopy as well. The excited state lifetime studies indicate a bi-exponential decay for both pristine and ground forms. The ground form has a shorter lifetime (τ_{avg} ~ 0.647 ns) than the pristine form (τ_{avg} ~ 0.834 ns), but the k_r for the ground form is augmented almost 2.58

times to that of the pristine form, further suggesting the MIEE effect (Figure 4.25, Table 4.4).

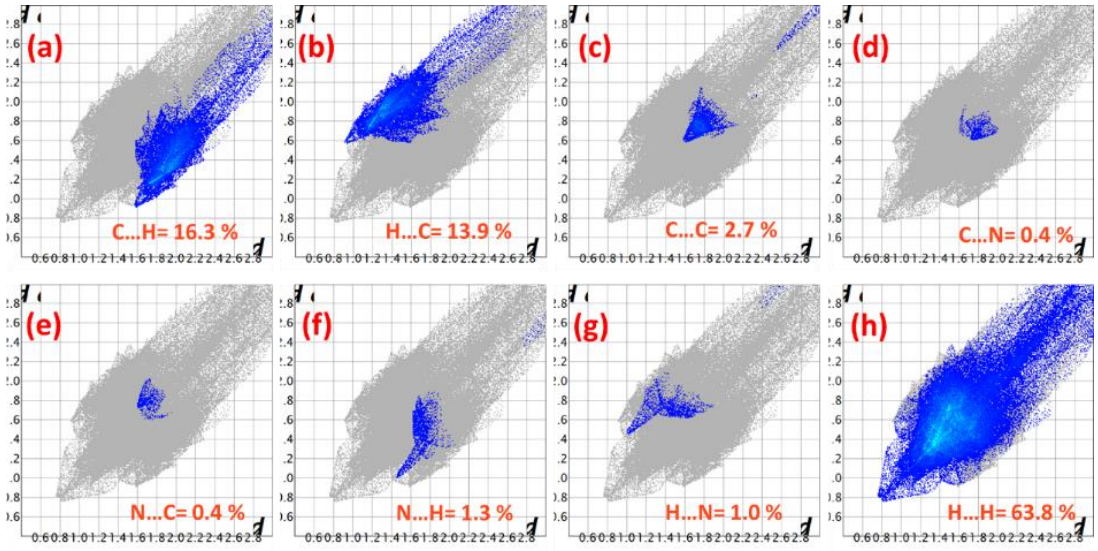

Figure 4.24 Hirshfeld surface and van der Waals and the non-covalent interactions to the packing for **SB3**

SEM images reveal that the pristine form has a well-organized sheet-like morphology that gets crumpled upon being ground, and the recovered form also does not fully recover to the original arrangements (Figure 4.26a, 4.26c).

4.3.4.1.2 Solid-state emission and mechanofluorochromism (MFC) from *D-π-D'* systems SB6 (IAT) & SB7 (IAP)

The compound **SB6** is significantly emissive in solids (absolute Φ_f = 20.11%) (Figure 4.27). Despite several attempts, we could not produce suitable single crystals of **SB6** for X-ray diffractions; therefore, we refrain from discussing the exact noncovalent interactions and their possible modulations under stimuli. However, differences in the powder X-ray diffraction (PXRD) pattern and Differential Scanning Calorimetry (DSC) studies assisted us in deciphering the possible causes. On grinding using a mortar/pestle, **SB6** displays a 23 nm mechanofluorochromic (MFC) redshift from 517 nm to 540 nm by transiting from its crystalline nature (approx. crystallinity 66.16 %, origin software-based calculations from PXRD pattern) to an amorphous state as found in the PXRD pattern (Figures 4.28a). Its original pristine emission is recovered after exposing low-boiling dichloromethane (DCM) solvent.

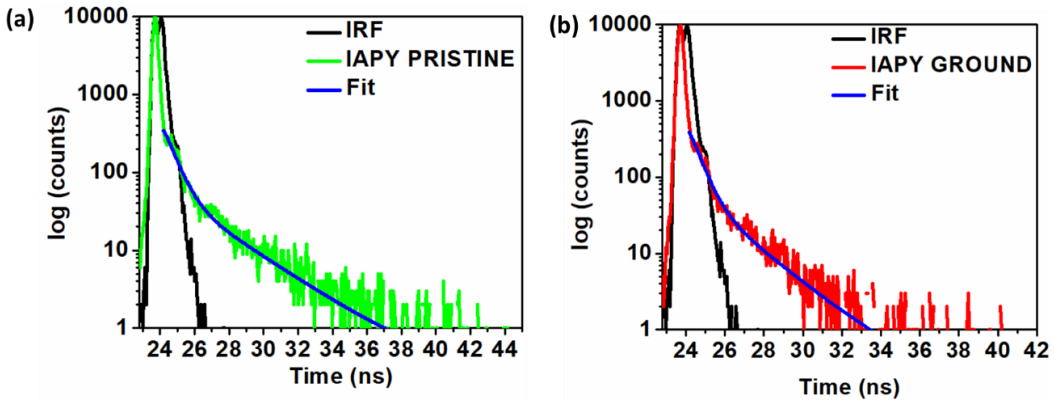

Figure 4.25 Decay profile of **SB3** (**IAPY**) for MIEE property

Table 4.4 Results of times-resolved studies for MIEE

Compound/Solvent	χ 2	λ_{em} max (nm)	τ_1	τ_2	τ_3	τ_4	$\alpha 1$	$\alpha 2$	$\alpha 3$	$\alpha 4$	$\tau_{avg.}$ (ns)	Φ_f (%)	$k_r(s^{-1})$ x 10^{-6}	$k_{nr}(s^{-1})$ x 10^{-6}
SB3 Pristine	1.012	517	0.6068	2.9607	-	-	0.9032	0.0967	-	-	0.8344	26.64	319.271	879.194
SB3 Ground	1.067	534	0.4983	2.1100		-	0.9079	0.0920		-	0.6467	53.32	824.493	721.818

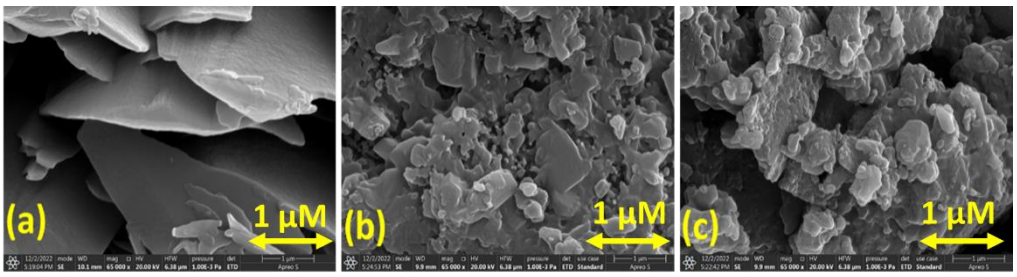

Figure 4.26 SEM images for **SB3** (a) pristine (b) ground (c) recovered

The DCM vapor facilitates regeneration of the crystalline nature (approx. crystallinity= 59.58%) (Figure 4.28a). This mechanical-force-induced emission shift is reversible and accompanied by an enhancement in quantum yield from Φ_f = 20.11% to 23.16% (Figure 4.27b). Notably, the MFC property of **SB6** can be repetitive up to ten times (Figure 4.28c). After the first cycle of reversibility, the diffraction signals become broader [larger average FWHM (Full Width Half Maxima)] for the recovered form of

SB6 than **SB6** pristine (Figure 4.28a). This broadness indicates looser molecular packing in the recovered sample than in the pristine form.[62]

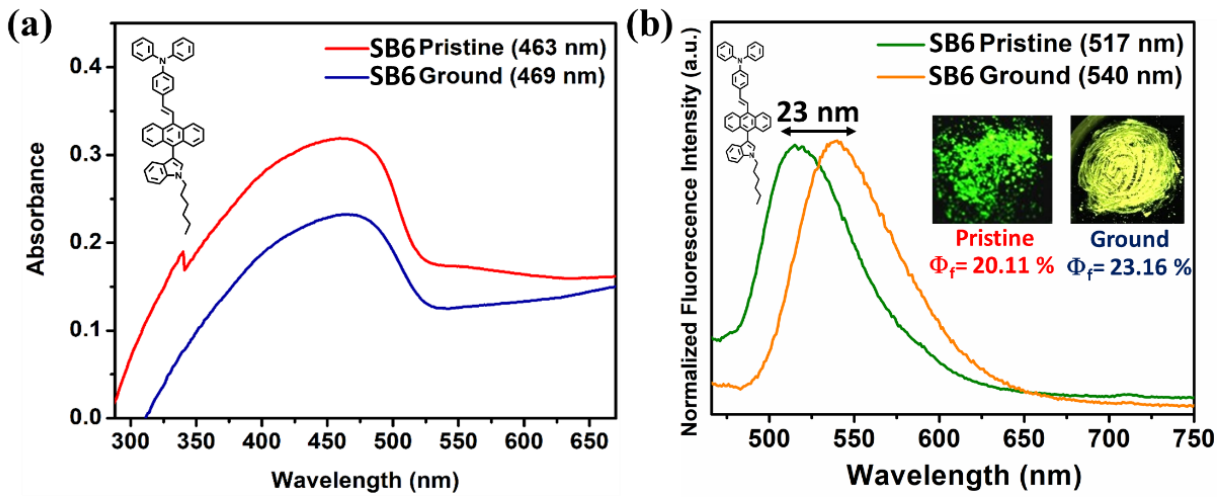

Figure 4.27 Mechanofluorochromic emission of **SB6** (a) absorbances, (b) emissions (images are captured under a 365-nm UV lamp)

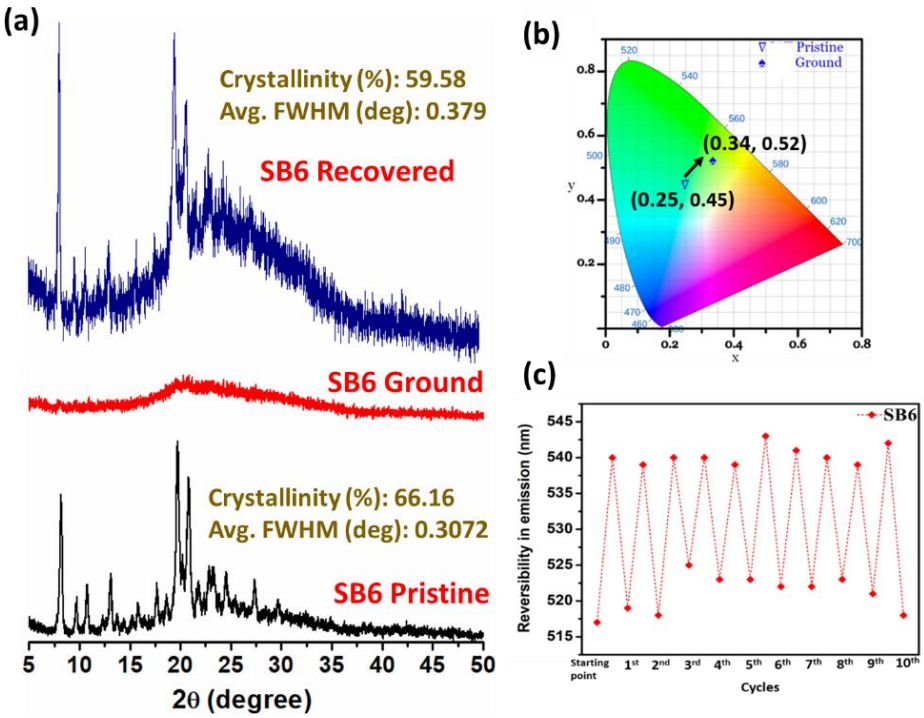

Figure 4.28 For MFC of **SB6** (a) PXRD patterns (b) CIE-1931 diagram (c) reversibility

Also, the crystallite in the recovered form is more strained than the pristine. In recovered form after 1st cycle, the diffractions at 2θ ~19°, 20°, 13°, and 8° are regenerated very well when other signals either reduced or disappeared (Figure 4.28a). After the 10th cycle, most possibly, the molecular packing is almost destroyed and unable to display

reversibility anymore. In general, a concomitant redshift is classically observed with the generation of an amorphous state, resulting in a decrease in the quantum yield.[63] Accordingly, **SB6** shows a usual trend to enhance emission by destroying the ordered lattice structure. The excited state planarity may cause enhanced emission upon applying mechanical force, and the excited-state configurations with more oscillator strength may display lower emission energy.[64-66] A subtle balance is required to tune the noncovalent intermolecular interactions in the solid, which enable facile amorphization and recrystallization under the respective stimuli.[63]

On the other hand, **the SB7** solid has a decent emission (absolute Φ_f = 2.66 %) (Figure 4.29b). Despite several attempts, we could not produce suitable single crystals of **SB7** for X-ray diffractions. Interestingly, **SB7** appeared remarkably delicate even with fingertip rubbing, displaying a 35 nm blue shift (red to yellow) with an enhanced intensity (Figure 4.29b).

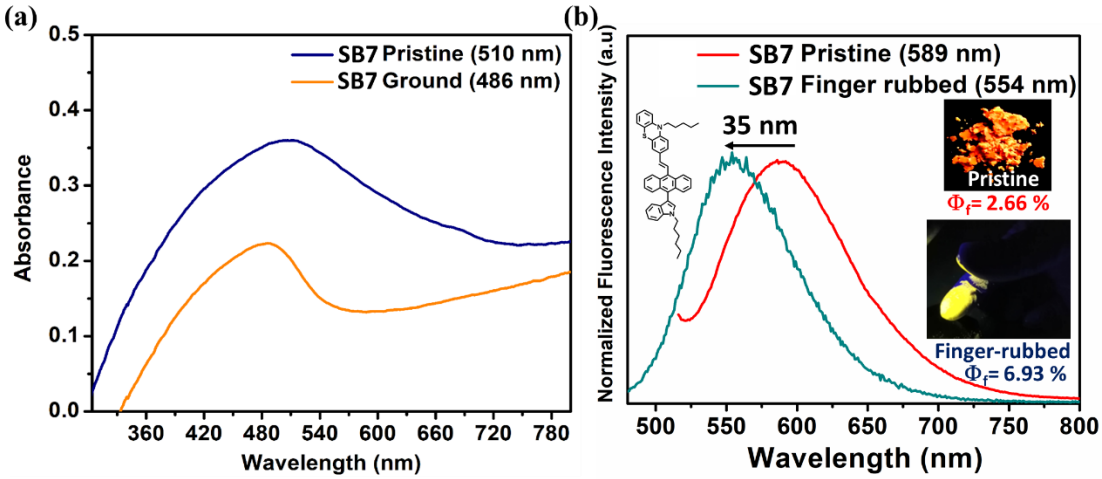

Figure 4.29 Mechanofluorochromic emission of **SB7** (a) absorbances, (b) emissions (images are captured under a 365-nm UV lamp)

The PXRD results showed a conversion from a less crystalline pristine state (approx. crystallinity: 15.88 %) to a more crystalline state (approx. crystallinity: 26.30 %) after applying mechanical force using a fingertip (Figure 4.29a, 4.30a). The enhancement in quantum yield (from Φ_f = 2.66% to 6.93%) can be explained due to the crystalline-induced enhanced emission (Figure 4.30a). A gentle scratch with a spatula is enough for the emission shift and quantum yield enhancement (Figure 4.30c). However, the mechanical-force-induced emission shift could not be fully recovered after DCM

treatment; instead, it displays an intermediate emission with the signal at 572 nm, indicating reaching a transition phase, not in the original.

A relatively heavier S-atom in **SB7** induces a butterfly-shaped non-planar phenothiazine ring. Further, two alkyl chains and the *N*/*S* atoms tend to create numerous sensitive supramolecular interactions in pristine solids. The twisted structure would also facilitate tuning the supramolecular interactions to achieve a decent emission in the solid. A subtle mechanical force perhaps rearranges the supramolecular interactions, improving the periodic arrangement of molecules in the **SB7** solid, leading to a better crystallinity, as pointed out before in the PXRD pattern. In addition, the disparity in crystal lattice strain might elucidate the high MFC sensitivity of the **SB7** pristine.[65,66]

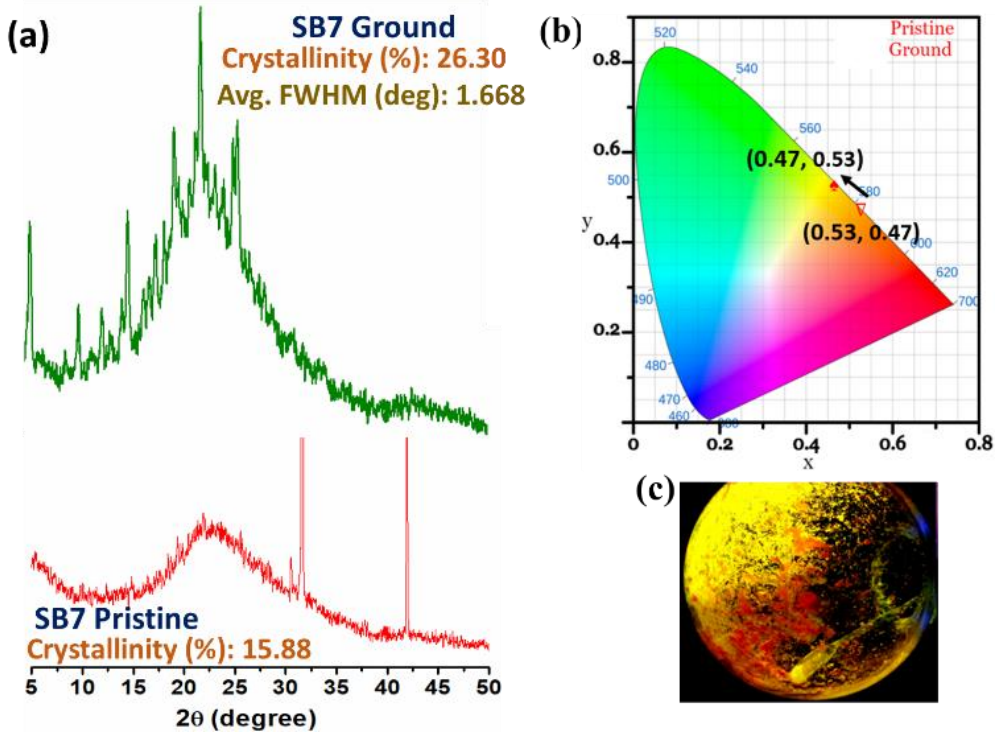

Figure 4.30 For MFC of **SB7** (a) PXRD patterns (b) CIE-1931 diagram (c) a gentle scratch with a spatula to switch emission

Broad signal and a few sharp diffractions at higher angles in the PXRD pattern (Figure 4.30a) indicate inhomogeneously strained crystallites. Upon rubbing with a fingertip, the crystallinity feature is enhanced, as estimated from the PXRD studies; hence, we expect a rise in crystallite size. Further, crystallite strain in the fingertip-

rubbed sample will reduce and adopt a better homogeneity as a preferred crystallite state. Furthermore, a notable diffraction at a small angle (2θ ~5°) indicates creating a long-range molecular order of the **SB7** ground sample, gaining a better crystallinity upon grinding. Thus, the pressure/mechanical sensitivity of **SB7** pristine can be elucidated. An additional alkyl chain and nonplanar phenothiazine ring in **SB7** contribute to the MFC sensitivity compared to **SB6**.Further, DSC studies confirmed the mechanical force applied phase transition for **SB6** and **SB7** (Figures 4.31a-b). For **SB6** pristine sample, only an endothermic signal appeared at 199 °C for melting, but the ground sample indicated an exothermic crystallization at 99 °C apart from the melting signal at 189 °C and a glass transition baseline shift at 54 °C. This confirms that pristine and ground **SB6** samples hold different states/phases from other molecular packing arrangements. On the other hand, the ground form of **SB7** displayed an exothermic hump at ~82 °C apart from the melting point endotherm, indicating a different phase transition compared to the pristine state (Figures 4.31c-d).

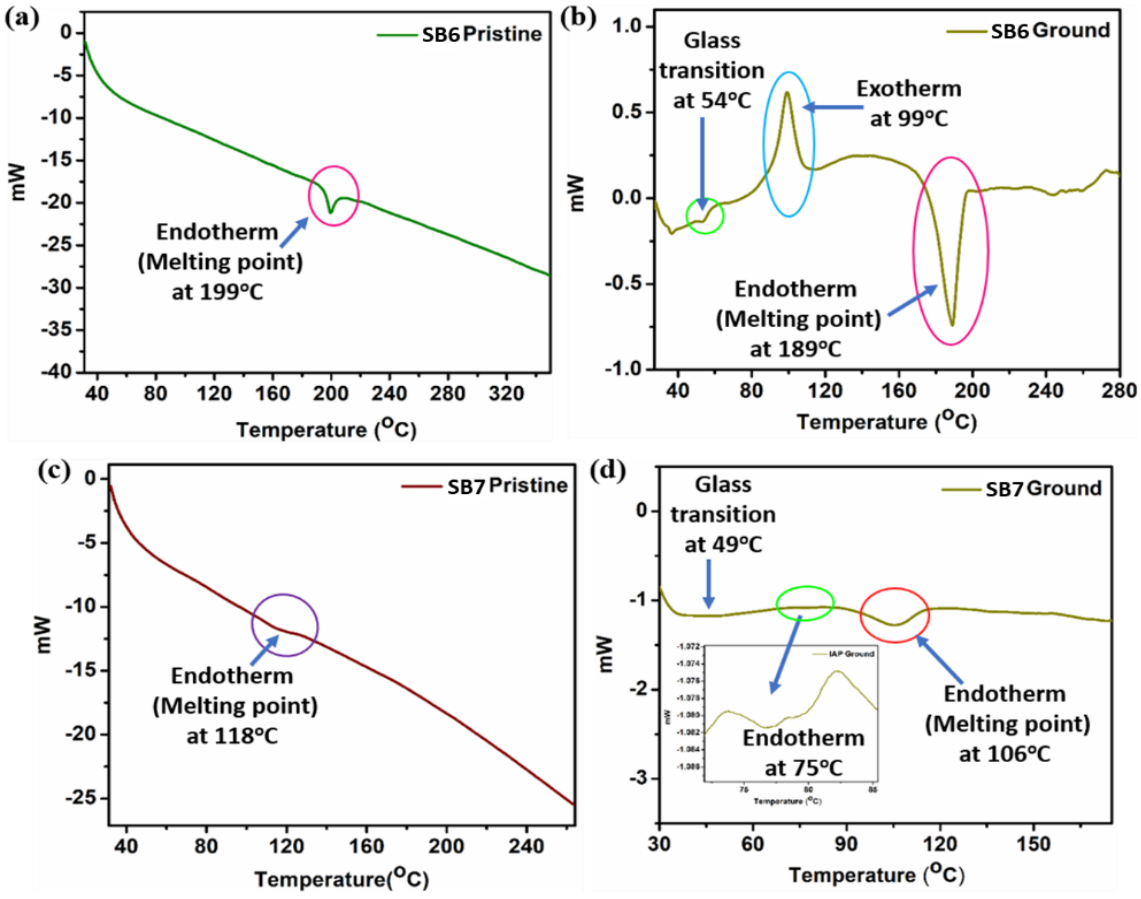

Figure 4.31 DSC curves for **SB6** (a) pristine form (b) ground form; DSC curves for **SB7** (c) pristine (d) ground

Furthermore, the morphology of the pristine and ground samples for **SB6** and **SB7** was determined using Scanning Electron Microscopy (SEM). The **SB6** pristine holds a sheet-like smooth surface that disappears and becomes random after grinding (Figures 4.32a-b), whereas the layered structure of **SB7** pristine was lost once ground (Figures 4.32c-d). Such morphological changes indicate variation in the pristine and ground sample's molecular arrangement, possibly responsible for exhibiting various solid-state emission features.

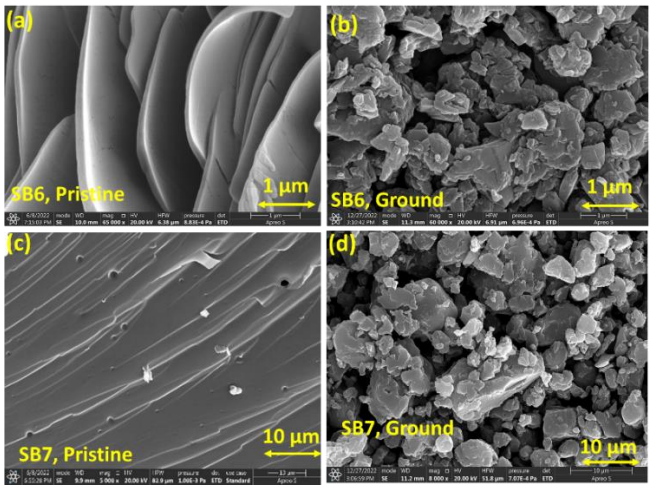

Figure 4.32 SEM images

The MFC emission switching with enhanced efficacy was also designated from the time-correlated single photon counting (TCS-PC) studies. The excited state decay profiles for **SB6** pristine and ground forms were fitted biexponentially (Figure 4.33, Table 4.5), leading to a slight decrement in the lifetime for the ground form (0.52 ns) compared to its pristine state (0.65 ns) (Figure 4.33). However, the radiative rate constant [k_r (10^8 s^{-1})] was higher for the ground form (4.45) than the pristine form (3.09). This result further supports the mechanical force-induced emission enhancement for **SB6**. Interestingly, the **SB7** fingertip-ground sample showed a rise in the lifetime of 1.63 ns [k_r (10^7 s^{-1}) = 4.25] than the pristine sample, showing a lifetime of 1.43 ns [k_r (10^7 s^{-1}) = 1.86]. Thus, a significant 2.3 times increment of kr (Table 4.5), realized for the SB7, explains a much better sensitivity and response than the **SB6** sample.

4.3.4.1.3 Solid-state acidofluorochromism (SSAC) from *D-π-A* system SB3

The pyridinyl N-atom of **SB3** offers a fascinating solid-state emission switching upon exposure to acid fumes (5-10 min) with a 75 nm redshift (517 nm to 592 nm), with

a diminished emission efficacy (Φ_f =1.16%) (Figures 4.34a-b, 4.36a). The single crystal generation for the **SB3H** was challenging; however, the DFT studies were performed to find the optimized geometry, which revealed a better planarity development at each twisted site at the S_1 state (Figure 4.35).

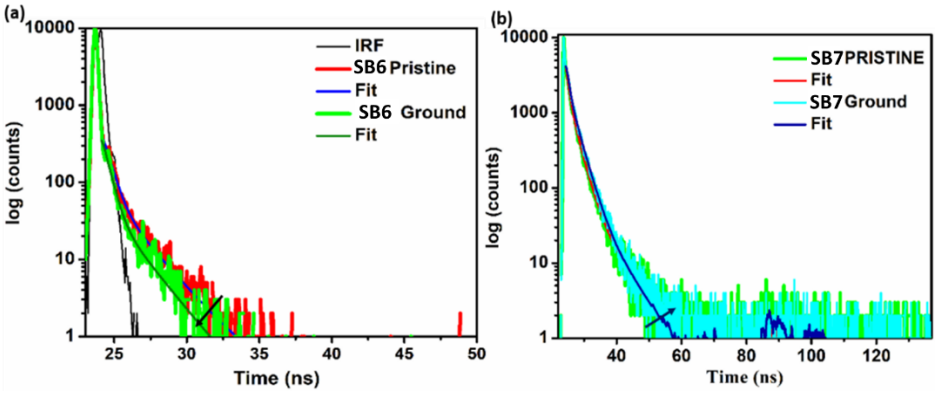

Figure 4.33 MFC decay profile (a) **SB6** (b) **SB7**

Table 4.5 Summary of the results of time-resolved fluorescence studies for MFC of **SB6** and **SB7**

Sample	$\lambda_{em\ max}$ (nm	τ_1	τ_2	τ_3	$\alpha 1$	$\alpha 2$	$\alpha 3$	$\tau_{avg.}$ (ns))	χ 2	Φ_f (%)	k_r(s^{-1}) x 10^6	k_{nr}(s^{-1}) x 10^9
IAT Pristine	517	0.4687	2.0401	-	0.8838	0.1162	-	0.65	1.004	20.11	309.3846	1229.0769
IAT Ground	540	0.3984	1.8439	-	0.9162	0.0838	-	0.52	1.006	23.16	445.3846	1477.6923
IAP Pristine	589	2.3524	0.7124	6.6161	0.3609	0.6183	0.0208	1.43	1.013	2.66	18.6013	680.6993
IAP Ground	554	0.7529	2.7093	9.8024	0.5834	0.4078	0.0087	1.63	1.029	6.93	42.5153	570.9815

It results in conjugation improvement and enhanced planarity, bringing molecules closer to cause π-stacking, leading to emission quenching. Again, the original deprotonated state could not be achieved simultaneously on exposure to the base ic (Et3N) vapor. The base-treated **SB3H** emits yellow at 544 nm (Φ_f =7.24%) (Figure 4.34a-b), designating a different packing mode. There were dissimilarities in the PXRD patterns between protonated and pristine samples, where the crystallinity of pristine was significantly decreased (Figure 4.34c). The surface morphology change was manifested in SEM analysis (Figure 4.36). Further, excited state lifetime profiles disclose

that **SB3H** has a comparatively longer lifetime (τ_{avg} ~1.024 ns) than the base-fumed form (τ_{avg} ~0.581 ns). The k_r (10^6 s^{-1}) value is inferior for **SB3H** (11.331) than **IAPY** pristine (319.271), possibly due to increased π-π stacking between planar **SB3H** molecules at S_1 (Figure 4.37, Table 4.6).

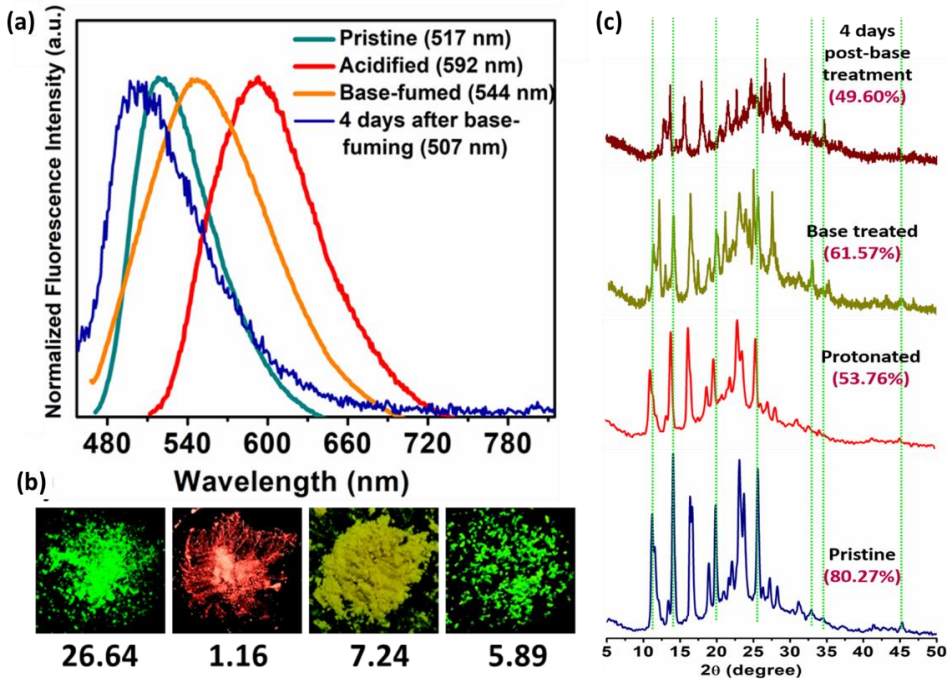

Figure 4.34 For **SB3**; (a) emissions due to solid state acidofluorochromism (SSAC) (b) pictures taken under UV-365 nm bulb, the quantum yields are written below each picture (c) changes in PXRD pattern for **SB3** due to acidofluorochromism

Excitingly, the emission is returned to green (λ_{max}=507 nm, Φ_f =5.89%) after 4 days on its own for the base treated sample that emitted at 544 nm initially, and the PXRD patterns appeared to be slightly broader with a difference in diffractions, indicating a different molecular arrangement (Figure 4.34c). Notably, no phase change was observed in the DSC (Figure 4.36b).

The auto-reversible nature must appear from the presence of acidic water vapor during acid vapor fumigation. It might cause partial dissolution on the crystal surfaces through the condensation process. A similar process can be perceived in response to base vapor, and thus, changes in crystallinity are anticipated. All these outcomes indicate that **SB3H** crystals can attain diverse molecular arrangements.

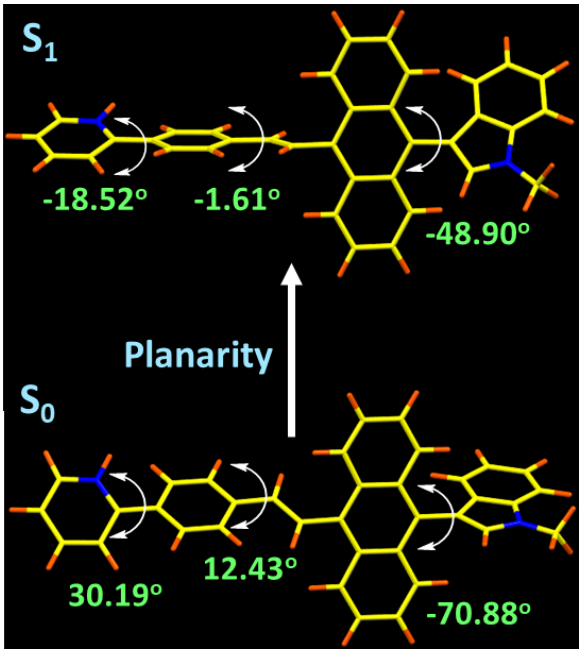

Figure 4.35 DFT optimized structures for **SB3H**

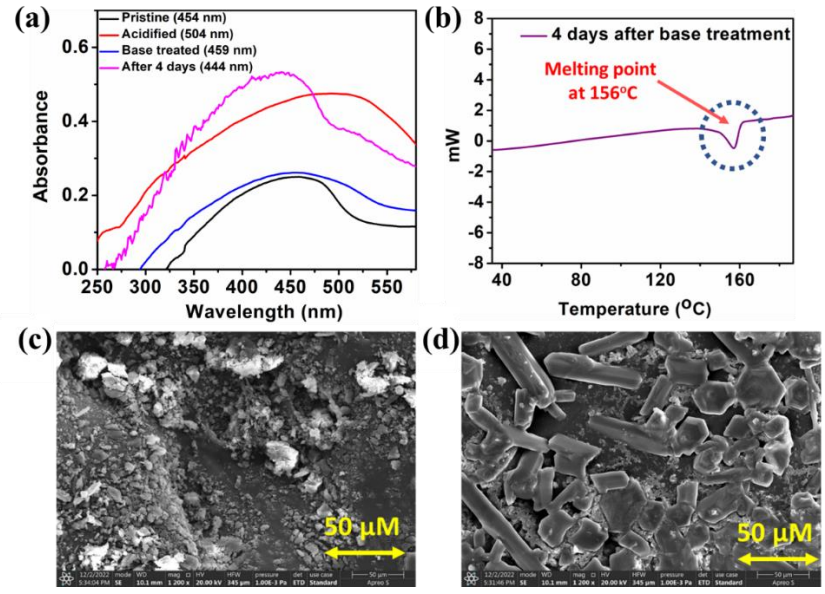

Figure 4.36 For **SB3**; (a) absorbances for **SB3** SSAC (b) DSC for the 4th day post to base treatment' form of **SB3**; SEM images for **SB3** (c) acid-fumed (d) base-fumed

The pristine form's intramolecular interactions may be altered in the protonated form as the chemical environment will change once the nitrogen is protonated. On base exposure, the deposition of triethylamine hydrochloride salt over the crystals will be hard to remove through the fumigation process thus, the deposited salt layer also may contribute to emission quenching.

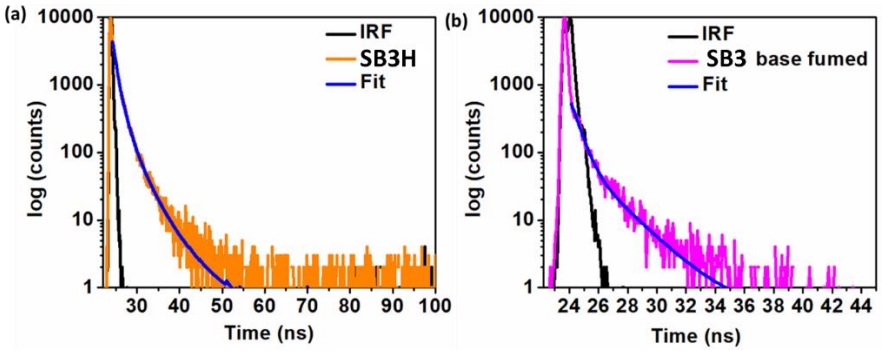

Figure 4.37 Decay profile for **SB3** (a) acid-fumed (**SB3H**) (b) base-fumed

Table 4.6 Results of times-resolved studies, SSAC of **SB3**

Compound/Solvent	χ 2	$\lambda_{em\ max}$ (nm)	τ_1	τ_2	τ_3	τ_4	$\alpha 1$	$\alpha 2$	$\alpha 3$	$\alpha 4$	$\tau_{avg.}$ (ns)	Φ_f (%)	k_r(s^{-1}) x 10^{-6}	k_{nr}(s^{-1}) x 10^{-6}
SB3H	1.000	530	0.6004	1.4100	3.449	-	0.6269	0.3189	0.0531	-	1.0237	1.16	11.331	965.517
SB3 base fumed	1.058	539	0.5186	2.1016			0.9098	0.0908			0.5806	5.89	101.447	1620.909

4.3.4.2 Dual State Emission (DSE) properties and Solvatofluorochromic (SFC) features

An organic molecule, conserving its emission in both solids and fluids, is recognized as DSEgens.[7,67] DSEgens with solvatochromic features are relatively sporadic in the literature.[68]

4.3.4.2.1 Dual State Emission (DSE) properties and solvatofluorochromic (SFC) features from SB6 and SB7 *D-π-D'*system

However, solvents with different polarities [polarity scale E_T (30)] were initially screened to investigate the DSE and SFC nature of **SB6** and **SB7**. Efficient DSE-gen should have intact emissions in nonpolar and polar solvents displaying SFC. Both were emissive in nonpolar and polar solvents, and the emission was redshifted with the increased polarity. **SB6** has a subtle 33 nm solvatochromic redshift from hexane to DMF, but **SB7** displays a 91 nm solvatochromic redshift. The **SB6** reveals strong green emission ($\lambda_{max.}$ = 517 nm; Φ_f = 62.78 %) in hexane (nonpolar) and yellow (λ_{max} = 550 nm; Φ_f = 14.94

%) in DMF (polar) (Figures 4.38a-b), while **SB7** also emits green in hexane ($\lambda_{max.}$ = 523 nm; Φ_f = 15.40 %) but red (λ_{max} = 614 nm; Φ_f = 3.99 %) in DMF (Figures 4.38c-d). **SB7** shows a slightly better Stokes shift in hexane but a significantly higher Stokes shift in DMF than **SB6** (Figure 4.38e, Table 4.7). The appearance of a more significant Stokes shift illustrates efficient emissions in solution. The relatively poor Φ_f for **SB7** can be described as two long-chain alkyl groups and heavier S-atom. This emission Φ_f slightly varies with polarity for **SB7,** while significant variation was observed for **SB6** (Figure 4.38f).[7,69]

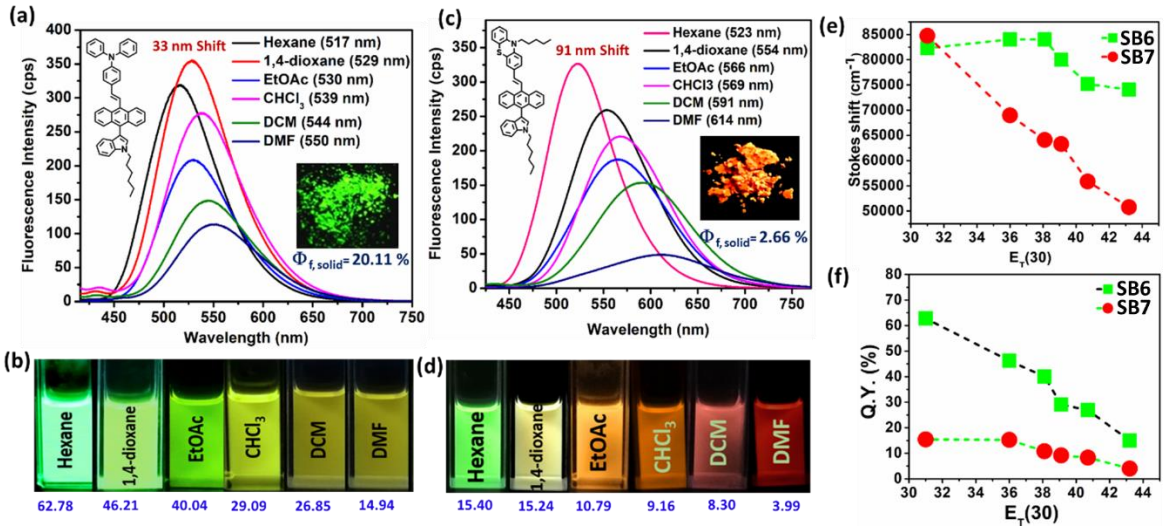

Figure 4.38 Emissions in solvents in 10^{-5} M concentration of (a) **SB6** (c) **SB7**; images captured under a UV-365 nm lamp for (b) **SB6** (d) **SB7**; The inset images show their emission intensity in the solid. (e) Stokes shift *vs* $E_T(30)$ values (f) emission efficacy vs ET_{30} (Q.Y. stands for relative quantum yield (Φ_f% and written in blue color)

However, unaffected absorption spectra for both these probes under different polarities indicate no effect in the ground state under different environments (Figures 4.39a-b). Notably, we notice **SB6** and **SB7** emitting at λ_{max} (nm) 517 and 589 in the solid state (Figures 4.38a-b insets; emission spectra are discussed earlier).

Further, in time-resolved fluorescence studies, the DSEgen behavior was specified. **SB6** and **SB7** retain a shorter lifetime (ns) of 0.063 and 0.083 in hexane but become longer, i.e., 1.051 and 3.13, respectively, in DMF. The k_r (radiative rate constant) and k_{nr} (non-radiative rate constant) are well-fitted to the observed results (Figures

4.40-4.41, Table 4.8). **SB6** and **SB7** experience superior k_r values in hexane, and consecutively, k_r decreased with the high polarity of the solvent.

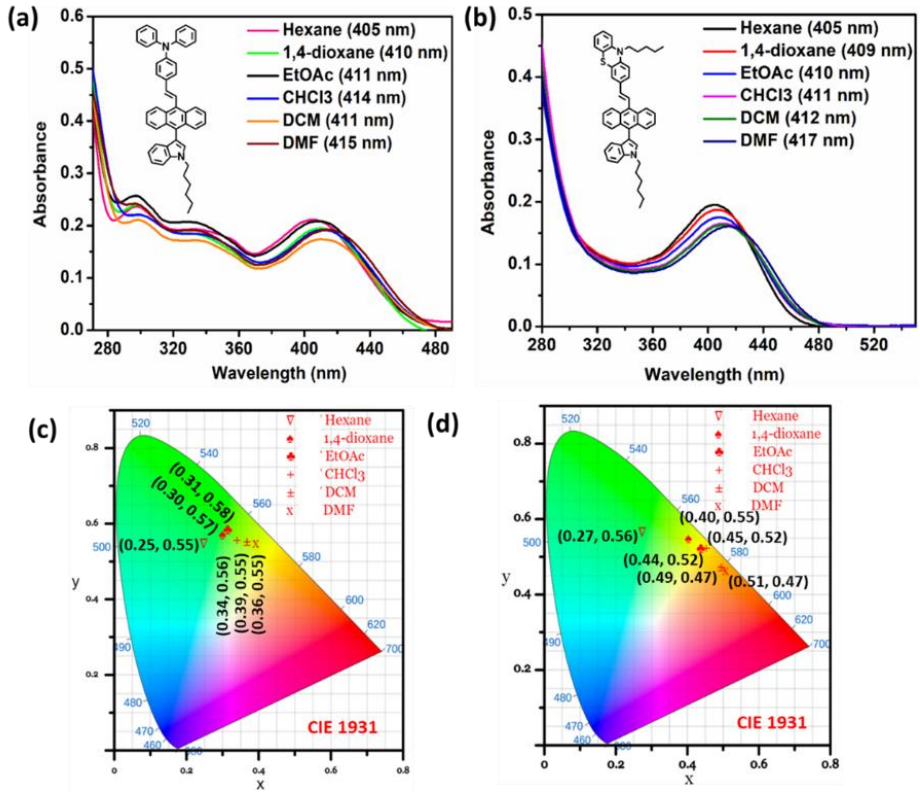

Figure 4.39 Absorbance in solvents (10^{-5} M) (a) **SB6** (b) **SB7**; CIE diagram for emissions of (c) **SB6** (d) **SB7**

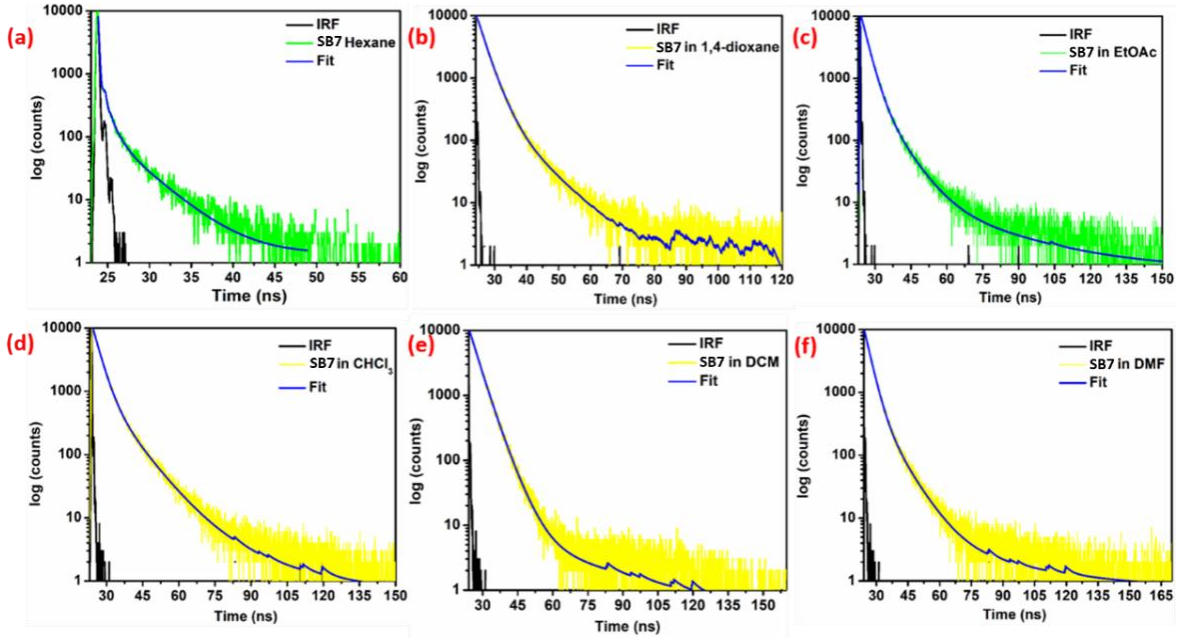

Figure 4.40 Lifetime decay profiles for **SB7** in different solvents

Table 4.7 The DSE-genic and solvatochromic properties are tabulated herein

Compounds with SSE	Solvent	ET_{30}	$\lambda_{abs.max}$ (nm)	$\lambda_{em.max}$ (nm)	CIE 1931 coordinates (x,y)	Stokes shift (cm^{-1})	DSE-shift (nm)	Solvatochromic shift (nm)	Φ_f (%)
SB6 with $\lambda_{em.max}$ (Solid) = 517 nm	Hexane	31.0	405	517	0.25, 0.55	82285.714	0	0	62.78
	1,4-dioxane	36.0	410	529	0.30, 0.57	84033.613	12	12	46.21
	EtOAc	38.1	411	530	0.31, 0.58	84033.613	13	13	40.04
	$CHCl_3$	39.1	414	539	0.34, 0.56	80000.00	22	22	29.09
	DCM	40.7	411	544	0.36, 0.55	75187.969	27	27	26.85
	N,N-DMF	43.2	415	550	0.39, 0.55	74074.074	33	33	14.94
SB7 with $\lambda_{em.max}$ (Solid) = 589 nm	Hexane	31.0	405	523	0.27, 0.56	84745.762	-66	0	15.40
	1,4-dioxane	36.0	409	554	0.40, 0.55	68965.517	-35	31	15.24
	EtOAc	38.1	410	566	0.44, 0.52	64102.564	-23	43	10.79
	$CHCl_3$	39.1	411	569	0.45, 0.52	63291.139	-20	46	9.16
	DCM	40.7	412	591	0.49, 0.47	55865.921	2	68	8.30
	N,N-DMF	43.2	417	614	0.51, 0.46	50761.421	25	91	3.99

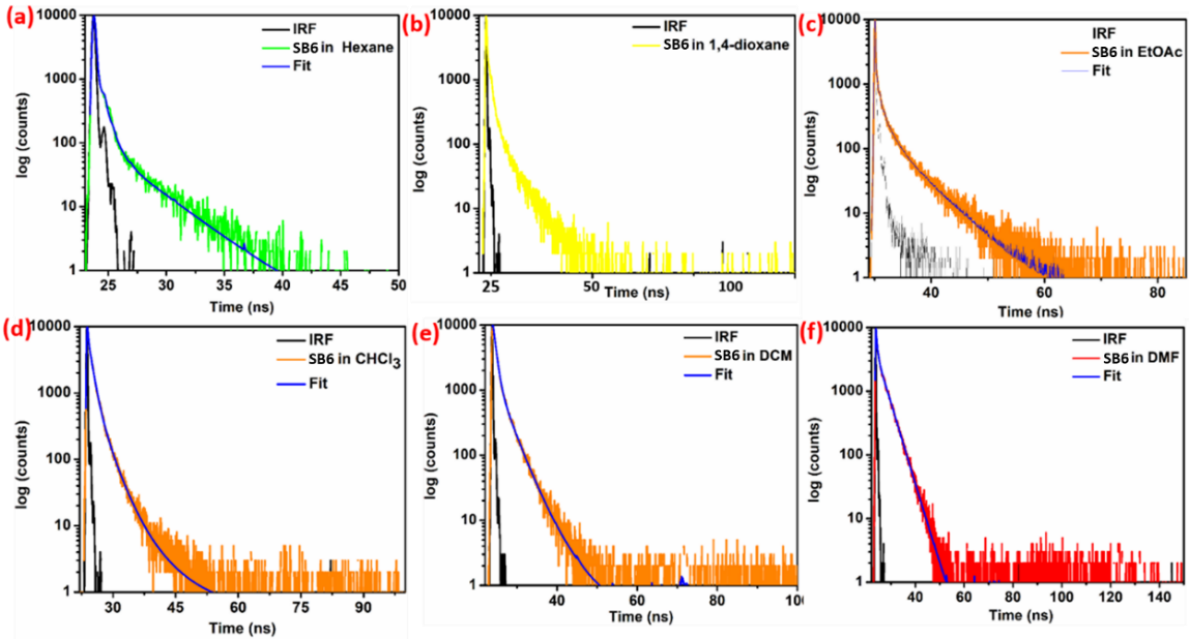

Figure 4.41 Lifetime decay profiles for **SB6** in different solvents

The cause for diverse emission efficiency from **SB7** can be elucidated by considering excited state planarity, f_{em}, RMSD, and the HOMO-LUMO energy gap in certain solvents.

Table 4.8 Summary of the results of time-resolved fluorescence studies with different solvents for **SB6** and **SB7**

Compound/ Solvent	$\lambda_{em\ max}$ (nm)	τ_1	τ_2	τ_3	τ_4	$\alpha 1$	$\alpha 2$	$\alpha 3$	$\alpha 4$	$\tau_{avg.}$ (ns)	$\chi 2$	Φ_f (%)	$k_r(s^{-1})$ x 10^{-6}	$k_{nr}(s^{-1})$ x 10^{-6}
SB6 /Hexane	517	0.0647	0.0639	-	-	0.9999	0.0001	-	-	0.0637	1.012	62.78	9855.5729	5843.0141
SB6/ Dioxane	529	0.8740	0.0784	4.1012	-	0.0607	0.9349	0.004	-	0.1804	1.067	46.21	2561.5299	2981.7073
SB6/ EtOAc	530	0.5925	3.2531	0.0600	-	0.0184	0.0012	0.9804	-	0.2545	1.039	40.04	1573.2809	2355.9921
SB6/ $CHCl_3$	539	0.15561	0.93201	6.0608	2.3645	0.5843	0.3505	0.002	0.0628	0.5806	1.0175	29.09	501.0334	1221.3228
SB6/ DCM	544	0.6207	1.8644	3.9976		0.0181	0.0173	0.0397		0.9039	1.012	26.85	297.0461	809.2709
SB6/ DMF	550	0.8162	0.8107	3.4130		0.4717	0.4831	0.0109		1.0508	1.019	14.94	0.1422	0.8095
SB7/ Hexane	523	0.9005	3.7764	0.0685		0.0096	0.0018	0.9886		0.083	1.085	15.40	1855.4216	10192.771
SB7/ Dioxane	554	1.1012	1.0984	9.4100	2.9313	0.4983	0.4976	0.0001	0.0039	1.11	1.070	15.24	0.1373	0.7636
SB7/ EtOAc	566	0.0629	7.1335	29.8626	2.6171	0.5678	0.034	0.001	0.3889	1.31	1.15	10.79	82.3664	680.9923
SB7/ $CHCl_3$	569	2.8678	8.7301	25.1591		0.8969	0.1011	0.0019		3.50	1.067	9.16	26.1714	259.5429
SB7 /DCM	591	3.3897	35.9403	5.4249		0.8306	0.0008	0.1687		3.76	1.036	8.30	22.0745	243.8829
SB7 /DMF	614	2.7442	7.9271	39.5027		0.9286	0.0709	0.0005		3.13	1.0685	3.99	12.7476	306.7412

TD-DFT studies were conducted for nonpolar (hexane) and polar (DMF) solvents to gain a deeper insight into these quantum chemical descriptors. In hexane and DMF, the excited state planarity is improved significantly at both twisted sites of the **SB7** molecule. Since the excited-state conformation largely determines molecular emission properties, such a favored planar geometry will offer bright emissions in solution.[14] Interestingly, the higher RMSD value in DMF than in hexane would prefer a higher non-

radiative rate, thus **SB7** emits with lesser Φ_f in DMF. The reduced energy gap between the HOMO-LUMO contributes to the low energy emission of **SB7** in DMF (Figures 4.42-4.43) .[11]

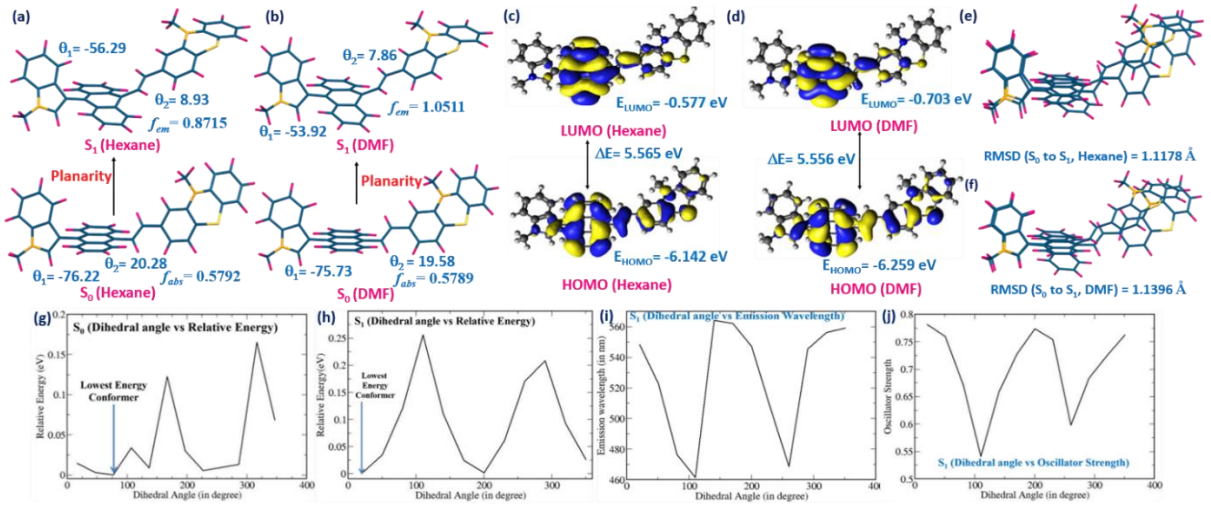

Figure 4.42 TD-DFT optimized structures for **SB7** in (a) hexane (b) DMF; HOMO-LUMO distribution of **SB7** in (c) hexane (d) DMF; RMSD of **SB7** in (e) hexane (f) DMF. The chain length is cut short as it does not contribute to differences; for **SB7** (g) dihedral angle vs. relative energy plot at S_0 state (h) dihedral angle vs. relative energy plot at S_1 state (i) dihedral angle vs. emission wavelength plot at S_1 state (j) dihedral angle vs. oscillator strength plot at S_1 state

However, **SB7**'s excited state configuration with high oscillator strength still favors the emission with decent intensity.[64-66] Similar to **SB7,** the achievement of excited-state planarity in **SB6** is also very high in hexane and DMF. However, a higher RMSD value and stronger emission oscillator strength (f_{em}) in DMF than in hexane control judiciously and results in a weaker but visually detectable emission from **SB6**. The reduced HOMO-LUMO energy gap with the increased polarity causes a redshift with lesser Φ_f (Figure 4.44, Table 4.8).

Thus, **SB7** is recognized as a rarely realized dual-state *red emitter* (Figures 4.37c-d).[70] Additionally, the redshifted emission in **SB7** was clarified by performing a dihedral angle scanning within the optimized molecular structure (Figures 4.42g-4.42j).[13]

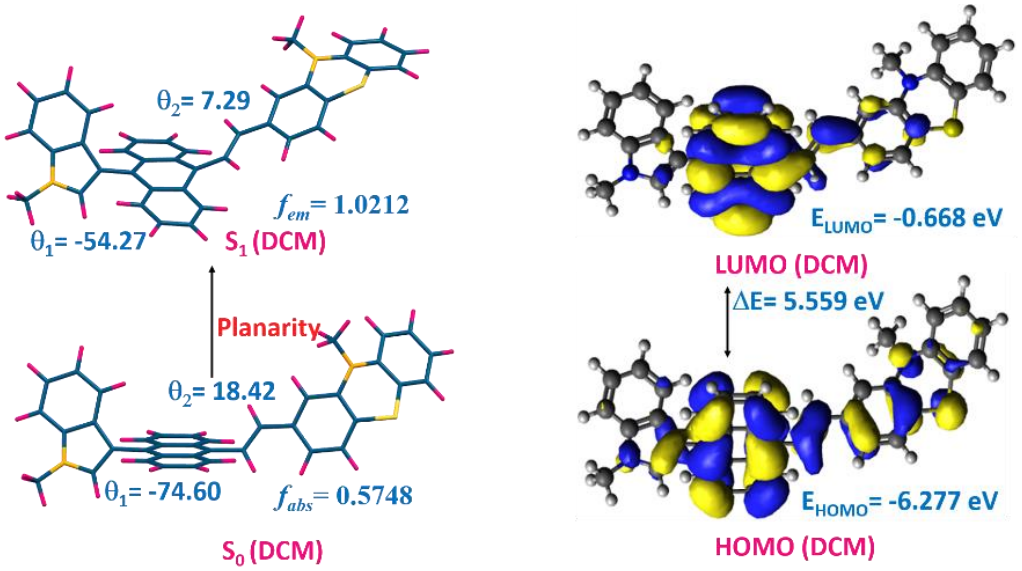

Figure 4.43 TD-DFT optimized structures for **SB7** in DCM and the HOMO-LUMO distribution

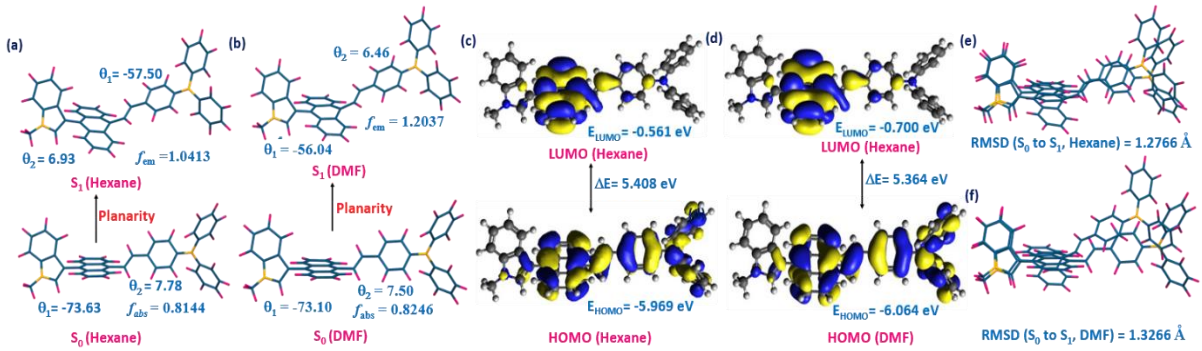

Figure 4.44 TD-DFT optimized structures for **SB6** in (a) hexane (b) DMF; HOMO-LUMO distribution of **SB7** in (c) hexane (d) DMF; RMSD of **SB6** in (e) hexane (f) DMF

Moving the θ_2 (dihedral angle) from 90° to 0° in the excited state S_1, the molecule **SB7** leads to occupy the low-energy conformer, possessing stronger oscillator strength and redshifted emission. The ups and downs of the critical parameters f_{em} and emission switching with dihedral angle are shown in Figures 4.42g-4.42j. This theoretical observation supported well the polarity-based SFC variation.

The molecule has no scope to possess the charge transfer state (as observed in Molecular orbital analysis). Still, the red-shifted solvatofluochromism was clarified by generating Natural Transition Orbitals (NTOs) in hexane and DMF for both **SB7** and **SB6**. We observed a perfect match (~97%) of the hole as HOMO and electrons as LUMO. Interestingly the LUMO (i.e., π* orbital) is more stable with an increase in the

polarity of the solvent. Thus, the HOMO-LUMO gap decreases with a polarity enhancement, leading to a red-shifted emission (Figures 4.45, 4.46, Tables 4.9-4.10).

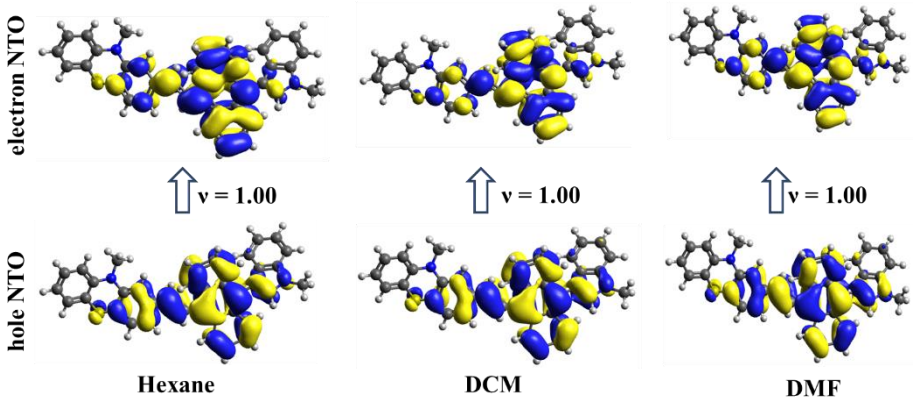

Figure 4.45 TD-DFT optimized NTOs for **SB7** in hexane and DMF (HOMO and LUMO calculated for Excited state S_1 geometry; hole NTO is HONTO and electron NTO is LUNTO)

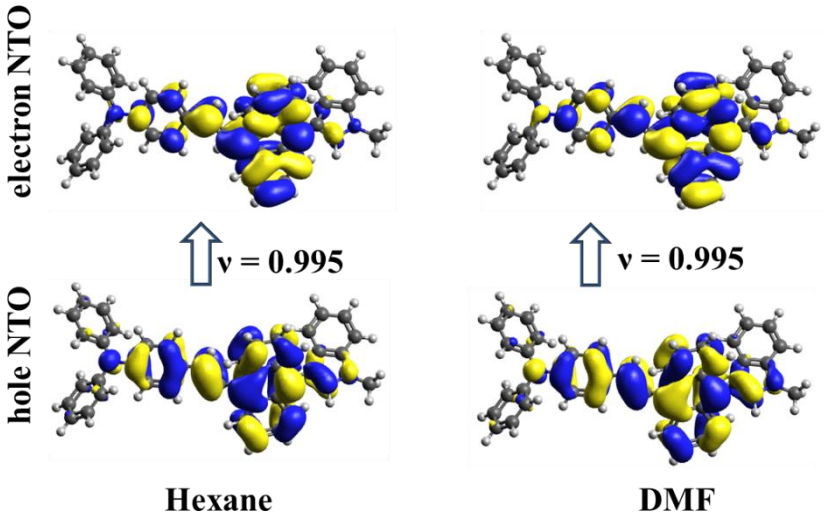

Figure 4.46 TD-DFT optimized NTOs for **SB6** in hexane and DMF (HOMO and LUMO calculated for excited state S_1 geometry; hole NTO is HONTO and electron NTO is LUNTO)

4.3.4.2.2 Dual State Emission (DSE) properties, solvatofluorochromic (SFC) features and whitish emission in solvents from SB3, a *D-π-A* system

The **SB3** displays commendable green emission (λ_{max}=517 nm, Φ_f =20.22%) in hexane (nonpolar) and yellowish green emission (λ_{max}=526 nm, Φ_f =9.79%) in *N,N*-dimethylformamide (DMF, polar).

Table 4.9 Summary of the results of TD-DFT studies for dual-state emission

Molecule	Solvent	ET_{30}	$\theta_1(S_0)$	θ_2 (S_0)	$\theta_1(S_1)$	θ_2 (S_1)	f_{abs}	f_{em}	$\Delta E_{HOMO-LUMO}$ (eV)	RMSD (Å)
SB7	Hexane	31.0	-76.22	20.28	-56.29	8.93	0.5792	0.8715	5.565	1.1178
	DCM	40.7	-74.60	18.42	-54.27	7.29	0.5748	1.0212	5.559	1.1396
	DMF	43.2	-75.73	19.58	-53.92	7.86	0.5789	1.0511	5.556	1.1396
SB6	Hexane	31.0	-73.63	7.78	-57.50	6.93	0.8144	1.0413	5.408	1.2766
	DMF	43.2	-73.10	7.50	-56.04	6.46	0.8246	1.2037	5.364	1.3266

Table 4.10 Summary of the results of NTO studies (HOMO and LUMO calculated for Excited state S_1 geometry)

Compound	Solvent	HOMO(π)	LUMO(π*)	ΔE_{HL} (eV)	Relative Energy (eV)
SB6	Hexane	-5.969	-0.561	5.408	-0.375
	DMF	-6.064	-0.7	5.364	-0.868
SB7	Hexane	-5.425	-1.312	4.113	-0.376
	DCM	-5.473	-1.451	4.022	-0.664
	DMF	-5.482	-1.476	4.006	-0.864

The appearance of larger stokes shifts in solvents further signifies the emissive capability of **SB3** (Figure 4.47, Table 4.11) with the reduced emission efficacy in polar solvents. However, the change in the absorbance λ_{max} under different solvent polarities was subtle, signifying an unchanged ground state (Figure 4.47a).

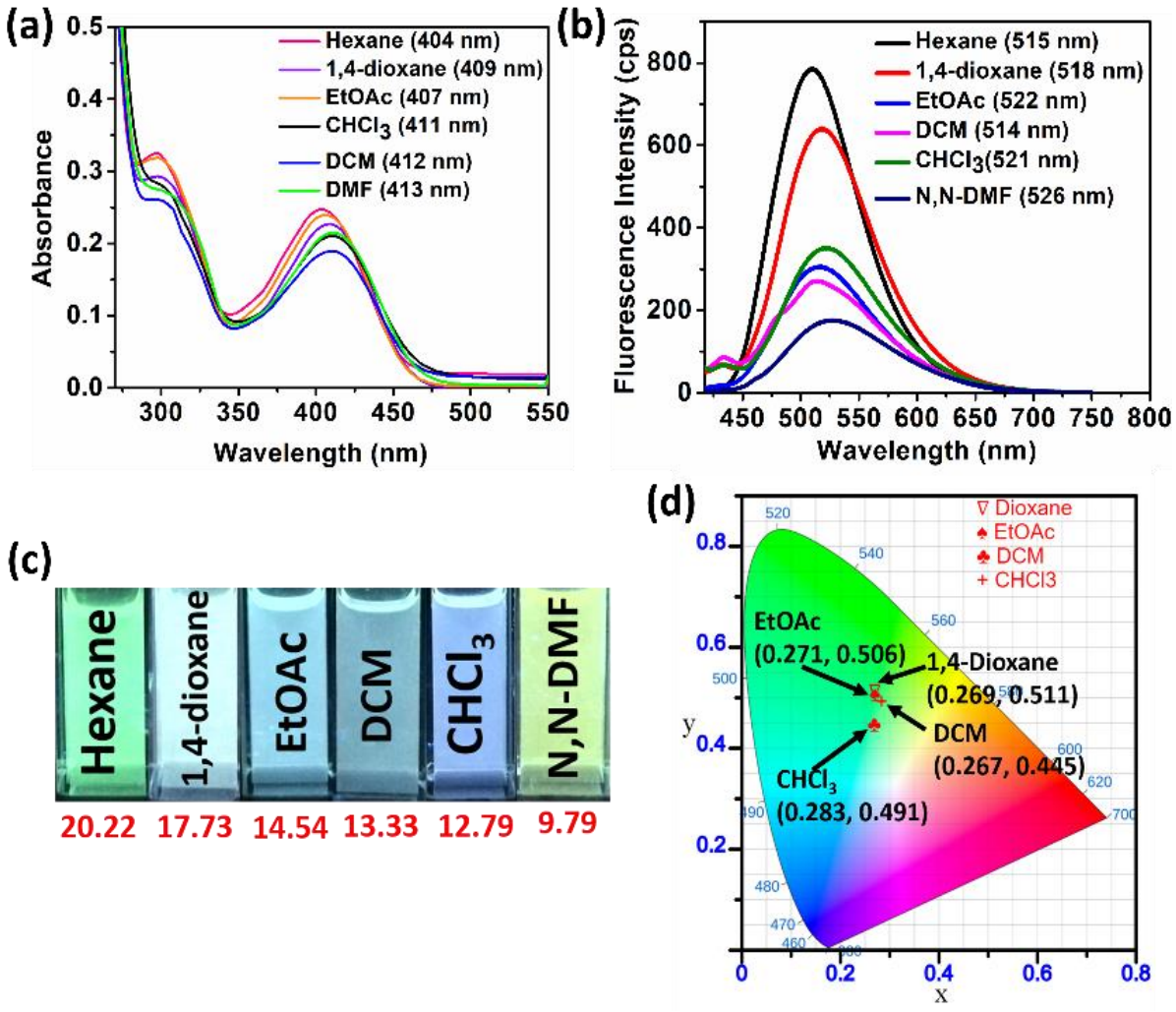

Figure 4.47 For **SB3** (a) Absorbances in different solvents, (b) DSE emission (c) the corresponding images (under UV-365 nm lamp) (d) CIE-diagram of selected solvents

TD-DFT studies were conducted for nonpolar (hexane) and polar (DMF) solvents to gain profound insight into these quantum chemical descriptors. In both the solvents, the excited state planarity is improved significantly in all three twisted sites of the **SB3** molecule. Typically, the excited-state conformation largely determines molecular emission properties and a favored planar geometry will offer bright emissions in solution.[14] The H→L contribution is also increased with the increased planarity in the excited state (Figure 4.48).

Table 4.11 DSE properties of **SB3**

Compound	Solvent	ET_{30}	$\lambda_{abs.max}$ (nm)	$\lambda_{em.max}$ (nm)	Stokes shift (cm^{-1})	Φ_f (%)
SB3 with $\lambda_{em.max}$ (Solid) = 517 nm	Hexane	31.0	404	515	90090.09	20.22
	1,4-dioxane	36.0	409	518	91743.119	17.73
	EtOAc	38.1	407	522	86956.521	14.54
	$CHCl_3$	39.1	411	521	90909.09	13.33
	DCM	40.7	412	514	98039.216	12.79
	N,N-DMF	43.2	413	526	88495.575	9.79

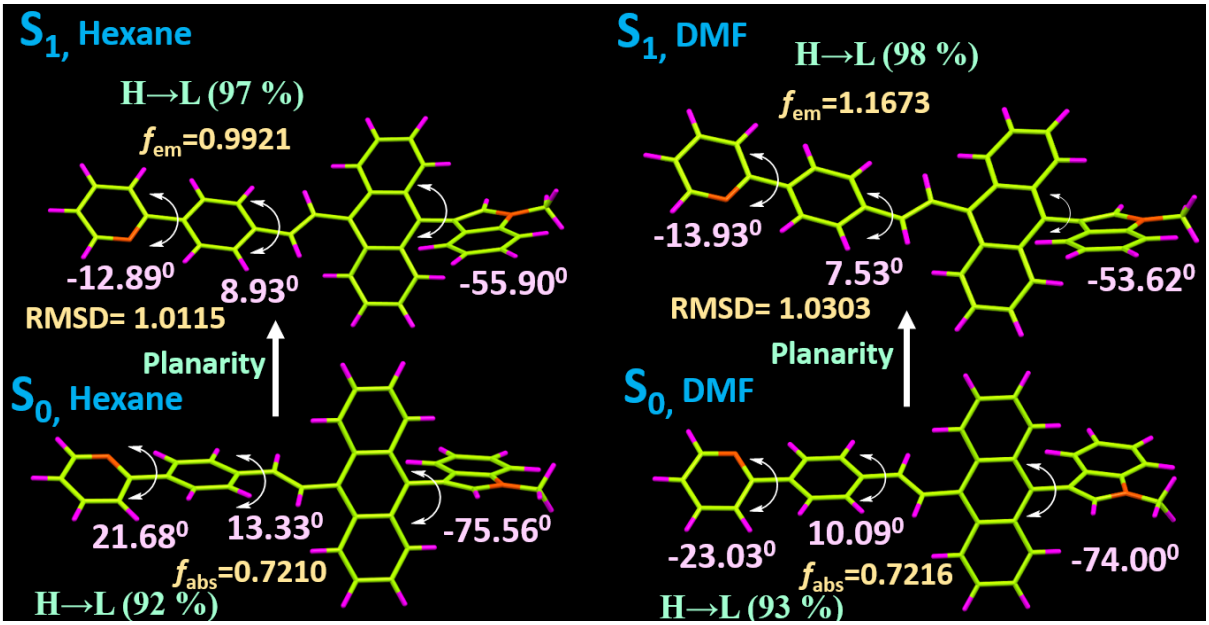

Figure 4.48 TD-DFT optimized structures and calculations for **SB3** in Hexane and N,N-DMF

Again, the higher RMSD in DMF (1.0303 Å) than in hexane (1.0115 Å), and stronger f_{em} in DMF with a slightly reduced HOMO-LUMO energy gap maintain to afford a decent recognizable emission. The NTO analysis for **SB3** in hexane and DMF reveals that the hole and electron NTOs are π and π* in nature, respectively, almost the same (~99%) as HOMO and LUMO. The LUMO (i.e., π* orbital) is more stable with the increased polarity of the solvent. Thus, the HOMO-LUMO gap decreases with increased polarity, and redshifted emission is observed (Figure 4.49). Actually, for the NTO analysis, we performed calculations based on two functions, CAM-B3LYP and PBE0/6-

31G, to crosscheck the accuracy of the calculations. The NTO analysis results were found neck to neck for both functions (Figure 4.50). It should be noted that during the calculation of the S_0 state HOMO-LUMO energy gap, we found a significant difference in values to use CAM-B3LYP, B3LYP, PBE0/6-31G, and other functions (Table 4.12).

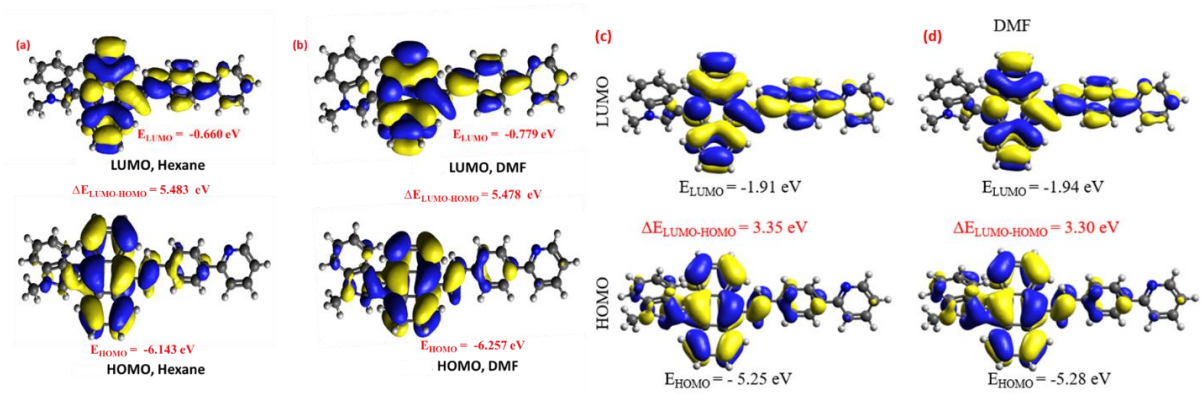

Figure 4.49 HOMO-LUMO for **SB3** in Hexane and *N,N*-DMF using (a-b) CAM-B3LYP/6-31G* (c-d) PBE0/6-31G* level of theory

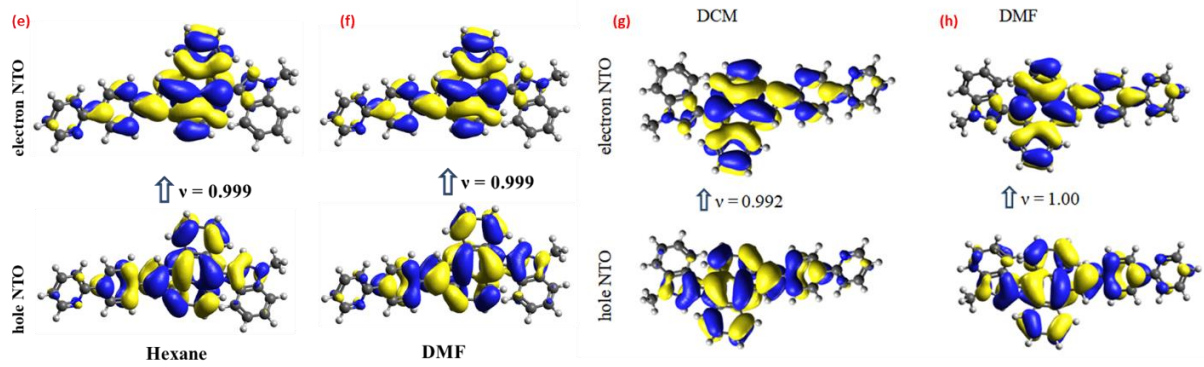

Figure 4.50 (e-f) NTOs for **SB3** in Hexane and N,N-DMF using CAM-B3LYP/6-31G* (g-h) hole and electron NTOs in the S_1 state of **SB3** in DCM and DMF solvent with PBE0/6-31G* level of theory

However, the experimentally calculated energy gaps from the cyclic voltammograms of **SB3** in DCM and *N,N*-DMF (Figure 4.51), were closer to the outputs of the B3LYP and PBE0/6-31G functions (Figure 4.51, Table 4.12) for S_0 state (ground state) HOMO-LUMO. In whatever way, the emission is an excited state phenomenon, and to our delight, for **SB3,** the NTO analysis for the S_1 (excited state) was very close for both CAM-B3LYP and PBE0/6-31G functions (Figure 4.50).

Table 4.12 Calculation of Electronic Properties in DMF and DCM Solvent

Properties/ Functionals	**B3LYP**	**CAM-B3LYP**	**M062X**	**BHnad HLYP**	**PBE0**	**WB97X**
HOMO (DMF)	-4.9482	-6.2572	-6.1992	-5.8986	-5.2752	-7.18
LUMO (DMF)	-1.8683	-0.779	-1.2049	-0.8648	-1.9327	0.019
Energy gap (DMF)	3.080	5.478	4.994	5.034	3.343	7.199
HOMO (DCM)	-4.9274	-6.2353	-6.2675	-5.8744	-5.2505	-7.1559
LUMO (DCM)	-1.8461	-0.7561	-1.1696	-0.8399	-1.9057	0.0456
Energy gap (DCM)	3.081	5.479	5.098	5.035	3.345	7.202

However, we relied on the CAM-B3LYP function for the structural optimizations as it had been reported to be better at yielding the most accurate geometrical characteristics and electronic descriptions of molecules in their excited states both in the gas phase and in solution.[71-72]

A dihedral angle scanning within the optimized molecular structure was undertaken to support the DSE nature further. The θ_3, θ_2, and θ_1 are designated as downside, middle, and upside dihedral angles, respectively (Figure 4.52). All three sites were scanned to monitor the f_{em} change against the dihedral angle, signifying the importance of the dihedral angle to emit in the anticipated range with a favorable f_{em}. In θ_2, and θ_1, with the increase in dihedral angle, the f_{em} decreases, but for θ_3, with the rise in dihedral angle, the f_{em} also increases (Figure 4.53). Hence a suitable dihedral angle contributes to not only twisting but also to the favorable f_{em}.

Also, the time-resolved fluorescence studies of **SB3** were conducted to confirm the DSEgen behavior. In all the solvents, **SB3** exhibits bi-exponential decay (Figure 4.54, Table 4.13) and possesses a shorter lifetime of 0.056 ns in hexane, but a comparatively longer lifetime of 0.074 ns in DMF. In a few solvents such as 1,4-dioxane, EtOAc, DCM, and $CHCl_3$, the emission spectra are generated from the combined contribution of locally excited (LE, a tiny signature at ~435 nm) and intramolecular charge transfer (ICT) state (Figures 4.47b, 4.55a).

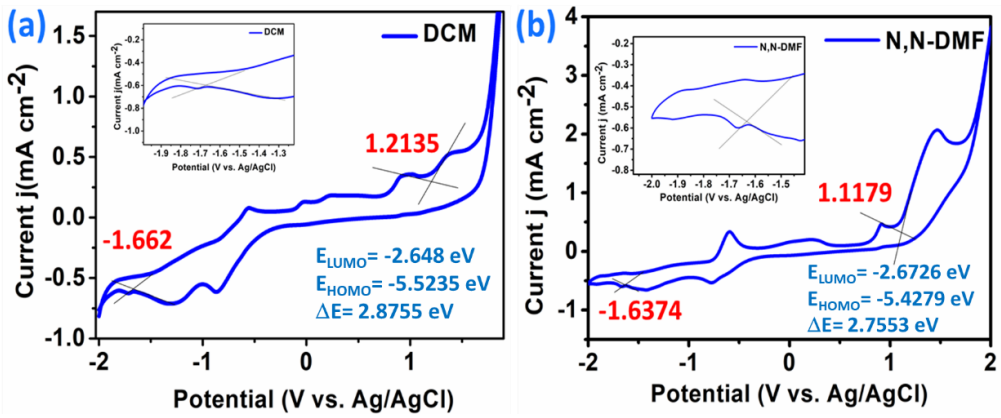

Figure 4.51 HOMO-LUMO calculation from CV for **SB3** in Hexane, and N,N-DMF

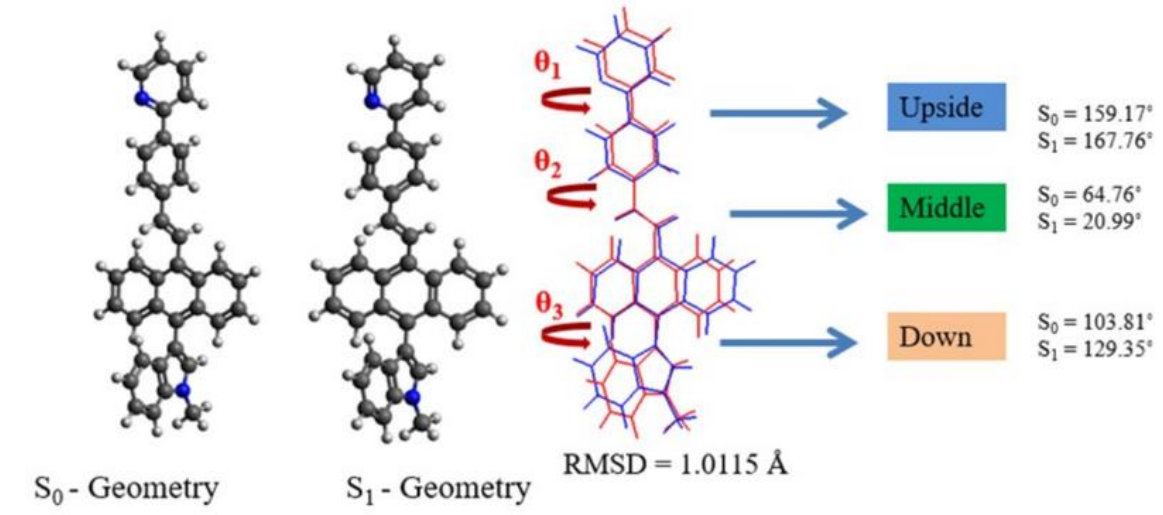

Figure 4.52 Geometry comparison between Ground state (S_0) geometry and S_1-state optimized geometry **SB3** in DMF using CAM-B3LYP/6-31G* level of theory

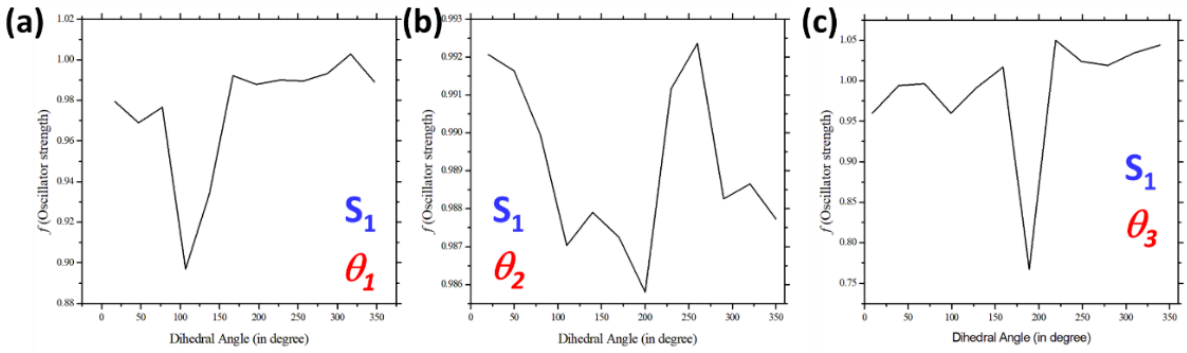

Figure 4.53 Dihedral scanning for emission oscillator strength at different twisted sites of **SB3**

Thus, the emission from two different excited states broadens the emission spectra, resulting in a whitish emission with CIE-coordinate near ~ (0.3, 0.5) (Figure

4.47d).[73,74] However, the donor-acceptor systems with twisted architecture were previously reported to produce a twisted charge-transfer state in their excited state.[73-79] Notably, earlier reports suggested that the twisting motion is controlled by the solvent polarity where EtOAc, DCM, and $CHCl_3$ (moderately polar) can open the ICT channel by stabilizing the excited state charge transfer species.[73-79] The extent of planarization in the excited state will facilitate the stabilization of the ICT state in *N, N*-dimethylformamide (DMF, a highly polar solvent).[73-79] A similar trend was noticed for **SB3,** and moreover, the three-site twisted structure and high donor-acceptor property of **SB3** would enable the creation of a dominant CT state in moderately polar solvents.[73-79] A marginal energy difference between LE and CT states would bring them into equilibrium, resulting in broad spectra (Figure 4.54a).[73,74] Thus, a fine-tuning of LE/CT energy will lead to the display of different emissions. Therefore, the impact of LE and CT state is regulated by modifying the ratio of 1,3-dioxane and $CHCl_3$ as a binary mixture, resulting in the whitish light emission from this system (Figure 4.55b, d). Other binary mixtures of EtOAc and $CHCl_3$ finally culminated in a greenish-yellow emission (Figure 4.55c, e). The k_r and k_{nr} for the emission in solvents are well-fitted to the observed results. **SB3** experiences better k_r values in hexane, and consecutively, k_r decreased with the high polarity of the solvent. This result validates the observed outcomes. All the time-resolved fluorescence study results are tabulated herein (Table 4.13).

4.3.4.3 Aggregation-Induced Enhanced Emission (AIEE) properties

Aggregation-induced emission (AIE) is a well-explored photophysical phenomenon where molecular aggregates emit brighter than a single molecule.[80] We noticed that due to aggregation, there were two types of emission displays *D-π-D′ systems exhibited blue-shifted enhanced emission*, whereas the *D-π-A system exhibited normal enhanced emission*. These two kinds of phenomenon are discussed in two subordinate sections to bring clarity.

4.3.4.3.1 Aggregation-Induced Blue-shifted Enhanced Emission (AIBSEE) properties of SB7 and SB6 *D-π-D′* systems

The aggregation-induced blue-shifted enhanced emission (AIBSEE) is a surprising experimental finding as the underlying mechanism is still uncertain.[81-84] Thus, exhibiting a blue-shifted bright emission on the aggregation of **SB6** and **SB7** is fascinating (Figure 4.59) because of the typical red-shifted emission observed for the aggregates for analogous systems.[84]

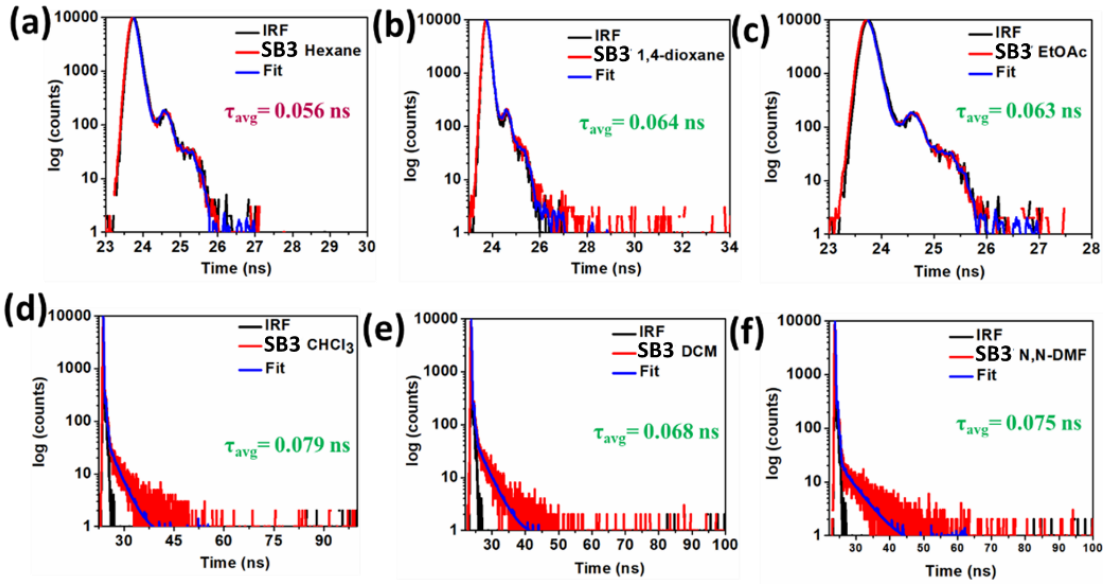

Figure 4.54 Decay profiles of **SB3** in different solvents

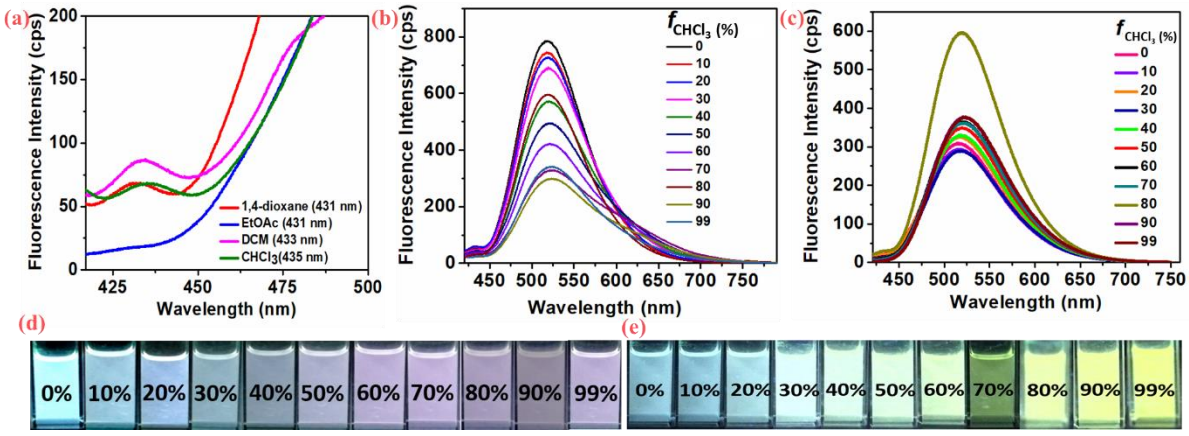

Figure 4.55 (a) Absorbances for whitish emission for **SB3** in the binary mixture of 1,4-dioxane and $CHCl_3$, (b) whitish emission for **SB3** in the binary mixture of 1,4-dioxane and $CHCl_3$, (c) binary mixture of $CHCl_3$ and EtOAC with a gradual increment of $CHCl_3$

fraction, (d, e) images captured under UV-365 nm bulb for 4.54b and 4.54c the percentage of $CHCl_3$ has been increased gradually, and the excitation wavelength was in the range of 409-425 nm). The CIE coordinates for 0% to 99% are as 0% (0.27, 0.52), 10% (0.27, 0.52), 20% (0.28, 0.58), 30% (0.29, 0.52), 40% (0.30, 0.52), 50% (0.32, 0.51), 60% (0.32, 0.50), 70% (0.34, 0.50), 80% (0.39, 0.46), 90% (0.34, 0.51), 99% (0.31, 0.52) for 4.54d

Table 4.13 Results of times-resolved studies for DSE-gen **SB3**

Solvent	χ 2	$\lambda_{em\ max}$ (nm)	τ_1	τ_2	$\alpha 1$	$\alpha 2$	$\tau_{avg.}$ (ns)	Φ_f (%)	$k_r(s^{-1})$ x 10^{-6}	$k_{nr}(s^{-1})$ x 10^{-6}
Hexane	1.037	515	0.0559	0.5962	0.4907	0.5093	0.0556	20.22	3636.69	14348.92
1,4-dioxane	1.069	518	0.0645	0.0634	0.4842	0.5157	0.064	17.73	2770.312	12854.688
EtOAc	1.023	522	0.0629	0.0625	0.4949	0.5051	0.063	14.54	2307.936	13565.079
DCM	1.071	514	3.177	0.064	0.0012	0.9988	0.068	13.33	1960.294	12745.588
$CHCl_3$	1.006	521	2.9433	0.0759	0.0011	0.9988	0.079	12.79	1618.987	11039.241
N,N-DMF	1.019	526	0.0719	5.0988	0.9995	0.0005	0.074	9.79	1322.972	12190.5405

Water-miscible DMF solvent was chosen herein to investigate the AIE behavior because the compounds displayed the lowest Φ_f in DMF. The compounds are already emissive in DMF; therefore, it is appropriate to define the phenomenon as *aggregation-induced blue-shifted enhanced emission* (AIBSEE). The emission for **SB6** was 19 nm blue-shifted from solution λ_{max}= 550 nm (Φ_f = 14.94 %) to aggregate (50% water/DMF, *v*/*v*) λ_{max}= 531 nm (Φ_f = 16.88 %) with four times rise in emission efficiency (Figure 4.57). The effect in the absorption spectra by increasing $f_w(\%)$= 50 is negligible for both **SB6** and **SB7**, indicating aggregate formation with an unaffected ground state (Figure 4.56). For **SB7**, a *remarkable 62 nm blue-shifted emission* from λ_{max} = 614 nm to 552 nm with 12

times enhanced emission efficacy (Figure 4.57) is noticed. It could be ascribed to the effect of the close packing of molecules on aggregation and freezing of low-frequency out-of-plane vibrations of peripheral bulky TPA/PTZ groups.[81-84] It is pertinent to mention that **SB6** and **SB7** DSE-gens have blue-shifted emissions in solids than in the DMF solution.

The impact from a typical strong donor-acceptor core may be excluded for these molecules; however, in such a system, more electron-rich parts (TPA or PTZ) will act as donors, and eventually, other parts (anthracene/indole) will contribute as acceptors. Again, the solid-state blue-shifted emission for **SB6** might arise from the twisted conformation, showing inadequate π-conjugations.[85,86]

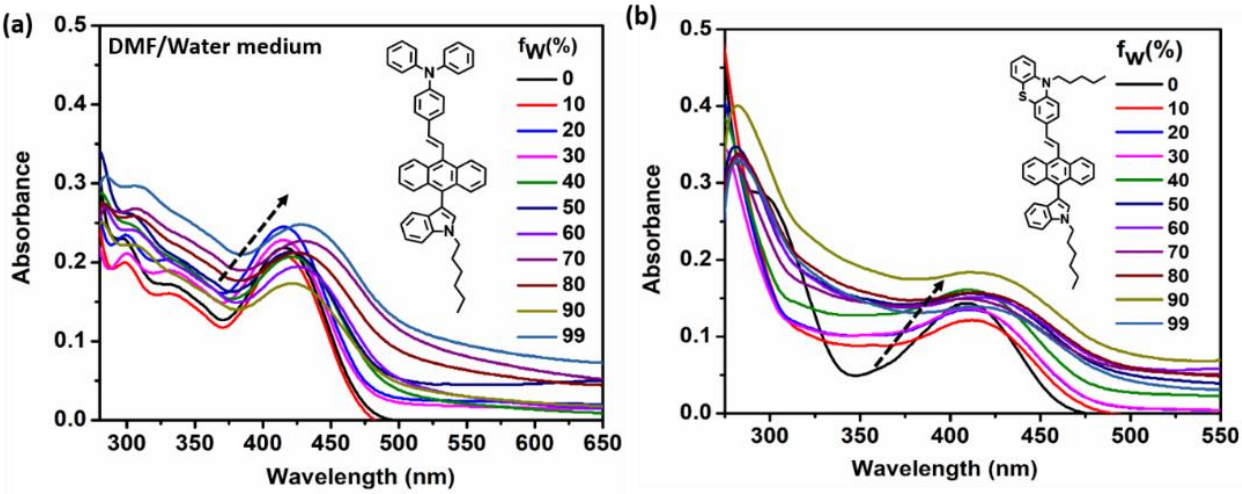

Figure 4.56 AIBSEE studies in DMF/Water binary medium (v/v %); absorbances for (a) **SB6** (b) **SB7**

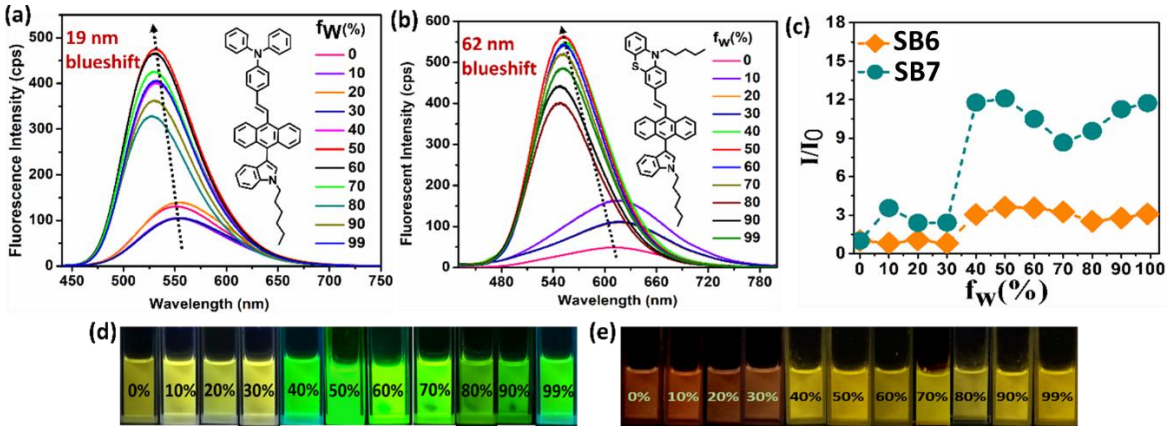

Figure 4.57 AIBSEE studies for (a) **SB6** (b) **SB7** (c) AIBSEE emission efficacy comparison between **SB6** and **SB7**; images taken under UV-365 nm lamp for (d) **SB6** (e) **SB7**

The twisted sites prevent intermolecular π-π interactions upon aggregation because aromatic rings cannot approach closer. But this substantial blueshift for **SB7** aggregates can be explained by the disparity in the reorganization energy.[81] If λ_{gs} is the reorganization energy of the ground state S_o, and λ_{es} is the reorganization energy of the first excited state S_1, in that case, the total reorganization energy λ is the combination of these two parameters. If E_{ab} is the absorption energy and E_{em} is the emission energy, $E_{em} = E_{ab} - \lambda$. For **SB7**, the experimental E_{ab} is 2.9732 eV, and the calculated λ is 1.390 eV (λ_{gs} is 0.632 eV and λ_{es} is 0.758).

Table 4.14 Summary of the results of AIBSEE properties for **SB6** and **SB7**

Compds	λ_{max} (nm) (in DMF)	λ_{max} (nm) (50% water)	λ_{max} (nm) (in DMF)	λ_{max} (nm) (50% water)	AIBSEE Shift (nm)	$\tau_{avg.}$ (ns) (aggr./solution)	K_r (aggr./solution)	K_{nr} (aggr./solution)
SB6	415	417	550	531	-19	0.284/ 1.051	594.3661/ 142.1503	1926.7605/ 809.3244
SB7	413	416	614	552	-62	0.206/ 3.13	285.4369/ 12.7476	4568.9320/ 306.7412

Again, the experimental E_{ab} for the **SB7** solid is 2.4311 eV. Accounting for a similarly reported molecule[81], we assume that the λ for **SB7** solid can never be less than 0.5 eV. The (E_{ab} - λ) eV value becomes more significant for **SB7** solids than **SB7** in DMF. The blue-shifted emission can be expected as their aggregated state was akin to the solid state.[81] The theoretical insight thus matches well the experimental output for **SB7**.

A comparative time-resolved fluorescence study between the aggregate and solution of **SB6** and **SB7** (Figure 4.58, Table 4.14) revealed that k_r (aggregate/solution) is ~1.5 -1.75 times higher than in k_{nr}. It supports the emission intensity enhancement in the aggregate state than in the solution.

The aggregate size (average) was determined by DLS (Dynamic Light Scattering) study and found to be 217 nm (PDI: 0.293) for **SB6** and 180 nm (PDI: 0.187) for **SB7**. The SEM images (Figure 4.59) demonstrate a more organized morphology of the aggregates than the solution state for both **SB6** and **SB7**.

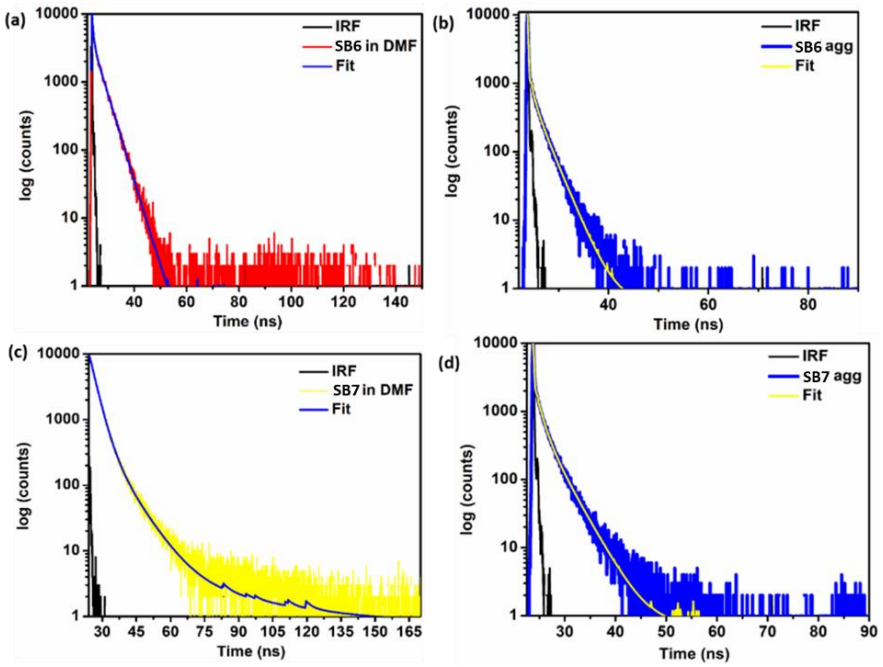

Figure 4.58 Lifetime decay profiles for **SB6** and **SB7** in DMF and aggregates

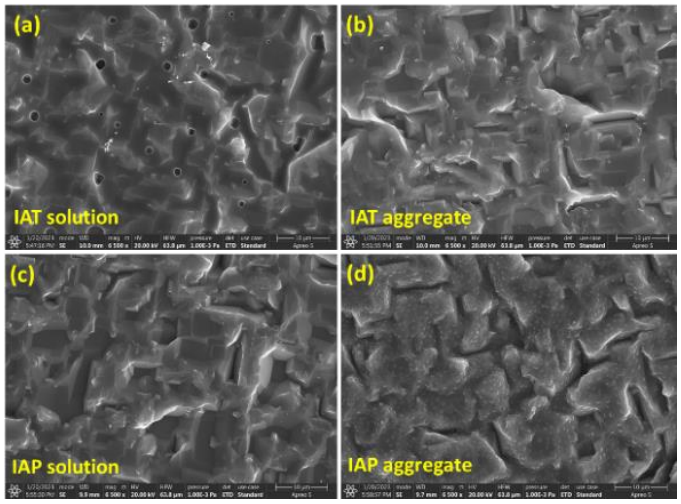

Figure 4.59 Drop-casted SEM images

4.3.4.3.2 Aggregation-Induced Blue-shifted Enhanced Emission (AIBSEE) properties of SB3, a *D-π-A* system

The AIE behavior was also observed in water-miscible DMF for this highly twisted **SB3** molecule. **SB3** is already emissive in DMF, so it is better to define it as aggregation-induced enhanced emission (AIEE) (Figure 4.60a,b,d). The aggregated state may behave like a solid state, although it may differ significantly due to the fundamental differences in the intermolecular interactions. A considerably large centroid to centroid distances (8.663 Å) and constrained alkyl chain in between two

anthracene rings offer a notable 17 times enhancement in emission (λ_{max}=530 nm, f_w= 70%) in the aggregated state (Figure 4.60b-c).

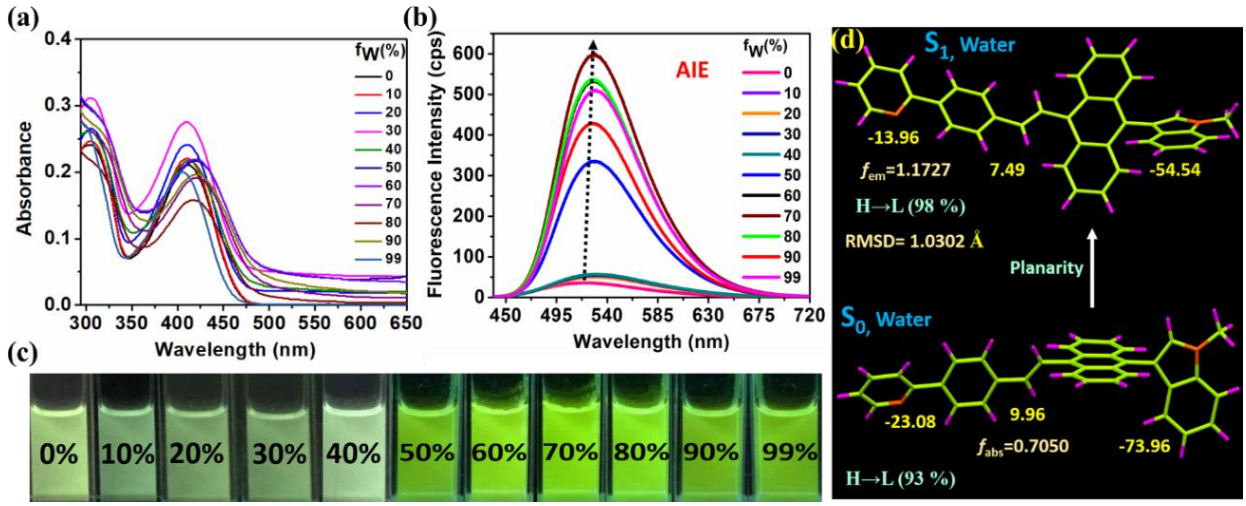

Figure 4.60 AIE feature of **SB3** (a) absorbances (b) emission (c) Intensity of emission increment for AIE at 10^{-5}M concentration (d) images under UV-365 nm bulb

As per DLS (Dynamic Light Scattering) study, the average size was 193.7 nm with PDI (Polydispersity Index) of 0.293 for aggregates of **SB3**. The TD-DFT optimized structure of **SB3** at S_1 state was almost similar to the exact crystal structure of **SB3,** although little deviation is there at θ_2 site (Figure 4.14, Figure 4.60d). The DFT study revealed that in water, the S_1 state configuration gets more planar at all three twisted sites, and the excited state f_{em} is increased with almost intact RMSD (1.0302 Å) as compared to that in hexane, favoring the AIE behavior.

4.3.4.4 Viscosity-Induced Enhanced Emission (VIEE) properties

Of note, twisted rotors against an olefinic stator have proven effective in displaying viscosity-induced emission.[21] We noticed that due to the viscous environment, there were two types of emission displays-*the D-π-D′ systems exhibited blue-shifted enhanced emission*, whereas the *D-π-A system exhibited normal enhanced emission*. Herein, these two kinds of phenomenon are discussed in two subordinate sections for clarification.

4.3.4.4.1 Viscosity-Induced Blue-shifted Enhanced Emission (VIBSEE) properties from SB6 and SB7, the *D-π-D'* systems

SB6 (Φ_f = 3.74 %) and **SB7** (Φ_f = 1.41%) have a considerable emission in MeOH. **SB6** becomes more planar around θ_2 in its excited state configuration than **SB7,** and the RMSD is less with stronger f_{em}, enabling **SB6** to emit brighter in MeOH than **SB7** (Figures 4.64a-b). With consecutive increments of glycerol percentage [f_g (v/v)] (miscible with MeOH)[87], the viscosity increases, and the emission efficiencies for **SB6** and **SB7** also substantially improve. The longer alkyl chain is less likely to participate in viscosity-induced emission.[88] Two twisted sites in **SB6** and **SB7** become more rigid in the denser medium, leading to relaxation through radiative channels.[89] Similar to AIE activity, the emission maxima were blue-shifted in the viscous environment compared to the emission maxima in pure MeOH. The two long alkyl chain movements were relatively reduced in **SB7** in a viscous medium and offered a 45 nm blue shift (Figures 4.63a-b), a distinct color switching from orange to yellow. On the other hand, **SB6** shows only an 8 nm blue shift in the viscous medium (Figures 4.63a-b). However, both **SB6** and **SB7** display emission enhancement in a viscous medium (Figure 4.64c), with a slight redshift in absorption maxima (Figure 4.62).

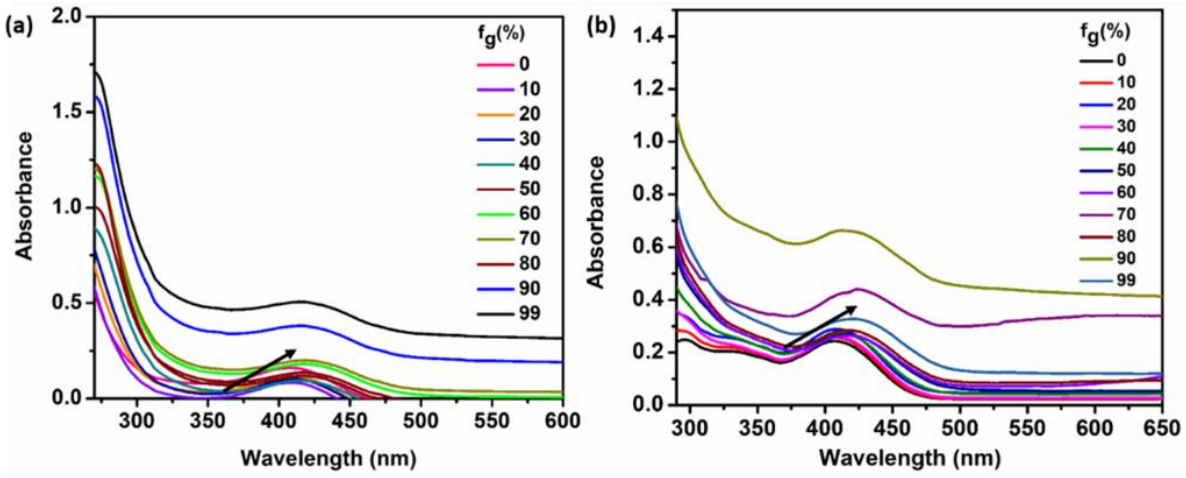

Figure 4.61 Viscofluorochromic absorbances from (a) **SB6** and (b) **SB7**

The decay profiles were determined for intensely emissive **SB6** and **SB7**, revealing a 0.103 ns and 0.208 ns excited state lifetime, respectively (Figure 4.64). The emission shift variance through AIBSEE and VIBSEE is presented through the CIE diagram (Figures 4.63d-e).

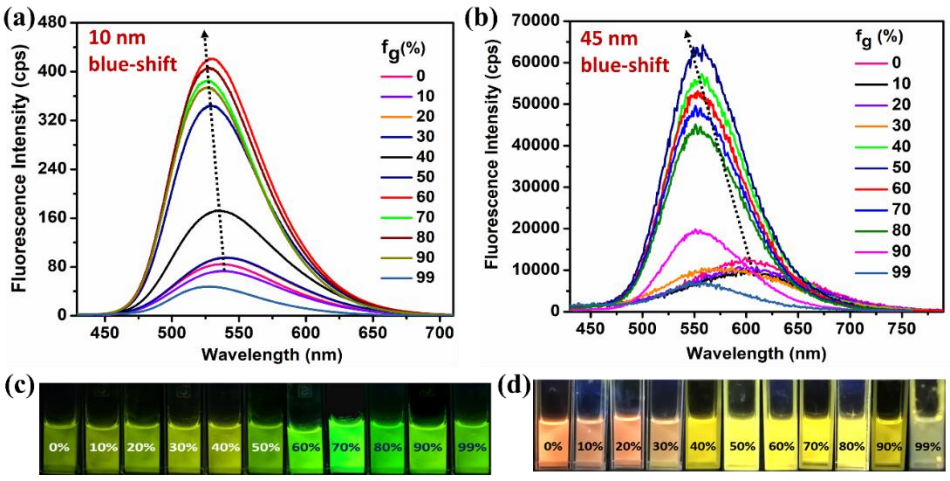

Figure 4.62 VIBSEE spectra for (a) **SB6** (b) **SB7**; images under UV-365 nm bulb for (c) **SB6** (d) **SB7**

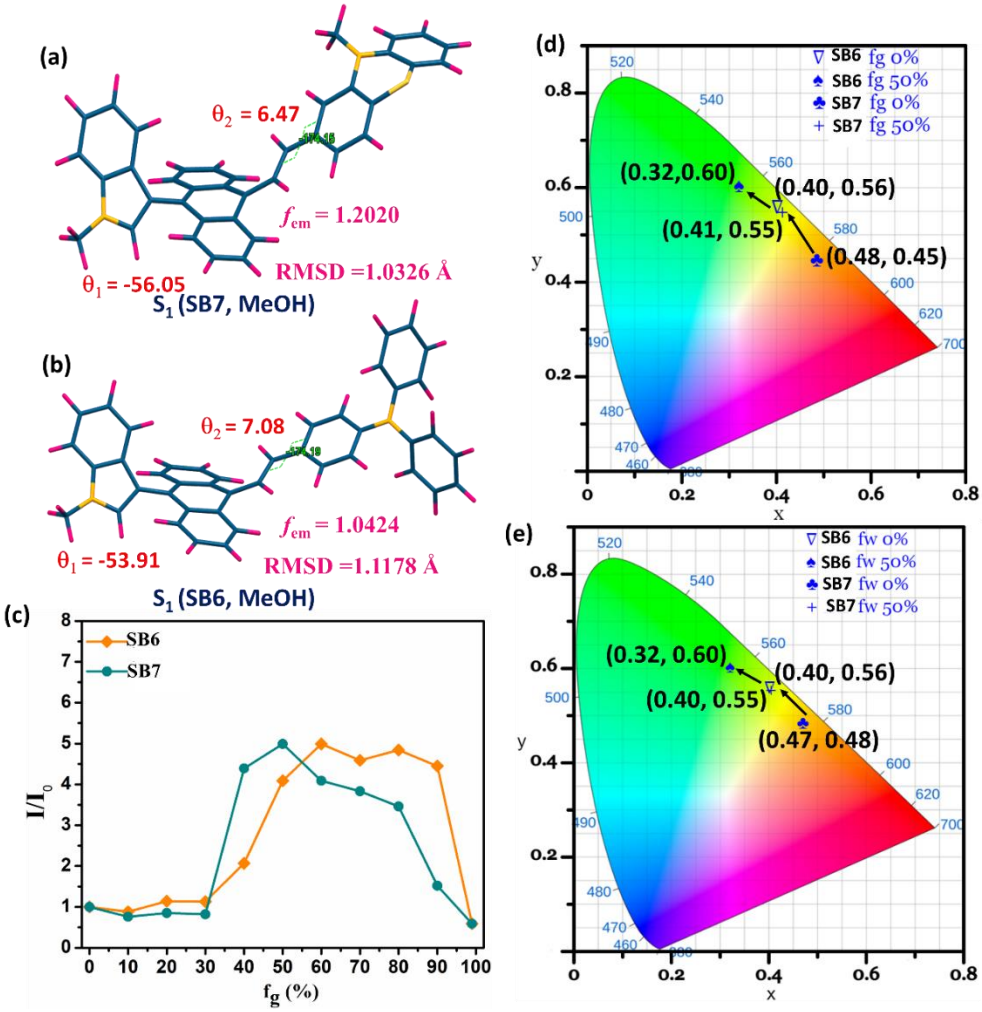

Figure 4.63 Optimized structure in MeOH for (a) **SB7** (b) **SB6**; (c) VIBSEE emission efficacy comparison between **SB6** and **SB7**; comparison through CIE-coordinates for blueshifted emission due to (d) viscosity (e) AIE behavior

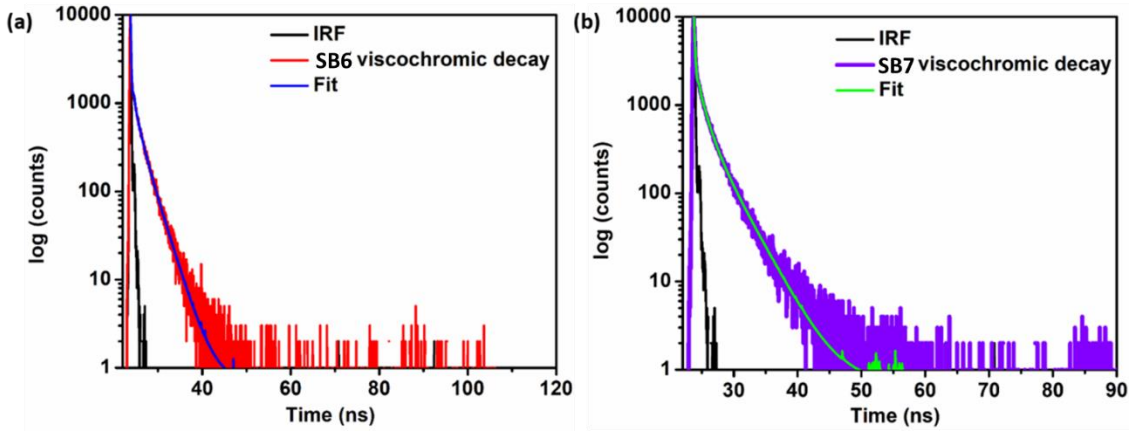

Figure 4.64 VIBSEE decay for (a) **SB6** (b) **SB7**

4.3.4.4.2 Viscosity-Induced Enhanced Emission (VIEE) property from SB3, the *D*-*π*-*A* system

The molecular motion can be restricted by increasing the viscosity of the solution, which would facilitate the excited state decay through a radiative fashion and enhance the FL intensity significantly (23 times) (Figure 4.65d). Having a three-site twisted rotor, **SB3** reveals an RMSD of 1.1655 Å and comparable f_{em} in MeOH than other solvents like hexane and *N,N*-DMF, leading to a weaker emission in MeOH. Further, the rotation barrier was ~6 kcal/mol, as noticed from dihedral scanning in the θ_3 site, suitable for the free rotation (Figure 4.66), resulting in non-radiative decay despite gaining excited state planarity (Figure 4.66).

4.3.5 Real-world optical applications

4.3.5.1 Hidden patent fingerprint memory and software assisted-comparison to detect fake people

Typical fingerprint dyes are detected visually in ambient light, while **SB6** offers a patent fingerprint, obscure under ambient light. A dilute ethanol solution of **SB6** (10^{-7} M) was soaked into a sponge. Later, the donor's fingers were pressed onto the sponge and placed on the silica gel layer, homogeneously distributed on an aluminum plate. The fingerprint will be invisible to the naked eye but easily recognizable under a 365 nm UV lamp, which is advantageous over conventional dyes and valuable in the security sector for anti-counterfeiting applications. Hence, noncytotoxic **SB6** is appropriate for

real-world applications. Further, we have extended this application to match previously recorded fingerprinting using an available online source.[90]

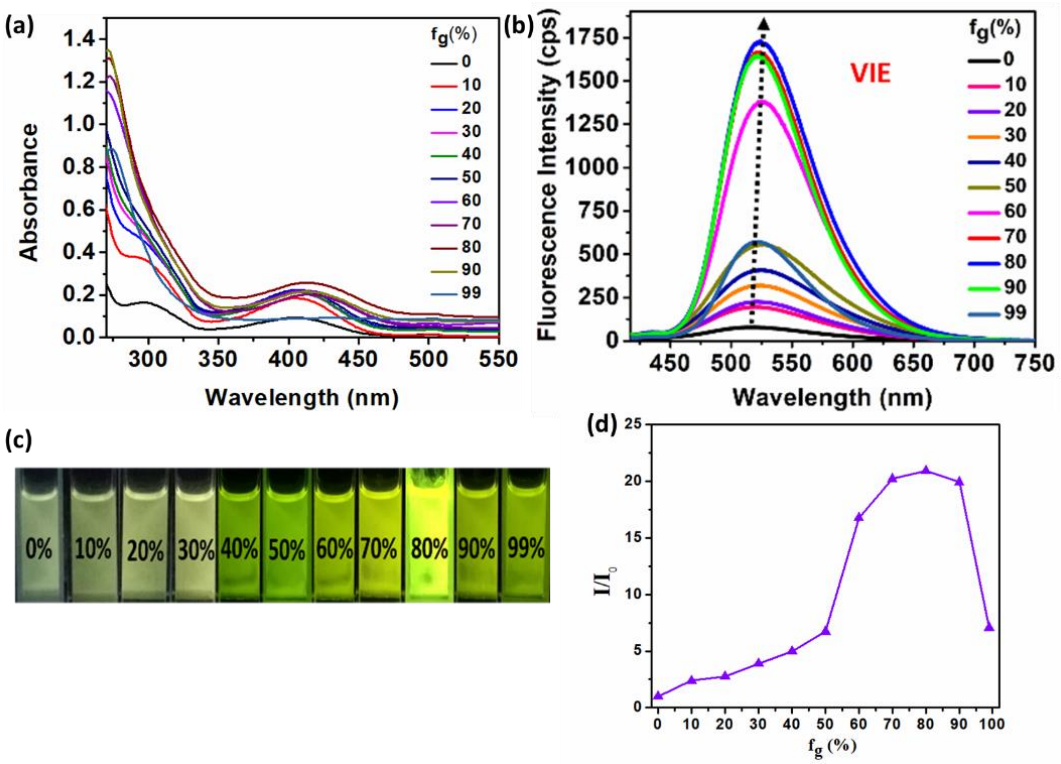

Figure 4.65 VIEE of **SB3** (a) absorbances (b) emissions (c) picture under UV-365 nm bulb (d) VIEE efficiency

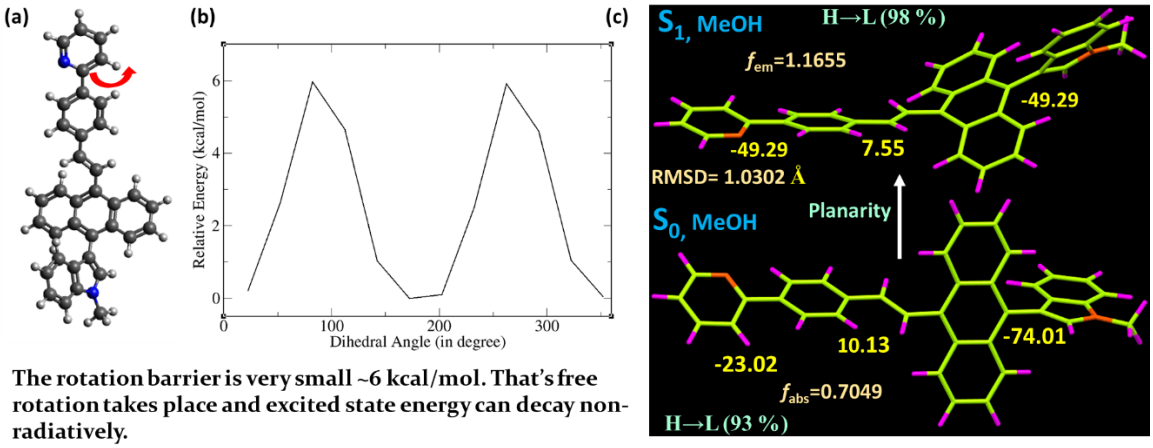

The rotation barrier is very small ~6 kcal/mol. That's free rotation takes place and excited state energy can decay non-radiatively.

Figure 4.66 (a-b) Rotation barrier of the pyridine group in S_1 state of the (c) TD-DFT optimized structure of **SB3** in MeOH

The hidden fingerprint of donor 1 was optically recorded by capturing an image under a 365 nm UV lamp and uploaded to the software. This software-stored fingerprint

could match the actual fingerprint of donor 1, while tested (Figure 4.67b) but does not match the fingerprint imaging of donor 2 (Figure 4.67d) and donor 3 (Figure 4.67e). The orientation of the images was manually set up and analyzed. When any two images were compared, less noise (as shown blue overlapped area) was observed for the matching fingerprint patterns. Still, prominent noise appears if there is a mismatch (red overlapped area). Thus, this dye is fruitfully demonstrated as a tool for hidden fingerprint detection and matches the previously recorded data, a crucial part of security-based investigations.

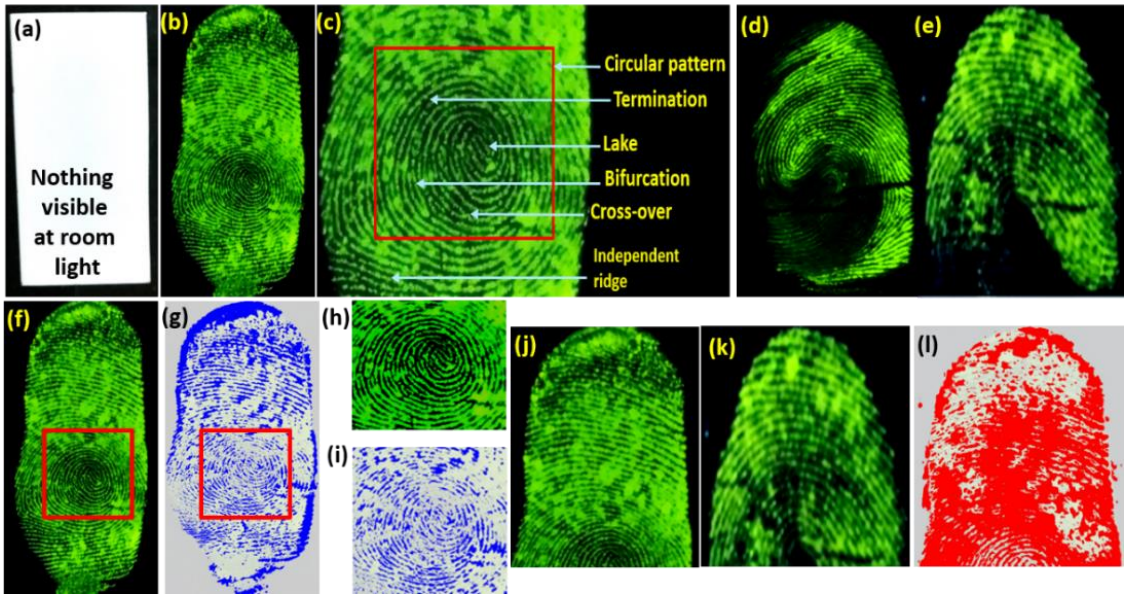

Figure 4.67 (a) Silica-gel coated Al-plate after pressing the thumb of donor 1 under ambient light (b) fingerprint of donor 1 visible under the UV-365 nm lamp on the same plate (c) different curves of fingerprint of donor 1; Fingerprint of (d) donor 2 (e) donor 3 under UV-365 nm lamp (f) two fingerprints images (earlier stored and recently captured) of donor 1 are uploaded to the software (g) outcome of comparison in software (less noise with blue-shade represents well-matched data) (h) zoomed portion of 'f' (i) zoomed portion of 'g' (j) selected portion of 'b' (donor 1 fingerprints) uploaded to software (k) selected portion of 'e' (donor 3 fingerprints) uploaded to software (*l*) outcome of comparison in software (more noises with red-shade indicate a poor agreement)

4.3.5.2 Ink-free reusable writing

The MFC properties of **SB6** and **SB7** allow them to be utilized in ink-free reusable security writing (Figure 4.68a-d). An **SB6**-appended polymethyl methacrylate (PMMA) polymer matrix and an **SB7**-coated Whatman filter paper were introduced to prepare the solid platform for security writing. Here 1 mg of **SB6**/**SB7**, 10 mg of PMMA, 1 ml of propylene carbonate, and 1 ml dichloromethane were sonicated for 15 min and then laid down and dried over a glass slide. Later, solidifying the polymer matrix made it possible to write '*MC*' on it with a spatula (Figure 4.68c). The solvent vapor erased the letters; thus, this platform can be reused (Figure 4.68d). The SEM image of **SB6** pristine and the polymer matrix of **SB6** clearly illustrated a sheet-like array of **SB6** (Figure 4.68b), which remains intact in the polymer matrix. However, the polymer matrix has blue-shifted absorbance maxima (λ_{max}= 433 nm) with a still bright emission at 510 nm (Φ_f = 5.97 %) (Figure 4.68a-d). For **SB7**, the sonicated solution was soaked with Whatman paper, followed by subsequent drying, producing a suitable writable platform (Figure 4.69).

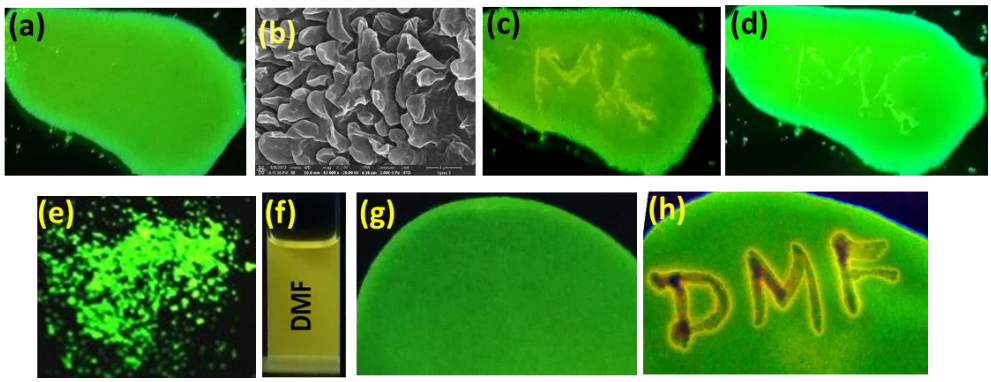

Figure 4.68 (a) image of PMMA-**SB6** polymer matrix under 365 nm UV lamp (b) SEM image of the matrix (c) '*MC*' is written with a spatula on this matrix (d) dichloromethane vapor was exposed for 5 min; For **SB6**, fluorescent color at e) solid-state, (f) solution in DMF [*N, N*-dimethylformamide] (10^{-5} M) (g) Whatman filter paper soaked and dried with 10^{-5} M stock solution of **SB6** in 1,4-dioxane (h) 'DMF' is written with *DMF* and emits yellow

4.3.5.3 Self-color switchable writing with solvent

Dual-state emitting feature of **SB6** with bright green emission in solids (Figure 4.68e) and yellow emission in DMF (Figure 4.68f) was utilized as a solvent-mediated self-color switchable writing platform. A Whatman paper was soaked with 10^{-5} M stock of **SB6**

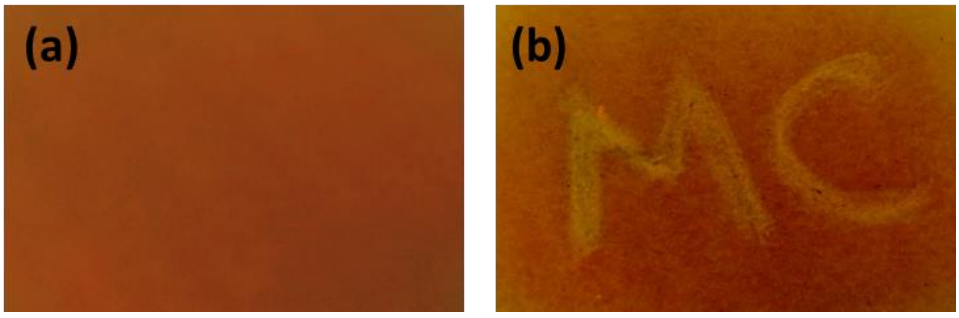

Figure 4.69 (a) image of PMMA-SB7 polymer matrix dried on Whatman paper under UV-365 nm bulb (f) '*MC*' is written with a spatula on this matrix

in 1,4-dioxane, followed by subsequent drying. **SB6** shined green once dried and became ready as a writing platform (Figure 4.68g), and then a tiny piece of DMF-soaked cotton bud was used to write over it. The writing turns yellowish (Figure 4.68h) but automatically switches its color to green upon solvent evaporation.

4.3.5.4 Data storage and hidden stimuli-responsive QR code/stamp-based anticounterfeiting applications

Fluorescent materials-based information storage and anticounterfeiting applications have gained ample recognition.[91,92] The acidofluorochromic feature of **SB3** was realistic in data storage and device fabrication for hidden quick response (QR) code-based anticounterfeiting applications. We utilized two dyes with the same emission wavelength (λ_{max} = 517 nm) **SB6** which does not display SSAC property, and **SB3**, which has SSAC property. A formulation was prepared with **SB6** to design a green emitting platform (Figure 4.69a), and on this green fluorescent platform, the QR code was screen printed using a formulation prepared with **SB3**. The QR code is also green-emitting and cannot be easily distinguished (for being printed on an already green-emitting platform) (Figure 4.70a).

Meanwhile, upon fuming acid vapor for 5 min on the green surface, the hidden QR code became visible (Figure 4.70b) with yellowish emission, but the rest of the

platform remained greenish, and the *stored hidden information* about '*Prof. MC Group*' could be received by scanning the yellow emitting QR code with a smartphone (Figures 4.70c-d).

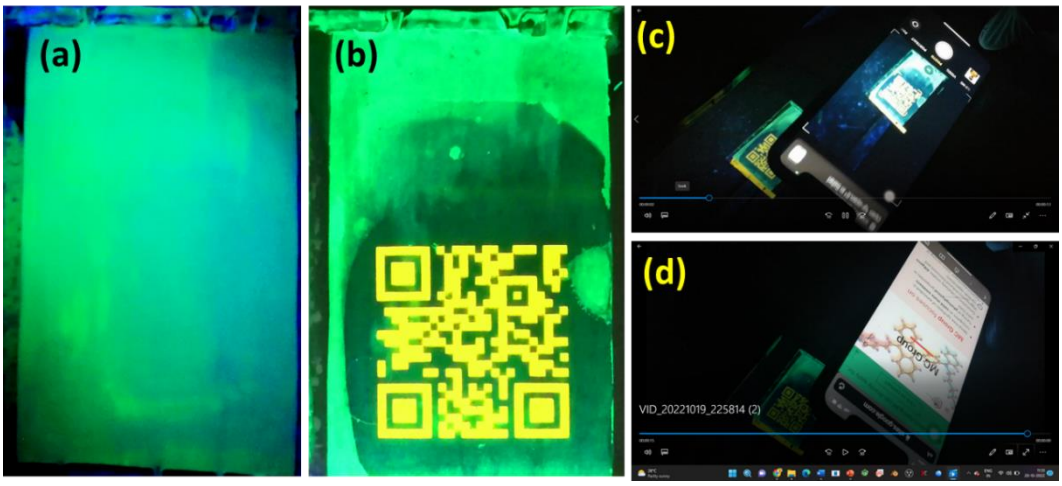

Figure 4.70 Data storage and hidden QR-code-based anticounterfeiting application: (a) green emitting platform made of **SB6** fluorophore, the QR code is screen printed on this platform with **SB3** fluorophore; the QR code is not visible now; (b) acid-fumed over the platform and QR code is visible as **SB3** is sensitive towards acid vapor; (c) QR code is scanned with a smartphone; (d) the hidden data about 'MC Group' is accessed

Without acid fumigation, the QR code will not be visible (Figure 4.70a), and the hidden information thus cannot be unveiled. A short video is uploaded for further clarification. Pure **SB3** displays orange-red emission upon acid fuming, but the dried formulation of **SB3** could switch its emission from green to yellow, possibly due to the changed chemical environment. The process of preparing the formulation is discussed in the supporting information.

Actually, a market-available screen-printing liquid (SPL) white non-fluorescent dye of 4000 cP was purchased. Later 30 mg of **SB3** dye was dissolved in 10 ml of DMSO and sonicated unless the solution became clear. This solution was added with 30 ml of the screen-printing liquid white non-fluorescent dye and appropriately mixed to prepare an **SB3-SPL** media. Again, using another dye **SB6**, the **SB6**-SPL media was prepared similarly. The QR code was drawn with CAD tool solid works, and on the PVC sheet the QR code was engraved with the universal laser system CO_2 laser with 10-micron wavelength with 10% into 30 watts. The **SB6-SPL** was first painted on a glass

surface and subsequently dried. The surface emitted green under a 365-UV lamp. Later, the laser-cut QR code pattern was screen printed with **SB3-SPL** on the surface of **SB6-SPL**. With the naked eye the QR code is not visible under ambient light. Even under 365-UV lamp also, the entire surface remains green. Once the acid fumigation is done, the QR code will be visible under the 365-UV lamp as it glows yellow on a green surface.

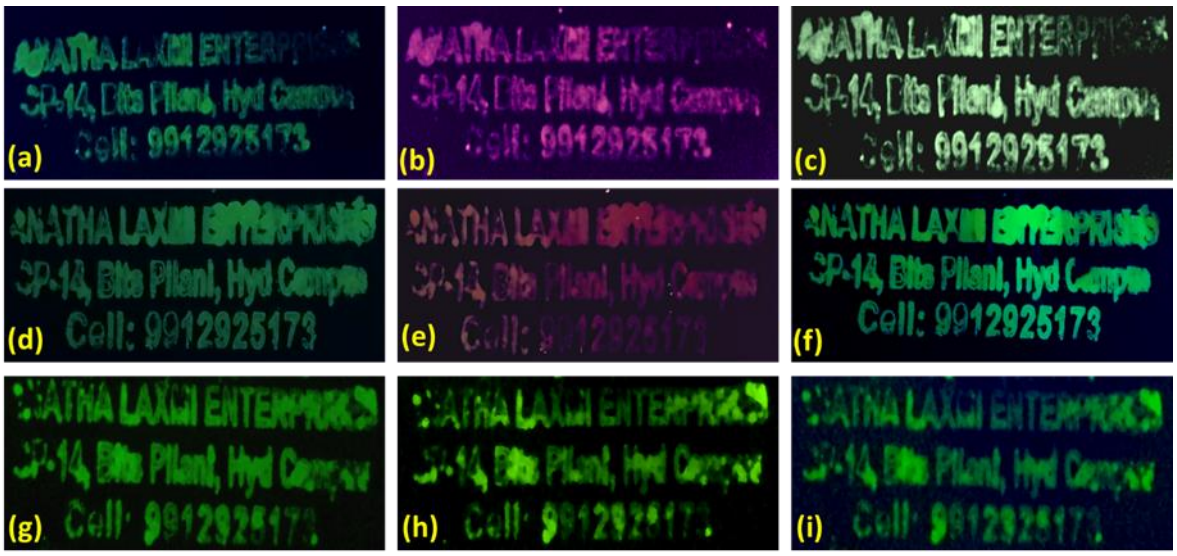

Figure 4.71 Data storage and anticounterfeiting applications with stimuli-responsive hidden stamp; (a) stamp prepared with **SB3** (b) acid-fumed over 'a' (c) base-fumed over 'b' (d) stamp prepared with **ATh4P** [chapter III] (e) acid-fumed over 'd' (f) base-fumed over 'e' (g) stamp prepared with **SB6** (h) acid-fumed over 'g' (i) base-fumed over 'h'

Further, **SB3** was utilized for preparing the stimuli-responsive hidden stamps aiming for anti-counterfeiting applications (Figures 4.71a-i). Three dyes- **SB3**, **ATh4P**, and **SB6** were initially chosen as they are green emitters (λ_{max}= 501-517 nm). An ethanolic solution of 10^{-7}M concentration was prepared for each dye and soaked with three different sponges. A wooden stamp was pressed on the **SB3** solution-soaked sponge and placed on a TLC plate to get an **SB3** led stamp. Later on, the wooden stamp was washed with acetone properly, and consecutively, two more **ATh4P** and **SB6** led stamps were prepared on the TLC plates. Now, none of the stamps are visible to the naked eye, but all the stamps glow green under the UV-365 nm lamp. Now how to identify which stamp is real and which ones are counterfeited? Let us say that the **SB3** is the real dye; hence, the **SB3** led stamp will be the real stamp. **SB3** emits orange-red on acid-fumigation but immediately does not revert to green on base-fumigation as it turns yellow. But this

information is secret. The counterfeiters might mimic a dye (**SB6**), which is a green emitter but not acidofluorochromic or can mimic a dye (**ATh4P**), which can emit red on acid fuming and again revert to green on base fuming. Reversible acidofluorochromism is usually used in most the cases. So, if an unknown stamp that looks like the real one is acid-fumed and still emits green, the dye is counterfeited, and the stamp is unreal. Next, if an unknown stamp that looks alike again as the real one is acid-fumed and turns red emitting, then that stamp may or may not be real. But again, with base-fuming, if it turns green emitting instantly, then the stamp (made of dye **ATh4P**) is fake, with no doubt. But on further base-fuming, if it turns yellowish, then the stamp is the real stamp.

4.3.5.5 Data encryption application

The **SB3** was feebly emissive in MeOH but highly emissive in solid-state, and this nature is utilized in a data encryption application[93] by spraying MeOH on a specific part of a letter or numerical (Figures 4.72-73). Almost every digit could be encrypted from digital '8' (Figures 4.72-73) due to the partial dissolution of the compound in MeOH from the selected part of the 'letter' or 'number'.

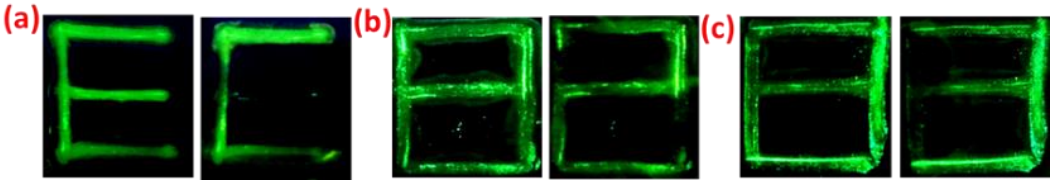

Figure 4.72 Data encryption with **SB3**

4.3.5.6 Detection of food-additive xanthan gum and sodium carboxymethyl cellulose

The applications are further extended using the viscofluorochromic emission sensitivity of fluorescent dye in checking food quality.[94] Here, **SB3** was utilized to detect the added thickeners such as xanthan gum (food additive) and Na-CMC (Sodium carboxymethyl cellulose, widely used in eyedrops) in water. Initially, we used water because it is the common constituent of any liquid food beverage. From zero addition

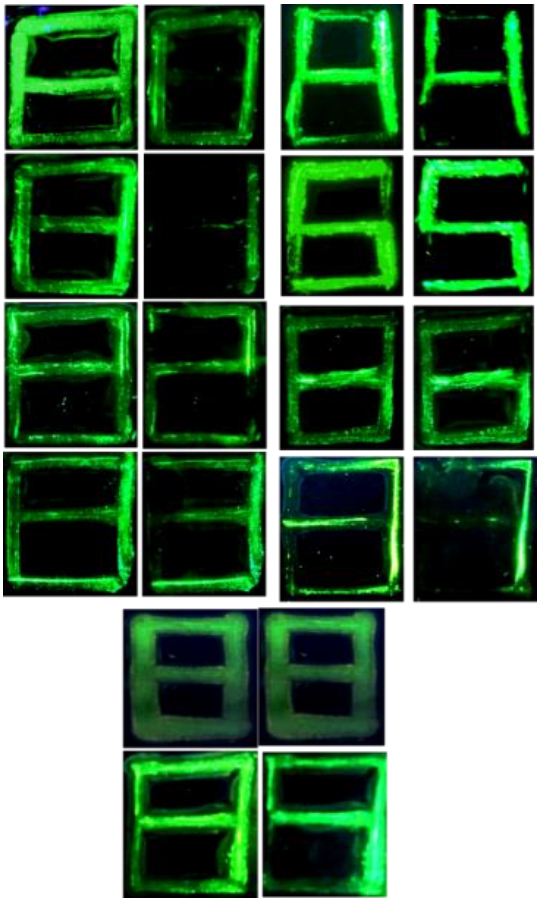

Figure 4.73 Data encryption with **SB3** to make different digits from '8'

to the addition of 5 mg of xanthan gum per 2 ml of water, the emission intensity raised gradually. So, the water fractions with or without food additives could be compared by visualization if the cuvettes are placed under a UV-365 nm lamp (Figure 4.74). The presence of Na-CMC in water could also be indicated in the same way (Figure 4.75). Detailed studies are presented in the supporting information.

4.3.5.7 Detection of blood stains and blood-smeared fingerprints for forensic utility

Besides, forensic applications using **SB3** were commendable in staining unclear fingerprints and patches of blood on glass and wood surfaces and making them brightly visible through green fluorescence. Detection of faint blood-smeared fingerprints and patches of blood is crucial to portray the crime scene for forensic investigation.[95] First, the blood stains were fixed with a 4% formaldehyde solution and then washed with 1X PBS. Next, 10^{-5} M solution of **SB3** in DMSO was sprayed over the blood stains and kept for 50 mins.

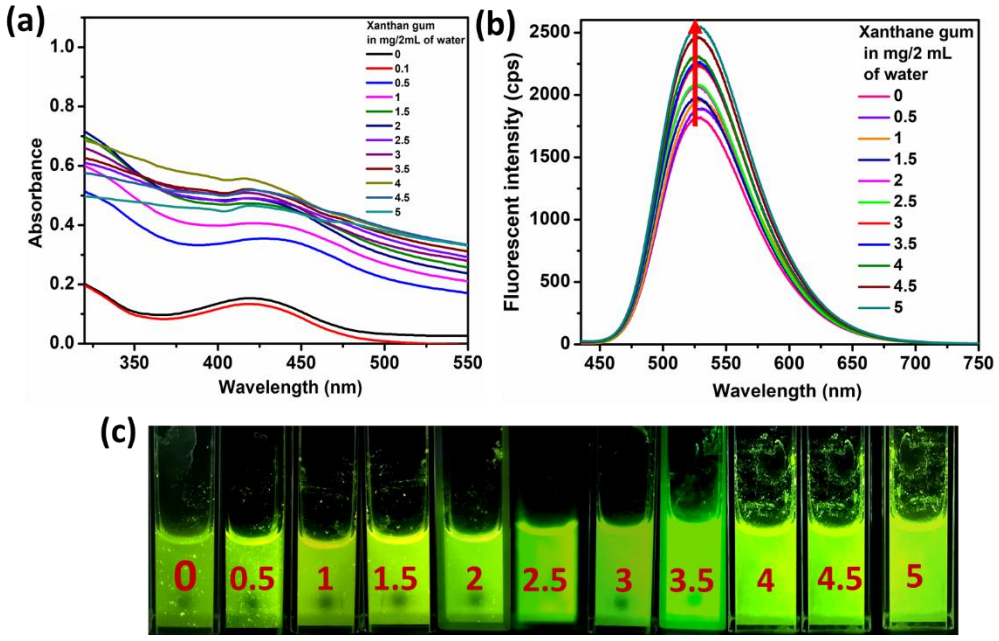

Figure 4.74 Xanthan gum sensing (a) absorbances (b) emission (c) picture taken under UV-365 nm lamp (the mg of Xanthan gum taken per 2ml of water is written on each cuvette picture)

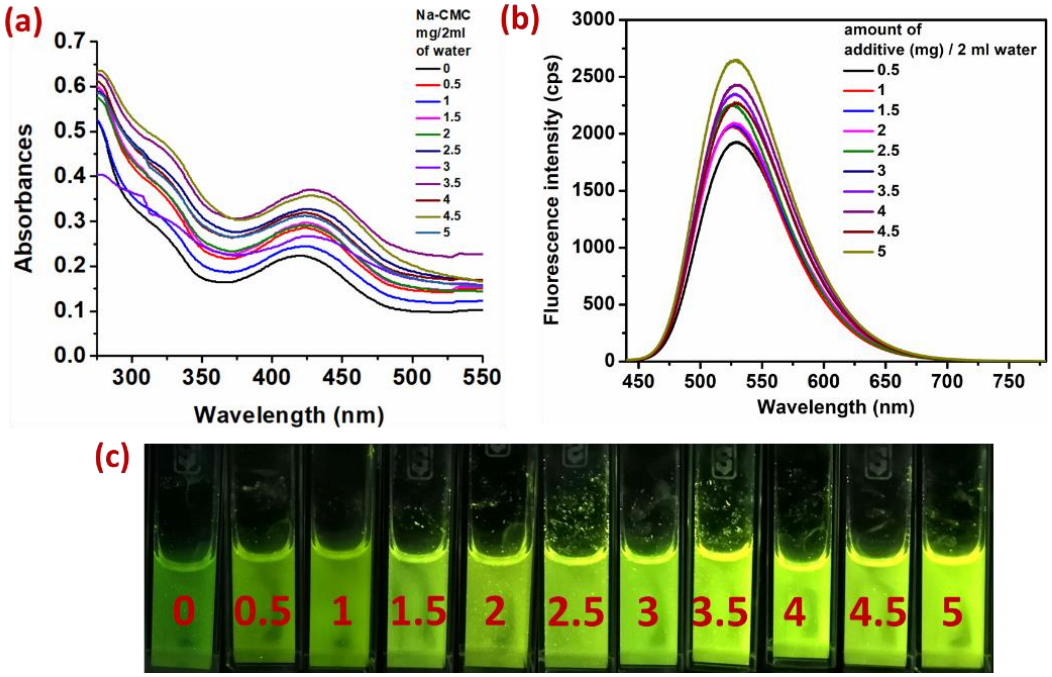

Figure 4.75 Na-CMC sensing (a) absorbances (b) emission (c) picture taken under UV-365 nm lamp (the mg of Na-CMC taken per 2ml of water is written on each cuvette picture)

DMSO was suitably chosen as a solvent with its high volatility and stain-development duration. Later, the stains were rewashed with PBS. After that, a 365 nm UV lamp was illuminated on the slide, and the bold stains or fingerprints displayed greenish fluorescence (Figure 4.76).

The false positive taste was done with dry cold drink patches and tomato sauces, but **SB3** displayed a faint or no stain (Figure 4.77). The ^{1}H-NMR-experiment (DMSO-d^{6}), after adding the serum of human blood with the probe (10^{-5} M) displayed a de-shielded resonance signal of the blood serum[96], indicating interactions between the probe with the blood serum (Figure 4.78-79).

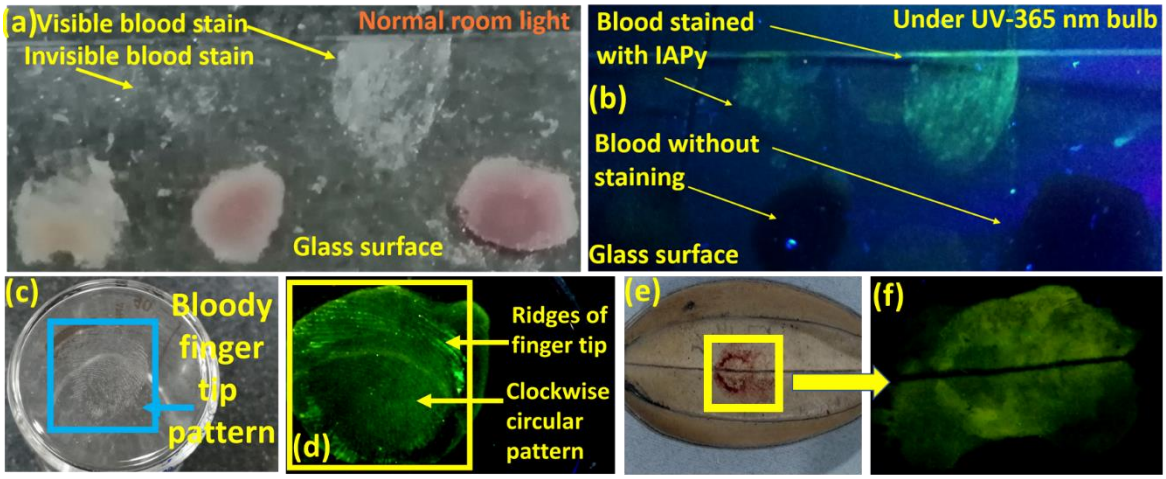

Figure 4.76 Forensic utilization of **SB3**; (a) blood stains under normal room light on glass slide (b) **SB3** stains blood patches to emit green fluorescence color under UV-365 nm lamp (c) blood-smeared fingerprint under room light on glass surface (d) fluorescent detection of blood-smeared fingerprint by **SB3** stain (e) blood patches on dry wood (f) fluorescent detection

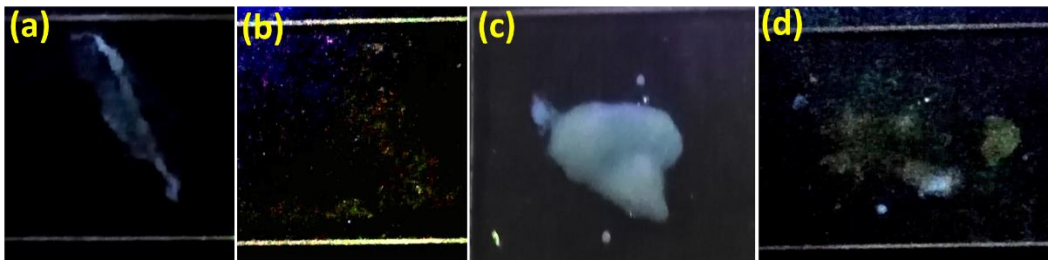

Figure 4.77 False-positive taste under UV-365 nm lamp; (a) dried patches of cold drinks (b) almost no fluorescence after staining with **SB3** (c) tomato sauce (d) feeble green fluorescence after staining with **SB3**

4.3.5.8 Fluorescent detection of hospital-disposed-of biohazards

Hospital-disposed biohazards such as cotton, blood-containing slides, gauze, sanitary napkins, and gloves can also spread germs and thus must be identified with advanced techniques. Encouraged by our probe's forensic utility, we applied it to perform a fluorescent detection of these hospital disposals. In the same way, the blood stains were initially fixed with a 4% formaldehyde solution followed by 1X PBS wash. **SB3**-DMSO solution of 10^{-5}(M) concentration was sprayed over the blood stains and kept for 50 mins.

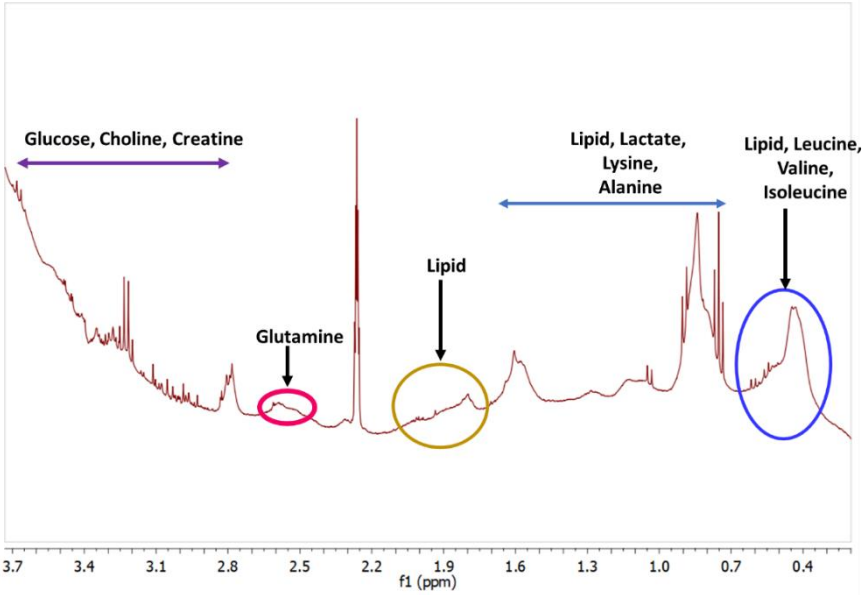

Figure 4.78 Blood serum NMR

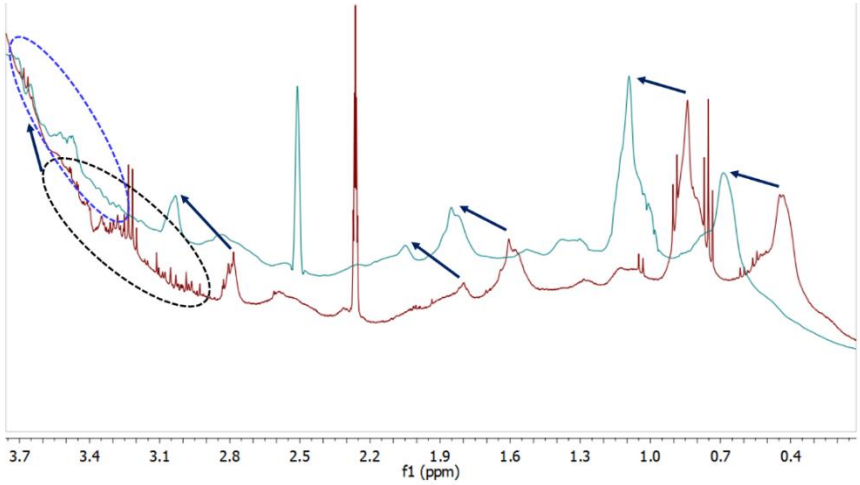

Figure 4.79 Blood serum-NMR comparison (the maroon color line for **normal serum** and the sea-green color line for (**SB3+serum**). The peaks for (**SB3+serum**) are de-shielded from that of **normal serum**

Next, the stains were rewashed with PBS and exposed under the 365 nm UV lamp to observe the greenish fluorescent detection of blood patches (Figures 4.80-81). We grew faint, dried blood patches with human blood for the experiments on glass, cotton, sanitary napkin, glove, and wood surfaces.

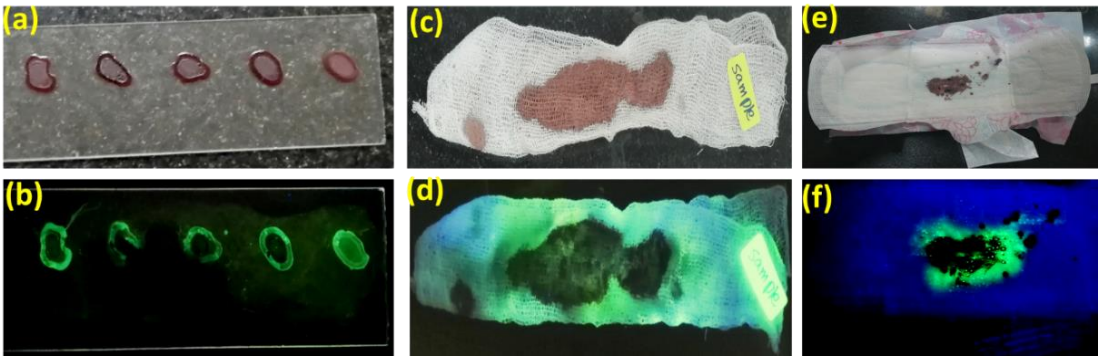

Figure 4.80 Fluorescent detection of hospital-disposed biohazards; under normal room light (a) blood-containing slide (c) blood-smeared gauze (e) blood patch containing sanitary pad; under UV-365 nm lamp (b) blood-containing slide (d) blood-smeared gauze (f) blood patch containing sanitary pad

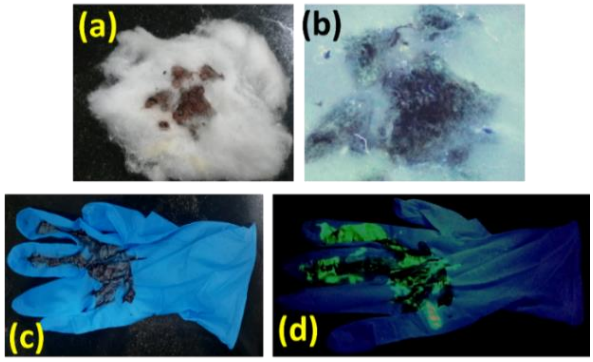

Figure 4.81 Hospital-disposed biohazards detection by fluorescence; under normal room light (a) blood-smeared cotton (c) blood-containing glove; under UV-365 nm lamp (b) blood-smeared cotton (d) blood-containing glove

4.3.6 Summary

Potential and judicious designs are successfully recognized in newly designed twisted systems, which can display six different photophysical facets, escaping the pitfalls of mutual exclusiveness of the photophysical properties. In the solid state, the double-site twisted conformation with transformability between more or less crystalline

and amorphous forms, the crystallite size alteration along with the strain regulates the respective emissions and its switching. In solution, absorbance and emission oscillator strengths, RMSD, and HOMO-LUMO energy gaps were realized to be effective behind the emissions in nonpolar and polar solvents. These theoretically determined parameters are crucial to elucidate blue-shifted aggregate emissions, and the twisted conformation may have been attributed to the crystal similar to the environment preventing π-π stacking, resulting in an emission enhancement in the aggregate. The restricted rotation in the aggregate plays a crucial role in this enhanced emission, as evident from viscofluorochromic studies. Especially the fingertip pressure-induced blueshifted MFC property of **SB7** and AIBSEE of **SB7** with 62 nm shift were even more fascinating. **SB7** was established as a DSE-gen in the near-red region, which is rarely identified. Most notably, all these features originated from every small single molecule. Moreover, diverse real-world optical applications were remarkable, that include (i) ink-free security writing and (ii) hidden patent fingerprints memory suitable for anti-counterfeiting applications with only **SB6**.

Again, we established an organic fluorescent dye **SB3** which can display seven different photophysical properties as a single material with seven multifarious applications in various domains. **SB3** exhibits a distinct '*V*' shape herringbone type packing with a centrosymmetric C2/c space group, three sites twisted structure with 22 different non-covalent interactions, and a substantial contact surface and solvent accessible void spaces. Again, the facially translated molecular columns, equidistant centroids, and stacking of two parallel molecules in a glide fashion with the presence of two-fold rotation axes and one-two screw axes induce the fascinating molecular packing. The relinquished π-π stacking results in a bright solid-state emission and AIE display. The system is susceptible to transitioning from a more crystalline state to a less crystalline state to display mechanical-force-induced enormous enhancement in emission. Almost free pyridyl nitrogens with 8% crystal void enable **SB3** to exhibit acidofluorochromic emission shift. Moreover, the three-site twisted structure contributes to presenting viscofluorochromic behavior. The favorable extent of quantum chemical descriptors and the appearance of LE and CT states simultaneously facilitate dual state emission and whitish light emission by tuning the solvent polarity.

Realizing a wide range of real-world applications using **SB3** is very much adequate. Further, **SB3** performs as a wash-free cancer cell bioimaging dye is notable and at the same time finds applications for forensic utility and fluorescent detection of hospital-disposed biohazards. The acidofluorochromism of **SB3** was utilized for hidden QR-code based/security stamp-based data storage and anticounterfeiting. Moreover, data encryption and food additive detection added extra fervor to its smartness.

4.3.7 Experimental section

The experimental part is described earlier in '*Materials, General Conditions and Measurements*.'

4.3.8 References

1 N. A. Kukhta and M. R. Bryce, ***Mater. Horiz.***, 2021, **8**, 33-35.

2 H. Ding, J. Li, G. Xe, G. Lin, R. Chen, Z. Peng, C. Yang, B. Wang, J. Sun, C. Wang, ***Nat. Commun.***, 2018, **9**, 5234.

3 H. T. Feng, J. Zeng, P. A. Yin, X. D. Wang, Q. Peng, Z. Zhao, J. W. Y. Lam, B. Z. Tang, ***Nat. Commun.***, 2020, **11**, 2617.

4 Q. Di, L. Li, X. Miao, L. Lan, X. Yu, B. Liu, Y. Yi, ***Nat. Commun.***, 2022, **13**, 5280.

5 X. Hou, C. Ke, C. J. Bruns, P. R. McGonigal, R. B. Pettman, J. F. Stoddart, ***Nat. Commun***,. 2015, **6**, 6884.

6 H. Ma, C. Zhao, H. Meng, R. Li, L. Mao, D. Hu, M. Tian, J. Yuan, Y. Wei, ***ACS Appl. Mater. Interfaces***, 2021, **13**(7), 7987-7996.

7 J. L. B. Vázquez, Y. A. A. Sánchez, L. A. R. Cortés, B. R. Molina, ***Chem. Mater.***, 2021, **33**(18), 7160-7184.

8 G, Chen, W. Li, T. Zhou, Q. Peng, D. Zhai, H. Li, W. Z. Yuan, Y. Zhang and B. Z. Tang, ***Adv. Mater.***, 2015, **27**, 4496-4501.

9 Q. Qiu, P. Xu, Y. Zhu, J. Yu, M. Wei, W. Xi, Dr. H. Feng, Prof. J. Chen and Prof. Z. Qian, ***Chem. Eur. J.***, 2019, **25**, 15983-15987.

10 Y. Yin, A. Ding, L. Yang, L. Kong and J. Yang, ***Mater. Chem. Front.***, 2022, **6**, 1261-1268.

11 L. Zou, S. Guo, H. Lv, F. Chen, L. Wei, Y. Gong, Y. Liu and C. Wei, ***Dyes Pigm.***, 2022, **198**, 109958.

12 J. Zhang, A. Li, H. Zou, J. Peng, J. Guo, W. Wu, H. Zhang, J. Zhang, X. Gu, W. Xu, S. Xu, S. H. Liu, A. Qin, J. W. Y. Lam and B. Z. Tang, ***Mater. Horiz.***, 2020, **7**, 135-142.

13 W. Yang, Y. Yang, Y. Qiu, X. Cao, Z. Huang, S. Gong and C. Yang, ***Mater. Horiz.***, 2020, **4**, 2047-2053.

14 F. Yu, H. Zhao, Y. Li, G. Xia and H. Wang, ***Mater. Chem. Front.***, 2022, **6**, 155.

15 M. Huang, J. Zhou, K. Xu, X. Zhu and Y. Wan, ***Dyes Pigm.***, 2019, **160**, 839-847.

16 W. Xi, J. Yu, M. Wei, Q. Qiu, P. Xu, Z. Qian and H. Feng, ***Chem. Eur. J.***, 2020, **26**, 3733-3737.

17 S. Mukherjee and P. Thilagar, **Chem. Eur. J.**, 2014, **20**, 9052-9062.

18 D. Su, C. L. Teoh, L. Wang, X. Liu and Y. T. Chang, ***Chem. Soc. Rev.***, 2017, **46**, 4833-4844.

19 M. A. Haidekker and E. A. Theodorakis, ***Org. Biomol, Chem.***, 2007, **5**, 1669-1678.

20 Y. Qu, Y. Zhu, J. Wu, J. Wu, Z. Gu and Y. Wu, ***Dyes Pigm.***, 2020, **172**, 107795.

21 J. Karpenko, Y. Niko, V. P. Yakubovskyi, A. O. Gerasov, D. Bonnet, Y. P. Kovtun and A. S. Klymchenko, ***J. Mater. Chem. C***, 2016, **4**, 3002-3009.

22 R. Yadav, A. Rai, A. K. Sonkar, V. Rai, S. C. Gupta and L. Mishra, ***New J. Chem.***, 2019, **43**, 7109-7119.

23 M. K. Kuimova, G. Yahioglu, J. A. Levitt and K. Suhling, ***J. Am. Chem. Soc.***, 2008, **130**(21), 6672-6673.

24 L. Xu, L. Ni, F. Zeng and S. Wu, ***Analyst***, 2020, **145**, 844-850.

25 U. P. Pandey and P. Thilagar, ***Adv. Optical Mater.***, 2020, **14**, 1902145.

26 B. K. Dwivedi, V. D. Singh and D. S. Pandey, ***J. Phys. Chem. C***, 2020, **124**(16), 9056-9067.

27 C. Ma, B. Xu, G. Xie, J. He, X. Zhou, B. Peng, L. Jiang, B. Xu, W. Tian, Z. Chi, S. Liu, Y. Zhang and J. Xu, ***Chem. Commun.***, 2014, **50**, 7374-7377.

28 J. Wang, Z. Liu, S. Yang, Y. Lin, Prof. Dr. Z. Lin and Prof. Dr. Q. Ling, ***Chem. Eur. J.***, 2018, **24**, 322-326.

29 W. J. Shi, R. Chen, J. Yang, Y. F. Wei, Y. Guo, Z. Z. Wang, J. W. Yan and L. Niu, ***Anal. Chem.***, 2022, **94**(42), 14707-14715.

30 W. Xi, J. Yu, M. Wei, Q. Qiu, P. Xu and Z. Qian and H. Feng, ***Chem. Eur. J.***, 2020, **26**, 3733-3737.

31 P. Gopikrishna and P. K. Iyer, ***J. Phys. Chem. C***, 2016, **120**, 26556-26568.

32 J. A. Lin, S. W. Li, Z. Y. Liu, D. G. Chen, C. Y. Huang, Y. C. Wei, Y. Y. Chen, Z. H. Tsai, C. Y. Lo, W. Y. Hung, K. T. Wong and P. T. Chou, ***Chem. Mater.***, 2019, **31**(15), 5981-5992.

33 Dr. S. Kumar, Prof. P. Rajamalli, Dr. D. B. Cordes, Prof. A. M. Z. Slawin and Prof. E. Z. Colman, ***Asian J. Org. Chem.***, 2020, **9**(9), 1277-1285.

34 F. Lafzi, Y. Taskesenligil, B. Canimkurbey, S. Piravadili, H. Kilic and N. Saracoglu, ***ACS Omega***, 2022, **7**, 44322-44337.

35 S. Tongsuk, R. Malatong, T. Unjarern, C. Wongkaew, P. Surawatanawong, T. Sudyoadsuk, V. Promarak and N. Ruangsupapichat, ***J. Lumin.***, 2021, **238**, 118287.

36 B. Prusti and Prof. Manab Chakravarty, ***ChemPlusChem***, 2020, **85**(12), 2652-2656.

37 B. Prusti and Prof. Manab Chakravarty, ***Dyes Pigm.***, 2020, **181**, 108543.

38 L. Qian, Y. Zhou, M. Liu, X. Huang, G. Wu, W. Gao, J. Ding and H. Wu, ***RSC Adv.***, 2017, **7**, 42180-42191.

39 Y. Ma, Y. Li, L. Chen, Y. Xiong and G. Yin, ***Dyes Pigm.***, 2016, **126**, 194-201.

40 B. Prusti and M. Chakravarty, ***Analyst***, 2020, **145**,1687-1694.

41 B. Prusti and M. Chakravarty, ***Mater. Adv.***, 2021, **2**, 1752-1759.

42 H. Liu, Y. Gu, Y. Dai, K. Wang, S. Zhang, G. Chen, B. Zou and B. Yang, ***J. Am. Chem. Soc.***, 2020, **142**(3), 1153-1158.

43 H. Liu, Y. Dai, Y. Gao, H. Gao, L. Yao, S. Zhang, Z. Xie, K. Wang, B. Zou, B. Yang and Y. Ma, ***Adv. Optical Mater.***, 2018, **6**(15), 1800085.

44 Y. Zhan, ***Dyes Pigm.***, 2020, **173**, 108002.

45 Dr. H. Wu, Dr. Z. Chen, Dr. W. Chi, A. K. Bindra, Dr. L. Gu, Dr. C. Qian, B. Wu, B. Yue, Dr. G. Liu, Dr. G. Yang, Prof. Dr. L. Zhu and Prof. Y. Zhao, ***Angew. Chem. Int. ed.***, 2019, **58**(33), 11419-11423.

46 S. Qu, Q. Lu, S. Wu, L. Wang and X. Liu, ***J. Mater. Chem. C***, 2012, **22**, 24605-24609.

47 P. Josse, M. Allain, J. P. Calupitan, Y. Jiang, C. Cabanetos and J. Roncali, ***Adv. Opt. Mater.***, 2020, **8**(13), 2000420.

48 D. Su, C. L. Teoh, L. Wang, X. Liu and Y. T. Chang, ***Chem. Soc. Rev.***, 2017, **46**, 4833-484.

49 M. R. Han and M. Hara, ***New J. Chem.***, 2006, **30**, 223-227.

50 H. Gao, D. Xu, Y. Wang, Y. Wang, X. Liu, A. Han and C. Zhang, ***Dyes Pigm.***, 2018, **150**, 59-66.

51 Dr. S. Suzuki, Dr. S. Sasaki, A. S. Sairi, R. Iwai, Prof. Dr. B. Z. Tang and Prof. Dr. G. Konishi, ***Angew. Chem. Int. Ed.***, 2020, **59**(25), 9856-9867.

52 Y. Liu, Y. Lei, M. Liu, F. Li, H. Xiao, J. Chen, X. Huang, W. Gao, H. Wu and Y. Cheng, ***J. Mater. Chem. C***, 2016, **4**, 5970-5980.

53 T. Shu, X. Gao, S. Chen, S. Wang, K. K. Lai and L. Gan, ***Sustainability***, 2016, **8**, 250.

54 T. Zhang, W. Shi, D. Wang, S. Zhuo, Q. Peng and Z. Shuai, ***J. Mater. Chem. C***, 2019, **7**, 1388-1398.

55 M. Rivera, L. Stojanovic and R. C. Otero, ***J. Phys. Chem. A***, 2021, **125**, 1012-1024.

56 Q. Zhu and S. Hattori, ***J. Mater. Res.***, 2023, **38**, 19-36.

57 N. P. Słomka, M. Małecka, M. Wierzchowski and B. Kupcewicz, ***Int. J. Mol. Sci.***, 2023, **24**, 7200.

58 M. P. Singh, A. Tarai and Prof. J. B. Baruah, ***ChemistrySelect***, 2018, **23**, 6364-6373.

59 Dr. H. Wu, Dr. Z. Chen, Dr. W. Chi, A. K. Bindra, Dr. L. Gu, Dr. C. Qian, B. Xu, B. Yue, Dr. G. Liu, Dr. G. Yang, Prof. Dr. L. Zhu and Prof. Y. Zhao, ***Angew. Chem. Int. Ed.***, 2019, **33**, 11419-11423.
60 R. Rotaru, M. Savin, N. Tudorachi, C. Peptu, P. Samoila, L. Sacarescu, V. Harabagiu, ***Polym. Chem.***, 2018, **9**, 860-868.
61 S. Banerjee, A. K. Both and M. Sarkar, ***ACS Omega***, 2018, **3**, 11, 15709-15724.
62 S. Hayashi, A. Asano, N. Kamiya, Y. Yokomori, T. Maeda, T. Koizumi, ***Sci. Rep.***, 2017, **7**, 9453.

63 P. Sudhakar and T. P. Radhakrishnan, ***J. Mater. Chem. C***, 2019, **7**, 7083-7089.

64 Y. Gu, H. Liu, R. Qiu, Z. Liu, C. Wang, T. Katsura, H. Zhang, M. Wu, M. Yao, H. Zheng, K. Li, Y. Wang, K. Wang, B. Yang, Y. Ma and B. Zou, **J. Phys. Chem. Lett.**, 2019, **10**(18), 5557-5562.

65 L. Wilbraham, M. Louis, D. Alberga, A. Brosseau, R. Guilot, F. Ito, F. Labat, R. Metivier, C. Allain and I. Ciofini, ***Adv. Mater.***, 2018, **30**, 1800817

66 Internet course by Paul Barnes, Simon Jacques, Martin Vickers, http://pd.chem.ucl.ac.uk/pdnn/peaks/size.htm.

67 L. A. R. Cortes, A. N. Huerta and B. R. Molina, ***Matter***, 2021, **4**, 2582-2685.

68 X. Mei, J. Wang, Z. Zhou, S. Wu, L. Huang, Z. Lin and Q. Ling, ***J. Mater. Chem. C***, 2017, **5**, 2135.

69 Y. Liu, L. Teng, C. Xu, T. B. Ren, S. Xu, X. Lou, L. Yuan and X. B. Zhang, ***CCS Chem.***, 2022, **4**, 2135-2164.

70 P. Gopikrishna and P. K. Iyer, ***J. Phys. Chem. C***, 2016, **120**, 26556-26568.

71 C. A. Guido, S. Knecht, J. Kongsted and B. Mennucci, ***J. Chem. Theory Comput.***, 2013, **9**, 2209-2220

72 D. Presti, F. Labat, A. Pedone, M. J. Frisch, H. P. Hratchian, I. Ciofini, M. C. Menziani and C. Adamo, ***J. Comput. Chem.***, 2016, **9**, 861-870.

73 K. T. Kamtekar, A. P. Monkman and M. R. Bryce, ***Adv. Mater.***, 2010, **5**, 572-582.

74 P. Das, A. Kumar, A. Chowdhury and P S. Mukherjee, ***ACS Omega***, 2018, **3** (10), 13757-13771.
75 M. B. Smykaj, K. Rachuta, G. L. Hug, M. Majchrzak and B. Marciniak, ***J. Phys. Chem. C***, 2021, **125**, 12488-12495.
76 Prof. Dr. G. Haberhauer, ***Chem. Eur. J.***, 2017, **23**, 9288-9296.
77 Y. Luo, Y. wang, S. Chen, N. Wang, Y. Qi, X. Zhang, M. Yang, Y. Huang, M. Li, J. Yu, D. Luo and Z. Lu, ***Small***, 2017, **13**, 1604113.
78 R. Ghosh, A. Nandi and D. K. Palit, ***Phys. Chem. Chem. Phys.***, 2016, **18**, 7661-7671.
79 X. H. Jin, C. Chen. C. X. Ren, L. X. Cai and J. Zhang, ***Chem. Commun.***, 2014, **50**, 15878-15881.
80 Dr. Z. Zhao, Dr. H. Zhang, Dr. J. W. Y. Lam and Prof. B. Z. Tang, ***Angew. Chem. Int. Ed.***, 2020, **25**, 9888-9907.
81 Q. Wu, T. Zhang, Q. Peng, D. Wang and Z. Shuai, ***Phys. Chem. Chem. Phys.***, 2014, **16**, 5545-5552.

82 H. Yin, B. Li, X. Zhao, Y. Liu, Y. Shi and D. Ding, ***Dyes Pigm.***, 2022, **201**, 110192.
83 J. Lee, Y. Park, J. Jung and W. S. Han, ***Photochem. Photobiol. Sci.***, 2017, **16**, 1495.
84 M. Z. K. Baig, D. Majhi, R. N. P. Tulichala, M. Sarkar and M. Chakravarty, ***J. Mater. Chem. C***, 2017, **5**, 2380-2387.
85 Y. Hong, J. W. Y. Lam and B. Z. Tang, ***Chem. Commun.***, 2009, 4332-4353.

86 J. He, B. Xu, F. Chen, H. Xia, K. Li, L. Ye, and W. Tian, ***J. Phys. Chem. C***, 2009, **113**(22), 9892-9899.

87 J. D. Vincent, K. Srinivas and J. W. King, ***J. Am. Oil Chem Soc.***, 2012, **89**(9), 1585-1597.

88 M. A. Haidekker, T. P. Brady, D. Lichlyter and E. A. Theodorakis, ***J. Am. Chem. Soc.***, 2006, **128**(2), 398-399.

89 Dr. S. Chen, Dr. Y. Hong, Dr. Y. Zeng, Q. Sun, Dr. Y. Liu, E. Zhao, G. Bai, Prof. J. Qu, Prof. J. Hao and Prof. B. Z. Tang, ***Chem. Eur. J.***, 2015, **21**(11), 4315-4320.

90 https://online-image-comparison.com/result

91 H. Wang, X. Ji, Z. A. Page and J. L. Sessler, ***Mater. Chem. Front.***, 2020, **4**, 1024-1039.

92 D. Hu, W. Xu, G. Wang, K. Liu, Z. Wang, Q. Shi, S. Lin, Z. Liu and Y. Fang, ***Adv. Funct. Mater.***, 2022, **45**, 2207895.
93 Q. Qiu, P. Xu, Y. Zhu, J. Yu, M. Wei, W. Xi, Dr. H. Feng, Prof. J. Chen and Prof. Z. Qian, ***Chem. Eur. J.***, 2019, **70**, 15983-15987.
94 L. Xu, L. Ni, F. Zeng and S. Wu, ***Analyst***, 2020, **145**, 844.
95 H. L. Barros, T. Mileski, C. Dillenburg and V. Stefani, ***Forensic Chem.***, 2017, **5**, 16-25.
96 F. Fathi, L. M. Kasmaee, A. M. Varnosfaderani, A. Kyani, M. R. Nejad, K. Sohrabzadeh, N. Naderi, M. R. Zali, M. R. Tavirani, M. Tafazzoli and A. A. Oskouie, ***Magn. Reson. Chem.***, 2014, **52**, 370-376.

Chapter V

Heteroatom Replacement Guided Emission Contrast from Twisted Dicyanoethylenes: Transpiring Non-cytotoxic SSEOF into Wash-Free LD Bioimaging of Living FaDu Cells

Objectives:

- Develop a new class of dicyanoethylene-based SSEOF for wash-free lipid droplet bioimaging in living cancer cells
- Understanding a common strategy for photophysical modulation accompanied by bioimaging modalities

Abstract:

Escaping from the conventional xanthene, cyanine, oxazine, or trisubstituted dicyanoethylene-based structures, heterocycle, and naphthalene-attached tetrasubstituted dicyanoethylene-based designs have been foreseen, and a three-step synthetic route has been established to produce five different fluorophores. In their design, the donor naphthalene, the acceptor 'dicyano' groups, and the 'diene' as a π-extension are common. Just by replacing the heteroatom/s in the attached heterocyclic part, it was possible to alter their extent of the '*J*'-type of crystal packings with other relevant quantum chemical descriptors. This contributed to astonishing artistry in solid and solution state emission tuning accompanied by a variation of their cell permeability, cytotoxicity, and bioimaging competence. The photo-physically sound, biocompatible, and a cell-permeable, hydrophobic core containing lead fluorophore **OXNCN** was transpired in wash-free lipid droplet (LD)-specific bioimaging of live cancer and normal cells. Moreover, the colocalization investigation with the standard dye Nile red, the outcomes of the cholesterol depletion and repletion studies, and oleic acid treatment-based bioimaging further confirmed the LD specificity of **OXNCN**. It was found that **OXNCN** performed better in robust FaDu cancer cells than in normal HEK-293 cells. By calculating the percentage area covered by LDs in cells it was even possible to discriminate the cancer cells from the normal ones.

5.1 Introduction

The strategic inception of non-cytotoxic smart organic fluorogens with omnipresent tunable emission, aided by microscopy imaging modalities, can't be averted as this helps to illuminate biological systems[1-9] by avoiding the mutually exclusive principles of photophysical outputs.[10,11] Fluorescence imaging has become a crucial contrivance to investigating the structure and function of cells and organelles in recent decades by virtue of its good operationality, high spatiotemporal resolution, and compatibility with living biosamples.[12-16] On the other hand, recent research has revealed that almost a ~20 times elevation in the number of lipid droplets is generally observed in cancerous cells compared to that in a normal cell.[17-19] Hence, lipid droplet (LD) targeting probes for living cancer cells are invaluable tools for investigating localized information.[20-23] Meanwhile, the art of strategy for converting key organic fluorophores into a successful LD bioimaging agent necessitates the combination of several layers of logic from the standpoints of photophysical competence, biocompatibility, and non-invasive, photostable bioimaging capability. Predicting the local environments that a designed probe will face inside the cell is difficult. It is always preferred if a non-cytotoxic probe can emit in the solid state, solution state, aggregates, and viscous medium everywhere.[24,25] Being a cause of concern, a small number of organic molecules is there to display emissions in aggregate, solids, solutions, and viscous medium as well, and still, cellular cytotoxicity becomes a pitfall for them, minimizing their ultimate applicability for living cell bioimaging.[26,27]

Of late, heterocycles attached-organic π-conjugates have rendered ardent attention to receive a commendable emission both in solids and solution states,[28-30] and many of them have been established through the π-extension,[31,22] charge-dependent strategy,[32] sol-gel molecular assembly,[33] donor-acceptor based ICT modulation[34,35] and by incorporating strongly electron-withdrawing -CN groups for effective LD bioimaging (Figure 5.1).[36-44]

Herein, we developed a series of a new class of planar or puckered heterocycles and naphthalene-conjugated tetra-substituted twisted dicyanoethylenes-**DBFNCN**, **DBTNCN**, **OXNCN**, **PONCN**, and **TANCN** with many astounding emission contrasts and tunings in solids, solvents, aggregates, and viscous medium. Notably, a common

synthetic route was established to prepare all of them with decent synthetic yields. Strikingly, **OXNCN,** with the flattest heterocyclic ring, exhibited the brightest solid-state emission, and **TANCN,** with a puckered heterocyclic scaffold, displayed the most intense solution-state emissions. Even though **OXNCN** showed green emission in aggregates, surprisingly, it exhibited yellow emission in a viscous medium. On the other hand, unlike other dyes, **TANCN** exhibited concentration-dependent off/on emission tuning in a viscous medium. Moreover, only **TANCN** and **PONCN** were effective dual-state emitters with ~99 nm/150 nm solvatochromic shifts. The science behind unusual photophysical contrasts and tuning was established through several steady-state and time-resolved fluorescence spectroscopy studies, single-crystal structure analysis, and detailed TD-DFT studies. The cytotoxicity of the synthesized probes was thoroughly screened, and the lead biocompatible and cell-permeable dye **OXNCN** was established for LD bioimaging of living FaDu cancer cells with a profound investigation of confocal experiments concerning market-available LD probe Nile red. To be noted, FaDu is a stubborn cancerous cell line that creates many challenges against the administered drugs, and the cells agglomerate to make lumps creating problems during bioimaging of LDs.[45,46] Since the inception of LD bioimaging dyes like Nile red [47] and BODIPY,[48], many endeavors have been conferred for LD bioimaging of different cancer cells, mainly focussing on A549/HeLa cells as a model.[49-52] Yet, the exploration of LD bioimaging with FaDu cells is rare, and thus, it is chosen for our bioimaging studies as inspired by earlier critical endeavors.[53] With **OXNCN**, it was possible to investigate concentration-dependent, time-dependent, and temperature-dependent LD bioimaging of FaDu cells, and the colocalization with standard dye Nile red was thoroughly examined in terms of different imaging-related parameters. The fluorescence intensity, staining efficiency, colocalization percentage, photostability, non-invasiveness, and live-cell imaging capability of **OXNCN** were commendable compared to Nile red. The cholesterol depletion and repletion studies confirmed the LD specificity of **OXNCN**, and oleic acid treatment-based bioimaging succeeded in the semi-quantification of LDs with this newly synthesized probe in FaDu. Thus, designing a new class of organic fluorophores and transpiring the lead **OXNCN** as an LD imaging probe aggravated the logical pursuits of the work.

5.2 Literature review on 'dicyano'-based organic fluorophores for lipid droplet bioimaging

Wu *et al*. developed a coumarin-based (5**A**) lipid-droplet targeting ratiometric fluorescent probe for hypochlorous acid in live cells.[36] Their probe displayed dual-emission signal changes in blue and red spectral windows (470.672 nm) upon HClO/ClO^- treatment. Wang *et al*. could discover one 1,4-dihydro quinoline-based probe (5**B**) that acted as a dual-functional AIE fluorescent probe to image β-amyloid plaques and lipid droplets.[37] An interesting work was reported in 2016 by Prof. Tang's research group when triphenylethylene (TPE) based dicyano functionalized probe **5C** could monitor even the process of LD accumulation in cells to diagnose early-stage fat-related diseases.[38] Huang *et al*. established a dansyltrimethylfuranylidene-based lipid droplet targeting fluorescent probe **5D**for specific detection of SO_2 derivatives in living cells.[39] The research group of Prof. Bin Liu established an ultrabright tetrasubstituted dicyanoethylene-based probe 5**E** for three-photon imaging of lipids, but no heterocyclic chemistry was involved in the designing of the probe.[40] From the lab of Prof. Voskuhl, an effort was made to produce a heterocycle containing organic fluorophore to image bacterial cell walls. Still, the probe (5**F**) had a conventional design of being a charged species aiming for bioimaging.[42]

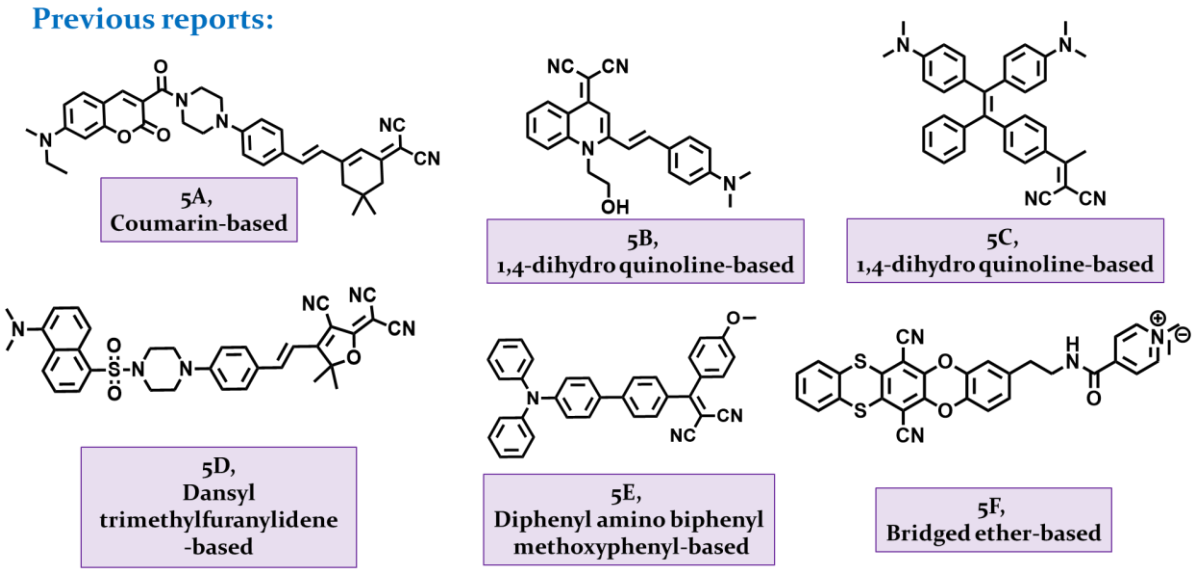

Figure 5.1 Some earlier reported LD bioimaging dyes that contain the 'dicyano' functional group (taken from refs. 36-42)

5.3 Results and Discussion

5.3.1 Design concept

For photophysical properties, the designed molecules have two different types of donors connected to the strong electron-withdrawing 'dicyano' group linked through a 'diene' π-extension, thus resulting in a tetrasubstituted D-π-A dicyanoethylene structures. Now, one donor in the flat/kinked heterocyclic scaffold and the introduction of 'S'/'O' heteroatom(s) may achieve different extents of planarity in the ring. It would tune the polarizability, electronegativity, electron density, orbital overlap and contribution. The other donor is the naphthalene which will create a twist with the other parts of the molecule, eliminating π-π stacking in different molecular planes. Thus, the combined effect would produce different slip angles, resulting in various crystal packing with a different extent of *J*-stacking. The D-π-A core with strong -CN acceptors would facilitate a higher degree of ICT in solvents, and the overall twisted design can adopt a bent-to-planar / planar-to-bent conformation at their respective excited states. However, it would alter the extent of some important quantum chemical descriptors such as RMSD, oscillator strength, HOMO-LUMO gap, and NTO distributions to differ in emission wavelength and efficiency. The twisted structure would facilitate the AIE property (Aggregation-Induced Emission), and restriction of the twisted molecular rotor would favor the VIE property (Viscosity-Induced Emission). As the naphthalene scaffold, 'diene,' and 'dicyano' parts remain unchanged in all the molecules, the emission contrast would originate from the direct and indirect effects of the present heteroatom in the respective heterocycles. Hence, the heteroatom replacement strategy would be anticipated to monitor the emission tuning.

On the other hand, high lipophilicity is crucial *for effective LD bioimaging*.[54,55] Of note, the naphthalene and dicyano cores would possess moderate lipophilicity of almost log *P* ~ 3.3 and *c*Log *P* ~ 2.606. Now, introducing different heteroatom/s in the heterocyclic part would render different degrees of cell permeability and effective log *P*/ *c*Log *P* values, which may facilitate LD specificity. The predicted effective Log *P* order was **OXNCN** (4.7) <**PONCN** (6.06) <**TANCN** (7.43), and *c*Log *P* order would be **OXNCN** (6.338) < **PONCN** (6.578) < **TANCN** (6.818). Again, the strong ICT would vary from non-polar to the polar environment, and the possibility of intramolecular *H*-bonding with

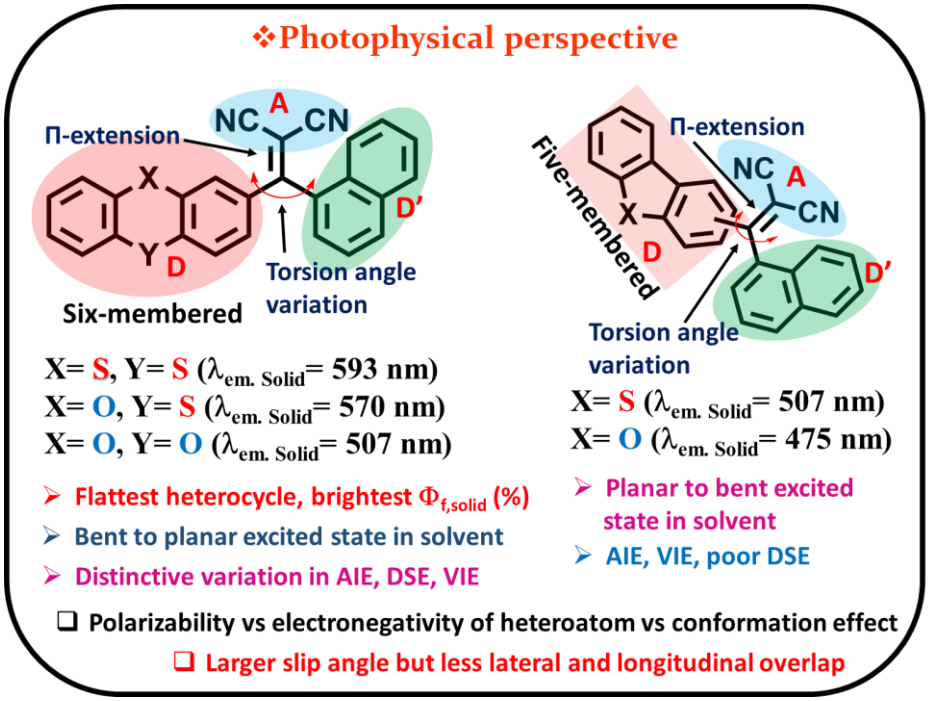

Figure 5.2.1 Design concept for favorable photophysical output

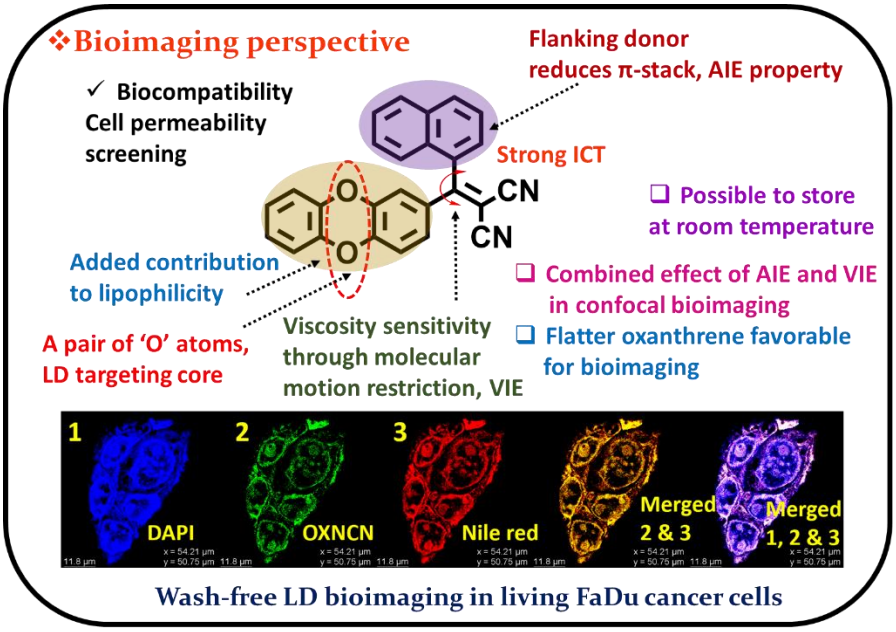

Figure 5.2.2 Design concept to transpire photophysical outputs into LD-targeted bioimaging

cyano groups would suppress cytosolic *H*-bonding interactions[56] to reduce background glitches during confocal imaging experiments. The probe should be irresponsive to the cytosolic polarity only to provide signals for LDs, and an uncharged chemical structure would disallow nucleus susceptibility. AIE property enhances fluorescence intensity

while the viscosity-responsive feature favors high-intensity emission with LD specificity.[57] In addition, combined AIE and VIE effects would assist in getting brighter imaging intensity even at lower probe concentrations (Figure 5.2).

5.3.2 Synthetic protocol and structural elucidation

Every dicyanoethylene derivative was prepared through a three-step reaction pathway (Scheme 1). The very first step is the electrophilic aromatic substitution (Friedel-Crafts- type arylation) onto diethyl (hydroxy(naphthalen-1-yl)methyl)phosphonate by utilizing the heterocyclic nucleophiles like thianthrene, phenoxathiine, oxanthrene, dibenzothiophene, and dibenzofuran in the presence of methane sulfonic acid, as recognized by our earlier efforts.[58,59] The synthetic procedure of the diethyl (hydroxy(naphthalen-1-yl)methyl)phosphonate was established earlier in our laboratory.[58,59] For thianthrene, oxanthrene, and dibenzothiophene, the attack happened through the '2' position, but for dibenzofuran, it prefered at the '3' position as expected. For phenoxathiine even though an 'O' atom is present, the attack happened through '3' position. According to earlier report,[60] frontier electron density values for an electrophilic attack would be greater at the '3' position of phenoxathiine. The extent of electron density does not vary much from dihedral angle ~120° to 180°.

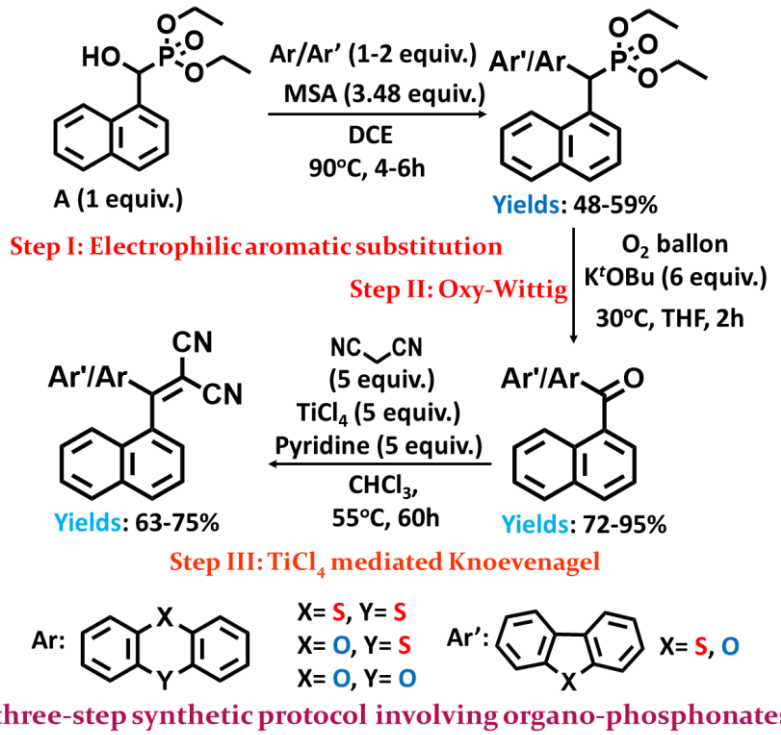

Scheme 1 Synthetic route for reporting tetrasubstituted dicyanoethylenes

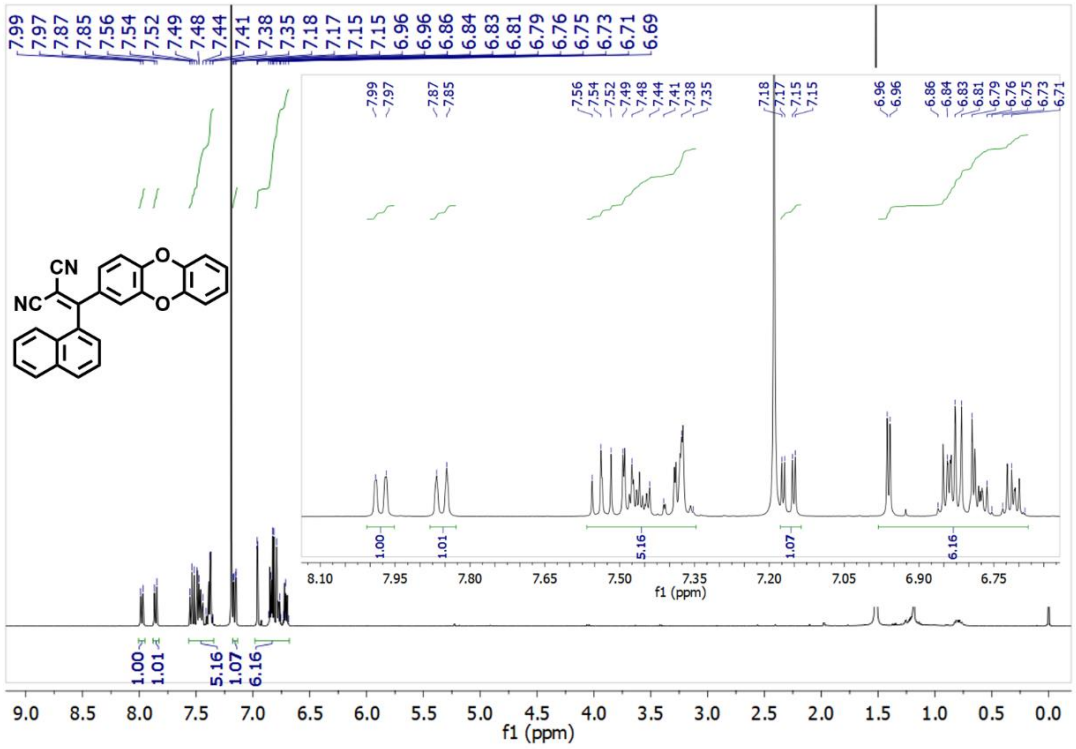

Figure 5.3 ^{1}H NMR spectra for 2-(dibenzo[b,e][1,4]dioxin-2-yl(naphthalen-1-yl)methylene)malononitrile)

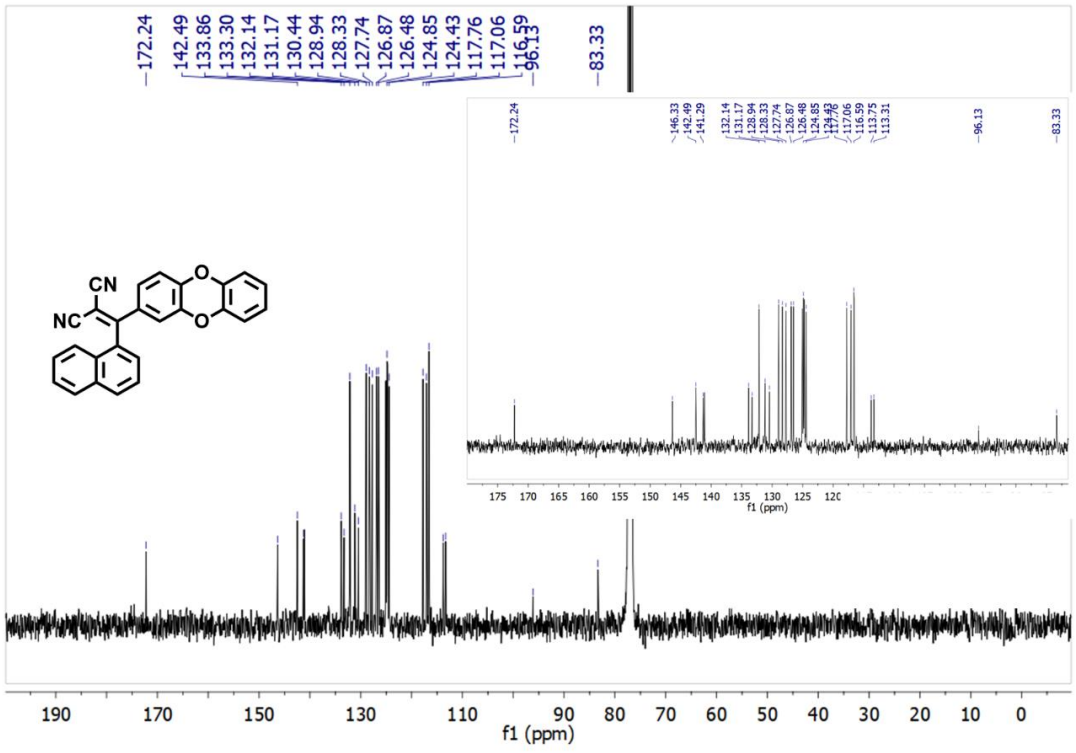

Figure 5.4 ^{13}C NMR spectra for 2-(dibenzo[b,e][1,4]dioxin-2-yl(naphthalen-1-yl)methylene)malononitrile)

This may be attributed to the observed '3' positional attack by phenoxathiine. As the second step of our synthetic protocol; the newly resulting phosphonates, through the electrophilic aromatic substitution reactions, were subjected to an oxy-Wittig reaction to form respective 'keto' derivatives following the previously reported pathway.[58] As the third and last step, the newly synthesized 'keto' derivatives underwent a Knoevenagel condensation with an excess of malononitrile, mediated by $TiCl_4$/pyridine (Lehnert reagent) to produce the final products with decent yields.[61]

The formation of phosphonates through electrophilic aromatic substitution reaction by different heterocycles was confirmed by distinctive peaks in ^{31}P NMR, P-CH peaks at $\delta \sim$ 5.17-5.51, and P-C coupling peaks at $\delta \sim$ 43-46, in ^{13}C NMR for most of the cases. The keto compounds had very typical peaks at $\delta \sim$ 195-197 in ^{13}C NMR. In IR spectrum, there were discerning peaks at ~ 2213-2220 cm^{-1}, indicating the -CN groups present for all the dicyanoethylene compounds. Again in ^{13}C NMR, there were distinctive peaks at δ ~112-114, confirming the presence of the cyano groups for all these dicyanoethylene derivatives.

5.3.3 Prompt Photophysical Properties

5.3.3.1 Solid-state emission tuning

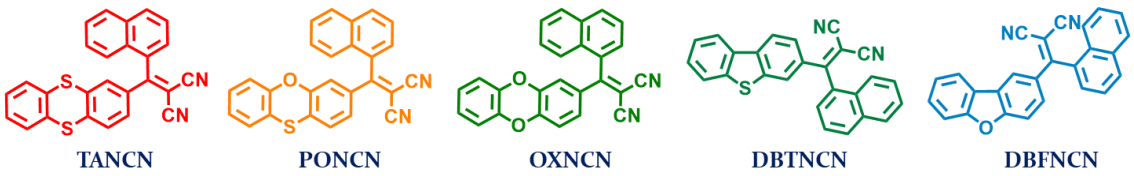

Figure 5.5 Structures of all five synthesized dyes at a glance

From the steady-state photophysical experiments, it is revealed that in solids, **PONCN** (*one 'S', one 'O' in the six-membered central ring*) absorbs (λ_{max}= 530 nm) almost at the same region as that of **TANCN** (*two 'S'in six-membered central ring*) (λ_{max}= 533 nm), but **PONCN** emits orange-yellow color (λ_{max}= 570 nm, Φ_f *(%)*= 3.00) while **TANCN** emits at near-red (λ_{max}= 593 nm, Φ_f *(%)*= 9.60) with enhanced emission efficacy. For **OXNCN** (*two'O'in six-membered central ring)*, the absorbance (λ_{max}= 465 nm) and emission wavelengths (λ_{max}= 507 nm) in solids are blueshifted as compared to that of

PONCN and **TANCN**. The emission quantum yield in solids for the flattest oxanthrene containing **OXNCN** was surprisingly found to be the highest (Φ_f (%)= 10.22), surpassing the quantum yields of **PONCN** and **TANCN**, which contain kinked heterocyclic rings. Again, for **DBTNCN** (*one 'S' in five-membered central ring*), the absorbance (λ_{max}= 461 nm) and emission wavelength (λ_{max}= 507 nm) are redshifted than that the absorbance (λ_{max}= 425 nm) and emission (λ_{max}= 475 nm) of **DBFNCN** (*one 'O' in five-membered central ring*,). Even the solid-state emission quantum yield is again higher for **DBFNCN** (Φ_f (%)= 8.36) than that of **DBTNCN** (Φ_f (%)= 6.79). So, the inclusion of a '*S*' atom or increasing the number of '*S*' atoms replacing '*O*' could help to exhibit bathochromic shift (86 nm emission shift from 507 nm to 593 nm for the *six-membered central heterocyclic ring* series and 32 nm emission shift from 475 nm to 507 nm for the *five-membered central heterocyclic ring* series).

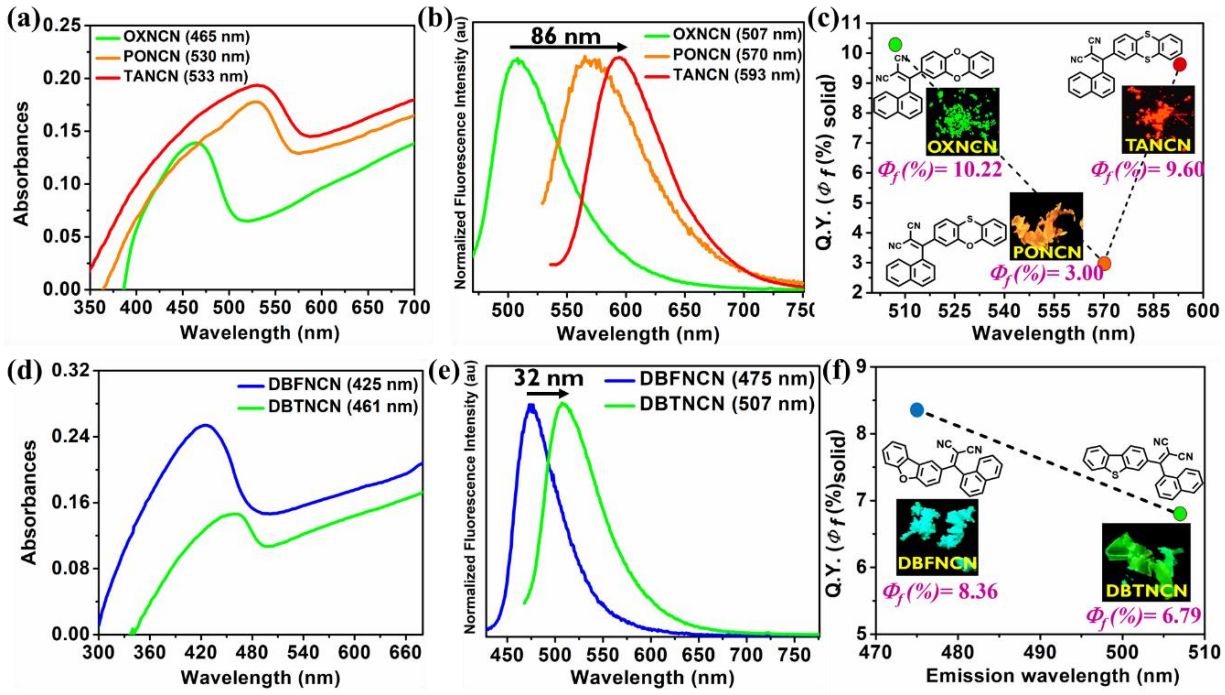

Figure 5.6 In **s**olid-state; for **OXNCN**, **PONCN**, and **TANCN** (a) absorbances (b) emissions (c) quantum-yield vs emission wavelength plot; for **DBFNCN** and **DBTNCN** (d) absorbances (e) emissions (f) quantum-yield vs emission wavelength plot (Inset pictures were captured under a UV-365 nm bulb, the reported Φ_f (%) is the absolute quantum yield in solid with ± 0.2-2% error)

However, the addition of an '*O*' atom or increasing the number of '*O*' atoms replacing '*S*' could assist enhancing the emission efficiency in this class of molecules (Figure 5.6).

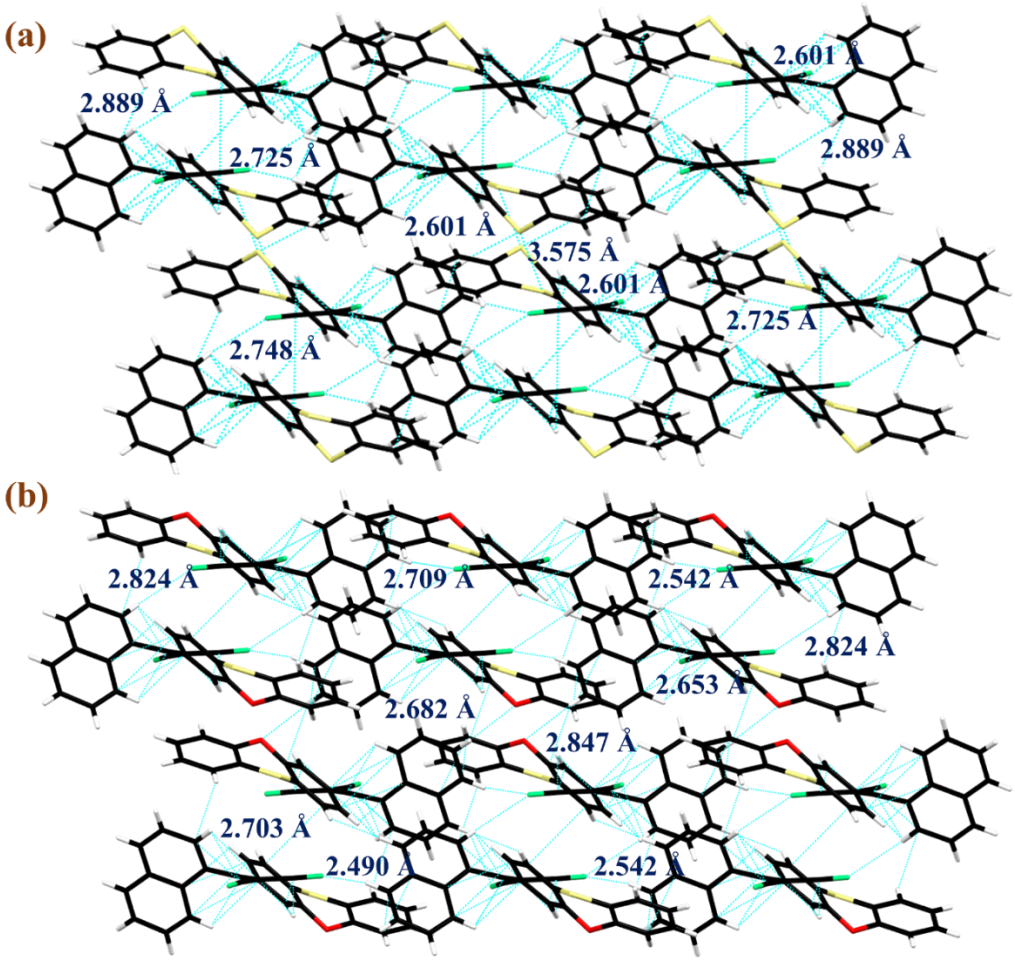

Figure 5.7 Crystal packing and non-covalent interactions (a) **TANCN** (c) **PONCN** ('b' axis view, atom-representations by color: yellow for '**S**', red for '**O**', green for '**N**')

This outcome is noteworthy because of the deviation towards from the previously recognized event in a relevant system.[42] Soliciting crystal packing with the non-covalent interactions of the respective single-crystals was highly important to have deep insight into the fact of surprising emission tuning and variance in emission efficacy. Single crystals for **TANCN**, **PONCN**, and **DBTNCN** were produced from both a $CHCl_3$:DMSO (3:1) solvent combination and a hexane: EtOAc (3:1) medium, and it was also possible to deduce their respective crystal structures. **TANCN** and **PONCN** both were found to be monoclinic crystal systems containing P 1 21/n 1 space group with a similar type of lattice parameters, volume, glide planes, screw axes, and negligible voids

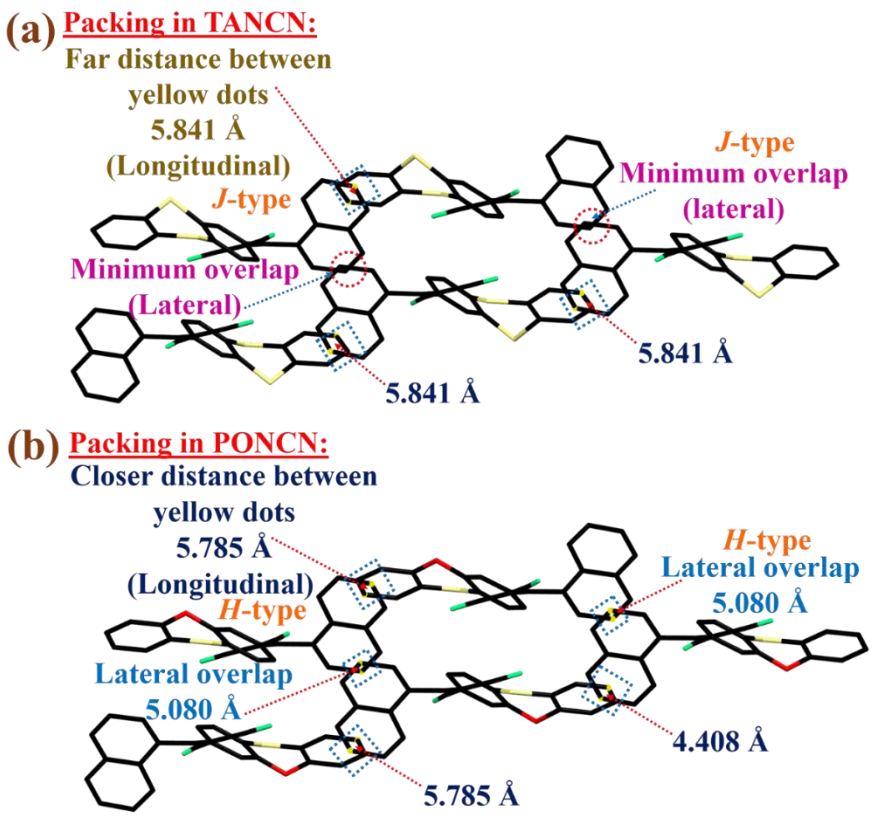

Figure 5.8.1 Longitudinal and lateral displacements for (a) **TANCN (b) PONCN**

(Table 5.1, Figures 5.9, 5.10). The crystal packing for both **TANCN** and **PONCN** looks almost the same with alternative and translated parallel end-to-end molecular rows (Figure 5.7), but the replacement of one 'S' atom with one 'O' atom created a contrast between **TANCN** and **PONCN**. There are 22 intra/intermolecular non-covalent interactions for **PONCN** and 21 interactions for **TANCN**. Both the **TANCN** and **PONCN** molecular packings include 8 different types of π...π interactions; however, **PONCN** holds slightly more number of C-H...π interactions than **TANCN**. Although three different types of N...H interactions are noticed for both of them, only one O...H interaction is accompanied by one H...H interaction in **PONCN**. Again, **TANCN** has one S...H interaction and even one S...S interaction, but there a lack of such interactions in **PONCN** holding one 'S' atom. (Table 5.2). Earlier, the molecular exciton model indicated that head-to-tail alignment of the transition dipoles for the monomeric dye aligns in a co-planar inclined fashion, having a slip angle of less than 54.7°.[62] As shown in Figure 5.8.1a, two adjacent highly twisted molecules are packed in an end-to-end arrangement

through intermolecular S...S interactions (3.575 Å). The thianthrene 'S' of one molecule to thethianthrene 'S' of another row molecule is organized *via* head-to-tail fashion with

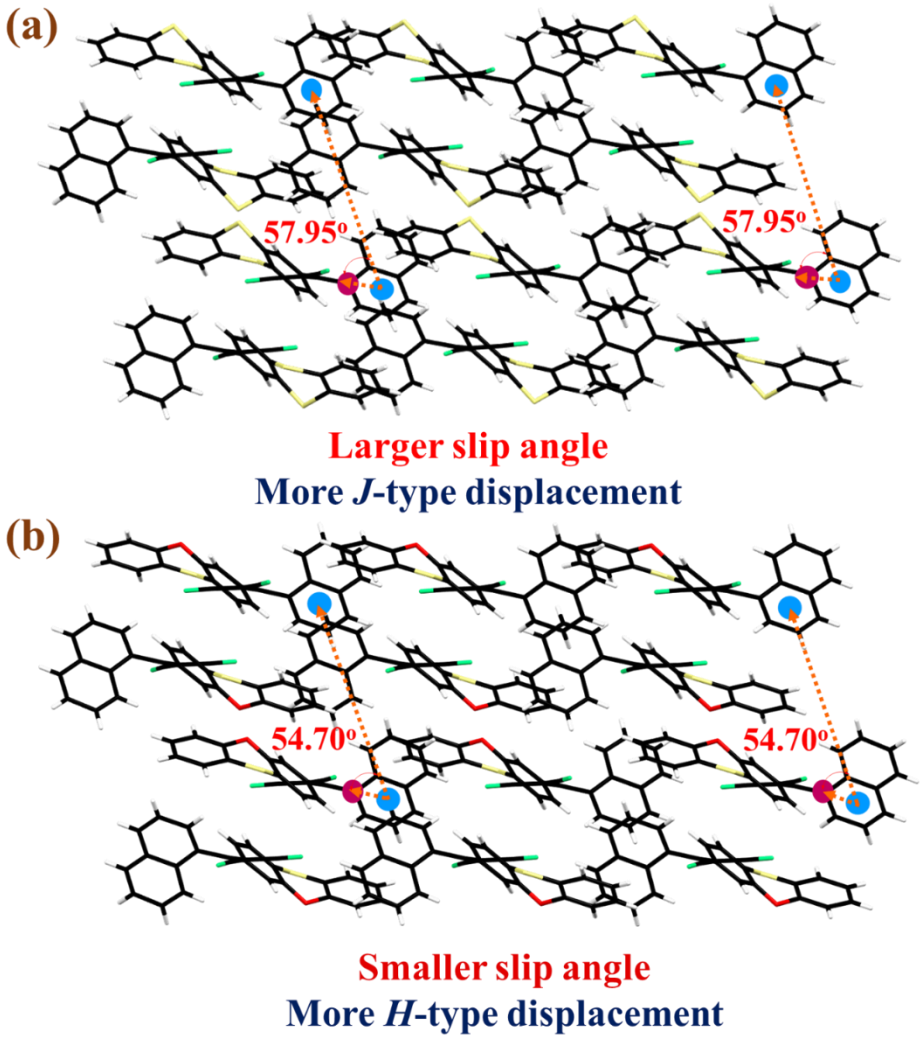

Figure 5.8.2 Slip-angles in crystal packing of (a) **TANCN** and (b) **PONCN** ('b' axis view)

a slip angle of 57.95° (Figure 5.8.2a). These twisted dimers again are extended *via* C...H π-interactions of various distances (2.507-2.889 Å) to maintain almost uniform rows. This highly twisted end-to-end with the head-to-tail arrangement is favorable for the *J*-type arrangement and can induce the bathochromic emission shift. This finding is notable with the observed near-red emission at 593 nm for **TANCN**. By analyzing the longitudinal and lateral displacements, we found that in the case of **TANCN**, the longitudinal overlap (depicted in Figure 5.8.1a) between the naphthalene ring and the benzene ring of thianthrene is 5.841 Å, with a minimum lateral overlap between two

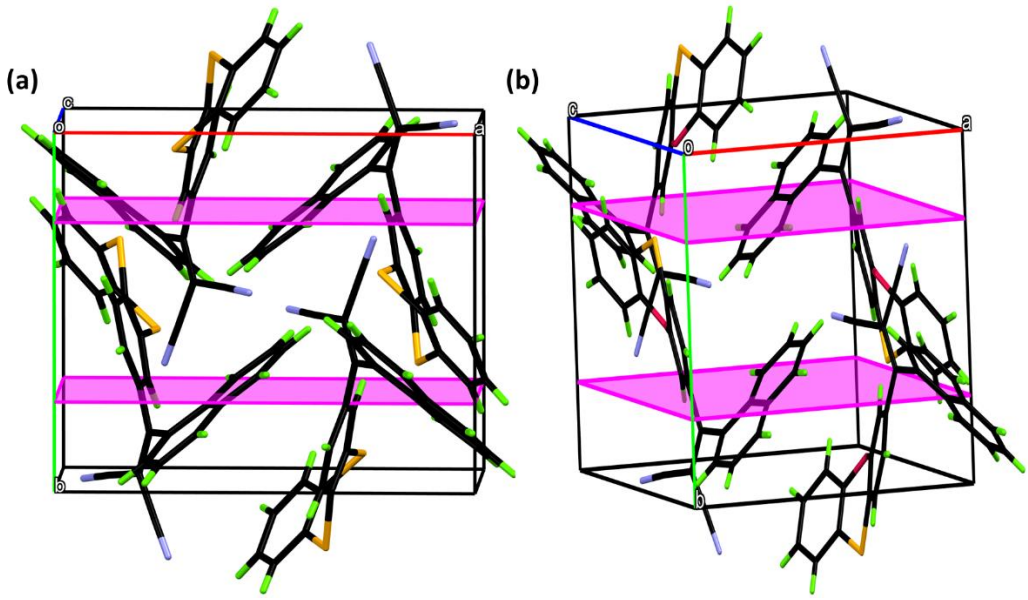

Figure 5.9 Glide planes from 'b' axis view for (a) **TANCN** (b) **PONCN**

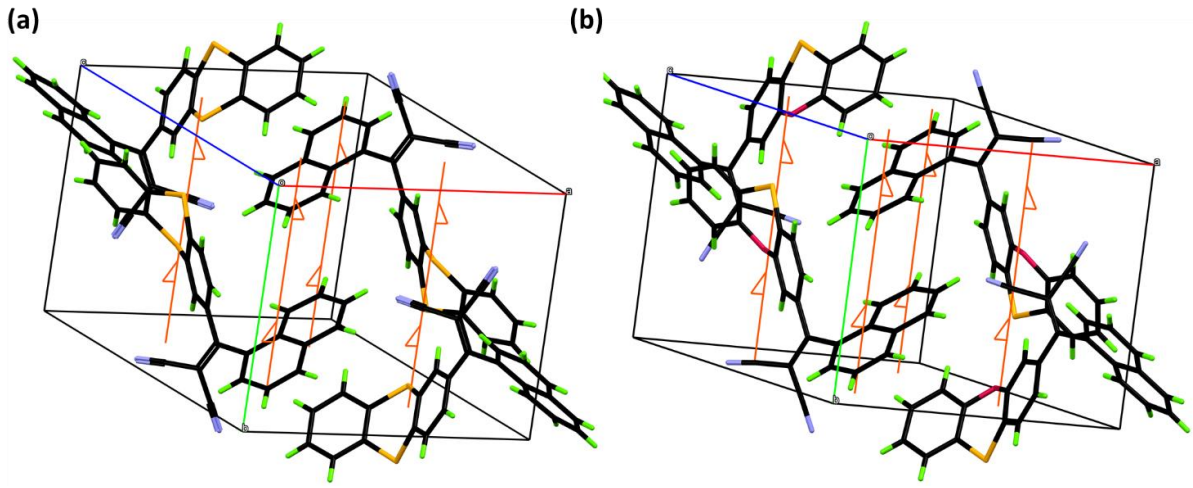

Figure 5.10 Two-fold Screw-axes from 'b' axis view for (a) **TANCN** (b) **PONCN**

naphthalene rings of two adjacent molecules. For **PONCN**, the longitudinal overlap varies from 4.408 Å to 5.785 Å, while the lateral overlap is 5.080 Å (Figure 5.8.1b). It is recognized that a reduction in the *J*-type arrangement may cause blueshifted emission.[42,63] The lateral displacement of **PONCN** leads to form *H*-type arrangement than that of **TANCN**. Even, the longitudinal displacement of **PONCN** would enable a *H*-type packing than that of **TANCN** (Figure 5.8.1). This may cause a slightly blueshifted emission for **PONCN** (Figure 5.6). This trend may become more prominent if both the 'S' atoms of **TANCN** are replaced with the 'O' atoms. Unfortunately, suitable single crystals of **OXNCN** could not be grown for X-ray diffraction studies.

Table 5.1 Crystal parameters for **TANCN**, **PONCN**, and **DBTNCN**

Topic	**TANCN**	**PONCN**	**DBTNCN**
Emp. Formula	$C_{26}H_{14}N_2S_2$	$C_{26}H_{14}N_2OS$	$C_{26}H_{14}N_2S$
Formula weight	418.5320	402.4710	386.4720
Crystal system	Monoclinic	Monoclinic	Monoclinic
Space group	P 1 21/n 1	P 1 21/n 1	P 1 21/c 1
a/Å	11.9694 (1)	11.6522 (2)	10.2590 (2)
b/Å	10.1347 (1)	10.1365 (2)	23.9746 (5)
c/Å	16.2523 (2)	16.2509 (3)	7.6877 (2)
/degree	90	90	90
/degree	96.470 (1)	98.031 (2)	94.982 (2)
/degree	90	90	90
V/ *Å*^{3}	1958.95 (4)	1900.61 (6)	1883.69 (7)
Z	4	8	4
$D_{calc/g\ cm-3]}$	1.419	1.406	1.363
/mm^{-1}	2.570	1.677	1.627
F(000)	809.0	832.0	803.5
Data/restraints/parameters	4135/0/272	4029/0/272	3976/0/263
S	1.053	1.078	1.018
+R1 [I>2(I)]	0.0342 (3946)	0.0525 (3761)	0.0366 (3607)
wR2 [all data]	0.0916 (4135)	0.1340 (4029)	0.0998 (3976)
Max./min. residual electron dens. [eÅ^{-3}]	0.324/-0.321	0.841/-0.501	0.2754/-0.4077
CCDC No.			

However, the PXRD analysis helped us understand the different crystal packing for **OXNCN** compared to **TANCN** and **PONCN** (Figure 5.11). The solid-state absorbance for **OXNCN** is also 68 nm blueshifted than that of **TANCN**. This indicates that **OXNCN** crystal packing is more *H*-type than **PONCN**, making the order of the extent of plausible longitudinal and lateral *J*-type arrangement as **OXNCN<PONCN<TANCN**. This scenario for **OXNCN** crystal packing could be suspected even by analyzing the slip-angle variations in **TANCN** and **PONCN**. As the slip angles were calculated in terms of the naphthalene of parallel molecular rows, the extent of planarity of the naphthalene ring would directly impact the slip angle. Surprisingly, the torsion angle among the heterocycle ring and naphthalene ($\theta_{h\text{-}n}$) was less planar for **TANCN** than that of **PONCN**. As the TD-DFT optimized structures of **TANCN** and **PONCN** were relevant to their respective solved crystal structures (Figure 5.12), the optimized form of **OXNCN**

was reliable to account for the necessary analysis. Surprisingly, the crystal structure analysis revealed that the slip angle for **TANCN** is more (57.95°) than that of **PONCN** (54.70°) (Figure 5.8.2). Now, from the observation of solid-state emissions of **TANCN** and **PONCN**, along with the consideration of respective slip angles, lateral and longitudinal overlap, it can be understood that the extent of longitudinal and lateral *J*-arrangement plays a critical role in the most red-shifted emission from **TANCN** despite of the opposite trend in slip angles. **PONCN** had more lateral *H*-slip than **TANCN**, which is surprising as **PONCN** had a smaller slip angle (Figure 5.8).

Table 5.2 Non-covalent interactions in **TANCN** and **PONCN**

Molecules	**C…C (Å)**	**C…H/H…C (Å)**	**N…H/H…N (Å)**	**H…H (Å)**	**O…H (Å)**	**S…S (Å)**	**S…H (Å)**
PONCN	3.153, 3.266, 2.924, 2.957, 3.327, 3.335, 3.315, 3.390	2.653, 2.731, 2.767, 2.703, 2.679, 2.490, 2.614, 2.847, 2.824	2.746, 2.709, 2.542	2.372	2.682	absent	absent
TANCN	2.916, 3.303, 3.116, 2.975, 3.350, 3.294, 3.272, 3.273	2.739, 2.722, 2.739, 2.717, 2.507, 2.601, 2.631, 2.889	2.738, 2.748, 2.725	absent	absent	3.575	2.906

From TD-DFT calculations, it was again revealed that $\theta_{h\text{-}n}$ of **OXNCN** was comparable to that of **PONCN**, and perhaps **OXNCN** crystal packing would have a smaller slip angle, making the longitudinal arrangement the least *J*-type (hence the most *H*-type) among the three fluorophores **OXNCN**, **PONCN**, and **TANCN**. Therefore, its emission would be the most blueshifted. On the other hand, **DBTNCN** crystallized in a monoclinic system with space group P 1 21/c 1 and one significantly long axis of 23.9746 Å. A two-fold screw axis was still present, but the crystal packing of **DBTNCN** consisted of end-to-end dimeric herringbone packing with four types of π…π interactions, seven types of

C...H π, two types of N...H and, surprisingly, two types of S...H interactions, but interestingly, no S...S interaction is present there (Table 5.1, Table 5.3). The crystal structure of **DBFNCN** could not be solved, but the attempted unsolved structure still could provide some clues (Figure 5.13b).

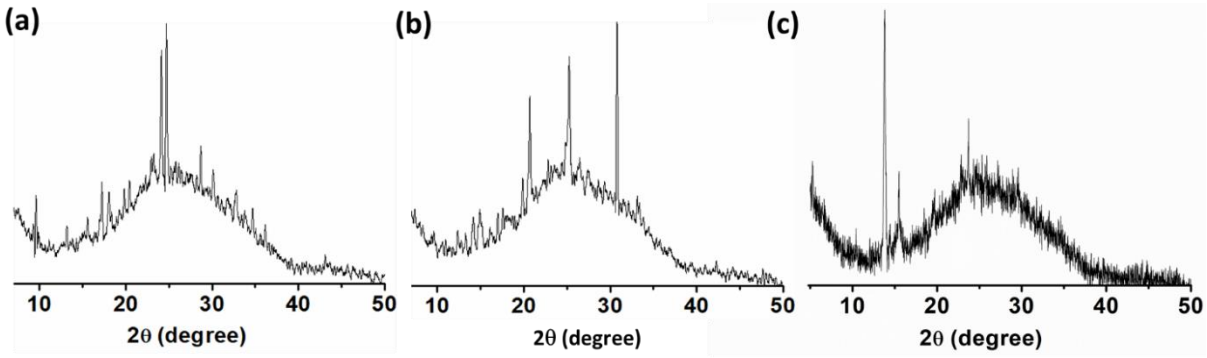

Figure 5.11 PXRD diffraction patterns for (a) **TANCN** (b) **PONCN**, and (c) **OXNCN**

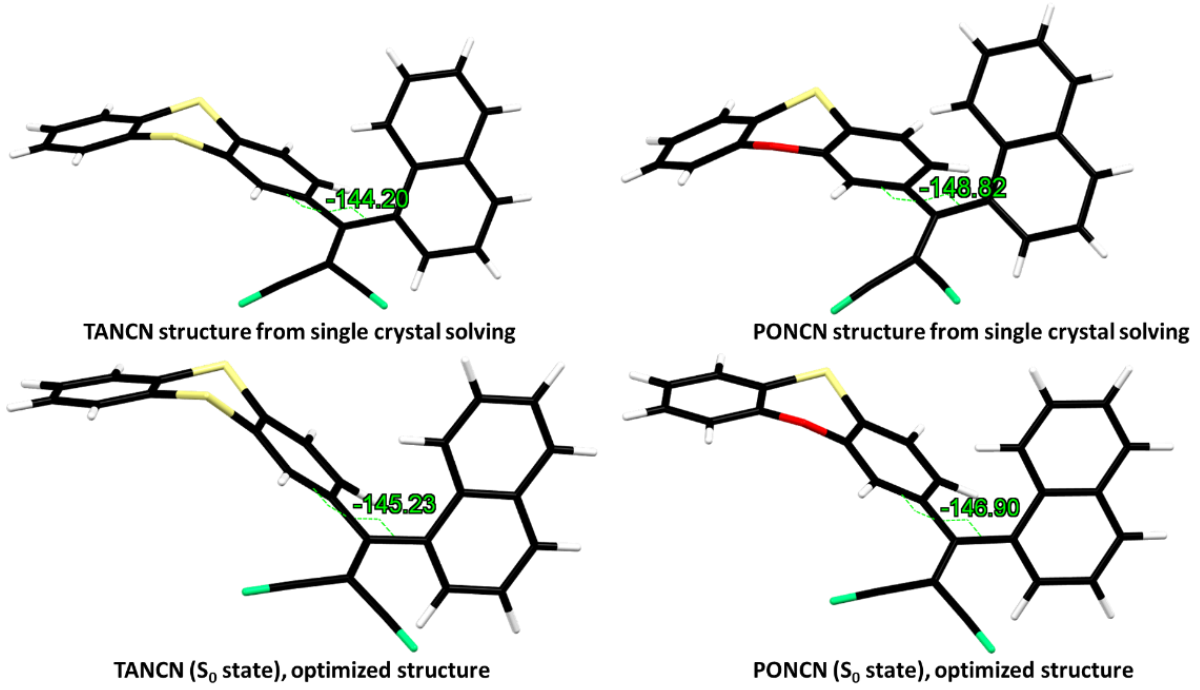

Figure 5.12 Comparison between single-crystal solved structures and TD-DFT optimized structures (gas phase) of **TANCN** and **PONCN**

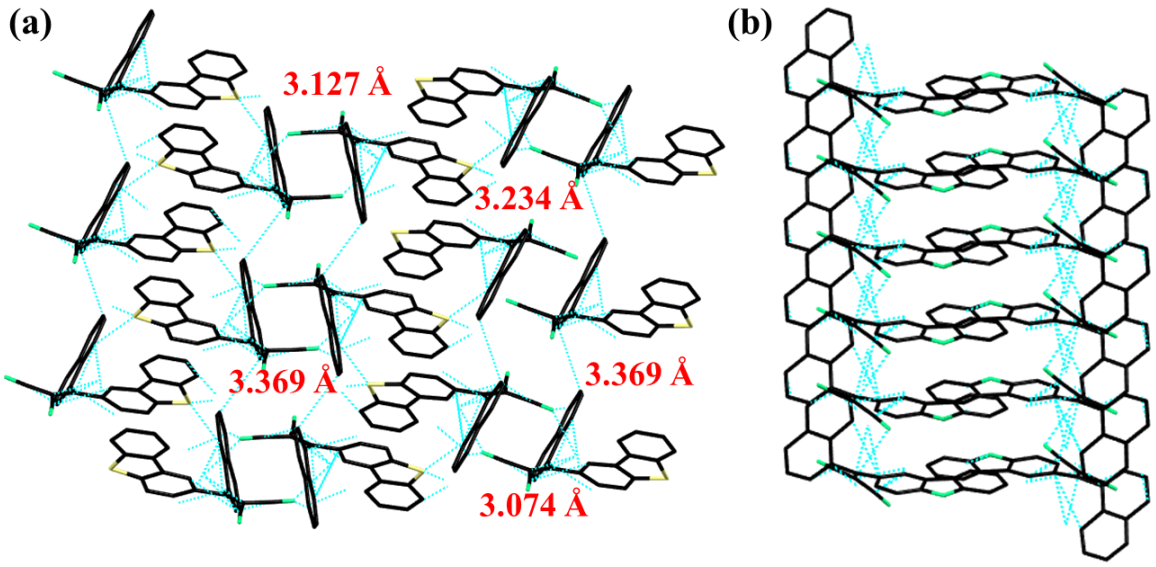

Figure 5.13 Crystal-packing with non-covalent interactions for (a) **DBTNCN** (solved) and (b) **DBFNCN** (attempted crystal structure, could not be solved due to bad diffraction)

DBFNCN might have an orthorhombic system with P2(1)/c space group with a short and a comparably longer cell axis, and most possibly, there would not be any H...H or O...H interactions despite the presence of one 'O' as the core heteroatom. The overall packing is anticipated to prefer an *H*-type for **DBFNCN** and a *J*-type arrangement for **DBTNCN** (Figure 5.13). The PXRD patterns for **DBFNCN** and **DBTNCN** were different than expected (Figure 5.15). For information, the surface morphology for all five solid compounds was also dissimilar (Figure 5.16). However, the UV-absorbance peak for solid **DBFNCN** was 36 nm blueshifted compared to the absorbance of solid **DBTNCN**, which further indicates the presence of an *H*-type arrangement for **DBFNCN**. Hence, this trend was the same as observed in **OXNCN** and **TANCN**.

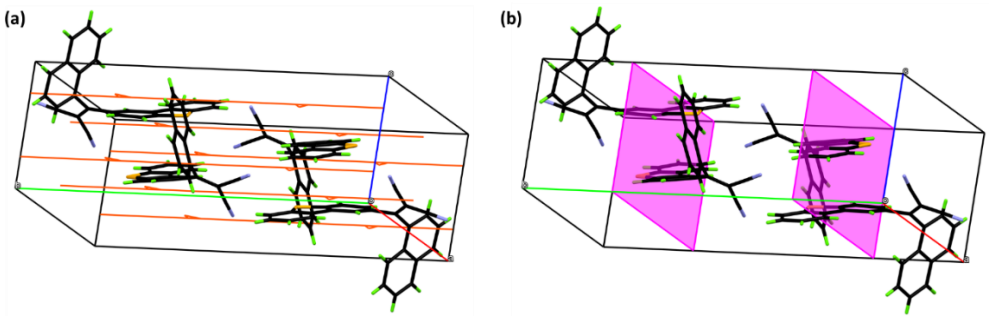

Figure 5.14 Screw-axes and glide planes for **DBTNCN**

Table 5.3 Non-covalent interactions in **DBTNCN** crystal

Compound	C...C (Å)	C...H/H...C (Å)	N...H/H...N (Å)	S...H (Å)
DBTNCN	3.234, 3.074, 3.127, 3.369	2.759, 2.631, 2.647, 2.838, 2.625, 2.831, 2.898	2.650, 2.644,	2.972, 2.961

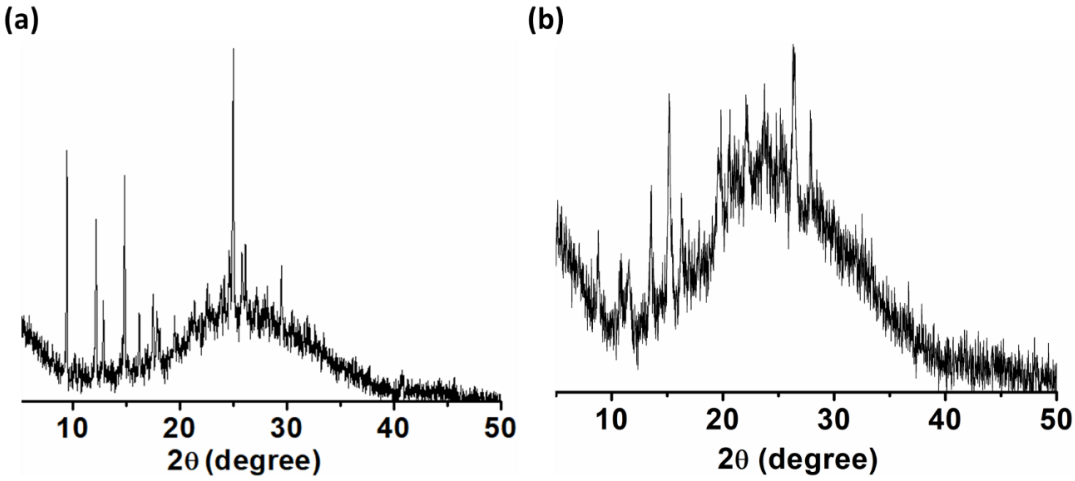

Figure 5.15 PXRD patterns for **DBTNCN** and **DBFNCN**

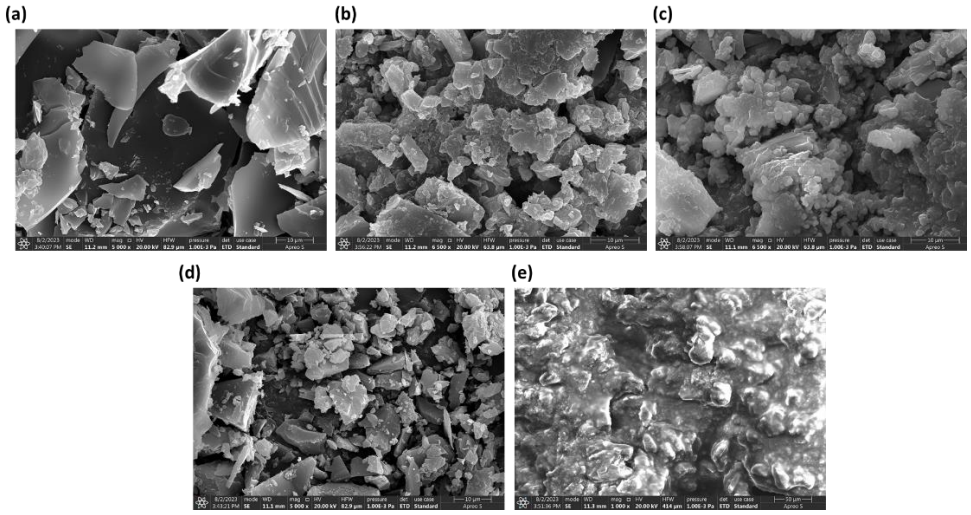

Figure 5.16 Solid-state SEM images (a) **TANCN** (b) **PONCN** (c) **OXNCN** (d) **DBTNCN** (e) **DBFNCN**

However, the anomaly lies in expecting the solid-state emission quantum yield from all these five compounds as **OXNCN,** with the flattest oxanthrene, displayed the highest

emission efficacy as compared to puckered **PONCN** and **TANCN,** which consists of kinked phenoxathiine and thianthrene heterocyclic rings respectively. The same trend

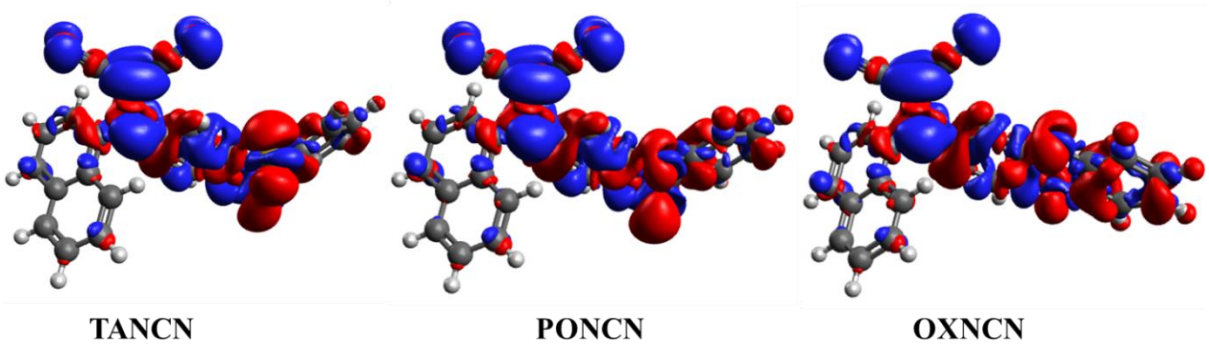

Figure 5.17 Electron density map, the blue and red color denote the high electron density in the ground and excited states, respectively. The isovalue is 0.001 a.u.

was observed in solids, even for **DBFNCN**, which contains a flatter dibenzofuran ring but exhibited a higher quantum yield than **DBTNCN**, which contains a less planar dibenzothiophene core. Factually, for **TANCN**, the inclusion of the 'S' atom into the planar aromatic skeleton would result in a twist of the ring due to the rendered polarizability. Notably,the peripheral benzene rings would deviate from the plane, taking a folded configuration. Due to the presence of sulfur atoms in thianthrene, there is sp^3 unequal hybridization mode with two lone pair electrons in its valence shell, and ultimately, there are four lone pairs of electrons on two sulfur atoms. It would create some primogenial repulsion even in **TANCN**.[64] The plane consisting of '*S*' atoms and a central acceptor determines the position vector of the transition dipole moment. This fact has been indicated in the literature even.[65,66] The powerful electron-donating ability of sulfur atoms may induce short-range multi-site distribution of molecular orbit, which is conducive to achieving small exchange energy while ensuring effective FMOs overlap. Owing to the folded peripheral benzene rings, the electron transfer caused by the molecular orbital overlap gets prevented, and the coplanar packing also becomes hindered, resulting in a lower energy but a bright emission. The crystal packing and the electron density map of **TANCN** indicated the same possibility (Figures 5.7, 5.17). We found interesting variations for **TANCN**, **PONCN,** and **OXNCN** on gaining their respective excited state planarity, and the flanking donor naphthalene played a crucial role in maintaining the torsion angle ($\theta_{\text{h-n}}$), with the heterocycle part reducing the

chances of π…π stacking. As the S_0 state-optimized structures for **TANCN, PONCN**, and **DBTNCN** were almost similar to their respective structures received by single-crystal solving, we could again rely on the TD-DFT optimized ground and excited state structures that concluded in favor of the experimental findings (Table 5.4). The **OXNCN** seems to gain even more planarity at the S_1 state. However, its S_0 state planarity was the highest among all the six-membered heterocyclic compounds. Hence, planarity relaxation from S_0 to S_1 state was less. Rather, the naphthalene and tilted dicyano acceptor groups were situated in the least extent of *J*-type crystal arrangement. The naphthalene alignment in the molecular packing would not allow π…π stacking, keeping the flat oxanthrene units far . This might cause surprising blueshifted emission , yet, the strongest emission efficiency for **OXNCN** surpassing puckered **PONCN** and **TANCN** in solids. **TANCN** receives favorable planarity at the S1 state and experiences the most planarity relaxation from the ground to the excited state (Figure 5.18, Table 5.4), well-harmonizing with the observed most redshifted emission with commendable efficiency. Factually, in **PONCN**, the ∠C-O-C angle tends to remain almost perpendicular, shaping an unusual twising in the phenoxathiin ring even at the S_1 state (Table 5.4). This unfavorable twisting may induce adverse excited-state vibrational frequency and cause higher energy emission for **PONCN** than **TANCN**. Except for **PONCN**, the H…H interactions were absent in other crystals, and probably, it wouldn't be present for **DBFNCN**. The intermolecular potential and cluster energy could be understood by processing the solved crystal data of **PONCN** and **TANCN** in the mercury software that generates the data following its own in-built programmes.[67,68] The packing energy of **PONCN** was undesirable than that of **TANCN**. For **PONCN**, the presence of van der Waals (H…H) and O…H interactions with a probable unfavoured S_1 state vibrational frequency seemed responsible for surprisingly weaker quantum yield. Even though **TANCN** displayed low energy emission, the stable packing might reduce reorganization energy significantly, suppressing non-radiative channels. This is even observed and discussed later based on the experimental results. Again, high-frequency out-of-plane vibrations could be reduced at the less kinked heterocycle scaffold of **TANCN** as compared to that of **PONCN**. This further might help **TANCN** emit brighter than **PONCN** in solids. On the other hand, $\theta_{h\text{-}n}$ of **DBFNCN** attained the required S_1 state planarity (~-153.11°), but surprisingly, S_1 state planarity at $\theta_{h\text{-}n}$ was very high (~-173.08°)

for **DBTNCN** (Table 4)**.** In addition, **DBFNCN** most likely attains weak *J*-type arrangement, while **DBTNCN** a prominent *J*-type arrangement. For **DBTNCN**, excessive $\theta_{h\text{-}n}$ planarity in the S_1 state might increase π…π stacking between naphthalenes. Indeed, the emission efficiency of **DBFNCN** was considerably higher than that of **DBTNCN**. Overall, there was certainly a role of S…H interaction for redshifted emission for **DBTNCN** and **TANCN**. Although only **PONCN** had O…H interaction, **DBFNCN** probably did not have such interaction as had been indicated by the attempted crystal structure. Of note, only **TANCN** with the lowest emission energy had the S…S interaction. So, the heteroatom replacement varied S…H, O…H, H…H, and S…S interactions most unexpectedly. However, few variations were noticed for C…C, N…H, or C…H π interactions.

Table 5.4 TD-DFT calculated bond angles at heteroatomic centers and torsion angle ($\theta_{h\text{-}n}$) between heterocycles and tilted naphthalene

Compounds	S_0 ∠C-S-C	S_1 ∠C-S-C	S_0 ∠C-O-C	S_1 ∠C-O-C	$\theta_{h\text{-}n}$ (S_0)	$\theta_{h\text{-}n}$ (S_1)
OXNCN	-	-	116.31 116.23	118.27 118.59	-146.18	-157.76
PONCN	117.89	124.57	97.86	102.27	-146.90	-158.09
TANCN	100.55 100.18	107.04 107.39	-	-	-145.23	-159.51
DBFNCN	-	-	106.05	105.96	-147.39	-153.11
DBTNCN	91.01	90.81	-	-	148.34	173.08

A time-resolved fluorescence spectroscopic study also indicated the variation of solid-state quantum yield. A higher K_r (s^{-1}) revealed better radiative decay. The K_r value appeared better for **OXNCN**, low for **PONCN**, and commendable for **TANCN**. For **OXNCN**, **PONCN**, and **TANCN**, two exponential decay was preferred where the lifetime of one component (~ 4 ns) was almost double that of the other species (~2 ns). However, the average lifetime increased with the enhanced quantum yield from **PONCN** (τ = 2.15 ns), **TANCN** (τ = 3.13 ns) to **OXNCN** (τ = 3.20 ns) (Figure 5.18, Table 5). The shorter wavelength emission with a shorter lifetime indicated less *J*-type packing for **PONCN** than **TANCN**, with more than one component in the excited state. For **OXNCN**, a longer

lifetime with a shorter emission wavelength indicates a smaller oscillator strength.[69] Further, TD-DFT analysis revealed that at the S1 state, **OXNCN** has a smaller oscillator strength (0.2343) than that of **PONCN** (0.2613), which had a shorter lifetime. On the other hand, the respective average lifetime (ns) for **DBFNCN** and **DBTNCN** were 2.99, and 0.42 ns. While **DBFNCN** had two-exponential decay, **DBTNCN** relaxed through three-exponential decay (Table 5). However, the maximum had two excited state species, as revealed by the time-resolved spectroscopic study. These two excited species could be due to two different structural motifs in the same emissive electronic state or two different structures in two different states.

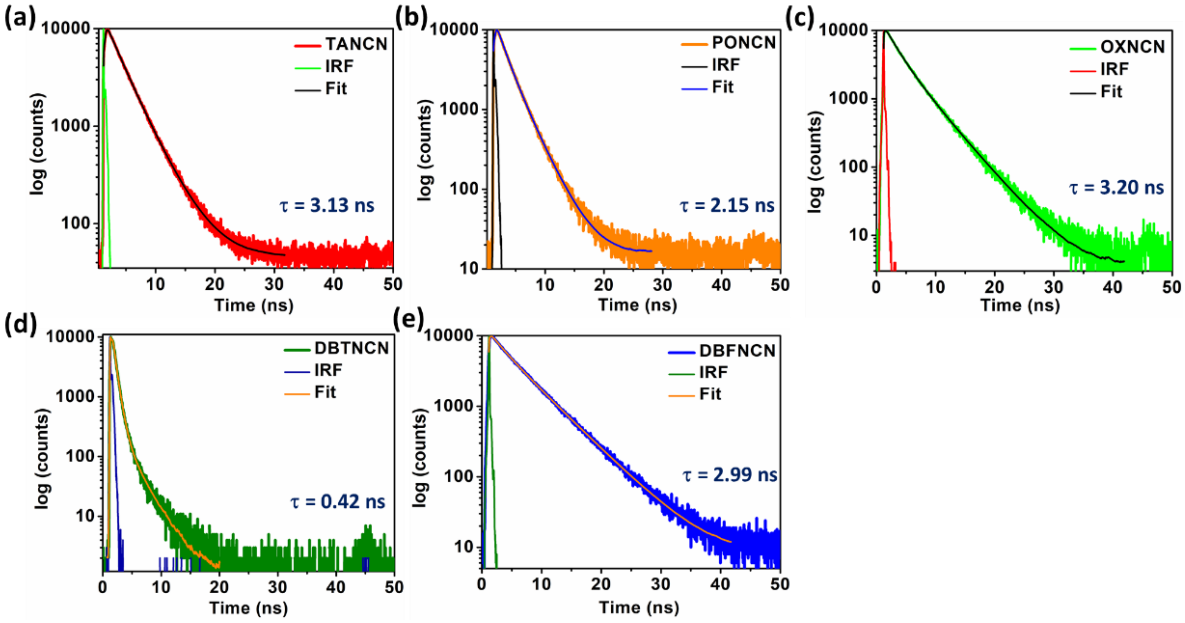

Figure 5.18 Decay profile revealed by time-resolved spectroscopic studies

Table 5.5 Summary of the results of solid-state time-resolved spectroscopic studies

Compounds	τ_1 (ns)	τ_2 (ns)	τ_3 (ns)	α_1	α_2	α_3	χ^2	τ (ns)	Φ_f (%)	K_r(s^{-1})×10^6	K_{nr}(s^{-1})×10^6
TANCN	2.735	4.044	-	0.698	0.302	-	0.977	**3.13**	**9.60**	30670.927	288817.891
PONCN	1.546	2.829	-	0.532	0.468	-	1.16	**2.15**	**3.00**	1395.349	463720.93
OXNCN	2.075	4.385	-	0.514	0.486	-	1.104	**3.20**	**10.22**	31937.5	280562.5
DBTNCN	0.183	0.611	2.354	0.603	0.448	0.017	1.17	**0.42**	**6.79**	161666.666	2219285.714
DBFNCN	2.163	5.235	-	0.728	0.272	-	1.087	**2.99**	**8.36**	27959.866	306488.294

5.3.3.2 Solution state emission tuning

Steady-state and time-resolved fluorescence studies were explored for the synthesized dyes in several solvents,with diverse polarities. There was no considerable

absorbance shift for **TANCN**, indicating non-responsiveness of S_0 state with varying solvent polarity (Figure 5.19a). However, **PONCN** showed almost no change in the absorbance peak shift from hexane to dichloromethane (DCM); a considerable shift of 26nm was observed in highly polar solvent medium such as DMF (Figure 5.19b). Interestingly, **TANCN** displayed a 99 nm solvatochromic emission shift from hexane (λ_{max}= 530 nm) to DCM (λ_{max}= 629 nm), but its emission became negligible in DMSO and DMF (Figure 5.20a, 5.20c). For **TANCN**, the bluish color in DMF resulted from the typical structure bands (Figure 5.20a, 5.20c inset image). It is noteworthy that **PONCN** exhibits a 150 nm solvatochromic emission shift from hexane (λ_{max}= 530 nm) to DMF (λ_{max}= 626 nm), retaining its decent emission at λ_{max}= 635 nm even in DMSO (Φ_f (%) = 1.23%) (Figure 5.20b, 5.20d). In all the cases, the structure bands were present, and the emission profile was composed of monomeric and excimer emissions, which are discussed later in detail. However, the variations in Stokes Shift, DSE-shifts, and quantum yields with changes in solvent polarity were very prominent for **TANCN** and **PONCN** (Figures 5.22, 5.26, Table 5.6).

The dual state emission was realized by in-depth TD-DFT investigations considering root-mean-square-displacement (RMSD), emission oscillator strengths (f_{em}), excited state planarity and $S_0 \rightarrow S_1$ planarity relaxation, HOMO-LUMO, and natural transition orbitals (NTOs). To understand the fact, a non-polar solvent hexane and a polar solvent DCM were taken initially for TD-DFT calculations. For **TANCN**, the HOMO-LUMO energy gap ($\Delta E_{H\text{-}L}$) reduced from hexane (3.254 eV) to DCM (3.239 eV), indicating a lower energy emission in DCM. The calculated extent of charge transfer (CT) associated with orbital contribution for **TANCN** was H-1→L (74%) and H-1→L (92%), respectively, in hexane and DCM (Table 5.7). The calculated $\Delta E_{H\text{-}L}$ for **PONCN**, in hexane was lower (3.034 eV) than that of **TANCN** (3.254 eV), signifying an anomaly as **PONCN** emits blue in hexane (λ_{max}= 485 nm), whereas, **TANCN** emits green (λ_{max}= 530 nm). In DCM, **PONCN** fluoresces (λ_{max}= 586 nm) again at a higher energy wavelength than **TANCN** (λ_{max}= 629 nm). that **PONCN** itself has almost the same calculated $\Delta E_{H\text{-}L}$ value in hexane and DCM. Even for **PONCN,** the emission was a CT type with H→L (89%) and H→L (87%) orbital contribution, respectively, in hexane and DCM (Table 5.7). Considering NTOs would be more logical as the emission is an excited state property.

The NTO analysis showed that the hole and electron NTOs were π and π* in nature, and in the S_1 state, there were 99.2% contributions from hole NTO (*h*NTO) to electron NTO (*e*NTO) for **TANCN** in both the solvents (hexane and DCM; Figure 5.21.1). **PONCN** had 98.8% contributions from *h*NTO to *e*NTO in hexane and DCM solvents (Figure 5.21.2). This might be a reason for overall blueshifted emission (high energy) for **PONCN**. For **TANCN** and **PONCN**, the S_1 state charge transfer is significantly high in hexane and DCM, with a very good FMO overlap, as indicated by NTO analysis. The inclusion of the 'S' atom led to a kink in the thianthrene or phenoxathiin ring with folded conformation. Yet, it did not affect breaking conjugation and making the molecule less polarizable. Instead, it favored significant polarizability components along the charge transfer direction. By considering a model of atomic contribution to polarizability,[70] it was earlier found that conjugation hindrance due to a kinked conformation may favor the stability of a twisted fluorophore and result in a zwitterionic state in which positive and negative charges are separated in the donor and acceptor moieties.

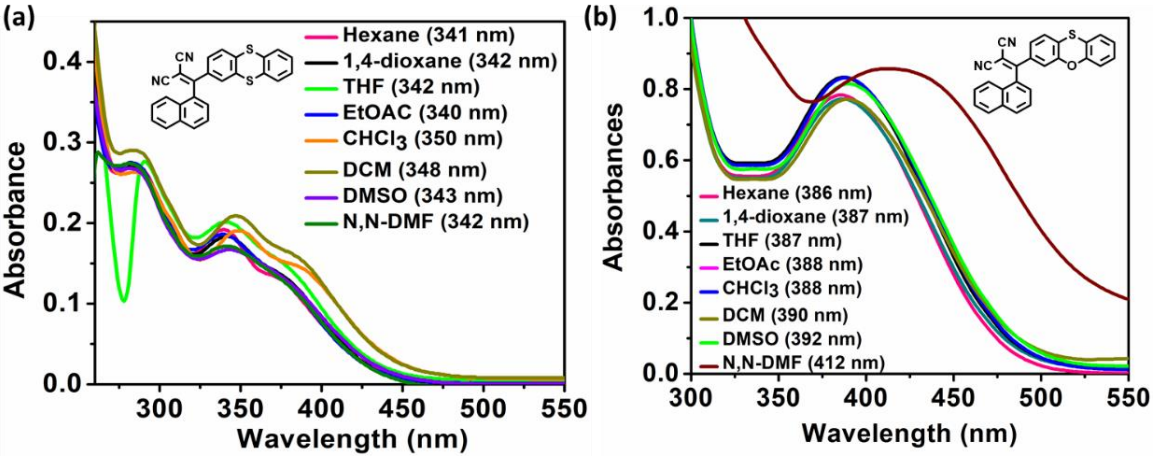

Figure 5.19 Solution-state absorbances in different solvents with different polarity for (a) **TANCN** (b) **PONCN**

Consequently, the CT polarizability (μ_z, CT) becomes dominant over LE polarizability for a twisted D-π-A system, as it might happen for twisted D-π-A structures like **TANCN** and **PONCN**. At least, the extent of TD-DFT calculated CT (%) harmonized well with this concept (Table 5.7). Even CT contribution to polarizability was sensitive to the torsion angle, and the intramolecular charge transfer influenced molecular planarization in different solvents for our systems, **TANCN** and **PONCN**.

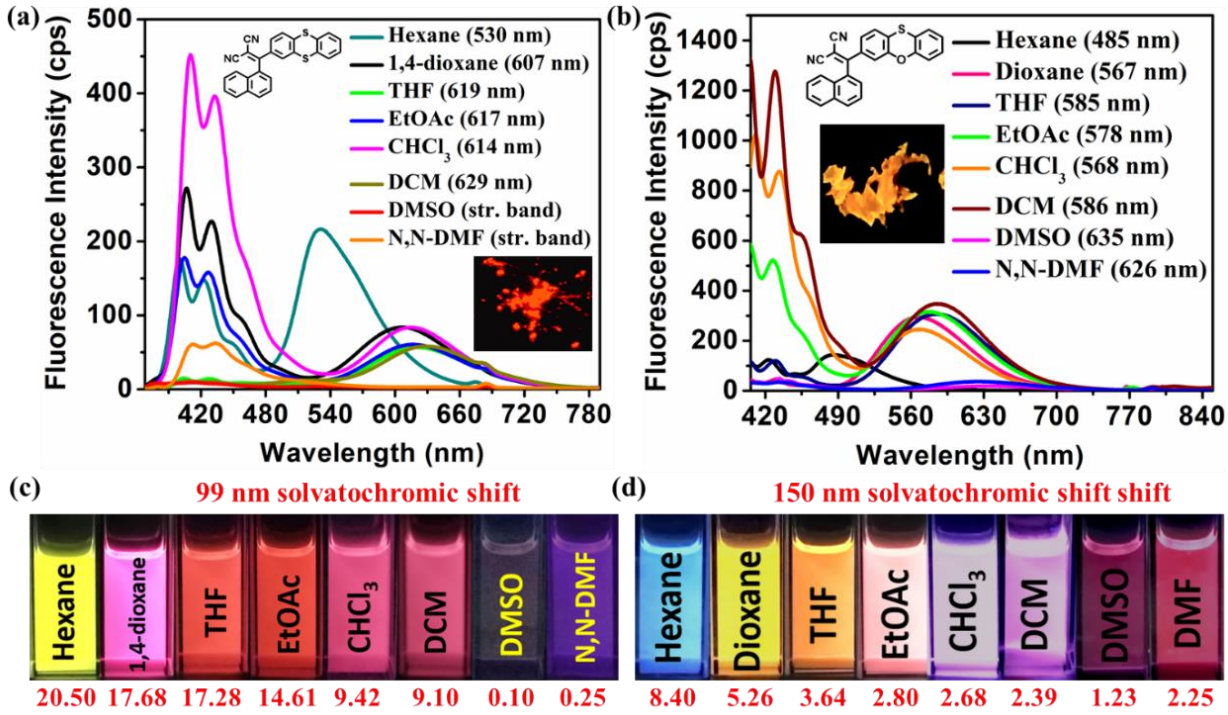

Figure 5.20 Dual-state emission with solvatochromic shifts (a,c) **TANCN** (b,d) **PONCN**; solid-state images are kept inset and all the images were taken under UV-365 nm bulb and the fluorophore concentration for emission study in all the solvents was 10^{-5}M; the Φ_f (%) in respective solvents are written in red color below the picture; 'str' means structure band; the reporting quantum yields are relative quantum yields (Φ_f (%) with respect to 10^{-5}M quinine sulfate dye with ±5% error

As discussed earlier, in hexane solvent, **TANCN** experienced 99.2% *h*NTO-*e*NTO overlap at the S_1 state with smaller emission oscillator strength (f_{em}=0.2092) and larger RMSD (0.5030 Å). In hexane, **PONCN** had 98.8% *h*NTO-*e*NTO overlap, but just as opposite to **TANCN**, it had larger emission oscillator strength (f_{em}=0.3548) and smaller RMSD (0.4026 Å). With these facts, the S_1 state $\theta_{h\text{-}n}$ was again more planarized for **TANCN** (-159.74°) than **PONCN** (-158.96°). In the S_1 state, the ∠C-O-C angle in **PONCN** was still found to remain almost perpendicular (102.33°), but both the ∠C-S-C angles in **TANCN** managed to become more planar (107.46°, 107.50°).

This was the reason for a high-energy emission for **PONCN** in hexane with a ~2.44 times reduction in quantum yield than that of **TANCN** in the same solvent. To our astonishment, in DCM, the f_{em}, RMSD, and S_1 state planarity for **TANCN** and **PONCN** were found to be comparable. Hence, the extent of FMO overlap is responsible

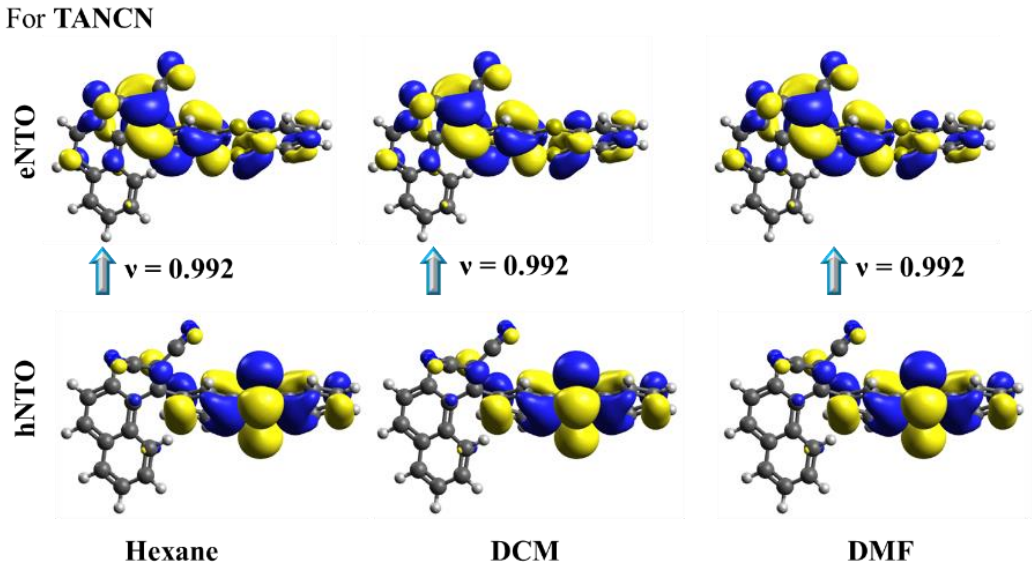

Figure 5.21.1 For **TANCN**, NTOs in respective solvents

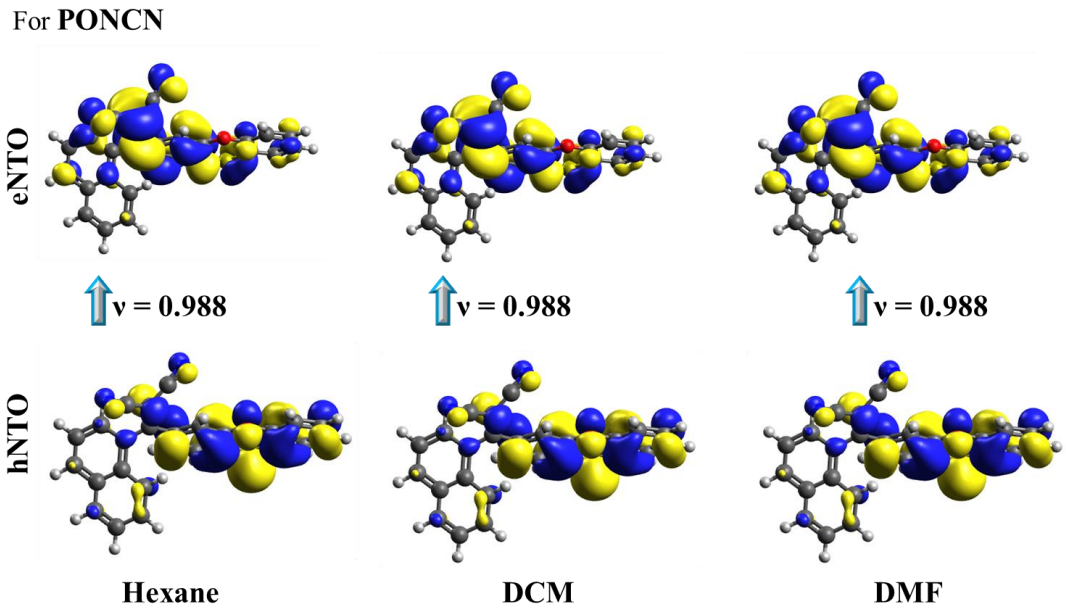

Figure 5.21.2 For **PONCN**, NTOs in respective solvents

for a brighter TANCN emission in DCM than **PONCN**. However, the extent of planarity relaxation of **TANCN** was better than **PONCN** in DCM. Thus, **TANCN** emits at a more redshifted wavelength than **PONCN** in DCM. As an observed fact, **TANCN** was almost non-emissive in DMSO (Φ_f (%) = 0.10), while **PONCN** retained its emission in DMSO to a commendable extent (Φ_f (%) = 1.23).

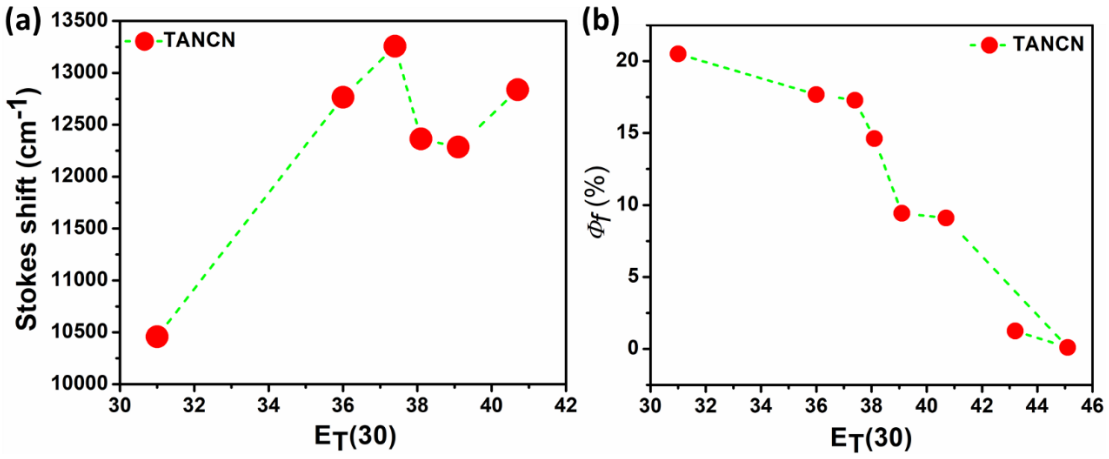

Figure 5.22 Plots for solvatochromism of **TANCN** (a) Stokes Shift vs $E_T(30)$ (b) Φ_f (%) vs $E_T(30)$

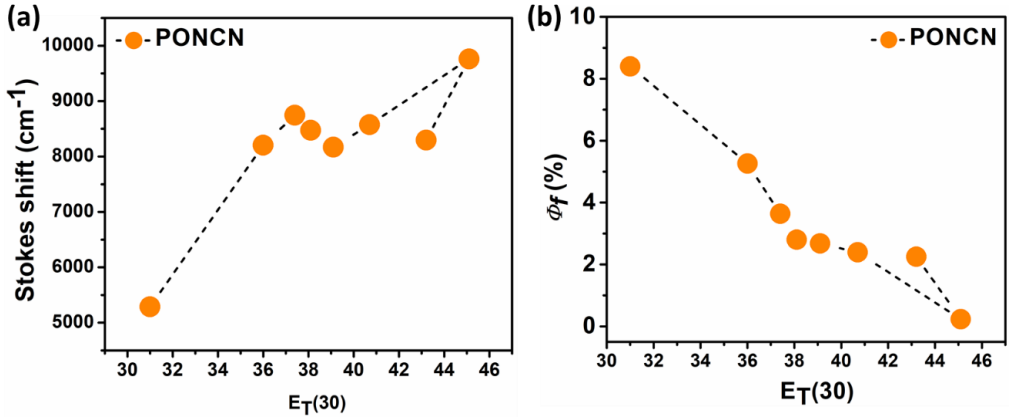

Figure 5.23 Plots for solvatochromism of **PONCN** (a) Stokes Shift vs $E_T(30)$ (b) Φ_f (%) vs $E_T(30)$

TANCN was calculated to experience the highest displacement (RMSD = 0.5706 Å) and the highest f_{em} (0.3994) in DMSO accompanied with the highest planarity relaxation (S_o state, $\theta_{h\text{-}n}$ =.-143.97° → S_1 state, $\theta_{h\text{-}n}$=.-160.93°). Gaining extended planarity relaxation extended π-π stacking in a harmful way to quench its emission significantly in DMSO. In DMF, **TANCN** was faintly bluish emissive with the structure bands, almost missing in DMSO. According to the TD-DFT calculation, the S_1 state planarity of **TANCN** was a little less in DMF than in DMSO. This fact was not that harmful in the case of **PONCN**, although even **PONCN** emitted better in DMF (Φ_f (%) = 2.25) than DMSO (Φ_f (%) = 1.23) (Table 5.8).

Despite a flatter oxanthrene ring, **OXNCN** emitted the brightest in solid-state with a 10.22% quantum yield. But in solvents, **OXNCN** somehow managed to emit better only in non-polar hexane (Φ_f (%) = 2.05%) and 1,4-dioxane (Φ_f (%) = 1.66), and its emission intensity was too very weak in polar DCM (Φ_f (%) = 0.16) and DMF solvent (Φ_f (%) = 0.12) (Table 5.6).

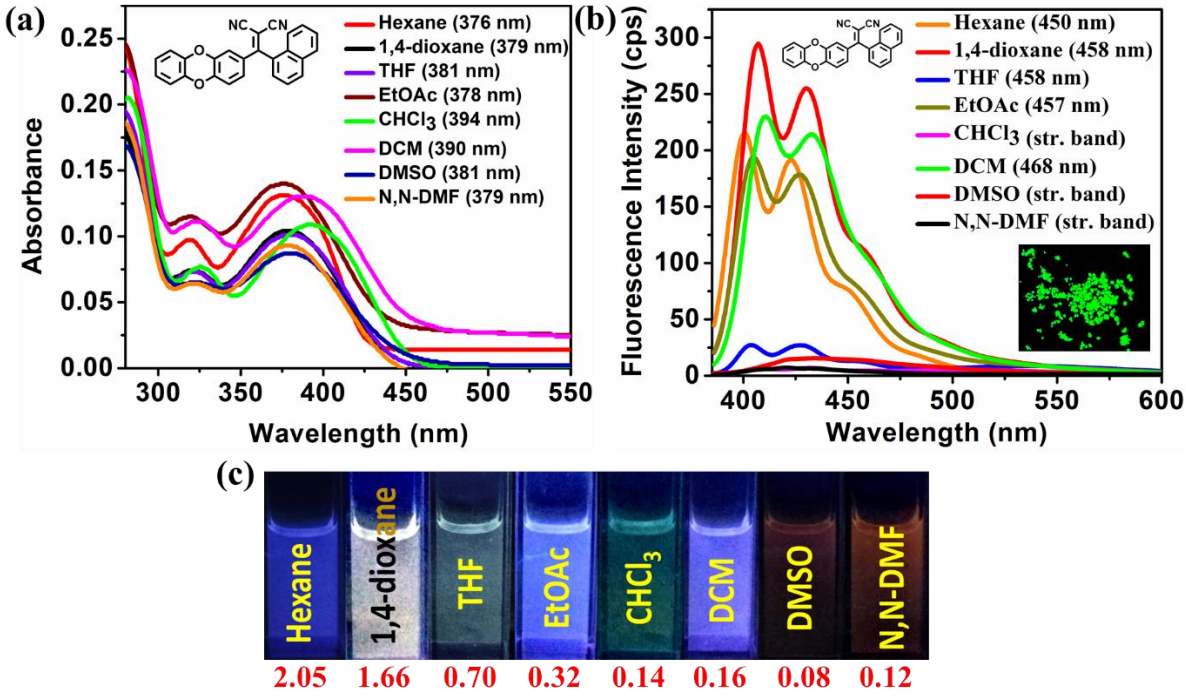

Figure 5.24 Solution state emission for **OXNCN** (a) absorbances (b) emissions (c) images captured under UV-365 nm bulb; the probe concentration was 10^{-5} M and the quantum yields in respective solvents are written in red color, the image of green solid-state emission is kept inset

The structure bands were very prominent, and CT-based solvatochromic peak shifts were negligible. TD-DFT analysis on **OXNCN** inferred, the FMO overlap between *h*NTO and *e*NTO, was reduced to 98.6% in hexane, DCM, and DMF (Table 5.7) and from hexane to DMF the f_{em} and RMSD increased consecutively. Due to this comparably less S_1 state FMO overlap and the more electronegativity of oxygen, the electron density was expected to be located on the oxanthrene ring to a greater extent. The $\mathbf{\Delta}E_{H\text{-}L}$ was higher in hexane (~3.11 eV) and lower in DMF (~3.025 eV), harmonizing the observed redshift in emissions. From the **OXNCN** optimized S_1 state structures, it was revealed that the

Table 5.6 DSE-genic and solvatochromic properties for **TANCN**, **PONCN,** and **OXNCN**

Compounds with solid-state emission	Solvent	$E_T(30)$	Abs. $\lambda_{.max}$ (nm)	Em. λ_{max} (nm) CT peak only	Stokes shift (cm^{-1})	DSE-shift (nm)	Solvatochromic shift (nm)	Φ_f (%)
TANCN with λ_{max} (Solid) = 593 nm	Hexane	31.0	341	530	10457.59	-63	0	20.50
	1,4-dioxane	36.0	342	607	12765.30	14	77	17.68
	THF	37.4	340	619	13256.68	26	89	17.28
	EtOAc	38.1	350	617	12363.97	24	87	14.61
	$CHCl_3$	39.1	350	614	12284.78	21	84	9.42
	DCM	40.7	348	629	12837.38	36	99	9.10
	DMSO	45.1	343	strb.	-	-	-	0.103
	N,N-DMF	43.2	342	strb.	-	-	-	1.25
PONCN with λ_{max} (Solid) = 570 nm	Hexane	31.0	386	485	5288.18	-85	0	8.40
	1,4-dioxane	36.0	387	567	8203.11	-3	82	5.26
	THF	37.4	387	585	8745.78	15	100	3.64
	EtOAc	38.1	388	578	8472.16	8	93	2.80
	$CHCl_3$	39.1	388	568	8167.56	-2	83	2.68
	DCM	40.7	390	586	8576.18	16	101	2.39
	DMSO	45.1	392	635	9762.17	65	150	1.23
	N,N-DMF	43.2	412	626	8297.40	56	141	2.25
OXNCN with λ_{max} (Solid) = 507 nm	Hexane	31.0	376	450	4373.52	57	0	2.05
	1,4-dioxane	36.0	379	458	4551.16	49	8	1.66
	THF	37.4	381	458	4412.66	49	8	0.70
	EtOAc	38.1	378	457	4573.19	50	7	0.32
	$CHCl_3$	39.1	394	strb.	-	-	-	0.14
	DCM	40.7	390	468	4273.50	39	18	0.16
	DMSO	45.1	381	strb.	-	-	-	0.08
	N,N-DMF	43.2	379	strb.	-	-	-	0.12

Note: 'strb.' implies a structural band without any distinctive CT emission peak. 'Abs.' implies absorbances and 'Em.' Is to indicate emission. The used probe concentration is 10^{-5}M. The 'DSE-shift' is the emission difference between the solid and a particular solution. The positive value represents redshift, while the negative value signifies blueshifted emission in solvent from the emission in solids. The solvatochromic shifts are written for each solvent concerning hexane. For **OXNCN**, only the structure bands were observed in DMSO and DMF. In $CHCl_3$, there was almost no emission from **OXNCN**.

$\theta_{h\text{-}n}$ (S_1) in the gas phase was smaller (-157.76°) than that of in hexane (-158.45°) and DMF (-159.83°). The ∠C-O-C angles did not vary considerably from S_0 to S_1 in hexane and DMF. Thus, gaining excited state planarity of $\theta_{h\text{-}n}$ might lead to favorable vibrational relaxation and extend π...π stacking between the excimers, reducing the emission efficacy in solvents for **OXNCN**.

Table 5.7 Solvent-wise orbital contribution

Compounds	Solvent	Orbital contribution	CT/LE
TANCN	Hexane	H-1→L (74%)	CT
	DCM	H-1→L (92%)	CT
	N,N-DMF	H-1→L (93%)	CT
PONCN	Hexane	H→L (89%)	CT
	DCM	H→L (87%)	CT
	N,N-DMF	H→L (85%)	CT
OXNCN	Hexane	H→L (90%)	CT
	DCM	H→L (89%)	CT
	N,N-DMF	H→L (89%)	CT

Strikingly, the presence of the 'S' atom in **DBTNCN** could not result in commendable emissions (Figure 5.25), although the HOMO-LUMO and NTO distributions were not unusual. Indeed, the S_1 state planarity of **DBTNCN** was unfavorable in hexane in terms of ∠C-S-C angle, and its $\theta_{h\text{-}n}$ became even more bent at its S_1 state than its comparably planar S_0 state in DMF. The excited state planarity relaxation was almost absent in the case of **DBFNCN,** causing it to be faintly emissive in respective solvents (Figures 5.26).

Apart from the structure band, there was a prominent signature of monomeric and excimer emission peaks in almost all the solvents for **TANCN** and **PONCN**. For **TANCN**, the excitation spectra in hexane and DCM were almost the mirror image of the UV-visible absorption spectrum (Figure 5.27). Still, for **PONCN**, the excitation spectra differed slightly from the UV-visible absorption spectra in hexane and DCM (Figure 5.28).

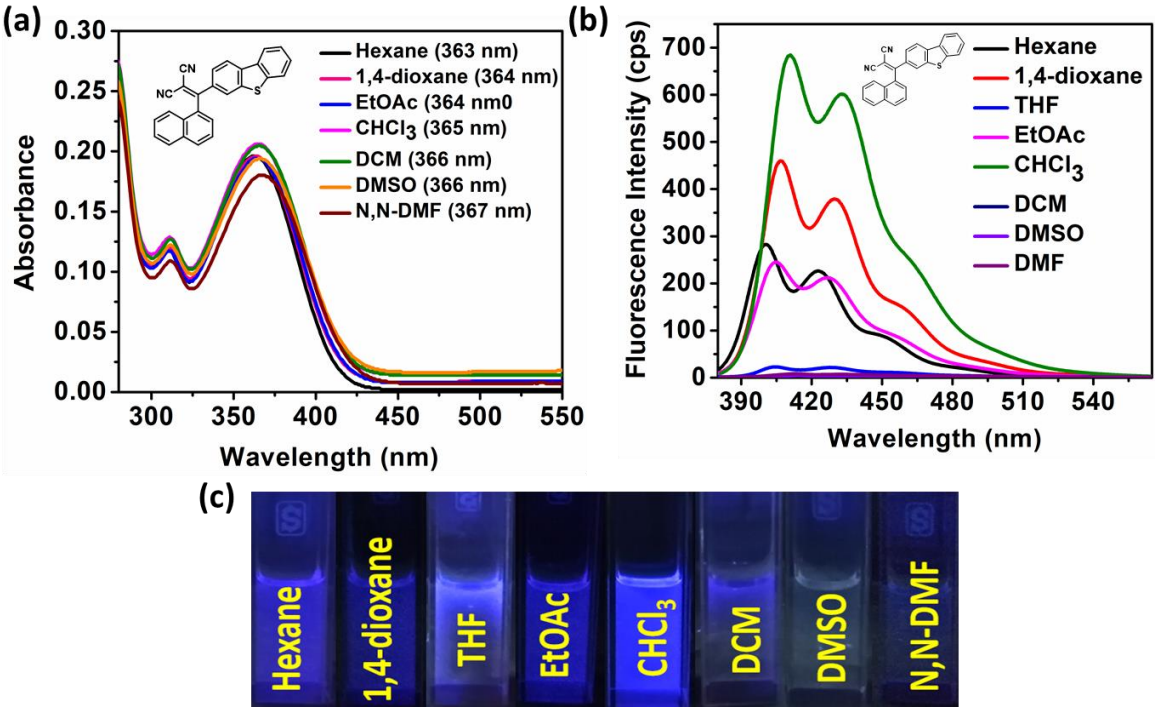

Figure 5.25 Solution state photophysical profile for **DBTNCN** (a) absorbances (b) emissions (c) picture captured under UV-365 nm bulb for respective solvents

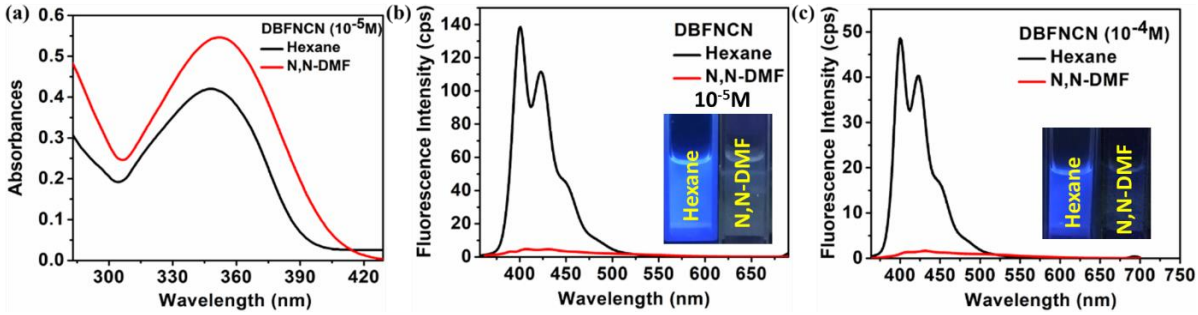

Figure 5.26 Solution state photophysical profile for **DBFNCN** (a) absorbances (b) emissions at 10^{-5}M probe concentration (c) emissions at 10^{-4}M probe concentration, inset pictures were captured under UV-365 nm bulb for respective solvents; excited at respective absorbances [$\lambda_{max.}$(hexane)= 349 nm, $\lambda_{max.}$(*N,N*-dimethylformamide) = 352 nm] that remained the same for both the concentrations

Excitation-wavelength-dependent emission spectra for **TANCN** were identical in hexane and DCM in different probe concentrations (Figures 5.29, 5.30), and it confirmed emission from single emitting species for **TANCN**. In different probe concentrations,

Table 5.8 TD-DFT calculated bond angles at heteroatomic centers and torsion angle ($\theta_{h\text{-}n}$) between heterocycles and tilted naphthalene in different solvents

Compounds	Solvents	S_0 ∠C-S-C	S_1 ∠C-S-C	S_0 ∠C-O-C	S_1 ∠C-O-C	$\theta_{h\text{-}n}$ (S_0)	$\theta_{h\text{-}n}$ (S_1)
TANCN	Hexane	101.69 101.27	107.46 107.50	-	-	-145.81	-159.74
	DCM	101.75 101.31	107.77 107.53	-	-	-145.11	-160.60
	DMSO	100.69 100.33	107.87 107.59	-	-	-143.97	-160.93
	N,N-DMF	101.75 101.31	107.86 107.59	-	-	-144.94	-160.89
PONCN	Hexane	98.85	102.33	119.38	124.55	-147.27	-158.96
	DCM	98.93	102.41	119.41	124.50	-146.47	-160.62
	DMSO	97.98	102.43	117.86	124.48	-145.37	-161.06
	N,N-DMF	98.95	102.43	119.42	124.48	-146.26	-161.03
OXNCN	Hexane	-	-	116.67 116.56	118.42 118.55	-148.20	-158.45
	DCM			116.74 116.57	118.65 118.51	-147.78	-159.47
	N,N-DMF			116.76 116.57	118.72 118.50	-147.75	-159.83
DBTNCN	Hexane	91.03	90.91	-	-	147.09	153.09
	N,N-DMF	90.91	90.95	-	-	153.09	146.95
DBFNCN	Hexane			106.08	106.03	-146.59	-149.48
	N,N-DMF			106.13	106.13	-145.19	-145.30

the excitation-wavelength-dependent emission spectra of **PONCN** were identical in DCM, but in hexane, the emission efficiency got quenched with a little spectral redshift., There will be a possibility of forming more than one emitting species in hexane from the S_1 state. Another observation was that excitement at 404 nm could eliminate the structure band in hexane for **PONCN** (Figures 5.31, 5.32). Furthermore, concentration-dependent emission studies in hexane and DCM for **TANCN** and **PONCN** confirmed the formation of excimers with increasing probe concentrations (Figures 5.33, 5.34). The short wavelength emission decreased consecutively while the long wavelength emission increased gradually with the increased probe concentration.

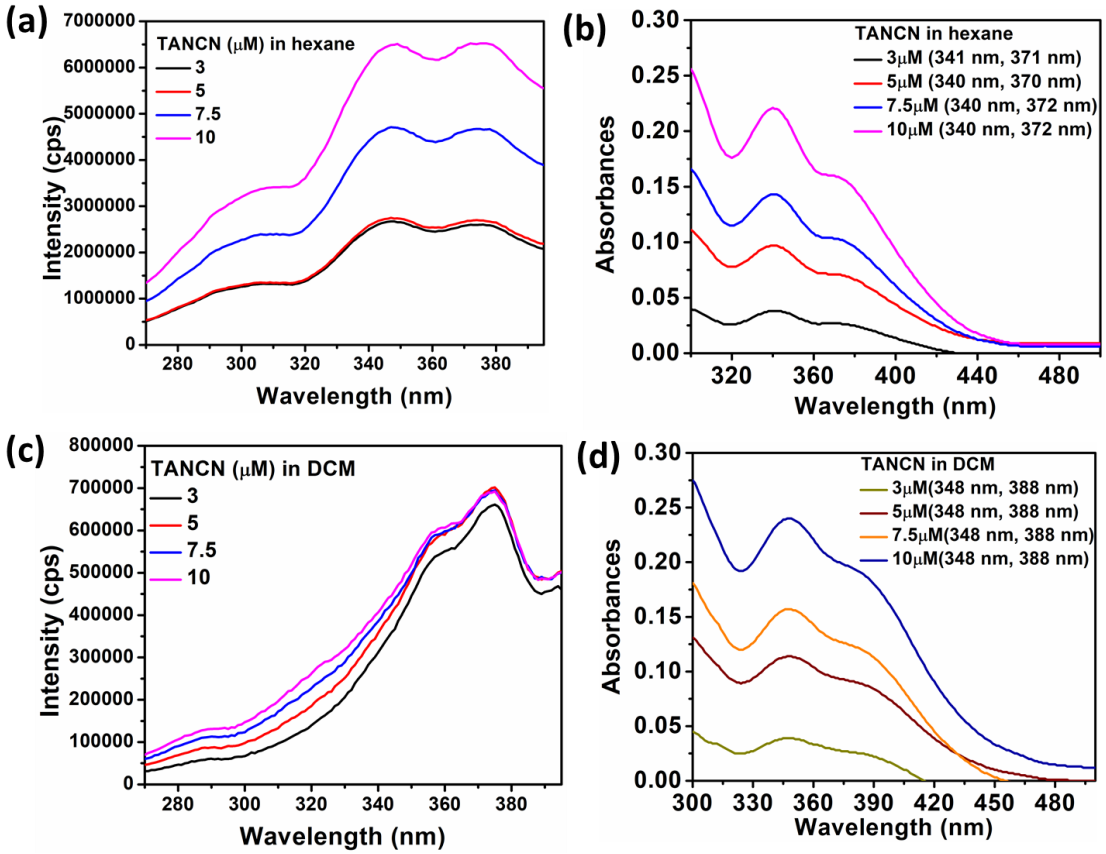

Figure 5.27 For **TANCN**, concentration-dependent excitation spectra in (a) hexane (c) DCM and UV-vis absorption spectra in (b) hexane (d) DCM

The excimer formation reduced the structured emission. The high polarizability of present 'S' atoms and puckered geometry probably disallowed π...π stacking between excimers with favorable reorganization energy to retain commendable emissions in respective solvents. The detailed reasonings were already explained before. The detailed reasonings were explained earlier, though. **TANCN**, **PONCN**, and **OXNCN** exhibited a similar trend in increasing their excited-state lifetime significantly from non-polar hexane to polar DCM.

All the lifetimes were found to be on a nanosecond (short time) span, which is very much possible for excimer emission (Figure 5.35, Table 5.9).[70] Of note, an organic fluorophore that conserves its emission in solids and solvents is called dual-state emitting fluorogens (DSE-gens).[10] **TANCN** and **PONCN** displayed fascinating solid-state emissions at 593 nm and 570 nm, respectively, and displayed near-red emissions in polar solvents with decent quantum yields.

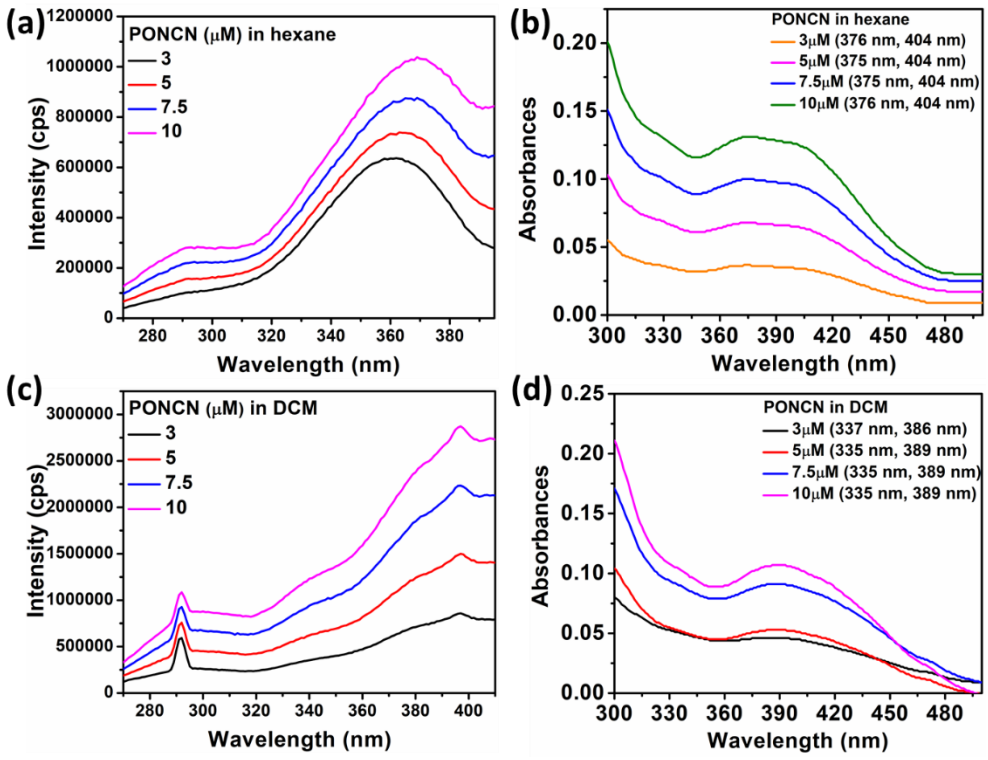

Figure 5.28 For **PONCN**, concentration-dependent excited spectra in (a) hexane (c) DCM and UV-vis absorption spectra in (b) hexane (d) DCM

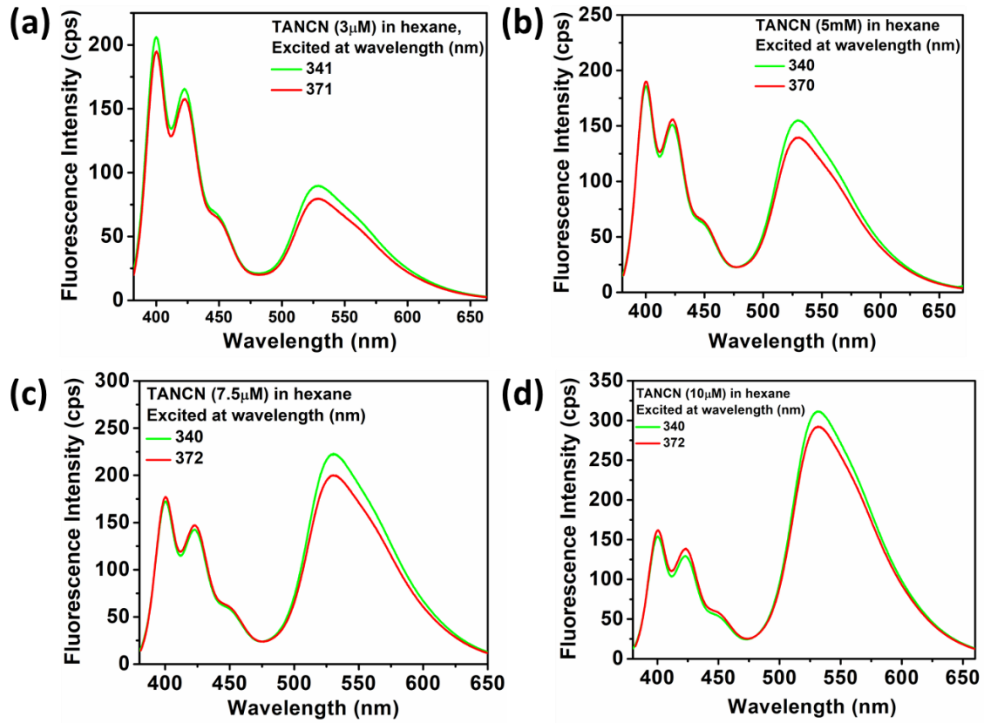

Figure 5.29 For **TANCN** in hexane, excitation wavelength-dependent emission spectra in different concentrations

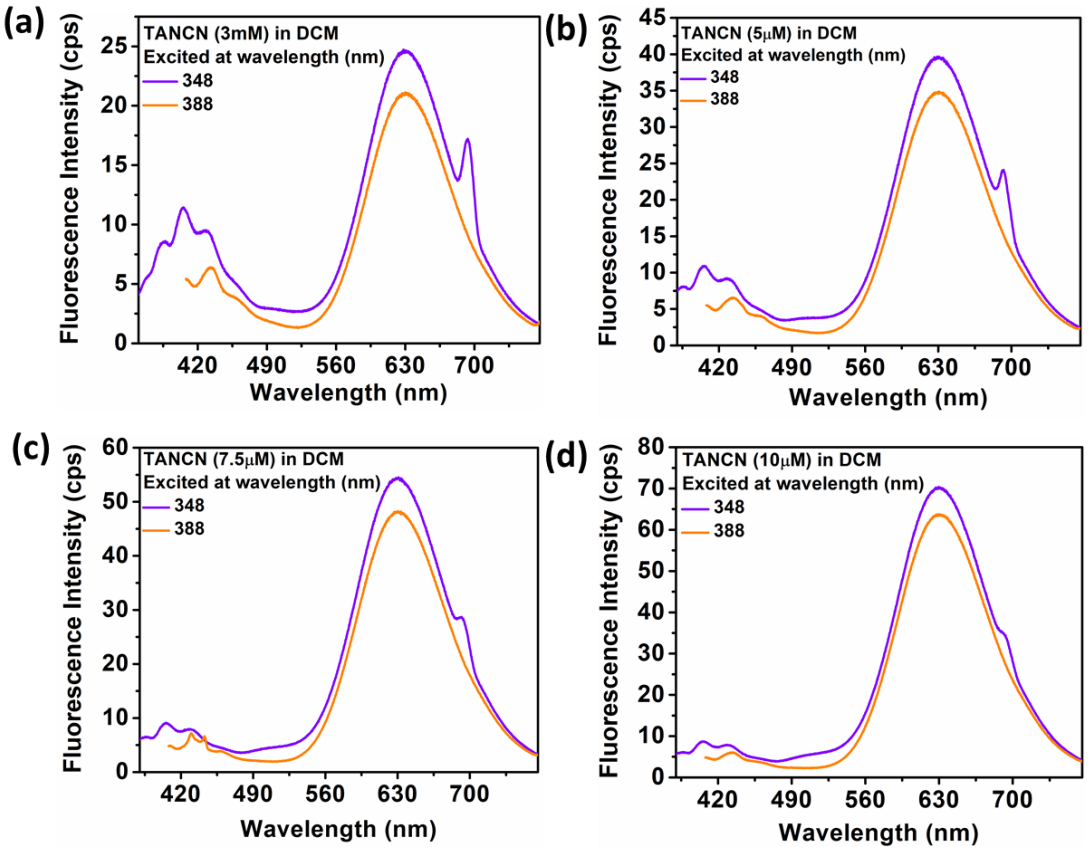

Figure 5.30 For **TANCN** in DCM, excitation wavelength-dependent emission studies in different concentrations; the peak near 700 nm is a double harmonic peak

Hence, these are a class of near-red-emitting DSE-gens, and red-emitting DSE-gens are sporadic in literature.

5.3.3.3 Tuning of AIE wavelengths from blue to near-red

Every dual-state emitter can't become AIE-gen, as observed in many earlier studies from our group and other research groups.[29,72,73] To our delight, with the new design concept, all the synthesized dyes were proven to be AIE-gens, although their extent of AIE efficacy and emission tuning was different (Figure 5.36). Like solids, **OXNCN** with the flattest oxanthrene scaffold again displayed the highest emission enhancement on aggregation among **TANCN**, **PONCN**, and **OXNCN**, as revealed by I/I_o *vs* f_w (%) plotting (Figure 5.36b).

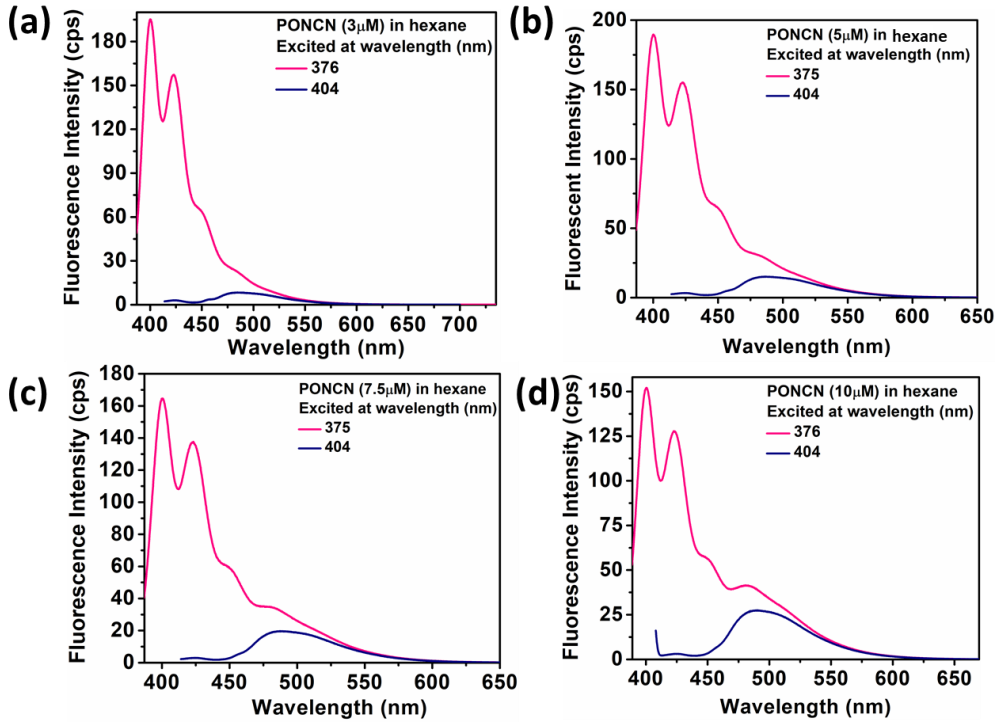

Figure 5.31 For **PONCN** in hexane, excitation wavelength-dependent emission studies in different concentrations

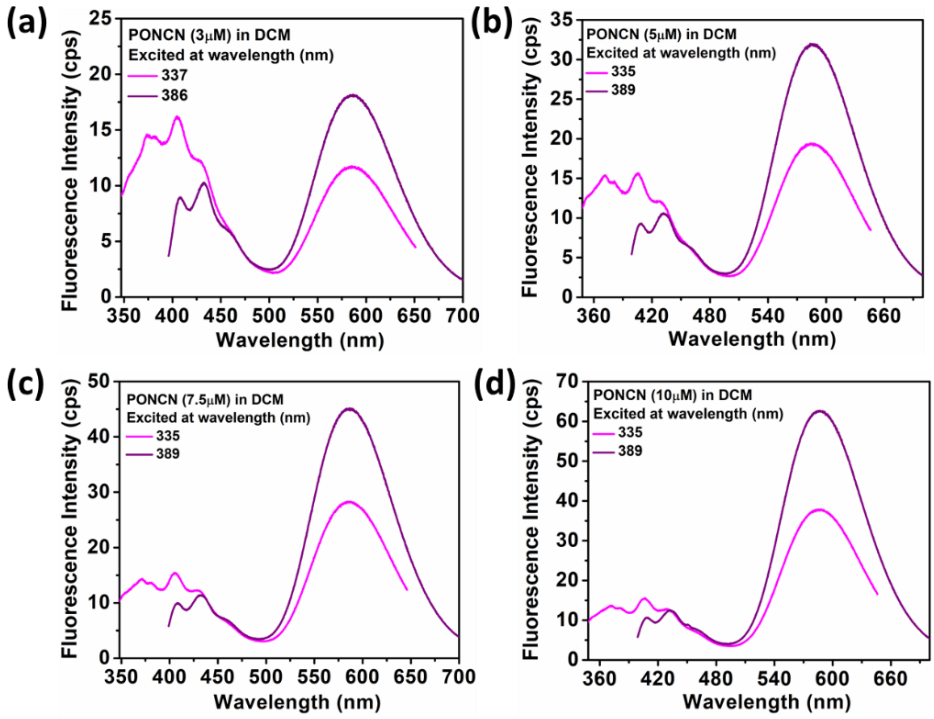

Figure 5.32 For **PONCN** in DCM, excitation wavelength-dependent emission studies in different concentrations

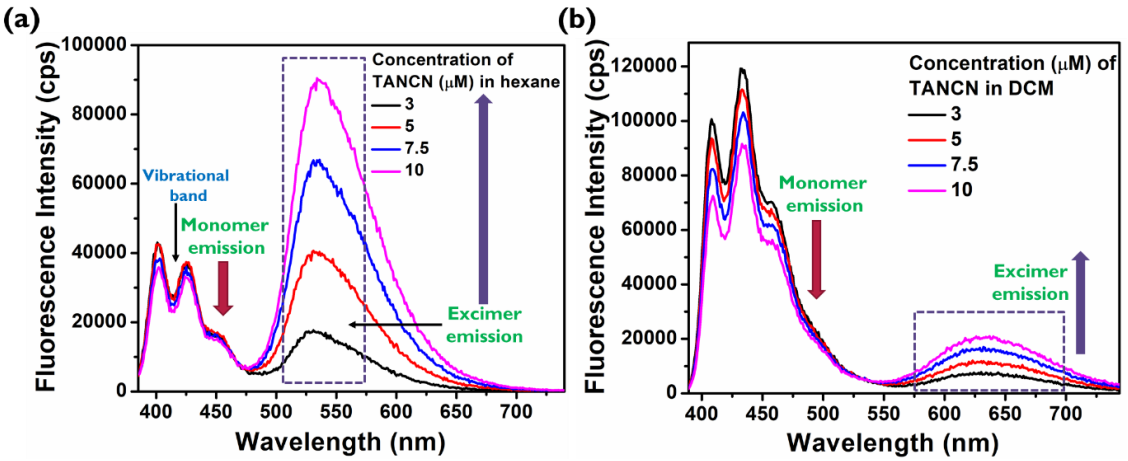

Figure 5.33 Concentration-dependent emission for **TANCN** in hexane and DCM

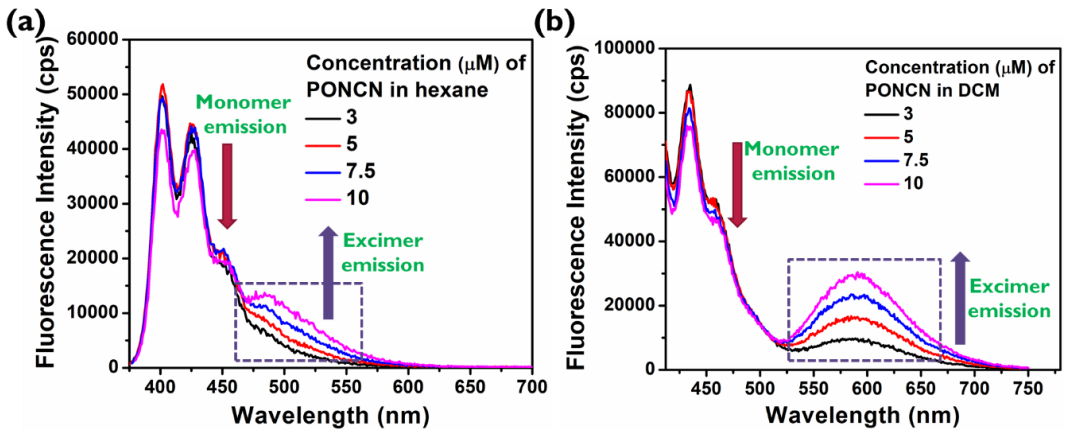

Figure 5.34 Concentration-dependent emission for **PONCN** in hexane and DCM

For all of the dyes, the excimer formation with water fraction increment in a MeCN/water (*v*/*v*) binary solvent system was very prominent at a higher probe concentration (10^{-4} M) as compared to a lower probe concentration (10^{-5} M) (Figures 5.37-5.41). On aggregation at 10^{-5} M concentration, there was a 57 nm absorbance redshift for **TANCN,** indicating the formation of strong *J*-aggregates. The absorbance redshift was 33 nm for **PONCN** and 18 nm for **OXNCN** on aggregation. So, on aggregation, the extent of *J*-stacking might be **OXNCN** < **PONCN** < **TANCN**, causing continuous redshifted emission from **OXNCN** to **TANCN**. As a strongly aggregated form tends to form closely solids (although not precisely), the reason for bright excimer

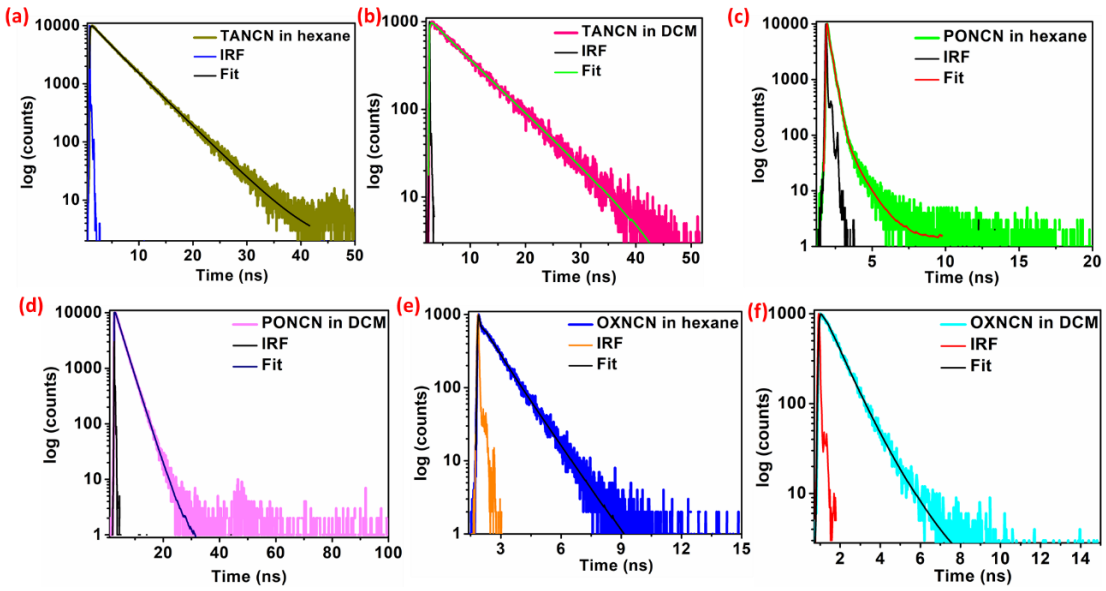

Figure 5.35 Time-correlated single photon counting (TCSPC) decay curves for **TANCN**, **PONCN**, and **OXNCN** in hexane and DCM

Table 5.9 Summary of TCSPC results for emissions in solvents, $K_r = \Phi_f/\tau$; $K_{nr} = (1- \Phi_f)/\tau$

Compds. (solvents)	τ_1 (ns)	τ_2 (ns)	τ_3 (ns)	α_1	α_2	α_3	χ^2	τ (ns)	Φ_f (%)	$K_r(s^{-1})\times10^6$	$K_{nr}(s^{-1})\times10^6$
TANCN (hexane)	2.344	4.819	-	0.1196	0.8799	-	1.107	**4.52**	20.50	45353.9823	175884.9557
TANCN (DCM)	5.264	7.444	-	0.1619	0.8381	-	1.121	**7.09**	9.10	12834.9788	128208.7447
PONCN (hexane)	0.076	0.224	0.9184	0.3844	0.6036	0.012	0.976	**0.18**	8.40	46666.6666	5088888.8888
PONCN (DCM)	2.09	2.939	-	0.155	0.855	-	1.19	**2.84**	2.39	8415.4929	343697.1830
OXNCN (hexane)	0.02	0.534	1.085	0.9219	0.0574	0.0207	0.96	**0.0715**	2.05	286713.2867	13699300.6993
OXNCN (DCM)	0.762	1.323	-	0.8033	0.1972	-	1.022	**0.873**	0.08	916.3803	1144558.9919

emissions could be attributed to their respective twisted structure and the extent of *J*-type arrangement avoiding deleterious π...π stacking. Even the extent of the *J*-type arrangement for the five-membered series was **DBFNCN** < **DBTNCN**. As a consequence, in both concentrations, **DBFNCN** aggregates emitted almost at 475 nm (cyan-blue), **DBTNCN** at 493 nm (greenish), **OXNCN** at 523 nm (yellowish green), **PONCN** at 587 nm (yellowish-orange), and **TANCN** aggregates emitted at 600 nm (reddish-orange). I/I_o vs. f_w (%) plotting revealed that the AIE emission efficacy followed **PONCN** < **TANCN** < **OXNCN**, which resembled the emission efficiency in their respective solids.

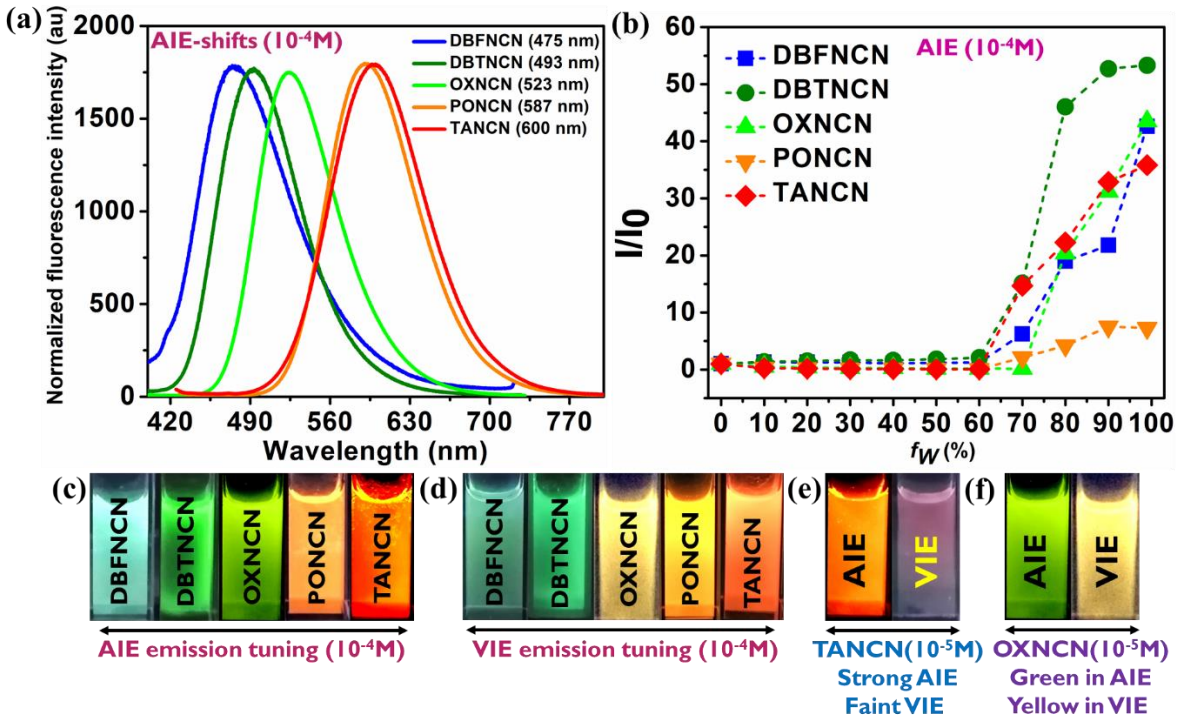

Figure 5.36 (a) Normalized AIE emission shifts for all dyes at their respective 10^{-4} M concentrations (b) excimer emission peak intensities for all dyes at different water fractions f_w (%) at their respective 10^{-4}M concentrations; images captured under UV-365 nm lamp for their (c) AIE emission tuning at 10^{-4} M concentration (d) VIE emission tuning at their respective10^{-4} M concentration (e) present AIE but absent VIE for **TANCN** at 10^{-5} M concentration (f) different color AIE and VIE display from **OXNCN** at 10^{-5} M (detailed information are kept in the supporting file)

DBTNCN displayed better I/I_0 increment than **DBFNCN** with a 14 nm blueshifted emission from its solids. Again, for **PONCN** and **OXNCN**, the AIE emission was ~17 nm redshifted from their respective emissions in solids due to their different extent of reorganization energy, most possibly.

For the lead fluorophore **OXNCN**, the aggregate formation was indicated from its respective SEM images as due to aggregation, square-shaped morphology was noticed (Figure 5.42). The particle size variation of **OXNCN** aggregates in 99% water was investigated by DLS (Dynamic Light Scattering) studies with the TCSPC lifetime measurement. The average particle size understood from DLS measurement was 719.2 nm (τ=2.92 ns) for 10^{-4} M and 356.2 nm (τ=2.92 ns) for 10^{-5} M **OXNCN** (Figure 5.43).

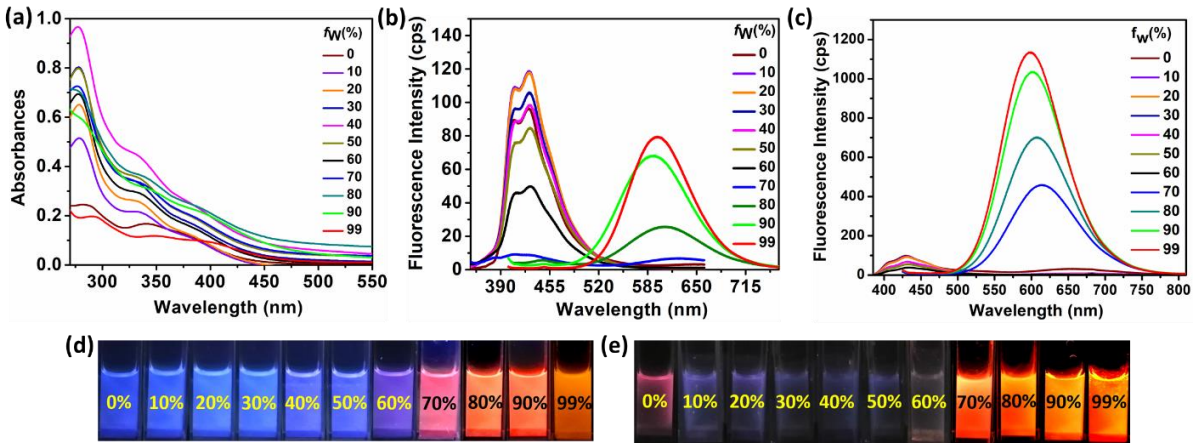

Figure 5.37 AIE-property of **TANCN** (a) absorbances with probe concentration of 10^{-5} M (b) emissions with probe concentrations of 10^{-5} M (c) emissions with probe concentrations of 10^{-4} M (absorbance wavelength was same as of 10^{-5} M); images captured under UV-365 nm bulb for **TANCN** (d) 10^{-5} M (e) 10^{-4} M concentrations

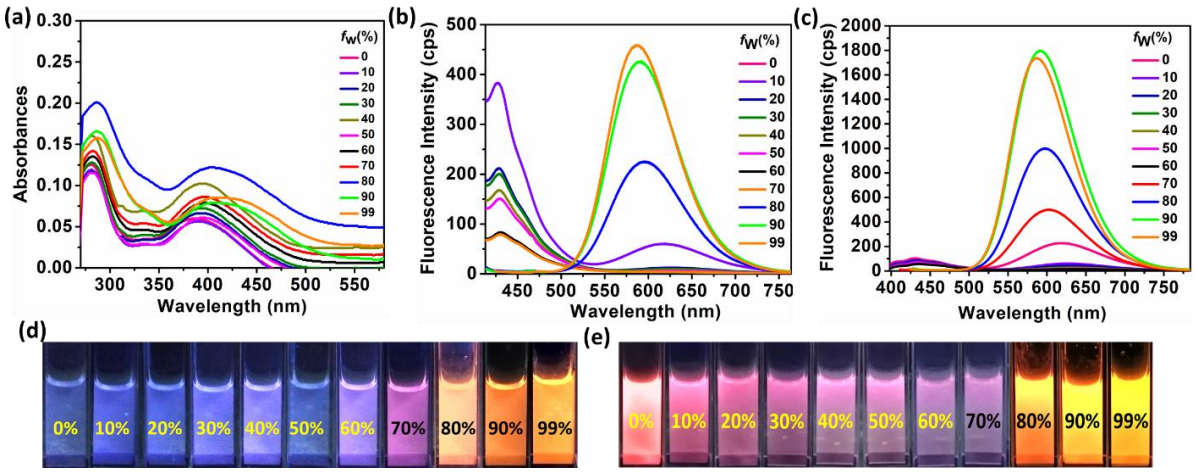

Figure 5.38 AIE-property of **PONCN** (a) absorbances with probe concentration of 10^{-5} M (b) emissions with probe concentrations of 10^{-5} M (c) emissions with probe concentrations of 10^{-4} M (absorbance wavelength was same as of 10^{-5} M); images captured under UV-365 nm bulb for **PONCN** (d) 10^{-5} M (e) 10^{-4} M concentrations

5.3.3.4 Tuning of VIE wavelengths from blue to near-red

Except for **TANCN**, all other dyes exhibited VIE at both higher (10^{-4} M) and lower probe concentration (10^{-5} M) (Figures 5.44-5.48). Although the VIE was very poor at 10^{-5} M concentration, **TANCN** displayed more than 80 times emission increment in 90% glycerol into MeOH medium (v/v) at 10^{-4} M concentration (Figure 5.44).

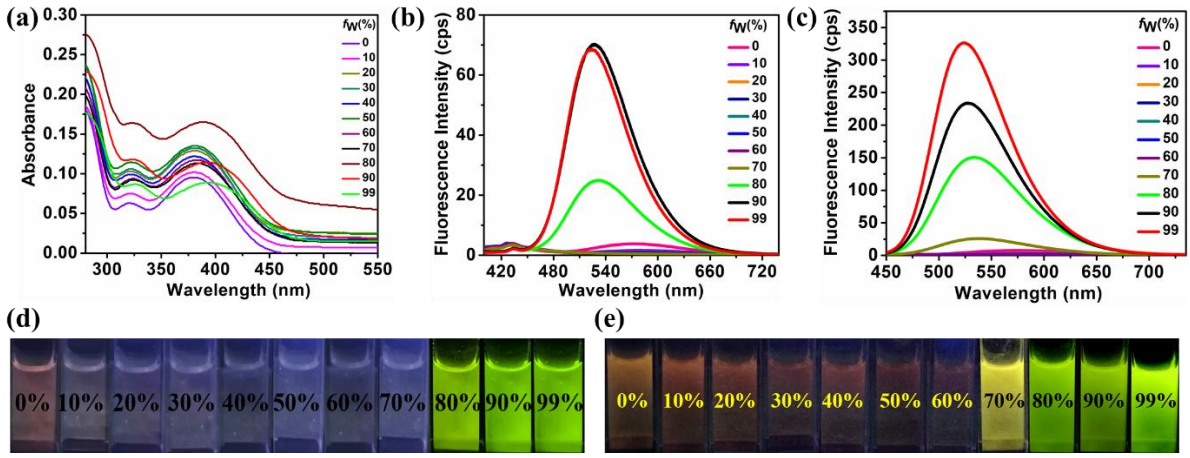

Figure 5.39 AIE-property of **OXNCN** (a) absorbances with probe concentration of 10^{-5} M (b) emissions with probe concentrations of 10^{-5} M (c) emissions with probe concentrations of 10^{-4} M (absorbance wavelength was same as of 10^{-5} M); images captured under UV-365 nm bulb for **OXNCN** (d) 10^{-5} M (e) 10^{-4} M concentrations

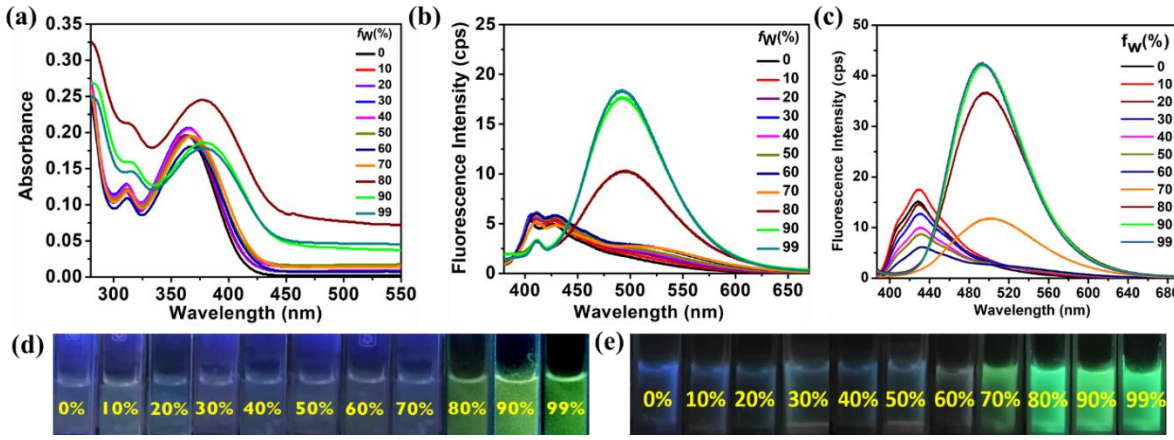

Figure 5.40 AIE-property of **DBTNCN** (a) absorbances with probe concentration of 10^{-5} M (b) emissions with probe concentrations of 10^{-5} M (c) emissions with probe concentrations of 10^{-4} M (absorbance wavelength was same as of 10^{-5} M); images captured under UV-365 nm bulb for **DBTNCN** (d) 10^{-5} M (e) 10^{-4} M concentrations

Hence, probe concentration was critical for the VIE of **TANCN**. When every other compound exhibited almost the same VIE and AIE colors, **OXNCN** displayed green AIE emission (λ_{max}= 523 nm). Still, its VIE emission turned yellow (λ_{max}= 545 nm) in 90% glycerol/MeOH medium at both concentrations. In 99% glycerol/MeOH, its emission turned green due to the deposition of solids, resulting from lack of solubility (Figure 5.46).

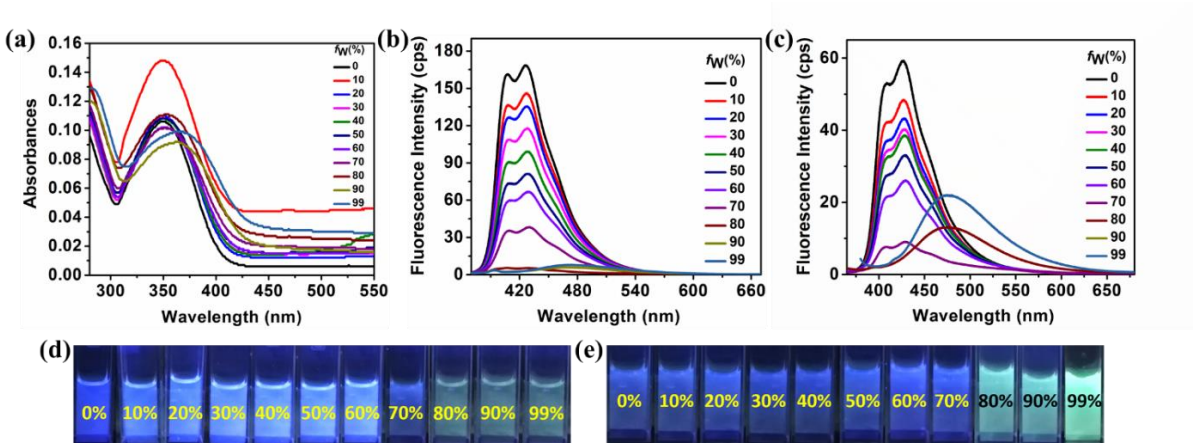

Figure 5.41 AIE-property of **DBFNCN** (a) absorbances with probe concentration of 10^{-5} M (b) emissions with probe concentrations of 10^{-5} M (c) emissions with probe concentrations of 10^{-4} M (absorbance wavelength was same as of 10^{-5} M); images captured under UV-365 nm bulb for **DBFNCN** (d) 10^{-5} M (e) 10^{-4} M concentrations

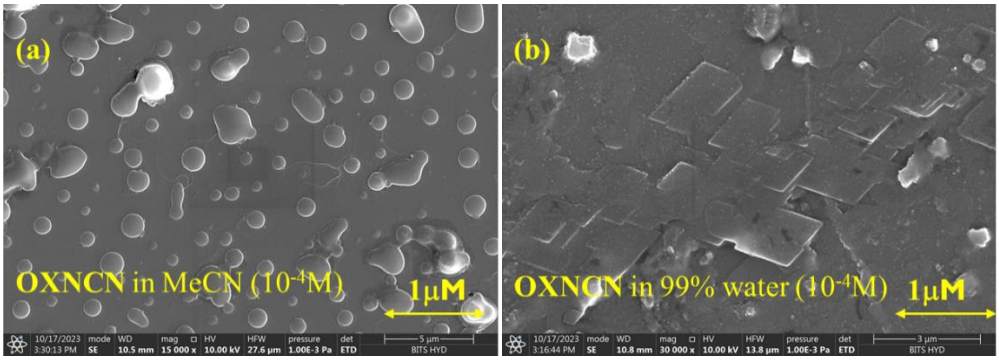

Figure 5.42 SEM images for **OXNCN** in solvent and as aggregate

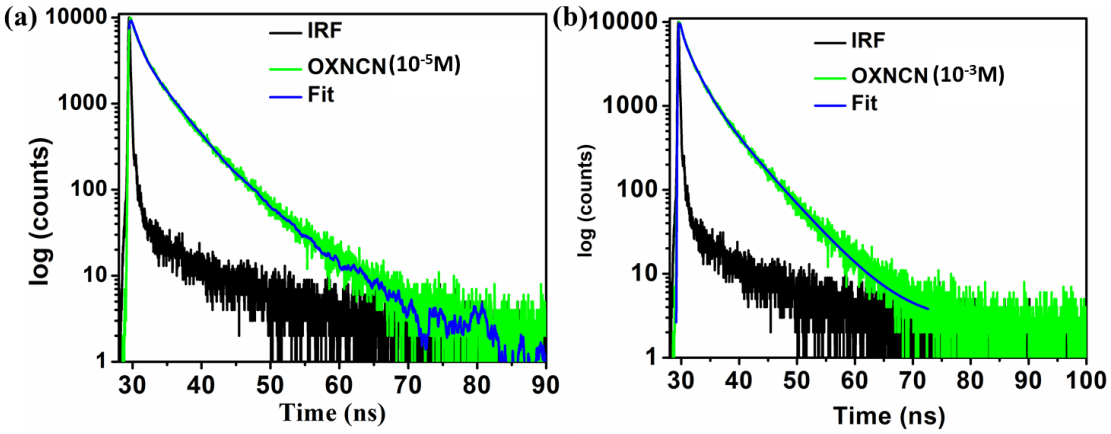

Figure 5.43 TCSPC lifetime decay profiles for **OXNCN** on aggregation in respective concentrations

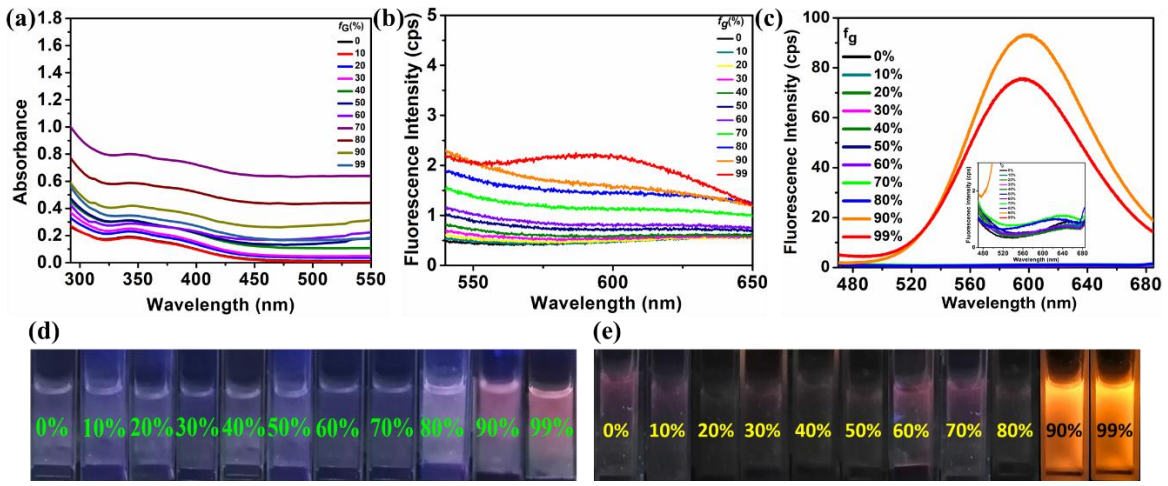

Figure 5.44 VIE-property of **TANCN** (a) absorbances with probe concentration of 10^{-5} M (b) emissions with probe concentrations of 10^{-5} M (c) emissions with probe concentrations of 10^{-4} M (absorbance wavelength was same as of 10^{-5}M); images captured under UV-365 nm lamp for **TANCN** (d) 10^{-5} M (e) 10^{-4} M concentrations

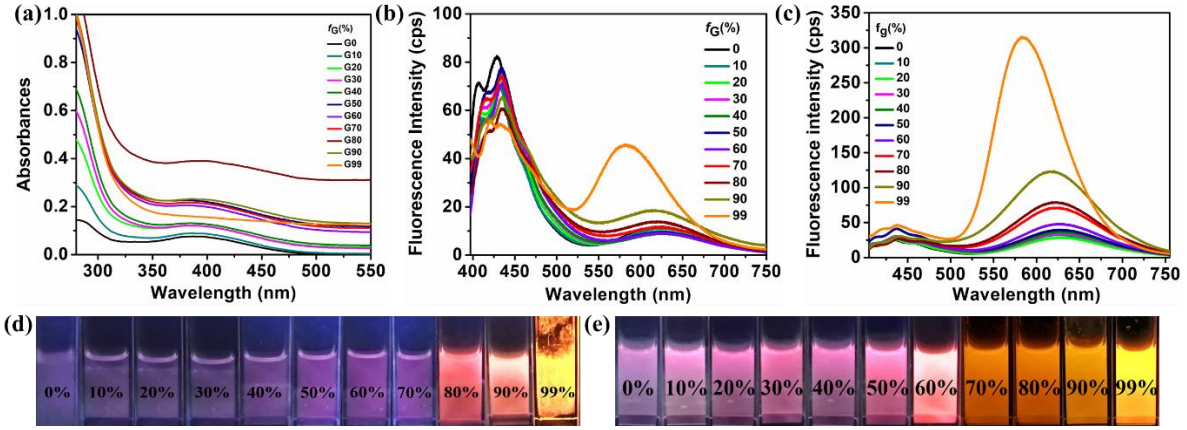

Figure 5.45 VIE-property of **PONCN** (a) absorbances with probe concentration of 10^{-5} M (b) emissions with probe concentrations of 10^{-5} M (c) emissions with probe concentrations of 10^{-4} M (absorbance wavelength was same as of 10^{-5} M); images captured under UV-365 nm bulb for **PONCN** (d) 10^{-5} M (e) 10^{-4} M concentrations

As an established fact, VIE is associated with the restriction of molecular motion.[74] Hence, the $\theta_{h\text{-}n}$ of **OXNCN** might experience favorable planarity, increasing the conjugation a bit more favoring redshifted emission in a higher percentage of glycerol. Again, the restriction of rotational and vibrational molecular motion would open up radiative pathways to emit with increased efficacy in a viscous medium. Ultimately, as

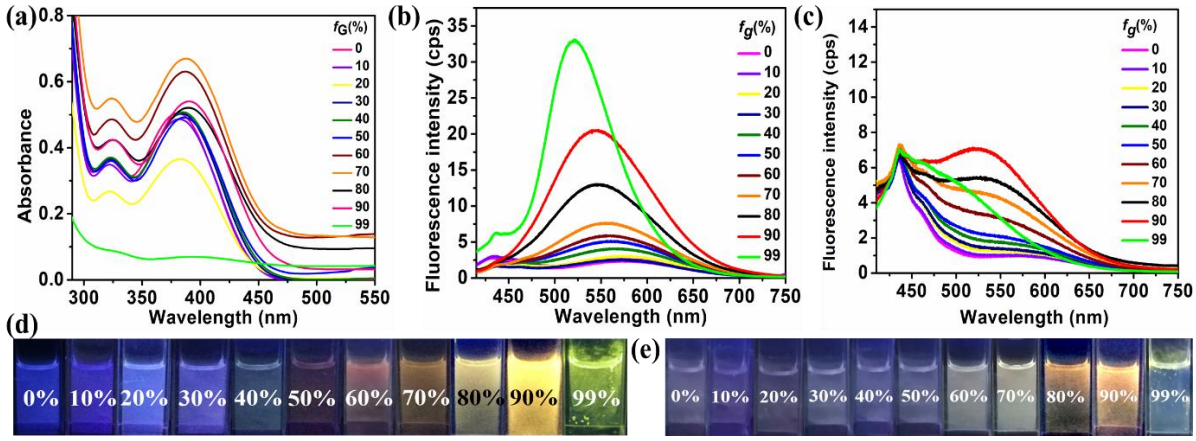

Figure 5.46 VIE-property of **OXNCN** (a) absorbances with probe concentration of 10^{-5} M (b) emissions with probe concentrations of 10^{-4} M (c) emissions with probe concentrations of 10^{-5} M (absorbance wavelength for 10^{-4} M was same as of 10^{-5} M); images captured under UV-365 nm lamp for **OXNCN** (d) 10^{-4} M (e) 10^{-5} M concentrations

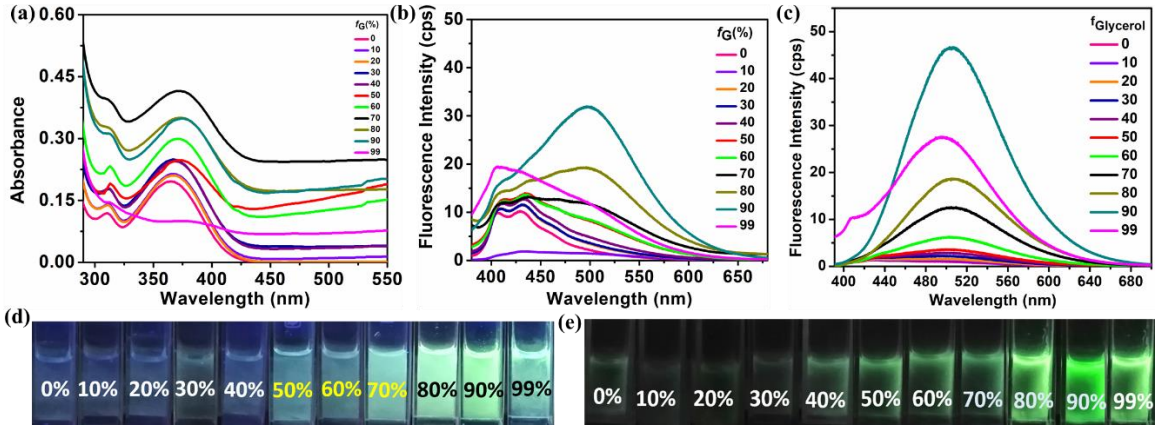

Figure 5.47 VIE-property of **DBTNCN** (a) absorbances with probe concentration of 10^{-5} M (b) emissions with probe concentrations of 10^{-5} M (c) emissions with probe concentrations of 10^{-4} M (absorbance wavelength was same as of 10^{-5} M); images captured under UV-365 nm bulb for **DBTNCN** (d) 10^{-5} M (e) 10^{-4} M concentrations

a combined effect, the emission is bright yellow instead of green. **DBTNCN** and **DBFNCN** were also found to be responsive to the viscosity enhancement (Figures 5.47, 5.48). Overall, at 10^{-4} M concentration, the viscofluorochromic emission maxima were observed at 498 nm, 504 nm, 545 nm, 584 nm, and 598 nm, respectively, for **DBFNCN**,

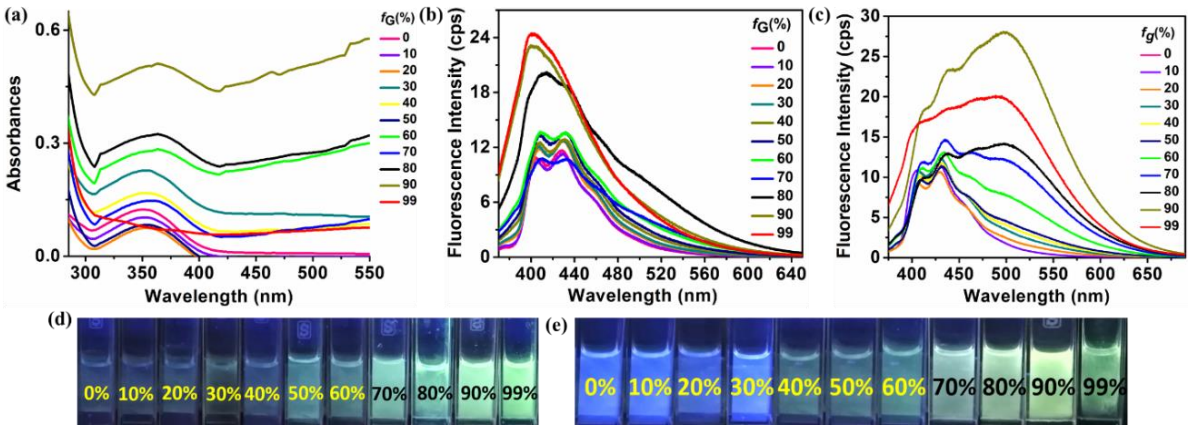

Figure 5.48 VIE-property of **DBFNCN** (a) absorbances with probe concentration of 10^{-5} M (b) emissions with probe concentrations of 10^{-5} M (c) emissions with probe concentrations of 10^{-4} M (absorbance wavelength was same as of 10^{-5} M); images captured under UV-365 nm bulb for **DBFNCN** (d) 10^{-5} M (e) 10^{-4} M concentrations

DBTNCN, **OXNCN**, **PONCN**, and **TANCN**. All of them emitted at different redshifted VIE wavelengths from their respective AIE wavelengths. Incidentally, AIE and VIE emissions of **OXNCN** fell into the green and yellow range, while others were in the same spectral range to display almost the same AIE and VIE color.

5.3.4 Cytotoxicity investigation and selection of bioimaging agent

The GI_{50} of all the compounds was >100 μM, indicating a safe window to derive the working concentrations for bioimaging experiments (Figure 5.49). As noticed from confocal images of **TANCN** and **PONCN** molecules, the cell penetration was not significant enough to be considered further for bioimaging studies (discussed in 2.10 paragraph). Excitingly, **OXNCN** showed a good amount of uptake by FaDu cells and, hence, a significant fluorescence intensity.

From photophysical investigations, **OXNCN** was proven to be a D-π-A fluorophore, exhibiting solid-state emission, viscosity and aggregation-dependent emission switching, but no solvatofluorochromism. Thus, it comprises a molecular design expected to remain nonresponsive to cellular environment. On the other hand, the combined AIE and VIE features might be useful for LD imaging, and hence, **OXNCN** was explored as the lead bioimaging agent. **OXNCN** was the safest, while the rest of the probes were more cytotoxic than **OXNCN**, hence kept restrained from bioimaging

exploration. Further, unlike to commercially available Nile red dye, **OXNCN** solids are stable at -20 °C to 40 °C; thus, no refrigerator storage is needed and can be considered with an added benefits with this newly discovered dye **OXNCN**.

5.3.5 Lipid droplet bioimaging in FaDu cancer cells

5.3.5.1 Wash-free LD bioimaging of live FaDu cancer cells with OXNCN at different probe concentrations and colocalization studies

Initially, 10 μM (1/10th of 100 μM) of **OXNCN** was utilized to investigate the wash-free LD bioimaging efficiency concerning 10 μM of Nile red and 3 μM of DAPI. Moreover, this concentration is biologically safe and typically used for Nile red in bioimaging studies. .[74] The LD specificity was excellent with Pearson's Correlation (PC) and overlap coefficient (OC) above 0.90 with a colocalization rate (CR%) of ~99% (Figure 5.50).

Notably, **OXNCN** displayed emission in the range of 523-527 nm in biologically relevant PBS medium andcells Further, this probe emits at 543-545 nm in 90% glycerol into MeOH (*v*/*v*), but almost non-emissive in polar DMSO. As PBS is rich in water and simultaneously a viscous medium, the emission of **OXNCN** in PBS and cells is probably a combined effect of its AIE and VIE- nature.

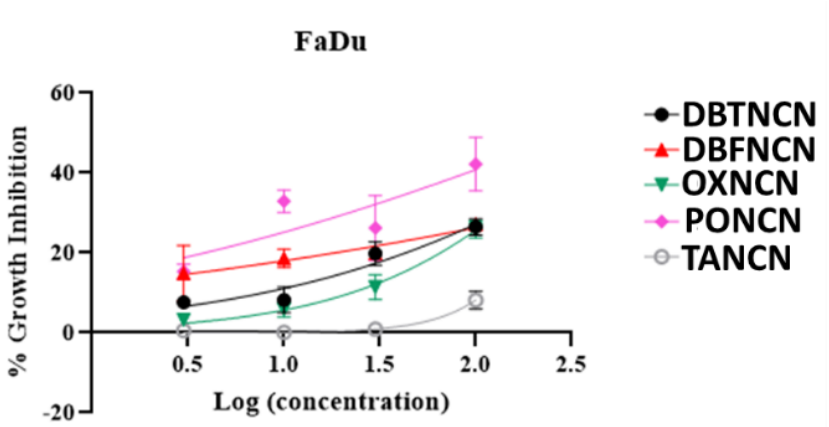

Figure 5.49 Cytotoxicity results against FaDu cells , for the synthesized dyes

Most possibly in cells, this combined effect is helping **OXNCN** display bright emission in lipid droplets because the most effective bioimaging studies could be carried out by opening a 534 nm laser channel. However, during confocal imaging, the merged profiles (Figure 5.50) and full projection between **OXNCN** and Nile red images indicated a perfect overlap supporting its final output of all *Z*-stacks to find a complete depth of the

area (Figure 5.51). To avoid interactions with DNA, **OXNCN** was designed as an uncharged molecule. A colocalization comparison with respect to DAPI and Nile red together could further help us spot the LD depositions surrounding the nucleus without staining the nucleus (zoomed version in Figure 5.50).

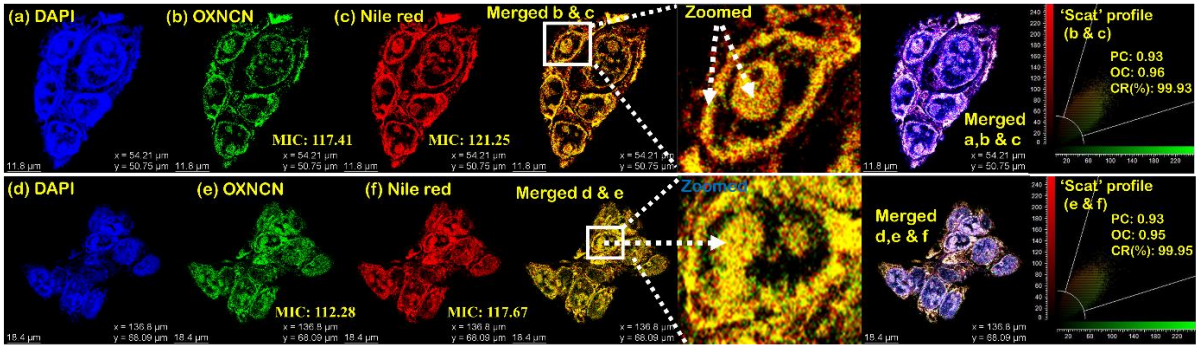

Figure 5.50 LD bioimaging with **OXNCN** (10μM) in FaDu cancer cells and colocalization comparison (a-c, d-f) with respect to DAPI (3 μM), and Nile red (10μM) in terms of several imaging parameters (the bright filed images are kept in the supporting information file); the LDs are marked by white color arrows and boxes in different zones

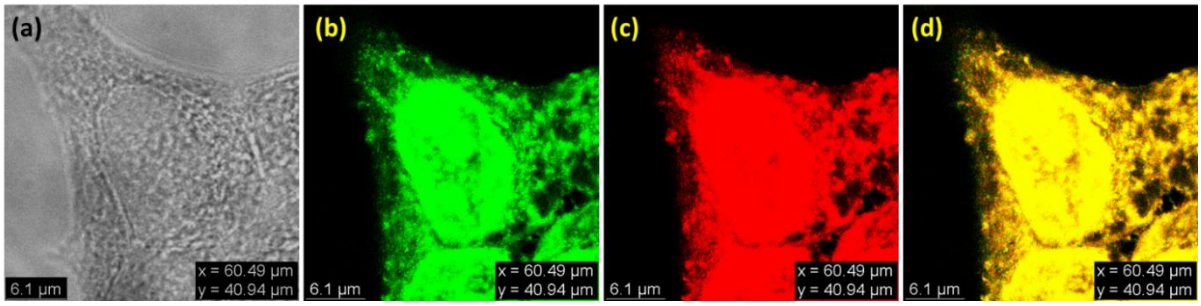

Figure 5.51 Images taken with full laser projection (a) bright field (b) **OXNCN** (10μM) (c) Nile red (10μM) (d) full laser projection image on colocalization with 20 times *Z*-stack

The mean intensity colocalization (MIC) and intensity vs. distance profiles were also encouraging, accompanying an excellent PC factor for staining with 10 μM of **OXNCN** with respect to 10 μM of Nile red (Figure 5.52). To investigate intensity vs distance outcome, 10 different spot selections (ROI: region of interest) were made for **OXNCN** and **Nile red** stained images with the 'line profile' tool in the 'quantify' option

of Las X software, and the MIC was found to be comparable further indicating commendable efficacy of **OXNCN** for LD bioimaging.

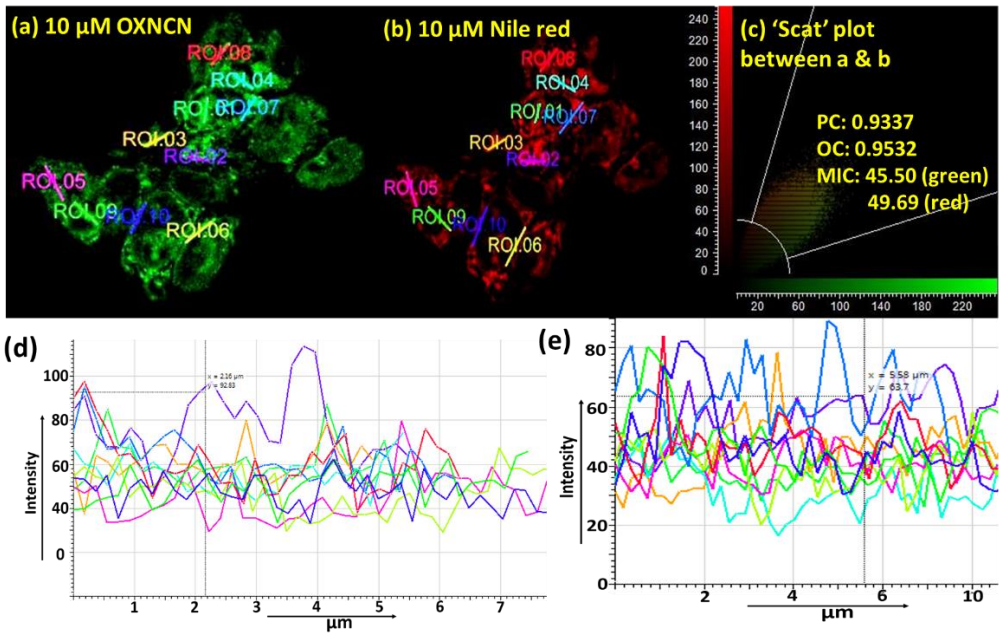

Figure 5.52 (a) Cells stained with **OXNCN** (10µM) with 10 selected 'ROI's (b) same cells stained with Nile red (10µM) with 10 selected 'ROI's at the same 10 regions of interest (c) 'Scat' profile comparison between the stain done by '**OXNCN**' in and 'Nile red' (d) intensity vs distance profile comparison for the cells stained with **OXNCN** (10µM) (e) intensity vs. distance profile comparison for the cells stained with Nile red (10µM)

To find the minimum requirement of the probe concentration for LD detection, we used ~1/3rd of 10 µM concentration of **OXNCN**. It is pertinent to note that Nile red was used earlier as low as 4 µM concentration for the imaging..[76] As PC >0.30, OC > 0.50, and CR(%) >50 are highly acceptable in LD bioimaging,[77-79] with PC ~ 0.33, OC ~ 0.71, and CR (%) > 60, the *Z*-stack (20 steps) merged profiles of **OXNCN** and Nile red stained images indicated a satisfying colocalization of the synthetic and standard dye. With a ~3 times magnified visualization of the cells (14.2 µm scale bar instead of 49.1 µm), the deposition of LDs was more clearly noticeable, as highlighted with white circles. (Figure 5.53).

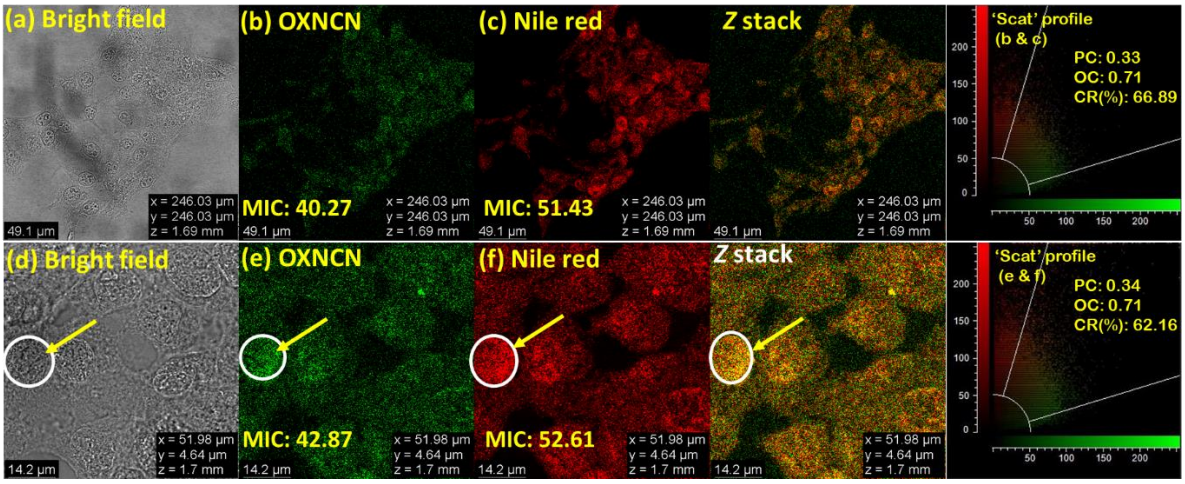

Figure 5.53 LD bioimaging with **OXNCN** (3 μM) in FaDu cancer cells and colocalization comparison (a-c, d-f) with respect to Nile red (4 μM) in terms of several imaging parameters

The mean intensity colocalization (MIC) and intensity vs distance profiles were also (stop using found to be; so many) encouraging, accompanying an excellent PC factor for staining with 3 μM of **OXNCN**, while comparing with 4 μM of Nile red (Figure 5.54).

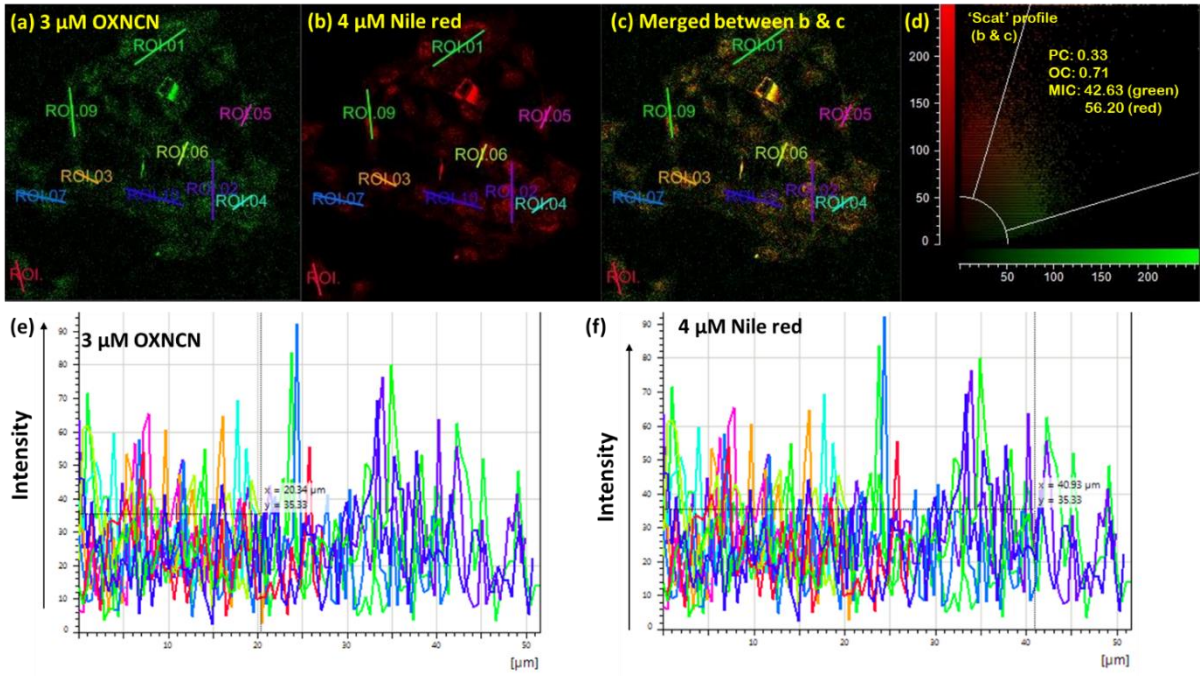

Figure 5.54 (a) Cells stained with **OXNCN** (3 μM) with 10 selected 'ROI's (b) same cells stained with Nile red (4 μM) with 10 selected 'ROI's at the same 10 regions of interest (c) colocalization between 'a' and 'b' (c) 'Scat' profile comparison between the stain done by '**OXNCN**' in 'a' and 'Nile red' in 'b' (d) intensity vs distance profile comparison for

the cells stained with **OXNCN** (3 μM) in 'a' (e)) intensity vs distance profile comparison for the cells stained with Nile red (4 μM) in 'b'

5.3.5.2 Wash-free LD bioimaging of live FaDu cancer cells at different time points at respective concentrations and photostability of fluorescence in cells

Time-dependent bioimaging can provide an idea about the dye performance regarding invasiveness, photostability, and specificity maintenance.[80] The time-dependent wash-free LD bioimaging experiments were performed again at both the probe concentrations, 10 μM and 3 μM of **OXNCN** with respect to 10 μM and 4 μM of Nile red respectively (Figures 5.55, 5.56, difference between **OXNCN** and Nile red and the merged version column-wise). The mean intensity colocalization (MIC) vs time point plotting revealed that 10 μM **OXNCN** displayed good MIC for up to 30 min, but after that, its intensity was reduced to some extent. The MIC was poor for 3 μM **OXNCN**, and again, after 30 mins the MIC began reducing. Of note, the MIC also fell after 30 mins for 10 μM Nile red, but its MIC for 4 μM concentration almost remained the same (Figure 5.57). The PC was ~ 0.66 for 10 μM **OXNCN** even at 30 minute time-point, but the PC of 0.23 appeared for 3 μM **OXNCN**, indicating a moderate PC value. However, the OC was satisfying for **OXNCN** even after 1 h at both concentrations. Overall, for time-dependent experiments, 10 μM concentration was commendable for **OXNCN** as it could maintain good visualization and colocalization even at 1 h time-point. Of note, 10 μM probe concentration was superior than standard 10 μM Nile red .

5.3.5.3 Wash-free LD bioimaging of live FaDu cancer cells at different time points at respective concentrations and photostability of fluorescence in cells

Fluorescent probes with temperature-dependent spectral properties help to get thermal images of living organisms without affecting them.[81] Herein, we were interested in investigating emission shifts in LDs inside cancer cells arising from the utilized fluorophore **OXNCN** at lower concentration i.e. 3 μM.

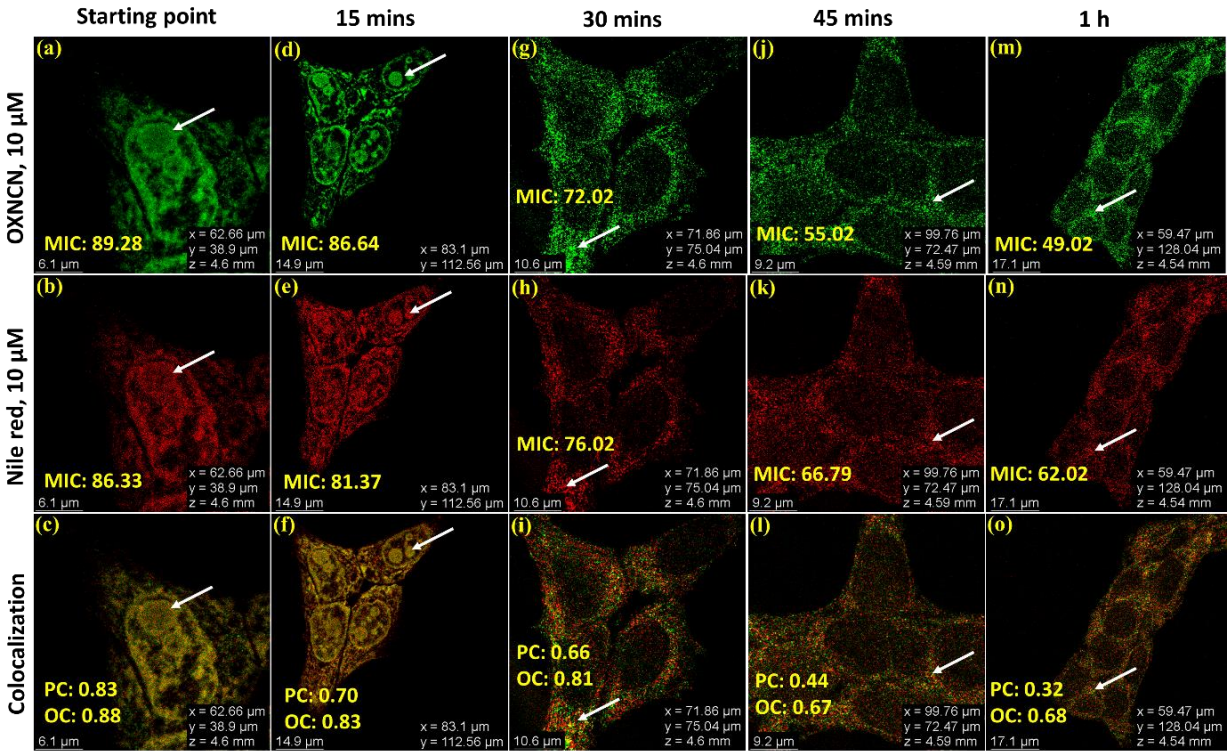

Figure 5.55 Time-dependent bioimaging of LDs in FaDu with **OXNCN** (10 µM) and colocalization comparison column-wise with standard dye Nile red (10 µM) at different time points; bioimaging of FaDu cells with **OXNCN** (10 µM) for time-point of (a) starting time (d) 15 min (g) 30 min (j) 45 min (m) 1h; with Nile red (4µM) for time-point of (b) starting time (e) 15 min (h) 30 min (k) 45 min (n) 1h; colocalization comparison (c) between 'a' and 'b' at starting-time point (f) between 'd' and 'e' at 15 min (i) between 'g' and 'h' at 30 min (l) between 'j' and 'k' at 45 min (o) between 'm' and 'n' at 1h

Planning for a simple experiment, with 25°C to 37°C limit of temperature, the images of the same cells were captured, keeping the bioimaging parameters the same for all the captured images. The viscosity-sensitive emission enhancement of **OXNCN** has been discussed earlier, and the temperature change is attributed to viscosity alteration in the cellular environment. We studied the photophysical outcomes of **OXNCN** (3 µM) even in a PBS medium (Figure 5.58d). With decreasing temperature, the viscosity of the medium would enhance to a certain degree , and the molecular motion of a fluorophore would be typically more restricted to open up the radiative channel.[74]

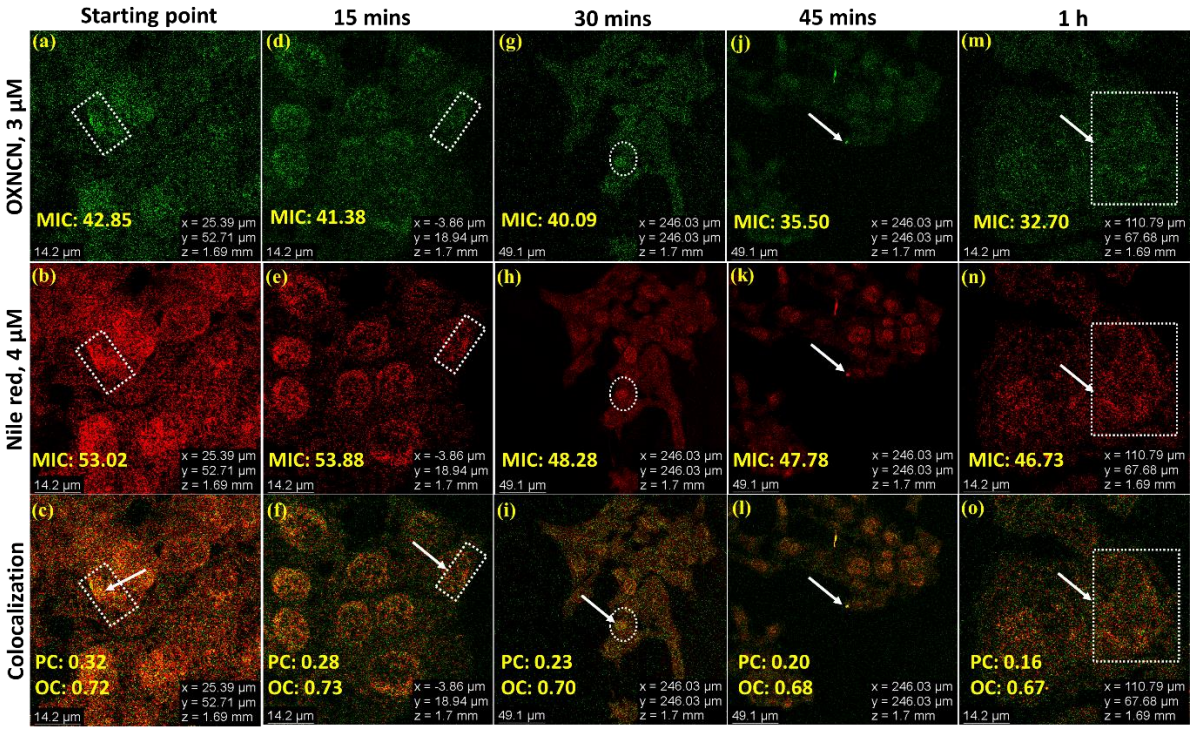

Figure 5.56 Time-dependent bioimaging of LDs in FaDu with **OXNCN** (3 µM) and colocalization comparison column-wise with standard dye Nile red (4 µM) at different time points; bioimaging of FaDu cells with **OXNCN** (3µM) for time-point of (a) starting time (d) 15 min (g) 30 min (j) 45 min (m) 1h; with Nile red (4µM) for time-point of (b) starting time (e) 15 min (h) 30 min (k) 45 min (n) 1h; colocalization comparison (c) between 'a' and 'b' at starting-time point (f) between 'd' and 'e' at 15 min (i) between 'g' and 'h' at 30 min (l) between 'j' and 'k' at 45 min (o) between 'm' and 'n' at 1h

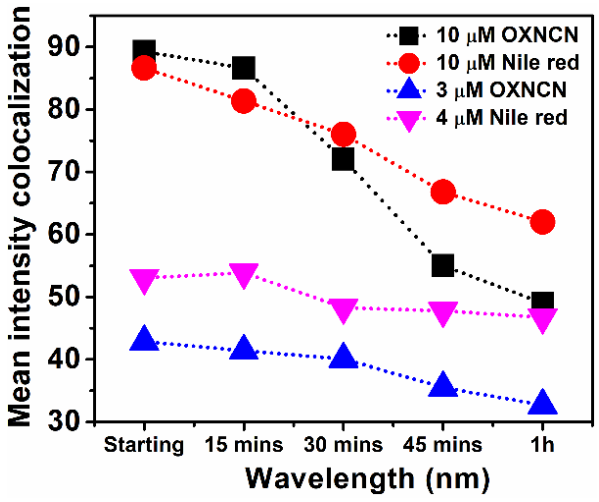

Figure 5.57 Mean intensity colocalization (MIC) comparison plot for time-dependent LD bioimaging with **OXNCN** and colocalization with Nile red

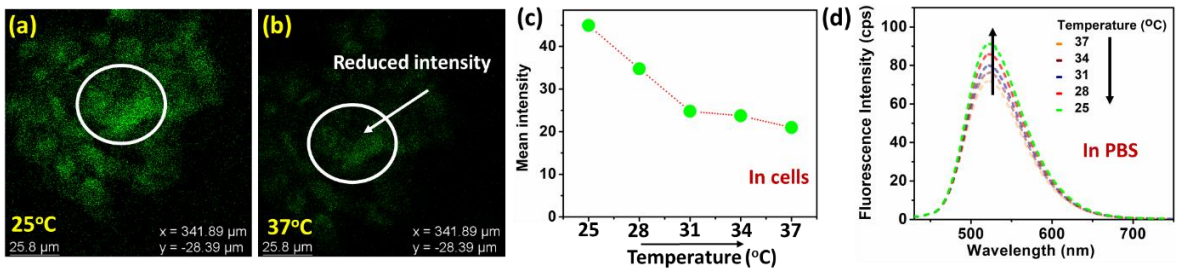

Figure 5.58 Temperature-dependent LD bioimaging with **OXNCN** (3 µM) in FaDu cancer cells at (a) 25 °C (b) 37 °C (c) fluorescence intensity comparison at different temperatures in cells (d) fluorescence intensity comparison at different temperatures in PBS

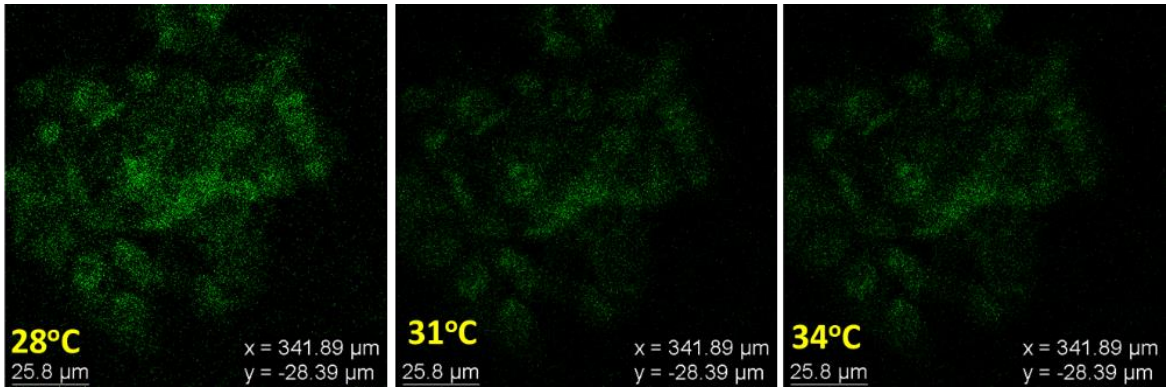

Figure 5.59 Temperature-dependent LD bioimaging with OXNCN (3 µM) in FaDu cancer cells at 28 °C, 31 °C and 34 °C

The image captured at 37 °C displayed the poorest intensity (Figure 5.58c) as quantified with ImageJ software. The intensity inside cells gradually increased with the fall of temperature and was the brightest at 25 °C (Figures 5.58, 5.59), following the same trend previously observed in the PBS medium.

5.3.5.4 LD depletion and cholesterol repletion studies with living FaDu cells

Methyl-β-cyclodextrin (MβCD) is often utilized to target and deplete cholesterol in lipid rafts. Cholesterol depletion by MβCD enhances cell membrane tension, and cholesterol gets removed to a great extent.[82] Acute cholesterol depletion by MβCD is the most widely used method to investigate the LD specificity of organic fluorophores. Still, it should be performed to avoid the common side-effect of cell death. FaDu cells were treated with 50 µM of MβCD and incubated for 30 mins at 37 °C. The cells were

washed twice with IC RPMI and then treated with 3 μM of **OXNCN**. In fresh (not undergone an M*β*CD treatment) cells, bright emission from LDs was received with 3 μM of **OXNCN** (Figure 5.60a). However, in M*β*CD treated cells, the signals got quenched drastically (Figure 5.60b). The cells were subjected to a cholesterol repletion experiment further. Hence, the cholesterol-depleted cells were again treated with 50 μM of cholesterol and incubated for 1 h at 37°C. After that, the cells were washed twice with IC RPMI and then treated with 3 μM of OXNCN. Now, the cells started to regain their fluorescence signal (Figure 5.61c); thus, the LD staining ability of OXNCN was further confirmed. As mentioned, this experiment was not done in a wash-free manner to avoid glitches caused by interference of left-over utilized reagents like M*β*CD and cholesterol.

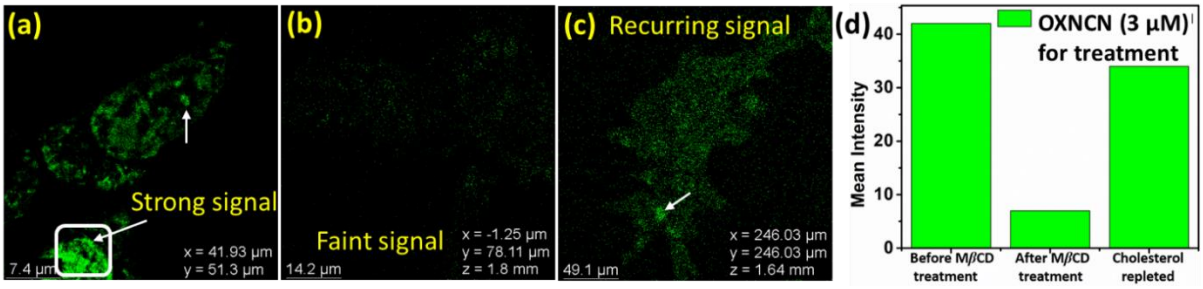

Figure 5.60 For LD bioimaging (a) FaDu cells stained with **OXNCN** (3 μM) (b) M*β*CD treated FaDu cells (cholesterol depleted cells) tried to stain with **OXNCN** (3 μM) (c) cholesterol repleted cells stained with **OXNCN** (3 μM) (d) mean fluorescence intensity in cells to compare among 'before M*β*CD treatment' 'after M*β*CD treatment', and 'cholesterol repletion treatment

5.3.5.5 Oleic acid treatment in living FaDu cells and semi-quantification

To investigate the ability of **OXNCN** in semi-quantifying LD content,[83] oleic acid treatment was followed to induce LD formation in living FaDu cells. Fresh FaDu cells were treated with 3 μM of **OXNCN** and 50 μM of oleic acid to be incubated for 30 min. With each 40-minute gap, the images of cells were captured up to 2 h. With the increment of inducing time of oleic acid to cells, more LDs should be formed during 2 h.[83] As shown below, by prolonging the oleic acid-inducing time, FaDu cells gradually became brighter. It indicates that oleic acid-induced the formation of more LDs, which **OXNCN** illuminated. The ratio of the fluorescence intensity of **OXNCN** in oleic acid-treated cells was plotted versus the time points. It showed that the fluorescence intensity increased with the increment of treatment time, implying that **OXNCN** can

reveal the change in LD content in living FaDu cells (Figure 5.61). Before investigation with cells, the photophysical emission responsiveness of **OXNCN** with varying concentrations of oleic acid was tested in the cuvette. Utilizing 3 μM **OXNCN**, a 0.17 % quantum yield was achieved in PBS only. Still, there was a sharp increment in the emission quantum yield with gradually increasing oleic acid concentration, and ultimately, it reached 1.28 % at 50 μM concentration of oleic acid (Figure 5.62). Hence, the photophysical outcome and cell imaging results with oleic acid treatment match further to claim probe efficiency.

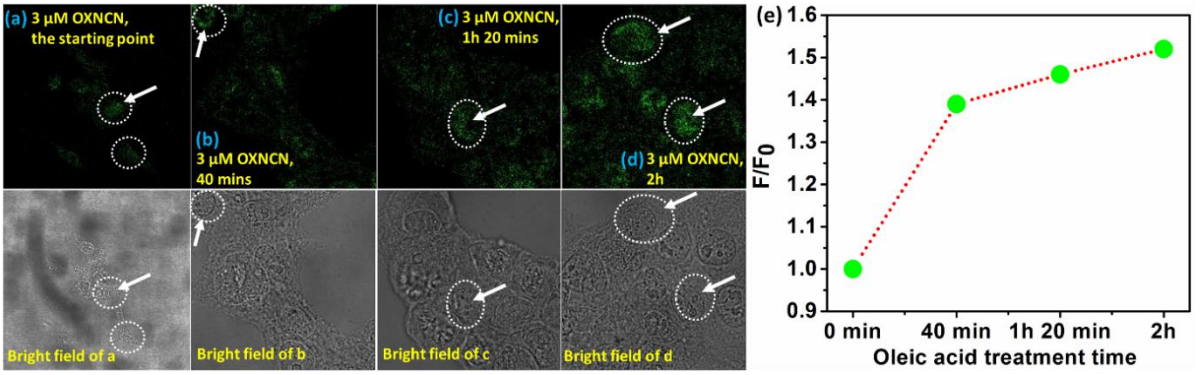

Figure 5.61 Utilizing 3 μM **OXNCN**, (a-d) confocal images of oleic acid treated FaDu cells at different time-points (e) plot of intensity variation vs oleic acid treatment time in FaDu cells

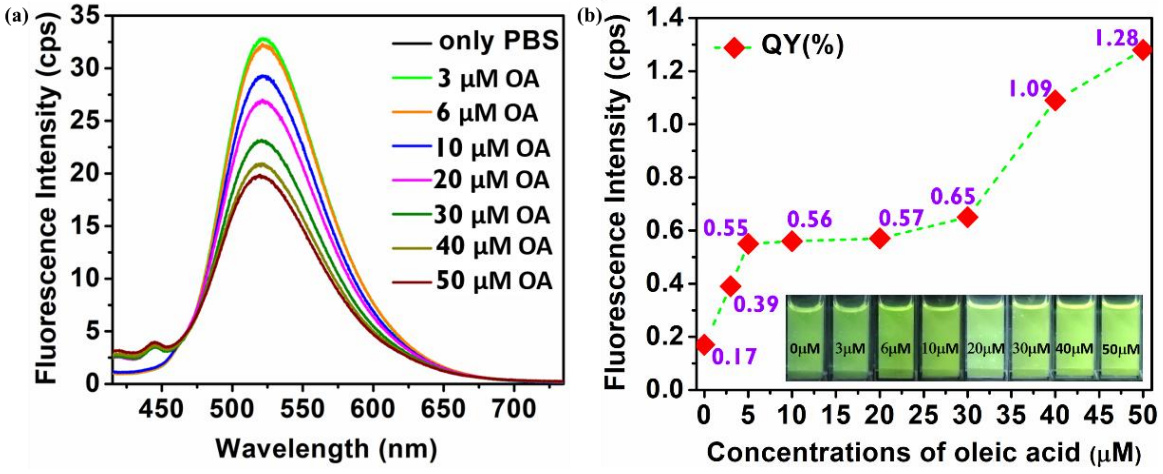

Figure 5.62 (a) Emission of **OXNCN** (3 μM) in PBS and simultaneous increment of oleic acid concentrations (b) fluorescence intensity vs concentrations of the oleic acid plot with the respective quantum yields written in the purple inset

5.3.5.6 Investigation of LD bioimaging in FaDu with TANCN and PONCN

OXNCN, being a green emitter, was selected to be the standard dye for colocalization experiments to investigate the LD bioimaging capability of **TANCN** (orange-red) and **PONCN** (orange-yellow) at 3 μM probe concentration for all of them, including standard **OXNCN**. But both of them were invasive and non-LD specific. There was unprecedented cytosolic staining, and that too, was noticed to be unstable (Figures 5.63, 5.64). The reason for non-LD-specificity for **TANCN** and **PONCN**, and the LD-specificity of **OXNCN** are unknown to us and subjected to carry out many other detailed investigations. It is observed that the '*dioxin*' moiety of **OXNCN** is favorable for non-cytotoxic LD imaging in FaDu with good photostability. Because except for the heteroatoms, the rest structure of the dyes is the same for all. As our future perspective, we aim to translate this work into FaDu-injected tumor *in vivo* imaging with **OXNCN**.

5.4 Summary

The present work concentrated on developing a new class of small organic fluorophores with omnipresent but multitudinous emission variation. A three-step facile synthetic

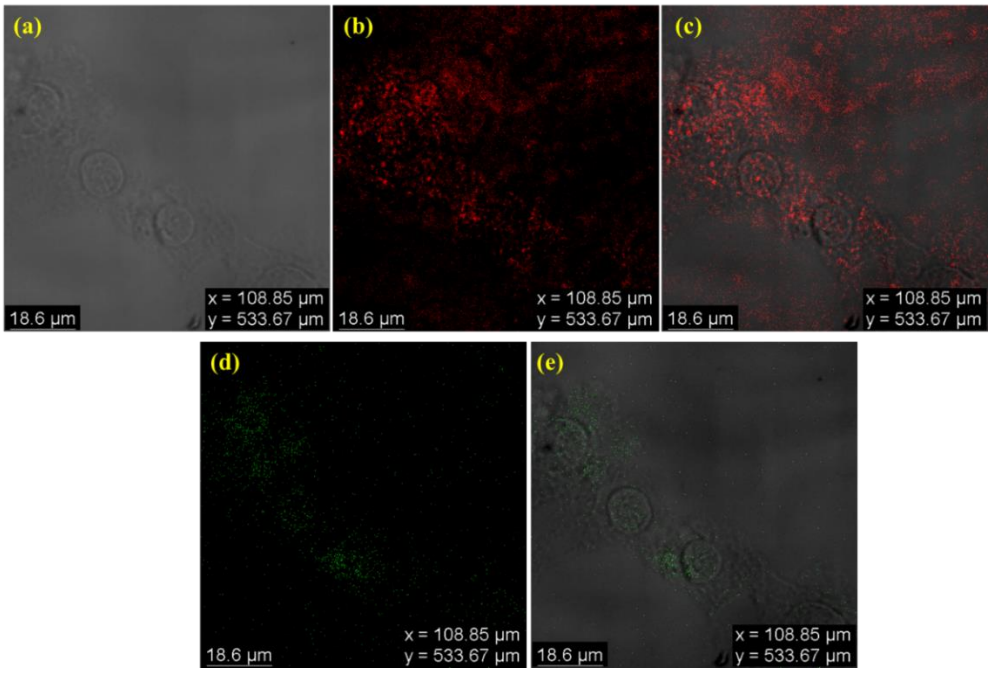

Figure 5.63 (a) Bright-field image of FaDu cells (b) non-specific staining by **TANCN** (3 μM) (c) merged between 'a' and 'b' (d) specific staining by **OXNCN** (3 μM) (e) merged images between 'a' and 'd'

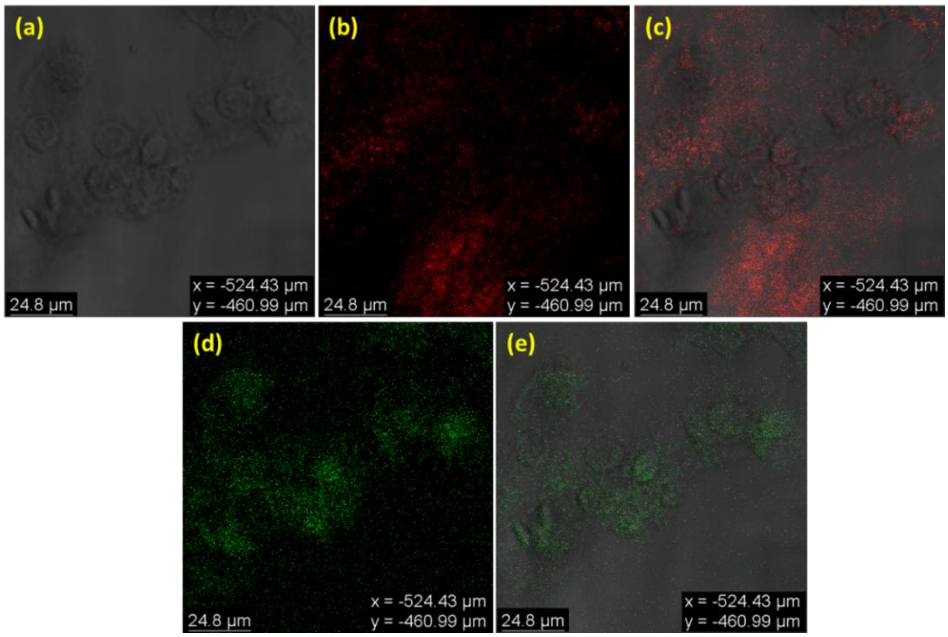

Figure 5.64 (a) Bright-field image of FaDu cells (b) non-specific staining by **PONCN** (3 µM) (c) merged between 'a' and 'b' (d) specific staining by **OXNCN** (3 µM) (e) merged images between 'a' and 'd'

route was successfully established utilizing organophosphonate chemistry, and the contrast in their photophysical properties was thoroughly investigated in solids, solvents, aggregates, and viscous environments. Single-crystal studies with non-covalent interactions, lateral and longitudinal displacement, different slip-angles, and TD-DFT analysis were deeply investigated to reach scientific explanations of the observed uncanny solid-state emission contrast. The emission phenomena in solution were ascribed with detailed TD-DFT analysis concerning excited planarity, relaxation, and other crucial quantum chemical descriptors. The different heterocyclic scaffolds influenced not only photophysical characteristics but also modified the cell permeability and cytotoxicity to a significant extent. The non-cytotoxic, cell-permeable lead **OXNCN** was selected for LD bioimaging explorations in aggressive FaDu cancer cells. The thoughtful design of **OXNCN** with a hydrophobic core specified LD location to provide emission in FaDu cells, most possibly as a combined effect of its AIE and VIE properties without responding to polarity. Hence, multipurpose concentration, time, and temperature-dependent LD bioimaging were successfully undergone with **OXNCN** in FaDu cells. Cholesterol depletion and repletion studies along with oleic acid

treatment experiments, further supported its LD specificity, whereas the bioimaging capabilities were profoundly compared with the standard LD dye Nile red. **OXNCN** was proven to be a visionary LD dye in terms of several parameters to manifest bioimaging audacity in robust FaDu cells; therefore, it translated itself from a conceptualized design into a real-world applicable bioimaging dye.

5.5. Synthetic procedures with characterization detailing

The synthesized phosphonates and some of the keto compounds were separated as gummy compounds, which were solidified after sufficient vacuum drying and keeping for a few days. All the phosphonates, keto, and dicyano compounds were prepared following the same respective procedures. For the phosphonates the R_f calculation and column chromatography were performed with 30% EtOAc into hexane (*v*/*v*) medium, whereas, fro the keto and dicyano compounds the R_f calculation and column chromatography were performed with 15% EtOAc into hexane (*v*/*v*) medium.

5.5.1 Synthesis of diethyl (naphthalen-1-yl(thianthren-2-yl)methyl)phosphonate

Diethyl (hydroxy(naphthalen-1-yl)methyl)phosphonate (1.699 mmol, 1 equiv., 0.5 g) was taken inside one 250 mL round bottom flask and subjected to vacuum drying for 10 min. Next, under N_2, dichloroethane (30 mL) was poured into it, and stirred well for 10 mins again. Now, methane sulfonic acid (5.91 mmol, 3.48 equiv., 0.39 mL) was added under N_2 and stirred for another 15 mins. Later, thianthrene (1.699 mmol, 1 equiv., 0.37 g) was added into the reaction mixture to receive a bluish solution, and the reaction was kept at 90 ^oC to reflux up to 4h. After cooling down to room temperature, the progress of the reaction was monitored with the formation of a bright spot at R_f= 0.32. The reaction mixture was worked up with 30 mL×3 of an EtOAC and brine water mixture of 1:2 EtOAc:H_2O ratio (*v*/*v*). The maroon color organic layer was separated and made into a slurry with silica gel (60-120 mesh) to perform column chromatography (30% EtOAc into hexane (*v*/*v*), which yielded ~51% (427.3 mg); **IR** (cm^{-1}): 3050, 2979, 2923, 2850, 1694, 1552, 1436, 1245, 1017; **mp**: 85^o-87^{o}C; **^{1}H NMR** (400 MHz, $CDCl_3$, 25^{o}C, δ) 8.10-8.09 (m, 1H), 7.92-7.90 (d, *J*= 8 Hz, 1H), 7.78-7.71 (m, 2H), 7.54-7.53 (m, 1H), 7.46-7.30 (m, 7H), 7.14-7.10 (m, 2H), 5.21 (d, *J*= 24 Hz, P-CH, 1H), 4.00-3.86 (m, 4H), 1.12 (t, *J*= 7.2 Hz, 3H), 0.94 (t, *J*= 7.2 Hz, 3H); **^{13}C NMR** (100 MHz, $CDCl_3$, 25^{o}C, δ) 136.8, 135.8, 135.4,

134.3, 134.2, 131.9, 131.5, 129.7, 129.6, 129.1, 128.9, 128.8, 128.6, 128.3, 127.7, 126.6, 125.7, 125.4, 122.9, 62.9, 45.9 (d, *J*= 140 Hz, P-C coupling), 16.3; **^{31}P NMR** (162 MHz, $CDCl_3$, 25°C, *δ*) 24.84; **HRMS** (ESI) m/z: calcd. for $C_{27}H_{25}O_3PS_2$ 493.1016, found 493.1946 $[M]^+$.

5.5.2 Synthesis of diethyl (naphthalen-1-yl(phenoxathiin-3-yl)methyl)phosphonate

Required chemicals and stoichiometry: Diethyl (hydroxy(naphthalen-1-yl)methyl)phosphonate (1.019 mmol, 1 equiv., 0.3 g), dichloroethane (30 mL), methane sulfonic acid (3.55 mmol, 3.48 equiv., 0.23 mL), phenoxathiin (2.038 mmol, 2 equiv., 0.41 g); R_f= 0.32; yield ~55% (267.1 mg); **IR** (cm^{-1}): 3066, 2981, 2925, 2902, 1724, 1595, 1466, 1230, 1015; **mp**: 57°-59°C; **^{1}H NMR** (400 MHz, $CDCl_3$, 25°C, *δ*) 8.13-8.09 (m, 1H), 7.94-7.91 (d, *J*= 12 Hz, 1H), 7.85-7.77 (m, 2H), 7.54-7.21 (m, 4H), 7.14-7.08 (m, 2H), 7.01-6.83 (m, 4H), 5.17 (d, *J*= 28 Hz, P-CH, 1H), 4.01-3.66 (m, 4H), 1.13 (t, *J*= 6.85 Hz, 3H), 0.95 (t, *J*= 7.2 Hz, 3H); **^{13}C NMR** (100 MHz, $CDCl_3$, 25°C, *δ*) 149.4, 146.9, 134.3, 131.7, 131.3, 129.5, 129.0, 128.5, 126.6, 125.7, 125.2, 124.2, 124.0, 123.2, 123.1, 122.9, 122.3, 121.9, 120.4, 117.1, 116.5, 116.4, 115.3, 60.2, 43.5 (d, *J*= 140 Hz, P-C coupling), 13.7; **^{31}P NMR** (162 MHz, $CDCl_3$, 25°C, *d*) 25.01; **HRMS** (ESI) m/z: calcd. for $C_{27}H_{25}O_4PS$ 477.1245, found 477.1264 $[M]^+$.

5.5.3 Synthesis of diethyl (dibenzo[b,e][1,4]dioxin-2-yl(naphthalen-1-yl)methyl)phosphonate

Required chemicals and stoichiometry: Diethyl (hydroxy(naphthalen-1-yl)methyl)phosphonate (1.019 mmol, 1 equiv., 0.3 g), dichloroethane (30 mL), methane sulfonic acid (3.55 mmol, 3.48 equiv., 0.23 mL), and oxanthrene (1.634 mmol, 1.6 equiv., 0.3 g); R_f= 0.30; yield ~48% (225.1 mg); **IR** (cm^{-1}): 3056, 2988, 2918, 2850, 1586, 1485, 1284, 1228, 1042, 1016; **mp**: 94°-96°C; **^{1}H NMR** (400 MHz, $CDCl_3$, 25°C, *δ*) 8.35-8.31 (m, 1H), 8.15-8.09 (m, 2H), 7.93-7.78 (m, 3H), 7.66-7.38 (m, 7H), 7.32-7.27 (m, 1H), 5.49 (d, *J*= 28 Hz, PCH, 1H), 4.05-3.95 (m, 2H), 3.89-3.78 (m, 2H), 1.14 (t, *J*= 7 Hz, 3H), 1.05 (t, *J*= 7 Hz, 3H). ^{13}C NMR (100 MHz, $CDCl_3$, 25°C, *δ*) 146.3, 142.5, 141.1, 133.9, 133.3, 132.1, 131.2, 130.4, 128.9, 128.3, 127.7, 126.9, 126.5, 124.9, 124.4, 117.8, 117.1, 116.6, 113.8, 113.3, 96.1, 83.3 (P-C coupling), 29.7. ^{31}P NMR (162 MHz, $CDCl_3$, 25°C, *d*) 25.01. Mass spectrometry: HRMS (ESI) m/z: calcd. for $C_{27}H_{25}O_5P$ 461.1473, found 461.2395 $[M]^+$.

5.5.4 Synthesis of diethyl (dibenzo[b,d]thiophen-3-yl(naphthalen-1-yl)methyl)phosphonate

Required chemicals and stoichiometry: Diethyl (hydroxy(naphthalen-1-yl)methyl)phosphonate (1.019 mmol, 1 equiv., 0.3 g), dichloroethane (30 mL), methane sulfonic acid (3.55 mmol, 3.48 equiv., 0.23 mL), and dibenzothiophene (2.038 mmol, 2 equiv., 0.38 g); R_f= 0.31; yield ~52% (244.1 mg); **IR** (cm^{-1}): 3053, 2979, 2928, 2902, 1733, 1597, 1474, 1238, 1019; **mp**: 63°-65°C; **^{1}H NMR** (400 MHz, $CDCl_3$, 25°C, δ) 8.35-8.31 (m, 2H), 8.17-8.03 (m, 2H), 7.86-7.75 (m, 4H), 7.64-7.42 (m, 6H), 5.51 (d, J= 24 Hz, PCH, 1H), 4.07-3.78 (m, 4H), 1.15 (t, J= 6.6 Hz, 3H), 1.05 (t, J= 7.2 Hz, 3H); **^{13}C NMR** (100 MHz, $CDCl_3$, 25°C, δ) 145.8, 139.8, 138.3, 135.8, 135.3, 134.2, 133.2, 133.1, 132.6, 131.8, 131.7, 129.1, 128.5, 128.2, 127.8, 126.8, 126.5, 125.6, 125.5, 124.3, 123.1, 122.8, 121.8, 62.9, 46.59 (d, J= 140 Hz, P-C coupling), 16.32; **^{31}P NMR** (162 MHz, $CDCl_3$, 25°C, *d*) 25.57; **HRMS** (ESI) m/z: calcd. for $C_{27}H_{25}O_3PS$ 461.1296, found 462.1316 $[M+H]^+$.

5.5.5 Synthesis of diethyl (dibenzo[b,d]furan-2-yl(naphthalen-1-yl)methyl)phosphonate

Required chemicals and stoichiometry: Diethyl (hydroxy(naphthalen-1-yl)methyl)phosphonate (1.019 mmol, 1 equiv., 0.3 g), dichloroethane (30 mL), methane sulfonic acid (3.55 mmol, 3.48 equiv., 0.23 mL), and dibenzothiophene (2.038 mmol, 2 equiv., 0.38 g); R_f= 0.30; yield ~59% (267.21 mg); **IR** (cm^{-1}): 3066, 2981, 2925, 2906, 1707, 1595, 1473, 1239, 1022; **mp**: 56°-58°C; **^{1}H NMR** (400 MHz, $CDCl_3$, 25°C, δ) 8.35-8.31 (m, 1H), 8.15-8.09 (m, 2H), 7.93-7.78 (m, 3H), 7.65-7.38 (m, 7H), 7.32-7.27 (m, 1H), 5.49 (d, J= 28 Hz, PCH, 1H), 4.05-3.78 (m, 4H), 1.14 (t, J= 7.2 Hz, 3H), 1.05 (t, J= 7 Hz, 3H); **^{13}C NMR** (100 MHz, $CDCl_3$, 25°C, δ) 156.6, 155.4, 134.2, 132.8, 131.8, 131.2, 129.1, 128.9, 128.1, 127.7, 127.2, 126.5, 125.6, 124.5, 124.1, 123.1, 122.7, 121.9, 120.9, 120.6, 113.0, 111.6, 62.8, 46.8 (d, J= 140 Hz, P-C coupling), 16.3. ^{31}P NMR (162 MHz, $CDCl_3$, 25°C, *d*) 25.79; **HRMS** (ESI) m/z: calcd. for $C_{27}H_{25}O_4P$ 445.1524, found 445.1544 $[M]^+$.

5.5.6 Synthesis of naphthalen-1-yl(thianthren-2-yl)methanone

Diethyl (naphthalen-1-yl(phenoxathiin-3-yl)methyl)phosphonate (0.5075 mmol., 1 equiv., 0.25 g) and K^{t}OBu (3.045 mmol., 6 equiv., 0.34 g) were taken into a 250 mL round bottom flask and subjected to vacuum drying for 10 min. Later on, under the

N_2 environment, a septum was capped up, and N_2 was continued thoroughly to be purged into it through a needle for 15 min. Next, 25 mL of dry THF was added to it, and the reaction was stirred for 2h under the O_2 environment. The progress of the reaction was checked with the formation of a green fluorescent spot at R_f = 0.64. The reaction mixture was worked up with 30 mL×3 of an EtOAC and brine water mixture of 1:2 EtOAc:H_2O ratio (*v*/*v*). The organic layer was separated and made into a slurry with silica gel (60-120 mesh) to perform column chromatography (15% EtOAc into hexane (*v*/*v*), which yielded ~95% (178.62 mg); **IR** (cm^{-1}): 3051, 2915, 2842, 2776, 1719, 1653, 1566, 1440, 1278, 1237, 103; **mp**: 80°-82°C; **^{1}H NMR** (400 MHz, $CDCl_3$, 25°C, δ) 8.05-8.01 (m, 2H), 7.95-7.92 (m, 2H), 7.71-7.69 (m, 1H), 7.56-7.43 (m, 6H), 7.28-7.26 (m, 2H), 7.25-7.24 (m, 1H); **^{13}C NMR** (100 MHz, $CDCl_3$, 25°C, δ) 196.5, 142.0, 137.8, 135.9, 135.8, 134.7, 134.3, 133.8, 131.6, 130.8, 130.1, 129.5, 128.9, 128.5, 128.2, 127.7, 127.5, 126.6, 125.5, 124.4; **HRMS** (ESI) m/z: calcd. for $C_{23}H_{14}OS_2$ 370.4840, found 371.0540 $[M+H]^+$.

5.5.7 Synthesis of naphthalen-1-yl(phenoxathiin-3-yl)methanone

Required chemicals and stoichiometry: Diethyl (naphthalen-1-yl(phenoxathiin-3-yl)methyl)phosphonate (0.5246 mmol., 1 equiv., 0.25 g), K^{t}OBu (3.1477 mmol., 6 equiv., 0.353 g), 25 mL of dry THF; R_f = 0.61; yield ~85% (158.04 mg); **IR** (cm^{-1}): 3058, 2955, 2914, 2850, 1726, 1654, 1581, 1463, 1404, 1277, 1223, 1083; **mp**: 164°-166°C; **^{1}H NMR** (400 MHz, $CDCl_3$, 25°C, δ) 8.05-8.01 (m, 2H), 7.94-7.92 (m, 1H), 7.58-7.46 (m, 6H), 7.15-6.94 (m, 5H); **^{13}C NMR** (100 MHz, $CDCl_3$, 25°C, δ) 196.4, 151.8, 151.4, 137.9, 135.9, 134.9, 133.7, 131.4, 130.8, 128.4, 128.3, 127.5, 127.4, 127.2, 126.7, 126.5, 125.6, 125.2, 124.9, 124.4, 119.0, 118.5, 117.9; **HRMS** (ESI) m/z: calcd. for $C_{23}H_{14}O_2S$ 355.0748, found 355.0769 $[M]^+$.

5.5.8 Synthesis of dibenzo[b,e][1,4]dioxin-2-yl(naphthalen-1-yl)methanone

Required chemicals and stoichiometry: Diethyl (dibenzo[b,e][1,4]dioxin-2-yl(naphthalen-1-yl)methyl)phosphonate (0.4343 mmol., 1 equiv., 0.2 g), K^{t}OBu (2.606 mmol., 6 equiv., 0.29 g), 25 mL of dry THF; R_f = 0.61; yield ~76% (111.68 mg); **IR** (cm^{-1}): 3053, 2958, 2922, 2849, 1724, 1651, 1461, 1405, 1274, 1222, 1083; **mp**: 159°-161°C; **^{1}H NMR** (400 MHz, $CDCl_3$, 25°C, δ) 8.02-7.99 (m, 2H), 7.93-7.91 (m, 1H), 7.58-7.48 (m, 4H), 7.43-7.40 (m, 2H), 6.93-6.82 (m, 5H); **^{13}C NMR** (100 MHz, $CDCl_3$, 25°C, δ) 195.9, 162.3, 159.2,

146.5, 142.1, 141.7, 136.2, 134.3, 133.7, 131.1, 128.4, 127.2, 126.5, 125.6, 124.6, 124.4, 124.2, 118.4, 116.5, 116.2; **HRMS** (ESI) m/z: calcd. for $C_{23}H_{14}O_3$ 339.0976, found 339.0999 $[M]^+$.

5.5.9 Synthesis of dibenzo[b,d]thiophen-3-yl(naphthalen-1-yl)methanone

Required chemicals and stoichiometry: Diethyl (dibenzo[b,d]thiophen-3-yl(naphthalen-1-yl)methyl)phosphonate (0.4343 mmol., 1 equiv., 0.2 g), K^{t}OBu (2.605 mmol., 6 equiv., 0.29 g), 25 mL of dry THF; R_f= 0.58; yield ~93% (136.69 mg); **IR** (cm^{-1}): 3052, 2946, 2894, 2835, 1712, 1642, 1578, 1478, 1409, 1234, 1070; **mp**: 134°-136°C; **^{1}H NMR** (400 MHz, $CDCl_3$, 25°C, δ) 8.69 (s, 1H), 8.14-8.04 (m, 3H), 7.97-7.86 (m, 4H), 7.66-7.44 (m, 6H); **^{13}C NMR** (100 MHz, $CDCl_3$, 25°C, δ) 197.7, 144.9, 139.7, 136.6, 135.7, 135.2, 134.9, 133.8, 131.3, 131.0, 128.5, 128.4, 127.6, 127.5, 127.3, 126.6, 125.8, 124.9, 124.5, 123.8, 122.9, 122.7, 122.0; **HRMS** (ESI) m/z: calcd. for $C_{23}H_{14}OS$ 339.0799, found 339.0820 $[M]^+$.

5.5.10 Synthesis of dibenzo[b,d]furan-2-yl(naphthalen-1-yl)methanone

Required chemicals and stoichiometry: Diethyl (dibenzo[b,d]furan-2-yl(naphthalen-1-yl)methyl)phosphonate (0.4499 mmol., 1 equiv., 0.2 g), K^{t}OBu (2.6994 mmol., 6 equiv., 0.30 g), 25 mL of dry THF; R_f= 0.58; yield ~72% (104.42 mg); **IR** (cm^{-1}): 3054, 2954, 2921, 2847, 1714, 1654, 1578, 1466, 1399, 1273, 1226, 1085; **mp**: 105°-107°C; **^{1}H NMR** (400 MHz, $CDCl_3$, 25°C, δ) 8.52 (s, 1H), 8.09-7.96 (m, 5H), 7.94-7.89 (m, 1H), 7.66-7.62 (m, 1H), 7.60-7.55 (m, 2H), 7.54-7.48 (m, 3H), 7.42-7.37 (m, 1H); **^{13}C NMR** (100 MHz, $CDCl_3$, 25°C, δ) 197.4, 136.6, 133.8, 131.3, 130.9, 130.2, 128.8, 128.5, 128.0, 127.6, 127.3, 126.5, 125.7, 125.3, 124.4, 123.8, 123.3, 121.5, 121.1, 120.4, 113.9, 112.1, 111.7; **HRMS** (ESI) m/z: calcd. for $C_{23}H_{14}O_2$ 323.1027, found 323.2246 $[M]^+$.

5.5.11 Synthesis of 2-(naphthalen-1-yl(thianthren-2-yl)methylene)malononitrile (TANCN)

Naphthalen-1-yl(thianthren-2-yl)methanone (0.5398 mmol., 1 equiv., 0.2 g) and malononitrile (2.699 mmol, 5 equiv., 0.178 g) were added to a two-necked 250 mL round bottom flask and subjected to a vacuum drying followed by N_2 purging, and the opening was capped up with septum. Then, 100 mL of $CHCl_3$ was injected into it under the N_2 environment, and the reaction mixture was allowed to stir for 10 min. Next, $TiCl_4$ (2.699 mmol, 5 equiv., 0.295 mL) and pyridine (2.699 mmol, 5 equiv., 0.22 mL) were injected

into the reaction mixture under the N_2 environment, and again the reaction was allowed to stir for 10 min. Once the fumes of TiCl4 inside the round bottom flask were clear, the reaction was allowed to reflux for 60 h. But at every 12 h, an identical amount of malononitrile, $TiCl_4$, and pyridine were added. The completion of the reaction was monitored by observing a bright reddish-orange fluorescent spot on TLC at R_f = 0.50. The reaction mixture was poured into ice water and extracted with $CHCl_3$ (3×100 mL). The combined organic layers were dried (Na_2SO_4), concentrated in vacuo, washed with Et_2O to remove excess malononitrile, and made into a slurry with silica gel (60-120 mesh) to perform column chromatography (15% EtOAc into hexane (*v*/*v*), which yielded (~75%, 169.44 mg) brightly orange-red fluorescent solids that could be easily crystallized; **IR** (cm^{-1}): 3050, 2975, 2915, 2832, 2217, 1709, 1652, 1564, 1444, 1331, 1240, 1215, 1031; **mp**: 231°-233°C; **^{1}H NMR** (400 MHz, $CDCl_3$, 25°C, δ) 8.07-8.05 (d, J = 8 Hz, 1H), 7.94-7.92 (d, J =.8 Hz, 1H), 7.61 (t, J = 8 Hz, 1H), 7.55-7.49 (m, 5H), 7.46-7.40 (m, 4H), 7.29-7.27 (m, 1H), 7.26-7.24 (m, 1H); **^{13}C NMR** (100 MHz, $CDCl_3$, 25°C, δ) 172.7, 142.3, 136.9, 135.1, 133.9, 133.8, 133.1, 132.4, 131.6, 130.3, 129.0, 128.9, 128.7, 128.5, 128.3, 127.9, 126.9, 125.1, 124.7, 113.4, 113.0, 96.1, 84.9; **HRMS** (ESI) m/z: calcd. for $C_{26}H_{14}N_2S_2$ 418.0598, found 442.0515 $[M+Na]^+$.

5.5.12 Synthesis of 2-(naphthalen-1-yl(phenoxathiin-3-yl)methylene)malononitrile (PONCN)

Required chemicals and stoichiometry: Naphthalen-1-yl(phenoxathiin-3-yl)methanone (0.2821 mmol., 1 equiv., 0.1 g), malononitrile (1.41 mmol, 5 equiv., 0.093 g), 100 mL of $CHCl_3$, $TiCl_4$ (1.41 mmol, 5 equiv., 0.15 mL), and pyridine (1.41 mmol, 5 equiv., 0.11 mL); R_f = 0.50; yield ~71% (80.53 mg, brightly orange-yellow fluorescent); **IR** (cm^{-1}): 3056, 2956, 2909, 2835, 2211, 1705, 1520, 1456, 1402, 1311, 1268, 1217, 1080, 1026; **mp**: 160°-162°C; **^{1}H NMR** (400 MHz, $CDCl_3$, 25°C, δ) 8.00-7.98 (d, J = 8 Hz, 1H), 7.87-7.85 (d, J =.8 Hz, 1H), 7.55 (t, J = 8 Hz, 1H), 7.50-7.44 (m, 2H), 7.41-7.33 (m, 2H), 7.22-7.20 (m, 1H), 7.07-6.01 (m, 5H), 6.84-6.82 (m, 1H); **^{13}C NMR** (100 MHz, $CDCl_3$, 25°C, δ) 172.5, 151.8, 150.8, 134.9, 133.9, 133.2, 132.2, 130.4, 128.9, 128.4, 127.8, 127.5, 127.1, 126.9, 126.7, 125.6, 125.1, 125.0, 124.7, 118.2, 117.9, 117.7, 113.5, 113.2, 96.1, 84.2; **HRMS** (ESI) m/z: calcd. for $C_{26}H_{14}N_2OS$ 402.0827, found 425.0626 $[M+Na]^+$.

5.5.13 Synthesis of 2-(dibenzo[b,e][1,4]dioxin-2-yl(naphthalen-1-yl)methylene)malononitrile) (OXNCN)

Required chemicals and stoichiometry: Dibenzo[b,e][1,4]dioxin-2-yl(naphthalen-1-yl)methanone (0.2955 mmol., 1 equiv., 0.1 g), malononitrile (1.4775 mmol, 5 equiv., 0.097 g), 100 mL of $CHCl_3$, $TiCl_4$ (1.4775 mmol, 5 equiv., 0.16 mL) and pyridine (1.4775 mmol, 5 equiv., 0.12 mL); R_f = 0.49; yield ~65% (74.21 mg, brightly orange-yellow fluorescent); **IR** (cm^{-1}): 3049, 2956, 2921, 2851, 2215, 1721, 1578, 1463, 1419, 1317, 1222, 1113, 1030; **mp**: 194°-196°; **^{1}H NMR** (400 MHz, $CDCl_3$, 25°C, δ) 7.99-7.97 (d, J = 8 Hz, 1H), 7.87-7.85 (d, J =.8 Hz, 1H), 7.56-7.35 (m, 5H), 7.18-7.15 (m, 1H), 6.96-6.69 (m, 6H); **^{13}C NMR** (100 MHz, $CDCl_3$, 25°C, δ) 172.2, 146.3, 142.5, 141.3, 133.9, 133.3, 132.1, 131.2, 130.4, 128.9, 128.3, 127.7, 126.9, 126.5, 124.9, 124.4, 117.8, 117.1, 116.6, 113.8, 113.3, 96.1, 83.3; **HRMS** (ESI) m/z: calcd. for $C_{26}H_{14}N_2O_2$ 386.1055, found 409.0925 $[M+Na]^+$.

5.5.14 Synthesis of 2-(dibenzo[b,d]thiophen-3-yl(naphthalen-1-yl)methylene)malononitrile (DBTNCN)

Required chemicals and stoichiometry: Dibenzo[b,d]thiophen-3-yl(naphthalen-1-yl)methanone (0.2955 mmol., 1 equiv., 0.1 g), malononitrile (1.478 mmol, 5 equiv., 0.098 g), 100 mL of $CHCl_3$, $TiCl_4$ (1.478 mmol, 5 equiv., 0.16 mL) and pyridine (1.478 mmol, 5 equiv., 0.12 mL); R_f = 0.48; yield ~74% (84.51 mg, brightly cyan green fluorescent); **IR** (cm^{-1}): 3052, 2942, 2898, 2826, 2213, 1702, 1590, 1524, 1411, 1325, 1238, 1152, 1065; **mp**: 217°-219°C; **^{1}H NMR** (400 MHz, $CDCl_3$, 25°C, δ) 8.46 (s, 1H), 8.11-8.07 (m, 2H), 7.95 (d, J = 8 Hz, 1H), 7.88-7.85 (m, 2H), 7.67-7.63 (m, 2H), 7.57-7.45 (m, 5H), 7.41-7.37 (m, 1H); **^{13}C NMR** (100 MHz, $CDCl_3$, 25°C, δ) 174.2, 144.9, 139.8, 136.1, 134.6, 133.9, 133.7, 132.2, 131.9, 130.6, 128.9, 128.6, 127.9, 127.7, 127.4, 126.9, 125.2, 124.9, 123.5, 123.0, 122.7, 122.1, 114.1, 113.5, 96.1, 83.9; **HRMS** (ESI) m/z: calcd. for $C_{26}H_{14}N_2S$ 386.0878, found 410.0793 $[M+Na]^+$.

5.5.15 Synthesis of 2-(dibenzo[b,d]thiophen-3-yl(naphthalen-1-yl)methylene)malononitrile (DBFNCN)

Required chemicals and stoichiometry: Dibenzo[b,d]furan-2-yl(naphthalen-1-yl)methanone (0.3102 mmol., 1 equiv., 0.1 g), malononitrile (1.551 mmol, 5 equiv., 0.102

g), 100 mL of $CHCl_3$, $TiCl_4$ (1.551 mmol, 5 equiv., 0.17 mL) and pyridine (1.551 mmol, 5 equiv., 0.13 mL); R_f = 0.47; yield ~63% (72.39 mg, brightly cyan fluorescent); **IR** (cm^{-1}): 3059, 2954, 2929, 2851, 2220, 1747, 1579, 1534, 1430, 1321, 1250, 1188, 1127, 1025; **mp**: 169°-171°C; **^{1}H NMR** (400 MHz, $CDCl_3$, 25°C, δ) 8.23-8.06 (m, 2H), 8.03-7.90 (m, 2H), 7.73-7.55 (m, 5H), 7.54-7.43 (m, 3H), 7.41-7.34 (m, 2H); **^{13}C NMR** (100 MHz, $CDCl_3$, 25°C, δ).166.5, 157.6, 155.7, 149.6, 133.9, 132.3, 130.6, 129.3, 129.2, 128.9, 128.6, 127.7, 126.8, 125.1, 124.9, 124.4, 123.6, 123.5, 122.9, 122.7, 121.6, 121.3, 121.2, 113.9, 113.3, 112.1; **HRMS** (ESI) m/z: calcd. for $C_{26}H_{14}N_2O$ 370.1106, found 393.0999 $[M+Na]^+$.

5.6 References

1 M. Rosenberg, K. R. Rostgaard, Z. Liao, A. Ø. Madsen, K. L. Martinez, T. Vosch and B. W. Laursen, ***Chem. Sci.***, 2018, **9**, 3122-3130.

2 X. Tian, L. C. Murfin, L. Wu, S. E. Lewis and T. D. James, ***Chem. Sci.***, 2021, **12**, 3406-3426.

3 A. S. Klymchenko, ***Acc. Chem. Res.***, 2017, **50**, 2, 366–375.

4 J. Bouffard, Y. Kim, T. M. Swager, R. Weissleder and S. A. Hilderbrand, ***Org. Lett.***, 2008, **10**, 1, 37–40.

5 Dr. Z. Li, P. Z. Liang, Dr. T. B. Ren, Prof. Dr. L. Yuan and Prof. Dr. X. B. Zhang, ***Angew. Chem. Int. Ed.***, 2023, **62**, 37, e202305742.

6 C. D. Andrade, C. O. Yanez, L. Rodriguez and K. D. Belfield, ***J. Org. Chem.***, 2010, **75**, 12, 3975–3982.

7 R. R. Nani, J. B. Shaum, A. P. Gorka and M. J. Schnermann, ***Org. Lett.***, 2015, **17**, 2, 302-305.

8 C. Yin, F. Huo, M. Xu, C. L. Barnes and T. E. Glass, ***Sens. Actuators B: Chem.***, 2017, **252**, 592-599.

9 C. H. Wu, Y. Chen, K. A. Pyrshev, Y. T. Chen, Z. Zhang, K. H. Chang, S. O. Yesylevskyy, A. P. Demchenko and P. T. Chou, ***ACS Chem. Biol.***, 2020, **15**, 1862-1873.

10 J. B. Vázquez, Y. A. A. Sánchez, L. A. R. Cortés and B. R. Molina, ***Chem. Mater.***, 2021, **33**, 7160-7184.

11 L. L. Bras, K. Chaitou, S. Aloise, C. Adamo and A. Perrier, ***Phys. Chem. Chem. Phys.***, 2019, **21**, 46-56.

12 T. Nagano, ***Proc. Jpn. Acad. Ser. B***, 2010, **86**, 837-847.

13 C. Li, G. Chen, Y. Zhang, F. Wu and Q. Wang, ***J. Am. Chem. Soc.***, 2020, **142**, 35, 14789–14804.

14 C. Zhu, R. T. K. Kwok, J. W. Y. Lam and B. Z. Tang, ***ACS Appl. Bio Mater.***, 2018, **1**, 6, 1768–1786.

15 M. J. Schnermann and L. D. Davis, ***Curr. Opin. Chem. Biol.***, 2023, **75**, 102335.

16 L. G. Wang, A. R. Montano, A. M. Masillati, J. A. Jones, C. W. Barth, J. R. Combs, K. A. S. U. Kumarapeli, N. A. Shams, N. V. D. Berg, A. L. Antaris, S. N. Galvis, I. McDowall, S. Z. H. Rizvi, A. W. G. Alani, J. M. Sorger and S. L. Gibbs, ***Adv. Mater.***, 2023, 2304724.

17 R. Chowdhury, Md. A. Amin and K. Bhattacharyya, ***J. Phys. Chem. B***, 2015, **119**, 34, 10868–10875.

18 Y. Jin, Y. Tan, J. Wu and Z. Ren, ***Cell Death Discov.***, 2023, **9**, 254.

19 A. L. S. Cruz, E. de A. Barreto, N. P. B. Fazolini, J. P. B. Viola and P. T. Bozza, ***Cell Death Dis.***, 2020, **11**, 105.

20 Y. Tatenaka, H. Kato, M. Ishiyama, K. Sasamoto, M. Shiga, H. Nishitoh and Y. Ueno, ***Biochemistry***, 2019, **58**, 6, 499–503.

21 D. Singh, R. Regar, P. Soppina, V. Soppina and S. Kanvah, ***J. Photochem. Photobiol. A Chem.***, 2022, **237**, 112589.

22 T. Yoshihara, R. Maruyama, S. Shiozaki, K. Yamamoto, S. I. Kato, Y. Nakamura and S. Tobita, ***Anal. Chem.***, 2020, **92**, 7, 4996–5003.

23 S. I. Suarez, C. C. Warner, H. B. Harding, A. M. Thooft, B. VanVeller and J. C. Lukesh III, ***Org. Biomol. Chem.***, 2020, **18**, 495–499.

24 R. Yang, T. Zhu, J. Xu, Y. Zhao, Y. Kuang, M. Sun, Y. Chen, W. He, Z. Wang, T. Jiang, H. Zhang and M. Wei, ***Molecules***, 2023, **28**, 8, 3455.

25 S. Bhuin, P. Chakraborty, P. Sivasakthi, P. K. Samanta and M. Chakravarty, ***ACS Appl. Opt. Mater.***, 2023, **1**, 7, 1289-1300.

26 L. Wang, M. S. Frei, A. Salim and K. Johnsson, ***J. Am. Chem. Soc.***, 2019, **141**, 7, 2770–2781.

27 F. Wurthner, ***Angew. Chem. Int. Ed.***, 2020, **132**, 14296-14301.

28 Y. Chen, D. G. Chen, Y. A. Chen, C. H. Wu, K. H. Chang, F. Y. Meng, M. C. Chen, J. A. Lin, C. Y. Huang, J. Su, H. Tian and Prof. P. T. Chou, ***Chem. Asian J.***, 2019, **25**, 72, 16755-16764.

29 W. Xi, J. Yu, M. Wei, Q. Qiu, P. Xu, Prof. Z. Qian and Prof. H. Feng, ***Chem. Asian J.***, 2020, **26**, 17, 3733-3737.

30 S. Riebe, Dr. S. Adam, Dr. B. Roy, Dr. I. Maisuls, Dr. C. G. Daniliuc, J. Dubbert, Prof. Dr. C. A. Strassert, Prof. Dr. I. Schapiro and Prof. Dr. J. Voskuhl, ***Chem. Asian J.***, 2021, **16**, 16, 2307-2313.

31 H. Xu, H. Zhang, G. Liu, L. Kong, X. Zhu, X. Tian, Z. Zhang, R. Zhang, Z. Wu, Y. Tian and H. Zhou, ***Anal. Chem.***, 2019, **91**, 977–982.

32 X. Li, C. Long, Y. Cui, F. Tao, X. Xu and W. Lin, ***ACS Sens.***, 2021, **6**, 1595-1603.

33 S. Kundu, B. Sk, N. Saha, S. Das, T. K. Dutta, A. Batra, R. S. Tomar and A. Patra, ***ACS Mater. Lett.***, 2023, **5**, 1, 27-35.

34 Z. L. Lai, J. S. Chang, Y. C. Chan, C. C. Chang, C. Y. Li and S. W. Huang, ***Sens. Actuators B***, 2021, **330**, 129269.

35 X. Zhang, L. Yuan, J. Jiang, J. Hu, A. du Rietz, H. Cao, R. Zhang, X. Tian, F. Zhang, Y. Ma, Z. Zhang, K. Uvdal and Z. Hu, ***Anal. Chem.***, 2020, **92**, 5, 3613-3619.

36 W. L. Wu, H. L. Ma, L. L. Xi, M. F. Huang, K. M. Wang, J. Y. Miao and B. X. Zhao, ***Talanta***, 2019, **194**, 308-313.

37 Y. Wang, Y. Qiu, A. Sun, Y. Xiong, H. Tan, Y. Shi, P. Yu, G. Roy, L. Zhang and J. Yan, ***Anal. Chim. Acta***, 2020, **1133**, 109-118.

38 M. Kang, X. Gu, R. T. K. Kwok, C. W. T. Leung, J. W. Y. Lam, F. Li and B. Z. Tang, ***Chem. Commun.***, 2016, **52**, 5957-5960.

39 M. F. Huang, L. N. Chen, J. Y. Ning, W. L. Wu, X. D. He, J. Y. Miao and B. X. Zhao, ***Sens. Actuators B Chem.***, 2018, **261**, 196-202.

40 S. Wang, X. Li, S. Y. Chong, X. Wang, H. Chen, C. Chen, L. G. Ng, J. W. Wang and B. Liu, ***Adv. Mater.***, 2021, **33**, 11, 2007490.

41 Dr. H. Wang, C. Zhang, L. Hu, Dr. F. Tang, Y. Wang, F. Ding, J. Lu and Prof. A. Ding, ***Chem. Asian J.,*** *2023*, **18**, 7, e202201291.

42 J. Dubbert, Dr. A. Hoing, Dr. N. Graupner, Dr. L. Rajter, Prof. Dr. M. Dunthorn, Prof. Dr. S. K. Knauer, Prof. Dr. A. Galstyan, Dr. F. Rizzo and Prof. Dr. J. Voskuhl, ***Chem. Asian J.***, 2023, **29**, 38, e202300334.

43 M. Y. Wu, J. K. Leung, C. Kam, T. Y. Chou, D. Wang, S. Feng and S. Chen, ***Mater. Chem. Front.***, 2021,**5**, 3043-3049.

44 C. Li, W. Zhuang, Y. Wang, S. Li, J. Chen, L. Zhou, Y. Liao, M. Chen and J. You, ***Dyes Pigm.***, 2022, **204**, 110439.

45 P. Chakraborty, S. B. Ahil, T. Jamma and P. Yogeeswari, ***Future Med. Chem.***, 2022, **14**, 7, 463-478.

46 J. Ma, S. Lu, L. Yu, J. Tian, J. Li, H. Wang and W. Xu, ***Oncol. Rep.***, 2011, **26**, 5, 1189-1195.

47 P. Greenspan, E. P. Mayer and S. D. Fowler, ***J. Cell Biol.***, 1985, **100**, 965-973.

48 E. E. Spangenburg, S. J. P. Pratt, L. M. Wohlers and R. M. Lovering, ***J. Biotechnol. Biomed.***, 2011, Article ID: 598358.

49 T. K. Fam, A. S. klymchenko and M. Collot, ***Materials***, 2018, **11**, 9, 1768.

50 L. Guo, M. Tian, Z. Zhang, Q. Lu, Z. Liu, G. Niu and X. Yu, ***J. Am. Chem. Soc.***, 2021, **143**, 8, 3169-3179.

51 W. Zhuang, P. Tan, S. Li, C. Li, J. Zhang, J. Ai, L. Yang, G. Li, Q. Wei, M. Chen and Y. Wang, ***J. Mater. Chem. B***, 2021, **9**, 9553-9560.

52 L. Fan, X. Wang, Q. Zan, L. Fan, F. Li, Y. Yang, C. Zhang, S. Shuang and C. Dong, ***Anal. Chem.***, 2021, **93**, 22, 8019-8026.

53 L. K. van Dijk, B. A. W. Hoeben, J. H. A. M. Kaanders, G. M. Franssen, O. C. Boerman and J. Bussink, ***J. Nucl. Med.***, 2013, **54**, 12, 2118-2124.

54 J. P. P. Ramalho, P. Gkeka and L. Sarkisov, ***Langmuir***, 2011, **27**, 7, 3723-3730.

55 J. K. Zehmer, R. Bartz, P. Liu and R. G. W. Anderson, ***J. Cell Sci.***, 2008, **121**, 11, 1852-1860.

56 A. P. Demchenko, Y. Mely, G. Duportail and A. S. Klymchenko, ***Biophys. J.***, 2009, **96**, 3461-3470.

57 C. W. Song, U. Tamima, Y. J. Reo, M. Dai, S. Sarkar and K. H. Ahn, ***Dyes Pigm.***, 2019, **171**, 107718.

58 M. B. Z. Khalid, G. Pallikonda, R. N. P. Tulichala and M. Chakravarty, ***Tetrahedron***, 2016, **72**, 17, 2094-2101.

59 G. Pallikonda and M. Chakravarty, ***Eur. J. Org. Chem.***, 2013, **5**, 944-951.

60 M. Kamiya, ***Bull. Chem. Soc. Jpn.***, 1972, **45**, 1589-1594.

61 F. Bures, W. B. Schweizer, C. Boudon, J. P. Gisselbrecht, M. Gross and F. Diederich, ***Eur. J. Org. Chem.***, 2008, **6**, 994-1004.

62 Prof. Dr. F. Wurthner, Dr. T. E. Kaiser and Dr. C. R. Saha-Moller, ***Angew. Chem. Int. Ed.***, 2011, **50**, 15, 3376-3410.

63 P. Gopikrishna and P. K. Iyer, ***J. Phys. Chem. C***, 2016, **120**, 46, 26556-26568.

64 Y. Wen, H. Liu, S. T. Zhang, G. Pan, Z. Yang, T. Lu, B. Li, J. Cao and B. Yang, ***CCS Chem.***, 2020, **2**, 1940–1948.

65 H. L. Lee, W. J. Chung and J. Y. Lee, ***Small***, 2020, **16**, 1907569.

66 Dr. M. Li, Dr. W. Xie, Dr. X. Cai, X. Peng, Dr. K. Liu, Q. Gu, Dr. J. Zhou, W. Qiu, Z. Chen, Y. Gan and Prof. S. J. Su, ***Angew. Chem. Int. Ed.***, 2022, **61**, 35, e202209343.

67 A. Gavezzotti, ***ACS Chem. Res.***, 1994, **27**, 10, 309-314.

68 A. Gavezzotti, G. Fillippini, ***J. Phys. Chem.***, 1994, **98**, 4831-4837.

69 F. Witte, P. Rietsch, N. N. Budau, F. Weigert, J. P. Gotze, U. R. Genger, S. Eigler and B. Paulus, ***Phys. Chem. Chem. Phys.***, 2021, **23**, 17521-17529.

70 L. Liu, Y. Xue, X. Chu, Q. Zeng and M. Yang, ***Chem. Phys. Lett.***, 2011, **511**, 12-15.

71 Y. Appiarius, P. J. Gliese, S. A. W. Segler, P. Rusch, J. Zhang, P. J. Gates, R. Pal, L. A. Malaspina, K. Sugimoto, T. Neudecker, N. C. Bigall, S. Grabowsky, A. A. Bakulin and A. Staubitz, ***J. Phys. Chem. C***, 2022, **126**, 4563-4576.

72 S. Bhuin, S. Bhattacharya and M. Chakravarty, ***New J. Chem.***, 2021,**45**, 21236-21247.

73 C. Zhu, R. T. Kwok, J. W. Y. Lam and B. Z. Tang, ***ACS Appl. Bio Mater.***, 2018, **1**, 6, 1768-1786.

74 D. Su, C. L. Teoh, L. Wang, X. Liu and Y. T. Chang, ***Chem. Soc. Rev.***, 2017,**46**, 4833-4844.

75 Z. Wang, C. Gui, E. Zhao, J. Wang, X. Li, A. Qin, Z. Zhao, Z. Yu and B. Z. Tang, ***ACS Appl. Mater. Interfaces***, 2016, **8**, 16, 10193-10200.

76 L. Guo, M. Tian, R. Feng, G. Zhang, R. Zhang, X. Li, Z. Liu, X. He, J. Z. Sun and X. Yu, ***ACS Appl. Mater. Interfaces***, 2018, **10**, 10706-10717.

77 L. Fan, X. Wang, Q. Zan, L. Fan, F. Li, Y. Yang, C. Zhang, S. Shuang and C. Dong, ***Anal. Chem.***, 2021, **93**, 22, 8019-8026.

78 M. A. de la R. Rodriguez, L. Deng, A. Gemmink, M. van Weeghel, M. L. Aoun, C. Warnecke, R. Singh, J. W. Borst and S. Kersten, ***Mol. Metab.***, 2021, **47**, 101168.

79 L. Yang, J. Wang, B. Liu, G. Han, H. Wang, L. Yang, J. Zhao, M. Y. Han and Z. Zhang, ***Sens. Actuators B: Chem.***, 2021, **333**, 129541.

80 K. Y. Zhang, Q. Yu, H. Wei, S. Liu, Q. Zhao and W. Huang, ***Chem. Rev.***, 2018, **118**, 4, 1770-1839.

81 A. Bednarkiewicz, J. Drabik, K. Trejgis, D. Jaque, E. Ximendes and L. Marciniak, ***Appl. Phys. Rev.***, 2021, **8**, 011317.

82 H. M. Kim, B. H. Jeong, J. Y. Hyon, M. J. An, M. S. Seo, J. H. Hong, K. J. Lee, C. H. Kim, T. Joo, S. C. Hong and B. R. Cho, ***J. Am. Chem. Soc.***, 2008, **130**, 4246-4247.

83 X. Shi, S. H. P. Sung, M. M. S. Lee, R. T. K. Kwok, H. H. Y. Sung, H. Liu, J. W. Y. Lam, I. D. Williams, B. Liu and B. Z. Tang, ***J. Mater. Chem. B***, 2020,**8**, 1516-1523.

Chapter VI

Evincing Triphenylamine-Anthracene-Based Twisted Organic π-Conjugate as Nucleus-Specific Bioimaging Probe with Motion-Restricted Emission Enhancement Strategy: A 'Made in India' Bioimaging Dye

Objectives:

- Develop a new class of nucleus-specific indigenous bioimaging dye for multipurpose cellular bioimaging
- Investigate if motion-restricted emission strategy with an uncharged probe works out and becomes a new tool for nucleus bioimaging in cancer cells and detection over normal cells

Abstract:

Developing biocompatible fluorescent molecules to light up biological systems has become a dependable and convenient tool nowadays. Especially the nucleus is the largest and most important cellular organelle that governs the cell. Most of the market-available dyes are developed in a foreign country; hence, establishing an indigenous dye is the need of the hour. Moreover, most of the nucleus bioimaging dyes are intercalating agents that rupture the DNA, and hence, long-term bioimaging is affected. Envisaged **PCSB1** dye is basically a non-charged twisted π-conjugate made of a triphenylamine-linked anthracenyl structure conjugated with trimethoxybenzene through a diene linker. **PCSB1** only fits itself into the DNA minor groove and restricts its molecular motion to display emission. It does not intercalate with DNA, as reflected in various scientific experiments. This newly established indigenous dye is capable of undergoing different types of nucleus-specific bioimaging. As an extra added advantage, it can discriminate cancer cells from normal cells with enhanced emission in cancer cells. The bioimaging performances of **PCSB1** were thoroughly compared with well-known nucleus staining dye DAPI, and **PCSB1** was proven to be better performing than DAPI in many aspects of nucleus-targeted live cancer cell bioimaging and discrimination.

6.1 Introduction:

Bio-imaging is a twig of science concerned with efficient and structural images of complex biological systems.[1] Small organic fluorescent probes unveil immense aspects in safe and vast bio-imaging studies of academic, clinical, and industrial pursuits.[2] Developing biocompatible fluorescent molecules to light up biological systems has become a dependable and convenient tool.[3] Especially, the nucleus is the largest and most vital cellular organelle that governs the cell,[4] and tracing the nucleus can assist unlocking various critical cellular phenomena.[5] In this regard, there are a few well-known market-available dyes like 'DAPI'(4′,6-Diamidino-2-phenylindole), Hoechst, SYBR Green, which generally contains short hydrophobic chains and planar aromatic cationic structures and these dyes can selectively bind to double-stranded DNA (dsDNA) at the minor groove.[6,7] The global bio-imaging market is expected to reach $ 10.98 billion by 2026,[8] *while no India-made bioimaging probe is commercially available*. Under these circumstances, the discovery and development of an indigenous novel fluorescent bioimaging probe '**PCSB1**' is envisioned here. The '**PCSB1**' is the lead dye of the **PCSB-Indifluores** series that consists of extensive π-conjugations with the conformationally twisted core. The production cost of those dyes is considerably less than the imported dyes,[9] and salient structural modification is achieved as per the raised necessities. Molecular engineering is conjectured so that the structurally twisted dyes would *fit into the DNA grooves to display bright fluorescence without undergoing any chemical reaction* with DNA base pairs. This mechanism is *exclusively conceptualized* as most of the nucleus-specific dye reacts with DNA-base pairs.[10] The developed nucleus stain is a non-charged D-*π*-D system with a twisted stature. It is effective in non-invasive live cells, fixed cell, wash-free imaging, and nuclear invasion studies of different cancerous and normal cells. By their viscosity and temperature-dependent fluorescence switching, they may contribute to detecting cancer cells to normal cells and cellular viscosity semi-quantification.

6.2 Literature review on organic fluorophores for nucleus-specific bioimaging

Maximum established nucleus-specific bioimaging dyes are charged species, widely utilized and market available. 4′,6-Diamidino-2-Phenylindole, Dihydrochloride (B), known as DAPI, is a market-available probe consisting of charged indolyl and

piperazine scaffolds. DAPI, being a charged species, interacts with the negatively charged DNA and intercalates with the DNA base pairs to generate bright fluorescence.[7] Hoechst dye (**A**) and SYBR (**C**) Green also follow the same working principles, being charged species.[11,12] In 2019, Deng *et al.* reported 9,9-dimethyl-9H-fluorene and thiophene conjugated charged pyridinyl dye **FTI** (**D**) for nucleus imaging in live cells.[13] **FTI** displayed sensitive fluorescent enhancement when bound to DNA in vitro with a 6.4-fold quantum yield increase. In 2019, Zhang *et al.* developed a notable dye **HoeSR** (**E**), developed by , which was a conjunction of Hoechst and sulforhodamine through a triazolyl propanol linker. **HoeSR** enabled wash-free fluorescence imaging of the nucleus and was applicable for dSTORM super-resolution imaging of nucleus DNA in live cells.[14] The work published by Mendoza *et al.*in 2020 focussed on developing a curcumin-based nucleus-specific fluorescent probe, and their probe '**2**' (**F**) was live-cell membrane permeable ultimately to produce bright fluorescence in the nucleus.[15] Gonzalez *et al.* reported naphthalimide-based macrophage nucleus imaging probes in 2020,[16] and they found that naphthalimides and quinolimides carrying the 2-(dimethylamino)ethyl chain at the imide ring (**G**) had resulted in suitable probes for macrophage imaging.

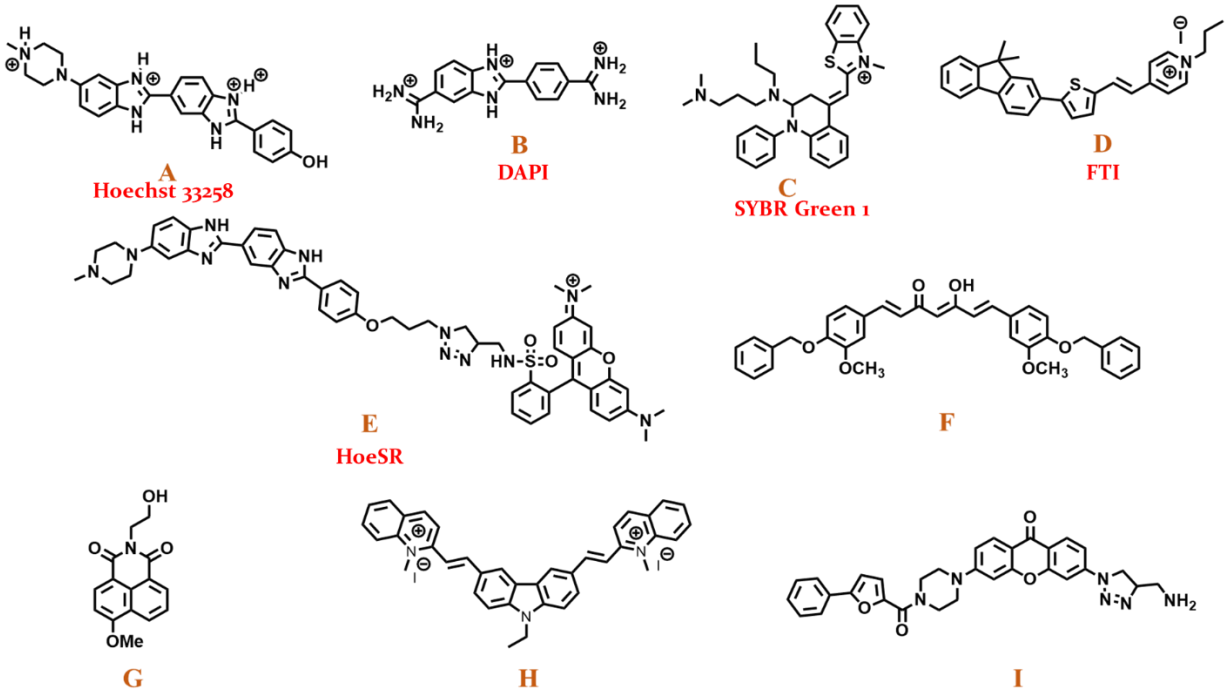

Figure 6.1 Market available nucleus dyes and a few noteworthy and recently reported synthesized nucleus-specific bioimaging dyes (the name of the market available dyes or its analogs are written inset, taken from refs. 11-18)

In 2019, Feng *et al.*, discovered mono, bi-quinolinium branches carbazole had groove binding mode and could serve as a two-photon excited fluorescent probe (**H**) for nucleus imaging.[17] In 2015, Ghosh *et al.*, reported a low cytotoxic nucleus staining fluorescent probe **CDb12** (**I**), for real-time mitosis imaging in live cells.[18] Non-charged nucleus targeting fluorescent probes are therefore rare, as understood from the literature. To the best of our knowledge, there is no reported dye on twisted triphenylamine-anthracene conjugated tri methoxy benzene stature. Hence, the system is explored.

6.3 Results and Discussion

6.3.1 Design strategy

Herein, we have developed seven molecules as triphenylamine conjugated anthracenyl styryl derivatives as dual-state emitting fluorogens (DSE-gens) with omnipresent emissions in solids, solutions, aggregates, and viscous medium. The synthesis of such probes is easy and cost-effective, and no column chromatography is needed. Their biocompatibility has been checked through MTT-Cytotoxicity assay, and finally, probes named '**PCSB**' dyes have been envisaged for the nucleus-specific bioimaging studies.

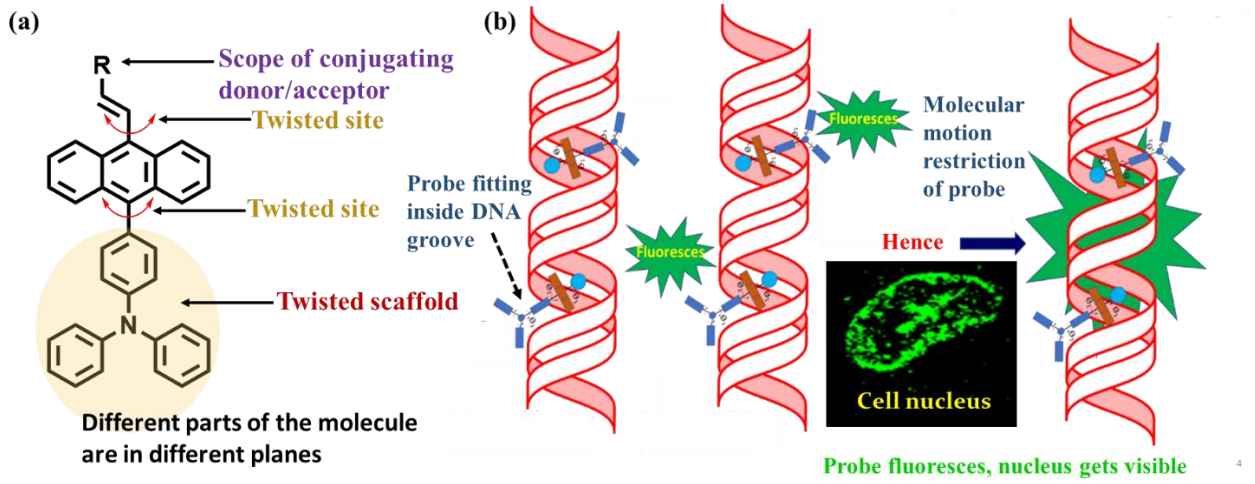

Figure 6.2 Design concept for '**PCSB**' dyes

The technique of fluorescence generation is relatively new here. Lead '**PCSB**' dye fits itself into the DNA grooves. Structurally, it is a π-conjugate system with twisted

conformation. Once it fits itself into the DNA grooves, the molecular motion gets restricted and starts to fluoresce upon exciting with a certain wavelength of UV light. Hence, the cell nucleus will also be glowing.

6.3.2 Synthetic protocol and structural elucidation

The TPA-AN-Phosphonate was synthesized through an easy electrophilic aromatic substitution reaction using triphenylamine (TPA) as a nucleophile under the presence of methanesulfonic acid. The designed D-π-D (**PCSB1-PCSB4**) and D-π-A combinations (**PCSB5-PCSB7,** Figure 6.3) could be generated by Horner-Wadsworth-Emmons (HWE)-reactions followed by the same protocol described in chapter III.

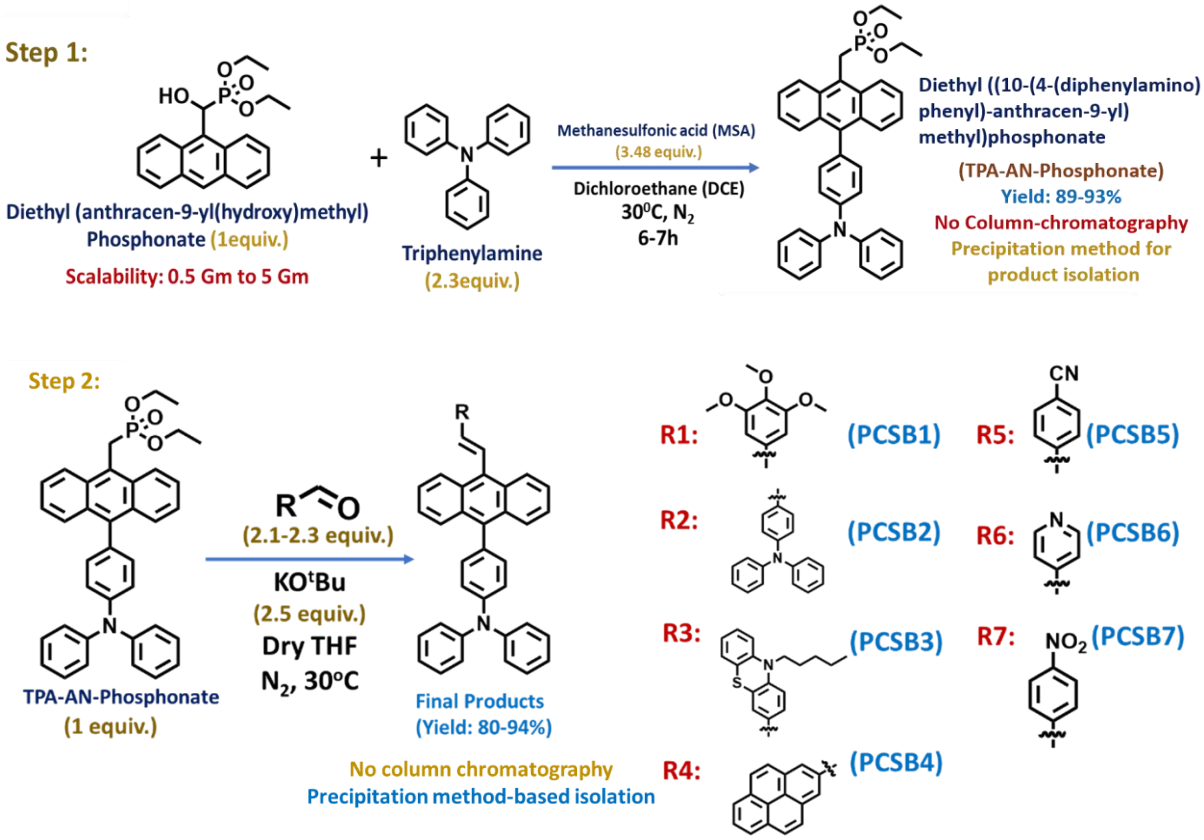

Figure 6.3 Synthetic route for '**PCSB**' dyes

6.3.3 Structural elucidation

6.3.3.1 NMR spectroscopic analysis of the synthesized compounds

The synthesized **TPA-AN-Phosphoante** was initially identified with a distinctive signal at 25.87 ppm in ^{31}P NMR, a P-CH2 coupling peak at 4.31 ppm (J = 20 Hz) in ^{1}H NMR, and a P-C coupling at 27.9 ppm (J = 140 Hz) in ^{13}C NMR. The lead compound **PCSB1** shows two very high-intensity peaks at 3.98 ppm and 3.93 ppm in ^{1}H

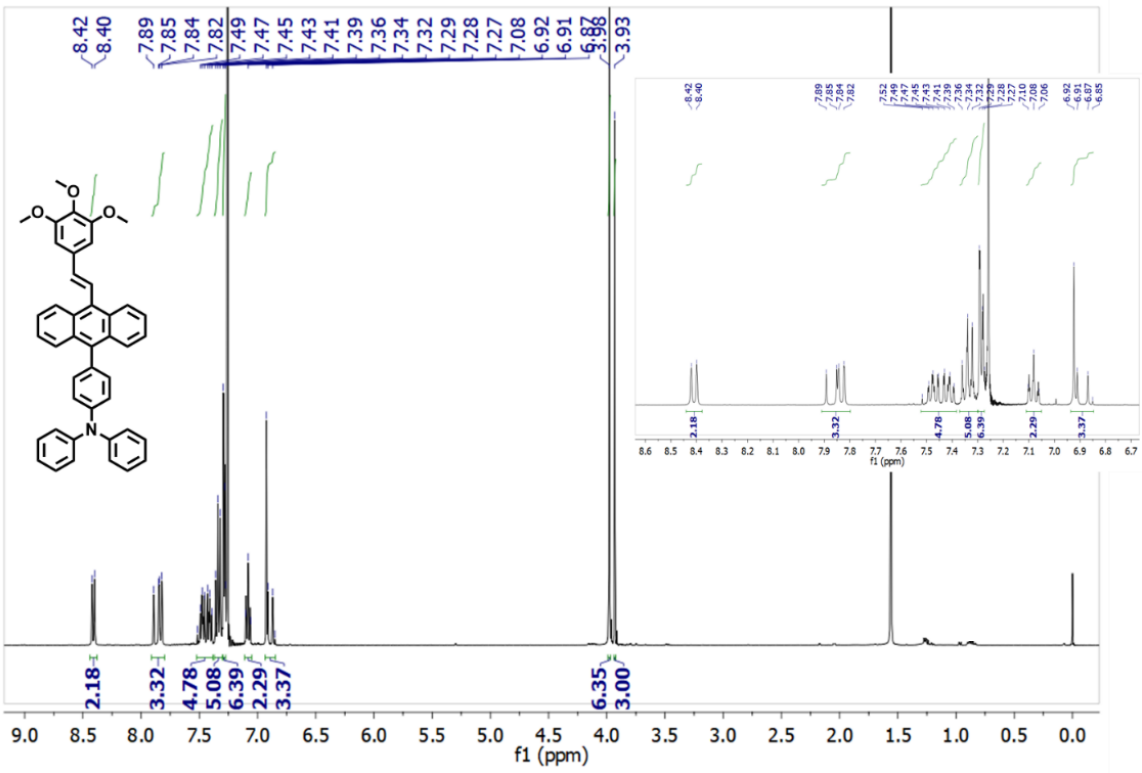

Figure 6.4 ^{1}H NMR of (E)-N,N-diphenyl-4-(10-(3,4,5-trimethoxystyryl)anthracen-9-yl)aniline (**PCSB1**) (water peak is there at ~1.52 ppm)

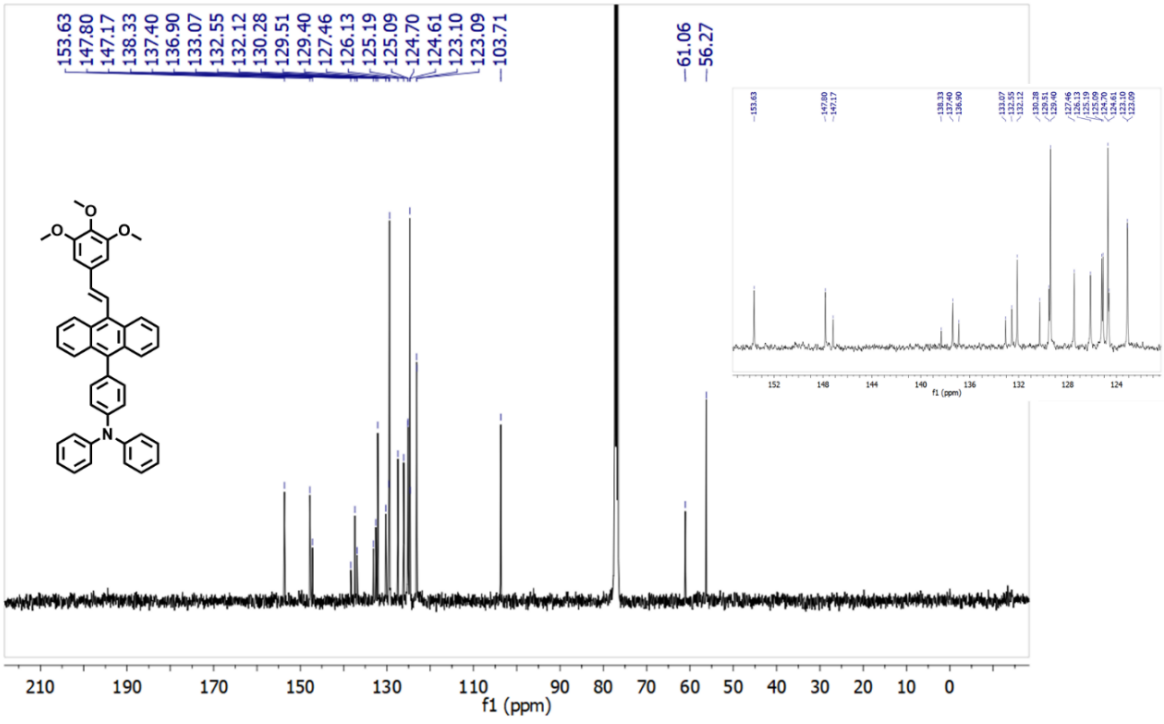

Figure 6.5 ^{13}C NMR of (E)-N,N-diphenyl-4-(10-(3,4,5-trimethoxystyryl)anthracen-9-yl)aniline (**PCSB1**)

NMR and two peaks at 61.1 ppm and 56.3 ppm in ^{13}C NMR due to the presence of methoxy groups of two different chemical environments within the molecule. All the synthesized compounds were thoroughly characterized by ^{1}H, ^{13}C, ^{31}P NMR, IR, HRMS, and even the single crystal structure elucidation for **PCSB1** was possible

6.3.3.2 Single crystal analysis

The **PCSB1** single-crystal was grown from a hexane/EtOAc (3:1) medium by a slow solvent evaporation process at ~ 30°C. The single-crystal X-ray diffraction analysis revealed that **PCSB1** crystallized in a monoclinic system with $P2_1/n$ space group. The crystal parameters are tabulated below in Table 6.1.

Table 6.1. Crystal-parameters for **PCSB1**

Compound	**PCSB1**	V /Å^3	6565.46(12)
Emp. Formula	$C_{43}H_{35}NO_3$	Z	8
Formula weight	613.7570	D_{calc} /g cm^{-3}]	1.242
Crystal system	monoclinic	μ /mm^{-1}	.606
Space group	$P2_1/n$	F (000)	2592.0
a /Å	16.8145(2)	Data/ restraints/ parameters	13926/0/854
b /Å	11.14890(10)	S	1.075
c /Å	35.0230(4)	+R1 [I>2σ(I)]	0.0396 (11829)
α/degree	90	wR2 [all data]	0.1055(13926)
β/degree	90.2530(10)	Max./min. residual electron dens. [eÅ^{-3}]	0.21/ -0.21
γ/degree	90		

6.3.4 Cytotoxic investigation of the synthesized dyes

The half-maximal inhibitory concentration (IC_{50}) for cancer cell FaDu and normal cell HEK-293 were determined for the synthesized fluorophores through MTT-assays, and **PCSB1** was found to be the best compound as it was very low toxic. The solid-state photophysical quantum yield (*discussed later*) was also promising. Against FaDu, the IC_{50} of **PCSB1** was ~136.7 μM, and against normal cell HEK-293, the cytotoxic concentration (CC_{50}) of **PCSB1** was ~76.96 μM (Figures 6.6, 6.7). Of note, from ATCC data bank, it is known that FaDu cell line has epithelial morphology which was first established in 1968 from a punch biopsy of a hypopharyngeal tumor from a 56-year old

male patient with squamous cell carcinoma. It is a very robust and aggressive cell line, and worthy to be investigated for bioimaging-based detection.

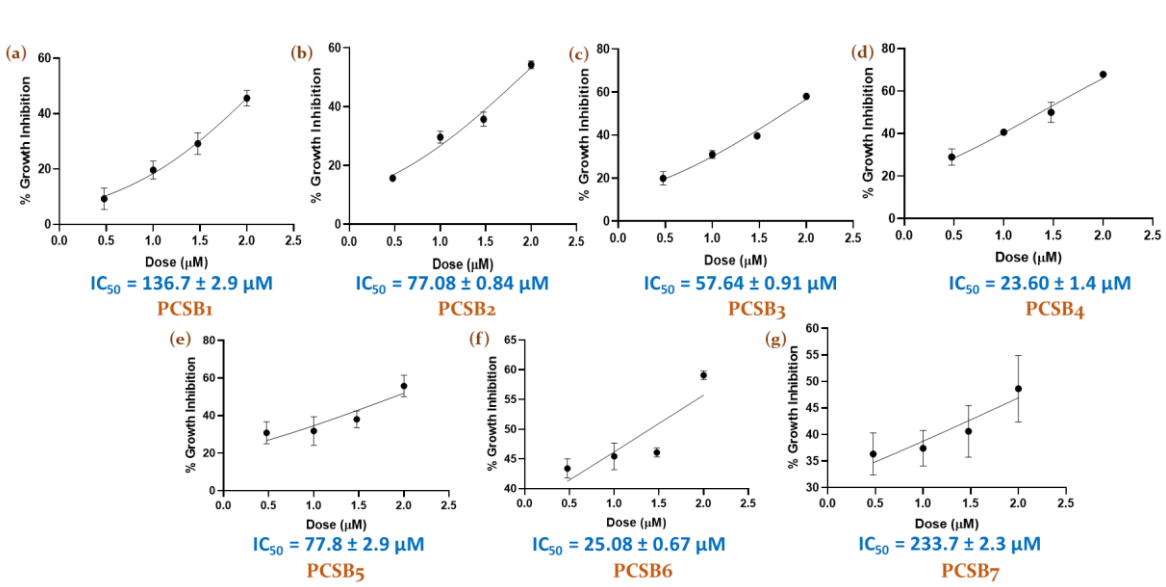

Figure 6.6 IC_{50} values for compounds of **PCSB** series against Fadu

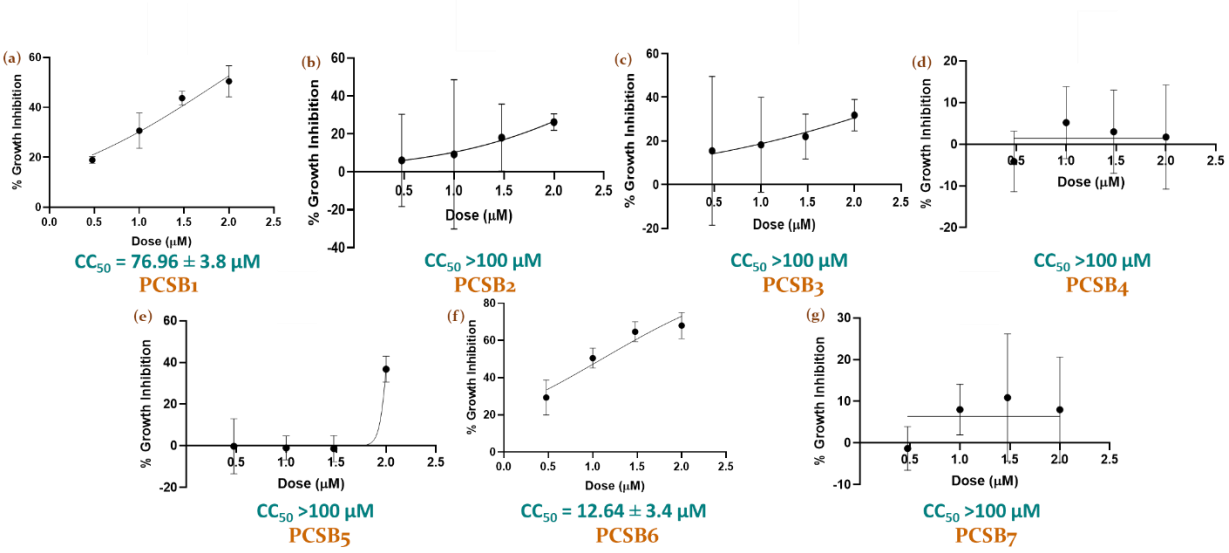

Figure 6.7 CC_{50} values for the compounds of **PCSB** series against HEK-293

6.3.5 Investigation of Photophysical Properties of PCSB1

As **PCSB1** was the lead compound selected for the bioimaging application. Therefore, the photophysical properties of **PCSB1** in solids, solvents, aggregates, and viscous medium were investigated thoroughly.

Dual-state emitting probes exhibit utmost importance in the field of bioimaging as they emit both in solids and solution states.[19,20] Due to the mutually exclusive photophysical principles, accessing all the photophysical outputs from a single probe becomes tricky. The prediction of intracellular environment faced by the probe would be difficult. So, it is always better to retain the emission of the probe in aggregate/solids and solvents. Initially, the solid-state emissions with absolute quantum yields were measured for all the dyes, and it was noticed that, except for **PCSB7**, all other dyes were green or yellowish-green emitters (Figure 6.8). While comparing between **PCSB1** and **PCSB7**, we can easily understand the effect on the introduction of the electron-withdrawing -NO_2 group, which increases the electronic conjugation in D-π-A system **PCSB7**, leading to create a redshifted emission. The redshifted emission due to better conjugation is very well established.[21]

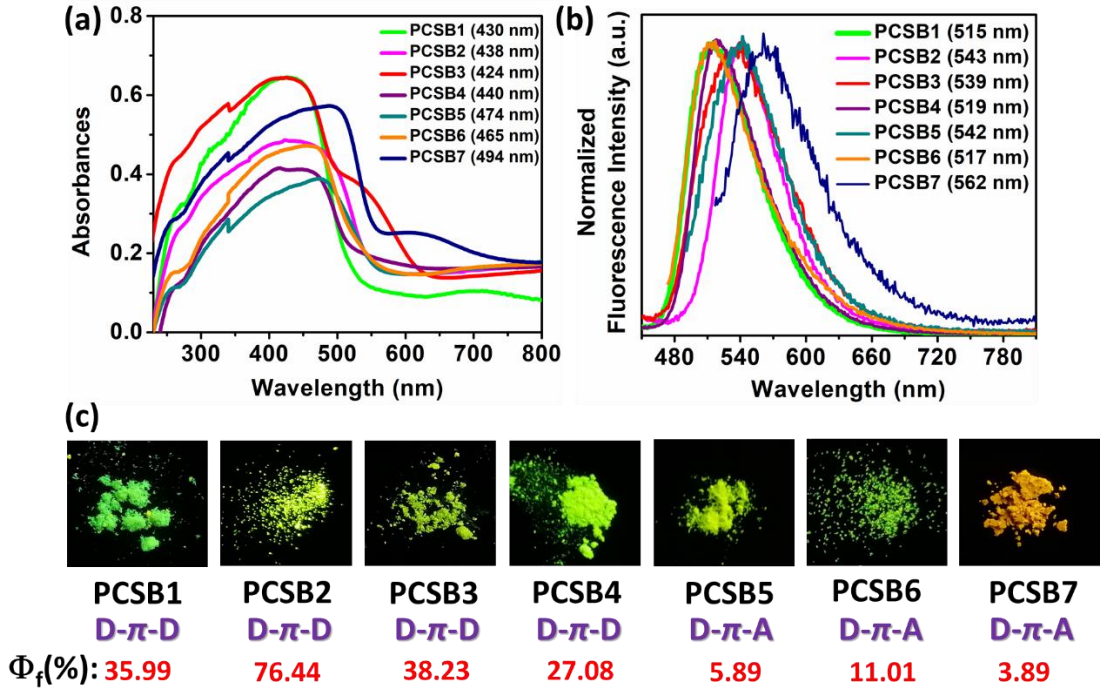

Figure 6.8 For **PCSB** dyes in solid-state (a) absorbances (b) emissions (c) images captured under UV-365 nm lamp and the respective solid-state quantum yields are written in red color

The **PCSB1** is a D-π-D system, and the tri methoxy benzene will make the system more electron-rich. Moreover, the molecular packing of **PCSB1** comprises of 101 different types of non-covalent interactions that include H...O, H...H, C...H, C...O, and C...C. The

number of C...H interactions was very high (58 different interactions), while π...π stacking (C...C) interactions were very few, although there were 20 types of H...H.

The unit cell of **PCSB1** contains twin crystals, and the crystal packing was done with alternative head-to-tail and then tail-to-head arrangements. The flat anthracene core of two immediate molecules is never π-stacked; on the other hand, the twisted triphenylamine (TPA) scaffolds of two neighboring molecules bring steric hindrance, eliminating the chances of π-stacking further. In addition, methoxy groups are also tilted (Figure 6.9); thus, the combined facts are responsible for the bright solid-state emission in **PCSB1**.

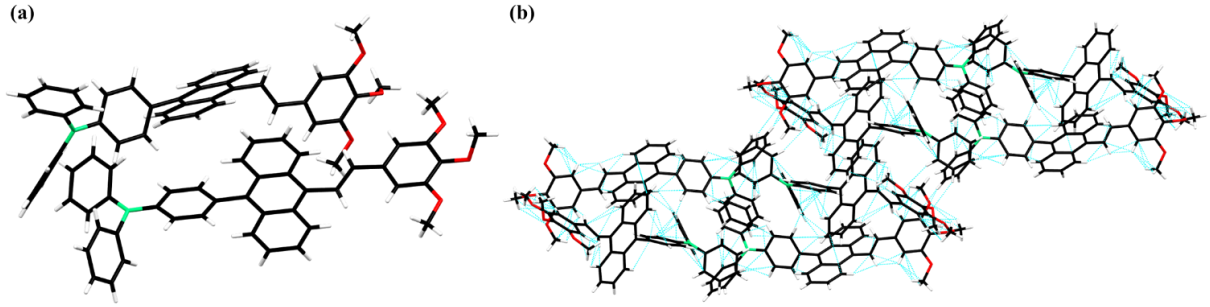

Figure 6.9 For **PCSB1** (a) twin-crystals in the unit cell (b) crystal-packing from 'b' axis view

To receive emission in solution, the excited state must gain optimum planarity, or there should be a considerable extent of planarity relaxation from the ground to the excited state.[22] In our earlier report,[23] it was shown how the excited state planarity became crucial for receiving emission in solvents with different polarities for the TPA-moiety-containing compounds. It was noticed that the emission oscillator strength (f_{em}), root-mean-square-displacement (RMSD), and the natural transition orbitals (NTOs) should be optimum for commendable emission in solvents. Being a TPA-analogue, **PCSB1** is expected to have optimum excited state planarity, $f_{em,}$ RMSD, and suitable contribution of NTOs in various solvents of different polarities. Our steady-state fluorescence studies in multiple solvents showed that **PCSB1** was a very good DSE-gen as it emitted brightly in solids (Figure 6.8c) and solvents (Figure 6.10).

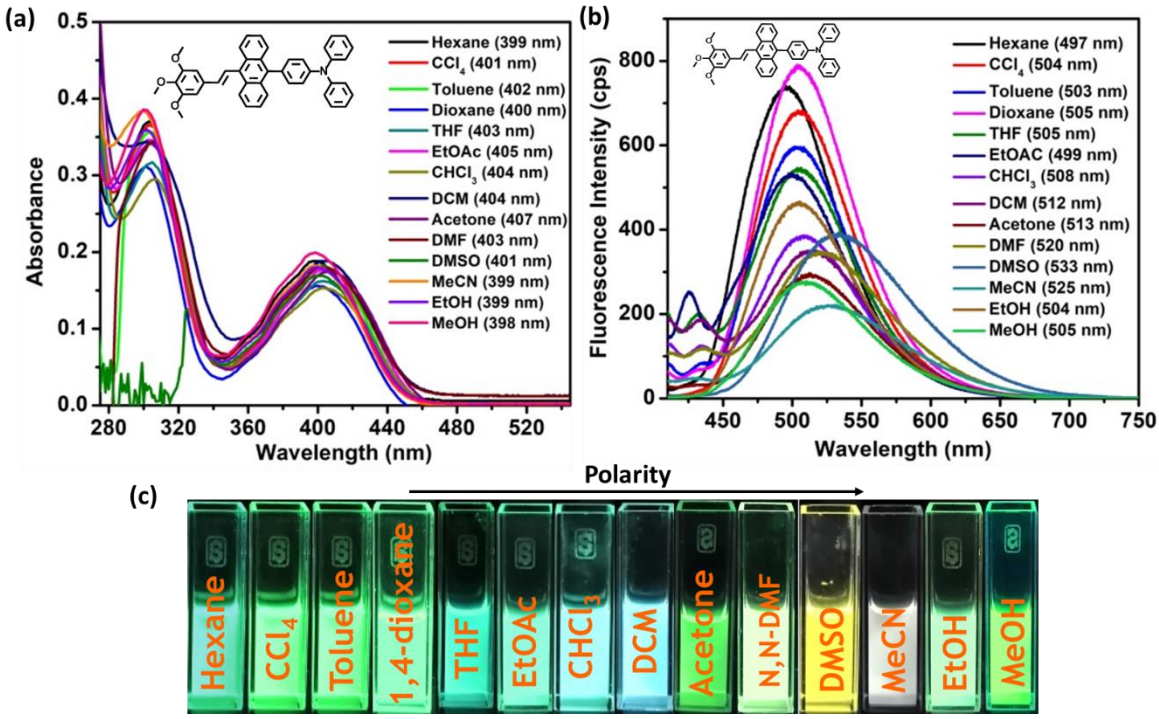

Figure 6.10 For steady-state fluorescence study of **PCSB1** (10^{-5} M) in multiple solvents (a) absorbances with λ_{max} written inset (b) emissions with λ_{max} written inset (c) images captured under a UV-365 nm lamp

The phenomenon of increased emission efficiency with the increment of water fraction in water miscible solvent medium is called the Aggregation-Induced Emission (AIE).[24] The aggregated state resembles the solid state, and considering this, **PCSB1** was expected to display AIE activity due to its twisted conformation. As from the single-crystal investigation, it was understood that the twisted structure of **PCSB1** would eliminate π...π stacking between two adjacent molecules to a greater extent. As in MeCN, **PCSB1** (10^{-5} M) was weakly emissive; the AIE activity was investigated in the MeCN/water medium. In 99% water fraction f_w (*v*/*v*), **PCSB1** exhibited the brightest emission, although the emission increment was observed in even in f_w = 70% (Figure 6.11). The respective absorbance for 99% water f_w (*v*/*v*) was redshifted from the 0% water f_w (*v*/*v*) absorbance peak, but the respective emission was found to be blueshifted. This happened possibly due to a certain extent of reorganization energy.[23] As DMSO is a suitable solvent in cell culture, the AIE-activity of **PCSB1** was also investigated in DMSO/water medium. The blueshifted AIE emission was repeatedly noticed (Figure 6.12).

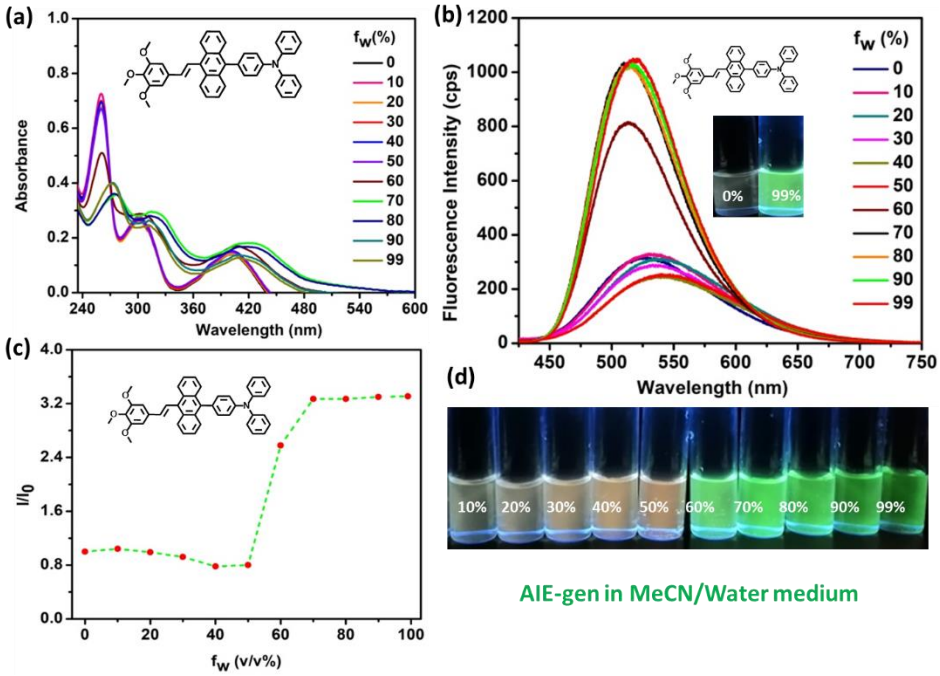

Figure 6.11 For **PCSB1** (10^{-5} M) in MeCN/water medium (a) respective absorbances (b) respective emissions (c) I/I_0 vs f_w (%) plot (d) images captured under UV-365 nm lamp

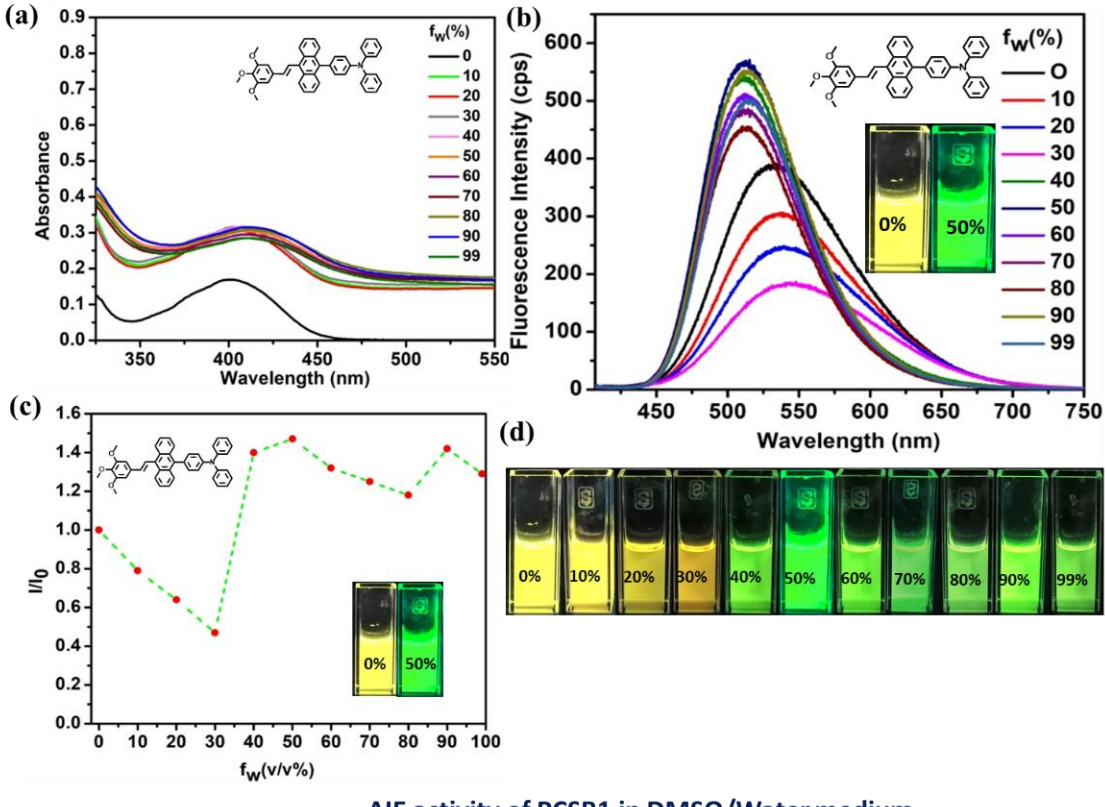

Figure 6.12 For **PCSB1** (10^{-5} M) in DMSO/water medium (a) absorbances (b) emissions (c) I/I_0 vs f_w (%) plot (d) images captured under UV-365 nm lamp

D-π-A system-based push-pull fluorophores with viscosity-sensitive emission enhancement were established earlier without being responsible for solvent polarity.[25-27] **PCSB1** is a D-π-D′ system, and its emission was previously investigated in MeCN and DMSO solvents. Instead, in both the solvents, **PCSB1** was proven to display the AIE phenomenon with the increment of water fraction. M eCN and DMSO both possess very close polarity, but the viscosity of DMSO is way better than MeCN, and thus, these two solvents are chosen to investigate the viscosity-induced emission (VIE) property of **PCSB1**. When the fluorescence emission of **PCSB1** rises with the increasing percentage of DMSO into MeCN (*v*/*v*), it proves the positive trend of VIE for **PCSB1** (10^{-5} M) (Figures 6.13a, b, e).

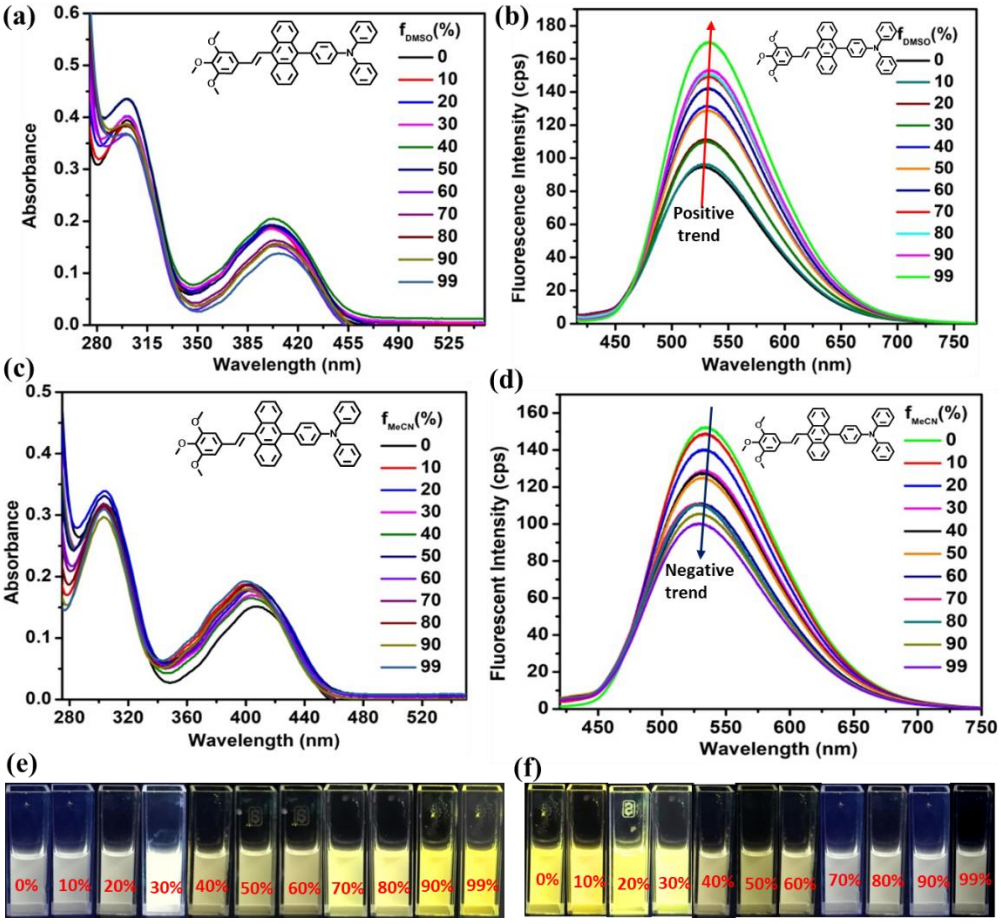

Figure 6.13 For VIE activity of **PCSB1** (10^{-5} M): (a, c) respective absorbances (b, d) respective emissions (e, f) respective images captured under UV-365 nm lamp; the excitation wavelengths were between 401-412nm)

Fluorescence emission decrement of **PCSB1** with the increasing percentage of MeCN into DMSO (*v*/*v*)was also investigated (Figures 6.13c, d, f). Thus, **PCSB1** was also proven to be a VIE-gen apart from its AIE activity.

The temperature-dependent emission change was also investigated for **PCSB1** (10^{-5} M) in DMSO to confirm the VIE characteristic of the dye. The emission change was observed while the temperature of DMSO was increased from 10 °C to 80 °C continuously (Figure 6.14c). The emission change was observed while the temperature of DMSO was decreased from 80 °C to 10 °C gradually (Figure 6.14a). The emission was yellowish at lower temperatures and greenish at higher temperatures, but the emission intensity was more at lower temperature (Figure 6.14b). However, the emission from **PCSB1** became greenish again at ~37 °C,. There is no color change at all in this study. 5-6 nm variation only. This part on color change should be excluded, spectra is fine to show almost no change, except intensity.

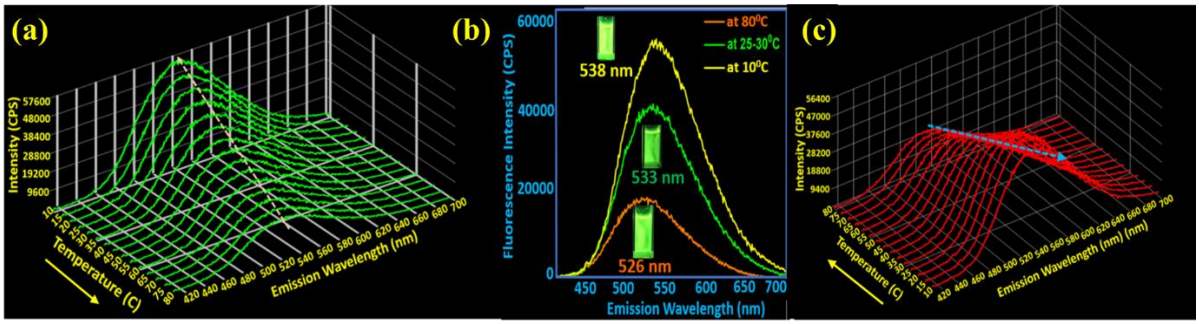

Figure 6.14 For temperature-dependent emission of **PCSB1** (10^{-5} M) in DMSO solvent (a) the temperature has been continuously reduced from 80 °C to 10 °C (b) fluorescence intensity vs emission wavelength plot at three representative temperatures (c) the temperature has been continuously increased from 10 °C to 80 °C

The increased viscosity causes a restriction in the molecular motion of the twisted fluorophore relaxing through radiative channel.[28] The extent of restriction may vary in different environments, thus altering the extent of the molecule's π-conjugation and emission oscillator strength. These things are expected to happen for **PCSB1** for VIE-based yellowish and green emissions.

From the time-correlated single photon counting (TCSPC) experiments, the lifetime of the **PCSB1** was determined in their respective solid state, MeCN and DMSO

solution, and aggregated states. The **PCSB1** has a lifetime of 0.59 ns in solids, but in MeCN, its lifetime is longer ~1.36 ns. A more excited state of 2.87 ns was determined in DMSO, a more viscous solvent. The aggregate lifetime is determined to be ~1.26 ns and 1.56 ns in MeCN/water and DMSO/water medium, respectively.(Figure 6.15).

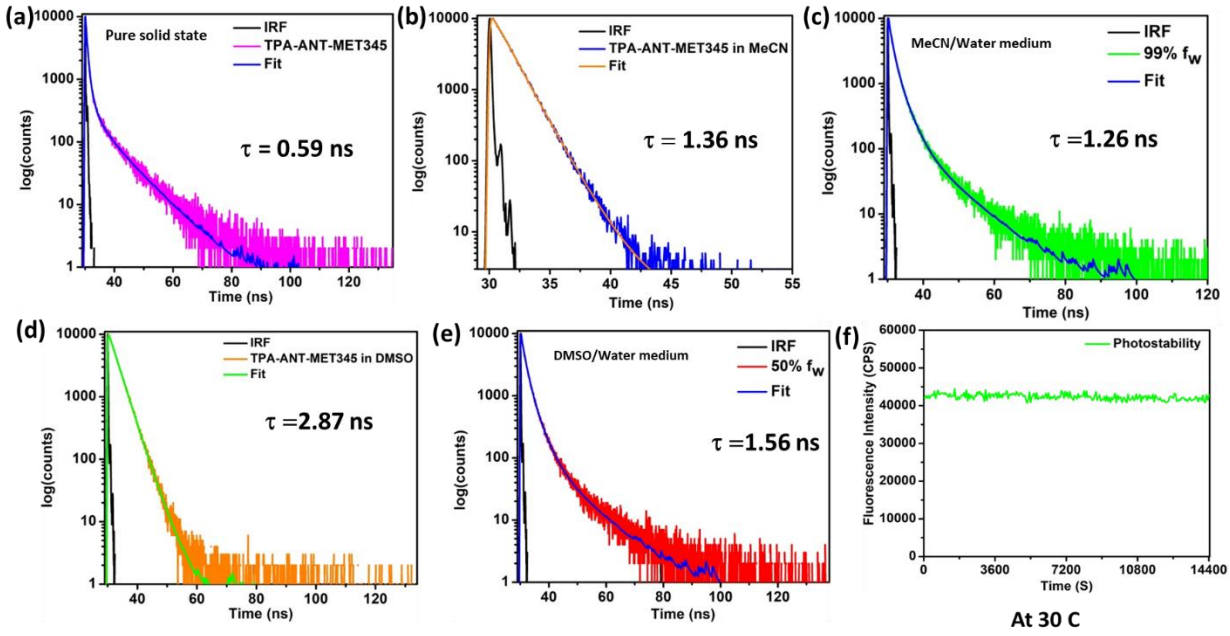

Figure 6.15 (a-e) Lifetime decay profiles for **PCSB1** solids, in solvents, and in aggregates (f) photostability of **PCSB1**

To check the photostability, we continuously irradiated UV on solid **PCSB1** for 4 h, but the probe is very much photostable, remaining with its intensity intact (Figure 6.15f), which is essential for a dye aimed to be useful for long-term bioimaging.

6.3.6 FACS experiments to investigate concentration-dependent cellular uptake of PCSB1

Through the 'Fluorescence-Activated Cell Sorting (FACS)' experiments, the cellular uptake into FaDu cells was investigated for the dye '**PCSB1**' with different probe concentrations ranging from 100 μM to 1 μM. We found the cellular uptake of the dye '**PCSB1**' very satisfying. The population towards the SSC-A represents the live cells, and the uptake graph shifts toward the P2 channel to describe the extent of cell permeability. For the unstained cells, the population in the P2 channel was almost ~1.1-2.4 %. However, even with 1 μM of **PCSB1** displayed ~29.1 - 32.6 % population in the P2

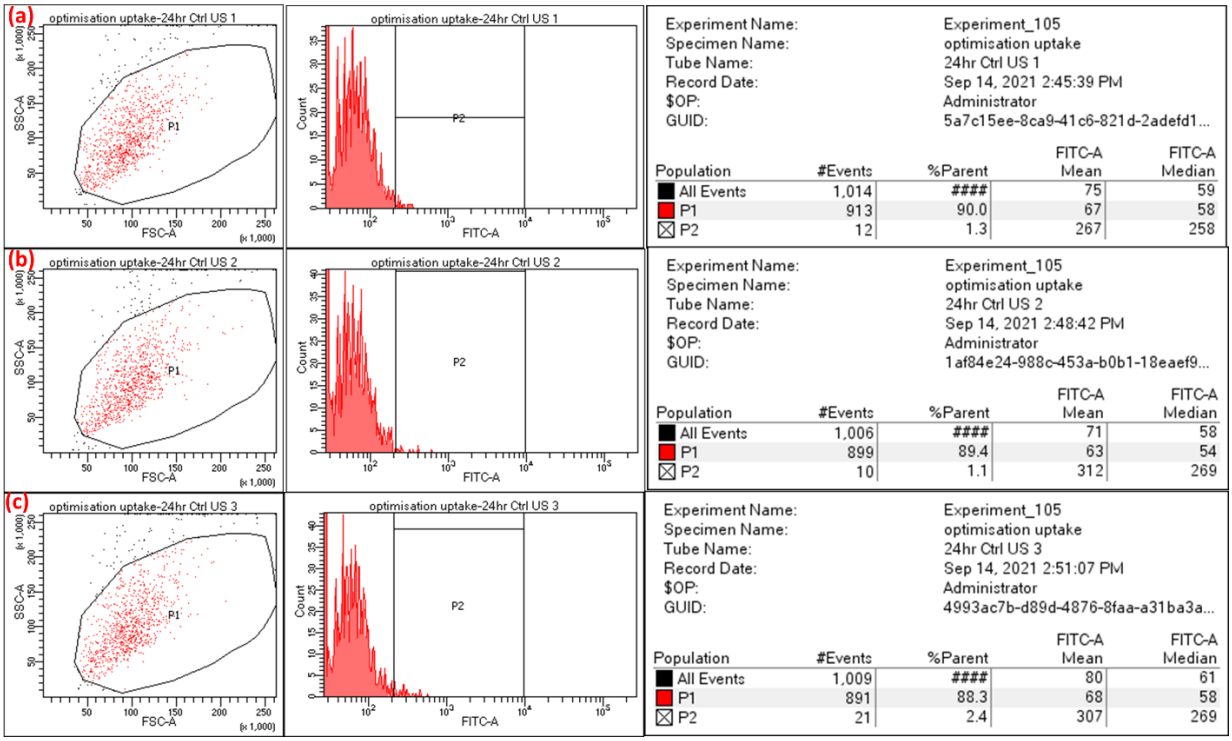

Figure 6.16 FACS experiments with unstained FaDu cells

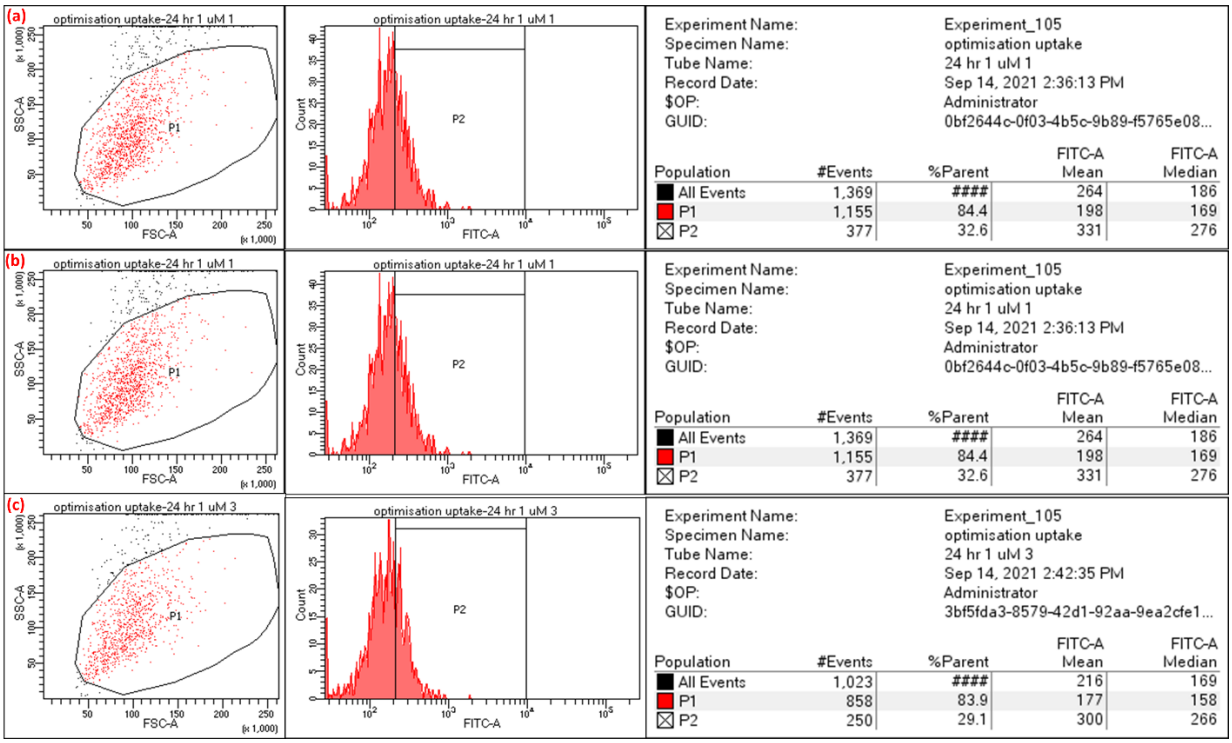

Figure 6.17 FACS experiments with **PCSB1** (1 μM) stained FaDu cells

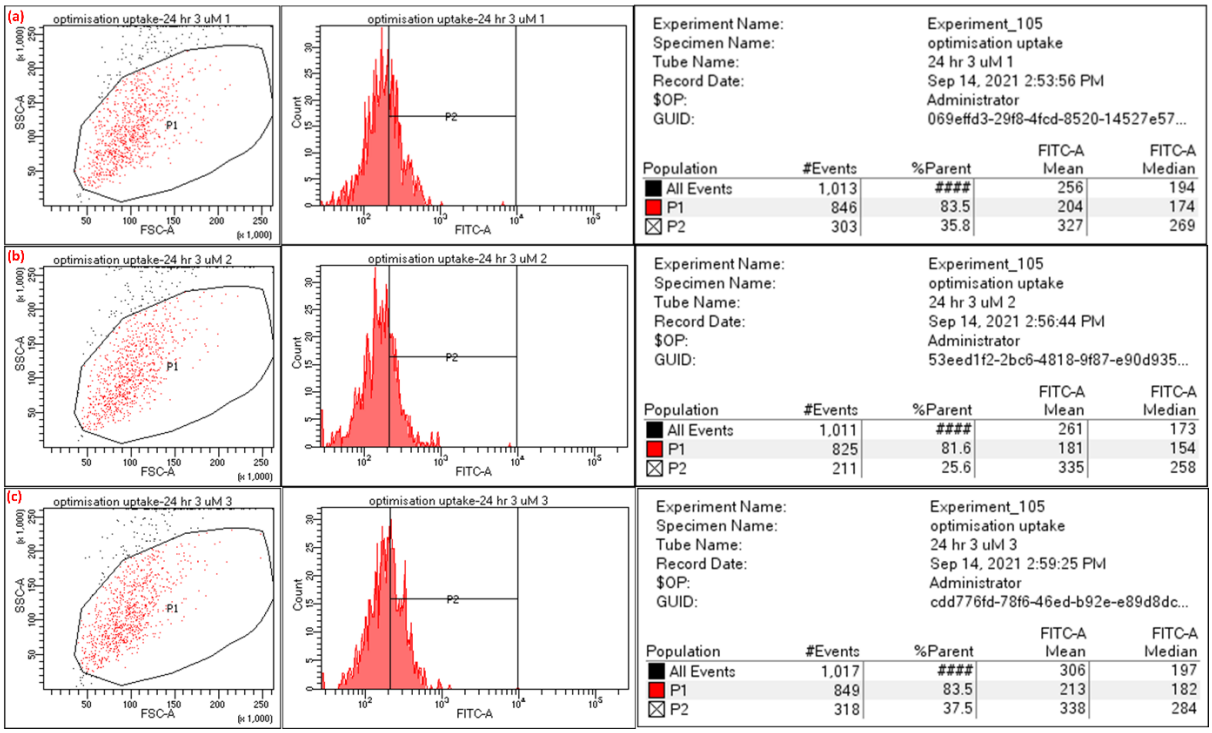

Figure 6.18 FACS experiments with **PCSB1** (3 μM) stained FaDu cells

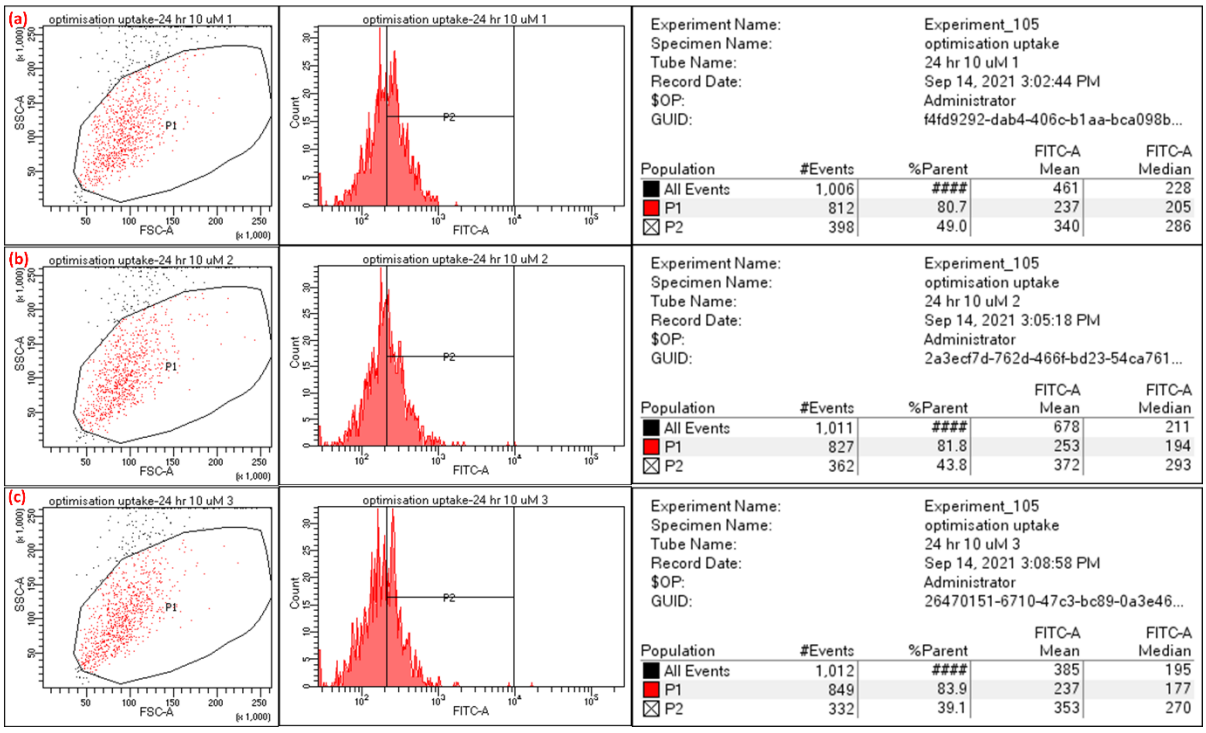

Figure 6.19 FACS experiments with **PCSB1** (10 μM) stained FaDu cells

channel, indicating a sufficient amount of cellular uptake for **PCSB1** at 1 µM concentration, There was an average of > 35 % of the population in the P2 channel with

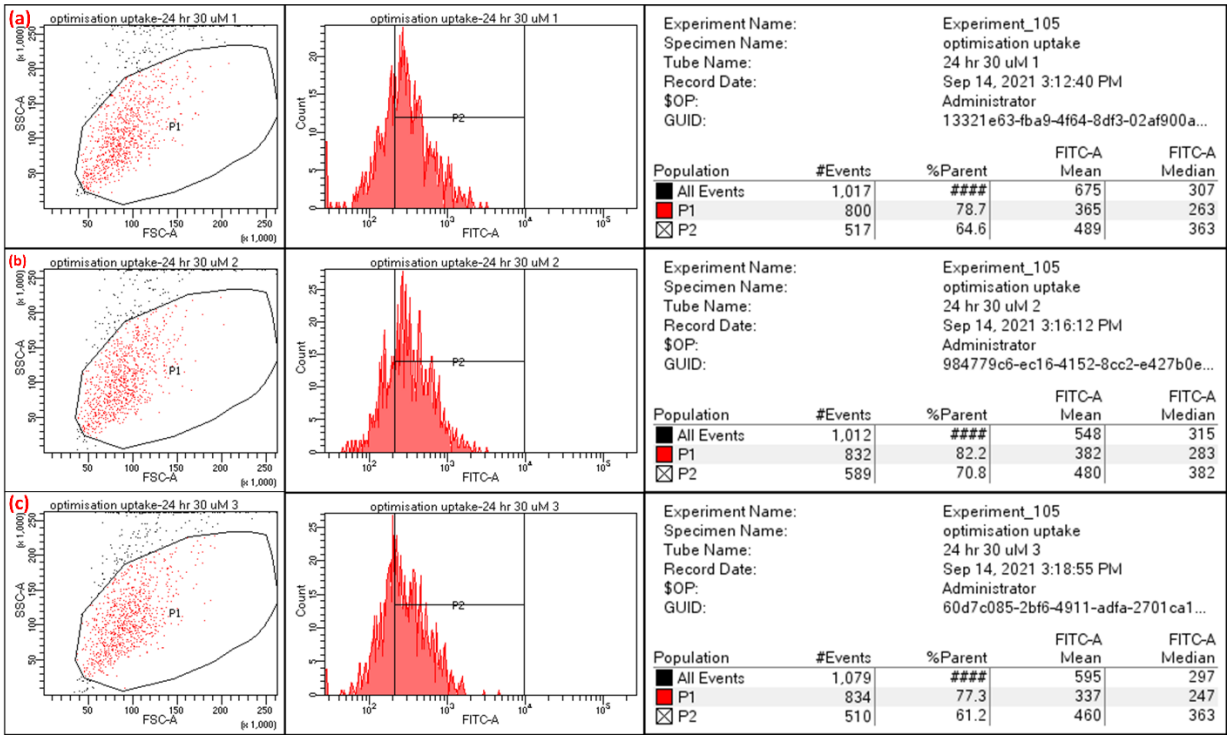

Figure 6.20 FACS experiments with **PCSB1** (30 μM) stained FaDu cells

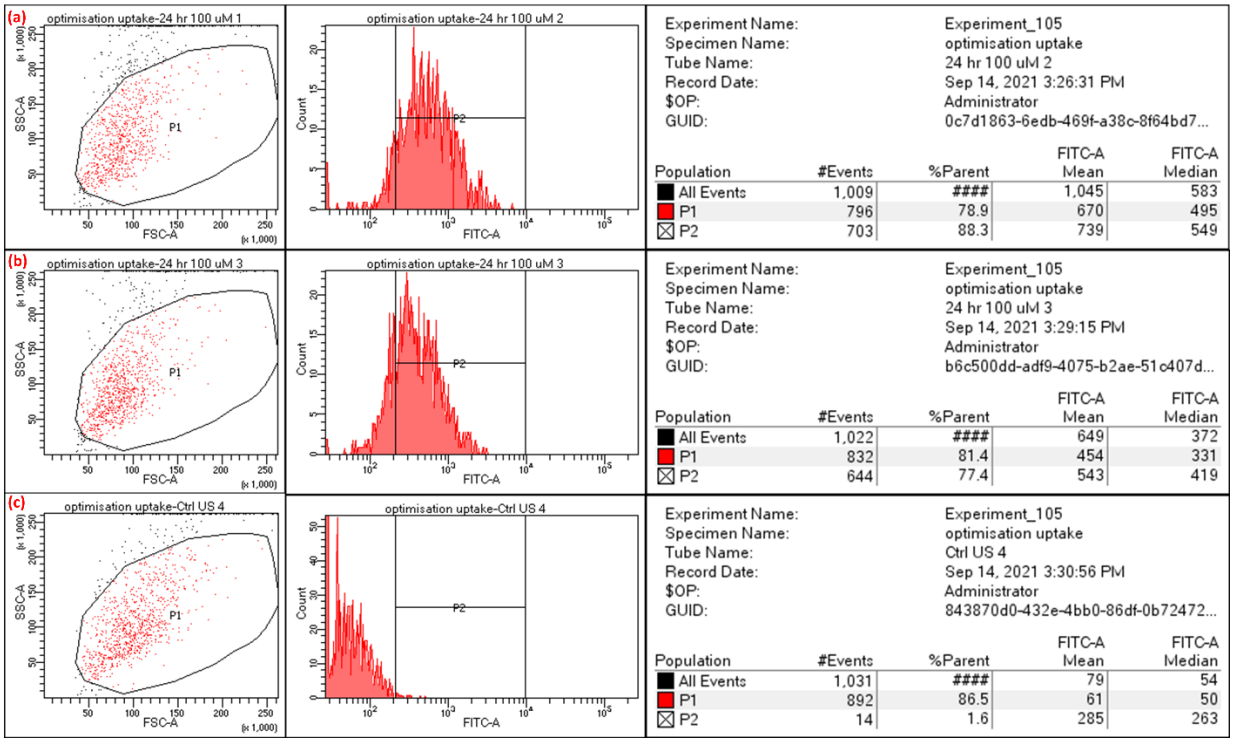

Figure 6.21 FACS experiments with **PCSB1** (100 μM) stained FaDu cells

3 μM of **PCSB1**. With 10 μM of **PCSB1**, up to 49% population was there in the P2 channel, while with 10 μM of **PCSB1**, it reached even ~70%, keeping the population inclined

towards SSC-A. With 10 μM of **PCSB1**, the dye uptake was the highest, with ~ 88% shift in the P2 channel. Hence, there was a sufficient amount of cellular uptake for the dye **PCSB1** (Figures 6.16-6.21) in every concentration, like 1 μM, 3 μM, 10 μM, 30 μM, and 100 μM. Of note, FaDu is a hypopharynx epithelial cell line, with the population doubling time of approximately 50 hours.[29]

6.3.7 Nucleus-specific bioimaging exploration with PCSB1

6.3.7.1 Live Cell Nucleus Bioimaging of FaDu cancer cell line with PCSB1 *at different probe concentrations*-wash-free (at 1 & 3 μM concentrations)

Live-cell imaging always provides a better understanding of biological function,[30] and every bioimaging dye cannot stain live cells. For example, propidium iodide is a popular red-fluorescent nuclear and chromosome-staining dye that cannot penetrate live cells.[31]

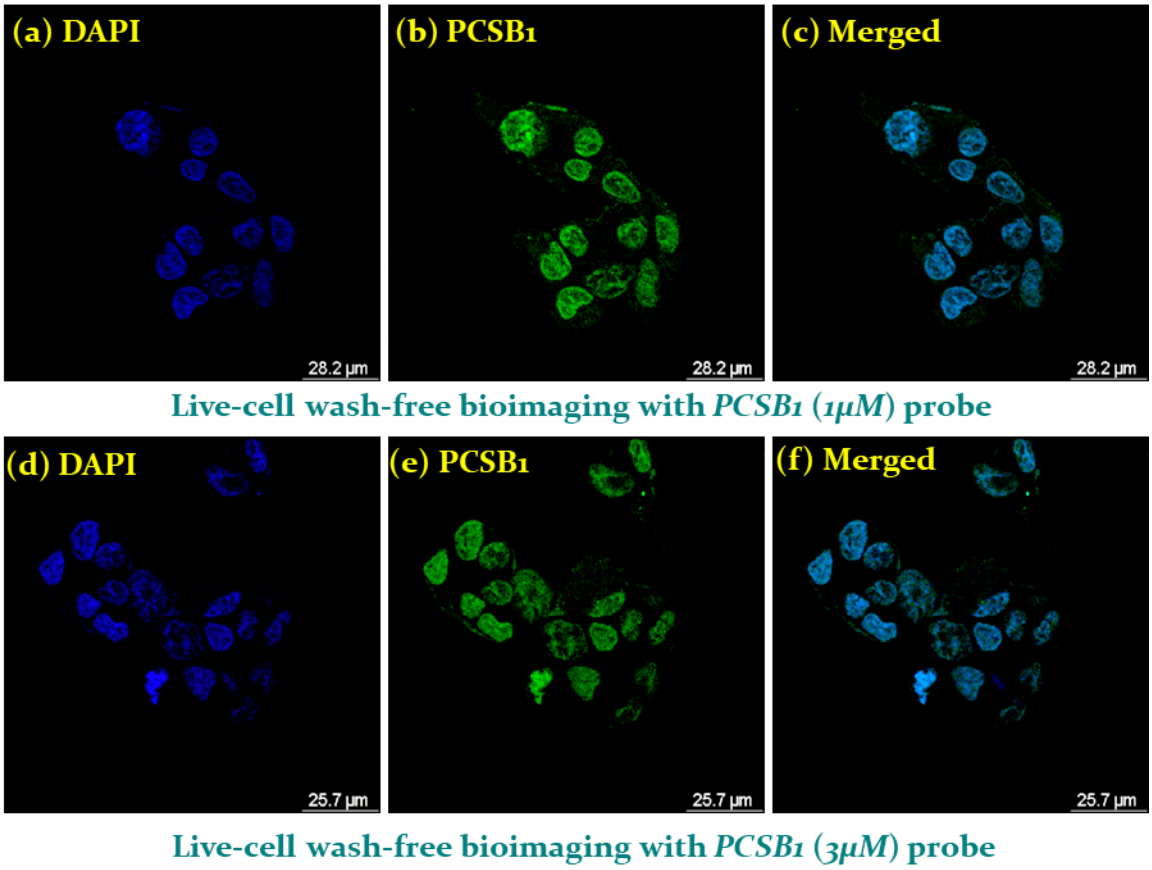

Figure 6.22 Nucleus-specific **FaDu** cancer live cells wash-free bioimaging with **PCSB1** at different concentrations

With **PCSB1,** we have tried live cancer cell imaging (PBS wash-free) of the FaDu cell line in two different probe concentrations (1 and 3 μM). DAPI was utilized as a standard dye with a 3 μM concentration. At both concentrations, **PCSB1** displayed good colocalization with DAPI. Notably, wash-free bioimaging of live cancer cells is always recommendable as it reduces both the cost and time of bioimaging (Figure 6.22).

6.3.7.2 Fixed Cell Nucleus Bioimaging of FaDu cancer cell line with PCSB1 *at a wide range of probe concentrations*-PBS-washed (at 1, 3, 10, 30, 100 μM concentrations)

Besides wash-free bioimaging, the probe **PCSB1** was also valuable in PBS-washed nucleus-specific bioimaging. The FaDu cells were fixated with cold MeOH, and the bioimaging experiments were explored at five different probe concentrations. At higher probe concentrations, the background glitches were noticed to interfere; this is the reason we also explored fixed cell bioimaging. We noticed that it was possible to eliminate the background glitches even at higher probe concentrations with a PBS wash (Figure 6.23).

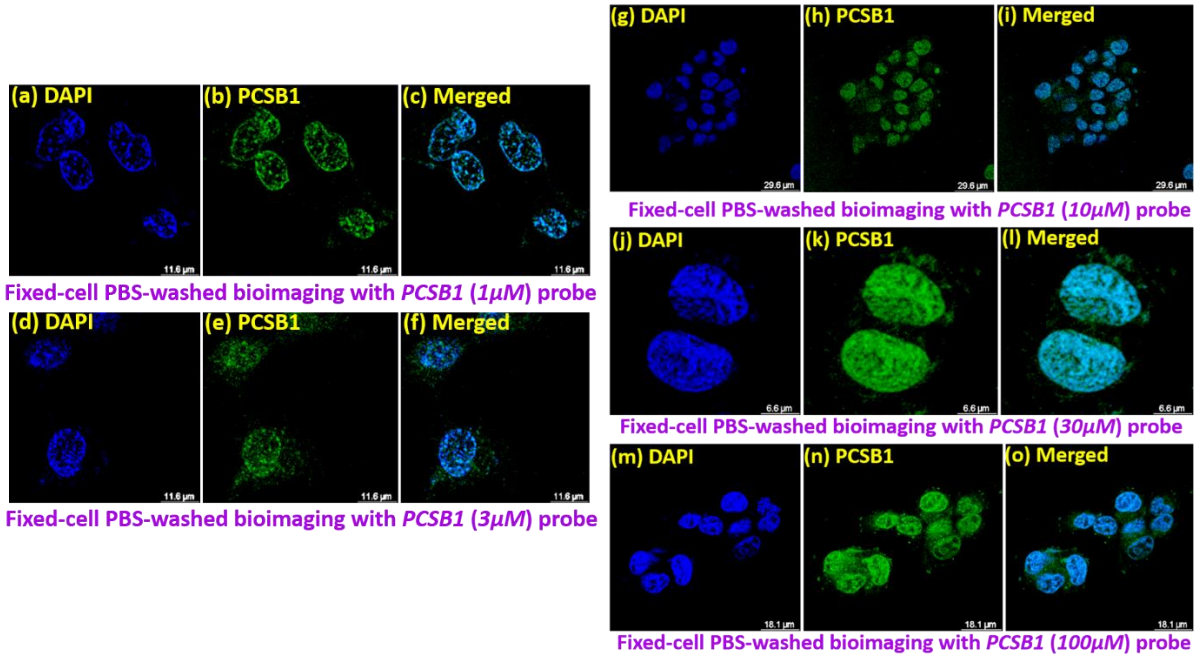

Figure 6.23 Nucleus-specific **FaDu** cancer fixated cells wash-free bioimaging with **PCSB1** at different concentrations

6.3.7.3 Time-dependent fixed cell nucleus-specific bioimaging of FaDu cancer cell line with PCSB1 *at a wide range of probe concentrations*-PBS-washed (at 1, 3, 10, 30, 100 μM concentrations): To study the non-invasive nature of the dye and photobleaching

Initially, we investigated the non-invasive nature of the dye **PCSB1** with three different concentrations (1 μM, 3 μM, and 10 μM) by performing a time-dependent bioimaging study. The dye **PCSB1** was proven to be a non-invasive dye as after 1 h of staining, the nucleus specificity was satisfying (Figure 6.24).

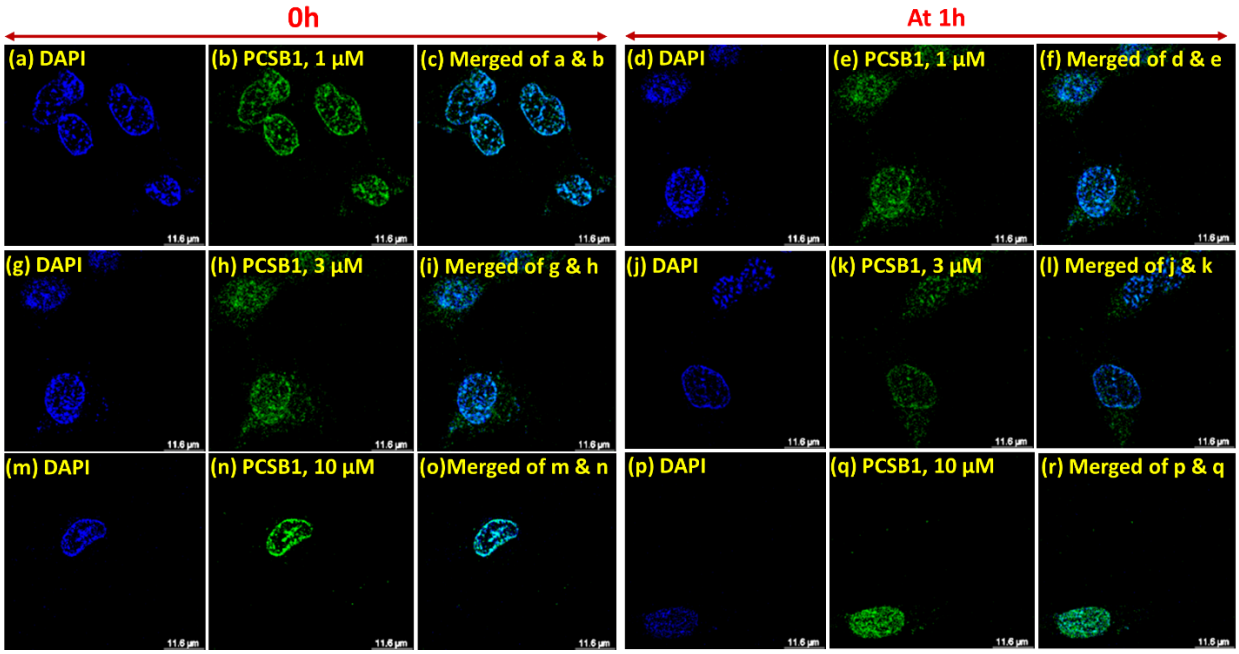

Figure 6.24 Fixed-cell cancer cell (FaDu) bioimaging with **PCSB1** at different concentrations (1 µM, 3 µM, and 10 µM) with different time points

We found **PCSB1** to be non-invasive in higher probe concentrations (30 μM and 100 μM) for up to 30-40 min (Figure 6.25). Thereafter, a slight invasiveness was revealed.

6.3.7.4 Fixed Cell Nucleus Bioimaging of A549 cancer cell line with PCSB1 *at different probe concentrations*

A549 cells are lung carcinoma epithelial cells widely used in research applications.[32] We also studied the bioimaging capability of **PCSB1** at five different

concentrations for A549. Similar to FaDu, a commendable colocalization of **PCSB1** and DAPI was detected while staining A549.

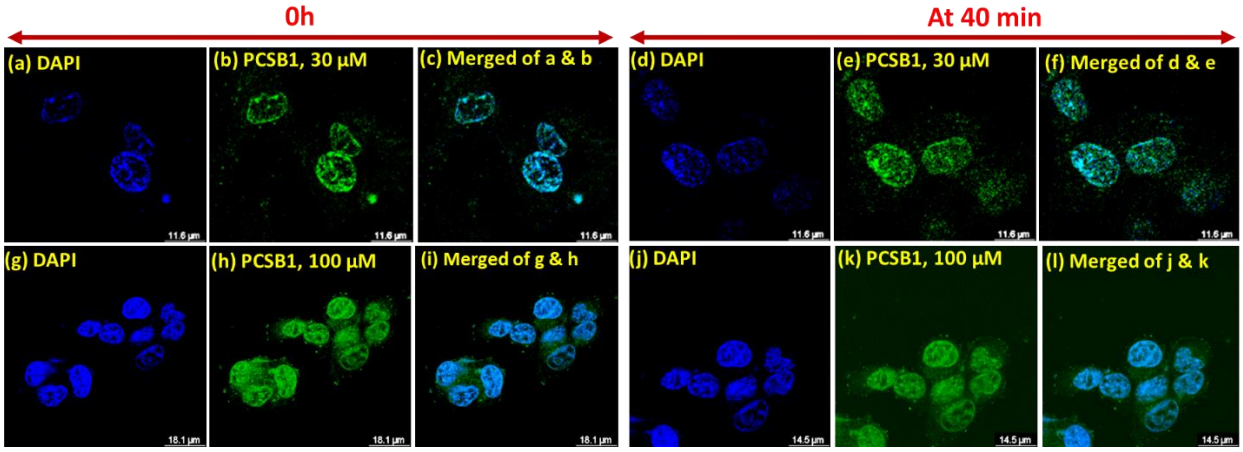

Figure 6.25 Fixated-cell cancer cell (FaDu) bioimaging with **PCSB1** at different concentrations (30 μM, and 100 μM) with different time points

The bioimaging was brighter for higher probe concentrations of 30 μM and 100 μM, but the bioimaging at lower probe concentrations was still admirable for DAPI. In this case, the 10 μM probe concentration was the most suitable moderate concentration with a sufficient amou nt of bioimaging intensity (Figure 6.26).

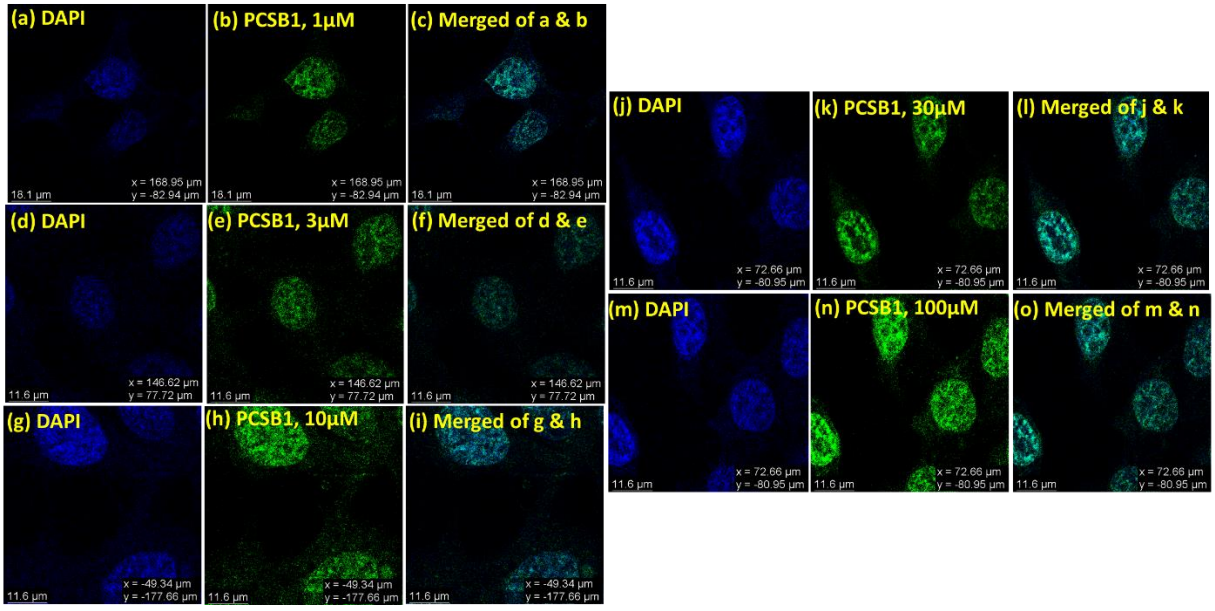

Figure 6.26 Fixed-cell cancer cell (A549) bioimaging with **PCSB1** at different concentrations

6.3.7.5 Fixed Cell Nucleus Bioimaging of A549 cancer cell line with PCSB1 *at different time points*

We also tried live cell nucleus-specific bioimaging for A549 cancer cell lines with five different probe concentrations of **PCSB1**. In addition, we studied time-dependent bioimaging for investigation of the non-invasive bioimaging capability without a major percentage of photobleaching (Figure 6.27).

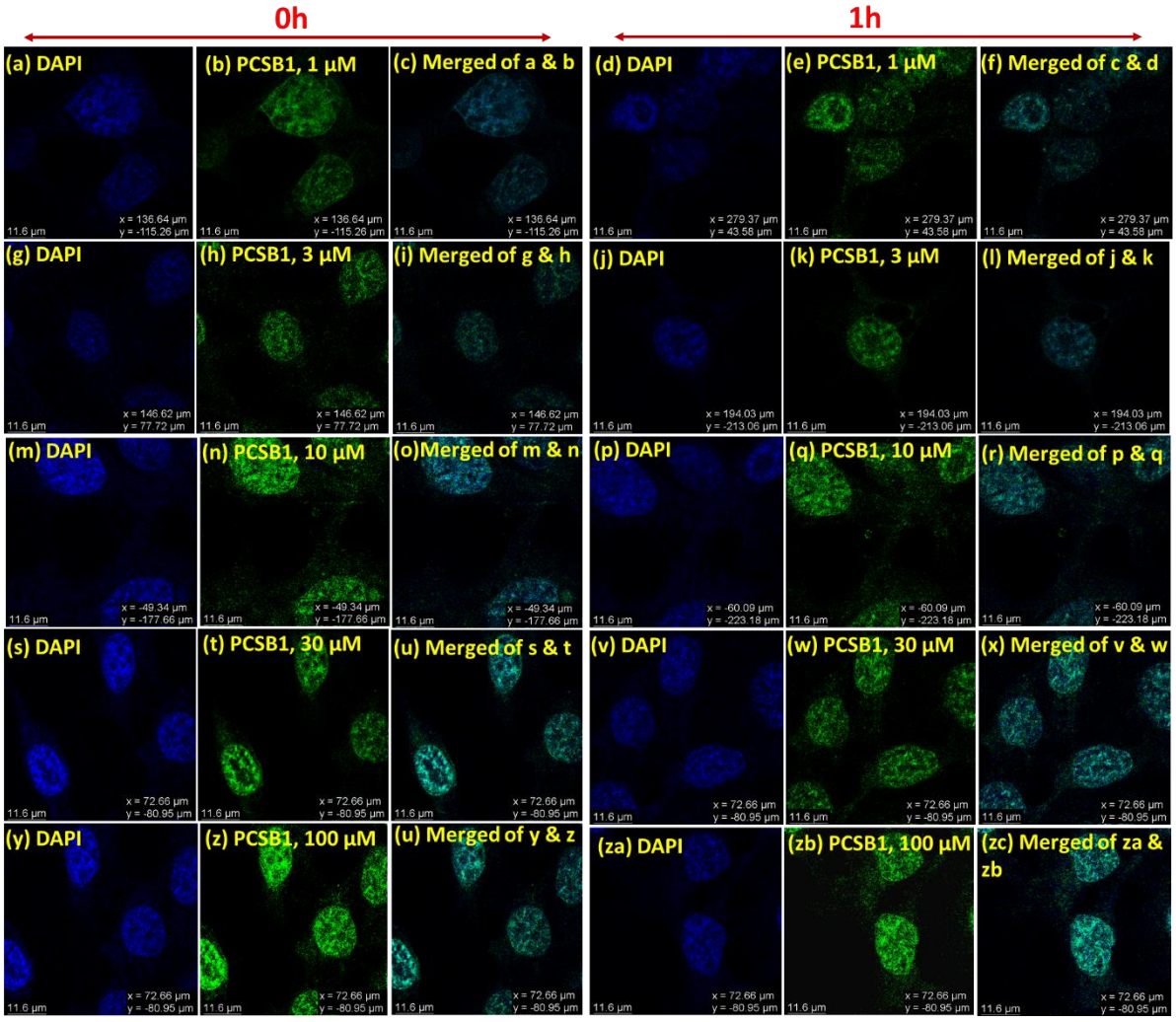

Figure 6.27 Fixed-cell cancer cell (A549) bioimaging with **PCSB1** at different time points

6.3.7.6 Fixed Cell Nucleus Bioimaging of HFF1 normal cell line with PCSB1 *at different probe concentrations*

HFF-1 is a human foreskin cell line, widely utilized in research investigations as a non-cancerous cell line. From our earlier studies, it was proven that **PCSB1** had the capability of bioimaging cancer cell lines like FaDu and A549. Hence, it was necessary

to investigate the bioimaging capability of **PCSB1** in a normal cell line. Surprisingly, **PCSB1** exhibited low-intensity bioimaging for normal cell HFF-1. The intensity was dull even at higher concentrations (30 μM or 100 μM). The colocalization was promising compared with DAPI in HFF-1 (Figure 6.28).

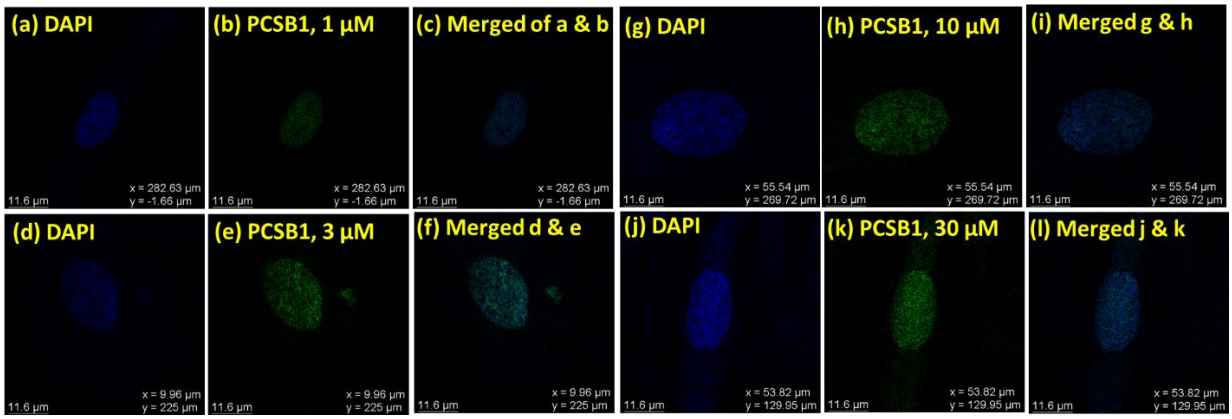

Figure 6.28 Fixed-cell normal cell (HFF1) bioimaging with **PCSB1** at different concentrations

6.3.7.7 Fixed Cell Nucleus Bioimaging of HFF1 normal cell line with PCSB1 *at different time points*

We explored the time-dependent bioimaging studies with HFF-1 and found that the dye **PCSB1** was good enough to sustain colocalization with DAPI at different time points. The bioimaging intensity was low at each time-point, but the background glitches were absent, indicating the non-invasiveness of the dye with passing time (Figure 6.29).

6.3.7.8 DNAse study to confirm the nucleus specificity

DNAse is an enzyme that can destroy the nucleus specifically. So, we intended to treat the FaDu cells with DNAse and destroy the nucleus. When the nucleus was destroyed, **PCSB1** could not image the cells. This experiment further indicates the nucleus-specificity of **PCSB1** dye (Figure 6.30).

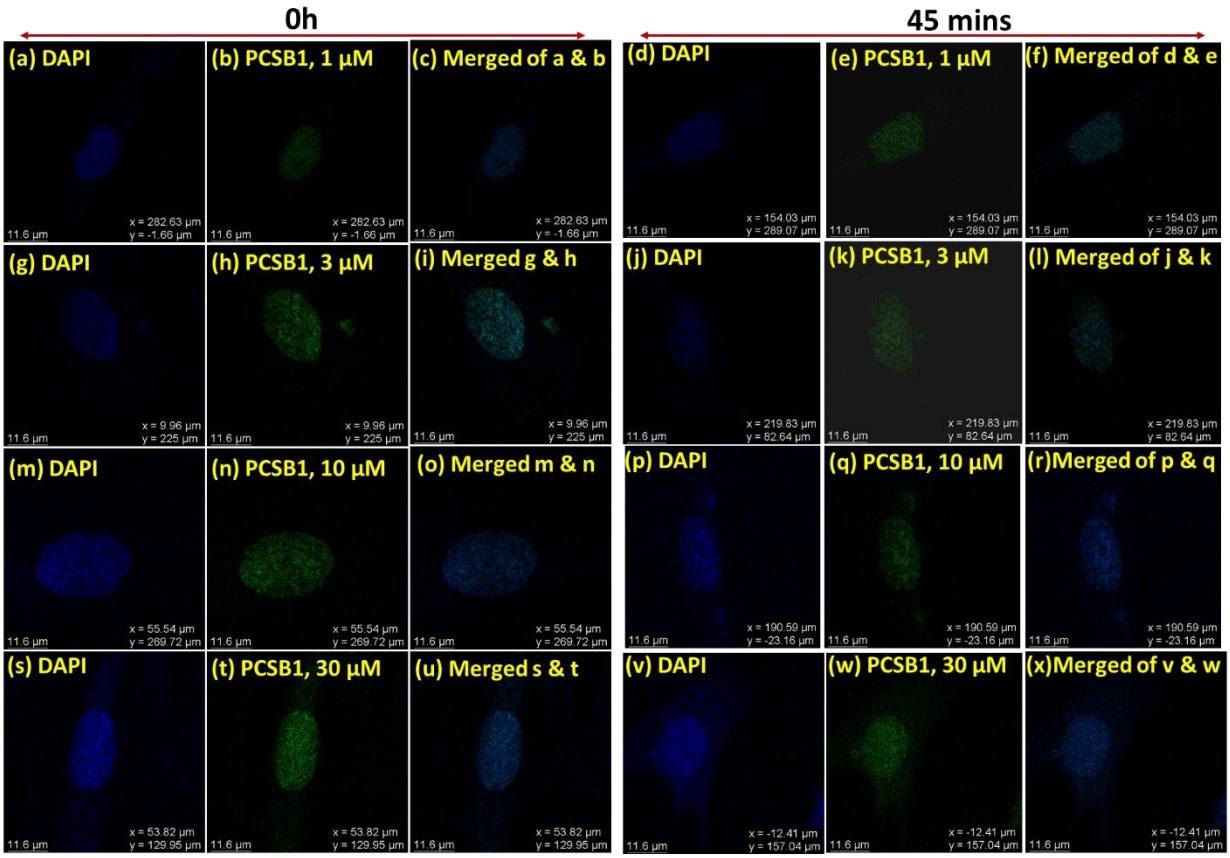

Figure 6.29 Fixed-cell normal cell (HFF1) bioimaging with **PCSB1** at different time points

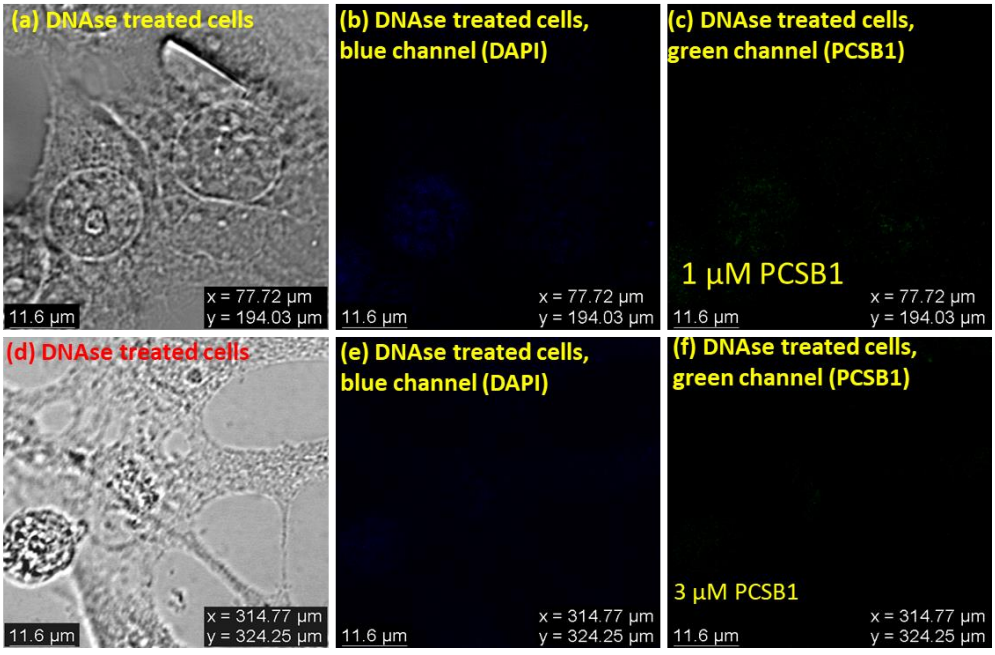

Figure 6.30 DNAse study with **PCSB1** with respect to DAPI for confirming the nucleus-specific bioimaging with **PCSB1**

6.3.7.9 Thermal Shift Assay (Protein Binding Study)

For a 25 μL reaction, 0.5X SYPRO orange dye (5000X stock concentration) was added with 3 μM BSA final concentration. A 10 μM final concentration of **PCSB1** probe was added to the sample, and an equivalent amount of DMSO was added to the control. PBS made up the rest volume. The thermal shift assay and melt curve analysis was carried out with a temperature rise from 25°C to 95°C with 1°C rise in temperature/ minute. SYPRO orange dye binds to unfolded protein with a temperature temperature rise and shows an increase in fluorescence of SYPRO orange. With 10 μM of dye only a negligible degree shift in melt temperature was observed with BSA protein, indicating minimum binding of the probe with protein (Figure 6.31).

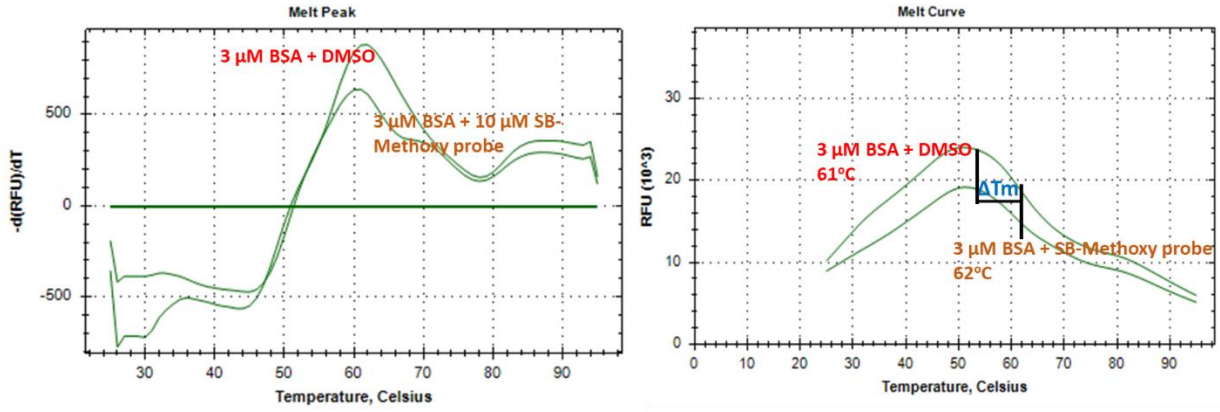

Figure 6.31 Thermal shift assay with **PCSB1**

6.3.7.10 Steady-state fluorescence studies with salmon sperm DNA and PCSB1

The steady-state fluorescence studies with increasing concentrations of salmon sperm DNA were performed with two different concentrations of **PCSB1**. In 1X PBS media, upon an increment of DNA concentration keeping the probe concentration fixed, the emission intensity gradually increased, indicating a certain interaction between the probe and DNA content (Figure 6.32).

6.3.7.11 Nucleotide docking

From the nucleotide docking, it was found that **PCSB1** had an interaction through the methoxy part 'oxygen' with 1BNA is the structure of left-handed helix BDNA

dodecamer (common in eukaryotes). The detailed docking is yet to be explored as our future perspectives (Figure 6.33).

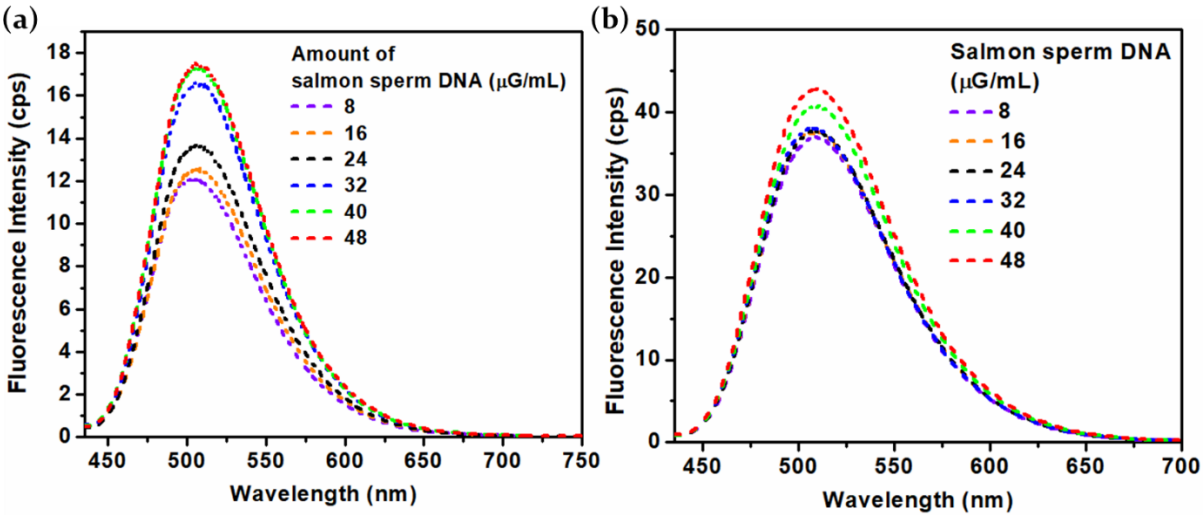

Figure 6.32 Steady-state fluorescence studies with DNA for **PCSB1** concentrations utilized (a) 1 μM (b) 3 μM

6.3.7.12 Detection of cancer cells over normal cells by live-cell/fixed-cell wash-free/PBS-washed bioimaging

Fluorescence bioimaging has become a dependable tool for cancer bioimaging and detection.[33-35] From our investigations, it was observed that the dye **PCSB1** displayed brighter emissions in cancer cells rather than in normal cells. Hence, we decided to quantify its bioimaging capability in respective cell lines. At each probe concentration of **PCSB1**, we have quantified the mean-fluorescence intensity for normal cell HFF1 and cancer cell lines like FaDu and A549 (Figures 6.34, 6.35).

6.4 Summary

A new triphenylamine-anthracenyl tri methoxy benzene-based nucleus-specific bioimaging dye **PCSB1** has been discovered and explored. The production and separation of the dye could be done by avoiding column chromatography and the usage of transition metal catalysts to claim greener pathway synthesis with excellent yields. The probe has a plausible mechanism to enlighten the cellular nucleus by restricting its molecular motion to open up a radiative channel. The photophysical properties in solids, solvents, aggregates, and viscous medium have been investigated thoroughly to

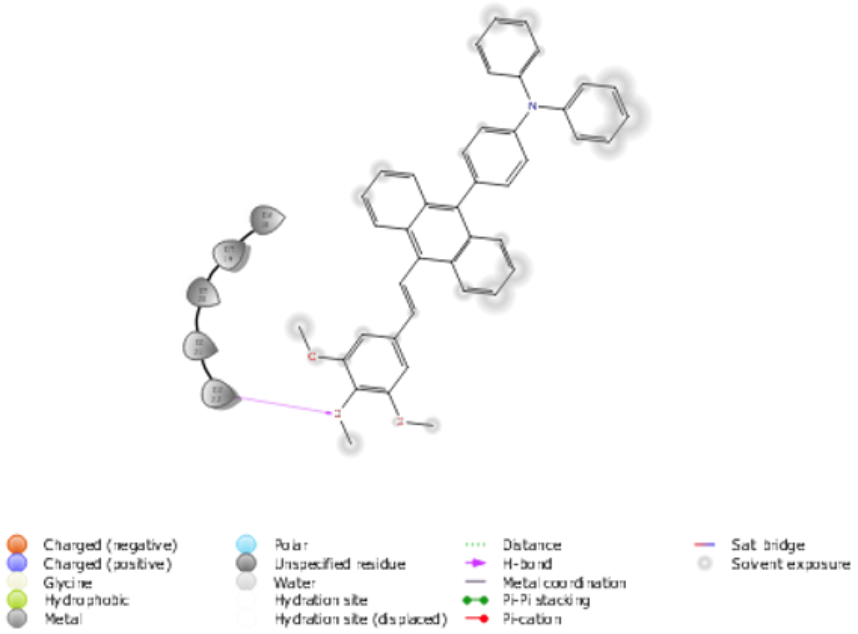

Figure 6.33 Nucleotide docking with **PCSB1**

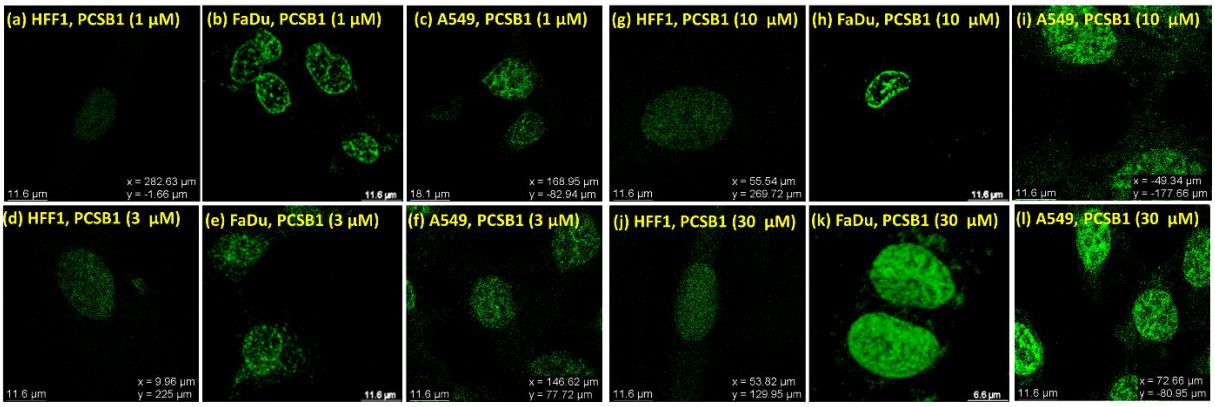

Figure 6.34 Cancer cell detection with **PCSB1**

The mean fluorescence intensity in cancer cells was considerably higher at each probe concentration, and **PCSB1** clearly could detect cancer cells from normal cells through confocal imaging (Figure 6.35).

accept that **PCSB1** displays an omnipresent emission in solids, solution, aggregates, and viscous medium to establish it as an AIE and VIE active DSE-gen. The cytotoxicity and cellular permeability were thoroughly determined and investigated. **PCSB1** was utilized in concentration-dependent, time-dependent nucleus-specific bioimaging in cancer cell lines and normal cells. The nucleotide docking, DNAse treatment-based bioimaging experiments, and thermal shift assay further confirmed its nucleus specificity.

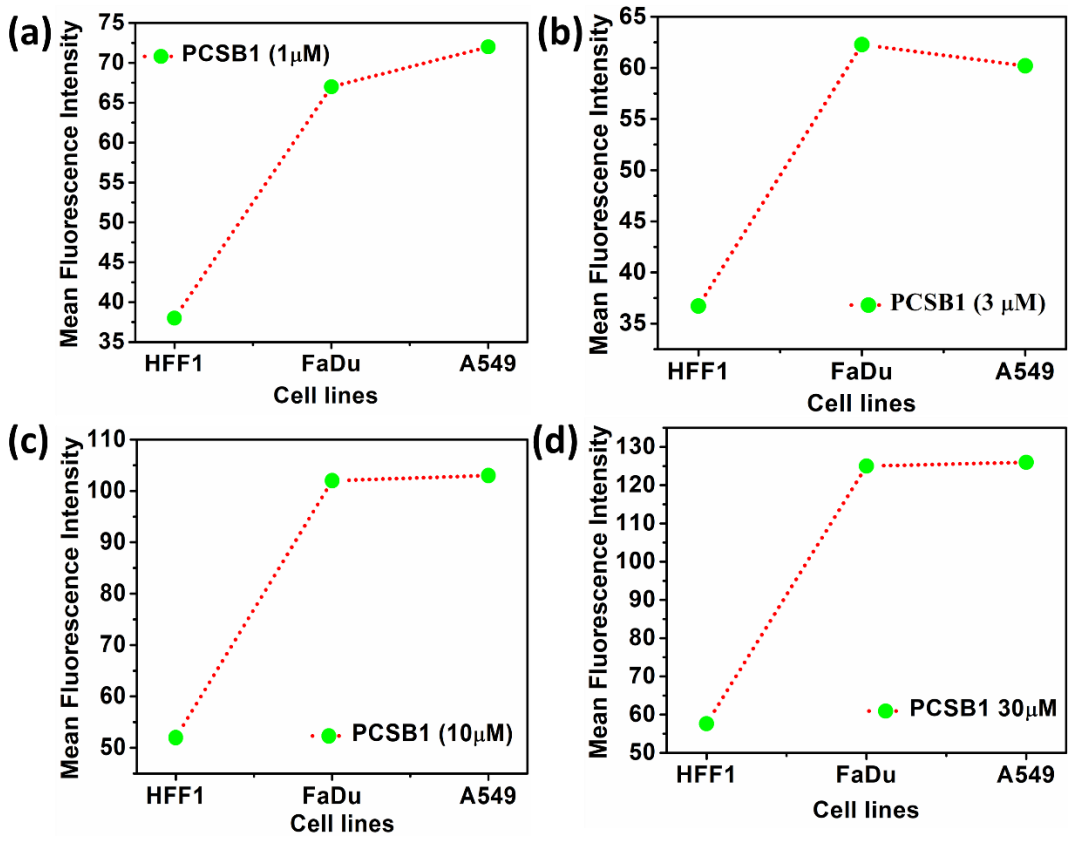

Figure 6.35 Comparison of mean fluorescence intensity in normal cells vs two types of cancer cells

The colocalization was thoroughly compared with respect to standard nucleus-specific dye DAPI. The probe **PCSB1** was able to detect cancer cells with 8 to 10 times brighter intensity than that of normal cells. Thus, **PCSB1** transpired itself as an indigenous nucleus-specific bioimaging probe.

6.5 Detailed synthetic procedures and characterizations

The general reaction procedure for **PCSB2-PCSB7** was the same as **PCSB1**, and the R_f was checked in 20% EtOAc into Hexane (v/v).

6.5.1 Synthetis of diethyl ((10-(4-(diphenylamino)phenyl)anthracen-9-yl)methyl)phosphonate

An 250 mL round bottom flask was subjected to vacuum drying and purged with N_2. Now solid substances diethyl (anthracen-9-yl(hydroxy)methyl)phosphonate (5.8081 mmol, 1 equiv, 2 gm) and triphenylamine (13.3586 mmol, 2.3 equiv., 3.27 g) with a clean

reaction pellet were taken into the same 250 mL round bottom flask and subjected to a vacuum drying for 10 mins followed by N_2 purging. Finally, the opening of the round bottom flask was sealed with silicon cap. Next, dichloroethane (50 mL) was injected into it and stirred for 10 mins in an ice bath. Later, methanesulphonic acid (MSA) (20.2122 mmol, 3.48 equiv, 1.26 mL) was injected into it at room temperature and allowed to stir for 10 h. The completion of the reaction was monitored by observing the formation of a cyan-green color fluorescent product spot at R_f= 0.17 while eluting the TLC (Thin Layer Chromatography) plate into Hexane/EtOAc medium (40% EtOAc into Hexane (v/v). The reaction mixture was subjected to work up with 30 mL×3 of EtOAc and brine water mixture with an EtOAc:H_2O (1:2) ratio. The organic layer was separated, and the volume was reduced by performing rotary evaporation. The reduced volume was added to 20 mL of 15% EtOAc into hexane medium to form precipitates within a day or two, which yielded (~ 91%, 3.052 gm) of a solid sand-like cyan-green fluorescent compound; **IR** (KBr, cm^{-1}): 3108, 3010, 2926, 1640, 1526, 1456, 1416, 1343, 1299, 1197, 1127, 1040; **mp**: 190-192°C; **^{1}H NMR** (400 MHz, $CDCl_3$, 25°C, δ): 8.40 (d, J = 8 Hz, 2H), 7.82 (d, J = 12 Hz, 2H), 7.58-7.52 (m, 2H), 7.41-7.31 (m, 6H), 7.28-7.26 (m, 4H), 7.25-7.23 (m, 4H), 7.09-7.05 (m, 2H), 4.31 (d, J= 20 Hz, P-CH_2 coupling, 2H), 4.02-3.84 (m, 4H), 1.13 (t, J= 8 Hz, 6H); **^{13}C NMR** (100 MHz, $CDCl_3$, 25°C, δ):147.8, 147.1, 137.5, 132.6, 132.1, 130.4, 130.2, 129.4, 127.8, 125.7, 125.2, 125.1, 124.8, 124.7, 123.6, 123.1, 62.3, 27.9(d, J = 140 Hz, P-CH_2 coupling), 16.4; **^{31}P NMR** (162 MHz, $CDCl_3$, 25°C, δ): 25.87; **HRMS** (ESI) m/z: calcd. for $C_{37}H_{34}NO_3P$ 571.6568, found: 594.2174 $[M+Na]^+$.

6.5.2 Synthetis of (*E*)-N,N-diphenyl-4-(10-(3,4,5-trimethoxystyryl)anthracen-9-yl)aniline (PCSB1)

A 250 mL round bottom flask was subjected to a vacuum drying and purged with N_2. Now solid substances diethyl ((10-(4-(diphenylamino)phenyl)anthracen-9-yl)methyl)phosphonate (0.8747 mmol, 1 equiv, 0.5 gm), 3,4,5-trimethoxybenzaldehyde (2.012 mmol, 2.3 equiv., 0.394 g), and potassium tert-butoxide (2.1868 mmol, 2.5 equiv., 0.25 g) with a clean reaction pellet were taken into the same 250 mL round bottom flask and subjected to a vacuum drying for 10 mins followed by N_2 purging and finally the opening of the round bottom flask was sealed with silicon cap. Next, dry THF (30 mL) was injected into it and allowed to stir at room temperature for 5-6 h. The completion

of the reaction was monitored by observing the formation of a greenish-yellow color fluorescent product spot at R_f = 0.44 while eluting the TLC (Thin Layer Chromatography) plate into Hexane/EtOAc medium (20% EtOAc into Hexane (v/v). The reaction mixture was subjected to work up with 30 mL×3 of EtOAc and brine water mixture with an EtOAc:H_2O (1:2) ratio. The organic layer was separated, and the volume was reduced by performing rotary evaporation. Now, the reduced volume was added to 15 mL of 15% EtOAc into hexane medium to form precipitates within a day or two. The upper layer of solvents was decanted, and the precipitates were washed with 5% EtOAc/hexane (v/v) solution three times and after subsequent drying it yielded (94%, 0.505 gm) of a solid green fluorescent compound. **IR** (KBr, cm^{-1}): 3116, 3102, 3042, 2964, 2918, 2851, 2788, 1611, 1526, 1429, 1357, 1189, 1154, 1086, 1046, 982, 878, 771; **M.p.**: 200-202°C; NMR spectroscopy: **^{1}H NMR** (400 MHz, $CDCl_3$, 25°C, δ): 8.42-8.40 (m, 2H), 7.89-7.82 (m, 3H), 7.52-7.39 (m, 5H), 7.36-7.31 (m, 5H), 7.29-7.27 (m, 6H), 7.10-7.06 (m, 2H), 6.92-6.85 (m, 3H), 3.98 (s, 6H), 3.93 (s, 3H); **^{13}C NMR** (100 MHz, $CDCl_3$, 25°C, δ): 153.6, 147.8, 147.2, 138.3, 137.4, 136.9, 133.1, 132.6, 132.1, 130.3, 129.5, 129.4, 127.5, 126.1, 125.2, 125.1, 124.7, 124.6, 123.1, 123.0, 103.7, 61.1, 56.3; Mass spectrometry: **HRMS** (ESI) m/z: calcd. for $C_{43}H_{35}NO_3$ 613.7570, found: 614.2688 $[M+H]^+$.

6.5.3 Synthetis of (*E*)-4-(2-(10-(4-(diphenylamino)phenyl)anthracen-9-yl)vinyl)-N,N-diphenylaniline (PCSB2)

Required chemicals and stoichiometry: Diethyl ((10-(4-(diphenylamino)phenyl)anthracen-9-yl)methyl)phosphonate (0.8747 mmol, 1 equiv, 0.5 gm), 4-(diphenylamino)benzaldehyde (2.012 mmol, 2.3 equiv., 0.55 g), and potassium tert-butoxide (2.1868 mmol, 2.5 equiv., 0.25 g), dry THF (30 mL); R_f = 0.42; yield ~ 80% (0.483 gm, greenish-yellow fluorescent); **IR** (KBr, cm^{-1}): 3113, 1609, 1522, 1441, 1357, 1299, 1236, 1086; **mp**: 258-260°C; **^{1}H NMR** (400 MHz, $CDCl_3$, 25°C, δ): 8.44-8.42 (m, 2H), 7.88-7.81 (m, 3H), 7.59-7.56 (m, 2H), 7.51-7.38 (m, 4H), 7.36-7.32 (m, 5H), 7.3-7.27 (m, 10H), 7.18-7.15 (m, 6H), 7.10-6.89 (m, 5H); **^{13}C NMR** (100 MHz, $CDCl_3$, 25°C, δ):147.8, 147.7, 147.6, 147.1, 136.9, 136.6, 133.0, 132.7, 132.1, 131.6, 131.5, 130.2, 129.5, 129.4, 129.3, 129.1, 127.5, 127.4, 126.3. 125.1, 124.7, 124.5, 123.8, 123.4, 123.1, 123.0; **HRMS** (ESI) m/z: calcd. for $C_{52}H_{38}N_2$ 690.8900, found: 691.3085 $[M+H]^+$.

6.5.4 Synthetis of (*E*)-4-(10-(2-(10-pentyl-10H-phenothiazin-3-yl)vinyl)anthracen-9-yl)-N,N-diphenylaniline (PCSB3)

Required chemicals and stoichiometry: Diethyl ((10-(4-(diphenylamino)phenyl)anthracen-9-yl)methyl)phosphonate (0.8747 mmol, 1 equiv, 0.5 gm), 10-pentyl-10H-phenothiazine-3-carbaldehyde (2.012 mmol, 2.3 equiv., 0.52 g), and potassium tert-butoxide (2.1868 mmol, 2.5 equiv., 0.25 g), dry THF (30 mL); R_f= 0.41 yield ~84% (0.525 gm, greenish-yellow fluorescent); **IR** (KBr, cm^{-1}): 3130, 1642, 1529, 1416, 1360, 1191, 1117, 1086; **mp**: 272-274°C; **^{1}H NMR** (400 MHz, $CDCl_3$, 25°C, δ): 8.40-8.38 (m, 2H), 7.84-7.80 (m, 2H), 7.55-7.50 (m, 1H), 7.47-7.43 (m, 2H), 7.42-7.38 (m, 2H), 7.36-7.31 (m, 4H), 7.28-7.26 (m, 5H), 7.23-7.15 (m, 3H), 7.11-7.03 (m, 2H), 6.99-6.82 (m, 4H), 3.90 (t, *J*= 8Hz, 2H), 1.87 (quint., 2H), 1.50-1.34 (m, 4H), 0.93 (t, *J*= 8Hz, 3H); **^{13}C NMR** (100 MHz, $CDCl_3$, 25°C, δ): 147.8, 147.1, 145.0, 136.7, 136.2, 132.9, 132.7, 132.1, 131.9, 130.3, 129.5, 129.4, 128.3, 127.5, 127.4, 127.3, 126.2, 125.9, 125.4, 125.2, 125.1, 125.0, 124.9, 124.7, 124.3, 123.4, 123.1, 122.5, 122.3, 115.4, 47.6, 29.2, 26.6, 22.4, 14.1; Mass spectrometry: **HRMS** (ESI) m/z: calcd. for $C_{51}H_{42}N_2S$ 714.9710, found: 715.3123 $[M+H]^+$.

6.5.5 Synthetis of (*E*)-*N,N*-diphenyl-4-(10-(2-(pyren-4-yl)vinyl)anthracen-9-yl)aniline (PCSB4)

Required chemicals and stoichiometry: Diethyl ((10-(4-(diphenylamino)phenyl)anthracen-9-yl)methyl)phosphonate (0.8747 mmol, 1 equiv, 0.5 gm), pyrene-1-carbaldehyde (1.9243 mmol, 2.2 equiv., 0.443 g), and potassium tert-butoxide (2.1868 mmol, 2.5 equiv., 0.25 g), dry THF (30 mL); R_f= 0.43; yield ~82% (0.465 gm, greenish fluorescent); **IR** (KBr, cm^{-1}): 3100, 1819, 1626, 1529, 1458, 1408, 1354, 1294, 1240, 1144; **mp**: 231-233°C; **^{1}H NMR** (400 MHz, $CDCl_3$, 25°C, δ) 8.74-8.32 (m, 4H), 8.28-8.01 (m, 6H), 7.95-7.87 (m, 2H), 7.72-7.43 (m, 5H), 7.37-7.28 (m, 13H), 7.10-7.00 (m, 3H); **^{13}C NMR** (100 MHz, $CDCl_3$, 25°C, δ): 164.4, 146.8, 146.2, 133.9, 132.7, 132.1, 131.6, 131.1, 130.9, 130.5, 130.0, 129.9, 129.3, 128.7, 128.6, 128.4, 127.4, 126.9, 126.5, 125.2, 125.1, 124.5, 124.4, 124.1, 123.7, 122.8, 122.1; **HRMS** (ESI) m/z: calcd.for $C_{50}H_{33}N$ 647.8210, found: 648.4627 $[M+H]^+$.

6.5.6 Synthetis of (*E*)-4-(2-(10-(4-(diphenylamino)phenyl)anthracen-9-yl)vinyl)benzonitrile (PCSB5)

Required chemicals and stoichiometry: Diethyl ((10-(4-(diphenylamino)phenyl)anthracen-9-yl)methyl)phosphonate (0.8747 mmol, 1 equiv, 0.5 gm), 4-formylbenzonitrile (2.0118 mmol, 2.3 equiv., 0.263 g), and potassium tert-butoxide (2.1868 mmol, 2.5 equiv., 0.25 g), dry THF (30 mL); R_f = 0.38; yield ~93% (0.442 gm, yellowish fluorescent compound); **IR** (KBr, cm^{-1}): 3027, 2219, 1584, 1482, 1379, 1317, 1264, 1024; **mp**: 251-253°C; **^{1}H NMR** (400 MHz, $CDCl_3$, 25°C, δ): 8.34-8.32 (m, 2H), 8.14 (d, *J*= 16H, 1H), 7.85-7.74 (m, 6H), 7.52-7.40 (m, 4H), 7.37-7.32 (m, 4H), 7.28-7.26 (m, 8H), 7.11-6.98 (m, 3H); **^{13}C NMR** (100 MHz, $CDCl_3$, 25°C, δ): 147.8, 147.3, 141.7, 137.7, 135.8, 135.5, 132.7, 132.3, 132.2, 132.0, 131.4, 130.2, 129.4, 127.6, 127.1, 125.7, 125.6, 125.2, 124.8, 123.2, 122.9, 119.0, 111.2; **HRMS** (ESI) m/z: calcd. for $C_{41}H_{28}N_2$ 548.6890, found: 549.2314 $[M+H]^+$.

6.5.7 Synthetis of (*E*)-N,N-diphenyl-4-(10-(2-(pyridin-4-yl)vinyl)anthracen-9-yl)aniline (PCSB6)

Required chemicals and stoichiometry: Diethyl ((10-(4-(diphenylamino)phenyl)anthracen-9-yl)methyl)phosphonate (0.8747 mmol, 1 equiv, 0.5 gm), isonicotinaldehyde (2.0118 mmol, 2.3 equiv., 0.22 g), and potassium tert-butoxide (2.1868 mmol, 2.5 equiv., 0.25 g), dry THF (30 mL); R_f = 0.37; yield ~81% (0.372 gm, greenish fluorescent compound); **IR** (KBr, cm^{-1}): 3019, 1610, 1527, 1442, 1347, 1301, 1222, 1093; **mp**: 250-252°C; **^{1}H NMR** (400 MHz, $CDCl_3$, 25°C, δ): 8.71-8.69 (m, 2H), 8.34-8.32 (m, 2H), 8.24 (d, *J*= 16 Hz, 1H), 7.86-7.83 (m, 2H), 7.57-7.40 (m, 6H), 7.36-7.32 (m, 4H), 7.29-7.26 (m, 8H), 7.11-7.06 (m, 2H), 7.00-6.92 (m, 1H); **^{13}C NMR** (100 MHz, $CDCl_3$, 25°C, δ): 150.3, 147.8, 147.3, 144.5, 137.8, 134.9, 132.2, 132.0, 131.2, 130.4, 130.2, 129.6, 129.4, 129.3, 127.6, 125.6, 125.2, 124.8, 123.2, 122.9, 121.0; **HRMS** (ESI) m/z: calcd. for $C_{39}H_{28}N_2$ 524.6670, found: 525.2326 $[M+H]^+$.

6.5.8 Synthetis of (*E*)-4-(10-(4-nitrostyryl)anthracen-9-yl)-N,N-diphenylaniline (PCSB7)

Required chemicals and stoichiometry: Diethyl ((10-(4-(diphenylamino)phenyl)anthracen-9-yl)methyl)phosphonate (0.8747 mmol, 1 equiv, 0.5 gm), 4-nitrobenzaldehyde (2.0118 mmol, 2.3 equiv., 0.30 g), and potassium tert-butoxide (2.1868 mmol, 2.5 equiv., 0.25 g), dry THF (30 mL); R_f= 0.37; yield ~90% (0.448 gm, greenish fluorescent compound); **IR** (KBr, cm^{-1}): 3109, 1613, 1531, 1416, 1360, 1299, 1222, 1090; **mp**: 281-283°C; **^{1}H NMR** (400 MHz, $CDCl_3$, 25°C, δ): 8.35-8.32 (m, 4H), 8.20 (d, *J*= 16 Hz, 1H), 7.86-7.82 (m, 4H), 7.52-7.41 (m, 4H), 7.37-7.32 (m, 4H), 7.29-7.27 (m, 8H), 7.11-7.05 (m, 3H); **^{13}C NMR** (100 MHz, $CDCl_3$, 25°C, δ): 147.8, 147.3, 147.2, 143.6, 137.9, 135.3, 132.2, 132.0, 131.2, 130.3, 130.2, 129.4, 127.7, 127.1, 125.7, 125.6, 125.2, 124.8, 124.3, 123.2, 122.9, 96.1; **HRMS** (ESI) m/z: calcd. for $C_{40}H_{28}N_2O_2$ 568.6760, found: 569.3142 $[M+H]^+$.

6.6 References

1 T. Terai and T. Nagano, ***Curr. Opin. Chem. Biol.***, 2008, **12**, 5, 515-521.

2 L. Li and H. Sun, ***Biochem.***, 2020, **59**, 3, 216-217.

3 H. Fang, Y. Chen, Z. Jiang, W. He and Z. Guo, ***Acc. Chem. Res.***, 2023, **56**, 3, 258-269.

4 Y. Cheng, C. Sun, X. Ou, B. Liu, X. Lou and F. Xia, ***Chem. Sci.***, 2017, **8**, 4571-4578.

5 D. M. Graham, T. Anderson, L. Sharek, G. Uzer, K. Rothenberg, B. D. Hoffman, J. Rubin, M. Balland, J. E. Bear and K. Burridge, ***J. Cell Biol.***, 2018, **217**, 3, 895-914.

6 T. R. Chen, ***Exp. Cell Res.***, 1977, **104**, 255–262

7 J. Kapuscinski, ***Biotech. Histochem.***, 1995, **70**, 220–233

8 https://www.wiseguyreports.com/sample-request/3764405-bio-imaging-global-market-outlook-2017-2026

9 https://www.marketsandmarkets.com/Market-Reports/near-infrared-imaging-market-174869738.html

10 L. C. Crowley, B. J. Marfell, A. P. Scott, J. A. Boughaba, G. Chojnowski, M. E. Christensen and N. J. Waterhouse, ***Cold Spring Harb Protoc***; doi:10.1101/pdb.top070318

11 M. A. A. F. de C. T. Carrondo, M. Coll, J. Aymami, A. H. J. Wang, G. A. Van der Marel, J. H. Boom and A. Rich, ***Biochem.***, 1989, **28**, 19, 7849-7859.

12 K. M. Bourzac, L. J. LaVine and M. S. Rice, ***J. Chem. Educ.***, 2003, **80**, 11, 1292-1296.

13 K. Deng, L. Wang, Q. Xia, R. Liu and J. Qu, ***Talanta***, 2019, **192**, 212-219.

14 X. Zhang, Z. Ye, X. Zhang, H. Man, Z. Huang, N. Li and Y. Xiao, ***Chem. Commun.***, 2019, **55**, 1951-1954.

15 M. A. O. Mendoza, I. I. A. Olguin, M. M. E. Carmona, W. M. Morales, Y. A. Ricardo, R. A. Toscano, F. A. Huertero, J. Cassani and R. G. Enriquez, ***Molecules***, 2020, **25**, 14, 3205.

16 F. F. Gonzalez, M. F. Gutierrez, D. G. Puentes, A. Orte, J. A. G. Vera and R. Herranz, ***Eur. J. Med. Chem.***, 2020, **200**, 112407.

17 Y. Feng, S. Chi, G. Gao, Y. Zhao and Y. Wu, ***Sens. Actuators B: Chem.***, 2019, **282**, 16-26.

18 K. K. Ghosh, Y. M. Jeong, N. Y. Kang, J. Y. Lee, W. Si Y. Diana, J. Y. Kim, J. Yoo, D. Kim, Y. K. Kim and Y. T. Chang, ***Chem. Commun.***, 2015, **51**, 9336-9338.

19 J. L. B. Vazquez, Y. A. A. Sanchez, L. A. R. Cortes and B. R. Molina, ***Chem. Mater.***, 2021, **33**, 18, 7160-7184.

20 K. Li, T. B. Ren, S. Huan, L. Yuan and X. B. Zhang, ***J. Am. Chem. Soc.***, 2021, **143**, 50, 21143-21160.

21 H. H. Park, P. Meti and Y. D. Gong, ***Dyes Pigm.***, 2021, **190**, 109320.

22 F. Yu, H. Zhao, Y. Li, G. Xia and H. Wang, ***Mater. Chem. Front.***, 2022, **6**, 155-162.

23 S. Bhuin, P. Chakraborty, P. Sivasakthi, P. K. Samanta and M. Chakravarty, ***ACS Appl. Opt. Mater.***, 2023, **1**, 7, 1289-1300.

24 J. Mei, N. L. C. Leung, R. T. K. Kwok, J. W. Y. Lam and B. Z. Tang, ***Chem. Rev.***, 2015, **115**, 21, 11718-11940.

25 R. D. Telore, M. A. Satam and N. Sekar, ***Dyes Pigm.***, 2015, **122**, 359-367.

26 L. Xu, K. Wu, R. Han, Y. Sui, C. Huang, W. Huang and L. Liu, ***Spectrochim. Acta A Mol. Biomol. Spectrosc.***, 2021, **261**, 120016.

27 L. Xu, Y. Zou, M. Zeng, S. Duan, K. Wu, R. Han and L. Liu, ***ACS Food Sci. Technol.***, 2022, **2**, 1, 49-56.

28 D. Su, C. L. Teoh, L. Wang, X. Liu and Y. T. Chang, ***Chem. Soc. Rev.***, 2017, **46**, 4833-4844.

29 S. R. S. Rangan ScD, ***Cancer***, 1972, **29**, 1, 117-121.

30 H. S. Lahoti and S. D. Jogdand, ***Cureus***, 2022, **14**, 9, e28923.

31 Y. Hirai, Y. Makita, J. Asaoka, Y. Aoyagi, A. Nomoto, H. Okamura and S. Fujiwara, ***ACS Omega***, 2023, **8**, 38, 35321-35327.

32 Y. Gao, P. Dorn, S. Liu, H. Deng, S. R. R. Hall, R. W. Peng, R. A. Schmid and T. M. Marti, ***Cancer Cell Int.***, 2019, **19**, 317.

33 Y. Zou, M. Li, Y. Xing, T. Duan, X. Zhou and F. Yu, ***ACS Sens.***, 2020, **5**, 1, 242-249.

34 M. Pirsaheb, S. Mohammadi and A. Salimi, TrAC, ***Trends Anal. Chem.***, 2019, **115**, 83-99.

35 Z. M. Yang, Q. Y. Mo, J. M. He, D. L. Mo, J. Li, H. Chen, S. L. Zhao and J. K. Qin, ***ACS Sens.***, 2020, **5**, 4, 943-951.

○ Future Scope ~

Each and every work explored and discussed herein has the potential to pave the way for future scopes of research and innovation. In *Chapter I*, new synthetic pathways were established to produce new organic fluorescent compounds that are crystallochromic. So far, crystallochromic dyes have not been utilized in bioimaging. The property to emit the same in solution but different in solids may become helpful in identifying the dryness of biological cells. We are currently considering aggravating their utilities in anticounterfeiting and bioimaging applications. In *Chapter II* and *Chapter IV*, two very sensitive SSAC dyes, '**ATh4P**' and '**SB3**' are well-established. Currently, those dyes are being utilized in stimuli-responsive hidden QR-code printing. We are actually targeting to implement this technique in medicine anticounterfeiting. Again, protonated '**ATh4P**' and '**SB3**' salts are being screened to find an application in mitophagy bioimaging. In *Chapter V*, a lipid-droplet-specific bioimaging dye, '**OXNCN**,' is explored. First and foremost, this dye contains a naphthalene scaffold, which is a new system for our research group. Because our maximum explorations were with anthracene moiety so far. There are scopes of structural modifications to explore new compounds and find their applications. The LD-specific bioimaging dye can be explored in hypoxia studies or bioimaging of fatty liver tissues in the coming days. In *Chapter VI*, a nucleus specific bioimaging dye '**PCSB1**' is established. The *in vivo* studies are currently being explored in mice models. However, we plan to marketize this compound as it already has the potential to be utilized as a cellular imaging dye for academic research purposes. But before entering the market, we will investigate a few more aspects- if it is useful for in vivo tumor detection or if it can be utilized in liquid biopsy. On successful consequences, in the coming future, '**PCSB1**' may find demand in the market as a '***Made in India***' **bioimaging dye** for academic, R&D, and diagnostic utilities.

Based on these works, we are looking to receive some grants for our lab so that any new student can be funded to continue her/his research. As discussed earlier, we are looking for some 'start-ups' on QR-code-based techniques and nucleus-specific bioimaging dyes. From a broader perspective, the scientific community around the globe will benefit from the outcome of this thesis work because these works are an addition to the continuous effort of the human race. These works are anticipated to help future Ph.D. students and other researchers.

The outcome of the Thesis:

List of publications from this thesis:

1. **S. Bhuin**, S. Bhattacharya and M. Chakravarty, Acceptor–donor–acceptor-linked triphenylamine and phenothiazine motifs as cousin molecules: the methyl effect on stimuli- responsiveness, crystallochromism, and dual-state emission, ***New J. Chem.***, 2021, **45**, 21236.
2. **S. Bhuin,** P.K. Samanta and M. Chakravarty, Efficient and reversible acidofluorochromic features on a solid platform for reusable security writing: A structure-property relationship study on anthracenyl π-conjugates, ***Dyes Pigm.***, 2022, **197**, 109944.
3. **S. Bhuin** and M. Chakravarty, Naked-eye optical recognition of ammonia vapor and melamine in water using a fluorophore appended polymer matrix, ***J. Fluoresc.***, 2023, **33**, 373-381.
4. **S. Bhuin**, P. Sharma, P. Chakraborty, O. Kulkarni and M. Chakravarty, Solid-state emitting twisted π-conjugates as AIEgens: In vitro anticancer properties against FaDu and 4T1 with biocompatibility and bioimaging, ***J. Mater. Chem. B***, 2023,**11**, 188-203.
5. **S. Bhuin**, P. Chakraborty, P. Sivasakthi, P. K. Samanta and M. Chakravarty, Double-Site Twisted D-π-D′ Conjugates with Versatile Photophysical Facets for Diverse Optical Applications and Wash-Free Bioimaging of Cancer Cells, ***ACS Appl. Opt. Mater.***, 2023, **1**, 7, 1289-1300.
6. **S. Bhuin**, P. Chakraborty, P. Sivasakthi, P. K. Samanta, P. Yogeeswari and M. Chakravarty, Asymmetrical Organic D-π-A Conjugate with 'V'-Shaped Crystal Packing: Quest to Transcend the Limits of Photophysical Properties and Applications, ***J. Mater. Chem. C***, 2023,**11**, 11270-11282.
7. **S. Bhuin**, P. Chakraborty, P. Sivasakthi, P. K. Samanta, P. Yogeeswari and M. Chakravarty Heteroatom Replacement Led Emission Contrast from Twisted Dicyanoethylenes: Employing Non-cytotoxic Fluorophore in Wash-Free LD Bioimaging of Live Cancer Cells, manuscript *under preparation*.

8. Motion-Restricted Enhanced Emission from Twisted Uncharged Organic Fluorophore: A Non-DNA-Intercalating Nucleus Specific Bioimaging Probe for Live *in vitro* Cancer Cell Detection and *in vivo* Imaging, **S. Bhuin**, P. Chakraborty, P. Yogeeswari and M. Chakravarty, *Manuscript to be communicated*.

List of publications not included in this thesis:

1. **S. Bhuin**, S. Halder, S.K. Saha and M. Chakravarty, Binding interactions and FRET betweenbovine serum albumin and various phenothiazine-/ anthracene-based dyes: a structure-property relationship, ***RSC Adv.***, 2021, **11**, 1679-1693. (not included in thesis)
2. **S. Bhuin**, S. Roy, C. Chakraborty and M. Chakravarty, Emission enhancement in twisted pyridyl salt using montmorillonite nano clay by intercalation and surface-fixation process, ***New J. Chem.***, 2022,**46**, 12856-12863. (not included in thesis)

List of filed patents:

1. Fluorescent indole-anthracenyl derivative molecules, method of synthesis, detection method and kit comprising the same, Indian Patent application no: **202211075459** , Feb 2023. Inventors: Mr. **Shouvik Bhuin**, Ms. Purbali Chakraborty and Prof. Manab Chakaravarty.

2. Made in India biocompatible organic dyes for nucleus-specific bioimaging studies: An accessible solution for academia/R&D industry research, and diagnostics. (Applied for Indian Patent). Inventors: **Mr. Shouvik Bhuin**, Ms. Purbali Chakraborty Prof. P. Yogeeswari and Prof. Manab Chakravarty.

National Conferences/Symposium:

1. ***Poster presentation*** in ***UGC, India-sponsored National Conference*** (2018) held at PSGR Krishnammal Women's College, Coimbatore, Tamil Nadu, India.

2. Poster presentation in 'Convergence of Chemistry & Materials (CCM-2023)' in Hyderabad, India.

International Conferences/Symposiums:

1. ***Oral presentation*** (virtual platform) in ***ACS Spring 2021*** (Abstract ID: 3553417; Inducing remarkable crystallochromic, thermochromic and piezochromic emission for TPA and PTZ based cousin molecules: Effect of methyl substituent)

2. ***Oral presentation*** (virtual platform) in ***ACS Spring 2022*** (Abstract ID: 3650752; Solid state reversible acidochromism of anthracene-π-conjugated pyridyl isomers: Application for security writing in a solid platform)

3. **Oral presentation** in '**ACS-India Pitch Your Research-2022**'

4. **Poster presentation** 'International Conference on Aggregation-Induced Emission: Fundamental to Application (**IC-AIEE-FA 2022**), Goa, India. ***It was the first international conference on 'AIE' in India.***

Award Received from the thesis work:

1. Best research pitch award in '***ACS Spring-India Satellite Event****-Pitch your Research 2022*'.

2. Best poster presentation award in 'International Conference on Aggregation-Induced Emission: Fundamental to Application (**IC-AIEE-FA 2022**), Goa, India.

Membership Received:

1. Associate Member, Royal Society of Chemistry (RSC), 2023-24 (ID: 742721)

2. Affiliate Member, Royal Society of Chemistry (RSC), 2022-23

Recommendation received / International Travel Grant and other related things:

1. HORIBA Academic Newsletter recommended the publication entitled 'Efficient and reversible acidofluorochromic features on a solid platform for reusable security writing: A structure-property relationship study on anthracenyl π-conjugates, ***Dyes Pigm.*, 2022, 197, 109944**' in the fields of Biology, Sensors and Materials, Issue 2 (2022) (https://ibook.antpedia.com/n/93358.html).

2. Finalist of DBT-BIG, India, 2022 (Department of Biotechnology-Biotechnology Ignition Grant, India).

3. SERB, CSIR, India granted an international travel grant to present the work from the published article ***J. Mater. Chem. B***, 2023,**11**, 188-203, in 'Tetrahedron Symposium-2022' in Lisbon, Portugal.

4. Our research on cancer cell inhibition and bioimaging was published in '*Know-Today*' news and is still available online (link: https://know-todays-news.com/valuate-anticancer-properties/)

Start-Up Endeavored:

1. One start-up approach has been endeavored with C-CAMP Meity on the basis of the acidofluorochromic work.
2. Another start-up is being endeavored on the work of 'Made in India' nucleus-specific bioimaging dyes.

Biography of the Candidate

Mr. Shouvik Bhuin was born at Narajole, West Midnapore, West Bengal, India. He completed his B.Sc. (Hons.) degree in Chemistry from Narajole Raj College, Vidyasagar University, Midnapore in 2013. Later, he moved to Chhattisgarh and completed his M.Sc. (Chemistry) from Bilaspur University with a 6th rank in the university merit list in 2015. He completed a teaching training-based course, B.Ed., from Pundit Ravishankar Shukla University, Raipur, in 2017. He qualified for the CUCET-RP examination in 2017 and joined the Central University of Tamil Nadu (CUTN) as an M.Phil. research scholar under Prof. M. Siva Prasad, the Department of Chemistry. He worked on asymmetric synthesis during his M.Phil tenure, and after completing that, he joined Prof. Manab Chakravarty's research group as an SRF (Senior Research Fellow) of a CSIR-granted project in January 2019. His Ph.D. work focussed on the synthesis and applications of organic solid-state emitters. He developed rare crystallochromic organic compounds, solid-state acidofluorochromic probes, and their utilization in acid vapor sensing, ammonia sensing, and melamine detection in liquid milk. He contributed to developing an anticancer active bioimaging agent that is the drug and the biomarker to detect dead cancer cells by virtue of its abated fluorescence. He also established an organic fluorophore that displayed the highest-ever blueshifted Aggregation-Induced Emission (AIE) and the highest-ever blueshifted Viscosity-Induced Emission (VIE). He developed organic fluorophore for wash-free cancer cell bioimaging, forensic detection of blood-smeared fingerprints, detection of food additives, hidden stimuli-responsive QR code and stamp-based anticounterfeiting material, detection of hospital disposed-of biohazards, inkless reversible writing platform. His special attention was on developing bioimaging probes, and he was successful in developing nucleus-specific, lipid-droplet-specific, and mitochondria-targeting bioimaging probes. Currently, he is investigating with his collaborators for organic fluorescent probe-based cancer cell detection in an in vivo model. His future aim is to join a research lab where he will be developing organic fluorescent probes to be directly implemented for cancer diagnostics in clinics. In his Ph.D., he published 6 papers, and a few more are yet to be published. He filed two Indian patents. He attended six national and international conferences/symposiums/workshops. He won the best poster award in Goa at an International Conference and the ACS-India Best Research Pitch award in 2022. His article was recommended in the Horiba Academic Newsletter in 2022 (Issue 2) in the section of 'sensors'. He was awarded a travel grant by CSIR and SERB to attend the 'Tetrahedron-2022' symposium in Lisbon, Portugal. He was the finalist of 'BIG-Grant Call-2023' (Biotechnology Ignition Grant). A few days ago, his work on cancer cell inhibition and detection was published in 'Know-Today' news (link: https://know-todays-news.com/valuate-anticancer-properties/). He was selected as an Affiliate Member of the Royal Society of Chemistry (RSC) in 2022, and further recognized as an Associate Member of RSC in 2023.

Biography of Professor Manab Chakravarty

Prof. Manab Chakravarty was born in Hooghly, West Bengal. He completed his M.Sc. from Visva-Bharati University, Shantiniketan, specializing in inorganic chemistry. He qualified CSIR JRF and registered for a Ph.D. degree in organophosphate chemistry from the School of Chemistry, the University of Hyderabad, under the supervision of Prof. K. C. Kumara Swamy. After completing his Ph.D. in 2007, he joined Chembiotek Pvt. Ltd. as a research associate for a few months. Then he moved to the Department of Chemistry, the University of New Mexico, Albuquerque, New Mexico, USA, for his postdoctoral studies with Prof. Robert T. Paine on synthesizing phosphorous-based compounds that act as ligands for radioactive elements. Prof. Manab Chakravarty joined BITS Pilani, Hyderabad Campus in 2010 as an assistant professor and was promoted to full professor in 2022. He served as the Head of the Department from October 2026 to 2022. He has 26 years of research experience and 14 years of teaching experience. He has interests in the metal-free synthesis of extended π-conjugates as solid-state emitters, tuning of photophysical properties in the solid state, generation of relatively smaller AIEgens (Aggregation-Induced Emission), and their wide applications, solid/solution/vapor states sensing of explosives, metals etc, smart and portable devices for the detection of Bas (Biogenic Amines) in real-life applications, bioimaging, and solid-state multicolored fluorescence switching and anticounterfeiting. He was the principal investigator for six completed projects funded by SERB, CSIR, and DST-FT. He is the PI of two ongoing projects funded by SERB, LSRB, and DRDO. He has given Ph.D. degrees to three students and supervised one postdoctoral candidate selected through the 'Women Scientist-DST, India.' Scheme. He has six active Ph.D. students in his laboratory and is also part of the DST-PURSE project of BITS-Pilani. He has published almost 100 research articles and filed for 5 Indian patents. He chaired many national and international conferences, symposiums, and workshops. His published article on low-cost, sensitive devices for ultralow detection of TNT was displayed in 'India Science Wire' on July 04, 2022, in New Delhi. His other article on mechanofluorochromic cocrystals was selected as a 'Potential News Item' in 'Chemistry Views' Magazine in 2021. Even in 2019, his article on anticounterfeiting applications was displayed in 'India Science Wire.' He has searched for the electron-rich microporous polymer as a single-component white light emitting device. He has already been successful in developing a device very recently. Again, he supervises a collaborative project aiming to detect cancer cells over normal cells with an organic fluorescent probe with motion-restricted emission enhancement.
